Stability of magnetic remanence in multidomain magnetite

by

Adrian Richard Muxworthy



Thesis submitted for the Degree of Doctor of Philosophy, University of Oxford.

Worcester College &
Department of Earth Sciences

Hilary Term 1998

Stability of magnetic remanence in multidomain magnetite

Adrian Richard Muxworthy
Worcester College and Department of Earth Sciences, University of Oxford.
Hilary Term 1998

Abstract

If a rock is to retain a geologically meaningful magnetic record of its history, it is essential that it contains magnetic minerals which are capable of carrying stable magnetic remanence. Of the natural occurring magnetic minerals, magnetite is the most important because of its abundance and strong magnetic signature. The stability, *i.e.,* the resistance to demagnetisation or re-orientation, of magnetic remanence is related to grain size; in smaller grains the magnetic moments align to have single domain (SD) structures, in larger grains complex magnetic patterns are formed (multidomain (MD)). "Classical" domain theory predicts that SD remanence is stable, whilst MD remanence is not. However experimental evidence has shown that both SD and MD grains can have stable remanences.

In this thesis the origin of stable MD remanence is examined. There are two opposing theories; one suggests that the stability is due to independent SD-like structures, the other postulates that the stability is due to metastable MD structure. A series of experiments were designed to examine the stability using a selection of characterised synthetic and natural samples. Low-stress hydrothermal recrystallised samples where grown for this study.

For the first time, the stability of thermoremanence induced in hydrothermal crystals to cooling was examined. The results agree with previous observations for crushed and natural magnetites, and support kinematic models.

The behaviour of SIRM and thermoremanences in MD magnetite to low-temperature cooling to below the crystallographic Verwey transition at 120-124 K (T_v) and the cubic magnetocrystalline anisotropy isotropic point (T_k) at 130 K was investigated. On cooling through T_v, SIRM was observed to decrease and demagnetise, however thermoremanence was found to display a large increase in the magnetisation at T_v, which was partially reversible on warming. The size of the anomaly is shown to be dependent on the temperature at which the thermoremanence is acquired, internal stress and grain size. The anomaly is attributed to the large increase in the magnetocrystalline anisotropy which occurs on cooling through T_v. It is postulated that low-temperature cycling demagnetisation is due to kinematic processes which occur on cooling between room temperature and T_k. Characterisation of low-temperature treated remanence and partially alternating field demagnetised remanence, suggest that the stable remanence is multidomain.

Low-temperature cooling of remanence in single sub-micron crystals was simulated using micromagnetic models. The models predict the observed anomaly for thermoremanence on cooling through T_v, and also the relative behaviour of SIRM and thermoremanence. The single domain threshold was calculated for the low-temperature phase of magnetite, and was found to be 0.14 μm, compared to 0.07 μm at room temperature.

Stability of magnetic remanence in multidomain magnetite

Adrian Richard Muxworthy
Worcester College and Department of Earth Sciences, University of Oxford.
Hilary Term 1998

Extended Abstract

For a rock to keep a geologically meaningful record of its magnetic history, it is essential that it contains carriers of stable magnetic remanence. Magnetic remanence is carried by ferromagnetic minerals; usually oxides of iron with titanium impurities. The most important magnetic mineral being magnetite because of its strong magnetic signature and abundance.

The stability of magnetic remanence is highly dependent on grain size. In smaller grains the atomic magnetic moments align in one direction and the magnetic structure is said to be single domain (SD). In larger grains the total magnetic flux leakage is reduced by the magnetisation breaking up into complex patterns (multidomain (MD)). "Classical" domain theory (Néel, 1949; 1955) predicts that remanence induced in SD grains is stable, whilst in MD grains it is not. However experimental evidence has demonstrated that both SD and MD grains can have stable remanences. The origin of MD remanence is at present uncertain. There are two opposing theories which attempt to explain it. The first theory postulates that the stability is due to stress-controlled SD-like areas in the grain which act independently (Verhoogen, 1959). There is substantial experimental evidence to support this idea (Dunlop & Argyle, 1991; Heider *et al.*, 1992; Argyle *et al.*, 1994; Dunlop &Özdemir, 1997). The second hypothesis suggests that the stability is a truly MD phenomenon, *i.e.*, the stability is due to *metastable* MD structures (Shcherbakov *et al.*, 1993; McClelland & Shcherbakov, 1995; McClelland *et al.*, 1996).

This study examines the origin of stable remanence in MD magnetite. A series of experiments were designed to examine the stability using a selection of characterised synthetic and natural samples. Because the first hypothesis postulates that stability is due to internal stress and the second theory does not, a selection of hydrothermal recrystallised samples were made following the method developed by Heider & Bryndzia (1987). Previous studies (*e.g.*, Heider, 1988; Heider *et al.*, 1988a) have demonstrated that hydrothermal crystals have *very* low residual stress compared to samples prepared by either crushing or the glass-ceramic method (Worm & Markert, 1987).

The stability of remanence is dependent on the method of acquisition. In rock magnetism there are two main remanence types of interest; thermoremanence and saturation isothermal remanence (SIRM). Thermoremanence is common in nature and is acquired by cooling from the Curie temperature, T_c, in small fields (earth's field $\approx 50\ \mu$T). SIRM is induced by applying large saturating fields at a given temperature. Generally SIRM is larger than thermoremanence, but relatively less stable. Understanding the stability of

thermoremanence is fundamental to palaeomagnetism. "Classical" thermoremanence theories (*e.g.,* Néel, 1955; Dunlop & Xu, 1994) are based on the hypothesis that a domain structure is "blocked" at a certain temperature during cooling, and on the removal of the inducing field the remanence varies as the spontaneous magnetisation. However it has been found (McClelland & Sugiura, 1987; Sholpo *et al.*, 1991) that the remanence does not vary as the spontaneous magnetisation, and instead domain reorganisation processes occur during cooling below the the acquisition temperature. This suggests that the domain structure is temperature dependent, and kinematic thermoremanence theories have been developed to explain this phenomenon (McClelland & Sugiura, 1987; Shcherbakov *et al.*, 1993). Previous experimental evidence of this phenomenon is sparse. These studies have only examined crushed or natural magnetites, which have either high-stress or impurities respectively. In this study similar experiments are reported for characterised hydrothermal crystals. The results from the hydrothermal crystals agree with previous observations for crushed and natural magnetites, and confirm the kinematic model.

The stability of MD magnetite is usually defined as being the fraction of remanence which remains after partial demagnetisation. One type of stability-test is low-temperature demagnetisation (LTD). It has been found (Yama-ai *et al.*, 1963; Ozima *et al.*, 1964a; Ozima *et al.*, 1964b), that MD remanence is partially demagnetised on cooling through the Verwey transition at 120-124 K (T_v) (Verwey, 1939), and the cubic magnetocrystalline anisotropy isotropic point (T_k) at 130 K (Bickford Jr., 1949). The remaining remanence after LTD is magnetically hard, and is often associated with the stability. However, due to the close proximity of T_v and T_k, and uncertainties in the physics of the Verwey transition, the controlling mechanism of demagnetisation during low-temperature cycling is unresolved. Because of these uncertainties low-temperature behaviour of the controlling magnetic energies are considered in this thesis. In particular the different models of the Verwey transition are extensively reviewed, and some of their hypothesis tested. Of the various models, the magneto-electronic model (Belov, 1993) is the only one to incorporate the anomaly in the spontaneous magnetisation at T_v. Because of this the magneto-electronic model is prefered in the remainder of this study. King (1996) argued that T_v and T_k are in fact the same transition, however after consideration of both my own and previous experimental data it is concluded in this thesis that T_v and T_k are separate transitions.

It was initially postulated in this study, that the low-temperature behaviour of remanence in the vicinity of T_v, might yield information about the origin of stability. Consequently, the low-temperature behaviour of various remanences during low-temperature cycling was measured. Previous studies have concentrated on the low-temperature behaviour of SIRM, however in this study the low-temperature behaviour of thermoremanence was also considered. This is the first extensive examination of the low-temperature behaviour of MD thermoremanence to be reported. On cooling through the transition SIRM remanence was observed to decrease and demagnetise, in agreement with the literature. However thermoremanence was found to display large positive anomalies in the magnetisation on cooling through T_v, *i.e.,* the remanences *increased* on cooling through T_v. On

warming to room temperature, the anomalies were found to be partially reversible. The experiments show that the size of the anomaly is dependent on the temperature at which the thermoremanence is acquired, internal stress and grain size, *e.g.,* the largest anomalies are for thermoremanences acquired at high temperatures in stressed magnetite crystals of only a few microns in diameter. Note, the anomaly is *not* due to stress, it is only enhanced by it. The anomaly is attributed to the large increase in the magnetocrystalline anisotropy which occurs on cooling through T_v. Previous studies have suggested that remanence demagnetises at either T_k or T_v during LTD (*e.g.,* Kobayashi & Fuller, 1968; Shcherbakova *et al.*, 1996; Dunlop & Özdemir, 1997), however in this study it is noted that remanences are largely reversible to cooling and warming through T_v, and that most of the demagnetisation occurs on cooling between room temperature and T_k. It is suggested in this study that the physical process which controls LTD is the kinematic process (McClelland & Sugiura, 1987; Shcherbakov *et al.*, 1993), *i.e.,* the same kinematic processes which occur on cooling remanence above room temperature continue to operate on cooling below room temperature. The rate of demagnetisation increases on approach to T_k, suggesting that the kinematic processes are partially controlled by the magnetocrystalline anisotropy. Characterisation of LTD treated remanence and partially alternating field demagnetised remanence, suggest that stable remanence is multidomain.

Low-temperature cooling of remanence in single sub-micron crystals was simulated using FFT micromagnetic numerical models developed by Wright *et al.* (1997). The models for single crystals predict the observed anomaly for thermoremanence on cooling through T_v. The model also predicts the relative behaviour of SIRM and thermoremanence, *i.e.,* the size of the anomaly is greater for thermoremanence than for SIRM structures. It is found from the model that SIRM domain structures are destroyed on cooling through T_v, whereas thermoremanence domain structures are partially reversible to cooling and warming through the Verwey transition.

The single domain threshold was calculated for the low-temperature phase of magnetite. It was found to be 0.14 μm, compared to 0.07 μm at room temperature (Williams & Wright, 1998). This difference is due to the large increase in the magnetocrystalline anisotropy on cooling through T_v. However the high resistance to changes in the domain structure in the low-temperature phase, means that it unlikely that grains already in vortex states will denucleate domain walls to become SD.

In summary this thesis has found that the origin of metastability is due to MD-like structures in agreement with McClelland & Shcherbakov (1995) and McClelland *et al.* (1996), rather than SD-like regions as suggested by Argyle *et al.* (1994). The metastable structures are associated with thermoremanence acquired at high-temperature near T_c. On cooling through the Verwey transition stable domain structures give rise to large reversible anomalies in the magnetisation which has not been documented previously. The positive anomalies and the stability of MD structures is supported by micromagnetic models. It is recommended that the relationship between domain structure and microstructure should be investigated in future studies.

Acknowledgements

Initially I thank my supervisors Buffy McClelland and Wyn Williams, for their advice and guidance through this thesis. I thank Buffy for reading the different versions of this thesis thoroughly and fast.

I would like to thank Steve Elphick for his help with the growth of the hydrothermal magnetite crystals in the high pressure labs at the Dept. of Geology and Geophysics, University of Edinburgh. Roy Thompson and Roy Gill informed me of the existence of the natural Shetland magnetites. I am grateful to Monica Price for helping with the infrared spectroscopy and for providing me with natural samples of hematite and goethite. Dr. W. O'Reilly donated a pure maghemite sample.

Thanks to the Institute for Rock Magnetism, University of Minnesota, for allowing me to become the first person to have visiting fellowships in two consecutive time slots. Peat Solheid undertook all the Mössbauer experimentation, and showed me how to interpret the Mössbauer results. Thanks to Mike Jackson and Jim Marvin for their help and infinite patience.

I am grateful to Dr K. O'Grady for permitting the use of his AGFM at the University of Wales in Bangor. Thanks also to John Cambridge for his assistance with the AGFM. Thanks to Andrew Harrison and Gavin Whittaker for their help during two visits to the Dept. of Chemistry, University of Edinburgh, to use their MPMS. I also thank Peter Battle (Dept. of Inorganic Chemistry) for allowing me to use the MPMS which they installed towards the end of my D.Phil.

I thank Franz Heider and James King for lending me copies of their theses. I acknowledge the use of Tom Wright's FFT micromagnetic code which allowed me to calculate the low-temperature domain structure of magnetite. I also acknowledge Rick Thomas for the results from the Thellier-Thellier experiment with liquid nitrogen step, which he measured in the summer before I started this thesis.

Colin Fagg deserves special thanks for his help and interpretation of XRD results and technical assistance with the SEM. Thanks to Will Reeve who analysed a few samples using a relatively new XRD in the Clarendon Laboratory, which allowed me to check the calibration of the rather old XRD in the Dept. of Earth Sciences. The glass blowers Steve Giles and Martin Miles excelled themselves when they vacuum sealed some of my samples. Thanks to Steve Wyatt for help in the geochemistry lab and his dry wit. Thanks also to Amanda Petford-Long and Mike Jenkins (Dept. of Material Science) for their help with my attempt to use TEM to examine dislocations at low-temperatures. Unfortunately I started this project a little late in this thesis, and did not have time to complete it. I would like to thank Brian Daniels for keeping the palaeomagnetic laboratory in working order.

I have benefited from discussions with several other people; Subir Banerjee, Bruce Moskowitz, Mitra Sahu, Andrew Newell, David Clark, Prof. Ekhard Salje, Richard Harrison, James King, David Virdee, Michael Urbat, Adry van Velzen and Conall MacNiocaill. I

would say that I benefited from numerous discussions with Yvo Kok but that would be a lie.

I would also like to thank to a few of the friends I have met whilst in Oxford; Rick, Charles, Captain Dave Kirk, Chuck, Rab, Jon, Dave, Suman, Kate, Liz, Leon, my officemate BJ Benny Ben Stephenson and Mark & Lard for their nonsensical attitude to the afternoon.

I would like to thank my parents and sister, and finally Emma for her patience and understanding.

Contents

Abstract i

Extended Abstract ii

Acknowledgements v

Contents vii

1 Introduction 1

1.1 Brief introduction to the thesis . . . 1
1.2 Historical review of palaeomagnetism and rock magnetism . . . 2
1.3 Physical principles of magnetism . . . 3
1.3.1 Diamagnetism . . . 4
1.3.2 The permanent magnetic moment . . . 4
1.3.3 Paramagnetism . . . 7
1.3.4 Spontaneous magnetisation . . . 8
1.4 Controlling magnetic energies . . . 10
1.4.1 Exchange energy . . . 11
1.4.2 Magnetostatic energy . . . 11
1.4.3 Anisotropy energy . . . 12
1.5 Domain theory . . . 16
1.5.1 Classical domain theory . . . 16
1.5.2 Micromagnetic models . . . 18
1.6 Remanence acquisition . . . 19
1.6.1 Isothermal remanent magnetisation . . . 21
1.6.2 Thermoremanent magnetisation . . . 21
1.6.3 Anhysteretic remanence . . . 21
1.6.4 Other remanences of interest to the rock magnetist . . . 22
1.7 Magnetic minerals . . . 23
1.7.1 Magnetite . . . 23
1.7.2 Maghemite . . . 25
1.7.3 Hematite . . . 27

1.7.4 Titanomagnetites and titanomaghemites 27
1.7.5 Other magnetic minerals 27
1.8 Standard rock magnetic laboratory techniques 28
1.8.1 Spectroscopic analysis 28
1.8.2 Demagnetisation of remanence 29
1.8.3 Palaeomagnetic equipment in Oxford 30
1.9 Thesis objectives and layout 33

2 Preparation of magnetite samples for experimental study 35
2.1 Introduction 35
2.2 Dankers samples 36
2.3 Hydrothermal recrystallisation 37
2.3.1 Hydrothermal recrystallisation method 37
2.4 Shetland magnetite 40
2.4.1 Collection of Shetland magnetites 40
2.4.2 Application of citrate-bicarbonate-dithionite treatment 40
2.4.3 Chemical analysis 42
2.5 Other samples 43
2.6 Vacuum sealed capsules 44

3 Magnetic characterisation of samples 46
3.1 Introduction 46
3.2 Hysteresis parameters and their relation to domain state and internal stress 46
3.3 Measurement of hysteresis loops 47
3.4 Hysteresis parameters as a function of grain size 48
3.4.1 Comparison of measured and published hysteresis parameters for Dankers material 48
3.4.2 Comparison of all measured hysteresis parameters with the literature 50

4 Behaviour of partial thermoremanences on cooling below the acquisition temperature 54
4.1 Introduction 54
4.1.1 Observational Data 55
4.1.2 Theoretical Approaches 58
4.2 Measurement of pTRM decrease below T_2 62
4.2.1 Notes on experimental technique 62
4.2.2 Field dependence of pTRM decay on cooling below T_2 64
4.2.3 Note on Viscous decay 67
4.2.4 Test on irreversibility of thermoremanence 67
4.2.5 Effect of grain size and pTRM type 67
4.3 Discussion 72

5 Low-temperature magnetic properties of magnetite **74**
5.1 Introduction . . . 74
5.2 Introduction to the Verwey transition . . . 75
5.2.1 Mössbauer spectroscopy study of pure magnetite at T_v . . . 77
5.3 Brief review of the various Verwey transition theories . . . 80
5.3.1 Structural-electronic model of the Verwey transition . . . 80
5.3.2 Magneto-electronic model of the Verwey transition . . . 81
5.3.3 Differences in the spontaneous and saturation magnetisation at T_v . . . 83
5.3.4 Comparison of the structural- and magneto-electronic models . . . 89
5.4 Behaviour of magnetic energies at low-temperatures . . . 90
5.4.1 Exchange Energy . . . 90
5.4.2 Magnetocrystalline Anisotropy Energy . . . 90
5.4.3 Magnetostrictive anisotropy constants and elastic moduli at T_v . . . 95
5.5 Variable stoichiometry at low-temperatures . . . 96
5.5.1 Effect of variable stoichiometry on the Verwey transition . . . 96
5.5.2 Effect of variable stoichiometry on the magnetic anisotropy below room temperature . . . 97
5.6 Importance of stress on the Verwey transition . . . 98
5.6.1 External stress at the Verwey transition . . . 98
5.6.2 Internal residual stress at the Verwey transition . . . 99
5.7 Measurement of susceptibility and hysteresis loops at low-temperatures . . . 99
5.7.1 Susceptibility at low-temperatures . . . 100
5.7.2 Low-temperature behaviour of the hysteresis parameters . . . 103
5.8 Summary . . . 109

6 Behaviour of magnetic remanences at low-temperature **110**
6.1 Introduction . . . 110
6.2 Previous investigations of low-temperature cycling of remanent magnetisations . . . 111
6.3 Definition of magnetic memory . . . 112
6.4 Notes on the technical capabilities of the MPMS . . . 113
6.4.1 Run-time problems with the MPMS . . . 114
6.4.2 Problem with back-field on inducing SIRM . . . 115
6.4.3 Residual field in the MPMS sample chamber . . . 115
6.5 Low-temperature cooling of SIRM . . . 119
6.5.1 Results of low-temperature cooling of SIRM . . . 119
6.5.2 Effect of small applied field on "zero-field" cooling . . . 123
6.5.3 Importance of T_v and T_k during low-temperature demagnetisation of SIRM . . . 125
6.5.4 Effect of internal residual stress on magnetic memory . . . 129
6.5.5 Oxidation as a source of internal stress . . . 130

6.5.6 Note on the effect of particle interaction on the Verwey transition . . 130
6.6 Low-temperature cooling of thermoremanences 131
6.6.1 Results of low-temperature cooling of weak-field thermoremanences 133
6.6.2 Low-temperature behaviour of high-field partial thermoremanences 139
6.7 Possible explanation for the difference between SIRM and thermoremanence low-temperature behaviour 142

7 Origin of metastability of multidomain magnetite 147
7.1 Introduction 147
7.2 Note on terminology 149
7.3 Relative behaviour of various magnetic remanences and their memories . . 150
7.3.1 Measurement of TRM memory and ARM memory acquisition curves 150
7.3.2 Magnetic memory of various initial remanences 157
7.3.3 AF demagnetisation of initial remanence and its magnetic memory . 164
7.3.4 Thermal demagnetisation of initial remanence and its magnetic memory 176
7.3.5 Step-wise thermal demagnetisation of low-field pTRM memory . . . 178
7.3.6 Summary of previous three sections 181
7.4 Characterisation of PDT_{C-AFD} and comparison with magnetic memory . . . 182
7.4.1 Calculation of calibrated AF demagnetisation step 182
7.4.2 Stability of remanence to repeated LTD or C-AFD treatment 183
7.4.3 Step-wise thermal demagnetisation of pTRM memory 186
7.4.4 Dependence of thermoremanence memory on thermal history 187
7.5 Further examination of PDT_{C-AFD} and memory 189
7.5.1 Progressive remagnetisation of TRM and TRM PDT 190
7.5.2 Thellier-Thellier type experiments 194

8 Micromagnetic models of pseudo-single domain grains near the Verwey Transition 197
8.1 Introduction 197
8.2 Micromagnetic Models 198
8.2.1 The Discrete Micromagnetic Model 199
8.3 Domain structure in the monoclinic phase of magnetite near the SD/MD transition 205
8.3.1 Test for the critical SD size 205
8.3.2 Orientation of magnetic moments in vortex structures in the monoclinic phase 213
8.4 Simulated low-temperature cycling of remanences 213
8.4.1 Solutions for $SIRM_x$ and $SIRM_z$ 215
8.4.2 Behaviour of thermoremanences 227
8.5 Comparison with experimental results 236
8.5.1 Remanent magnetisation versus temperature 236

8.5.2 Magnetic memory 238
8.6 Conclusions 239

9 Conclusions **242**

Bibliography **247**

Appendices

A Identification of magnetic minerals by infrared spectroscopy **264**
A.1 Introduction 264
A.2 Method 264
A.3 Common magnetic minerals 265
A.4 Detection of maghemite in the presence of magnetite 266
A.5 Conclusions 267

B Bitter pattern imaging at high temperatures **268**
B.1 Introduction 268
B.2 Calculation of domain wall visibility as a function of temperature 268

Chapter 1

Introduction

1.1 Brief introduction to the thesis

If a rock has stable magnetic remanence, then it is possible for it to retain a magnetic record of its geological history. Magnetic remanence is carried by magnetic minerals, the most important being magnetite because of it is abundant and has a strong magnetic signature.

The size of a magnetic crystal is crucial to its magnetic behaviour. Smaller grains behave like magnetic dipoles (single domain grains (SD)), whereas in larger grains the magnetisation breaks up into complex patterns (multidomain grains (MD)). According to the early remanence theories of Néel (1949; 1955) SD grains should carry stable remanence, whilst larger MD grains should not. However, experimental evidence has shown that both SD and MD grains can have stable remanences. The cause of MD stability is still unresolved. Verhoogen (1959) postulated that the stability is due to stress-controlled SD-like areas in the grain which act independently. Dunlop and co-workers have given evidence to support this theory (Dunlop & Argyle, 1991; Heider *et al.*, 1992; Argyle *et al.*, 1994; Dunlop & Özdemir, 1997). On the other hand, several studies have suggested that the stability is a truly MD phenomena (Sholpo *et al.*, 1991; Shcherbakov *et al.*, 1993; McClelland & Shcherbakov, 1995; McClelland *et al.*, 1996).

In this thesis, the stability of MD magnetite remanence and its origin is examined. In particular, the stability of remanence to low-temperature cooling of MD remanence through the Verwey crystallographic transition at $\approx$ 120-124 K (Verwey, 1939; Verwey & Haayman, 1941) is considered. Low-temperature cycling partially demagnetises MD remanence (Ozima *et al.*, 1964b; Kobayashi & Fuller, 1968), leaving a fraction (memory) which is relatively stable to other methods of demagnetisation. The memory is often associated with the stability of MD remanence.

In palaeomagnetic studies, low-temperature treatment is occasionally applied to remove unstable components of MD remanence (*e.g.*, McClelland & Briden, 1995), however the physics of the demagnetisation processes during low-temperature cycling has never

been truly understood. There are several reasons for this; firstly palaeomagnetists are primarily interested in the magnetic behaviour of minerals above room temperature, and consequently do not usually have specialised low-temperature equipment. Secondly, a large percentage of the low-temperature investigations were undertaken in the 1960's (*e.g.*, Yama-ai *et al.*, 1963; Nagata *et al.*, 1964; Ozima *et al.*, 1964a; Ozima *et al.*, 1964b; Creer & Like, 1967; Kobayashi & Fuller, 1968), before the introduction of SQUID based magnetometers to rock magnetism allowed examination of very weak remanences like magnetic memory. Because magnetic memory of MD remanence tends to be weak, most of the early low-temperature measurements only examined saturation isothermal remanences (remanences induced by applying a large field at a given temperature (SIRM)) which have large unstable, intensities relative to thermoremanence. The SIRMs were seen to demagnetise during low-temperature cooling. In nature SIRMs are uncommon. A more common natural remanence is thermoremanent magnetisation, which is acquired by cooling in a small field from the Curie temperature. Thermoremanence is magnetically more stable than SIRM, and display a greater resistance to demagnetisation during low-temperature cycling (Heider *et al.*, 1992; McClelland & Shcherbakov, 1995). It might be expected that its behaviour during low-temperature cycling yields information about the origin of its stability. To my knowledge, however, the direct measurement of thermoremanence during low-temperature cycling has never been extensively studied. I decided to investigate the behaviour of various remanences including thermoremanence, during low-temperature cycling, in the hope that it would yield information about the origin of stability in general.

Other features of MD stability are also examined, including the characterisation of memory and the stability of thermoremanence to cooling after acquisition.

To investigate this problem a largely experimental approach was undertaken. Some numerical models were also considered. Because of the importance of stress on the stability of magnetite, low-stress, synthetic hydrothermal recrystallised samples were made to examine this problem. To compliment the study of hydrothermal crystals, annealed crushed magnetites and natural magnetites are also considered.

In the earlier sections of this chapter, a brief introduction to rock magnetism is given (Sections 1.2–1.7). In Section 1.9 the thesis objectives and layout are detailed.

1.2 Historical review of palaeomagnetism and rock magnetism

The magnetic properties of lodestone have been known to the Chinese since about 2,500 BC. The "father" of Greek philosophy, Thales of Miletus (early 6th. century BC) refered to the ability of a magnet to move iron in his discussion of the soul (Honderich, 1995). The first compasses were invented by the Chinese in the 2nd. century BC, comprising of a lodestone spoon rotating on a smooth board (Smith & Needham, 1967). Compasses did not arrive in Europe until the 12th. century AD. Petrus Peregrinus reported a series of experiments conducted on spherical lodestone in his *Epistola de Magnete* in 1269 (Smith,

1968). He discovered the dipole nature of magnets, and became the first to formulate the law that like poles repel and unlike poles attract. It was William Gilbert in 1600, who first realised the similarities between the field lines around a lodestone and those around the earth (Smith, 1968). He concluded in his *De Magnete* that the earth is effectively a giant magnet.

The observation that some rocks are magnetised parallel to the direction of the Earth's magnetic field was made by the Italian Melloni in 1853 (Nagata, 1961). David (1904) and Brunhes (1906) found evidence for geomagnetic reversals from studies on material baked lavas.

The birth of rock magnetism did not occur until Koenigsberger (1938) and Thellier (1938) brought earth magnetism into the laboratory. Using ferromagnetic domain theories developed in the first half of this century (*e.g.*, Landau & Lifshitz, 1935), they attempted to reproduce and understand the processes by which rocks are magnetised in nature.

During the 1940's and 50's, there were great advances in both ferromagnetic domain theory and rock magnetism. The final developments of "classical" domain theory were made by Kittel (1949a), Rhodes & Rowlands (1954) and Amar (1958). These advances were then applied to problems in rock magnetism, *e.g.*, acquisition mechanisms of thermoremanent magnetisation (TRM), and the behaviour of small grains (*e.g.*, Néel, 1949; Roquet, 1954; Néel, 1955; Blackett, 1956; Stacey, 1958). The theories and results from the 1940's and 50's form the basis of what is now rock magnetism. However there are still many discrepancies between theory and experiment, hence the present study.

Rock magnetic studies have tended to concentrate on the magnetic properties of magnetite (lodestone), because it is often the dominant carrier of remanence in rocks.

1.3 Physical principles of magnetism

Oersted (1820) found that an electrical current flowing around a coil produces a magnetic field. In the same year, Ampère postulated that all magnetism was due to small circulating currents associated with each atom (Jiles, 1991). Ampère's theory can now be thought of as a simple approximation to the modern physics interpretation of a magnetic moment ($\mathbf{m}$), the circulating currents being electrons (e^-) in closed orbits around atomic nuclei (Figure 1.1).

The vector sum of the magnetic moments from many atoms gives rise to the net macroscopic magnetisation ($\mathbf{M}$) of a material. Materials can be broadly divided into two classes with regard to their magnetic properties: those that contain atoms or ions with permanent magnetic moments and those that do not (diamagnetic). The group containing permanent magnetic moments can be subdivided into materials that have magnetic long-range order below a critical temperature and those that do not (paramagnetic). The

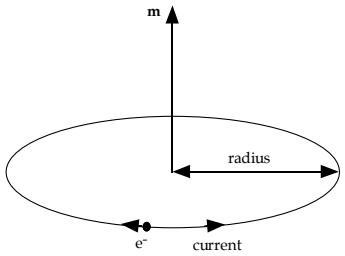


Figure 1.1: An electron in a circular orbit is equivalent to a current loop and hence to a magnetic moment. Note negatively charged electrons move in the opposite direction to the current.

magnetic ordering can be further classified depending on the particular orientations of the alignments that the moments exhibit (Figure 1.2).

With reference to the magnetic susceptibility $\boldsymbol{\chi}$, the magnetic behaviour of materials can be expressed by (Jiles, 1991),

$$\mathbf{M} = \mathbf{M}_0 + \boldsymbol{\chi} \cdot \mathbf{H} \tag{1.1}$$

where $\mathbf{H}$ is the applied field and $\mathbf{M}_0$ is the net magnetisation in the absence of a magnetic field, *i.e.,* the permanent magnetic moment. The susceptibility $\boldsymbol{\chi}$ is represented by a 3×3 matrix, however for isotropic materials the susceptibility can be treated as a scalar, *i.e.,* χ.

1.3.1 Diamagnetism

A magnetic field applied to any material will induce a magnetisation in the material directly opposed to the magnetic field. This phenomenon is called diamagnetism. The diamagnetic response can be considered in terms of Lenz's law; changes in the magnetic flux through the current loop, *i.e.,* the electron's orbit about the nucleus (Figure 1.1), gives rise to an electro-motive force in the current loop. This either accelerates or decelerates the electron's angular velocity depending on the relative orientation of the field with th current loop orientations, in such a way as to generate an internal magnetic field in opposition to the external magnetic field. The diamagnetic contribution to the total susceptibility is negative. However in materials containing permanent magnetic moments the diamagnetic contribution is usually insignificant. Typical diamagnetic materials are quartz (SiO_2) and calcite ($CaCO_3$).

1.3.2 The permanent magnetic moment

The nature of the permanent magnetic dipole moment can be understood by considering the model of an electron orbiting a nucleus with angular momentum $\mathbf{J}$ (Figure 1.1). The direction of $\mathbf{m}$ is parallel and proportional to $\mathbf{J}$, (French & Taylor, 1978),

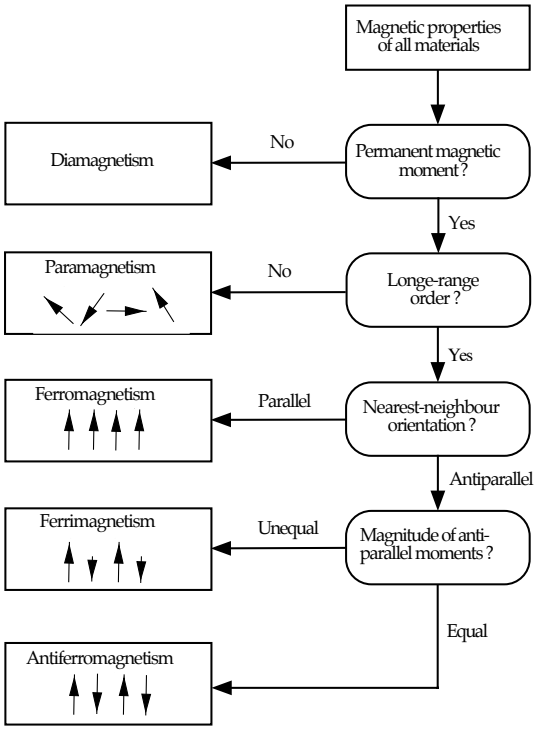


Figure 1.2: Classification of magnetic properties of material. Antiferromagnetism can be viewed as a special case of ferrimagnetism

$$\mathbf{m} = \gamma \mathbf{J} \tag{1.2}$$

where γ is the gyromagnetic ratio. The classical value for γ for an electron of charge $-e$ and mass m, is (Bleaney & Bleaney, 1965)

$$\gamma = \frac{-e}{2m} \tag{1.3}$$

The angular momentum $\mathbf{J}$ of an electron cannot be derived classically, however a simplified quantum mechanical approach can be used.

An electron's angular momentum has two components; orbital and intrinsic spin. The orbital angular momentum ($\mathbf{m}_l$) can be considered to be identical to classical orbital angular momentum, and is given by (Hook & Hall, 1991)

$$\mathbf{m}_l = -\frac{e\hbar}{2m}\mathbf{l} = -\mu_B \mathbf{l} \tag{1.4}$$

where $\hbar = h/2\pi$, h is Planck's constant and μ_B is the Bohr magneton. This quantum mechanical approach is identical in appearance to the classical approach given that the orbital

angular momentum of an electron is $\hbar\mathbf{l}$. Note, however, $\mathbf{l}$ is not an angular momentum vector but an angular momentum operator on an electron's wavefunction.

The intrinsic angular momentum or spin $\mathbf{m}_s$, is a consequence of relativistic classical dynamics (Jackson, 1975), and can be thought of as the angular momentum of the electron in its own rest frame. In effect, it can be treated as an angular momentum though it has no classical analogue. The magnetic momentum, associated with the intrinsic angular momentum, $\hbar\mathbf{s}$, is given by (Hook & Hall, 1991)

$$\mathbf{m}_s = -g_s\mu_B\mathbf{s} \tag{1.5}$$

where $\mathbf{s}$ is the intrinsic spin and g_s is the intrinsic spin Landé factor. g_s takes a value of 2.001, (Bleaney & Bleaney, 1965), which is often approximated to 2.

By the Pauli exclusion principle, (Bleaney & Bleaney, 1965), the contribution from closed electron shells to the total orbital and intrinsic angular momenta is zero (Figure 1.3). Therefore, only atoms with incomplete shells have permanent magnetic moments. Several "groups" have partially filled shells; $3d$ (iron group), $4d$ (palladium group), $4f$ (lanthanide group), $5d$ (platinum group) and $5f$ (actinide group).

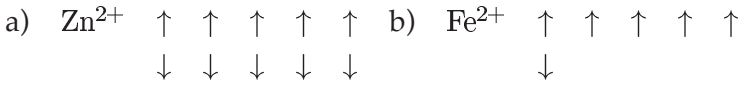


Figure 1.3: Examples of the Pauli exclusion principle for the $3d$ shell which has 10 possible electron states. Occupancy and alignment of electronic magnetic moments in; a) closed shell; the Zn^{2+} ion has 10 electrons in its $3d$ shell, zero net angular moment and no permanent magnetic moment. b) unclosed shell; the Fe^{2+} ion has 6 electrons in its $3d$ shell, the net angular momentum is non-zero and there is a permanent magnetic moment.

The total angular momentum is controlled by mutual quantum mechanical interactions between electrons in open shells. There are two main types of electron interaction; Russel-Saunders coupling and spin-orbit coupling, (Liboff, 1992). For 3d iron transition elements Russel-Saunders coupling is dominant. The spin-orbit interaction is only important in the heaviest atoms.

It is convenient to write the quantum mechanical value for the gyromagnetic ratio γ as

$$\gamma = -\frac{g\mu_B}{\hbar} \tag{1.6}$$

where g is the Landé factor and equals g_s for pure spin and 1 for pure orbital angular momentum. This equation is identical to Equation 1.3 if only orbital angular momentum is considered. g can be theoretically calculated (Rae, 1992),

$$g = 1 + \frac{J(J+1) + S(S+1) - L(L-1)}{2J(J+1)} \tag{1.7}$$

where $L(L+1)$, $S(S+1)$ and $J(J+1)$ are the eigenvalues of the quantum mechanical operators $\mathbf{L}^2$, $\mathbf{S}^2$ and $\mathbf{J}^2$ respectively, which are in turn representative of the square of the total orbital, intrinsic and coupled angular momenta.

However in the 3*d* iron group the open shell is the outer shell, which has a large interaction with the crystalline electric field of neighbouring ions. In a non-central crystalline field the plane of orbit is unstable, *i.e.,* the orbital angular momentum may average to zero, and the resulting moment is entirely due to spin (Kittel, 1975). The orbital angular momentum is said to be quenched or frozen. The intrinsic spin is unaffected by the crystalline electric field, and for a fully quenched orbital angular momentum the magnetic moment is due to "spin only". However in the 3*d* group, Russel-Saunders coupling energy causes the spin to "drag" some orbital momentum with it. Because of these two effects, the measured magnetic moment of iron group ions differs from that predicted for unquenched total angular momentum (Figure 1.4). The other groups, *e.g.,* 4*f* (lanthanide group), are not so strongly effected by the crystalline electric field because their open shells are deep within the atom.

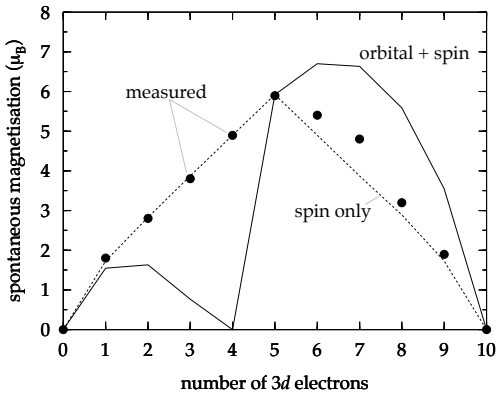


Figure 1.4: Comparison of experimental and theoretical values of the magnetic moments of isolated ions of the 3*d* iron group. Below five 3*d* electrons the measured magnetic moment is identical to that calculated for the spin only, however above five Russel-Saunders coupling "drags" some of the unquenched orbital moment. After Jiles (1991).

1.3.3 Paramagnetism

If the permanent magnetic moments in a material have no long-range order they are said to be paramagnetic (Figure 1.2). In such materials, thermal vibrations are sufficient to overcome any magnetic or quantum mechanical coupling effects and randomise the orientations of the permanent magnetic moments. This randomisation makes the net magnetisation zero.

Application of an external field causes partial alignment of the moments giving rise to a net magnetisation. The strength of the induced magnetisation depends on temperature as well as the applied field intensity. Since the moments tend to align parallel to the applied field, isotropic paramagnets have a positive susceptibility. For small fields the susceptibility is given by (Jiles, 1991)

$$\chi = \frac{C}{T} \tag{1.8}$$

where C is the Curie constant. If a large enough field is applied all the moments align, and the material is said to be saturated. In such a field the measured magnetisation is said to be the saturation magnetisation, M_{sat}. Typical paramagnetic minerals are pyrite (FeS_2) and ilmenite ($FeTiO_3$).

1.3.4 Spontaneous magnetisation

Ferro/ferri/antiferro-magnets are materials where there is an interaction between the permanent magnetic moments which causes them to spontaneously align (Figure 1.2). The resulting magnetisation is termed the spontaneous magnetisation M_s. At some critical temperature, the Curie temperature (T_c), the effect of thermal fluctuations is sufficient to break the long-range order, and the material becomes paramagnetic. There are two types of interaction (Stancil, 1993);

1. magnetic dipole-dipole interactions, arising from the magnetic field due to one dipole acting on another.
2. exchange interactions between the electrons in different ions, identical in nature to the spin interaction between electrons mentioned in Russel-Saunders coupling. The interaction can take negative values.

The latter interaction greatly outweighs the former. For example, the Curie temperature of nickel is 631 K (Bleaney & Bleaney, 1965). This is a rough indication of the temperature at which the interaction between neighbouring nickel ions (separation 2.5 Å) is of the order kT, where k is the Boltzmann constant and T is the absolute temperature. The purely magnetic interaction energy of two atomic dipoles at this distance would be equivalent to kT for $T < 1$ K. For the exchange interaction to be of comparable energy as the magnetic interaction energy, the nickel ions would need to have a separation of ≈ 6 Å.

For two separate atoms the exchange energy, E_{ex}, depends on the relative overlap of the two total spin vectors, $\mathbf{S}_i$ and $\mathbf{S}_j$, and is given by (Stancil, 1993)

$$E_{ex} = -2\mathcal{J}_{ij}\mathbf{S}_i \cdot \mathbf{S}_j \tag{1.9}$$

where $\mathcal{J}_{ij}$ is the exchange integral and has units of energy. If $\mathcal{J}_{ij} > 0$ the energy is minimised by the spins being parallel alignment (ferromagnetism). If $\mathcal{J}_{ij} < 0$ antiparallel alignment is favoured (ferrimagnetism).

Ferromagnetism

At absolute zero, the magnetic moments of a ferromagnet are aligned parallel to each other (Figure 1.5a). On warming to a temperature below T_c, thermal fluctuations cause the magnetic moments to precess around the average direction reducing the spontaneous magnetisation (Figure 1.5b). The degree of precession increases until T_c is reached, where the magnetic moments are randomly orientated (Figure 1.5c).

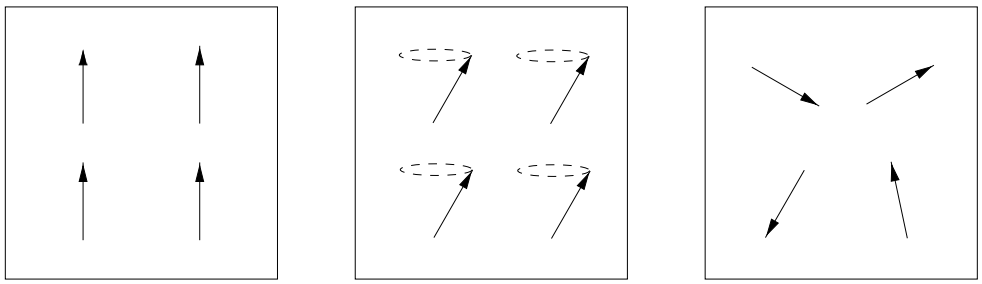


Figure 1.5: Alignment of individual magnetic moments at various temperatures: a) perfect alignment at 0 K, b) magnetic moments precess about the average direction due to thermal activation for 0 K $< T <$ T_c and c) random orientation above T_c.

For ferromagnets it can be shown (Bleaney & Bleaney, 1965), that the spontaneous magnetisation varies as

$$\frac{M_s(T)}{M_s(0)} = f\left(\frac{T}{T_c}\right) \tag{1.10}$$

The susceptibility for $T > T_c$ and low fields is given by the Curie-Weiss law (Stancil, 1993)

$$\chi = \frac{C}{T - T_c} \tag{1.11}$$

Examples of ferromagnetic materials are iron, cobalt and nickel.

Ferrimagnetism

In ferrimagnetic materials the exchange coupling mechanism causes adjacent moments to align antiparallel (Figure 1.2). The long-range order can be considered in terms of two

opposing ferromagnetic sublattices. If the net magnetisations of the two sublattices are unequal then, the material is a said to be a ferrimagnet. Ferrimagnets are not limited to two sublattices; the distinguishing characteristic is that the equilibrium magnetisation of at least one sublattice must oppose that of the others.

If the sublattices have similar thermal behaviour, the ferrimagnets can be simply treated as a ferromagnets with M_s determined by the net magnetisation of the sublattices (Figure 1.6a) . If the two sublattices have different temperature dependencies and magnetic intensities then the net magnetisation may exhibit either a peaked behaviour (Figure 1.6b) or an additional zero or compensation point at $T < \mathrm{T}_c$, where magnetic order still exists (Figure 1.6c). Examples of ferrimagnets are magnetite (Fe_3O_4), strontium ferrite ($SrO \cdot 6(Fe_2O_3)$ and yttrium-iron garnet ($5Fe_2O_3 \cdot 3Y_2O_3$) (Jiles, 1991).

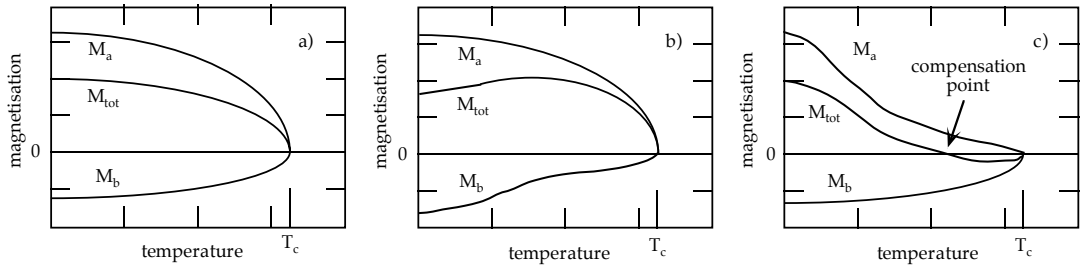


Figure 1.6: Possible forms of the temperature dependence of the net magnetisation M_{net} of a ferrimagnet; a) monotonic b) peaked and c) existence of a compensation point.

Antiferromagnetism

Antiferromagnets are similar to ferrimagnets in that the net magnetisation is a contribution from antiparallel sublattices, however in antiferromagnets the opposing moments are equal giving a net spontaneous magnetisation of zero.

Because the net spontaneous magnetisation is zero, antiferromagnets behave like anisotropic paramagnets. The susceptibility is very small in the parallel/anti-parallel direction of the moments (Figure 1.7a). The parallel susceptibility at finite temperatures is due to thermal agitations preventing the moments from being perfectly aligned. The parallel susceptibility only disappears at 0 K, where perfect alignment occurs. In the direction perpendicular to the moments, the susceptibility is much larger because the moments on both of the sublattices are able rotate towards the applied field (Figure 1.7b).

1.4 Controlling magnetic energies

The magnetic behaviour of a material is governed by the ascendancy of the controlling magnetic energies. The main magnetic energies are; the exchange energy, E_{ex}, the demagnetising energy E_d the anisotropy energy E_{anis}, and the external field energy, E_h.

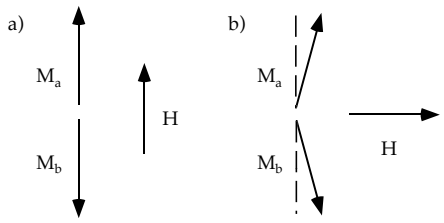


Figure 1.7: Antiferromagnetic susceptibilities: a) except for overcoming thermal deviations from collinear alignment, the parallel field has no effect, and b) application of a perpendicular field can induce comparatively large moments.

The total magnetic energy, E_{tot}, is given by

$$E_{tot} = E_{ex} + E_h + E_d + E_{anis} \tag{1.12}$$

1.4.1 Exchange energy

The exchange energy (Equation 1.9) is minimised by parallel (anti-parallel) alignment of the permanent magnetic moments of each atom for ferromagnets (ferrimagnets). Often in materials one inter-sublattice interaction dominates, *e.g.*, in magnetite the ferrimagnetic $\mathcal{J}_{AB}$ is dominant over ferromagnetic $\mathcal{J}_{AA}$ and $\mathcal{J}_{BB}$. Equation 1.9 can be simplified for such a material to (Jiles, 1991)

$$E_{ex} = -2\mathcal{J}\mathbf{S}_i \cdot \mathbf{S}_j \tag{1.13}$$

1.4.2 Magnetostatic energy

In a ferromagnetic material the exchange energy causes parallel alignment of all the permanent moments. As a result the material behaves like a large magnetic dipole. The magnetostatic energy, E_{stat}, for a magnetic dipole, $\mathbf{m}$, in a magnetic field, $\mathbf{H}$, is given by (O'Reilly, 1984)

$$E_{stat} = -\mu_0 \mathbf{m} \cdot \mathbf{H} \tag{1.14}$$

In rock magnetism it is often desirable to consider fields of external and internal origin separately.

External field energy

The external field energy, E_h, is simply

$$E_h = -\mu_0 \mathbf{m} \cdot \mathbf{H_{ext}} \tag{1.15}$$

where $\mathbf{H_{ext}}$ is the external field.

Demagnetising energy

The demagnetising energy (internal field energy) arises from the interaction of a crystal's magnetisation with itself.

In a magnetised material, the internal field due to $\mathbf{M}$ points in the opposite direction to the magnetic induction $\mathbf{B}$ and is called the demagnetising field, $\mathbf{H_d}$, see Figure 1.8. The magnetic induction field $\mathbf{B}$ is the response of a medium to a field $\mathbf{H}$, and is related to $\mathbf{M}$ and $\mathbf{H}$ by (Jiles, 1991),

$$\mathbf{B} = \mu_0(\mathbf{H} + \mathbf{M}) \tag{1.16}$$

The demagnetising field depends on $\mathbf{M}$ and the geometry of the material, and for a simple dipole moment is given by (Jiles, 1991)

$$\mathbf{H_d} = N_d \mathbf{M} \tag{1.17}$$

where N_d is the demagnetising factor which is calculated form the geometry of the material alone, (Nagata, 1961). For example for a sphere $N_d = 1/3$ and for a cylinder of length/diameter ratio of 20, $N_d = 0.00617$ (Jiles, 1991).

1.4.3 Anisotropy energy

The total anisotropy is the sum of the magnetocrystalline, magnetostrictive and magnetoelastic anisotropies.

Magnetocrystalline energy

As mentioned above, there is sometimes an interaction between the permanent magnetic moment and the anisotropic crystalline field (Section 1.3.2). The magnetocrystalline anisotropy energy E_k, is due to the presence of unquenched orbital angular momentum, *i.e.*, if there is no unquenched orbital momentum then there is no anisotropy. Interaction between the spin and orbital momenta via the exchange interaction causes the energy of the net magnetic moment of the ion to depend on its orientation with respect to certain favoured crystallographic axes.

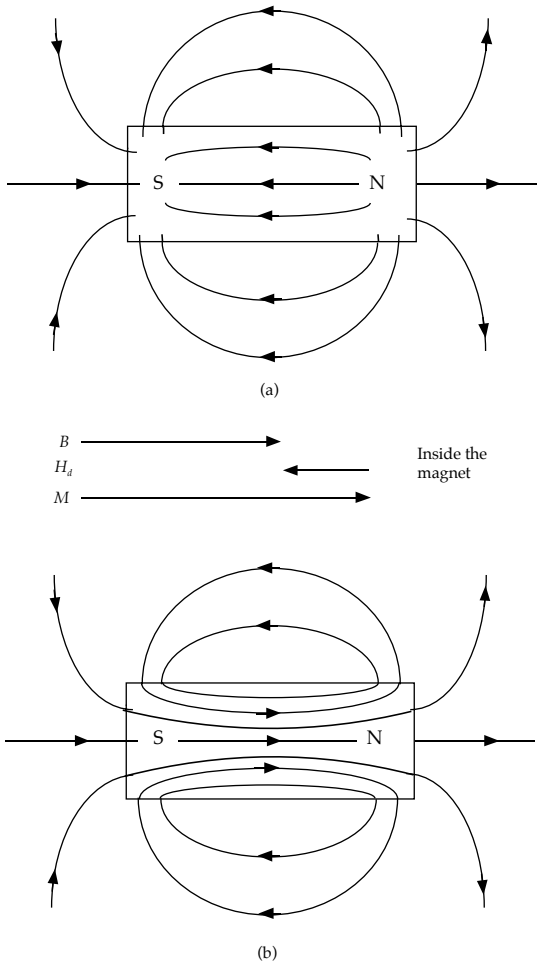


Figure 1.8: a) Magnetic field $\mathbf{H}$ both inside and outside a bar magnet, b) magnetic induction $\mathbf{B}$ both inside and outside a bar magnet. Notice in particular that the magnetic field and induction lines are identical outside the material, but inside they are quite different (they even point in opposite directions). Inside the material $\mathbf{H}$ is termed $\mathbf{H_d}$.

In hexagonal crystals the magnetocrystalline anisotropy is uniaxial (Jiles, 1991), *i.e.*, there is one axis which corresponds to maximum energy (hard axis), and one for minimum energy (soft axis). Because of the symmetry, the energy is the same whether the magnetisation is aligned up or down the easy axis. An even power series in $\sin\theta$ can be used to describe the uniaxial magnetocrystalline energy E_k^u (Stancil, 1993).

$$E_k^u = K_{u1}\sin^2\theta + K_{u2}\sin^4\theta + \cdots \tag{1.18}$$

where K_{u1} and K_{u2} are the first two uniaxial anisotropy constants respectively.

Most ferromagnetic materials have a cubic crystal structure, *e.g.*, magnetite. The cubic magnetocrystalline anisotropy E_k^c, is given by (Stancil, 1993)

$$E_k^c = K_1(\alpha_1^2\alpha_2^2 + \alpha_2^2\alpha_3^2 + \alpha_3^2\alpha_1^2) + K_2\alpha_1^2\alpha_2^2\alpha_3^2 + \cdots \tag{1.19}$$

where K_1 and K_2 are the first two cubic anisotropy constants respectively, and α_i is the directional cosine of the magnetisation vector with respect to the cubic axes. For cubic magnetocrystalline anisotropy there are three easy axes. The magnetocrystalline anisotropic constants are material and temperature dependent.

K_1 is often much larger than K_2, so that Equation 1.19 can be simplified to

$$E_k^c = K_1(\alpha_1^2\alpha_2^2 + \alpha_2^2\alpha_3^2 + \alpha_3^2\alpha_1^2) \tag{1.20}$$

Magnetostrictive energy

The previous three energies *i.e.*, E_{ex}, E_d and E_k, all vary with the state of strain. The material will spontaneously deform if this deformation reduces the total sum of the magnetic and elastic energies. This phenomenon is known as the magnetostriction or the induced magnetoelasticity. Of the various categories, linear magnetostriction is the most relevant to rock magnetism. This is a second order effect due to the interaction of the magnetocrystalline energy and elastic energies (Lee, 1955).

The equation for the cubic magnetocrystalline energy, (Equation 1.19), is for an unstrained material. The dependence of the cubic anisotropy energy (E_{anis}^c) on strain can be expressed using a Taylor series (Kittel, 1949a)

$$E_{anis}^c = (E_{anis}^c)_0 + \sum_{i\geq j}\left(\frac{\partial E_{anis}^c}{\partial e_{ij}}\right)_0 e_{ij} + \cdots = E_k^c + E_{strict}^c \tag{1.21}$$

where e_{ij} is the strain tensor, $(E_{anis}^c)_0$ equals E_k^c and refers to the undistorted lattice and must satisfy cubic symmetry. E_{strict}^c is the cubic magnetostrictive energy and represents the interaction between the magnetic anisotropy and strain. E_{strict}^c is given by (Kittel, 1949a)

$$\begin{aligned} E_{strict}^c &= [(9/4)(c_{11} - c_{12})\lambda_{100}^2 - (9/2)c_{44}\lambda_{111}^2](\alpha_1^2\alpha_2^2 + \alpha_2^2\alpha_3^2 + \alpha_3^2\alpha_1^2) \\ &= K_{strict}(\alpha_1^2\alpha_2^2 + \alpha_2^2\alpha_3^2 + \alpha_3^2\alpha_1^2) \end{aligned} \tag{1.22}$$

$$\text{where} \qquad \lambda_{100} = -\frac{2}{3}\frac{B_1}{c_{11} - c_{12}} \qquad \lambda_{111} = -\frac{1}{3}\frac{B_2}{c_{44}}$$

where c_{11}, c_{12} and c_{44} are elastic moduli (Kittel, 1975), λ_{100} and λ_{111} are the cubic magnetostriction anisotropy constants for the [100] and [111] crystallographic directions respectively (Moon, 1991), and B_1 and B_2 are the magnetoelastic coupling constants defined by Kittel (1949a).

Equations 1.20 and 1.22 can be combined to give (Ye *et al.*, 1994)

$$\begin{aligned} E^c_{anis} &= (K_1 + K_{strict})(\alpha_1^2\alpha_2^2 + \alpha_2^2\alpha_3^2 + \alpha_3^2\alpha_1^2) \\ &= K_1'(\alpha_1^2\alpha_2^2 + \alpha_2^2\alpha_3^2 + \alpha_3^2\alpha_1^2) \end{aligned} \tag{1.23}$$

Ye *et al.* (1994) correctly point out that the commonly measured K_1' is often misinterpreted as K_1. K_1 can only be directly measured by ferromagnetic resonance experiments (Bickford Jr., 1949; 1950).

Magnetoelastic energy

The anisotropy energy given by Equation 1.21 is for a material in a zero stress state.

If a magnetic material is subjected to external or internal stresses, then the stress will induce additional strains which alter the direction of the spontaneous magnetisation. This results in an addition to the anisotropic energy called the magnetoelastic energy or magnetoelastic coupling energy, E_{me}. For a cubic crystal E^c_{me} is (Träuble, 1969)

$$E_{me} = -\left(\frac{3}{2}\right)\lambda_{100}(\alpha_1^2\sigma 11 + \alpha_2^2\sigma 22 + \alpha_3^2\sigma_{33}) - 3\lambda 111(\alpha_1\alpha_2\sigma_{12} + \alpha_2\alpha_3\sigma_{23} + \alpha_3\alpha_1\sigma_{31}) \tag{1.24}$$

where σ_{ij} is the stress tensor.

External stress in rocks is common. It usually has a very slow spatial variation within a magnetic crystal and is referred to as the macrostress. Internal stress or microstress is due to crystal imperfections, *e.g.*, dislocations, inclusions *etc.* (Weertman & Weertman, 1992), and is rapidly varying within the crystal.

The two types of stress have different effects on the magnetic properties of a material. The magnetoelastic energy due to macrostress behaves in a similar fashion to E_k and E_{strict}. The microstress can only be averaged over the whole crystal (Moon, 1991). The microstress is very important when considering internal magnetic processes and remanence (Xu & Merrill, 1989).

Total anisotropic energy

The total anisotropic energy E_{anis}, is given by the addition of E_k, E_{strict} and E_{me} (Lee, 1955)

$$E_{anis} = E_k + E_{strict} + E_{me} \tag{1.25}$$

1.5 Domain theory

In ferromagnets below T_c and above a critical size (d_o), it is energetically favourable for the magnetic structure to break up into complex patterns called domains. The domain structure for a given temperature and sample is determined by the minimisation of E_{tot} (Equation 1.12). Attempts to calculate the domain structure are hampered by the need to determine the long range non-linear magnetostatic interaction, *i.e.*, E_d. Due to the large computational power and time required to calculate the magnetostatic energy, early work on domain prediction was obtained by guessing a simple domain structure for a particle with a known shape and then analytically solving Equation 1.12 (see Section 1.5.1). Recent advances in computing power has allowed for the direct, unconstrained calculation of E_{tot} (see Section 1.5.2).

1.5.1 Classical domain theory

Classical domain theory assumes that within each domain the moments are aligned parallel to each other, and they only change direction at boundaries (domain walls). The theory was first developed by Landau & Lifschitz (1935) and later refined by Kittel (1949a).

Figure 1.9 shows examples of some classical domain configurations. In Figure 1.9a E_{ex} dominates and a single domain (SD) structure results. In Figures 1.9b the contribution from E_d is too large for a SD structure to be stable and a two domain state is formed, which greatly reduces E_d. A domain state with two or more domain is said to be multidomain (MD). The introduction of closure domains (Figure 1.10c), further reduces the stray field and hence E_d, by aligning the magnetisation parallel to the surface of the grain.

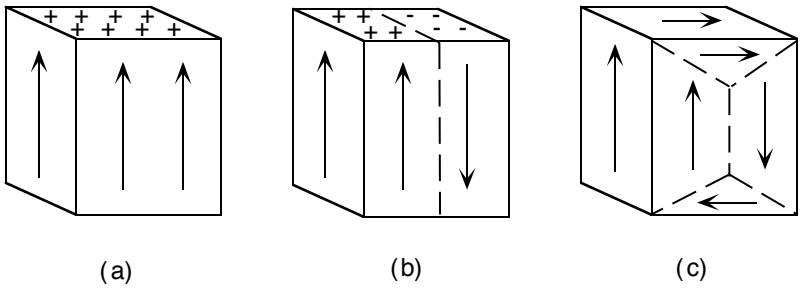


Figure 1.9: Schematic representations of a) single domain magnetic structure, b) two domain magnetic structure, and c) two domain structure with closure domains. The arrows represent the direction of M_s in each of the domains, and the dashed lines represent domain walls (see Figure 1.10).

Separating two domains is a domain wall, where the magnetic moments rotate between the orientations of the two domains (Figure 1.10). There are two types of domain wall; Bloch and Néel type (Figure 1.10). The magnetic moments of a Bloch wall (Figure 1.10a) rotate on a cone about the wall normal, *i.e.*, the rotation is perpendicular to the

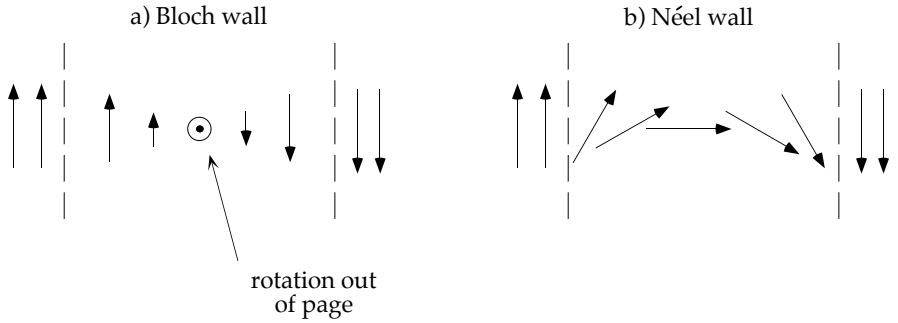


Figure 1.10: Schematic representations of a) Bloch wall and b) Néel wall. Bloch wall rotate out of the paper, whilst Néel wall rotates only in the plane of the paper.

domain magnetisation. Néel type walls rotate only in the plane of the domain magnetisation (Figure 1.10b). All domain walls in the centre of a domain structure are Bloch type walls. However when a Bloch wall meets a grain surface, Néel domain walls become energetically more favourable by rotating only in the plane of the surface, reducing the stray field. Néel walls which occur only at the surface of a grain are often referred to as "Néel caps" (Xu & Dunlop, 1996).

The domain wall width δ_w is controlled by two competing energies; E_{ex} and E_{anis}. E_{ex} makes the walls thicker, whilst E_{anis} is minimised for thin domain walls. δ_w is determined by minimising the domain wall energy, which is the sum of E_{ex} and E_{anis} across the domain wall. For a 180° domain wall with anisotropy K, δ_w is given by (Kittel, 1949a)

$$\delta_w = \pi\sqrt{\frac{A}{K}} \tag{1.26}$$

where A is the exchange constant and equals $\mathcal{J}S^2/a$ (S is the spin magnitude (see Equation 1.13), and a is the spacing between spins). $\delta_w \to \infty$ as $K \to 0$, and the domain structure becomes SD.

The equilibrium number of domains in a grain n_{eq} is a balance between E_d and the sum of all the domain walls' energies. For lamellar domains where the magnetocrystalline anisotropy dominates the anisotropy, n_{eq} is given by (Stacey & Banerjee, 1974)

$$n_{eq} = \left(\frac{\mu_0 N_{SD} M_s^2}{2(\pi A K_1)^{\frac{1}{2}}}\right)^{\frac{1}{2}} \tag{1.27}$$

where N_{SD} is the demagnetising factor of each identical lamellar domain.

The introduction of domains greatly reduces the demagnetising factor N_d given in Equation 1.14. The demagnetising factor depends on the number of walls and their positions (Dunlop & Özdemir, 1997).

For larger grains, *i.e.*, many domains, the classic domain configurations agree quite closely with patterns observed by the various optical methods; Bitter technique (Bitter, 1931; Bozorth, 1951), Lorentz electronic microscopy (Smith, 1979; Smith, 1980), magneto-optical Kerr effect (MOKE) (Hoffmann *et al.*, 1987; Ambatiello *et al.*, 1995) and magnetic force microscopy (MFM) (Williams *et al.*, 1992b; Proksch *et al.*, 1994).

However the first domain observations for grains with just a few domains have only recently been reported (*e.g.*, Geiß *et al.*, 1996; Pokhil & Moskowitz, 1997). These observations conclude that classical domain theory does not accurately model structures with only a few domains, instead unconstrained three-dimensional numerical models are required.

1.5.2 Micromagnetic models

Micromagnetic calculations are achieved by minimising the total energy of a specified number of interacting magnetic moments. Recent advances in computing technology has made the calculation of unconstrained three-dimensional models feasible (Schabes & Bertram, 1988; Williams & Dunlop, 1989).

These calculations follow the micromagnetic equations formulated by Brown (1963). An initial random domain configuration is chosen, and the system is optimised usually by the conjugate-gradient method (Press *et al.*, 1986) for a set of variable conditions, *e.g.*, external field and temperature. To minimise computer time many simplifications are made, *e.g.*, for materials like magnetite where the magnetocrystalline energy dominates the anisotropy, the magnetostriction is ignored (Fabian *et al.*, 1996).

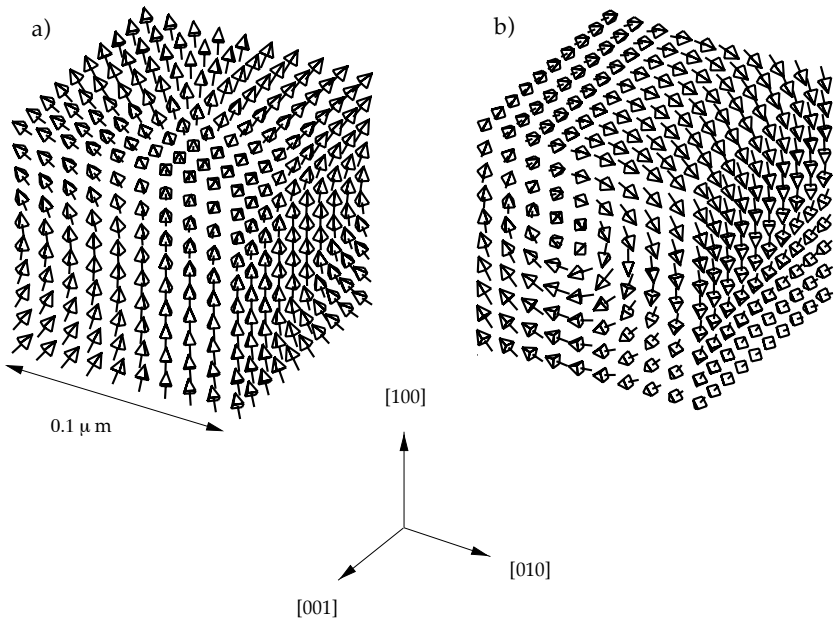


Figure 1.11: Examples of possible stable domain configurations for a 0.1 μm cubic grain of magnetites at room temperature, calculated using an unconstrained three-dimensional model. a) flower state, and b) vortex state.

Numerical modelling has produced domain structures very different to those of classical domain theory (*cf.* Figures 1.9 and 1.11). For example instead of the single domain state (Figure 1.9a), micromagnetic models find that "flower" states have lower energies (Figure 1.11a). Also, "vortex" structures (Figure 1.11b), are found to be energetically preferable to the classical two-domain structure with closure domains (Figure 1.9b).

Three-dimensional micromagnetic calculations have so far been limited to SD and small MD grains (≤ 4 μm (Wright *et al.*, 1997)), but with rapidly increasing computer capabilities it may soon be possible to model domain structures for larger MD grains. It would appear however, that classic domain theory and micromagnetic models converge as the grain size increases, *e.g.*, Williams & Wright (1998) found their model of a 4.0 μm cubic grain displayed many observed multidomain features.

Other optimisation methods have been applied in the calculation of the domain structure, *e.g.*, Monte Carlo simulation (Fukuma & Dunlop, 1997). However in the case Monte Carlo simulation, the required increase in computational power means that only two-dimensional models can be modelled. It is debatable (*pers. comm.* W. Williams, 1997) how well one- and two-dimensional models reflect reality.

1.6 Remanence acquisition

Here only a brief description of remanence acquisition is given. For a full account of the mechanisms see one of the following books; Nagata (1961), Stacey & Banerjee (1974), O'Reilly (1984) or Dunlop & Özdemir (1997).

When a field is applied to a domain structure the total energy (Equation 1.12) increases, the magnetic domain structure changes and the sample is said to be magnetised. The size of the magnetisation depends on the inducing field, temperature and on the domain structure's resistance to change. Figure 1.12 shows a schematic representation of the response of a magnetic material to an inducing field at a given temperature, *i.e.*, a hysteresis loop. The temperature is important because all the internal magnetic energies (Section 1.4) are temperature dependent. Because their temperature dependencies are different the shape of a hysteresis curve (Figure 1.12) is also temperature dependent.

According to classical domain theory, a domain will be unaffected by the external field until the field equals the coercive force H_c (Figure 1.12). H_c is a measurement of a grain's resistance to change, and is $\propto 1/\chi$. Coercive force is related to the number of domains (grain size) and the degree of internal stress. Experimental results show a gradual decrease in coercive force over many decades of grain size (*e.g.*, Dankers & Sugiura, 1981; Heider *et al.*, 1988a, see Figure 3.3).

Classically the response of SD grains is to rotate the entire moment, whereas MD grains respond by movement of domain walls (Figure 1.13). The coercive force associated with domain wall movement is substantially less than that of SD rotation, and subse-

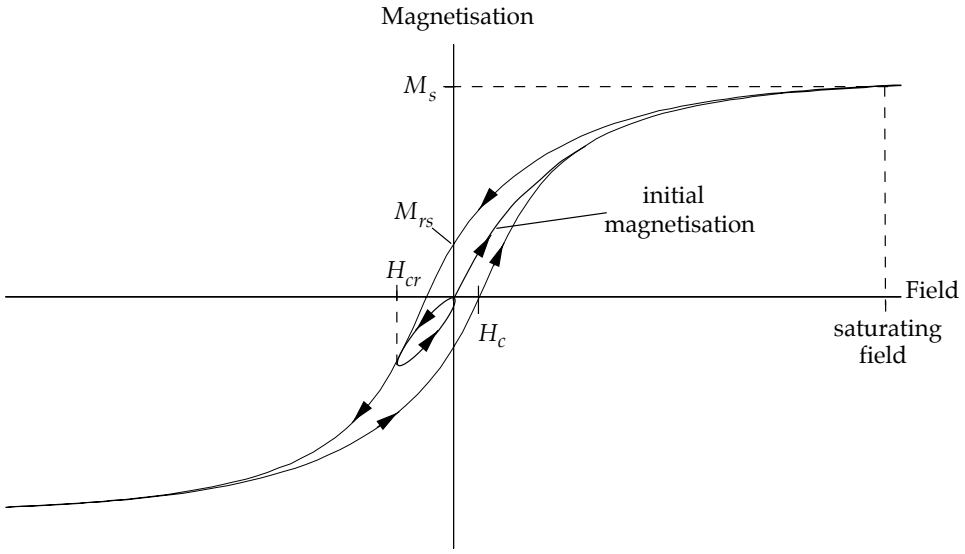


Figure 1.12: Schematic representation of an initial magnetisation and hysteresis loops for a ferro/ferri-magnetic material. The hysteresis parameters M_s, M_{rs}, H_c and H_{cr} are shown on the diagram. H_c is the field required to demagnetise M_{rs} *in* field, whilst H_{cr} is the field required to demagnetise M_{rs} when the field is removed.

quently MD grains have a lower H_c. Stress fields associated with dislocations impede both domain wall movement and the rotation of SD moments (Stacey & Wise, 1967; Shive, 1969; Xu & Merrill, 1989), which increases H_c. Domain structures have a range of coercive forces. The entire range is often termed the coercive force spectrum.

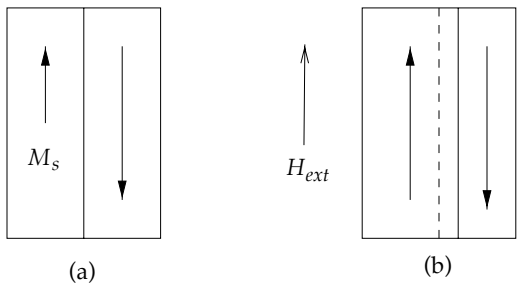


Figure 1.13: Domain configurations of a classical two-domain grain in a) zero external field, and b) with a field H_{ext}.

On removal of the field, the moments of the SD grains above a given size stay aligned in the direction of the inducing field, and the SD sample is said to have a remanence. For SD grains below the threshold size, thermal energy is sufficient to randomise the magnetic orientation, and the sample does not exhibit any remanence. These types of grains are termed superparamagnetic (Néel, 1955; Bean & Livingston, 1959). In MD grains on the removal of the external field, $\mathbf{H_d}$ acts to encourage the domain walls to return to their original position. Some domain walls do return and are said to be reversible. However in other cases $\mathbf{H_d}$ is insufficient to overcome the coercive force due to the stress fields around dislocations, and the walls are said to be "pinned" (irreversible). The irreversible move-

ment of domain walls gives rise to remanence, represented as M_{rs} for saturating fields in Figure 1.12.

There are several different types of remanence which can be induced in a sample. Brief descriptions are given below.

1.6.1 Isothermal remanent magnetisation

The easiest remanence to induce is an isothermal remanent magnetisation (IRM). This is simply achieved by applying a field for a short period of time at a given temperature. An IRM induced in a virgin sample follows the initial magnetisation curve. (Figure 1.12).

If a large field is applied to a MD grain, the domain walls move to the edge making the grain SD, and the sample is said to be saturated. Increasing the field further, causes reversible reduction in the precession of the moments (Figure 1.5b), which causing the magnetisation to increase slightly. Ultimately in a very high field the moments are completely aligned with the field (*cf.* Figure 1.5a). The IRM associated with a saturating field is termed a SIRM (M_{rs}). Generally SIRMs tend to be large and unstable.

IRM can be induced in nature by lightning strikes. Within a few metres of a strike, the surface rocks experience a DC field of short duration and varying intensity that remagnetises all or part of the original remanence (Collinson, 1983).

1.6.2 Thermoremanent magnetisation

Of great interest to the rock magnetist is thermoremanent magnetisation (TRM) which is acquired by cooling in a small field from T_c. At temperatures near T_c, the magnetic energies (Section 1.4) are small and a field as low as the earth's ($\approx$ 50 μT) can cause significant magnetisation. Because thermoremanences are acquired from a paramagnetic state, all energy barriers within domain a configuration can be overcome during acquisition, and TRM affects the entire domain structure or coercive force spectrum. Thermoremanences are very stable compared to IRMs, and are also stable over geological time-scales.

Thermoremanences acquired between temperatures other than T_c and room temperature are termed partial TRM (pTRM), *e.g.*, $\mathrm{pTRM}_{500}^{T_c}$ or $\mathrm{pTRM}_{300}^{500}$ (where the temperatures are in Celsius).

1.6.3 Anhysteretic remanence

Anhysteretic remanence is induced using a combination of two fields; a large AC field which effects the entire coercive spectrum of a grain, and a DC biasing field which induces a small remanence.

The AC field is decreased from a maximum field to zero. As the field decreases, the percentage of the total coercive force spectrum which it affects also decreases. The

small biasing field preferentially orientated the magnetisation in the direction of the DC field. Because the AC field affects the entire coercive force spectrum, ARMs have a greater intensity than IRM for the same DC field. Because ARM affects the entire coercive force spectrum like TRM, it is is sometimes used as an analogue for TRM in palaeointensity experiments (Banerjee & Mellema, 1974a; Stephenson & Collinson, 1974), because unlike TRM acquisition it does not require heating which can cause chemical alteration. However, recent experimental evidence suggests that this substitution is not appropriate (Dunlop & Argyle, 1997, Chapter 7).

There is some evidence to suggest that lightning strikes might induce ARM as well as IRM (Collinson, 1983).

1.6.4 Other remanences of interest to the rock magnetist

There are several other types of remanence of interest to the rock magnetist, although none of them are studied in this thesis. The main ones are listed below.

Chemical remanent magnetisation (CRM) This results from the formation of a new magnetic mineral in the presence of a magnetic field. The new magnetic mineral can either be formed by growth of a mineral (McClelland, 1996) or by chemical alteration from one mineral or phase to another, *e.g.*, γ-$Fe_2O_3 \rightarrow \alpha$-$Fe_2O_3$ (Özdemir & Dunlop, 1989). CRM is sometimes referred to as crystallisation remanent magnetisation.

Viscous remanent magnetisation (VRM) This remanence is acquired at a given temperature (usually room temperature) by a sample lying for a period of time in a small magnetic field. VRM is highly dependent on the grain size distribution of the magnetic minerals within a rock (Dunlop, 1973b; Dunlop, 1983).

Piezoremanent magnetisation (PRM) The application of an external stress to a magnetic grain can induce a remanence or alternatively it can rotate the original remanence (Nagata, 1961).

Detrital remanent magnetisation (DRM) DRM is acquired when sediments are deposited and consolidated and is no more than a reconstitution of the TRM, CRM, VRM *etc.*, of detrital magnetic grains from the source rock (or rocks) (O'Reilly, 1984). However it is weaker than TRM, CRM or VRM due to the randomisation of grains.

Gyromagnetic remanent magnetisation (GRM) This is a laboratory induced remanence, acquired by samples in alternating or rotating fields. It originates in the gyroscopic response of SD moments to the torque of an applied field. The moments precess about the direction of $\mathbf{H}_{ext}$ and only gradually relax into the direction of $\mathbf{H}_{ext}$. The net effect for anisotropic rocks is a GRM perpendicular to $\mathbf{H}_{ext}$ (Stephenson, 1981).

1.7 Magnetic minerals

The most important geological magnetic minerals are oxides of iron, often containing titanium, and sulphides of iron. Most of the minerals of interest are within the ternary system $FeO - TiO_2 - Fe_2O_3$ (Figure 1.14).

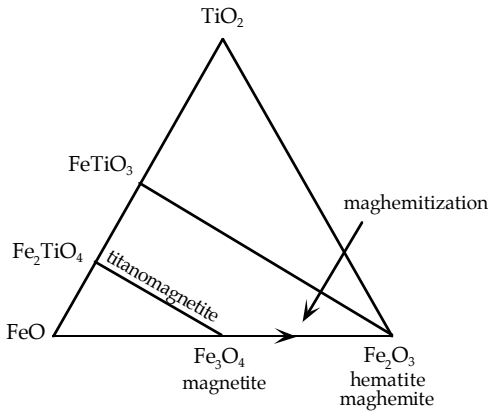


Figure 1.14: Ternary diagram of $Fe - TiO_2 - Fe_2O_3$, showing the composition of the most important magnetic minerals.

The ternary system can be split into two structural groups. The first group consists of the strongly magnetic cubic oxides; titanomagnetites and titanomaghemites. The second group is made up of the weakly magnetic rhombohedral minerals; hematite and solid-solution titanohematites.

1.7.1 Magnetite

Magnetite (Fe_3O_4 or $Fe^{2+}Fe_2^{3+}O_4$) is the most important naturally occurring mineral, because it is both strongly magnetic and common. It is the mineral chiefly studied in this thesis.

Magnetite is a cubic mineral with spinel structure. The oxygen anions form a face-centred cubic crystal structure with Fe^{2+} and Fe^{3+} cations in interstitial sites. There are two interstitial sites which are often referred to as A and B. The A sites or sublattice have a lattice constant $a = 8.396$ Å, and are tetrahedrally coordinated. The B sites are octahedrally coordinated. One Fe^{3+} ion is located on the A site, whilst the remaining Fe^{2+} and Fe^{3+} cations are located on the B site. This particular arrangement of cations defines an inverse spinel (Figure 1.15).

The magnetic moments of the cations on the two sublattices are antiparallel, making magnetite ferrimagnetic. The magnetic moments of the two Fe^{3+} cations cancel out, and the the net magnetic moment is due to the Fe^{2+} ion (Figure 1.16). The thermal dependencies of the two sublattices are identical and magnetite's ferrimagnetic behaviour is similar to that

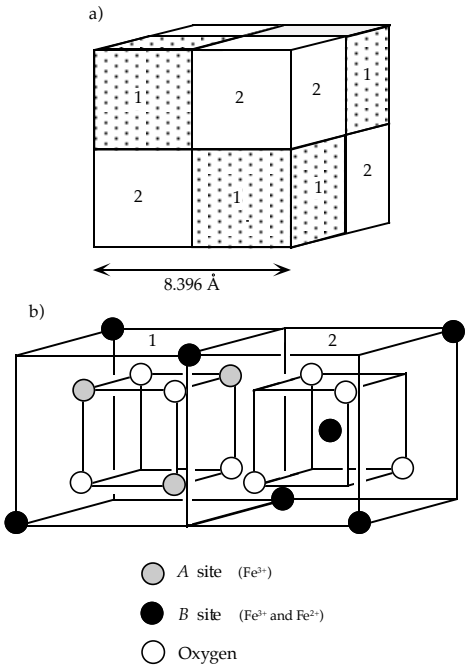


Figure 1.15: Schematic diagram of a unit cell of magnetite. The unit cell (a) consists of 8 different sub-cubes which can be split into two (1 and 2). In b) the ionic arrangement for two different sub-cubes 1 and 2 is shown. Redrawn from Calhoun (1954).

shown in Figure 1.6a. The behaviour of the total magnetisation is shown in Figure 1.17. Magnetite has a Curie temperature of 578 °C (Figure 1.17).

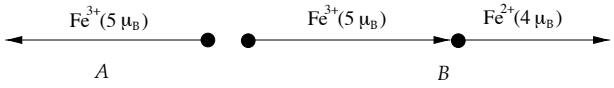


Figure 1.16: Arrangement of magnetic vectors in magnetite's A and B sublattices.

At room temperature the electrons are free to hop between the Fe^{2+} and Fe^{3+} cations ions on the B sublattice. The hopping rate is such that the Fe^{2+} and Fe^{3+} cations become indistinguishable. On cooling through the Verwey transition at 120-124 K (Verwey & Haayman, 1941), the cubic structure becomes monoclinic, and the rate of electron hopping dramatically decreases (Belov, 1993). The B sublattice Fe^{2+} and Fe^{3+} cations are distinguishable below the Verwey transition. The Verwey transition is discussed in detail in Chapter 5.

At room temperature the cubic magnetocrystalline anisotropy constant $|K_1| \gg |K_2|$ (see Equation 1.19). K_1 has a value of -1.08×10^4 Jm^{-3} at room temperature (Bickford Jr., 1950). To my knowledge K_1 has never been directly measured as a function of temperature above room temperature. Above room temperature K_1' (see Equation 1.23) varies as $\approx M_s^8$ (Fletcher & O'Reilly, 1974).

At room temperature the cubic magnetostriction constants (Section 1.4.3) λ_{100} and λ_{111} are -19×10^6 and 78×10^6 respectively (Ye *et al.*, 1994). The temperature variation of

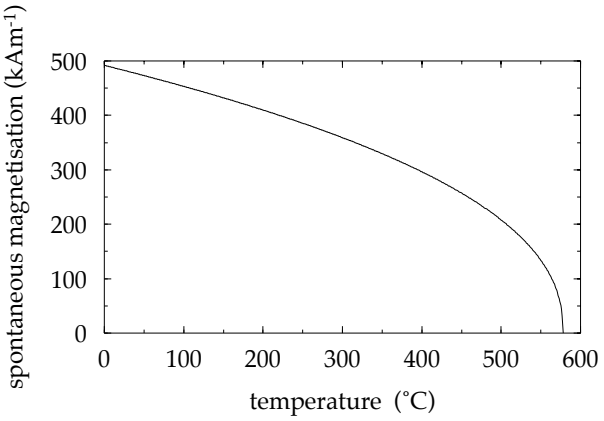


Figure 1.17: Spontaneous magnetisation versus temperature for magnetite above room temperature. After Pauthenet & Bochirol (1951).

λ_{111} above room temperature is ill-defined. It is thought to vary somewhere between $M_s^{2.2}$ and $M_s^{2.7}$ (Moskowitz, 1993a).

The low-temperature behaviour of M_s, K_1, K_2, λ_{100} and λ_{111} is considered in detail in Chapter 5.

Maghemitisation of magnetite

Magnetite is unstable in the presence of air at room temperature. It gradually oxidises to maghemite (Section 1.7.2). This process is called maghemitisation, and occurs on the surface of crystals. The centres of crystals can become oxidised by the diffusion of Fe^{2+} from the crystal interior to a free surface, where it is converted to Fe^{3+}. Oxidation is slow, being controlled by Fe^{2+} diffusion rates and distance to the surface. The centres of large grains remain relatively unaffected by maghemitisation, whilst smaller grains are susceptible to oxidation at room temperature. A partially oxidised or cation deficient magnetite has the structural formula $Fe^{3+}_{2+2/z}Fe^{2+}_{1-z}\square_{z/3}O^{2-}_4$, where z is the oxidation parameter and $\square$ represents a lattice vacancy. Figure 1.18 shows the saturation magnetisation as a function of the oxidation parameter.

1.7.2 Maghemite

Maghemite (γ-Fe_2O_3) is the fully oxidised equivalent of magnetite. It has a body centred cubic structure, and is magnetically very similar to magnetite. At room temperature M_{sat} of maghemite is 380 kAm^{-1}, compared to 480 kAm^{-1} for magnetite (Figure 1.18), and the thermal dependency of M_s for maghemite is similar to that of magnetite (Figure 1.17). The magnetocrystalline and magnetostrictive constants have values approximately one third that of magnetite (Dunlop & Özdemir, 1997).

At room temperature γ-Fe_2O_3 is metastable, but on heating it inverts to weakly magnetic hematite (Section 1.7.3). The inversion temperature has been reported as occurring

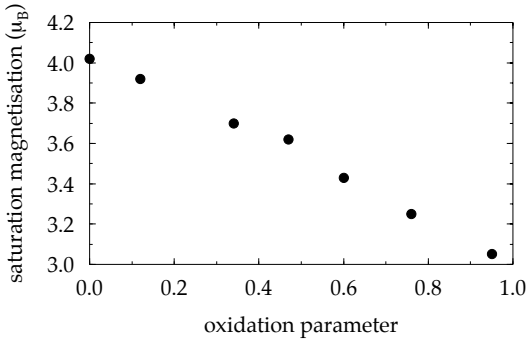


Figure 1.18: Saturation moment in number of Bohr magnetons μ_0 per molecule at 0 K as a function of oxidation parameter z in partially maghemitized magnetites. After Readman & O'Reilly (1972).

anywhere between 250 °C (Verwey, 1935) and 750 °C (Özdemir, 1990). I measured a high-temperature susceptibility curve (Section 1.8), for a maghemite sample whose purity had been tested using XRD. I found an inversion temperature of $\approx$ 550 °C (Figure 1.19).

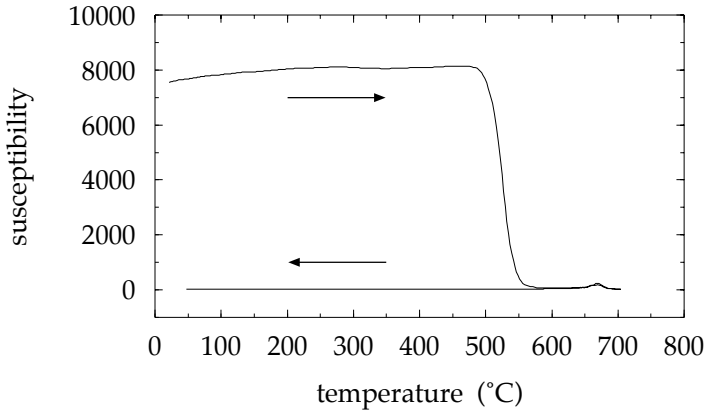


Figure 1.19: High-temperature susceptibility curve for maghemite (BASF, $\gamma - Fe_2O_3$). The maghemite was kindly provided by Dr. W. O'Reilly at the University of Newcastle. X-ray diffraction (XRD, Section 1.8.1) of this maghemite sample confirmed the purity of the sample to within the accuracy of the XRD spectrometer (≤ 5 %). An inversion temperature of 550 °C is observed.

At present it is unknown what causes this very wide range of inversion temperatures. Naturally occurring maghemites usually have higher inversion temperatures (Özdemir, 1990). Because of the inversion to hematite, an accurate determination of T_c becomes problematic. According to Dunlop & Özdemir (1997) the best present estimate for T_c for maghemite is 645 °C (Özdemir & O'Reilly, 1982), however a value as high as 695 °C has been reported (Readman & O'Reilly, 1972). Recently de Boer & Dekkers (1996) reported a Curie temperature of 610 °C for natural maghemite.

1.7.3 Hematite

Hematite (α-Fe_2O_3) has a rhombohedral structure. Below the Morin transition (-10 °C, Morin 1950), hematite is perfectly antiferromagnetic (Section 1.3.4). Above the transition there is a small canting of the A and B sublattice spontaneous magnetisations M_a and M_b, giving rise to a net spontaneous magnetisation perpendicular to M_a and M_b. This canting is similar in appearance to Figure 1.7b, but occurs without an external field (Dunlop & Özdemir, 1997). At room temperature the magnitude of M_s is 2.5 kAm^{-1}, ≈ 0.5 % of magnetite. The canted antiferromagnetism disappears at T_c = 675 °C, which is also known as the Néel point (Banerjee, 1991). Underlying the canted antiferromagnetism is an isotropic ferromagnetism that is unaffected by the Morin transition. Its origin is due to chemical or lattice defects, and is often termed the defect moment. The defect moment is less than 2 % of the spin-canted moment (Dunlop, 1971).

At room temperature hematite has a very high coercive force compared to similar sized grains of magnetite. This is partly because it is normally SD, and partly because of the significant contribution from impurities and crystal defects.

1.7.4 Titanomagnetites and titanomaghemites

Single-phase titanomagnetites $Fe_{3-x}Ti_xO_4$ ($0 \leq x \leq 1$), (Clark, 1983), are inverse spinels. Increasing substitution of Ti^{4+} weakens the exchange coupling and the Curie temperature falls almost linearly with increasing x (Xu *et al.*, 1996). $Fe_{2.4}Ti_{0.6}O_4$ (TM60) is the primary titanomagnetite in rapidly cooled basaltic lavas, and has been extensively studied (*e.g.*, Metcalf & Fuller, 1986; Moskowitz & Halgedahl, 1987; Sahu & Moskowitz, 1995; Brown & O'Reilly, 1996; Stumpf *et al.*, 1997). At room temperature TM60 has a M_s of ≈ 125 kAm^{-1}. Magnetically titanomagnetites behave in a similar manner to magnetite ($x = 0$), but with decreasing intensity as x increases.

A partially oxidised titanomagnetite is referred to as a titanomaghemite. Oxidation reduces the magnetic properties of a titanomagnetite, and the Curie temperature is similarly lowered (Parkinson, 1983).

1.7.5 Other magnetic minerals

Two important naturally occurring hydrous iron oxides are goethite (α-FeO(OH)) and lepidocrocite (γ-FeO(OH)) (Dunlop & Özdemir, 1997). These two minerals dehydrate to oxides on warming to 100–300 °C to give hematite and maghemite respectively. Pyrrhotite (FeS_{1+x} where $0 \leq x \leq 0.14$) is the only iron sulphide that is ferrimagnetic.

1.8 Standard rock magnetic laboratory techniques

In this section standard rock magnetic techniques and equipment utilised in this study are briefly discussed. Spectroscopic techniques used to determine the chemical composition of the samples in this study are described in Section 1.8.1. Section 1.8.2 discusses standard demagnetisation methods which examine stability of a remanence. In Section 1.8.3, the palaeomagnetic equipment used in the Oxford Palaeomagnetic laboratory is briefly described.

1.8.1 Spectroscopic analysis

In rock magnetic studies it is essential to characterise the magnetic mineralogy of the sample. If the concentration of the magnetic minerals within a sample is high, then spectroscopic analysis is the most accurate method of determining the mineralogy. Standard spectroscopic methods are X-ray analysis (Berti & Pinna, 1996; King, 1996), electron spectroscopy (Goss, 1987; Banfield *et al.*, 1994) and Mössbauer spectroscopy(Longworth *et al.*, 1979).

Distinguishing between similar minerals can significantly increase the measurement time. For example, when using XRD to distinguish between magnetite and maghemite, it is necessary to scan at large angles because these two minerals can only be separated for the reflection from the $hkl = 00\underline{24}$ plane, where for a CuKα_1 source (wavelength = 1.5418 Å) $2\theta = 94.5^\circ$ for magnetite (d = 1.0496 Å) and $2\theta = 95.2^\circ$ for maghemite (d = 1.043 Å) (ICDD, 1986). It is also necessary to increase the scan time as the relative intensities from the $hkl = 00\underline{24}$ plane for magnetite (6 %) and maghemite (9 %) are weak.

This particular problem of identifying small traces of maghemite and hematite in the presence of magnetite is common in rock magnetic studies, because magnetite oxidises in air to maghemite, which in turn transforms into hematite upon heating. Surface coatings strongly affect the magnetic behaviour of magnetite (Özdemir *et al.*, 1993), making it important to be able to detect oxidation products.

There are other non-magnetic methods for determining the purity of magnetite, *e.g.*, transmission electron microscopy (TEM). By using high-resolution TEM it is possible to detect small inclusions of foreign minerals of only a nanometer in diameter, stacking faults and other types of stress related features(Goss, 1987; Banfield *et al.*, 1994).

Two spectroscopic methods were used in this study; X-ray diffraction (XRD), and Mössbauer spectroscopy. An attempt to use infrared spectroscopy was made, but it was found to be less accurate than either XRD or Mössbauer spectroscopy. Results from a preliminary investigation are reported in Appendix A.

XRD Spectrometry

Most of the XRD analysis was carried out using a rather old Phillips PW1320 Diffractometer. To test the accuracy of the Phillips PW1320 Diffractometer, a few samples were examined on a more modern Phillips PW1710 Diffractometer located in the Clarendon Laboratory, University of Oxford. The differences in the spectra from the two diffractometers were negligible. The Phillips PW1320 lacked the modern software packages to aid interpretation of the spectra.

The Phillips PW1320 Diffractometer had not been calibrated for the identification of the relative iron oxide minerals of note, making the interpretation of the spectra semi-quantitative. It was estimated that it could detect magnetite:maghemite ratios of approximately 10:1 (*pers. comm.* C. Fagg, 1995).

The samples were prepared by grinding with a pestle and mortar before examination.

Mössbauer Spectrometry

Mössbauer spectroscopy was undertaken at the Institute for Rock Magnetism, University of Minnesota using a Ranger Scientific Mössbauer Spectrometer. The Mössbauer spectroscopic analysis software had been calibrated to examine the magnetite:maghemite ratio. Hematite has not yet been included in this calibration but assuming that it does not behave erratically and unexpectedly then its contribution can be calculated. Due to this uncertainty in the hematite concentration, any claims about the magnetite/maghemite/hematite content have a degree on uncertainty. It is estimated that the Mössbauer spectrometer could detect a magnetite:maghemite ratio as high as 20:1 (*pers. comm.* P. Solheid, 1996).

It was necessary to lightly grind whole crystals using a pestle and mortar before study.

1.8.2 Demagnetisation of remanence

One method of testing the stability of remanence is to demagnetise it. Remanence which is resistant to demagnetisation is said to be hard or stable, whilst remanence which is easily demagnetised is "soft".

Three different types of demagnetisation were used in this study; thermal demagnetisation, alternating field (AF) demagnetisation and low-temperature demagnetisation.

Thermal demagnetisation

The method of thermal demagnetisation is identical to thermoremanence acquisition, but with no inducing field. On heating to T_c, ferro/ferri-magnetic materials become paramagnetic and any record of the original remanence is lost. However on heating to a temperature

less than T_c in zero field, only part of the magnetisation is demagnetised. The degree of demagnetisation reflects the stability of the original magnetisation.

There are two kinds of thermal demagnetisation; continuous and step-wise. Continuous thermal demagnetisation involves measuring the magnetisation as a function of temperature during heating, *i.e.,* the magnetisation is measured at high temperature. During step-wise thermal demagnetisation, the sample is heated to a given temperature, cooled back to room temperature and the magnetisation measured. The sample is then heated to a higher temperature *etc.* Step-wise demagnetisation is easier to implement, because all the measurements are undertaken at room temperature. It should be realised that the two methods are not identical.

AF demagnetisation

AF demagnetisation works in a similar manner to ARM acquisition, except the DC biasing field is zero. The large AC field sweeps across the grain "unpinning" walls with microcoercive forces in the order of the AC field. In a similar manner to step-wise thermal demagnetisation, it is possible to partially AF demagnetise a sample in a series of steps, gradually increasing the maximum AC field. Remanent magnetisation which does not demagnetise in low and medium AC fields is said to be stable.

Low-temperature demagnetisation

Low-temperature demagnetisation is specific to minerals which have transitions below room temperature, *e.g.,* magnetite and hematite (Section 1.7). During low-temperature cooling from room temperature to liquid nitrogen temperature (77 K), magnetite passes through the cubic magnetocrystalline anisotropy isotropic point at $\approx$ 130 K and the Verwey transition at 120-124 K. The ascendancy of the controlling magnetic energies is strongly affected in both cases, and MD remanence partially demagnetises (Ozima *et al.*, 1964b; Kobayashi & Fuller, 1968).

One of the primary concerns of this study is the understanding of demagnetisation processes during low-temperature cooling.

1.8.3 Palaeomagnetic equipment in Oxford

In this section the experimental equipment used in the Oxford Palaeomagnetic Laboratory is briefly described. For a full description of palaeomagnetic methods and equipment see Collinson (1983).

To minimise the influence of the earth's field on the remanence of the samples, the samples were kept in reduced field space. The magnetometers, ovens and AF tumbling demagnetiser all have Helmholtz coils (Collinson, 1983) around the entrances to the sample

chambers, which reduce the ambient field to ≈ 1 μT, *i.e.*, ≈ 2 % of the earth's magnetic field. During transfer between apparatus, the samples were kept in μ-metal boxes with an internal field of ≤ 100 nT.

Magnetometers

Two different magnetometers were used in this study to measure the magnetisation at room temperature. Most of the measurements were undertaken on a CCL Cryogenic magnetometer which used a SQUID interface to measure the magnetisation. The term SQUID is an acronym for superconducting quantum interference device, and the physics behind the SQUID magnetometer have been well documented (*e.g.*, Schrieffer, 1974; Collinson, 1983; Hook & Hall, 1991) If used carefully the CCL magnetometer in Oxford has a sensitivity of $\approx 5 \times 10^{-11}$ Am^{-2}. The sample chamber has a residual field of ≤ 10 nT.

For samples with magnetic moments above the upper limit of the cryogenic magnetometer ($\approx 5 \times 10^{-6}$ Am^{-2}), the magnetisation was measured using a Molspin Ltd. spinner magnetometer (Collinson, 1983) with a sensitivity of $\approx 5 \times 10^{-8}$ Am^{-2}. This was only necessary during the measurement of H_{rc} for large natural magnetite crystals (Chapter 3).

IRM acquisition

Isothermal remanences were induced using a Molspin Ltd. pulse magnetiser with a maximum field of 0.8 T. The saturating field for magnetite is 0.3 T.

ARM acquisition

Anhysteretic remanent magnetisation was induced using an in-house static AF demagnetiser with biasing field. The AC field was applied in only one direction and the sample did not "tumble". The sample chamber was a μ-metal cylinder. The maximum AC field was 100 mT, and the maximum DC biasing field 180 μT. The AC field was 200 mT less than the 300 mT ideally required for magnetite, however for soft MD magnetites 100 mT should be sufficient to affect the entire coercive force spectrum (Collinson, 1983). The frequency of the AC field was 50 Hz.

The AC field interacted with DC field, causing the DC field to oscillate slightly. To counter act this a filter was placed in the system to dampen the interaction.

Thermoremanence acquisition and thermal demagnetisation

Thermoremanence was induced using a MMTD oven with a maximum temperature of $\approx$ 700 °C, and a maximum DC field of 300 μT. Unfortunately it was only possible to calibrate the field up to 200 μT. Above 200 μT, the current used to produce the field had to

be extrapolated. On heating to a set temperature the samples were held for 45 minutes at the set temperature, to allow the temperature to equilibrate.

Step-wise thermal demagnetisation was achieved using the same MMTD oven with the DC field switched off, and an in-house oven. The in-house oven had no DC field option. The residual field in both ovens during thermal demagnetisation was ≤ 10 nT.

During this study, the MMTD oven's temperature was calibrated first by myself in May 1995 and later by Dr. Adry van Velzen in the summer of 1996.

AF demagnetisation

AF demagnetisation was achieved using a NGU tumbling AF demagnetiser. The maximum AC field was 100 mT, which is thought to be sufficient to completely demagnetise magnetite (Collinson, 1983). The AC field had a frequency of 50 Hz. To reduce the possibility of accidental ARM acquisition, the AF demagnetiser was set inside Helmholtz coils. The residual field inside the Helmholtz coils was ≤ 20 nT.

Low-temperature demagnetisation

Low-temperature demagnetisation was achieved by placing samples in a μ-metal box filled with liquid nitrogen. The samples were kept at 77 K for 15 minutes, before warming to room temperature in a second μ-metal box filled with water. The samples spent a few seconds in the earth's magnetic field during transfer from hot to cold μ-metal boxes and *vice versa*. However, importantly, during cooling and warming the samples were not subjected to fields of ≥ 100 nT.

The minimum hold-time for vacuum sealed samples (Section 2.6) was tested. It was found that ≈ 5 minutes was sufficient for the sample to cool through the Verwey transition at 120 K. Erring on the side of caution a hold-time of 15 minutes was chosen.

High-temperature susceptibility

Measurement of susceptibility (Equation 1.1) as a function of temperature, can yield information about the magnetic mineralogy and the domain structure, *i.e.*, SD or MD, of a sample (Collinson, 1983; O'Reilly, 1984). The susceptibility can be used when the concentration of the magnetic minerals is too low for spectroscopic analysis.

High-temperature susceptibility was measured using a Geofyzika Kappabridge with CS2 attachment, which had been customised to allow the sample to be heated in an inert atmosphere (argon). The sensitivity of the Kappabridge was 4×10^{-8} SI, the frequency 920 Hz and the maximum temperature 700 °C. It was necessary to lightly grind the larger samples before measurement.

High-temperature susceptibility (HT-χ) curves are primarily used to determine T_c. It should be realised that although T_c depends on composition, T_c does not uniquely define it. For example a Curie point of 300 °C could indicate a titanomagnetite with $x \approx 0.4$, *i.e.,* $Fe_{0.6}Ti_{0.4}0_4$, a hematite-ilmenite solid solution ($Fe_{1.5}Ti_{0.5}0_3$) or a monoclinic pyrrhotite $Fe_{0.87}S$ (O'Reilly, 1984). HT-χ curves are insensitive at identifying traces of maghemite and hematite in the presence of magnetite, because the former is magnetically similar, and the later has a relatively weak susceptibility.

1.9 Thesis objectives and layout

It was the objective to understand the origin of metastability of remanence in multidomain magnetite with special note to thermoremanence stability during low-temperature cycling through the Verwey transition.

The stability of remanence in MD magnetite has never been fully understood. Previous studies have suggested that the origin of the stability is due to stress controlled SD like-regions (Dunlop & Argyle, 1991; Heider *et al.*, 1992; Argyle *et al.*, 1994; Dunlop & Özdemir, 1997), whilst the work of Shcherbakov *et al.* (1993), McClelland & Shcherbakov (1995) and McClelland *et al.* (1996) suggests that the source of the stability is a truly multidomain effect.

The stability of MD magnetite thermoremanence to low-temperature cycling through the Verwey transition has never been extensively studied.

To examine these problems a selection of sized magnetite samples were prepared. Hydrothermal crystals were grown following the techniques developed by (Heider & Bryndzia, 1987; Heider *et al.*, 1988a). Relatively pure, stress-free, large MD natural magnetites were collected from the Shetland Isles. Annealed magnetites with small traces of titanium made by Dankers (1981) were also investigated.

In the three experimental chapters the stability of remanence is considered. Initially the stability of remanence to heating and cooling above the Verwey transition is considered (Chapter 4). A series of experiments examining the stability of thermoremanence to cooling below the acquisition temperature are reported in Chapter 6. And lastly the magnetic stability of remanences after low-temperature cycling are considered in Chapter 7. In Chapter 8, micromagnetic numerical models which attempt to simulate some of the experiments in this study are reported.

An in depth review of the physics of the Verwey transition and other changes in the magnetic properties of magnetite during low-temperature cycling is considered in Chapter 5.

A brief description of each chapter is given below.

Chapter 2 Preparation of the synthetic samples and the collection of the natural samples used in the rest of the study are discussed. The samples are spectroscopically analysed.

Chapter 3 The samples described in chapter 2 are magnetically characterised by examining their hysteresis parameters.

Chapter 4 The behaviour and stability of partial thermoremanences to cooling below the acquisition temperature is examined. The results are compared to the literature (*e.g.,* McClelland & Sugiura, 1987; Sholpo *et al.*, 1991).

Chapter 5 The physics of low-temperature properties of magnetite are discussed in detail. This includes an in depth discussion of the Verwey transition.

Chapter 6 Direct measurement of various remanences during low-temperature cycling through the Verwey transition are reported. This includes the first extensive study of the low-temperature behaviour of both thermoremanences and partial-thermoremanences.

Chapter 7 Characterisation of the metastable fraction remaining after either low-temperature cycling or partial AF demagnetisation. All the experiments are performed at room temperature or above.

Chapter 8 Micromagnetic numerical models of simulated low-temperature cycling of remanence bearing of sub-micron cubic grains of magnetite are presented. The model simulates the experimental results in chapters 6 and 7. The single domain threshold size in the monoclinic phase of magnetite is calculated.

Chapter 9 Synthesises the results and conclusions of the five preceding chapters and makes recommendations for future work.

Chapter 2

Preparation of magnetite samples for experimental study

2.1 Introduction

To study stability of remanence in multidomain (MD) magnetite, it is necessary to have a selection of characterised MD magnetite samples. It is important to know both the composition and the magnetic properties of each sample. It is generally easier to characterise synthetic samples as their histories are controlled, however in a field which intends to understand the behaviour of magnetic minerals in rocks it is necessary to study samples of natural origin as well.

It has been suggested that the stability of remanence in MD magnetite is due to stress controlled areas which behave in a SD-like manner (Dunlop & Argyle, 1991; Heider *et al.*, 1992; Argyle *et al.*, 1994). However there is also evidence from crushed MD magnetite samples to suggest that stability is a truly MD phenomena (McClelland & Shcherbakov, 1995). If the latter hypothesis is correct then "low-stress" magnetites would be expected to show stability of remanence, however by the former hypothesis they would not. There is also evidence to suggest that stability is grain size dependent, *e.g.*, the coercive force decreases over many decades of grain size (Heider *et al.*, 1988a; Dunlop & Özdemir, 1997).

To investigate both grain size dependence and the influence of stress on stability of remanence, it was necessary to have a selection of sized, "low-stress" MD magnetite samples. Three different "sets" of multidomain (MD) samples were used in this study, each of different origin.

Dankers. The material from which these samples were made, was originally prepared by Dankers (1978). The original material consists of crushed natural multidomain magnetite with small traces of titanium. Crushing induces large residual stress within

samples. However the internal stress of samples used in this study had been reduced by subsequent annealing.

Hydrothermal recrystallised. Following the technique developed by Heider & Bryndzia (1987), stoichiometric MD magnetite crystals were made by hydrothermal recrystallisation. Hydrothermal recrystallised grains are known to have very low internal stress (Heider, 1988; Heider *et al.*, 1988a).

Natural Shetland. Natural MD magnetite samples collected from the Shetland Isles. Samples collected from the same location by Dr. R. Gill were known to have very low-coercive forces, *i.e.,* low-internal stress (*pers. comm.* R. Thompson, 1995).

In this chapter the preparation and chemical composition of the samples is discussed. The magnetic properties of the samples are considered in Chapter 3.

In Section 2.2, the Dankers samples used in this study are briefly discussed. The preparation of the hydrothermal samples is discussed in Section 2.3, and in Section 2.4 the collection and sizing of the natural magnetites is discussed.

Because this study is primarily interested in the study of thermoremanence, it was necessary to stop the oxidation of magnetite $\rightarrow$ maghemite $\rightarrow$ hematite, which occurs when magnetite is heated in air. This was achieved by vacuum sealing the samples in quartz capsules (Section 2.6).

2.2 Dankers samples

The "Dankers samples" consist of crushed natural magnetite prepared by Dankers (1978; 1981) from homogeneous unoxidised magnetite separated from gabbro. The samples do not have any optical visible lamellae (Dankers, 1981). The magnetite was crushed in a nitrogen atmosphere and ultrasonically sieved in acetone with photo-etched micro-precision sieves. The sieved grain fractions were; 5-10 μm, 15-20 μm, 20-25 μm, 25-30 μm, 30-40 μm, 75-100 μm and 100-150 μm.

The same material has been used in several other studies (*e.g.,* Dankers & Sugiura, 1981; McClelland & Sugiura, 1987; McClelland & Shcherbakov, 1995). Scanning electron microscope (SEM) analysis by McClelland & Shcherbakov (1995), confirmed the stated grain size fractions are correct to within 10 %; no fine adhering particles were observed.

Electron microprobe analysis and XRD conducted by Dankers (1981), indicated an ≈ 0.1 % Ti content and a small Fe_2O_3 content; maghemite and/or hematite. Using a standard Debye-Scherrer powder camera with FeKα radiation, McClelland & Shcherbakov (1995) measured the lattice parameter to be 8.392 ± 0.002 Å which is slightly less than stoichiometric magnetite (Figure 1.18). Rather than suggesting a small titanium content this suggests the presence of slightly cation-deficient magnetite. They also observed very

weak peaks corresponding to hematite. McClelland & Shcherbakov (1995) measured high-temperature susceptibility curves, however these did not indicate hematite.

2.3 Hydrothermal recrystallisation

Synthetic crystals were made by the method of hydrothermal recrystallisation documented by Heider & Bryndzia (1987). Hydrothermal recrystallisation was chosen over other possible methods, *e.g.*, glass-ceramic method (Worm & Markert, 1987), because it produces synthetic crystals upto 1 mm in size with extremely low-internal stress (Heider *et al.*, 1988a; King, 1996). Hydrothermal crystallisation does not produce crystals of uniform size, unlike some other methods, *e.g.*, electron beam lithography (King, 1996; King *et al.*, 1996) and gel ageing method (Ozaki & Matijević, 1985; Matijević, 1993). The gel aging method has to my knowledge not been used in the production of MD magnetite samples because of the difficulty in producing large grains, *i.e.*, ≥ 1 μm. However since making my hydrothermal magnetites, A. Harrison (Dept. of Chemistry, University of Edinburgh) has informed me that he has managed to grow uniform hematite crystals with a diameter of ≈ 20 μm. Reducing hematite crystals to magnetite is a relatively straight forward process (King, 1996). I suggest here, that future studies should consider using A. Harrison's gel aging technique as a method of producing medium sized MD magnetite crystals of uniform size.

The hydrothermal crystals were made during three visits in February 1995 to the NERC facility high-pressure laboratory at the Dept. of Geology and Geophysics, University of Edinburgh.

2.3.1 Hydrothermal recrystallisation method

The method used in this study closely follows that of Heider & Bryndzia (1987). Here only a brief description of the method is given.

Typically 200 mg of commercially obtained magnetite (Johnson-Matthey, 99.999 % pure Fe_3O_4, average diameter $\approx$ 0.5 μm) was placed in platinum capsules with 80 μl of mineraliser NH_4Cl. The capsules were then sealed, and vertically mounted in high-pressure vessels or "bombs". The bombs were made of a nicol alloy (NiMONiC), which is a suitable buffer to maintain the necessary oxygen fugacity for magnetite production. An air pressure of 2 kbar was applied to the bombs. In a series of experiments, a range of temperatures between 450 °C to 800 °C were applied. Increasing the temperature increases the size of the magnetite crystals (Heider & Bryndzia, 1987). The bombs were then monitored over the next eight days, whilst the magnetite seed material was given time to grow. At the end of the experiment, the bomb was quenched and the magnetite washed with distilled water, and dried with acetone.

A preliminary investigation of the particle sizes was undertaken using an optical microscope. As expected, crystal size was found to be dependent on the temperature,

however the grain distributions were very wide. It was decided to reduce the distribution widths by sieving (Figure 2.1). High-precision nylon sieves with mesh sizes as low as 5 μm were obtained from Sefar Inc., Switzerland.

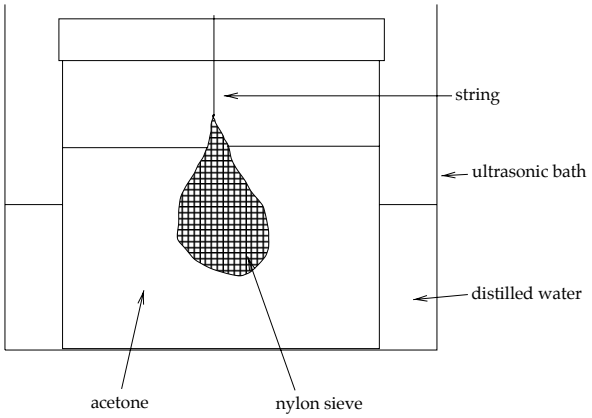


Figure 2.1: Schematic diagram showing the set-up used to sieve the hydrothermal crystals.

After sieving SEM micrographs were taken for size determination. The hydrothermal crystals have shapes similar to those reported for other hydrothermally grown magnetites (Heider & Bryndzia, 1987). The crystals shapes are combinations of rhombic dodecahedral, octahedral and cubic (Figures 2.2 and 2.3). They have rounded corners and edges, and take on spherical appearances. This is in contrast to natural magnetites and other grown magnetites, which are usually octahedral in shape (Figure 2.6). Heider & Bryndzia (1987) suggested that the "ideal" conditions result in decreased surface energy. Spherical and rhombic dodecahedral shapes have a lower surface:volume ratio than octahedra.

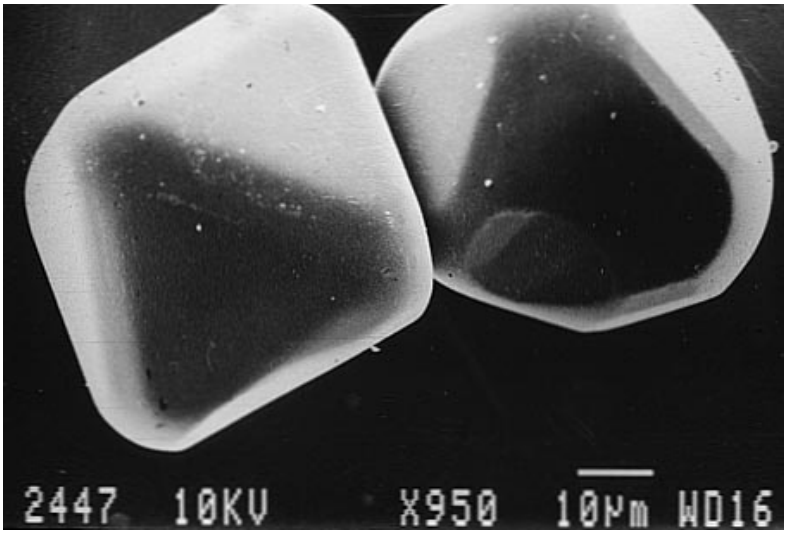


Figure 2.2: SEM photograph of two octahedral hydrothermal recrystallised crystals. Both crystals have rounded edges.

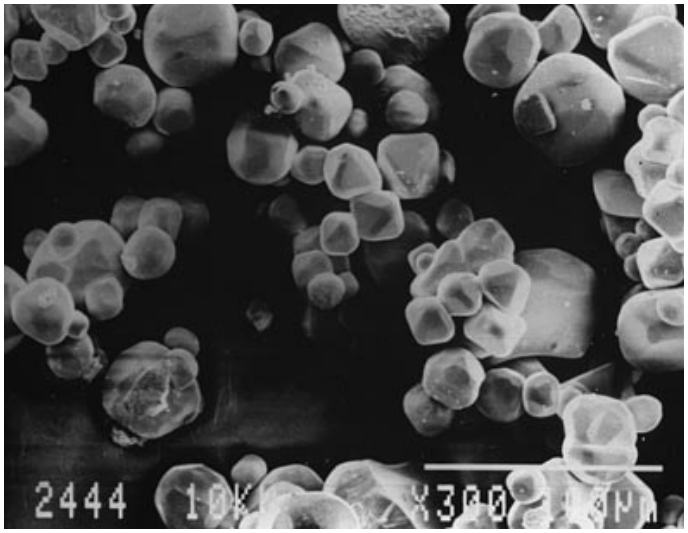


Figure 2.3: SEM photograph of the hydrothermal crystals after sieving. Mean grain size is 39 μm with $\sigma = 9$ μm (sample *H(39 μm)*). The scale bar is 100 μm.

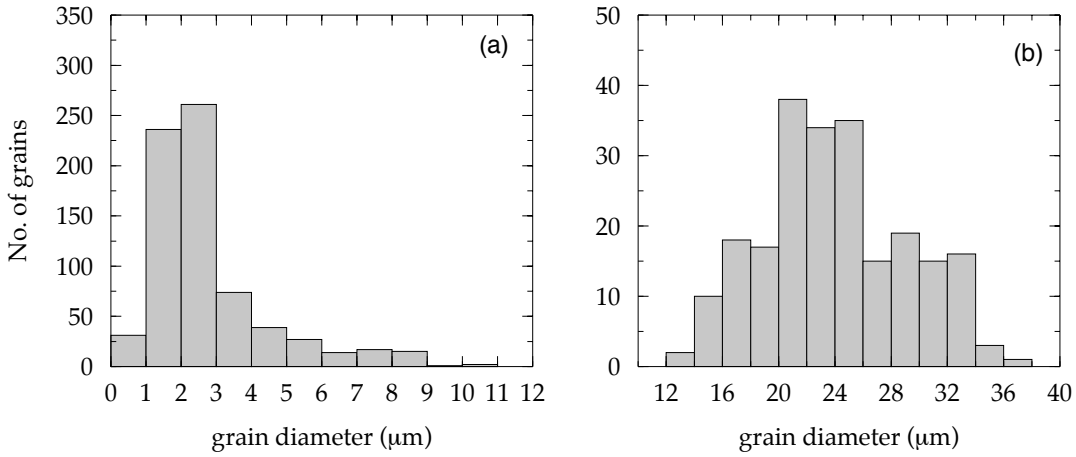


Figure 2.4: Grain size distribution of hydrothermal samples a) *H(3.0 μm)* and b) *H(24 μm)*. Mean grain size of *H(3.0 μm)* is 3.0 μm with $\sigma = 2.4$ μm, and *H(24 μm)* 24 μm with $\sigma = 5$ μm.

After discussions with several people from Dept. of Material Science, University of Oxford, it was decided to determine the size distribution manually. It was realised that there is a tendancy for operators to overestimate the size of the grains (Allen, 1990).

For the smaller sized samples, a large number of grains were counted (Table 2.1), however for the larger grain sizes there was not enough material to do this. Examples of grain size distributions are shown in Figure 2.4. The standard deviations are quite large (Table 2.1), which is a common problem for hydrothermal crystals. For the smaller crystals Heider & Bryndzia (1987) obtained grain size distributions with slightly lower standard deviations to those in Table 2.1, but comparible standard deviations for the larger crystals.

Both Mössbauer spectrometry and XRD analysis was performed on the seed material and the hydrothermal samples. There was no evidence for deviation from stoichiometric magnetite.

sample name	mean size (μm)	$\pm\sigma$ (μm)	particles measured
H(3.0 μm)	3.0	2.4	718
H(7.5 μm)	7.5	3.0	217
H(13 μm)	13	3	211
H(18 μm)	18	6	193
H(24 μm)	24	5	264
H(39 μm)	39	9	243
H(59 μm)	59	16	274
H(76 μm)	76	25	190
H(108 μm)	108	31	168

Table 2.1: Summary of mean grain size and standard deviated σ for the hydrothermal samples examined in the rest of this study. All the particles on several SEM micrographs were measured to deterimine the grain size distribution. The number of particles counted in shown in the last column.

2.4 Shetland magnetite

2.4.1 Collection of Shetland magnetites

Natural magnetites from Shetland were collected in August 1995 during a five day field trip to the Shetland Isles. I was initially informed of the existence of near-stoichiometric, low-coercive force natural magnetites on the Shetland Isles by R. Thompson. It was decided to collect some of these natural magnetites to compare with the Dankers and hydrothermal samples.

Several localities on the Shetland Isles were investigated. The sites were initially identified by Heddle (1878a; 1878b; 1878c), and a full description of the localities is given by Mykura (1976). Two localities were found to have relatively pure magnetites; Pundy Geo, Fethaland Point (OS 376936) and Evaland beach, Fetlar (OS 658914),(Figure 2.5). At both sites magnetite crystals exist in abundance in green chlorite schist matrix. At Pundy Geo the crystals are up to 1 cm in diameter, and at Evaland beach 0.1-0.5 mm in diameter. Whole samples of rock were collected.

On return to Oxford, the crystals from the Pundy Geo rock were removed individually from the soft matrix by a small hand drill. The Evaland beach rock was very soft. A large percentage of it could be broken by hand, the remaining fraction was very lightly crushed. Magnetite crystals were removed from the coarse powder with a hand magnet.

2.4.2 Application of citrate-bicarbonate-dithionite treatment

Because this study was concerned with the properties of stoichiometric magneties, it was decided to apply citrate-bicarbonate-dithionite (CBD) treatment to the Shetland samples. CBD treatment is known to remove surface iron oxide products in grains ≥ 1 μm, whilst grains of ≤ 1 μm are completely removed (Liu *et al.*, 1995; Hunt *et al.*, 1995). It is debatable

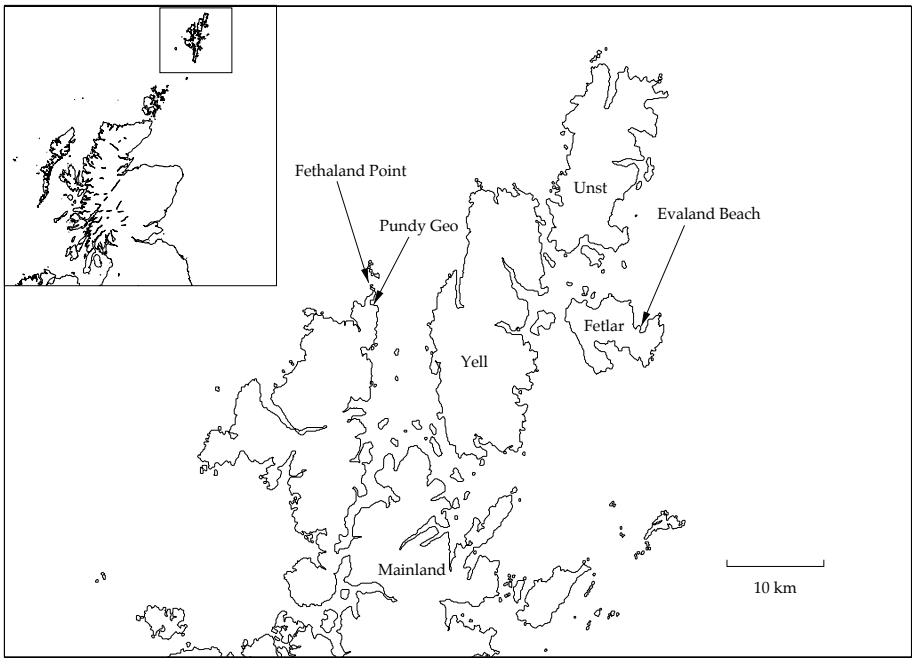


Figure 2.5: Map of the Shetland Isles showing the localities of sampled natural magnetite; Pundy Geo, Fethaland Point (OS 376936) and Evaland beach, Fetlar (OS 658914).

whether CBD treatment preferentially removes maghemite over magnetite (Fine & Singer, 1989; Liu *et al.*, 1995).

The application of CBD treatment to the Shetland samples was intended to remove any surface iron oxides including oxidation products of magnetite, *e.g.*, maghemite.

CBD treatment was applied following the procedure of Hunt *et al.* (1995). The steps are summarised below. Sodium-dithionate acts as a strong reducing agent, and reduces and solubilizes iron oxides including magnetite, maghemite and hematite. Once reduced, Fe^{2+} is chelated by the citrate. The pH of the system is buffered at 7.3 by the sodium bicarbonate. For further details on the chemistry behind the technique see Mehra & Jackson (1960).

Method

2 g of Shetland magnetite crystals were heated in 0.4 l citrate-bicarbonate solution to 70-75 °C. 5 g of dithonate was added and stirred until dissolved. A second 5 g of dithionate was added and stirred until dissolved. The temperature was held between 70-75 °C for 30 minutes. The magnetite crystals were removed from solution, and washed with dilute water. The procedure was repeated for a second time. After the second "extraction" the samples were dried with acetone.

2.4.3 Chemical analysis

The chemistry of the Shetland samples and the effect of CBD treatment are summarised in Table 2.2. Chemical analysis was performed using both Mössbauer spectroscopy and XRD. High-temperature susceptibility analysis (Section 1.8.3) was found to be too insensitive. The samples from Evaland beach were found to be pure iron oxide, whilst the Pundy Geo magnetites had titanium impurities. Samples taken from different sides of Pundy Geo had different titanium content. No maghemite was detected in the Evaland beach samples. No oxidation products were observed for the Pundy Geo samples. There are two possible reasons for this; firstly the Pundy Geo samples had no surface oxidation products, or alternatively the large volume:surface ratio made the presence of surface magnetite oxidation products undetectable to both Mössbauer spectrometry or XRD.

locality	size range (μm)	before CBD	after CBD
Evaland Beach	50-1500	95 % Fe_3O_4 + 5 % α-Fe_2O_3	Fe_3O_4 + trace α-Fe_2O_3
Pundy Geo (west)	500-3000	Fe_3O_4 + trace $FeTiO_2$	Fe_3O_4 + trace $FeTiO_2$
Pundy Geo (east)	500-3000	80 % Fe_3O_4 + 20 % $FeTiO_2$	80 % Fe_3O_4 + 20 % $FeTiO_2$

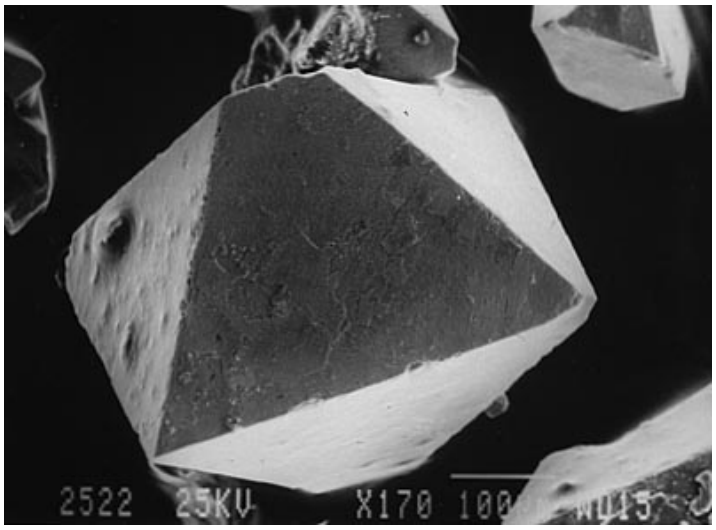
Table 2.2: Summary of the mineralogy of natural Shetland magnetites before and after the application of CBD treatment. The mineralogy was determined by a combination of XRD and Mössbauer spectrometry. The term "trace" is used when mineral content was too low to be quantifiable. Samples taken from different sides of Pundy Geo were found to have different compositions.

The smaller crystals from Evaland beach are seen to be affected by CBD treatment. The larger crystals from Pundy Geo are not. SEM photographs of Evaland beach samples clearly show the effect of CBD treatment (Figure 2.6). CBD treatment removes surface oxidation products revealing a fractured surface. The cracking is a result of maghemitization. Because maghemite and hematite have smaller cell edges than magnetite, the surface oxidation of magnetite $\rightarrow$ maghemite $\rightarrow$ hematite causes stress which induces surface cracking (Özdemir *et al.*, 1993). The crystals are octahedra (Figure 2.6).

The Evaland magnetites were separated into different grain sizes using the same sieving system as shown in Figure 2.1. Repeating the method used for the hydrothermal magnetite samples, grain distributions were obtained manually from SEM micrographs

The natural samples examined in the rest of the study are summarised in Table 2.3. The natural samples are larger than the hydrothermal samples (*cf.* Figures 2.1 and 2.3). The standard deviations of the Evaland beach samples are relatively small compared to the hydrothermal crystals. This difference reflects the difficulty in sieving at small mesh sizes.

a)



b)

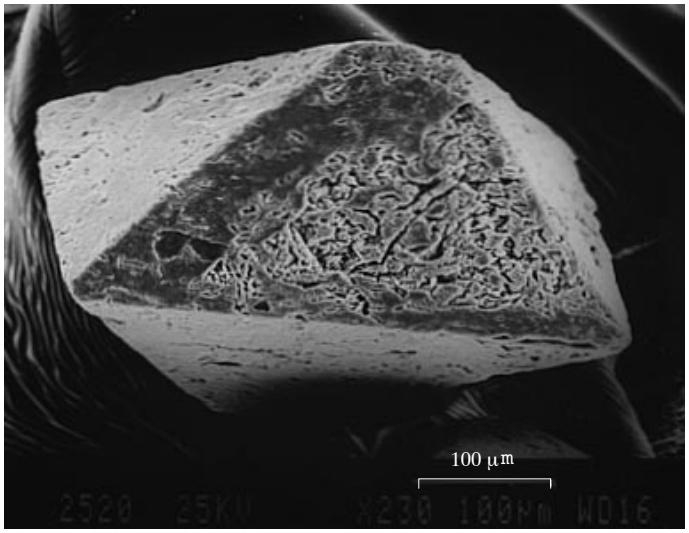


Figure 2.6: SEM photograph of Evaland beach samples a) before CBD treatment and b) after CBD treatment. In figure b) the faint scale is redrawn.

2.5 Other samples

Three other samples were examined in this study; firstly Johnson-Matthey 99.999 % pure Fe_3O_4, which has a mean diameter of ≈ 0.5 μm. XRD and Mössbauer spectroscopy confirmed the purity of the sample. This was the seed material for the hydrothermal crystals and is named *H(seed)*. Two other samples provided by E. McClelland were also examined; a acicular single domain magnetite sample (*SD(acic.)*) and a small multidomain magnetite sample with a mean grain size of ≈ 0.5 μm (*psd-1*). The chemical purity of the last two samples was not examined.

sample name	locality	mean size (μm)	$\pm\sigma$ (μm)	no. of particles measured	composition
E(150 μm)	Evaland	150	25	170	Fe_3O_4 + trace α-Fe_2O_3
E(190 μm)	Evaland	190	30	148	Fe_3O_4 + trace α-Fe_2O_3
E(250 μm)	Evaland	250	30	143	Fe_3O_4 + trace α-Fe_2O_3
E(1.5 mm)	Evaland	1500	···	1	Fe_3O_4 + trace α-Fe_2O_3
PW(1 mm)	Pundy (west)	1000	···	1	Fe_3O_4 + trace $FeTiO_2$
PW(2 mm)	Pundy (west)	2000	···	1	Fe_3O_4 + trace $FeTiO_2$
PW(3 mm)	Pundy (west)	3000	···	1	Fe_3O_4 + trace $FeTiO_2$
PE(3 mm)	Pundy (east)	3000	···	1	80 % Fe_3O_4 + 20 % $FeTiO_2$

Table 2.3: Summary of the natural Shetland magnetite samples used in the rest of the study. All the particles on several SEM micrographs were measured to deterimine the grain size distribution. The mineralogy was determined by both XRD and Mössbauer spectrometry. The term "trace" is used when mineral content was too low to be quantifiable.

2.6 Vacuum sealed capsules

One of the objectives of this thesis, was to experimentally investigate the stability of thermoremanence. It is necessary to heat magnetite to above T_c (578 °C) to induce thermoremanence. To prevent oxidation which occurs on heating in air, the samples were vacuum sealed in quartz capsules. The Dankers samples had been previously sealed in quartz capsules by E. McClelland.

Preparation of vacuum capsules

The magnetite crystals were first dispersed in KBr powder which had been ground by hand in a pestle and mortar. Typically 0.004 g of magnetite was mixed with 0.15 g of KBr, *i.e.*, 2-3 %. Time was taken to disperse the magnetite crystals in KBr. The MD samples did not stick together, however the acicular SD magnetite was prone to clumping. Interaction (clumping) between SD grains in a sample causes the magnetic signature to have MD-like characteristics (Dunlop & West, 1969; Davis & Evans, 1976). Producing synthetic samples containing SD material with no interaction has been a problem for many years. King and co-workers (1996; 1996) have recently developed the first method which avoides clumping and produces equal sized grains, *i.e.*, electron beam lithography. This technique was only fully developed after the preparation of the *SD(acic.)* sample. As it was not the primary aim of this study to examine single domain behaviour, this problem was not considered further, and the SD grains in the *SD(acic.)* sample were allowed to interact. Interactions between MD grains are thought to be less significant than for SD grains (*pers. comm.* W. Williams, 1995).

The dispersed mixture was lightly pressed into pellets using a hand press. Care was taken not to apply excess pressure which would induce dislocations in the sample (King, 1996; Sahu, 1997). The pellets were sealed into evacuated quartz capsules (Figure 2.7). The

glassblowers were careful not to oxidise the magnetite during production. KBr and quartz are both weak diamagnetic materials (Mulay & Boudreaux, 1976).

Two sizes of quartz capsule were made. The first set were similar in size to the Dankers capusles made by E. McClelland, *i.e.*, length = 36 mm and OD = 9 mm. A second set of quartz capsules were made which were designed to fit into the sample chamber of a Quantum Design Magnetic Property Measuring System (MPMS), *i.e.*, length = 36 mm, OD = 7.3 mm (Figure 2.7).

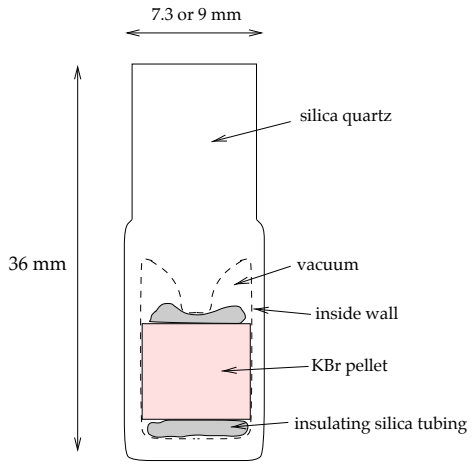


Figure 2.7: Schematic diagram showing a vacuum sealed quartz capsule. OD = 9 mm for the large capusles and 7.3 mm for capsules designed to fit into the MPMS.

Chapter 3

Magnetic characterisation of samples

3.1 Introduction

In magnetic studies it is important to classify and characterise the samples of interest before attempting to examine theoretical problems. Examination of hysteresis loops (Section 1.6) is a simple and standard method of classifying magnetic samples (Thompson & Oldfield, 1986).

In this chapter hysteresis loops and hysteresis parameters of the various samples prepared in Chapter 2 are presented. The hysteresis parameters considered in this chapter, are defined in Figure 1.12; coercive force (H_c), remanent coercive force (H_{rc}) and the reduced saturation isothermal remanence, *i.e.*, the saturation isothermal remanence (SIRM) divided by the saturation magnetisation (M_s). SIRM is often refered to as M_{rs} in hysteresis studies. In accordance with the literature the term M_{rs}/M_s is used to denote the reduced saturation isothermal remanence rather than SIRM$/M_s$.

3.2 Hysteresis parameters and their relation to domain state and internal stress

A grain's domain structure can respond to an applied field in one of three ways. For multi-domain (MD) structures in the presence of small fields, the domain structure rearranges by either the movement of domain walls (Figure 1.13) or nucleation/denucleation of domain walls. If the applied field is large enough then orientation of the domain can rotate. The method of rotation is unclear. For single domain (SD) grains it was originally thought that the entire domain rotated ("coherent rotation") (Néel, 1955), however recent micromagnetic models suggest vortex nucleation as an intermediate step during reversal (Williams & Dunlop, 1995). This has since been supported by experimental evidence (King, 1996). The energy associated with vortex nucleation is far greater than that of domain wall movement.

As SD grains can only respond to the field by vortex nucleation the hysteresis parameters associated with SD grains are larger.

The hysteresis parameters of MD grains reflect the degree of resistance to domain wall movement. Stress fields around impurities or dislocations control this resistance. The localised coercive force which a domain wall experiences in the vicinity of a dislocation is termed the microcoercive force h_c, whilst the measurable term H_c is refered to as the bulk coercive force. Calculations by several researchers (*e.g.*, Stacey & Wise, 1967; Aharoni, 1985; Xu & Merrill, 1989; 1990a; 1992; Moskowitz, 1993b) have shown how H_c is related to h_c for high and low dislocation densities. It is calculated that h_c is dependent on both dislocation density and the ratio of dislocation size to wall width. The dependency of H_c on microstructure is confirmed by experimental studies (*e.g.*, Banfield *et al.*, 1994; Harrison & Putnis, 1997). H_c is grain size dependent (Roquet, 1954; Néel, 1955).

Classically $M_{rs} \propto H_c$ (Xu & Merrill, 1990a). M_{rs} displays similar dependencies on grain size and microstructure as H_c (Heider *et al.*, 1988a). Theoretically, for randomly orientated single domain grains $M_{rs}/M_s = 0.5$ (Néel, 1955). For MD grains this ratio is reduced.

In the most extensive study to date of H_{rc} of MD magnetite, Heider *et al.* (1996) have shown experimentally that H_{rc} is less dependent on grain size and internal stress than either H_c or M_{rs}/M_s. This disagrees with theoretical considerations (Xu & Merrill, 1992).

3.3 Measurement of hysteresis loops

Hysteresis loops were measured using a Princeton Measurements alternating gradient force magnetometer (AGFM) for all the samples apart from the large single crystals, *i.e.*, natural Shetland crystals ≥ 0.5 mm in diameter. Two AGFMs were used in this study; one located at the School of Electronic Engineering Science, University of Wales, in Bangor, and the other at the Institute for Rock Magnetism, University of Minnesota. AGFMs became commercially available in the 1980's (O'Grady *et al.*, 1993), and have since become widely used in rock magnetism. The sample size on an AGFM is substantially smaller than for other more established methods, *e.g.*, vibrating sample magnetometer (VSM). Vlag *et al.* (1996) have verified that the smaller sample size does not affect the hysteresis parameters.

AGFMs are particularly simple to use; a few crystals from a sample are dispersed in silica gel and placed on the sample holder, ready for measurement. Measurement time for a hysteresis loop is typically fifteen minutes. Determination of H_{cr} takes approximately another ten minutes.

For the large natural Shetland samples, *i.e.*, *E(1.5 mm)*, *PW(1 mm)-PW(3 mm)* and *PE(3 mm)*, only H_{rc} was determined. This was measured in Oxford using a pulse magnetiser and magnetometer.

The hysteresis loops of hydrothermal magnetites *H(3.0 μm)* and *H(39 μm)*, and the hydrothermal seed material *H(seed)* are shown in Figure 3.1. The two hysteresis loops for

H(3.0 μm) and *H(39 μm)* are representative of all the hysteresis loops measured for the hydrothermal, Dankers and natural Shetland samples. The smaller samples, *e.g., H(3.0 μm)*, displayed slightly more hysteresis than the larger samples represented by *H(39 μm)* (Figure 3.1). The only sample to show significant hysteresis was *H(seed)* (Figure 3.1). The acicular magnetite sample was not measured.

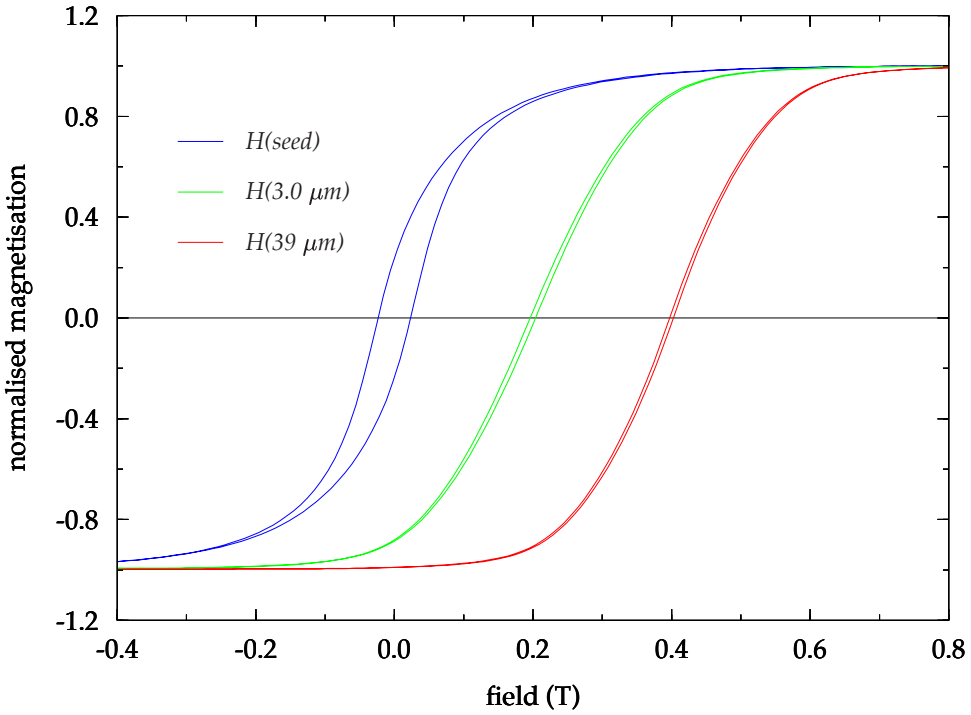


Figure 3.1: Hysteresis loops for hydrothermal samples *H(3.0 μm)* and *H(39 μm)*, and the hydrothermal seed materials *H(seed)*. *H(seed)* was the only sample measured to show significant hysteresis. The hysteresis loops for *H(3.0 μm)* and *H(39 μm)* have been shifted along the x axis. Maximum applied field was 1 T.

Inspection of hysteresis loops can provide useful qualitative information, especially for SD and small MD samples, however it is the comparison of hysteresis parameters such as H_c and M_{rs} which provides quantitative information.

3.4 Hysteresis parameters as a function of grain size

The hysteresis parameters were calculated by the AGFM support software.

3.4.1 Comparison of measured and published hysteresis parameters for Dankers material

The measured hysteresis parameters H_c and H_{rc} of my Dankers samples (*D(5-10 μm)-D(100-150 μm)*) are compared to identical measurements performed on the same source

material by Dankers (1981), Dankers & Sugiura (1981) or McClelland & Shcherbakov (1995) in Figure 3.2.

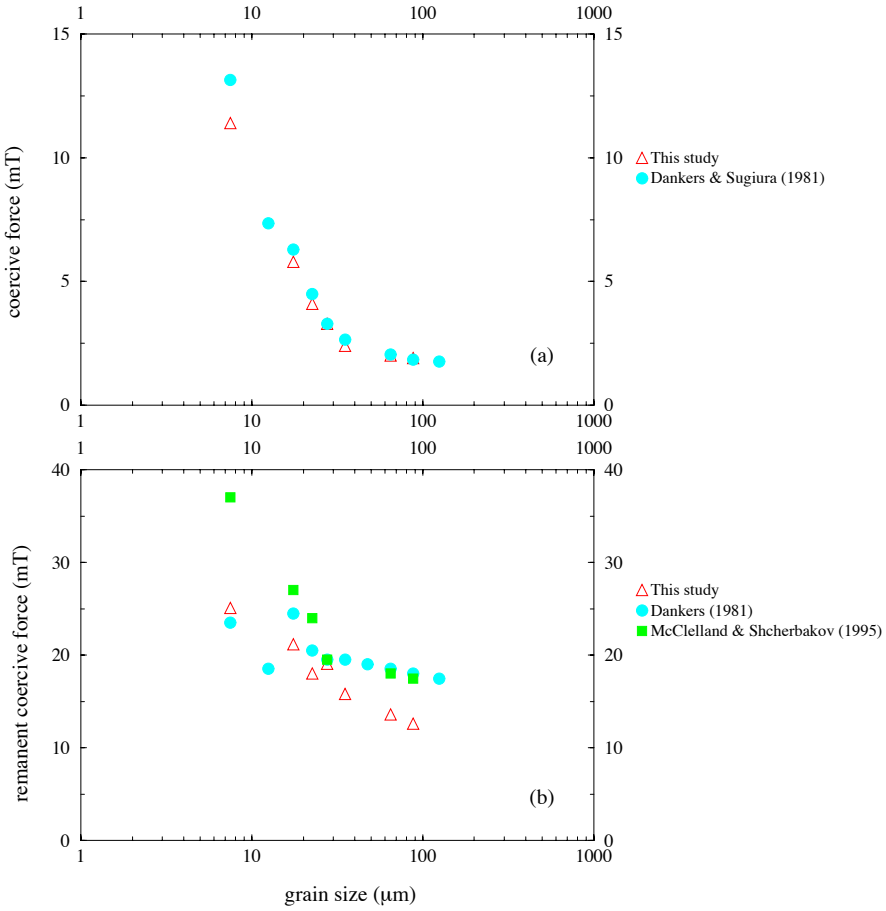


Figure 3.2: a) H_c and b) H_{cr} as function of grain size for Dankers material. All measurements were performed on unannealed Dankers material. The Dankers material is not stoichiometric magnetite, it has ≈ 0.1 % Ti content (Section 2.2).

For the smaller grains my values for H_c are slightly lower than the published data (Figure3.2a). There is no significant difference for the larger grains. Reduction in H_c can be an indicator of oxidation. Goss (1987) has shown that H_c decreases during maghemitisation of single domain magnetite grains. Özdemir & O'Reilly (1982) measured a similar decrease for low-grade maghemitisation of single domain $Fe_{2.4}Ti_{0.6}O_4$. The Dankers samples had been stored in air for several years, which previous studies have shown is sufficient for significant maghemitisation to occur (Hunt *et al.*, 1995). It seems likely that the reduction of H_c for the Dankers samples is due to oxidation since the samples were originally made. The smaller grains are particularly susceptible to oxidation as they have a larger volume:surface ratio.

Values for H_{rc} measured in this study, are slightly lower than those reported by Dankers (1981) and McClelland & Shcherbakov (1995) (Figure 3.2b), however a similar grain

size dependency is observed, *i.e.,* H_{rc} decreases with grain size. There are two possible reasons for the difference between the published data and my data for H_{rc}; firstly the oxidation suggested from the measurement of H_c would be expected to reduce H_{rc}. A second possible cause is variations in concentration. Dankers & Sugiura (1981) have shown that H_{rc} decreases with increasing concentration, and is more sensitive to variations in concentration than H_c. An increase in concentration for my samples would explain the decrease in H_{rc}. It should be noted that the reduction is probably not a result of different instrumentation, because Vlag *et al.* (1996) found that remanent coercive forces measured on an AGFM were slightly *larger* than those measured on a VSM.

In summary it appears that the Dankers material used in this study has oxidised slightly since it was prepared by Dankers (1981).

3.4.2 Comparison of all measured hysteresis parameters with the literature

Hysteresis parameters H_c and M_{rs}/M_s for the Dankers, hydrothermal and natural Evaland beach magnetites are shown with selected data from the literature in Figures 3.3 and 3.4. H_c and M_{rs}/M_s show similar grain size dependences. There is an offset in both H_c and M_{rs}/M_s between the size trends for crystals which were grown by either gel aging or hydrothermal recrystallisation, and grains which were crushed. It is assumed that the increase in both H_c and M_{rs}/M_s in the crushed grains is due to their higher dislocation densities. Both the effect of stress and size dependency on H_c and M_{rs}/M_s has been well documented (*e.g.,* Heider *et al.*, 1988a; King *et al.*, 1996; Dunlop & Özdemir, 1997).

The measured values for H_c and M_{rs}/M_s for the Dankers samples are slightly lower than for other crushed magnetites (Parry, 1965; Day *et al.*, 1977, Figures 3.3 and 3.4.). The origin of this difference is probably the nonstoichiometric nature of the Dankers samples which were slightly maghemitised titanomagnetites, *i.e.,* titanomaghemites. The titanium content (0.1 %) would not be expected to reduce H_c (Day, 1977), however the low-grade maghemitisation would.

My hydrothermal samples have slightly higher H_c and M_{rs}/M_s values than those reported by Heider *et al.* (1988a) for assemblages of dispersed magnetite (Figures 3.3 and 3.4 respectively). However they have comparable values for H_c and M_{rs}/M_s to the individual single crystals measured by Heider (1996). It is worth considering the results for the hydrothermal crystals of Heider *et al.* (1988a) and Heider (1996). Presuming the method of production is identical and that both sets of hydrothermal crystals are stoichiometric, there are only two possible causes for the difference in H_c and M_{rs}/M_s from these two studies (Figures 3.3 and 3.4). One is that systems used to measure the hysteresis parameters were not calibrated properly. Another is that grain interactions in the dispersed magnetite assemblages measured by Heider *et al.* (1988a) significantly reduce the hysteresis parameters. It should be noted that the hysteresis parameters for my hydrothermal magnetites and the single crystals of Heider *et al.* (1996) were measured using an AGFM, whilst the results

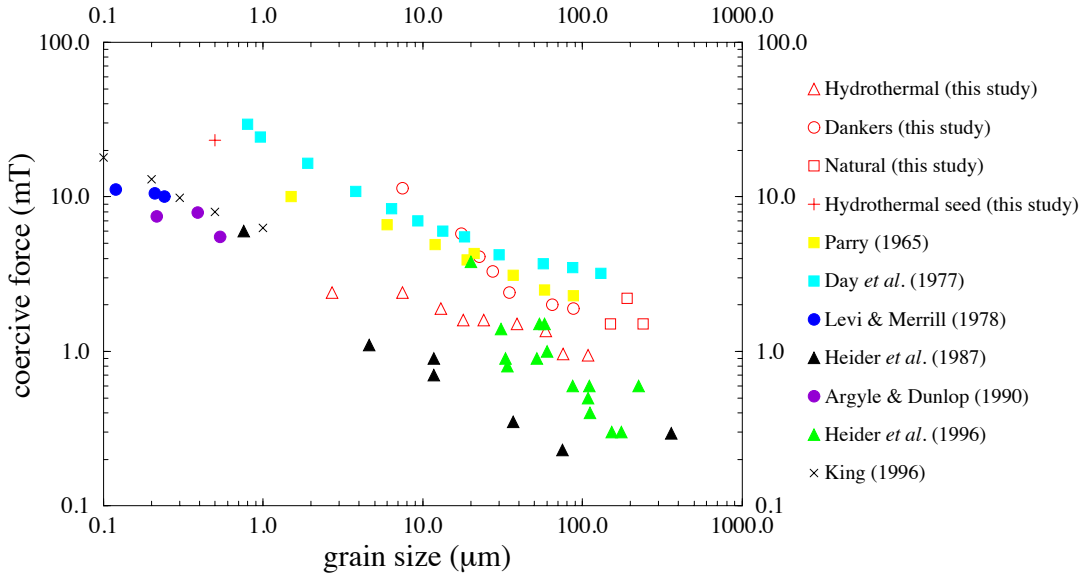


Figure 3.3: H_c as a function of grain size for the Dankers, hydrothermal and Evaland beach magnetites described in Chapter 2. In comparison with my results, data from selected studies are also presented. Hydrothermal crystals are represented by △, annealed crystals by ○, unannealed, crushed or natural by □ and crystals produced by electron beam lithography by ×. My samples are represented by open symbols, *e.g.*, ○, whilst previously published data are shown as closed symbols, *e.g.*, ●. Note the results of Heider *et al.* (1996) are for single crystals.

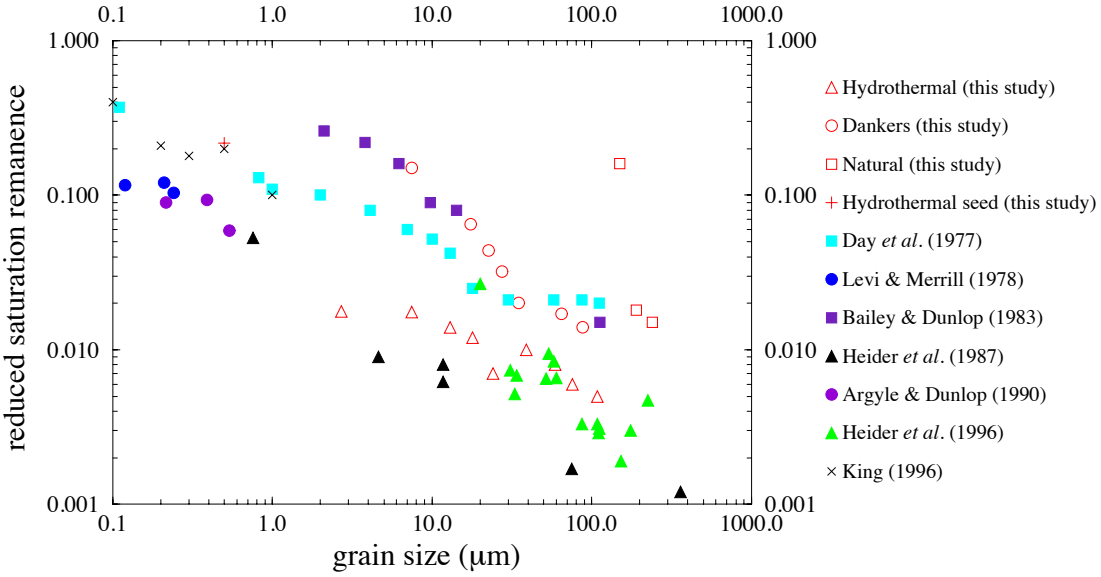


Figure 3.4: Reduced magnetisation (M_{rs}/M_s) as function of grain size for the Dankers, hydrothermal and Evaland beach magnetites described in Chapter 2. In comparison with my results, data from selected studies are also presented. Hydrothermal crystals are represented by △, annealed crystals by ○, unannealed, crushed or natural by □ and crystals produced by electron beam lithography by ×. My samples are represented by open symbols, *e.g.*, ○, whilst previously published data are shown as closed symbols, *e.g.*, ●. Note the results of Heider *et al.* (1996) are for single crystals.

of Heider *et al.* (1988a) were measured using a vibrating sample magnetometer VSM for the grains $\leq$ 50 μm and a magnetometer that used a superconducting quantum interference device (SQUID) for grains $\geq$ 50 μm. Presuming that the AGFM and the VSM/SQUID were correctly calibrated then the difference must be due to grain interactions. This would imply that my hydrothermal crystals did not significantly interact with each other. Ignoring the results from the single crystals, another possible explanation for the difference in H_c and M_{rs}/M_s (Figures 3.3 and 3.4 respectively) between my hydrothermal samples and those of Heider (1988a), is the variation in grain distribution widths. Generally speaking Heider and co-workers (Heider & Bryndzia, 1987; Heider, 1988; Heider *et al.*, 1988a; Heider *et al.*, 1992; Heider *et al.*, 1996) have managed to obtain narrower grain distributions, *e.g.*, my samples *H(18 μm)* and *H(24 μm)* had standard deviations of 6 μm and 5μm respectively (Table 2.1), whilst Heider *et al.* (1992) made 20 μm and 25 μm samples both with a standard deviation of only 3μm. Because the rate of decrease of both H_c and M_{rs}/M_s is approximately logarithmic with grain size, then my samples with a higher proportion of smaller grains should be expected to have higher values for H_c and M_{rs}/M_s. This is seen to be the case in Figures 3.3 and 3.4.

The natural Evaland beach magnetites (Section 2.4) have values for H_c and M_{rs}/M_s which are comparable with the crushed magnetites (Figures 3.3 and 3.4). This suggests that the Evaland beach magnetites were highly stressed. Note H_c and M_{rs}/M_s were not measured for the larger Shetland magnetites; *E(1.5 mm)*, *PW(1 mm)-PW(3 mm)* and *PE(3 mm)*.

The measured values of H_{cr} for the Dankers, hydrothermal and natural Shetland magnetites are shown with selected data from the literature in Figure 3.5.

The Dankers and hydrothermal samples display a grain size dependence, however this dependency is weaker than for either H_c and M_{rs}/M_s (Figures 3.3 and 3.4 respectively). The crushed Dankers samples display a slightly stronger grain size dependency than the hydrothermal samples, and there is a bigger scatter in the hydrothermal crystals remanent coercive forces. The remanent coercive forces of the Dankers samples are of a similar magnitude to those of the hydrothermal crystals. This is in agreement with the results of Heider *et al.* (1996), who observed that crushed grains $\geq$ 10 μm have similar H_{cr} to grown magnetites. The comparable H_{cr} values for hydrothermal and crushed magnetites indicate that hydrothermal crystals can carry stable remanence.

The large Shetland magnetites from Pundy Geo (*PW(1 mm)–PW(3 mm)* and *PE(3 mm)*) all have very low H_{cr} values, *i.e.*, 8–11.5 mT. The H_{cr} values for the Pundy Geo magnetites are slightly lower than those measured for "green schist" magnetites by Heider *et al.* (1996). This suggests that the Pundy Geo magnetites have exceptionally low internal stresses. Heider *et al.* (1996) noted that grains $\geq$ 110 μm in diameter had on average lower H_{cr} values. They tentatively speculated that 110μm is a the pseudo-single-domain/MD transition. The Shetland magnetites from Evaland beach (*E(150 μm)–E(250 μm)*) display similar H_{cr} values to the hydrothermal and crushed crystals. If the hypothesis of Heider *et al.* (1996) is correct, then the data from the Evaland beach magnetites indicate a higher pseudo-single-

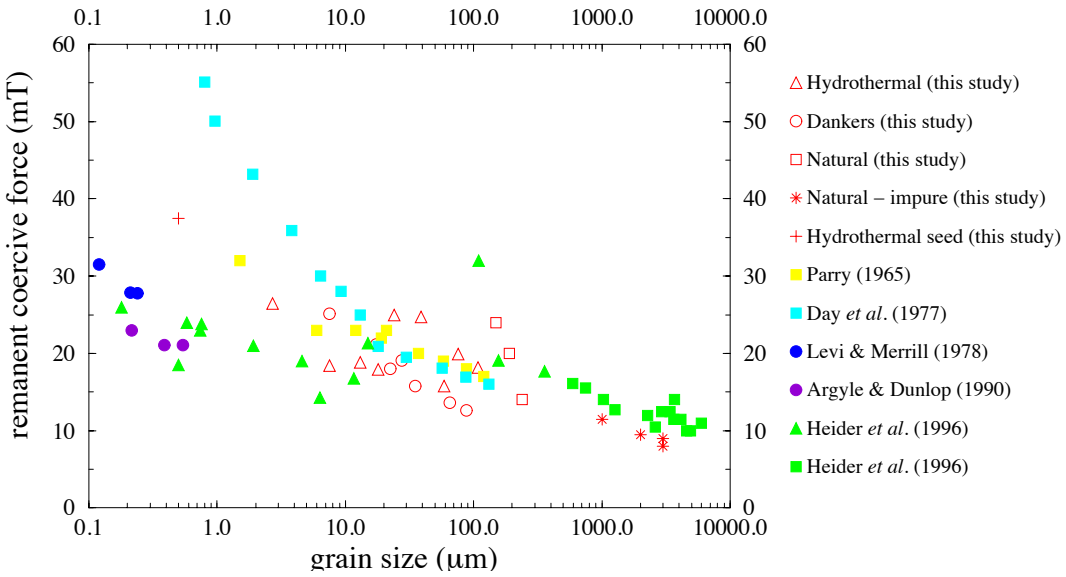


Figure 3.5: H_{cr} as function of grain size for all the samples considered in this study (Chapter 2). In comparison with my results, data from selected studies are also presented. Hydrothermal crystals are represented by △, annealed crystals by ○, and unannealed, crushed or natural by □. My samples are represented by open symbols, *e.g.*, ○, whilst previously published data are shown as closed symbols, *e.g.*, ●. The results for the natural crystals in this study, *i.e.*, Natural (∗) and "Natural - impure" (*) are for *E(150 μm)-E(250 μm)* and *PW(1 mm)-PE(3 mm)* respectively. Note the results for hydrothermal magnetites from Heider *et al.* (1996) are for *assemblages* of dispersed crystals.

domain/MD transition than 110μm.

Chapter 4

Behaviour of partial thermoremanences on cooling below the acquisition temperature

4.1 Introduction

A thermoremanence acquired between T_c and room temperature is referred to as a TRM, whilst thermoremanence acquired over any other temperature range as a partial thermoremanence or pTRM. This chapter examines the temperature dependent behaviour of pTRM on cooling after acquisition. All measurements are above room temperature.

According to "classical" hysteretic multidomain (MD) thermoremanence models (*e.g.*, Néel, 1955; Stacey, 1958; 1962; Everitt, 1962; Schmidt, 1973; Dunlop & Xu, 1994; Xu & Dunlop, 1994 and appendix of Shcherbakov *et al.*, 1993), during pTRM acquisition domain walls either block at some temperature T_b or will reequilibrate to a remanence carrying or demagnetised state when the field is removed at a temperature T_2, where $T_2 \leq T_b$. On cooling below T_2 it is assumed that pTRM will vary as the ratio of $M_s(T)/M_s(T_2)$ denoted by $m_s(T)$, where M_s is the spontaneous magnetisation and T the temperature. Because $M_s(T)$ increases with decreasing temperature (Figure 1.17), $m_s(T) \geq 1$ for all $T \leq T_2$. According to classical theory, the ratio pTRM$/m_s(T)$ is constant on cooling below T_2, however pTRM$/m_s(T)$ has been found to *decrease* on cooling below T_2 for MD magnetite (*e.g.*, Parry, 1979; Markov *et al.*, 1983; McClelland & Sugiura, 1987; Sholpo *et al.*, 1991, Figure 4.1). This decrease in the remanence on cooling indicates that domain reorganisation occurs, which violates the idea of a "blocked" domain structure fundamental to the classical model.

In a similar experiment, Sugiura (1981) found that isothermal remanences (IRM) induced at 240 °C in MD magnetite also decrease on cooling to room temperature when the change in $m_s(T)$ is taken into account. This again violates the classical MD theory and questions the concept of "blocked" domain structure.

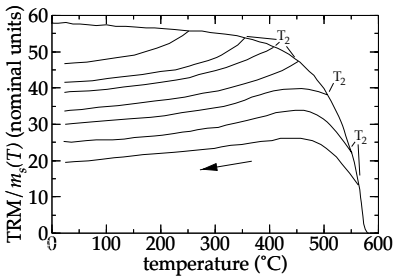


Figure 4.1: Changes in $\text{pTRM}_{T_2}^{T_c}$ as a function of temperature for a peridotite sample containing magnetite with MD hysteresis characteristics, *e.g.*, H_c = 3.8 mT, H_{cr} = 8.5 mT and M_{rs}/M_s = 0.08 (see Chapter 1 for definition of parameters). Field H = 100 μT between T_c and T_2, and zero below T_2. After Sholpo *et al.* (1991).

It should be noted that viscous decay (Dunlop, 1973b; 1983) is not the cause of this decrease in either pTRM or IRM, because no change is observed if the samples are held at a constant temperature (Sugiura, 1981; McClelland & Sugiura, 1987).

4.1.1 Observational Data

Domain structure of MD magnetite as a function of temperature

In addition to measurement of pTRM below T_2, direct observations of domain walls in MD magnetite using optical techniques have found a temperature dependence of domain structure which disagrees with classical domain models (*e.g.*, Heider *et al.*, 1988b; Heider, 1990; Ambatiello *et al.*, 1995). Using the Bitter pattern technique (Bitter, 1931; Bozorth, 1951), Heider and co-workers (1988; 1988b; 1990), found that heating MD grains of magnetite (natural and synthetic hydrothermal) to a temperature of 122 °C was sufficient to cause pronounced changes in fairly complicated domain structures; the number of domains decreasing with temperature. The samples had been previously alternating field (AF) demagnetised at room temperature (maximum field, H = 100 mT, Chapter 1) and had no remanent magnetisation. Few further changes were observed in the domain structure on heating up to 200 °C. On cooling back to room temperature some domain structures were found to (approximately) return to the initial domain state, whilst others did not. There appeared to be no particular reason as to why some domain structures were reversible and others irreversible. The possibility that the change in domain structure was caused by a small residual fields ($< 20\mu$T) was eliminated as the same type of changes were observed in variously orientated applied fields up to 1 mT. It was concluded that the temperature dependent changes in domain structure are intrinsic to multidomain magnetite. However between 10–20 % of the smaller grains ($\leq$ 10 μm in diameter), showed temperature independent behaviour on heating to as high as 350 °C.

In contrast to Heider and co-worker's results, using the magneto-optical Kerr effect (MOKE, Hoffmann *et al.*, 1987; Dunlop & Özdemir, 1997), Ambatiello *et al.* (1995) observed simple lamellar structures on a (110) polished surface of a 6 mm natural crystal. Only minor

reversible changes in the domain structure were observed on heating to 400 °C, but above this temperature strong irreversible changes occurred.

The discrepancy between the two observed domain patterns ,*i.e.,* complicated (Heider *et al.*, 1988b; Heider, 1990), and simple (Ambatiello *et al.*, 1995), is due to the orientation of the samples. Simple, "classic" domain structures in MD magnetite are observed when viewed on the (110) surface, but for "unfavourably" orientated samples, *e.g.,* (111) surface, the domain structures are more complicated (Özdemir & Dunlop, 1993; 1995; 1997). Ambatiello *et al.* used orientated samples ((110) plane) whilst Heider and co-workers did not, which explains the dissimilarities in the observed domain structures. However this does not explain the differences in temperature dependent behaviour, for which there appears to be no clear reason. The only possible cause is differences in the samples' compositions and internal stresses; Heider and co-workers studied both natural and stoichiometric, low-stress synthetic magnetites, whilst Ambatiello *et al.* examined only one natural crystal.

Domain structure during TRM acquisition

It is possible to directly observe changes in the domain structure during TRM acquisition, however to my knowledge there have been no such optical TRM studies of magnetite. This is mainly due to the technical difficulties of heating samples to T_c (≈ 578 °C). However there have been several optical studies of TRM acquisition for Ti-rich titanomagnetites (*e.g.,* Metcalf & Fuller, 1986; 1987a); Halgedahl, 1991), which have lower Curie temperatures *e.g.,* for $Fe_{2.4}Ti_{0.6}O_4$ (TM60), $T_c \approx 150$ °C (Readman & O'Reilly, 1972).

Metcalf & Fuller (1986; 1987a; 1988) have found that after cooling from T_c to room temperature in the earth's geomagnetic field, TM60 grains of $14 \times 7\mu$m in dimension, are sometimes in energetically unfavourable single domain (SD) states. Note the critical SD/MD threshold size for TM60 is $\approx 0.6\mu$m (Soffel, 1971; Moskowitz, 1980). Generally Metcalf & Fuller found that the number of domains increased due to domain wall nucleation (discussed in detail in Section 4.1.2), with decreasing temperature. They concluded that the inability of a SD or low-domained MD state to reach its absolute energy minimum (AEM), *i.e.,* some higher MD state, was due to nucleation failure.

Halgedahl (1991) observed the same SD states in $Al_{0.1}Mg_{0.1}Fe_{2.2}Ti_{0.6}O_4$ (AMTM60) grains when induced with a TRM, however contrary to the results of Metcalf & Fuller, she observed that during cooling the domain structure *denucleated* domain walls to reduce the total number of domains. On repeated measurements on the same samples, she found some of the room temperature TRM states had a very high number of domains (Figure 4.2a) compared to the number observed after AF demagnetisation (Figure 4.2b). Note, it is commonly assumed that the AF demagnetised state is a good indicator of the AEM state (Halgedahl, 1991; Ye & Merrill, 1995b). Halgedahl (1991) concluded that the range of TRM domain states (Figure 4.2a), was due to *denucleation* of domain walls from a high number of domains to a lesser number. The room temperature TRM states with large domain numbers

were due to denucleation failure during cooling.

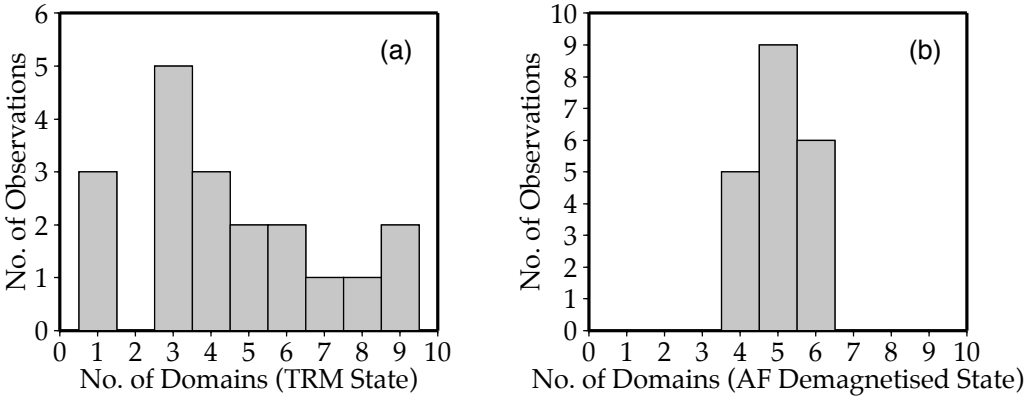


Figure 4.2: Histograms of the number of domains in a AMTM60 grain ($\approx 20 \times 25 \mu$m); a) after TRM experiments ($H = 0.42 \mu$T), and b) following AF demagnetisation (peak alternating field = 90 mT). After Halgedahl (1991).

There is a clear contradiction between the conclusions of Metcalf & Fuller (1986; 1987a; 1988) and Halgedahl (1991). However before attempting to resolve this, it is worth noting some technical difficulties with Bitter pattern imaging.

Note on Bitter pattern imaging

The Bitter pattern technique is achieved by placing fine magnetic particles suspended in oil or water on top of a highly polished surface of a magnetic crystal. The colloid particles are then attracted to the high field regions, namely domain boundaries (Bozorth, 1951).

There are several important limitations which can lead to experimental error and misinterpretation.

- *Preparation of samples.* Polishing samples in preparation for domain observation, can induce crystal defects within the sample. These aid nucleation of domain walls, but impede subsequent domain wall motion, hence altering the magnetic properties of the crystal under examination (Boyd *et al.*, 1984; Dunlop & Özdemir, 1997). Recent improvements in polishing techniques have greatly reduced the amount of stress induced in the sample (Hoffmann *et al.*, 1987).

- *The orientation of the sample.* As mentioned previously the orientation of the viewing plane can radically alter the observed Bitter pattern (Özdemir & Dunlop, 1993).

- *The invisibility of shallow domain walls.* Domain walls near the surface of a crystal are referred to as shallow domain walls. Shallow domain walls do not produce large enough stray fields to attract sufficient colloid to make them visible. Williams *et al.* (1992a) predicted that domain walls shallower $\leq 1.0 \mu$m are invisible to Bitter pattern imaging. This limitation makes shallow closure domains and domain structures in

small grains near the SD-MD threshold invisible. As a consequence Bitter patterns disappear near the edges of domains (*e.g.,* Figure 3 of Halgedahl (1991)). However recently Geiß *et al.* (1996) have managed to observe two domain structures in glass ceramic magnetite crystals of $\approx 0.5\mu$m (with difficulty).

This effect can be beneficial if one intends to examine the main-body domains.

- *Decrease in domain wall visibility with increasing temperature.* The intensity of Bitter pattern images decreases with increasing temperature. It is possible to calculate the domain wall visibility as a function of temperature, and this is done for both magnetite and TM61 in Appendix B. Domain structures in magnetite are visible to 350 °C (Heider, 1988; Heider *et al.*, 1988b), whilst in AMTM60 they are visible to nearly T_c (Halgedahl, 1991).

  The disappearance of a domain wall with increasing temperature does not necessarily indicate the denucleation of the domain wall, it may be due to reduced visibility. However by continuous observation it is possible to distinguish between the two possibilities, as Halgedahl (1991) demonstrates.

After considering these points, it is difficult to resolve the differences between Metcalf & Fuller's (1986; 1987a; 1988) and Halgedahl's (1991) results, because of the variety of possible causes. However I suspect the inclusion of small concentrations of Al and Mg in Halgedahl's AMTM60 may be a significant factor, although Dunlop & Özdemir (1997) ignore these impurities in their discussion. Before dwelling on the cause of the discrepancy, it is worth noting that it is incorrect to directly apply the results from titanomagnetite studies to magnetite, because of the greater importance of magnetostriction in titanomagnetite domain structures. However, some of the TRM results from TM60, if correctly considered can yield important information about the nature of TRM acquisition in magnetite (Ye & Merrill, 1995b)

In summary, optical observations also disagree with the classical MD theory idea of "blocked" domains, *e.g.,* Heider and co-workers (1988b; 1990) have shown that domain walls which according to the classical theory should be blocked and stable, can move easily at low-temperatures.

4.1.2 Theoretical Approaches

To explain these phenomena which disagree with the classical model, several new theories have been developed. Earlier models tried to explain the decrease in pTRM on cooling below T_2, by applying hysteretic models to MD structures of inhomogeneous magnetic hardness (Parry, 1979; Shcherbakov & Markov, 1982; Markov *et al.*, 1983). These models were later found to be flawed (McClelland & Sugiura, 1987; Shcherbakov *et al.*, 1993). More recent models are based on domain wall nucleation/denucleation theories.

Domain state and nucleation/denucleation theory

Moon & Merrill (1984; 1985) considered the discrepancy between classical "hysteresis" theory (Néel, 1955) and both the observed number of domains and the observed nucleation of domain walls in grains of magnetite and titanomagnetite (Halgedahl & Fuller, 1980, 1983; Boyd *et al.*, 1984); the number of domains was higher than theoretically expected and the nucleation of domain walls disagreed with theory.

Hysteresis theories presume that during TRM acquisition the domain structure is close to the global or absolute energy minimum (GEM/AEM) state at all times until certain domain walls became blocked. This leads to a limited number of domain states, however data such as that shown in Figure 4.2, clearly demonstrates this is not the case. Moon & Merrill showed that there are several minimum energy states available to the domain structure, which they termed local energy minima (LEM). Their calculations suggested that sometimes the energy barriers between the different states were too great to be overcome by the internal magnetostatic demagnetising field and thermal fluctuations, *i.e.*, the domain structure can get trapped in high energy, steep-sided LEM potential wells. Moon & Merrill postulated that as the conditions change, *e.g.*, changes in grain size, applied field, temperature *etc.*, energy barriers correspondingly alter, allowing domain wall nucleation and denucleation to occur.

The idea of domain wall nucleation and variable domain numbers led several researchers to calculate the ideal number of domain walls at each temperature and the likelihood of domain wall nucleation with temperature changes. Initially a variety of constrained Rhodes-Rhowlands-Amar (RRA) calculations (Rhodes & Rowlands, 1954; Amar, 1958 and Section 1.2), were used (Moskowitz & Halgedahl, 1987; Shcherbakov *et al.*, 1990; Shcherbakov & Tarashchan, 1990; Xu & Merrill, 1990b). These calculations broke away from classical hysteretic theory by letting the domain wall width to be incorporated into the model. This is especially important at high temperatures, where the domains for an "open domain structure" (ODS), *i.e.*, without closure domains (Shcherbakov *et al.*, 1990), disappear and only a corkscrew-like domain structure remains. Shcherbakov & Tarashchan (1990) present the only RRA calculations which include closure domains ("closed domain structure" (CDS)). The CDS total magnetic free energy is substantially lower than the ODS, however the number of domains at room temperature for the CDS model is very low at two for a 35 μm grain, whilst for the ODS model it is 27. The observed number of domains is around 5-10 for 30-50 μm grains (Worm *et al.*, 1991). By including stress into the model, Ye & Merrill (1995a) have found a better correlation between domain number per grain and observational data for titanomagnetite at room temperature.

These RRA models predict that the number of domains in a magnetite grain will increase with temperature until only domain walls fill the structure (Shcherbakov *et al.*, 1990; Xu & Merrill, 1990b). The remaining "corkscrew" structure gradually unwinds on warming to T_c (Xu & Merrill, 1990b). The number of domains decreases in agreement with the experimental evidence (Heider *et al.*, 1988b; Heider, 1990).

Moon (1991) used a highly-constrained, micromagnetic, corkscrew model for the entire domain structure, that is he allowed for a continuous rotating Bloch wall structure with no areas in the grain where magnetic vectors where in parallel alignment, *i.e.,* domains. He found for magnetite, that the number of LEM states decreased with temperature, in agreement with observation. The application of a field an order of magnitude greater than that of the earth's, made little difference to the number of LEM states at room temperature, but increased the number near T_c. Moon realised the limitations of his corkscrew model, however it does demonstrate the large number of domain states available to grains with temperature.

Unfortunately no reported three-dimensional micromagnetic modelling has tackled this problem, this is partly due to the uncertainties in the anisotropy energies near T_c. However Dunlop *et al.* (1994) considered the transdomain transitions; SD $\leftrightarrow$ 2 domain $\leftrightarrow$ 3 domain during TRM acquisition, using a one-dimensional, stress-free, micromagnetic model. In a development from Moon's (1991) model, they were able to calculate the energy barriers between the LEM states. They concluded domain nucleation only occurs at high temperatures, *i.e.,* $T \geq 553$ °C for SD $\leftrightarrow$ two domain and $T \geq 574$ °C for 2 domain $\leftrightarrow$ 3 domain, and the possibility of domain wall nucleation/denucleation during MD TRM acquisition was unlikely. It should be realised that their model was only one-dimensional which has been argued is an inaccurate approximation to reality (*pers. comm.* W. Williams, 1997).

Domain Nucleation and TRM

The theories and models discussed, have only been concerned with domain nucleation/denucleation as a function of temperature *etc.* They have suggested that nucleation/denucleation is possible, the likelihood increasing with grain size and temperature. Observational data is also limited yet revealing, because it has been found that domain walls move readily in weak fields at low temperatures (Heider *et al.*, 1988b; Heider, 1990).

Incorporating the idea of temperature dependent domain wall nucleation, a kinematic model has been developed to explain thermoremanence acquisition and its behaviour on cooling below T_2 (McClelland & Sugiura, 1987; Shcherbakov *et al.*, 1993). McClelland & Sugiura (1987) assumed that domain walls can be regarded as a statistical ensemble, each element of the ensemble being in one of two possible states: demagnetised or TRM state. During cooling, the domain walls jump randomly between the two states, however in zero-field the demagnetised state is preferred (Figure 4.3a) whilst in a field the TRM state is preferred (Figure 4.3b).

During TRM acquisition the net contribution from the statistical ensemble is a magnetised state, whilst on cooling below T_2 the net magnetisation demagnetises giving rise to the behaviour seen in Figure 4.1.

Shcherbakov *et al.* (1993) developed the theory of McClelland & Sugiura (1987) by considering a theoretical micromagnetic approach, *i.e.,* a number of uniformily-magnetised,

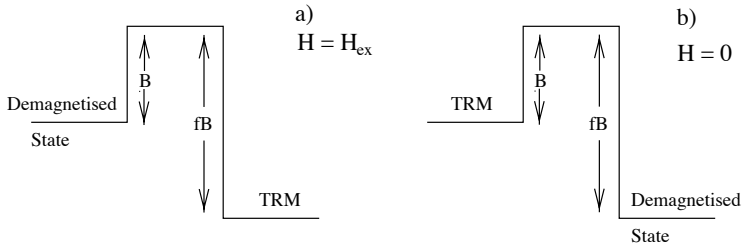


Figure 4.3: Schematic illustration of the two possible states for a domain wall during cooling (a) in a field (b) in zero field. After McClelland & Sugiura (1987).

discrete cells within the grain. Assuming uniaxial anisotropy for each discrete region, they considered a statistical probability that the cells would align in one of two possible directions. In effect they replaced the statistical ensemble of domain walls used by McClelland & Sugiura (1987), with an statistical ensemble of dipole moments. The model of Shcherbakov *et al.* (1993) is similar to that represented by Figure 4.3, but instead of the barrier B/fB representing the energy barrier between the two possible domain wall states, it represents the energy needed to rotate a magnetic dipole between two possible orientations. This model is similar to that of SD theory except that time is replaced by temperature.

The model of Shcherbakov *et al.* (1993) is abstract and unquantitative, and it makes some simplifications which rather invalidate the model; most importantly the model did not calculate the intercellular interaction effect. However the model does predict a decrease in thermoremanence after cooling in zero-field below T_2, allows for the possibility of the irreversibility of pTRM on heating and cooling, and shows the importance of thermal prehistory (Sugiura, 1981; Vinogradov & Markov, 1989). Shcherbakov *et al.* (1993), show that the model is analogous to a spin glass system (Chakravarty, 1980) which is known to be dependent on the thermal prehistory, have a range on metastable states, governed by kinetic equations and never reach thermodynamic equilibrium.

It is worth noting the model of Ye & Merrill (1995b), who have used renormalisation group theory to examine the magnetic structure near T_c for titanomagnetites (TM60). Near T_c the classical domain theory breaks down, because both the magnetocrystalline anisotropy and the magnetoelastic anisotropy tend to zero. Their model examines the probability of clustering when adjacent discrete cells interact with each other. They predict the range of observed domains after TRM acquisition (Figure 4.2a), is due to small thermal fluctuations which effect clustering formation close to the magnetic ordering temperature. These clustering formations Ye & Merrill termed "predomain" structures. They conclude that the final TRM LEM state is dependent on these predomain structures, which vary from experiment to experiment even for identical conditions, and not on nucleation processes which occur at lower temperatures. For magnetite they postulated that nucleation/denucleation processes are more common than for TM60, yet they still stress the importance of predomain structure. This model in some respects is similar to the classical hysteretic model in that once a predomain structure is formed, there will be little or no change in

the domain structure on cooling. In summary the model of Ye & Merrill (1995b) predicts a variety of domain structures, yet in disagreement with experiment does not allow for temperature dependent domain processes at temperatures much less than T_c.

4.2 Measurement of pTRM decrease below T_2

In this Section the behaviour of thermoremanences induced in hydrothermal magnetites to cooling below the acquisition temperature are reported.

Previous studies of pTRM decrease below T_2 have been measured on natural magnetites (Sholpo *et al.*, 1991), crushed natural magnetites (McClelland & Sugiura, 1987) and annealed synthetic samples of unknown preparation (Markov *et al.*, 1983). This is the first time, as far as I am aware, that synthetic magnetite produced by hydrothermal recrystallisation has been used to examine this effect. It has been well documented that hydrothermal crystals' magnetic behaviour is closer to that of natural samples than crushed magnetites (Heider *et al.*, 1988a; Dunlop & Özdemir, 1997, see also Chapter 3).

The results presented here add to the limited experimental evidence, and they also give further support to the kinematic theories of McClelland & Sugiura (1987) and Shcherbakov *et al.* (1993).

4.2.1 Notes on experimental technique

In conjunction with low-temperature experiments described in Chapter 6, continuous records for acquisition of thermoremanence from T_c to T_2 and subsequent cooling to 77 K were recorded on my second visit to the Institute for Rock Magnetism (I.R.M.), University of Minnesota. The I.R.M. is probably unique (certainly in the field of rock magnetism) in that it has equipment which allows the measurement of a complete record of magnetisation from 2 K to 1025 K. Admittedly it is necessary to use two pieces of equipment; above room temperature a Princeton Electronics μ-VSM (Vibrating Sample Magnetometer), whilst below a Quantum Design Magnetic Property Measuring Systems (MPMS).

In this section only the cooling behaviour of pTRM measured on the μ-VSM between T_2 and room temperature is considered. Subsequent measurements on the MPMS are presented in Chapter 6.

Two types of pTRM were induced in the samples;

Type 1 The samples are cooled from above T_c to T_2 in a field, where room temperature, rtp $< T_2 < T_c$ ($T_c \downarrow T_2$, H=ON; $pTRM_{T_2}^{T_c}$).

Type 2 This type of pTRM is acquired by cooling from T_c to a temperature T_1 in zero field, and from T_1 to T_2 in a field, where rtp $< T_2 < T_1 < T_c$ ($T_c \downarrow T_1$, H = OFF; $T_1 \downarrow T_2$, H=ON; $pTRM_{T_2}^{T_1}$).

In both cases below T_2, the samples were cooled in a zero field environment.

The vacuum sealed quartz capsules described in Chapter 2, could not be used on the μ-VSM because they were too large. Instead a set of KBr pellets from each grain size were made in the same manner as described in Chapter 2, *i.e.,* 2-3 % magnetite dispersed in KBr and lightly pressed into a pellet. The μ-VSM allowed the samples to be kept in an inert atmosphere of He during heating which reduced the possibility of oxidation. As an extra precaution against oxidation the pellets were coated in weak-diamagnetic (*pers. comm.* J. Marvin, 1997), high-temperature glue (Omega CC High Temperature Cement). Each sample from each grain size was examined only once.

Note on inducing field and thermoremanence

An immediate problem arose on using the μ-VSM; it had no shielding from the earth's magnetic field. This made it necessary to induce the thermoremanences in fields greater than $\approx 42\mu$T to produce a "step-down" in field when T_2 was reached.

Most experimental evidence in the literature suggests that TRM, *i.e.,* $TRM_{rtp}^{T_c}$, intensity measured is linear with applied field up to 200-400 μT (*e.g.,* Day, 1977; Shcherbakov *et al.*, 1993). However, Parry (1979) found a much higher breaking point of ≈ 3.1 mT for natural magnetite grains with a mean diameter of 200 μm. TRM induced in fields where there is a linear relationship between TRM intensity and field is usually referred to as "weak-field" TRM, and TRM induced in higher fields as "high-field" TRM.

A field of ≈ 200 μT would have been ideal for inducing pTRM, being "weak-field" TRM and with a reasonable step-down in field at T_2. Unfortunately, the low sensitivity of the μ-VSM (sensitivity = 5×10^{-9} Am^2), meant that this was not possible. It was therefore necessary to induce pTRM in higher fields. Initially an inducing field of 5 mT, *i.e.,* 5000 μT was used, however and a few later samples were induced with pTRM in a field of 500 μT.

Due to the uncertainty in the weak-field/high-field transition, on returning to Oxford, it was decided to measure the dependence of thermoremanence intensity on applied field using a selection of samples (hydrothermally recrystallised, crushed and natural multidomain magnetites). It was only possible to apply a calibrated field up to 200 μT, and an uncalibrated field up to 300 μT (Section 1.8). Typical results are shown in Figure 4.4.

The thermoremanence acquisition curves (Figure 4.4) display similar behaviour to the majority of previous results (*e.g.,* Day, 1977; Shcherbakov *et al.*, 1993; Dunlop & Argyle, 1997); the linearity in the relationship begins to break down at 200 μT. It is possible, that the break in linearity is due to errors in the field calibration, and that the linear relationship holds for higher fields. However this is only speculation and it must be assumed that the weak-field/high-field transition field is ≈ 200 μT. The result of Parry (1979) is considered to be sample specific.

In summary, thermoremanences induced in fields as high as 5 mT are probably not analogous to thermoremanences induced in the earth's field, and it is debatable that ther-

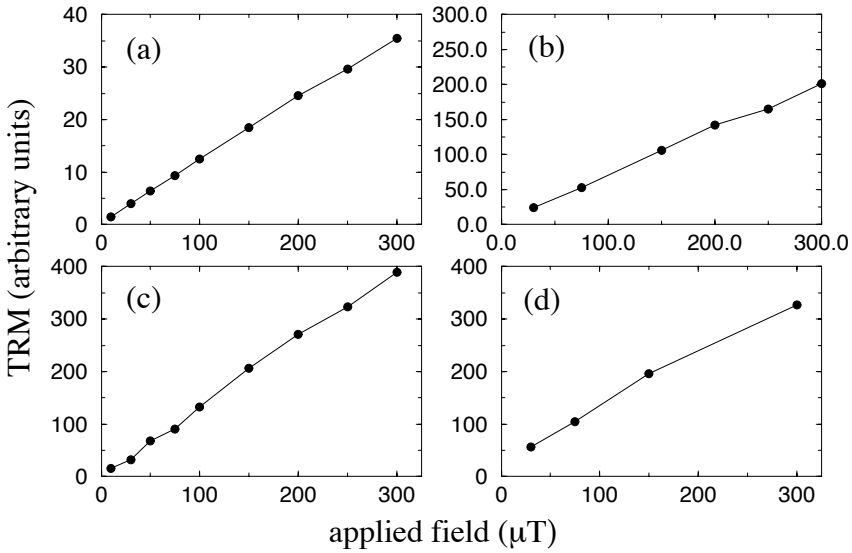


Figure 4.4: $TRM^{T_c}_{rtp}$ intensity versus field for a selection of magnetites, a) crushed synthetic *D(15-20 μm)*, b) hydrothermal synthetic *H(39 μm)*, c) natural *E(150 μm)* and d) natural *PW(3 mm)*.

moremanences induced in 500 μT are analogous either. That is not to say that these type of high-field thermoremanences are not of scientific interest, as they provide further contributions to thermoremanence theory even if the results are not directly applicable to naturally occurring thermoremanences. In fact most previous studies investigating the decrease in pTRM on cooling below T_2, have examined "high-field" thermoremanences, *i.e.*, $H > 300\mu$T, *e.g.*, Parry (1979) and Sugiura (1981) both used a field 1 mT, whilst McClelland & Sugiura (1987) used a field of 0.84 mT. However the observed decrease is not a property confined to high-field thermoremanences, as both Markov *et al.* (1983) and Sholpo *et al.* (1991) have observed the same effect for an inducing field of 100 μT.

4.2.2 Field dependence of pTRM decay on cooling below T_2

The pTRM inducing field in some of my experiments was considerably higher than those used in all previous studies except for Markov *et al.* (1983). Because of this difference it was decided to examine the dependency of pTRM cooling behaviour on H. Markov *et al.* (1983) examined this same problem and found that as H increased the observed demagnetisation in $pTRM^{400}_{300}$ below T_2 decreased (Figure 4.5).

In a similar experiment, Sugiura (1981) measured the decrease of IRM on cooling from an acquisition temperature of 240 °C. He found that as the inducing field increased the relative demagnetisation of IRM decreased (Figure 4.6). Although for a different type of remanence the results of Sugiura (1981, Figure 4.6), show a complimentary field dependency to that found for cooling thermoremanences by Markov *et al.* (1983, Figure 4.5).

Both sets of results are in disagreement with the theories of McClelland & Sugiura (1987) and Shcherbakov *et al.* (1993). Consider initially pTRM acquisition in the model of

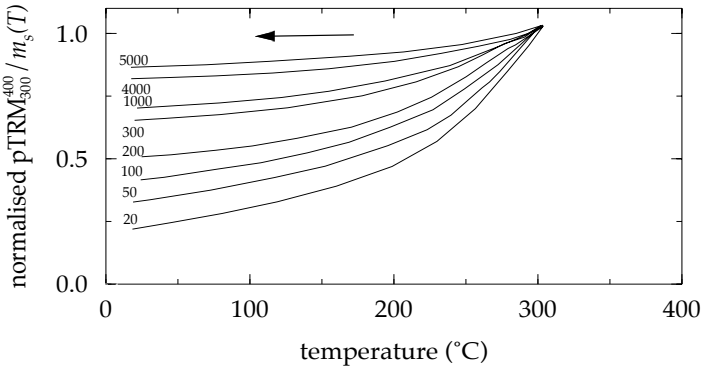


Figure 4.5: Field dependence of the decrease of normalised $\text{pTRM}_{300}^{400}/m_s(T)$ induced in synthetic magnetite (300-400 μm), during cooling to room temperature from 300 °C. Field units are in μT. After Markov *et al.* (1983).

McClelland & Sugiura (1987) represented by Figure 4.3a. Increasing H, increases the height of fB ($\propto H$), which in turn increases the total thermoremanence. Samples with a high-field TRM will have more walls in the TRM state than in the demagnetised state, when the field is switched off at T_2. As the "hopping" rate is dependent on temperature, the net decay should be expected to be greater for a high-field TRM than for the low-field case. From this approach, the demagnetisation of pTRM on cooling below T_2 increases with inducing field intensity. There are similar arguments for IRMs, and also for the model of Shcherbakov *et al.* (1993). The theory is obviously in clear disagreement with the results of Markov *et al.* (1983, Figure 4.5) and Sugiura (1981, Figure 4.6).

To examine this disagreement, I considered my pTRM experiments using hydrothermal recrystallised magnetite. Thermoremanences acquired over the same temperature range, but with different inducing field (5 mT and 0.5 mT), are shown in Figure 4.7 for Type 1 and Type 2 pTRM. As is standard in these type of diagrams, the increase in the spontaneous magnetisation is compensated for.

The reported decrease in $\text{pTRM}/m_s(T)$ on cooling (*e.g.*, Markov *et al.*, 1983; McClel-

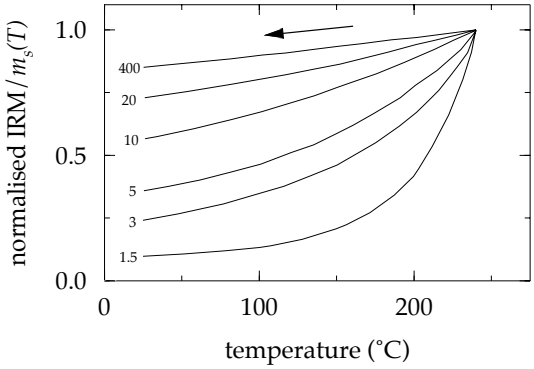


Figure 4.6: Inducing field dependence of the demagnetisation of normalised $\text{IRM}(T)/m_s(T)$ induced at 240 °C in 100-150 μm crushed magnetite. The sample had been previously heated to T_c in zero-field before cooling to 240 °C. Field units are in mT. After Sugiura (1981).

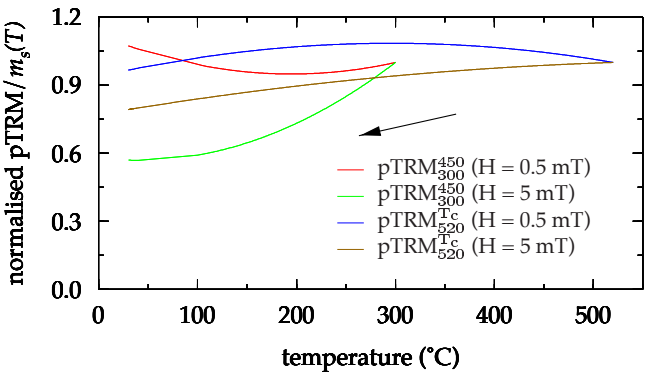


Figure 4.7: Cooling behaviour of normalised Type 1 (pTRM$^{T_c}_{520}$/$m_s(T)$) and Type 2 (pTRM$^{450}_{300}$/$m_s(T)$) for hydrothermal sample *H(76 μm)*, with variable inducing field.

land & Sugiura, 1987; Sholpo *et al.*, 1991) is repeated here (Figure 4.7). However the field dependency of behaviour is opposite to that reported by Markov *et al.* (1983), *i.e.*, the relative demagnetisation of pTRM on cooling below T_2 *increases* with increasing field strength, whilst Markov *et al.* (1983) found a decrease with field. There is no clear reason for the discrepancy, however there are a few possible contributory causes which may account for it. Firstly, my samples were relatively stress-free stoichiometric magnetites, whilst Markov *et al.* (1983, Figure 4.5) used synthetic magnetites (300-400 μm) of unknown origin. Secondly, the temperature range over which the thermoremanences were acquired was different; my thermoremanences were acquired over the range T_c–520 °C for Type 1 pTRM and 450–300 °C for Type 2 pTRM, whereas Markov *et al.* (1983) induced their pTRM (Type 2 only) over the temperature range 400–300 °C. However it is unlikely that pTRMs acquired over 450–300 °C and 400–300 °C should vary significantly in there response to applied field. Lastly, differences in initial domain state could play a significant role. In my Type 2 thermoremanences,the samples were cooled from T_c in zero-field (in fact the earth's field (discussed below)). This domain state is commonly referred to in the Russian literature as the absolute zero state (AZS) (Shcherbakov *et al.*, 1993). The experiments of Markov *et al.* (1983) were carried out before the importance of thermal history had been truly clarified (Vinogradov & Markov, 1989). Because of this Markov *et al.* have not commented on the thermal histories of their samples, only that they were induced with pTRM$^{400}_{300}$. It is unknown if differences in thermal histories affect the field dependency of pTRM cooling behaviour. It should be noted in support of the results of Markov *et al.* , that the behaviour observed by Sugiura (1981, Figure 4.6) was for IRMs induced in AZS MD grains.

It was noted previously that the pTRM$^{450}_{300}$ was not induced in hydrothermal samples in a true AZS, because they had been cooled from T_c in the earth's field. The pTRM$^{T_c}_{520}$ show a similar field dependency (Figure 4.7) as the pTRM$^{450}_{300}$ which suggests that the error in the AZS of pTRM$^{450}_{300}$ was not significant. Markov *et al.* (1983) obtained a residual field of only 1–2 μT.

4.2.3 Note on Viscous decay

At first it might appear that the reduction in thermoremanence on cooling below T_2 is a viscous affect. To check for this a sample was induced with a $pTRM^{T_c}_{480}$ and held at 480 °C for $\approx$ 20 minutes in zero field (earth's field). It was found to remain constant, confirming the theory that demagnetisation on cooling is truly temperature dependent. This corresponds to similar tests reported in the literature (Sugiura, 1981; McClelland & Sugiura, 1987).

4.2.4 Test on irreversibility of thermoremanence

Both direct observation of the domain structure (Heider *et al.*, 1988b) and measurement of the magnetisation (McClelland & Sugiura, 1987; Sholpo *et al.*, 1991) find that thermoremanences are irreversible to changes in the direction of heating/cooling below T_2. Both McClelland & Sugiura (1987) and Shcherbakov (1993) have incorporated this in their theories. A simple check for this phenomenum was done for a selection of samples. A typical result is shown in Figure 4.8. It is seen that hydrothermal recrystallised grains of magnetite (Figure 4.8a) behave in the same manner as crushed grains of magnetite (Figure 4.8b). The decay is larger in Figure 4.8a than in Figure 4.8b, because of the differences in field during pTRM acquisition and the temperature at which the pTRMs were acquired. (Figure 4.7).

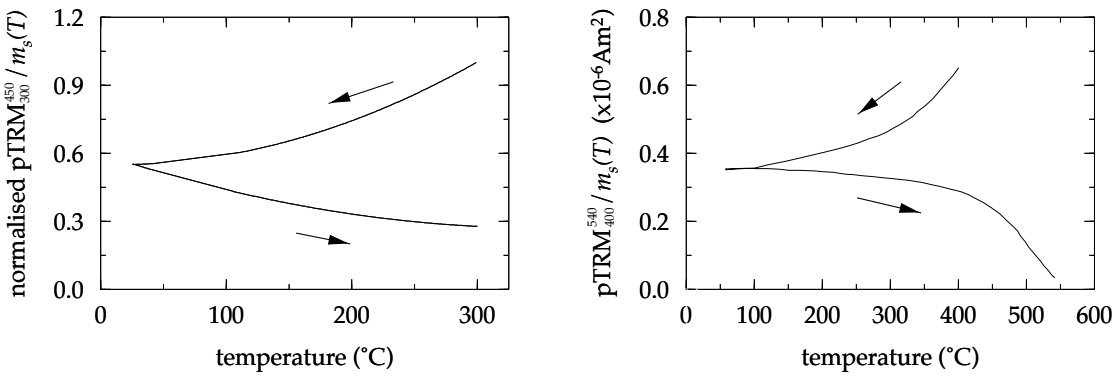


Figure 4.8: Irreversibility of pTRM to changes in heating/cooling direction. a) $pTRM^{450}_{300}$ (H = 5 mT) induced in hydrothermal magnetite sample *H(76 μm)*, and b) $pTRM^{540}_{400}$ (H = 0.84 mT) induced in 100-150 μm crushed magnetite, after McClelland & Sugiura (1987). *Note differences in temperature scale.*

4.2.5 Effect of grain size and pTRM type

In this section, the dependency of pTRM cooling behaviour on grain size and pTRM type is considered. For all experiments in this section a field of 5 mT was used to induce the thermoremanences. The two types of pTRM, *i.e.*, $pTRM^{T_c}_{T_2}$ and $pTRM^{T_1}_{T_2}$, are initially considered separately.

Behaviour of Type 1 pTRM

The Type 1 thermoremanences, *i.e.*, $pTRM^{T_c}_{T_2}$, were induced by cooling over the temperature range $T_c \rightarrow 520$ °C. The results are normalised and the temperature-dependent behaviour of $m_s(T)$ compensated for (Figure 4.9).

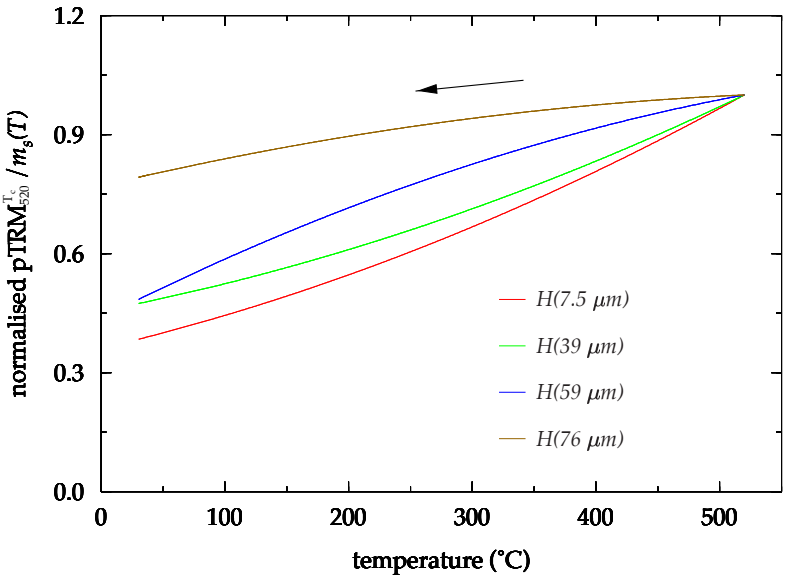


Figure 4.9: Behaviour of normalised $pTRM^{T_c}_{520}$ on cooling below 520 °C in the earth's field. $pTRM^{T_c}_{520}$ was induced in the hydrothermal samples *H(7.5 μm)*, *H(39 μm)*, *H(59 μm)* and *H(76 μm)* using a field of 5 mT.

It is seen in Figure 4.9, that the demagnetisation observed on cooling $pTRM^{T_c}_{520}$ decreases with increasing grain size.

Behaviour of Type 2 pTRM

Type 2 pTRM, *i.e.*, $pTRM^{T_1}_{T_2}$, was induced by cooling the samples over the temperature ranges 550 °C → 450 °C and 450 °C → 300 °C, having previously been cooled from T_c in the earth's field. As above, the results are normalised and the temperature-dependent behaviour of $m_s(T)$ compensated for (Figure 4.10).

For Type 2 pTRM (Figure 4.10), the demagnetisation during cooling $pTRM^{450}_{300}$ below 300 °C is less dependent on grain size than that observed for $pTRM^{550}_{450}$ on cooling below 450 °C. In fact, only $pTRM^{550}_{450}$ induced in sample *H(7.5 μm)* (Figure 4.10) displays any distinctive grain size dependency. Unfortunately no cooling behaviour was measured for sample *H(7.5 μm)* induced with $pTRM^{450}_{300}$. The rate of demagnetisation on cooling below T_2 is greater for $pTRM^{450}_{300}$ than for $pTRM^{550}_{450}$, but the amount of decay from T_2 to 20 °C is similar.

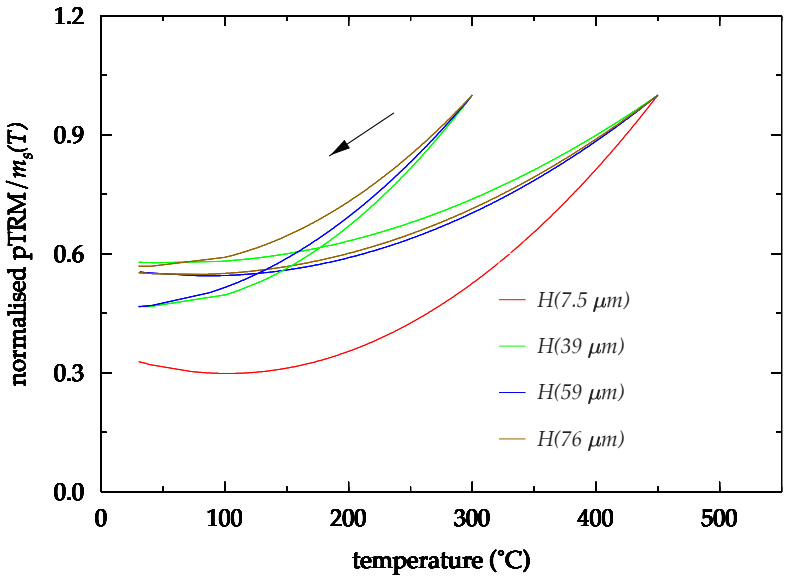


Figure 4.10: Change of normalised pTRM/$m_s(T)$ on cooling in the earth's field for two different $\text{pTRM}_{T_2}^{T_1}$ induced in hydrothermal samples using a field of 5 mT; pTRM_{450}^{550} induced in samples *H(7.5 μm)*, *H(39 μm)*, *H(59 μm)* and *H(76 μm)*, and pTRM_{300}^{450} induced in samples *H(39 μm)*, *H(59 μm)* and *H(76 μm)*.

Comparison of Type 1 and Type 2 pTRM

Figure 4.11 shows both Type 1 and Type 2 pTRM for the *H(76 μm)* sample. Type 2 pTRM *i.e.*, pTRM_{450}^{550} and pTRM_{300}^{450}, decrease more rapidly than Type 1 pTRM, *i.e.*, $\text{pTRM}_{520}^{T_c}$. This suggests that Type 2 pTRM domain structures are more susceptible to domain reconfigurations during cooling below T_2, *i.e.*, they are less stable than Type 1 pTRM.

Comparison with theory and literature

On cooling Type 1 pTRM the observed demagnetisation (Figure 4.9) decreases with increasing grain size contrary to previous experimental evidence which found an increase (Sugiura, 1981; McClelland & Sugiura, 1987). However there are differences in the detail; in this study thermoremanences were induced in a larger field ($H = 5$ mT) than either Sugiura (1981, $H = 1$ mT) or McClelland & Sugiura (1987, $H = 0.84$ mT) had used. Secondly Sugiura (1981) and McClelland & Sugiura (1987) both used crushed magnetites, whereas my samples were relatively stress-free hydrothermal magnetites (Chapters 2 and 3).

The increased inducing field can partially explain the discrepancy between the literature and my results. The larger inducing field would be expected to form domain configurations with fewer domains than those induced in the smaller field by McClelland & Sugiura (1987). On switching off the field at T_2, the domain structure of MD grains partially reverses, *cf.* the "reversible induced moment" of McClelland & Sugiura (1987), *i.e.*, the high self-demagnetising energy causes unblocked domain walls to demagnetise until pinned on a dislocation. Because hydrothermal crystals have lower internal stresses and less pinning

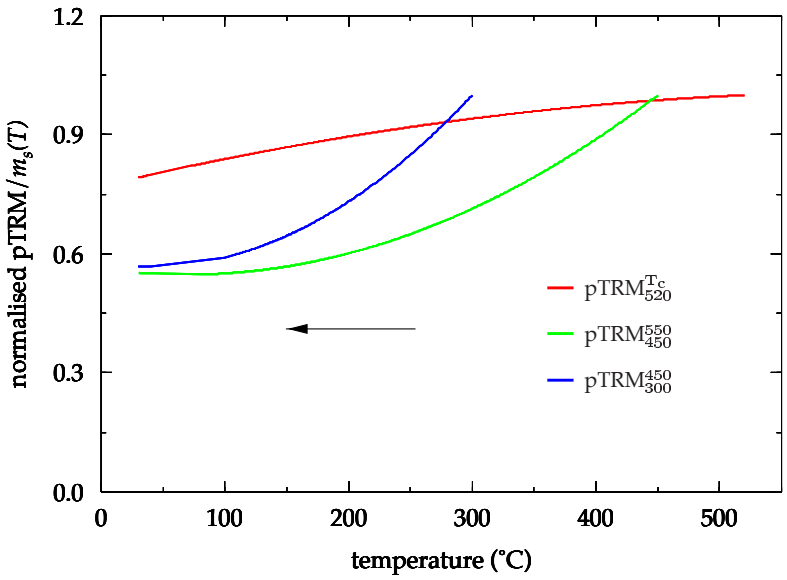


Figure 4.11: Change of normalised pTRM/$m_s(T)$ on cooling below T_2 in the earth's field for sample *H(76 μm)* induced with Type 1 pTRM (pTRM$^{T_c}_{520}$) and Type 2 pTRM (pTRM$^{550}_{450}$ and pTRM$^{450}_{300}$). An inducing field of 5 mT was used.

sites than crushed rocks, my hydrothermal samples are expected to have larger reversible induced moments than the crushed rocks of McClelland & Sugiura (1987). The smaller crystals, *e.g., H(7.5 μm)*, have smaller reversible induced moments than the larger crystals, *e.g., H(76 μm)*. There are two reasons for this; firstly the smaller grains have fewer domain walls to reverse, and secondly there is a relatively larger interaction between the domain walls and the crystals surfaces. It is even possible that small crystals are in a SD-like state after cooling from T_c in a field of 5 mT (Boyd *et al.*, 1984; Dunlop & Argyle, 1997). On cooling below T_2, the smaller crystals are expected to be in relatively unstable high-magnetisation states, making them susceptible to domain reconfigurations. Due to the low-number of domains, nucleation of even one wall contributes significantly to the domain structure, *i.e.*, changing from an odd to even number of domains in a grain with only a few domains significantly alters the net magnetisation (Dunlop & Özdemir, 1997). In larger grains with many more domains, the nucleation of one or two walls is less significant. On removal of the field at T_2, the crushed samples of McClelland & Sugiura (1987) have larger remanence per grain than hydrothermal crystals, because of the increased pinning site density, *i.e.*, domain walls are trapped in states further from the demagnetised state. The demagnetisation process which occurs on cooling, is expected to increase as the self-demagnetising energy domain structure increases, *i.e.*, the process is more pronounced in crushed grains than for hydrothermal grains. Increased dislocation density aids the ability of domain walls to nucleate/denucleate (Dunlop & Özdemir, 1997).

In summary the behaviour of the remanence behaviour appears to be grain size dependent. For the smaller grains, domain wall movement is partially controlled by the interaction of domain walls with the crystal surface. As the grain size increases this interaction

becomes less important, and domain wall movement is governed by the interaction of domain walls with stress fields around dislocations. The importance of dislocation density on the magnetic behaviour of a grain, increases with grain size. The reason for the difference in behaviour between my results and the results of McClelland & Sugiura (1987), can be summarised thus;

At T_2. The higher inducing field pushes my smaller grains domain structure into higher-energy states with fewer domains than that of McClelland & Sugiura (1987). Because of the lower number of pinning sites, my larger grains are relatively reversible at T_2 compared to the crushed samples of McClelland & Sugiura (1987).

Cooling below T_2. The smaller hydrothermal grains are in unstable domain states which nucleate domain walls causing large decreases in pTRM. The smaller crushed samples of McClelland & Sugiura (1987), are not initially in such unstable states, and the demagnetisation observed is relatively less. For the larger grains of McClelland & Sugiura (1987), both the higher self-demagnetising energy and the higher dislocation density makes nucleation easier than in my "stress-free" hydrothermal crystals. This gives rise to a relatively larger demagnetisation in the crushed samples.

Type 2 pTRM show less grain size dependence (Figure 4.10) than the Type 1 TRM (Figure 4.9). This may reflect a narrower range of possible domain configurations open to Type 2 pTRM.

In comparing Type 1 and Type 2 thermoremanences (Figure 4.11), it is immediately obvious that the Type 1 thermoremanences are more stable on cooling than the Type 2. This is in disagreement with McClelland & Sugiura (1987), but in agreement with Sholpo *et al.* (1991). This difference may be due to the nature of the samples, as the former used crushed samples, whereas the later used natural samples. Hydrothermal samples often display behaviour akin to natural samples, *e.g.,* hydrothermal and natural samples display similar coercive force, whereas crushed magnetites usually have larger coercive forces (Heider *et al.*, 1988a, Figure 3.3). A pTRM acquired at a higher temperature range, *i.e.,* $pTRM_{T_2}^{T_c}$ will form domain structures with higher self-demagnetising energies, than a pTRM acquired at lower temperatures. Increases in the dislocation density also cause domain structures with higher self-demagnetising energies to be formed. Therefore a pTRM acquired in a crushed grain at high temperatures has a very high self-demagnetising energy. During cooling domain structures with higher self-demagnetising energies are more likely to be demagnetised. A sample with low internal stress will have smaller remanences per grain, however the domain configuration will have a wider range of available metastable LEM states. The number of metastable LEM structures available decreases with temperature. In low-stress samples with smaller self-demagnetising energies, LEM structures acquired at high temperatures are stable to the self-demagnetising energy. Consequently pTRM acquired in low-stress samples is more stable if acquired at higher temperatures. Unstable domain structure will display the largest demagnetisation on cooling, *i.e.,* $pTRM_{T_2}^{T_c}$ is less

stable than $pTRM^{T_1}_{T_2}$ for crushed samples, and *vice versa* for natural and hydrothermal samples.

Note the difference in behaviour between the results of McClelland & Sugiura (1987) and this study, cannot be explained by the "zero field" approximation used in this study being non-zero , *i.e.*, earth's field, because the "zero field" approximation used by McClelland & Sugiura (1987) was 100 μT. Neither is it possible that the high-"zero field" approximation is the cause of demagnetisation on cooling below T_2, because Markov *et al.* (1983) have observed demagnetisation process in a "zero field" approximation as low as $H = 1$–2 μT.

4.3 Discussion

The results presented in this chapter agree with those previously published; they show a decrease in the normalised magnetisation/m_s on cooling below T_2, indicating domain re-organisation. This agrees with the kinetic theories (McClelland & Sugiura, 1987; Shcherbakov *et al.*, 1993) and domain observations (Heider *et al.*, 1988b; Heider, 1990), and strongly disagrees with the classical hysteretic models (Néel, 1955; Dunlop & Xu, 1994) which assume that the domain structure is "blocked" (Chapter 1).

The bulk of the thermoremanences were induced in a field of 5 mT (Figures 4.9, 4.10 and 4.11), which is approximately five times greater than previous studies (*e.g.*, Parry, 1979; Sugiura, 1981; McClelland & Sugiura, 1987). However it should be noted that both their and my results are for "high-field" thermoremanences. This variation in applied field plus the "stress-free" nature of my samples can be used to explain the differences between my results and those for crushed samples (*e.g.*, Parry, 1979; Sugiura, 1981; McClelland & Sugiura, 1987).

There are several fundamental points which arise from these results; firstly that the dependency of inducing field on pTRM cooling behaviour agrees with the theory (McClelland & Sugiura, 1987; Shcherbakov *et al.*, 1993) contrary to previous reports (Markov *et al.*, 1983), secondly $pTRM^{T_c}_{T_2}$ appears to more stable for ''low-stress" samples than $pTRM^{T_1}_{T_2}$ on cooling below T_2, and thirdly the importance of stress on the results.

The results continue to support the theories of McClelland & Sugiura (1987) and Shcherbakov *et al.* (1993), which are too abstract to be quantitative. These theories do not incorporate variations in dislocation density, which is the probable cause for the difference between my results and those of McClelland & Sugiura (1987). McClelland & Sugiura (1987) and Shcherbakov *et al.* (1993) suggests that domain wall nucleation is a relatively easy process, however it has been argued that it is not (Ye & Merrill, 1995b; Dunlop & Özdemir, 1997). These arguments, however, seem flawed. Dunlop & Özdemir (1997) have applied the results of Halgedahl (1991) for AMTM60 to magnetite, which as discussed previously is inappropriate (Section 4.1.1). The theoretical model of Ye & Merrill (1995b) can also be discredited because it does not incorporate the observed domain structure reorganisation on cooling below T_2. Following the discussion in Section 4.2.5, it appears that

nucleation is relatively easy, with increased dislocation density facilitating domain wall nucleation in larger grains.

The results in this chapter agree with the postulation by Heider (1990) that the demagnetisation processes on cooling are continuous rather than discrete as suggested by the simplified model of McClelland & Sugiura (1987).

Chapter 5

Low-temperature magnetic properties of magnetite

5.1 Introduction

Magnetite undergoes a phase transition called the Verwey transition at $\approx$ 120 K, T_v, (Verwey, 1939), whilst at 10 K above this temperature, *i.e.,* at 130 K, the first cubic magnetocrystalline anisotropy constant passes through an isotropic point, T_k, (*e.g.,* Bickford Jr., 1949; Kąkol & Honig, 1989). On zero-field cooling of rocks to temperatures below T_v, it has been found that the magnetic remanence carried by multidomain magnetite grains partially demagnetises (*e.g.,* Nagata *et al.*, 1964; Ozima *et al.*, 1964b; Creer & Like, 1967, Figure 5.1). The remaining remanence (memory) is relatively stable remanence (*e.g.,* Kobayashi & Fuller, 1968; McClelland & Shcherbakov, 1995).

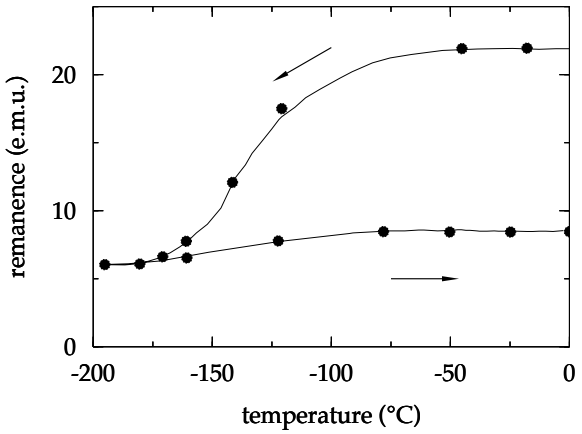


Figure 5.1: Temperature variation of room temperature IRM (H = 20 mT) of multidomain synthetic magnetite. After Ozima *et al.* (1964b).

The nature and origin of magnetic memory is of great interest to the palaeomagnetist, because there is evidence to suggest that it is associated with primary remanences (*e.g.*, Ozima *et al.*, 1964a; Kobayashi & Fuller, 1968). It has been suggested that low-temperature treatment could be used as a "magnetic cleaning" technique, *i.e.*, applying low-temperature treatment reduces multi-component magnetisations to the primary component (Figure 5.2).

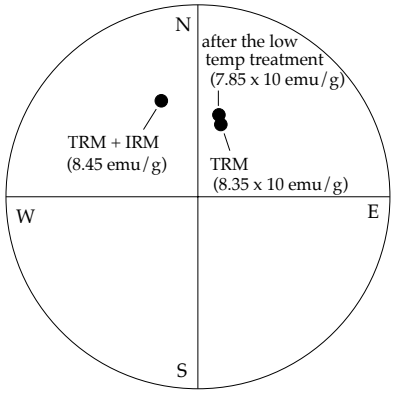


Figure 5.2: Stereonet plot showing the effect of low-temperature ''magnetic cleaning" on a composite remanent magnetisation induced in a basalt rock sample.. A secondary IRM (H = 1.2 mT (12 Oe)) is superposed at right angles to a TRM induced in the earth's magnetic field. Low-temperature treatment is applied to leave memory. The IRM component is said to be ''washed off". Stereonet plot after Ozima *et al.* (1964a).

However the effectiveness of "magnetic cleaning" has been contested (*e.g.*, Merrill, 1970; Borradaile, 1994), and it has not become a standard palaeomagnetic technique. This disagreement is partly due to a lack of understanding as to the processes which control low-temperature demagnetisation.

Before examining the behaviour of multidomain remanences at low-temperatures (Chapter 6), it is necessary to have a clear understanding of the low-temperature physics of magnetite, especially of the Verwey transition itself. In this chapter, the low-temperature physical properties are examined and discussed using a combination of my own experimental data collected from a selection of magnetite samples (natural, synthetic crushed samples, hydrothermally grown magnetite samples and commercial magnetite made by Johnson-Matthey (Chapter 2)), and experimental results and theories by previous researchers. Initially the general physical properties are considered, *e.g.*, crystal structure, followed by an examination of fundamental magnetic properties, *e.g.*, susceptibility and coercive force.

5.2 Introduction to the Verwey transition

Historically, the first report that magnetite exhibits a phase transition was by Millar (1929), who discovered an anomaly in the heat capacity near 120 K. However it was Verwey and co-workers (Verwey, 1939; Verwey & Haayman, 1941; Verwey & Heilmann, 1947; Verwey

Figure 5.3: Relationship between the low-temperature monoclinic unit cell (*a*, *b* and *c*) and the rhombohedrally distorted cell (solid line), and the high temperature cubic unit cell (dashed line). Each monoclinic unit cell consists of four rhombohedrally distorted cells. Redrawn after IIzumi *et al.* (1982).

Importantly, at the transition there is a sharp drop in the electrical conductivity (*e.g.*, Domenicali, 1950; Gleitzer, 1997, Figure 5.4), which is due to a reduction of electron mobility on the B-sublattice. As stated previously (Section 1.7.1), magnetite is a ferrimagnet, with one Fe^{3+} situated on the tetrahedral A-sublattice, whilst the remaining Fe^{3+} and Fe^{2+} are located on the octahedral B-sublattice (Figure 1.15). The magnetic moments of the two sublattices point in opposite directions (Figure 1.16).

Above T_v electrons from the *3d* shells move or "hop" between the Fe^{3+} and Fe^{2+} cations on the B-sublattice, and magnetite behaves like a semiconductor.

$$Fe^{3+} + e^{-} - Fe^{2+}$$

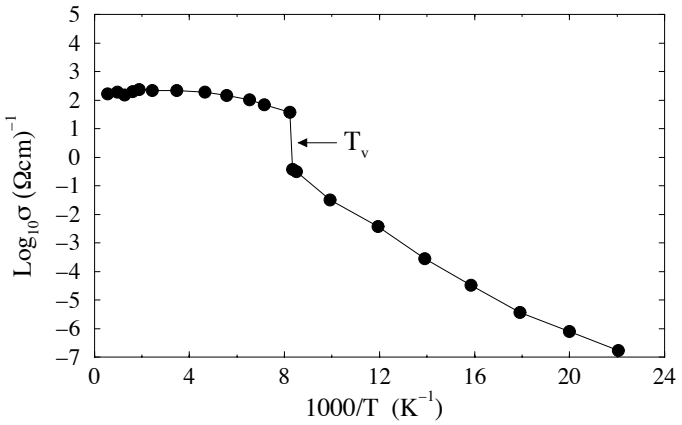


Figure 5.4: Conductivity of magnetite as a function of temperature. After Gleitzer (1997).

On cooling below T_v the hopping is sharply reduced due to a strong increase in the activation energy required for hopping of the electrons. The conductivity is reduced by a factor of almost 100 (Belov, 1993, Figure 5.4). The valency state of the Fe^{2+} and Fe^{3+} ions above and below T_v is examined in the next section.

5.2.1 Mössbauer spectroscopy study of pure magnetite at T_v

Both Mössbauer spectroscopy and nuclear magnetic resonance (NMR) enable the valency state of the magnetic ions in a mineral to be examined by measuring the hyperfine interaction field, H_{hf}, (Belov, 1993). In magnetic minerals the hyperfine interaction of interest is due to splitting of the nuclear energy levels by the magnetic field from the unpaired electrons in the $3d$ shell. This phenomenon is commonly termed the Zeeman effect (Krane, 1988). H_{hf} for magnetite yields information about the relative valency state of the Fe^{2+} and Fe^{3+} cations on the B-sublattice (McKie & McKie, 1974).

Using the Mössbauer spectroscopy techniques described previously (Section 1.8.1), the Mössbauer spectrum of commercial Johnson-Matthey magnetite sample *H(seed)* (see Chapter 2) was measured as a function of temperature on my second visit to the Institute for Rock Magnetism (I.R.M.), University of Minnesota. The Mössbauer spectrum of the Johnson-Matthey magnetite sample at five different temperatures is shown in Figure 5.5.

At 300 K, there are two distinct peaks with source velocities in the range -8 to -6 mms^{-1} range (at ≈ -7.5 mms^{-1} and ≈ -7.0 mms^{-1}, see Figure 5.5) which drift to lower source velocities on cooling. At 300 K, the peak at ≈ -7.5 mms^{-1}, is associated with the A-sublattice/maghemite Fe^{3+} cation, whilst the peak at ≈ -7.0 mms^{-1} is attributed to the B-sublattice Fe^{2+} and Fe^{3+} cations (*pers. comm.* P. Solheid, 1996).

On cooling through the transition the peak at ≈ -7.0 mms^{-1} collapses. It has been suggested by Sahu (1997), that the complete disappearance of the peak indicates the temperature of T_v, however as the peak takes ≈ 10 K to collapse this is not an appropriate

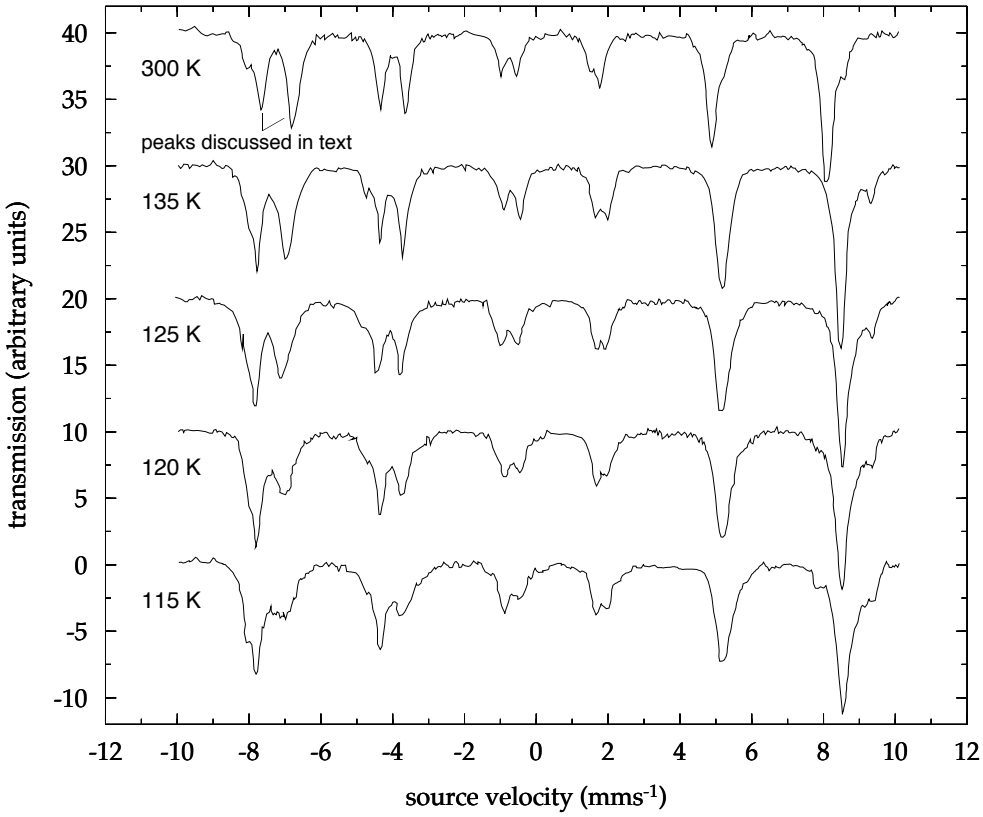


Figure 5.5: Mössbauer spectra as a function of temperature for commercial magnetite sample *H(seed)*. The two distinctive peaks above the transition referred to in the text are marked on the 300 K spectrum. The Mössbauer spectra for $T > 115$ K have been shifted up the page for clarity.

method of determining T_v.

Using the fitting techniques developed by P. Solheid at the I.R.M., four spectra were fitted; two spectra for magnetite's B-sublattice *i.e.,* B1 and B2, one spectrum for magnetite's A-sublattice and maghemite, and one for hematite. Note the signal from the iron ions on magnetite's A-sublattice and in maghemite give similar peaks in the Mössbauer spectrum. This gave estimates for H_{hf} and for the purity of the sample. From the 300 K spectrum it was found that the sample was approximately 71 % magnetite with 17 % hematite and 12 % maghemite. Previous examination (Chapter 2) of a different batch of Johnson-Matthey magnetite only detected magnetite (Section 3). There are three possible reasons for this discrepancy between the first and second batches; firstly, the second batch was not as pure as claimed by the manufacturers. Secondly it is possible that the second batch had oxidised during storage in Oxford; the first batch was tested and used to make the hydrothermal crystals almost immediately after purchase, then both the first batch and the hydrothermal samples were stored in a desiccator before measurement (Chapter 2). The second batch was not tested for nearly six months after purchase, and although it was in a sealed container, it was not kept in desiccator. It should also be noted that the commercial Johnson-Matthey magnetite was in a relatively fine powder form (mean grain size = 0.7 μm), which gave it a high volume to surface ratio. Initially it might appear that the magnetite had

oxidised to maghemite during this six month period, however this does not explain the presence of hematite in the sample. Maghemite is metastable at room temperature and atmospheric pressure (O'Reilly, 1984), so it is highly unlikely that as much as 17 % hematite could have inverted from maghemite to hematite at room temperature in six months (*pers. comm.* A. van Velzen, 1997). The third possibility is an error in the fitting program developed by P Solheid, however this idea can be quickly refuted by inspection of the 300 K spectrum (Figure 5.5). The presence of hematite is indicated by the small peak/shoulder at -8 mms^{-1} on the 300 K spectrum (Figure 5.5). It must be concluded that the second batch of Johnson-Matthey magnetite was initially impure. The effect of impurities on T_v is discussed in Section 5.22.

The calculated H_{hf} gives a much clearer indication of the processes occurring at the Verwey transition (Figure 5.6) than the raw Mössbauer spectra (Figure 5.5). The hyperfine splitting fields for the two B-sublattices B1 and B2 are strongly effected by the Verwey transition, whereas hematite and the A-sublattice and maghemite are not. Above T_v, B1 and B2 are indistinguishable due to the frequency of the hopping being considerably higher than the inverse of the Mössbauer measuring time (De Grave *et al.*, 1993). As a consequence, the Mössbauer effect sees an average valency state, often denoted as $Fe^{+2.5}$ (*e.g.*, Zhang & Satpathy, 1991). Below T_v, B1 and B2 are distinguishable due to a reduction in the hopping rate, *cf.* the reduction in the conductivity at T_v (Figure 5.4).

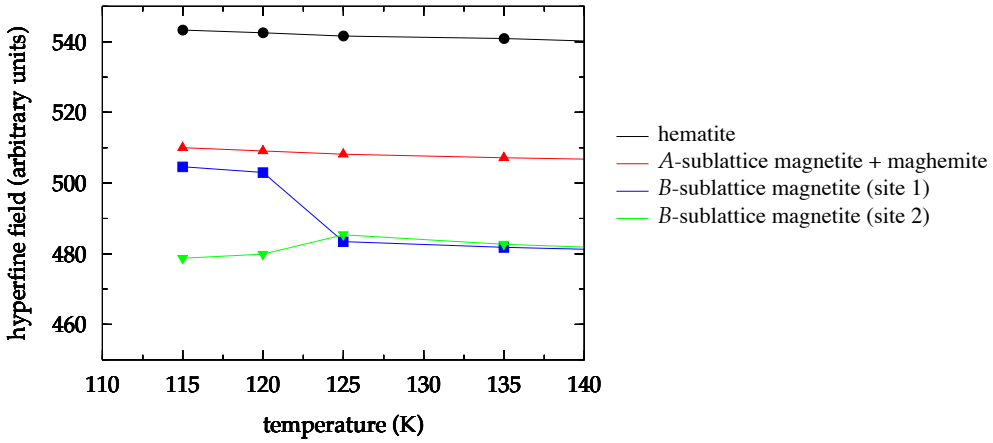


Figure 5.6: The hyperfine splitting field as a function of temperature for the second batch of non-stoichiometric Johnson-Matthey magnetite. B1 and B2 represents the Fe^{2+} and Fe^{3+} ions on the B-sublattice. Above T_v they are indistinguishable, below T_v they are distinguishable. However the relationship between B1 and B2, and Fe^{2+} and Fe^{3+} is unknown (*pers. comm.* P. Solheid, 1997). The hyperfine field associated with the A-sublattice + maghemite and hematite are also shown. They are uneffected by the Verwey transition.

The results are in approximate agreement with previous studies; Mössbauer spectroscopy (Hargrove & Kündig, 1970; Rubinstein & Forester, 1971; Persoons & De Grave, 1989) and NMR (Rubinstein & Forester, 1971; Mizoguchi, 1978b; Mizoguchi, 1978a). However as the second batch of Johnson-Matthey magnetite was not very pure, it was not possible to make as detailed an analysis as some of the previous studies (*e.g.*, Hargrove &

Kündig, 1970; Rubinstein & Forester, 1971).

Examination of the hyperfine splitting field (Figure 5.6), clearly demonstrates the reduction in electron hopping on cooling through the Verwey transition.

5.3 Brief review of the various Verwey transition theories

Many mechanisms have been proposed to account for the experimental data, *i.e.,* the structural change, the reduction in the conductivity (Figure 5.4) plus anomalies in the heat capacity (*e.g.,* Millar, 1929; Kozłowski *et al.*, 1996, Section 5.2), magnetic-relaxation processes (*e.g.,* Walz & Kronmüller, 1991; 1994, see Section 5.7.1), magnetocaloric effect (Belov, 1982), magnetoresistance (*e.g.,* Belov, 1994; Gridin *et al.*, 1996), spontaneous magnetisation (Belov, 1993, see Section 5.3.3), magnetocrystalline anisotropy (*e.g.,* Bickford Jr., 1949; Bickford Jr. *et al.*, 1957; Abe *et al.*, 1976, see Section 5.4.2), magnetostriction (*e.g.,* Tsuya *et al.*, 1977; Aksenova *et al.*, 1987, see Section 5.4.3) at T_v. It has also been found that variations in the stoichiometry (*e.g.,* Aragón *et al.*, 1985, 1992 and Honig, 1995, see Section 5.22) and pressure (Rozenberg *et al.*, 1996, see Section 5.6) strongly affect the Verwey transition. Unfortunately there is too much experimental evidence to discuss in detail here. Some of the topics will be discussed in the text as referenced, for the others I refer the reader to the suggested literature.

Although several theories exist (*e.g.,* Verwey, 1939; Cullen & Callen, 1971; Honig & Spałek, 1992; Belov, 1993), none has been able to explain all the experimental data. The different models can be roughly split into two camps; structural-electronic and magneto-electronic. The term "structural-electronic" was coined by Belov (1993) to describe models based on Verwey's original theory, and to differentiate from Belov's own magneto-electronic model developed more recently.

5.3.1 Structural-electronic model of the Verwey transition

Verwey (Verwey & Haayman, 1941) proposed that the transition is an ionic order-disorder transition. He suggested that below T_v, the Coulomb repulsion between neighbouring Fe^{2+} and Fe^{3+} B-sublattice site cations causes the two cations to arrange themselves on alternate (100) planes producing the crystal distortion. According to this model the reduction in the conductivity is a product of the ionic ordering. Anderson (1956) showed that the Coulomb interaction between the cations on the octahedral sites of ferrites, gives rise to short-range order (SRO) and is minimised by $\sim (\frac{3}{2})^{N_B/2}$ different configurations where N_B is the number of B sites. A few of these configurations, have long-range order (LRO), the Verwey structure being one of these LRO states (Zuo *et al.*, 1990). Anderson interpreted the Verwey transition as a loss of LRO upon heating through the transition. Mössbauer and NMR studies (Hargrove & Kündig, 1970; Rubinstein & Forester, 1971), using more detailed analysis than was performed in Section (5.2.1) , identified more Fe^{2+} and Fe^{3+} sites

than the single Fe^{2+} and single Fe^{3+} predicted by the Verwey model. Later Mizugouchi (1978b) found as many as five different Fe^{3+} sites on the B-sublattice using NMR. As a result a number of more complicated charge-ordering models have been proposed (*e.g.,* Mizoguchi, 1978a; Iida, 1980; Zuo *et al.*, 1990; Mishra & Satpathy, 1993).

5.3.2 Magneto-electronic model of the Verwey transition

The magneto-electronic model was developed by Belov (1993; 1994; 1996a; 1996b), in response to two important discrepancies between the structural-electronic model and experimental data; extremely low mobility of the conduction electrons above T_v and an unexplained anomaly in the spontaneous magnetisation at the transition, which is described latter.

Considering the low-electron mobility problem first, the Verwey model (Verwey, 1939; Verwey & Haayman, 1941), assumed a "hopping" mechanism for electrical conduction in magnetite. An alternative approach has been to apply band theory of electrical conduction to magnetite and other ferrites (*e.g.,* Cullen & Callen, 1971; 1973; Zhang & Satpathy, 1991; Samiullah, 1995). However neither of these two models explain the extremely low mobility of the conduction electrons in magnetite above T_v.

For example, for the hopping model, the concentration, N_e, of hopping electrons can be estimated assuming that there is one hopping electron per Fe_3O_4 molecule, consequently there are 8 per unit cell. Since the lattice parameter of magnetite is $a = 8.3963$ Å, this gives

$$N_e = \frac{1\text{cm}^3}{a^3} 8 \approx 1.35 \times 10^{22} \text{cm}^{-3}$$

This value of N_e is comparable to that which exists in metals, and is much greater than the value in ordinary semiconductors, however the conductivity of magnetite is akin to semiconductors (Belov, 1993). This low electron mobility has been attributed to the electrostatic interactions discussed previously in the structural-electronic model, however Belov (1993) notes that this is not sufficient to cause the large reduction in the conductivity. Belov (1993) points out that in semiconductors there is another important mechanism that causes localisation of conduction electrons; the Vonsovskiĭ exchange interaction (Vonsovskiĭ, 1946; Nagaev, 1971). This is the exchange interaction between valence and inner electrons in ferromagnetic materials. The spin of valence electrons is acted upon by the magnetic field exerted by the internal electrons (Vonsovskiĭ, 1946).

The magneto-electronic model applies the Vonsovskiĭ exchange interaction theory to magnetite. The valence electrons are the hopping electrons and the inner electrons are the fixed electrons on the A- and B-sublattice cations. At high temperatures thermal energy is sufficient to break the Vonsovskiĭ exchange interaction, however on cooling through

the Verwey transition the hopping electrons are magnetically ordered under the influence of the Vonsovskiĭ exchange interaction with the magnetic cations, to form an *e*-sublattice. Because the Vonsovskiĭ exchange interaction between the hopping electrons and the iron cations is negative (antiferromagnetic) (Belov, 1993), this leads to not only localisation of the conduction electrons but also to a partial screening of the total magnetic moment (Abrikosov, 1968), *i.e.,* the *e*-sublattice electrons align antiparallel to the net magnetic moment of the *A*- and *B*-sublattices (Figure 5.7).



Figure 5.7: Magneto-electron sub-lattice electron model. After Belov (1993).

This leads to a small decrease in the spontaneous magnetisation for $T < \mathrm{T}_v$. At $T > \mathrm{T}_v$, the thermal motion destroys the magnetisation of the *e*-sublattice, which results in a small experimentally detected anomaly in the spontaneous magnetisation (Figure 5.8).

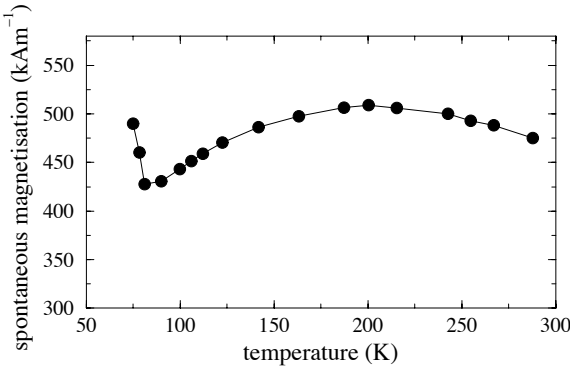


Figure 5.8: Spontaneous magnetisation as a function of temperature for magnetite. Data originally collected by Skipetrova (1978) and reported in Belov (1993).

According to theories of Belov (1996a), the interaction of a strong-sublattice (*A*- and *B*-sublattices) with a weak-sublattice (*e*-sublattice) retards the Verwey transition, *i.e.,* the transition is spread over a certain temperature interval (see Figures 5.8 and 5.9). This retardation is supported by results from photoemission spectroscopy (Chainani *et al.*, 1996). The low-temperature behaviour of the spontaneous and saturation magnetisation is considered further in Section 5.3.3.

The antiferromagnetic Vonsovskiĭ exchange interaction also explains the reduction in electron mobility above T_v. Above T_v the Vonsovskiĭ exchange interaction is insufficient to cause LRO order of the hopping electrons, however it is large enough to effect the orientation of the hopping electrons. Because the Vonsovskiĭ exchange interaction in

Figure 5.9: Schematic representation of the spontaneous magnetisation of magnetite's temperature dependence at low-temperature. Curve 1 = total M_s of $A-$ and $B-$sublattices, curve 2 = M_s of $e-$sublattice and curve 3 = total M_s of $A-$, $B-$ and $e-$sublattices. After Belov (1996a).

magnetite is antiferromagnetic, the hopping electrons periodically reverse (flip) their spin during hopping which requires an additional activation energy (Belov, 1996a). This results in a reduction in the electron mobility.

5.3.3 Differences in the spontaneous and saturation magnetisation at T_v

The spontaneous magnetisation, M_s, is the magnetisation within the centre of a domain in zero field (Section 1.3.4). At temperatures above absolute zero, the magnetic moments precess (Figure 1.5b). The saturation magnetisation M_{sat} is the magnetisation measured in a saturating field (Figure 1.12), *i.e.*, the field required to make a multidomain grain single domain (technical saturation). At technical saturation the magnetic moments precess around the field direction (Figure 1.5b). If the field is increased further the magnetisation increases slowly due to the gradual reduction of the precession. Ultimately at very high fields the magnetic moments are completely aligned in the direction of the field (Figure 1.5a), *i.e.*, similar to the spontaneous magnetisation at 0 K. For fields of same order of magnitude as the technical saturating field, *e.g.*, 1 T, the reduction in the precession is very small (Jiles, 1991). To ensure that technical saturation has been obtained it is common practice to determine M_{sat} by measuring in a field greater than the technical saturation field, *e.g.*, magnetite saturates at 0.3 T (Thompson & Oldfield, 1986), however M_{sat} is often determined by applying fields greater than this; 0.6 T (Heider *et al.*, 1996), 1 T (Heider *et al.*, 1988a; King, 1996) and 1.5 T (Dankers & Sugiura, 1981).

In rock magnetic literature, M_s and M_{sat} are often considered to be identical, and are indiscriminately interchanged (*e.g.*, O'Reilly, 1984; Banerjee, 1991; Dunlop & Özdemir, 1997). At room temperature and above this assumption is permitted, however according to the magneto-electronic model there is a significant difference between the saturation and spontaneous magnetisation at low-temperatures below the Verwey transition (Belov, 1993).

The structural-electronic models (section 5.3.1) make no reference to the decrease in M_s.

According to the magneto-electronic model, M_{sat} differs from M_s because of the interaction of the *e*-sublattice with the external saturating field. The effect of a field on the *e*-sublattice is two-fold; firstly if the external field is large enough then the electrons in the *e*-sublattice align in the direction of the field, and secondly for even greater external fields the *e*-sublattice is destroyed, *i.e.*, the electrons become delocalised (Belov, 1994). Collectively these two processes are termed the "paraprocess" (Belov, 1994). The paraprocess in magnetite reduces the magnetisation associated with the *e*-sublattice, which in effect increases the net magnetisation of the entire lattice (*cf.* Figure 5.7). The paraprocess gives rise to an increase in electron mobility which is documented in magnetoresistance studies (*e.g.*, Belov, 1994; Gridin *et al.*, 1996). In the low-temperature phase of magnetite, the paraprocess is not significant until fields of the order needed to cause technical saturation are applied (Belov, 1993). According to the magneto-electronic model, below the Verwey transition M_{sat} measured in a field greater than the minimum field necessary to cause technical saturation is significantly greater than M_{sat} measured in the minimum technical saturation field (Belov, 1993).

There is limited experimental data examining the low-temperature behaviour of M_s (Belov, 1996b). I decided to verify the behaviour of M_s shown in in Figure 5.8, and at the same time confirm or disprove the magneto-electronic theory of Belov (1993).

In the remainder of this section, the direct measurement of the saturation magnetisation and the determination of the spontaneous magnetisation from low-temperature hysteresis loops are reported. There is a general discussion and comparison of the structural-electronic and magneto-electronic models in Section 5.3.4.

Measurement of saturation magnetisation at T_v

In this study the saturation magnetisation was measured (Figure 5.10) by heating the hydrothermal magnetite sample *H(39 μm)* (see Chapter 2) from 20 K to 300 K in fields above the room temperature technical saturation field ($\approx$ 0.3 mT, see Figure 5.11). This was measured using the Magnetic Property Measurement System (MPMS) in Department of Chemistry, University of Edinburgh (a full discussion of the MPMS and its capabilities is given in Section 6.4).

Below T_v, increasing the applied field from 0.5 T to 0.8 T increases the measured magnetisation below T_v, which decreases the size of the sharp anomaly at T_v (Figure 5.10). The anomaly difference due to the paraprocess, *i.e.*, below T_v the field interacts with the *e*-sublattice which results in either rotation or delocalisation of the *e*-sublattice electrons. Above T_v the *e*-sublattice is destroyed by thermal energy. The increase in the paraprocess with field increases M_{sat} below T_v, and hence decreases the sharp jump in the magnetisation at T_v. Similar results are reported elsewhere (Domenicali, 1950; Matsui *et al.*, 1977; Aragón, 1992; King, 1996). Sampling on single crystals, Domenicali (1950) attributed the

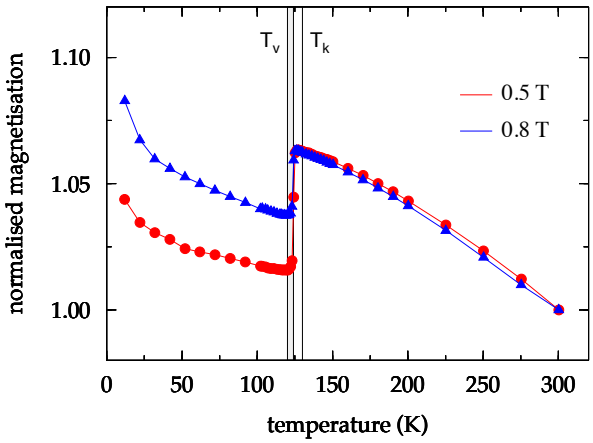


Figure 5.10: Magnetisation of magnetite sample *H(39 μm)* as a function of temperature in the presence of two different applied fields.

anomaly to changes in the magnetocrystalline anisotropy and its control on the preferred direction of magnetisation (see Section 5.4.2) , however I can reject this theory because in the present study the sample contained a large number of randomly orientated grains. For randomly orientated grains the mechanism suggested by Domenicali (1950) would average to zero, and no anomaly would be observed. Matsui *et al.* (1977) and Aragón (1992) both measured at only one applied field (1T), and both reported an anomaly of ≈ 0.1 % in the magnetisation at T_v. They postulated that the anomaly is due to small populations of anisotropic ions such as Fe^{1+} and Fe^{2+} in a doublet ground state (Slonczewski, 1958; Abe *et al.*, 1976), however this hypothesis does not explain the dependence of anomaly size on field strength, nor has it been experimentally tested.

In summary, in magnetite the net effect of the paraprocess is to increase the net magnetisation below T_v. The paraprocess is field dependent, *i.e.*, it increases with increasing field, and it is sometimes referred to as the paraprocess susceptibility. By incorporating the paraprocess effect the magneto-electronic model is the only model at present which can explain the field dependence of the anomaly in M_{sat} at T_v.

Measurement of spontaneous magnetisation at T_v

The spontaneous magnetisation was determined by measuring hysteresis loops at low-temperatures using an in-house built vibrating sample magnetometer (VSM) at the I.R.M. (this in-house VSM is discussed in more detail in Section 5.7.2). Hysteresis loops were measured as a function of temperature for two hydrothermal magnetites *H(3.0 μm)* and *H(76 μm)*. Two typical hysteresis loops for the sample *H(76 μm)* are shown in Figure 5.11.

At 300 K, magnetic saturation sets in at fields of ≈ 0.3 T, whereas at 120 K the magnetisation curve has not saturated in a field of 1.5 T (Figure 5.11). The intensity of magnetisation at ≈ 0.5 T for the 120 K hysteresis loop is less than for a similar field on the 300 K curve (Figures 5.11). The reason for these two differences can be explained by the magneto-

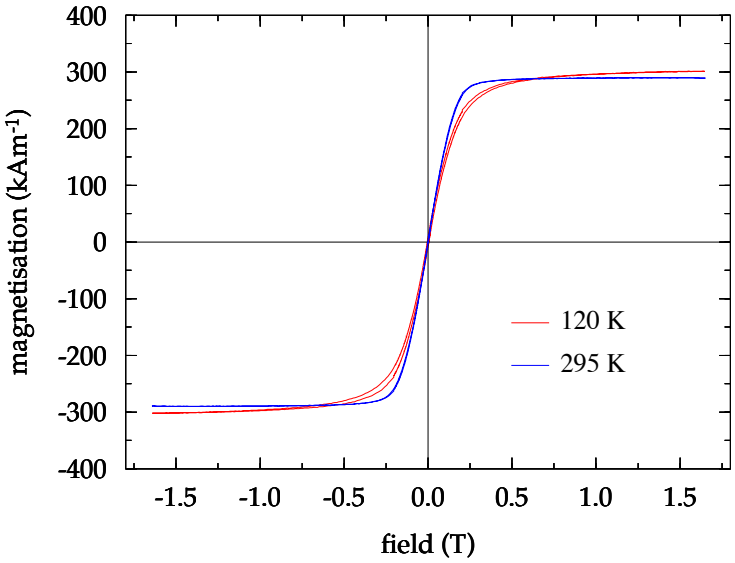


Figure 5.11: Hysteresis loops for hydrothermal sample *H(76 μm)*at two temperatures. The hysteresis loops where measured using the in-house VSM at the I.R.M.

electronic model. The difference in intensity for the two loops is due to the presence of the *e*-sublattice at 120 K, which reduces the net magnetisation (Figure 5.9). The difference in the saturation field is the due the paraprocess effect; at 300 K the paraprocess effect is very small, however on cooling to near T_v it becomes significant. The field-dependent paraprocess destroys the *e*-sublattice, which effectively increases the net magnetisation. At 120 K, the paraprocess does not completely saturate until $\approx$ 1.9 T (Belov, 1993; Belov, 1996b, (unfortunately the maximum reliable field on the VSM used in this study was only 1.6 T), and hence the difference between saturation fields at 120 K and 300 K. In a field of 1.9 T M_{sat} at 300 K $\approx$ M_{sat} at 120 K. Note at 120 K M_{sat} is slightly greater than at 300 K, due to the reduction in thermal energy which causes the magnetic moments to precess.

From the hysteresis loops it is possible to estimate the spontaneous magnetisation at each temperature by extrapolating the value of the magnetisation in a field near technical saturation to $H = 0$, *i.e.*, the spontaneous magnetisation is calculated at a given field near the technical saturation field from the *initial* forward curve of a hysteresis loop. The larger the field is above technical saturation, the larger the contribution from the paraprocess, *i.e.*, rather than the spontaneous magnetisation alone, the spontaneous magnetisation plus the effect of the field-dependent paraprocess is measured. Figures 5.12 and 5.13 show the error in calculating the spontaneous magnetisation from high fields where the effect of the paraprocess is large. It can be seen in Figure 5.13, that if the spontaneous magnetisation is calculated from a field substantially greater than the technical saturation field (0.3 T), *e.g.*, 1.4 T, where the paraprocess is large, then the anomaly in the calculated spontaneous magnetisation is significantly reduced.

The spontaneous magnetisation as a function of temperature for the hydrothermal samples *H(3.0 μm)* and *H(76 μm)* is shown Figure 5.14. These two curves were calculated

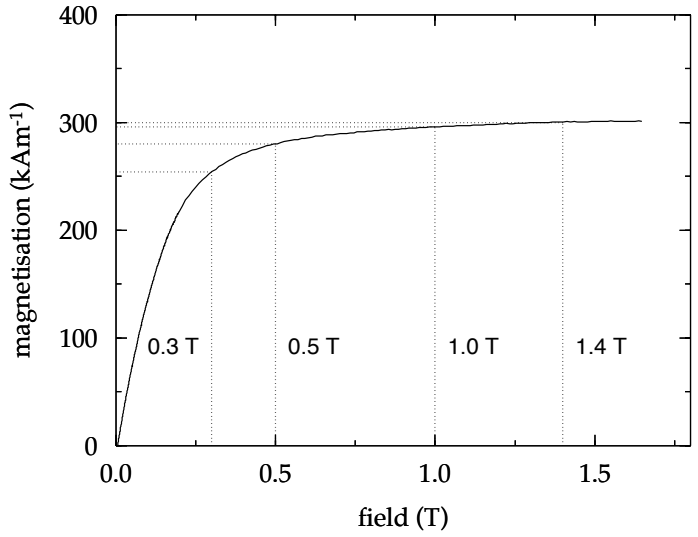


Figure 5.12: Various calculations of the spontaneous magnetisation at 120 K for sample *H(76 μm)*. The hysteresis loop is the initial forward loop.

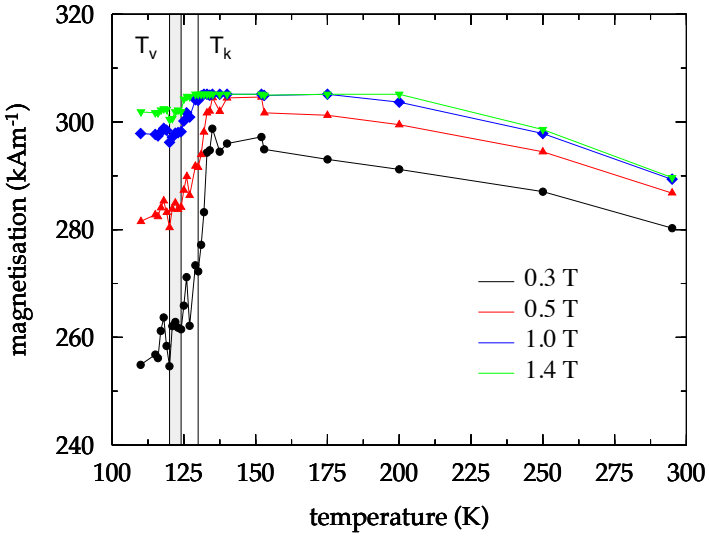


Figure 5.13: Various calculations of the spontaneous magnetisation as a function of temperature for the hydrothermal sample *H(76 μm)*. Each curve is calculated from hysteresis loops similar to those shown in Figure 5.11. The different curves represent the field value from which M_s is calculated. For example the "1.0 T" curve, is the magnetisation at 1.0 T on the *initial* forward curve in each hysteresis loop (see Figure 5.12). Many hysteresis loops were measured over the temperature range 105 K to room temperature. T_v and T_k are marked, T_v as a range 120-124 K.

assuming a technical saturation of $\approx$ 0.3 T, *i.e.*, each curve is calculated by taking the value for the magnetisation at 0.3 T from hysteresis loops similar to those shown in Figure 5.11.

Even at fields less than the technical saturation field, *i.e.*, $\leq$ 0.3 T, there is a small contribution from the paraprocess to the magnetisation, however it is difficult to calculate for this. The effect of the paraprocess contribution in fields less then 0.3 T, is to decrease the size of the low-temperature anomaly in the magnetisation at $T <$ T_v, *i.e.*, the paraprocess *increases* the measured magnetisation below T_v. Therefore the true spontaneous magneti-

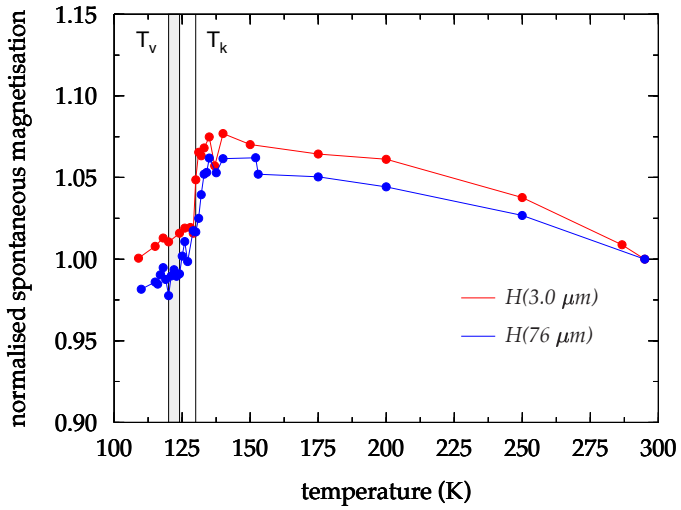


Figure 5.14: Spontaneous magnetisation as a function of temperature for the hydrothermal samples *H(3.0 μm)* and *H(76 μm)*. Each curve is calculated by taking the value for the magnetisation at 0.3 T from hysteresis loops similar to those shown in Figure 5.11. T_v and T_k are marked, T_v as a range 120-124 K.

sation for a sample in zero field is larger than that calculated at $H = 0.3$ T. However the general behaviour of the spontaneous magnetisation can be seen (Figure 5.14).

The spontaneous magnetisation which I measured (Figure 5.14), shows a sharper low-temperature anomaly than that measured by Skipetrova (1978, Figure 5.8) and reported in Belov (1993). The reason for this difference is unknown. No information is known about the origin of the sample used to determine Figure 5.8. However a sharp transition is in agreement with the saturation magnetisation results (Figure 5.10)

Belov (1996a) has asked for verification of the behaviour of the spontaneous magnetisation below 100 K as reported by Skipetrova (1978, Figure 5.8). Unfortunately in this study, it was not possible to verify the behaviour below 100 K shown in Figure 5.8, because there were difficulties with the VSM temperature control (see Section 5.7.2 for more details).

Whilst measuring low-temperature hysteresis loops of synthetic magnetites, King (*pers. comm.* 1996) found a similar anomaly at T_v as that shown Figure 5.14. However he only plotted the magnetisation measured in field of 1 T as a function of temperature, making the anomaly smaller than shown in Figure 5.14.

Note in theory it is possible to simply determine the spontaneous magnetisation by measuring the magnetisation of a sample in the technical saturation field on heating from below T_v to room temperature. However it is more accurate to determine M_s from hysteresis loops measured at a range of temperatures. There are two reasons for this; firstly there are uncertainties in a sample's technical saturation field below T_v which can only be determined by measuring its hysteresis loops, and secondly by determining M_s from hysteresis loops, any possible contributions to the magnetisation caused by heating and cooling a sample in a field below the Verwey transition are removed.

In low-field and remanence studies which are of interest to the rock magnetist it is important to know the behaviour of the spontaneous magnetisation rather than the saturation magnetisation.

5.3.4 Comparison of the structural- and magneto-electronic models

Both the structural-electronic and magneto-electronic models have experimental evidence in their favour. Strong support for the structural-electronic hypothesis comes from both Mössbauer spectroscopy (Hargrove & Kündig, 1970; Rubinstein & Forester, 1971) and NMR (Rubinstein & Forester, 1971; Mizoguchi, 1978b). For $T > \mathrm{T}_v$, Fe^{2+} and Fe^{3+} cations on the B-sublattice are indistinguishable to Mössbauer spectroscopy and NMR (see Section 5.2.1), however on cooling below T_v, they become distinguishable (Figure 5.6). This is interpreted by the structural electronic model as ordering of the Fe^{2+} and Fe^{3+} cations. However, Belov (1996a) provides a second interpretation of Mössbauer spectroscopy and NMR results in terms of the magneto-electronic model. He argues that at $\mathrm{T} < \mathrm{T}_v$, the Vonsovskiĭ exchange interaction between the iron cations and the hopping electrons which orders the hopping electrons to form the e-sublattice, localises the hopping electrons on the B-sublattice cations. This localisation gives rise to different values of H_{hf} for Fe^{2+} and Fe^{3+} cations of the B-sublattice (Figure 5.6). At $\mathrm{T} > \mathrm{T}_v$, where the magnetic order is partially destroyed, hopping electrons delocalise and migrate between the Fe^{2+} and Fe^{3+} cations, creating an averaged H_{hf} field (Figure 5.6).

In favour of the magneto-electronic model, there are the anomalies at T_v in the spontaneous magnetisation (Figure 5.8), the magnetocaloric effect (Belov, 1982) and the magnetoresistance (*e.g.*, Belov, 1994; Gridin *et al.*, 1996), which have only been explained by the magneto-electronic model. Another experimental observation to support the magneto-electronic model is an anomaly in the shape anisotropy found for grains of ≈ 88 Å, *i.e.*, single domain, (Hu *et al.*, 1991). Because the shape anisotropy $\propto M_s^2$ (Dunlop & Özdemir, 1997) this anomaly is expected by the magneto-electronic model which incorporates the anomaly in the spontaneous magnetisation (Figures 5.8, 5.9 and 5.14), but not by the structural-electronic model. Belov (1993) attributes the distortion in the cubic symmetry below T_v which is fundamental to the structural-electronic model, to the changes in the anisotropic magnetostriction (Section 5.4.3). The magneto-electron model can also explain the dependency on field during low-temperature cooling, *i.e.*, samples cooled in large fields show different behaviour at T_v compared to samples cooled in a zero field (Domenicali, 1950; Moskowitz *et al.*, 1993).

Most other effects, *e.g.*, anomalies in the magnetocrystalline anisotropy (*e.g.*, Abe *et al.*, 1976; Belov, 1993, see Section 5.4.2), have been explained by both theories.

In summary there is strong experimental support for both the magneto-electronic model and the structural electronic model, however the anomaly in M_s at T_v is only accounted for by the magneto-electronic model. Because the behaviour of M_s is fundamental

to the magnetic domain structure (Chapter 1), the magneto-electronic approach is used in the explanation of other magnetic phenomena of interest to this thesis.

5.4 Behaviour of magnetic energies at low-temperatures

To understand the demagnetisation processes which occur at the Verwey transition it is important to know how the controlling magnetic energies and parameters behave near the Verwey transition (Section 1.4). The behaviour of the spontaneous magnetisation across the Verwey transition was presented in Section 5.3.2.

5.4.1 Exchange Energy

Experimental evidence (*e.g.,* Alperin *et al.*, 1967; Torrie, 1967) suggests that the exchange energy is not effected by the Verwey transition. Theoretical attempts to calculate the exchange energy by applying band theory to magnetite have not ventured below the transition (*e.g.,* Pénicaud *et al.*, 1992; Uhl & Siberchicot, 1995).

5.4.2 Magnetocrystalline Anisotropy Energy

$T_v < T \leq$ 300 K

The behaviour of the magnetocrystalline anisotropy energy (Section 1.4.3) at low-temperatures is still a matter of debate. Are the first magnetocrystalline anisotropy constant K_1 isotropic point at 130 K (Bickford Jr., 1949; 1950; Bickford Jr. *et al.*, 1957, Figure 5.15) and the Verwey transition at $\approx$ 120-124 K, two separate low-temperature transitions or just one? King (1996) argues that they are actually identical, and any discrepancies between the two temperatures are due to the neglect of the second anisotropy constant K_2 and other higher order contributions. K_2 is usually ignored because K_1 dominates at and above room temperature, however at the K_1 isotropic point the contribution from K_2 becomes significant.

The two most complete sets of low-temperature magnetocrystalline anisotropy data (*i.e.,* Bickford Jr. *et al.*, 1957; Syono, 1965, Figure 5.15) are for K_1' and K_2', *i.e.,* $K_i, \mathcal{K}_i$ plus a magnetostrictive contribution (Equation (1.23). In theory it is possible to obtain $K_i, \mathcal{K}_i$ by either direct measurement using ferromagnetic resonance (FMR) as suggested by Ye *et al.* (1994), or by simply removing the experimentally measured magnetostrictive term from $K_i', \mathcal{K}_i'$ (*e.g.,* Kąkol *et al.*, 1991; Sahu & Moskowitz, 1995). However with regard to FMR, there are very few reports of its use (Bickford Jr., 1949; 1950), and these few reports only cover the temperature range $T_v < T \leq$ room temperature. The latter method of calculating $K_i, \mathcal{K}_i$ is fraught with errors, because for magnetite the values of the magnetostrictive constants are often smaller than the error in the measurement of $K_i', \mathcal{K}_i'$.

Using the data of Syono (1965, Figure 5.15), King (1996) shows that by adding K_1' and K_2', the isotropic point is decreased from 139 K for K_1' to 134 K for $K_1' + K_2'$. However if a similar approach is taken with the data collected by Bickford Jr. *et al.* (1957, Figure 5.15), then the value for the isotropic point is greater for $K_1' + K_2'$ than for K_1' alone. This raises the possibility that magnetocrystalline anisotropy E_k is zero at a higher temperature than 130 K, rather than lower as King (1996) suggests.

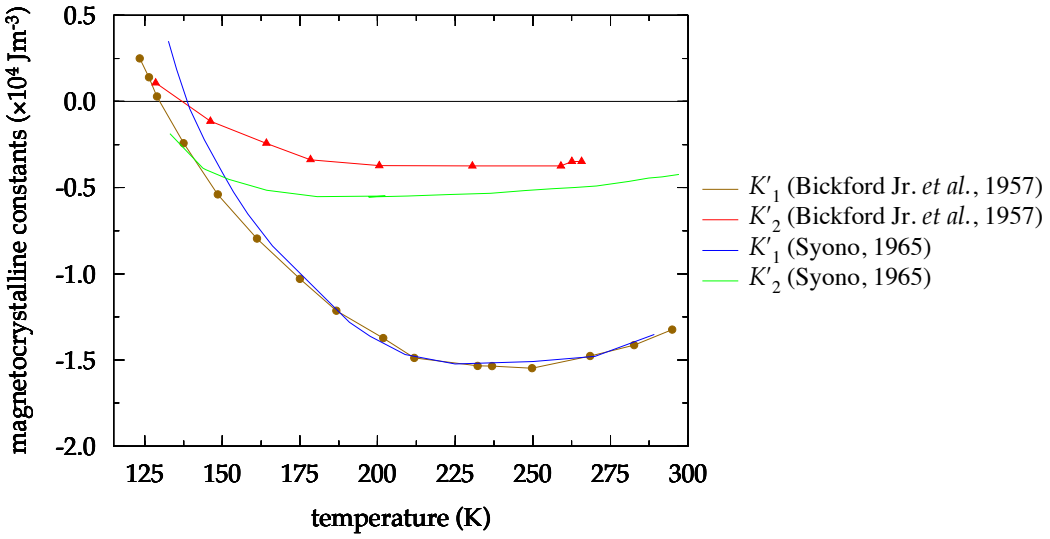


Figure 5.15: Magnetocrystalline anisotropy constants K_1' and K_2' as a function of temperature showing the large difference in the values of Bickford Jr. *et al.* (1957) and Syono (1965).

The reason for the high isotropic point for K_1' measured by Syono (1965, Figure 5.15) is unclear. King (1996) suggested that it was due to impurities, however it is shown in Section 5.22 that the effect of small deviations from stoichiometric Fe_3O_4 is to decrease the isotropic point. It is not until $x \approx 0.4$ for $Fe_{3-x}Ti_xO_4$, that the isotropic point increases to above 130 K (Syono, 1965; Kąkol *et al.*, 1991).

By examining the relative magnetic initial permeability ($\equiv \chi + 1$), Aragón *et al.* (1985, Figure 5.16) have produced very strong evidence in support of two transitions, and low-temperature hysteresis results reported in this study (Section 5.7), also suggest the existence of two separate transitions. It appears in answer to the initial question, that the magneto-crystalline isotropic point and the Verwey transition are separate transitions, and not the same as suggested by King (1996).

$T \leq T_v$

Below T_v the crystal structure transforms from a cubic to a to a less symmetric structure. The majority of the experimental results suggests that this structure is monoclinic with a tilt from the c axis of 0.23°(Figure 5.3). For the monoclinic low-temperature structure the magnetocrystalline energy E_k^m is expressed by (Abe *et al.*, 1976)

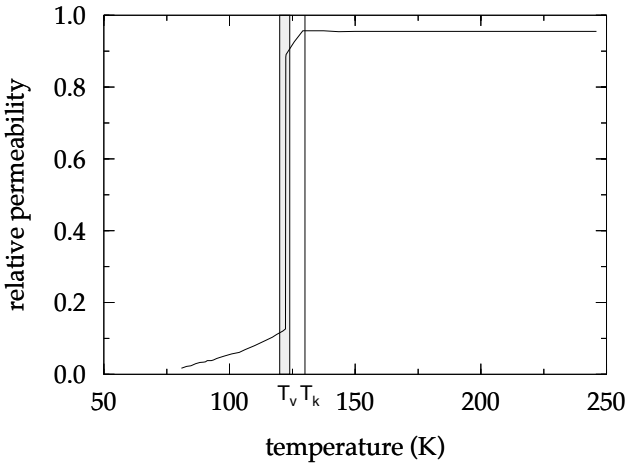


Figure 5.16: Relative magnetic initial permeability ($\equiv \chi + 1$) as a function of temperature for annealed magnetite single crystal. After Aragón *et al.* (1985). The two transitions T_v and T_k are marked. Aragón *et al.* (1985) associate the vertical anomaly with the Verwey transition, and the change in slope from $y = x$ to the horizontal at $\approx$ 130 K with the isotropic point.

$$E_k^m = \mathcal{K}_a\alpha_a^2 + \mathcal{K}_b\alpha_b^2 + \mathcal{K}_{aa}\alpha_a^4 + \mathcal{K}_{bb}\alpha_b^4\mathcal{K}_{ab}\alpha_a^2\alpha_b^2 - \mathcal{K}_u\alpha_{111}^2 \tag{5.1}$$

where α_a, α_b and α_{111} are the direction cosines of the magnetisation with respect to the monoclinic *a*-, *b*- and cubic [111] axes respectfully (see Figure 5.3 for coordinate system). Abe *et al.* (1976) added the $-\mathcal{K}_u\alpha_{111}^2$ term to the expression originally derived for an orthorhombic phase by Calhoun (1954), to deal with the small rhombohedral distortion.

The temperature dependent behaviour of magnetocrystalline constants for both the cubic and monoclinic phases is shown in Figure 5.17.

The low-temperature monoclinic magnetocrystalline anisotropy constants are considerably larger than the cubic magnetocrystalline anisotropy constants (Figure 5.17). The controlling monoclinic constant $\mathcal{K}'_a$ is approximately ten times greater than K'_1. Consequently the relative importance of the monoclinic magnetocrystalline anisotropy to the domain structure is far greater than the cubic magnetocrystalline anisotropy, *i.e.*, $E_k^m \gg E_k^c$ (where E_k^c is the cubic magnetocrystalline anisotropy energy (Equation 1.19)).

This abrupt jump in the magnetocrystalline anisotropy on cooling through T_v is expected, because the magnetocrystalline anisotropy is controlled by the mobility of the Fe^{2+} ions (or alternatively the mobility of the hopping electrons) (Fletcher & O'Reilly, 1974; Belov, 1993). As the mobility decreases the magnetocrystalline anisotropy increases (Belov, 1993). At T_v the electron mobility drops abruptly (Section 5.2), which strongly effects the intensity of the magnetocrystalline anisotropy constants (Figure 5.17).

There is also a large change in the symmetry of the magnetocrystalline anisotropy field. The magnetocrystalline energy fields for T = 290 K, 120 K and 100 K are plotted in Figures 5.18–5.20. In the cubic phase, for $T > 130$ K the easy-axis is the [111] (Figure 5.18),

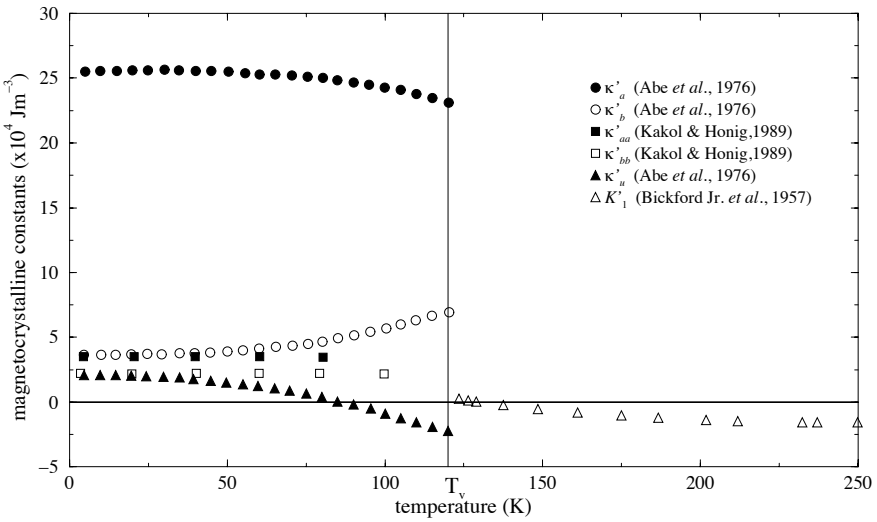


Figure 5.17: Temperature dependence of the cubic and monoclinic magnetocrystalline constants used in the model. K_1' is the first cubic magnetocrystalline anisotropy constant (Equation 1.19), and $\mathcal{K}_i'$ are the low-temperature monoclinic constants (Equation 5.1).

and for T$_v$< T < 130 K, K_1' is positive which switches the easy axis from the [111] axis to the [100] (Figure 5.19). The monoclinic magnetocrystalline anisotropy has a lower order of symmetry than the cubic phase, the easy-axis is the *c*-axis, however the *b*-axis is also relatively easy compared to the *a*-axis (Figure 5.20).

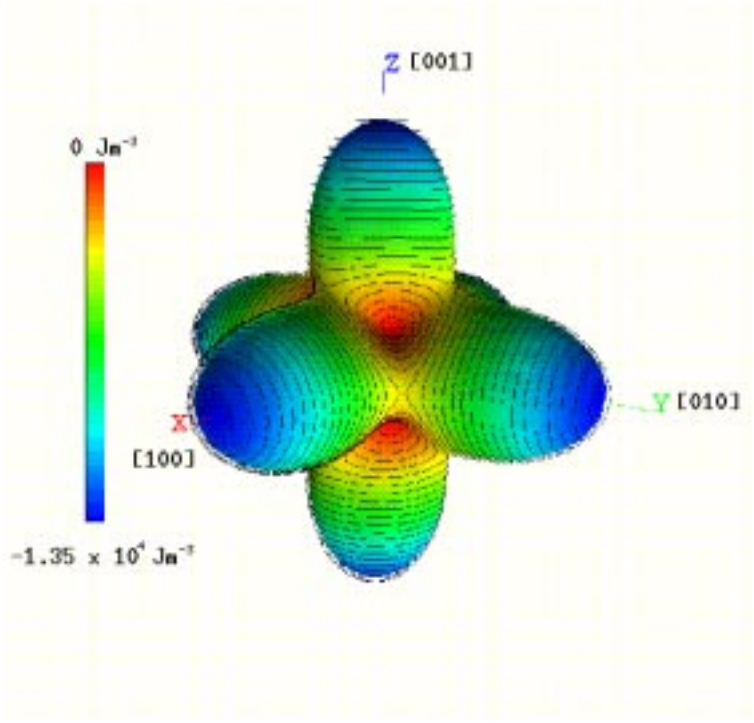


Figure 5.18: The cubic magnetocrystalline anisotropy of magnetite at 290 K. The hard axis is in the [100], [010] and [001] directions (red).

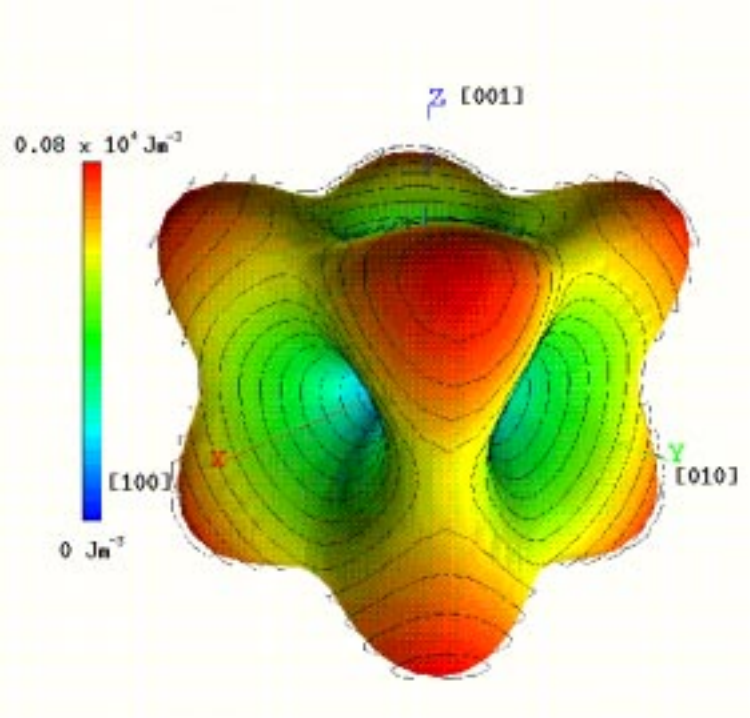


Figure 5.19: The cubic magnetocrystalline anisotropy of magnetite at 120 K. The hard axis is in the [111], direction (red). Note the smaller scale on this figure compared to Figures 5.18 and 5.20.

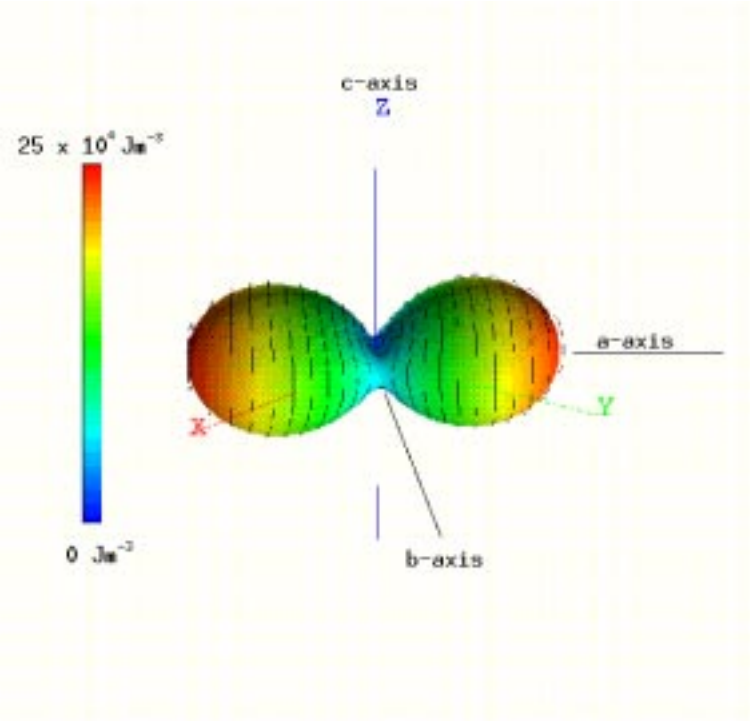


Figure 5.20: The monoclinic magnetocrystalline anisotropy of magnetite at 110 K. The are axis is the a axis (red). Note the larger scale on this figure compared to Figures 5.18 and 5.19.

5.4.3 Magnetostrictive anisotropy constants and elastic moduli at T_v

The magnetostrictive and magnetoelastic anisotropy energies are both controlled by the behaviour of the magnetostrictive anisotropy constants (Section 1.4.3). The magnetostrictive energy is also dependent on the behaviour of the elastic moduli c_{11}, c_{12} and c_{44} (Equation 1.22). It should be noted that the cubic magnetostrictive constants λ_{100} and λ_{111} are defined in terms of c_{11}, c_{12} and c_{44} (Equation 1.22).

Behaviour of the elastic moduli at T_v

Softening anomalies at T_v have been found for c_{11} and c_{44}, (Siratori & Kino, 1980; Isida *et al.*, 1996). The anomaly in c_{44} is much larger than the reported anomaly found in c_{11} (Isida *et al.*, 1996). c_{12} is relatively uneffected by the Verwey transition (Siratori & Kino, 1980).

A decrease in the elastic moduli, reduces the magnetostrictive energy term (Equation 1.22), however it also increases the magnetostrictive constants.

Magnetostrictive anisotropy constants at T_v

The temperature dependent behaviour of the magnetostrictive constants of magnetite between room temperature and T_v has been well documented (*e.g.*, Domenicali, 1950; Bickford Jr. *et al.*, 1955; Belov *et al.*, 1985b), however there have been fewer studies which examine the low-temperature behaviour as a function of temperature (Arai *et al.*, 1976; Tsuya *et al.*, 1977).

The magnetostrictive anisotropy is defined in terms of nine mutually independent constants below T_v (Arai *et al.*, 1976), however it is possible to crudely assign the low-temperature magnetostrictive constants in terms of the high-temperature constants λ_{100} and λ_{111} (Arai *et al.*, 1976; Tsuya *et al.*, 1977). This gives some estimate for the behaviour of the magnetostrictive constants across T_v.

The temperature dependence of all the constants becomes steeper, almost asymptotic, towards the transition (Figure 5.21).

The anomalies in λ_{100} and λ_{111} across T_v (Figure 5.21), have been attributed to reduction of the elastic moduli (Aksenova *et al.*, 1987), however there must also be temperature variations in the magnetoelastic coupling constants (B_0 and B_1, Equation 1.22) to explain the behaviour of the λ_{100} and λ_{111}.

On comparison with the magnetocrystalline anisotropy (Figure 5.17), the change in intensities of λ_{100} and λ_{111} (Figure 5.21) are considerably smaller than the changes in the magnetocrystalline anisotropy constants.

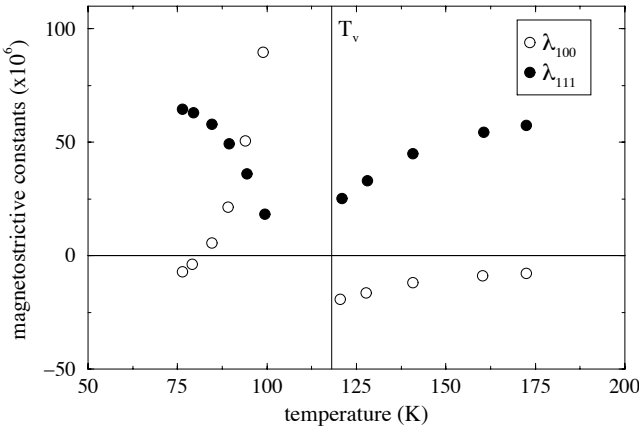


Figure 5.21: Temperature dependence of the magnetostriction constants across T_v. Above T_v λ_{100} and λ_{111} are directly measured. Below they are calculated from the seven low-temperature constants, which gives a rough estimate for the temperature dependent of the magnetostrictive constants. After Tsuya *et al.* (1977).

In summary it appears that the magnetostrictive and magnetoelastic anisotropy energies are both effected by the Verwey transition, however the changes in the energies is less significant than in the magnetocrystalline anisotropy energy.

5.5 Variable stoichiometry at low-temperatures

Before 1984, the importance of stoichiometry had not been realised (Honig, 1995). In the past ten years there have been many investigations which have examined the effect of non-stoichiometry at low-temperatures (*e.g.*, Aragón *et al.*, 1985; Kąkol *et al.*, 1991; Aragón, 1992; De Grave *et al.*, 1993; Kozłowski *et al.*, 1996).

5.5.1 Effect of variable stoichiometry on the Verwey transition

Deviations from stoichiometric magnetite, either by an oxygen deficiency ($Fe_{3(1-\delta)}O_4$) or an impurity, *e.g.*, $Fe_{3-x}Ti_xO_4$, shifts the Verwey transition to lower temperatures (Figure 5.22). Non-stoichiometry also depresses and broadens the transition (Honig, 1995; Dunlop & Özdemir, 1997).

There is a discontinuous anomaly in the Verwey temperature at $\delta = 0.0039$, *i.e.*, $3\delta = 0.012$, which has led to a reclassification (Aragón, 1992) of the Verwey transition into first-order ($-0.0005 \leq \delta < \delta_c \equiv 0.0039$) and second-order ($\delta_c < \delta < 3\delta_c$). For $\delta \approx 3\delta_c$ the magnetite-maghemite/hematite phase boundary is reached and the Verwey transition disappears (Honig, 1995). There is a corresponding system for impurities with $x = 3\delta$, *e.g.*, $Fe_{3-x}Ti_xO_4$ (Honig & Spałek, 1992). Similarly for $x \geq 9\delta_c$ no Verwey transition has been found (Honig & Spałek, 1992; Kozłowski *et al.*, 1996).

There have been several structural-electronic theories which explain the effect of the non-stoichiometry on the Verwey transition. The microscopic order-disorder model devel-

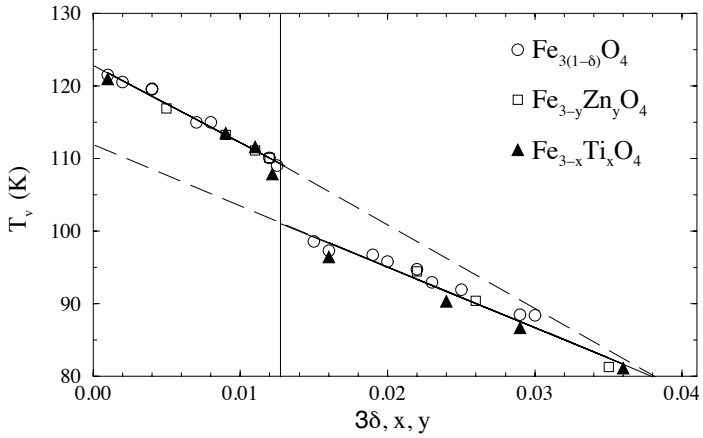


Figure 5.22: Variation of Verwey transition temperature T_v with composition of $Fe_{3(1-\delta)}O_4$, $Fe_{3-y}Zn_yO_4$ and $Fe_{3-x}Ti_xO_4$. After Honig (1995).

oped by Honig and co-workers (*e.g.*, Honig & Spałek, 1992; Honig, 1995), proposes that at the first- and second-order transition, *i.e.*, $\delta = \delta_c$, the the Fe^{2+} and Fe^{3+} B-sublattice cations are rearranged to minimise the free energy (Aragón, 1992; Honig, 1995). This theory has been very successful in explaining the experimental data.

The magneto-electronic model (Section 5.3.2), has not been explicitly applied to this problem, but it seems reasonable to assume that as x or δ increase, the negative Vonsovskiĭ exchange interaction between the *e*-sublattice and A- and B-sublattices weakens. Because the temperature of the Verwey transition is governed by the the balance between the Vonsovskiĭ exchange interaction and thermal energy; a decrease in the Vonsovskiĭ exchange interaction causes T_v to decrease. However this does not explain the first and second-order effects.

5.5.2 Effect of variable stoichiometry on the magnetic anisotropy below room temperature

For titanomagnetites ($Fe_{3-x}Ti_xO_4$) the anisotropy constant K_1' passes through a minimum at x=0.2, irrespective of temperature (Syono, 1965; Kąkol *et al.*, 1991, Figure 5.23). This coincides with the point where Fe^{2+} ions appear in the tetrahedral interstitial sites. For $x \geq 0.2$, there is a large magnetostrictive contribution to the anisotropy which dominates at high x (Kąkol *et al.*, 1991). The isotropic point for K_1' decreases from 130 K for Fe_3O_4 (Kąkol *et al.*, 1991) until $x = 0.2$ where K_1' is still negative at 77 K (Figure 5.23). Note for $x \geq 0.04$ there is no Verwey transition (Figure 5.22). For $x > 0.2$, both the magnetocrystalline anisotropy and the temperature of the isotropic point increases with x (Figure 5.23). For high values of x, *i.e.*, $x \approx 0.6$, K_1 is positive between 77 K and T_c (Kąkol, 1990; Sahu & Moskowitz, 1995). Similar result have been found for $Fe_{3-x}Co_xO_4$ (Slonczewski, 1958).

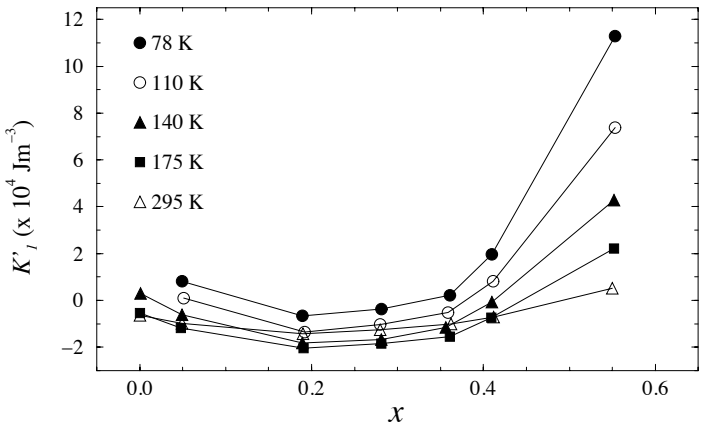


Figure 5.23: Anisotropy parameter K_1' against x parameter in $Fe_{3-x}Ti_xO_4$ at selected temperature in the 77 K–295 K range. After Kąkol *et al.* (1991).

5.6 Importance of stress on the Verwey transition

Around internal dislocations, there are residual stress fields which interact with the magnetisation (*e.g.*, Träuble, 1969; Xu & Merrill, 1989). It is therefore important to understand the effect of stress on the behaviour of the Verwey transition. By applying external stress it is possible to calculate the behaviour of the controlling magnetic energies at low-temperatures.

5.6.1 External stress at the Verwey transition

By examining the conductivity, Rozenberg *et al.* (1996) have shown that applying external stress to magnetite affects the temperature behaviour of the Verwey transition in a similar manner to variations in the stoichiometry, *i.e.*, the Verwey transition decreases with increases stress and is split into first and second-order phases (Figure 5.24). In the pressure range 0-6 GPa, T_v decreases continuously with pressure P from 122 K to 107.5 K (Figure 5.24). At $P \approx 6$ GPa there is a discontinuous jump in T_v from 107.5 K to 100 K, thereafter for 6 GPa $\leq P \leq$ 12.5 GPa there is second-order phase which decreases linearly to to 83 K for 12.5 GPa. For $P >$ 12.5 GPa no Verwey transition is observed, *i.e.*, there is no discontinuous drop in conductivity at low-temperatures.

The structure of the low-temperature phase at $P >$12 GPa is unknown, it is possible that the high pressure actually suppresses the phase transition to the simpler monoclinic/triclinic structure. Rozenberg *et al.* (1996) explain their results in terms of a simple "Wigner structure" type model rather than the order-disorder formulation (Section 5.5).

The behaviour of the elastic modulus c_{11} at T_v is strongly effected by external pressure, vanishing completely at T_v for pressures of $\approx$ 1.2 GPa (Isida *et al.*, 1996). c_{12} and c_{44} are unaffected by pressure changes.

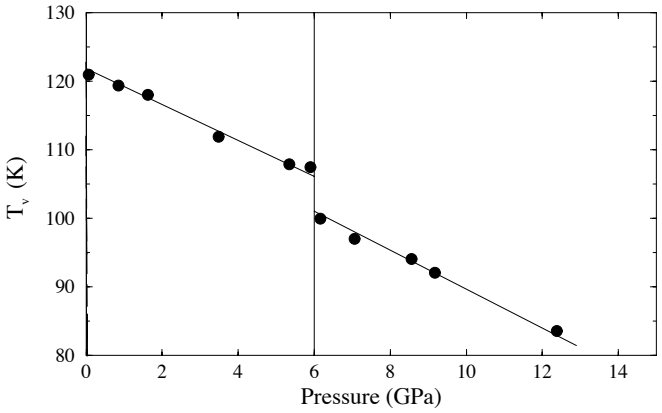


Figure 5.24: Pressure variation of the Verwey transition. After Rozenberg *et al.* (1996).

5.6.2 Internal residual stress at the Verwey transition

Presuming the results from external pressure studies are applicable to internal stress, *i.e.*, stress fields around dislocations, then these results have implications for magnetic domain structures; firstly stressed-areas of a grain near dislocations will have lower Verwey temperatures than stress-free areas (Figure 5.24), and secondly differences in the elastic moduli responses' to pressure will increase the anisotropic energy.

The effect of internal stress on the Verwey transition has by studied by King (1996) and Sahu (1997). King (1996) induced internal stress to his lithographic samples by quenching them from 600 °C at rates $\geq 30\ ^{\circ}Cs^{-1}$ (Lowrie & Fuller, 1969) and by piston pressing. By examining the demagnetisation of low-temperature induced SIRM at T_v (see chapter 6 for more details), he found that the stressed samples displayed a broader, less-well defined Verwey transition than the unstressed samples. This difference in low-temperature behaviour can be explained by a wider range of Verwey temperatures within the sample due to inhomogeneous internal stress.

5.7 Measurement of susceptibility and hysteresis loops at low-temperatures

To understand the demagnetisation mechanism of magnetic remanence during low-temperature cooling to below T_v, it is important to have a knowledge of both the behaviour of the controlling magnetic energies (discussed in Section 5.4), and the basic magnetic parameters, *e.g.*, susceptibility and hysteresis parameters (Chapter 3). The results of an experimental investigation of the basic magnetic parameters at low-temperature is presented here.

I measured the low-temperature initial susceptibility and hysteresis parameters of single domain and multidomain magnetite during a visit to the I.R.M., University of Min-

nesota. The vacuum sealed quartz capsules described in Chapter 2, could not be used on the equipment used in this section. Instead a set of KBr pellets from each grain size were made in the same manner as described in Chapter 2, *i.e.,* 2-3 % magnetite dispersed in KBr and lightly pressed into a pellet.

5.7.1 Susceptibility at low-temperatures

The susceptibility, χ, was measured between $\approx$ 20 K and room temperature at five frequencies (40, 140, 400, 1000 and 4000 Hz) for a selection of samples (*SD(acic.)*, *H(3.0 μm)*, *H(76 μm)* and *H(108 μm)*), using a Lakeshore Cryotronics Low-Temperature AC Susceptometer at the I.R.M. The frequency dependency of susceptibility, χ_{fd}, is usually used to distinguish between superparamagnetic and stable single domain grains (Thompson & Oldfield, 1986). Grains on the boundary between superparamagnetic and stable single domain grains will have lower χ values for the higher frequencies than for the lower frequencies. This is because their relaxation time is longer than half a period of the AC field, *i.e.,* they are affectively blocked to the high frequency range. The susceptibility of natural samples has been found to vary as much as 24 % with frequency, however natural coarse multidomain grains generally have $\leq$ 0.3 % frequency dependency (Thompson & Oldfield, 1986).

The *SD(acic.)* sample displayed no transition in the 120-130 K, whilst the hydrothermal crystals *H(3.0 μm)*, *H(76 μm)* and *H(108 μm)* displayed sharp transitions (Figure 5.25). The increases on heating through T_v and T_k are $\approx$ 120 %, $\approx$ 105 % and $\approx$ 100 % respectively (Figure 5.25). The large increase in χ for multidomain grains is in agreement with previous studies (*e.g.,* Walz & Kronmüller, 1991; Belov, 1993).

The *SD(acic.)* sample is unaffected by the transitions T_v and T_k (Figure 5.25a). This is because the susceptibility of randomly orientated *acicular* single domain grains is controlled by $\chi \propto 1/N$, where N is the self-demagnetising factor (Nagata, 1961). Any changes in N due to possible small changes in the crystal shape is unlikely to be significant. The controlling anisotropy energies of single domain grains is discussed in detail in Section 5.7.2. The hydrothermal crystals *H(3.0 μm)*, *H(76 μm)* and *H(108 μm)* are multidomain, whose susceptibility is governed by the behaviour of domain walls which are dependent on the magnetocrystalline and magnetoelastic anisotropy energies. The sharp increase in χ in the temperature range 120-130 K reflects this dependency (Figures 5.25b-5.25d).

Measurement of the low-temperature susceptibility of *H(108 μm)*, was repeated with smaller temperature steps in the range in 110-130 K (Figure 5.26). There was a very good repeatability in χ in this temperature range (*cf.* Figure 5.25d).

The anomaly associated with T_v and T_k occurs over the range of temperatures 118-126 K (Figure 5.25). That the transition is over a temperature range rather than a discontinuous jump is in agreement with the magneto-electronic model (Section 5.3.2). The transition width of $\approx$ 8 K is wider than the 3 K reported for single crystals (*e.g.,* Aragón *et al.*, 1985;

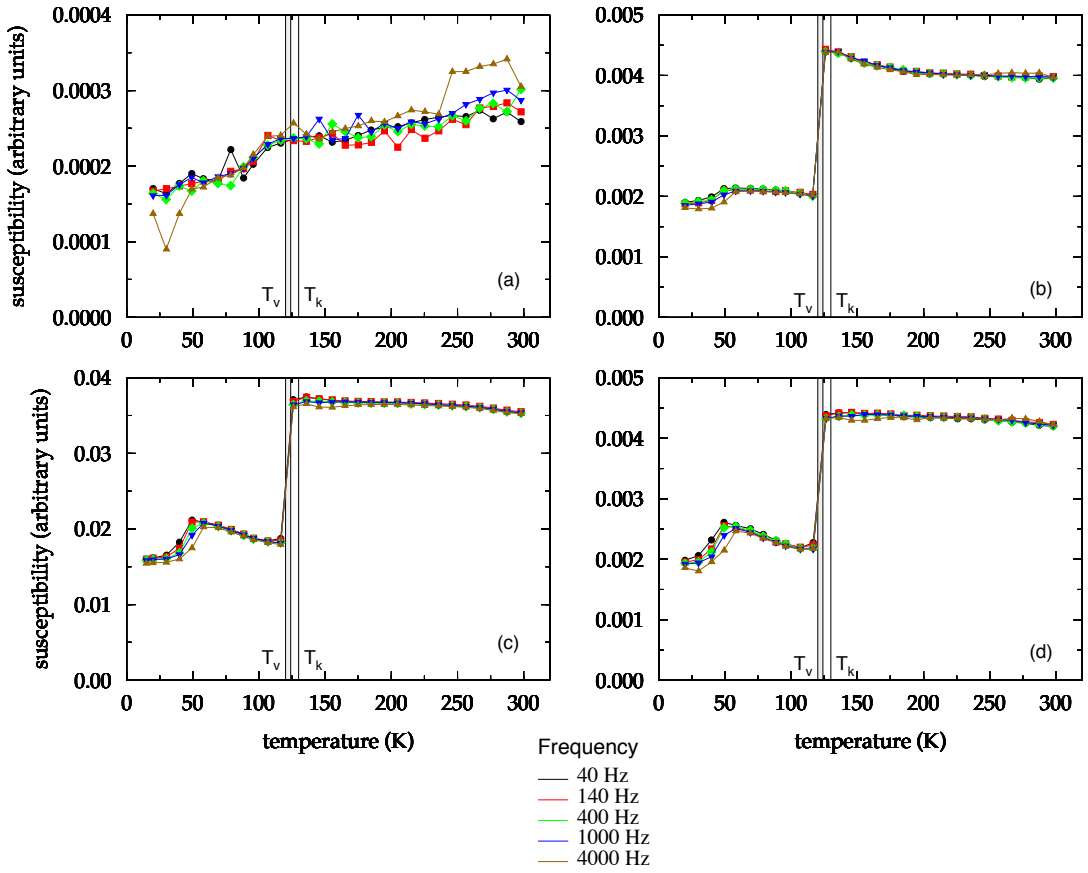


Figure 5.25: Susceptibility of temperature at various frequencies for a) *SD(acic.)*, and hydrothermal crystals b) *H(3.0 μm)*, c) *H(76 μm)* and d) *H(108 μm)*. The susceptibility curves were measured on warming from ≈ 20 K.

Walz & Kronmüller, 1991), however it is considerably narrower than the 17 K reported for powdered samples (Walz & Kronmüller, 1991). It is uncertain why the range of the transition is larger than the value for the single crystal. It is not due to temperature inhomogeneity across the sample, because the sample which should only take a minute or two to equilibrate, was held for between 10–20 minutes within 2 K of the temperature before measurement. Walz & Kronmüller attribute the large transition width for their powdered sample to internal stress induced during milling; stress around dislocation points has the effect of decreasing the Verwey transition temperature (see Figure 5.24). Therefore inhomogeneously stressed samples should be expected to display a range of transition temperatures. Applying this theory to the *H(108 μm)* sample, implies that there was a range of stresses within the samples, *i.e.*, either different grains within the sample or different areas within a grain had slightly different internal stress values giving rise to a wide transition temperature. Examination of the coercive force (Figure 3.3) suggests that the raw material *H(108 μm)* was relatively stress free (Chapter 3). Any stress within the sample must have been induced during the preparation of the lightly pressed KBr pellets. The difference in transition width cannot be explained by grain interactions, because crystals in the *H(108 μm)* sample are of a size where grain interactions are thought to be insignificant (*pers. comm.* W. Williams, 1996).

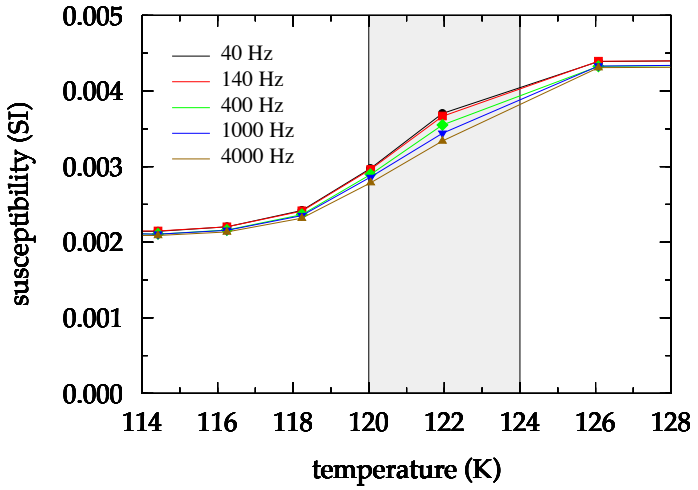


Figure 5.26: Susceptibility as a function of temperature at various frequencies for hydrothermal crystals *H(108 μm)*. The susceptibility was measured at smaller step intervals in the range 110-130 K than reported in Figure 5.25. The Verwey transition (120–124 K) is shaded in grey.

Another possible explanation for the large transition width of the *H(108 μm)* sample, is that the jump in χ is associated with the domain structure. The domain structure of each grain within a sample will have a slightly different degree of stability. In response to the AC field and changes in the magnetic energies in the vicinity of T_v, the domain structure will ''break" at some temperature, giving rise to the increase in χ. In a similar manner to the stress, different grains will have different degrees of domain stability. By measuring only one crystal, with one domain structure, then transition width will be relatively narrow (Walz & Kronmüller, 1991), however by measuring a number of grains then the width of the transition will be larger (Figure 5.26). It should be noted that different single crystals very rarely give the same temperature for the Verwey transition. Differences are normally attributed to small variations in the stoichiometry, however even for "perfect" magnetite there are a range of claimed temperatures for T_v, *e.g.*, 122-125 K (Aragón *et al.*, 1985), 125 K (Walz & Kronmüller, 1994), 100-120 K (Belov, 1996a), 120 K (Gridin *et al.*, 1996) and ≈121 K (Rozenberg *et al.*, 1996).

There is a slight frequency dependency for *H(108 μm)* across the transition, most noticeably at 122 K (Figure 5.26). For most temperatures outside the range 118-126 K, the susceptibility measured in 40 Hz χ_{40}, displayed an almost identical value to that measured at higher frequencies. However in the temperature range 118-126 K, χ is frequency dependent, *i.e.*, $\chi_{40} > \chi_{140} > \chi_{400} > \chi_{1000} > \chi_{4000}$. This was unexpected and to my knowledge has never been reported. It is clearly related to the Verwey transition. A possible cause for this frequency dependency is the reduction in the mobility of hopping electrons across the transition. Above the transition the electrons hop with an "attempt frequency", τ_0^{-1}, of $\approx 10^{14}\text{s}^{-1}$, however below the transition, $\tau_0^{-1} \approx 10^{12}\text{s}^{-1}$ (Walz & Kronmüller, 1994). Across the transition itself, there will be a temperature where the the *e*-sublattice is very weak, and is very susceptible to external changes. For multidomain grains χ is inversely related to the

magnetocrystalline anisotropy, which is due to the unquenched component of the orbital momentum of the Fe^{2+} (Section 1.4.3). The localisation of electrons/Fe^{2+} below T_v causes the large increase in the magnetocrystalline anisotropy (Figure 5.17), and a corresponding decrease in χ. Compared to the higher AC frequencies, at lower AC frequencies there is more time for the weakened Vonsovskiĭ exchange interaction to be broken by the weak AC field. Destroying the *e*-sublattice increases the hopping rate of the electrons/Fe^{2+} which in turn increases χ. As the AC frequency increases there is less time to respond, making the effective magnetocrystalline anisotropy higher, which in turn decreases χ. The temperature where the frequency dependency is greatest *i.e.,* 122 K for *H(108 μm)* (Figure 5.26), is probably a good indicator for T_v.

Another point of interest is the small anomaly in χ at $\approx$ 50 K observed for *H(3.0 μm)*, *H(76 μm)* and *H(108 μm)* (Figure 5.25). This anomaly has been reported before for single crystals of magnetite (*e.g.,* Walz & Kronmüller, 1991; 1994), and is attributed to magnetic after-effect/relaxation processes (Kronmüller, 1977; Belov *et al.*, 1985a). The magnetic-after effect is the change in magnetic properties with time, and is akin to viscous remanent magnetisation. The magnetic-after effect in magnetite is related to electron mobility. Walz and Kronmüller have shown in a series of papers (*e.g.,* Kronmüller *et al.*, 1974; Kronmüller, 1977; Walz & Kronmüller, 1990; 1991; 1994), that by repeatedly measuring χ over a period of 180 s for a range of temperatures (4-300 K), that depending on the temperature there can be up to a 10 % decrease in χ. Obviously T_v has a large effect on the magnetic after-effects, but Walz and Kronmüller have identified other magnetic-after affects at various temperatures, *e.g.,* electron-tunnelling (4-20 K) and restrained electron hopping (50-125 K) (Walz & Kronmüller, 1994).

The anomaly in χ at 50 K is attributed to a diminishment of the restrained electron hopping, from $\tau_0^{-1} \approx 10^{12}$ s^{-1} above 50 K to $\tau_0^{-1} \approx 10^{11}$ s^{-1} below it (Walz & Kronmüller, 1994). Changes in electron mobility effect χ in a similar manner as at T_v. The small frequency dependency found in samples *H(3.0 μm)*, *H(76 μm)* and *H(108 μm)* at 50 K (Figure 5.25) is analogous to the situation at T_v. *H(76 μm)* and *H(108 μm)* have larger anomalies than *H(3.0 μm)* because they are truly multidomain rather than pseudo-single domain (Chapter 3).

There are reports in literature of peaks in χ at T_k, (*e.g.,* Hodych, 1986; Belov, 1993), however the only sample to display a peak near T_v was the small *H(3.0 μm)* sample (Figure 5.25b). I suggest here that the peak could be an indicator of grain size.

5.7.2 Low-temperature behaviour of the hysteresis parameters

Hysteresis loops were measured using the in-house built VSM at the Institute for Rock Magnetism (Section 5.3.2). The temperature control on the VSM was rather unreliable; at temperatures less than $\approx$ 95 K the drift was $\approx$ 5 K during the 15 minutes it took to measure a hysteresis loops. At temperatures above this, with careful monitoring it was possible to

keep the temperature to within $\pm$ 0.2 K of the required temperature. It should be noted that even though the temperature control was not perfect the temperature could be measured accurately to within $\pm$ 0.1 K (*pers. comm.* J. Marvin, 1996).

Hysteresis loops at various temperatures in the range 100-300 K, were measured for three samples; the single domain *SD(acic.)* sample and two hydrothermal samples *H(3.0 μm)* and *H(108 μm)*. These samples had been previously used to measure the low-temperature χ curves (Section 5.7.1).

Measurement of coercive force as a function of low-temperature

Figure 5.27 shows coercive force, H_c, plotted as a function of temperature for the hydrothermal samples. In contrast *H(3.0 μm)* and *H(76 μm)* both show large decreases in H_c across the two transitions T_v and T_k with increasing temperature (Figure 5.27). The coercive force measured for *H(3.0 μm)* decreases sharply from $\approx$ 8.8 mT at 128 K to $\approx$ 2.1 mT at 132 K. The coercive force anomaly for *H(76 μm)* is not as large, dropping from $\approx$ 4.0 mT at 127 K, to $\approx$ 1.1 mT at 133 K. In both cases the coercive force drops by a factor of approximately four.

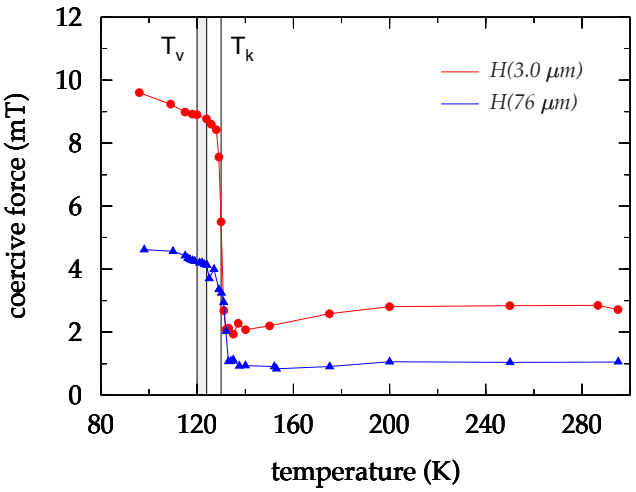


Figure 5.27: Coercive force as a function of temperature for hydrothermal crystals a) *H(3.0 μm)* and b) *H(76 μm)*. The coercive force was determined from hysteresis loops measured at a variety of temperatures. Data from the same hysteresis loops had previously been used to determine the spontaneous magnetisation in Figure 5.14.

On heating to T_v, H_c sharply decreases at T_v for both *H(3.0 μm)* and *H(76 μm)*, before reaching a minimum at T_k (Figure 5.27). It is expected that the minimum occurs at T_k rather than T_v. This is because at T_v there is a discontinuous jump in the magnetocrystalline anisotropy from a negative to a positive value *i.e.*, $E_k > 0$ at all times across T_v (Figure 5.17). However at T_k, $E_k \rightarrow 0$. That the two transitions appear as a single wide transition is due to their proximity and the retardation of the Verwey transition (Section 5.3.2). After a minimum in H_c at $\approx$ 135 K for *H(3.0 μm)*, there is a small increase in H_c with

increasing temperature, levelling off towards room temperature (Figure 5.27). *H(76 μm)* displays a similar though less pronounced trend as *H(3.0 μm)*(Figure 5.27). This trend has been previously observed for natural samples (Hodych, 1986; Hodych, 1990) and synthetic crystals (King, 1996; Schmidbauer & Keller, 1996). For Fe_3O_4 thin films, Zhou & Yan (1992) found a peak in H_c at $\approx$ 220 K which gradually decreased towards room temperature (*cf.* Figure 5.27). They split the behaviour of H_c, into contributions controlled by the shape anisotropy and by the magnetocrystalline anisotropy. They attributed the peak at $\approx$ 220 K to the magnetocrystalline anisotropy. The size of increase on heating from T_k appears to be grain size dependent, *i.e.,* the increase on warming from T_k to room temperature is larger for *H(3.0 μm)* than for *H(76 μm)* (Figure 5.27). This grain size dependency has been previously noted by King (1996), who postulated that it is indicative of pseudo-single domain behaviour.

Calculation of SD low-temperature coercive force

According to traditional theories, single domain (SD) remanence should not be affected on cooling by T_k or T_v because its behaviour is controlled by the shape anisotropy. However there is some experimental evidence to suggest that acicular SD grains do exhibit a remanence transition (Dunlop & Özdemir, 1997), but to my knowledge no explanation for this has been given in the literature. Traditional models do not include the anomaly in the spontaneous magnetisation (Section 5.3.3), and they assume that the anisotropy for SD grains is governed by the shape anisotropy at all temperatures. However, using Mössbauer spectroscopy, Hu *et al.* (1991) have shown that the anisotropy for SD grains of diameter 0.0088 and 0.011 μm exhibits a transition at T_v.

Here a simplified model which examines the controlling anisotropy energy and its influence on the coercive force as a function for single domain grains is presented. The coercive force H_c of a single domain single crystal is controlled by either shape, magnetostrictive or magnetocrystalline anisotropies. At room temperature the shape anisotropy is dominant for most single domain grains, apart from grains which are almost spherical (Schmidbauer & Keller, 1996). On cooling below the Verwey transition there is a very large increase in the magnetocrystalline anisotropy (Figure 5.17), which greatly influences the ascendancy of the anisotropy energies. In the following calculation only the shape and magnetocrystalline anisotropies are considered. Assuming uniaxial anisotropy (K_u), the coercive force of a single domain grain is given by (Nagata, 1961)

$$\begin{aligned} H_c &= \frac{2K_u}{\mu_0 M_s} && \text{(magnetocrystalline)} \\ &= NM_s && \text{(shape)} \end{aligned} \tag{5.2}$$

where μ_0 is the permeability of free space, N is the demagnetising factor of a single domain grain and K_u equals K_1 in the cubic phase of magnetite, and K_a in the monoclinic

phase. For an assemblage of crystals H_c given is Equation 5.2) is divided by two (Dunlop & Özdemir, 1997). At a certain value of N (N_{crit}), the coercive force due to the shape anisotropy and magnetocrystalline anisotropy are equal. N_{crit} is given by

$$N_{crit} = \frac{2K_u}{\mu_0 M_s^2} \tag{5.3}$$

In examining N_{crit} it is useful to consider the parameter N_b which is the value of N needed to block an SD grain by the shape anisotropy at a given temperature. N_b is given by (Néel, 1949; Dunlop & West, 1969)

$$N_b = \frac{2\mathrm{k}T(\ln C + 2\ln(2t))}{\mu_0 M_s^2 v} \tag{5.4}$$

where k is Boltzmann's constant (1.381 $\times 10^{-23}$ JK^{-1} (Jiles, 1991)), C is a rate constant which can be considered as the number of attempts per second that the magnetic vector tries to change direction. The exact value of C is unknown, it is usually quoted as being either 10^8 s^{-1} (*e.g.*, Stacey & Banerjee, 1974; Williams & Walton, 1986), 10^9 s^{-1} (*e.g.*, Crew *et al.*, 1996; Dunlop & Özdemir, 1997) or 10^{10} s^{-1} (*e.g.*, McElhinny, 1973; Dunlop, 1983). As part of an undergraduate project (Muxworthy, 1994), I personally calculated C to be 1.00 $\pm$0.05 $\times$ 10^{10} s^{-1} from SD viscous decay data collected by Williams (1986). This last value of 10^{10} s^{-1} is used for C in the calculation of N_b (Figure 5.28).

Using the low-temperature dependency of M_s shown in Figure 5.8, and the data shown in Figure 5.17 for K_u N_{crit}, N_b and H_c are calculated as a function of temperature (Figures 5.28 and 5.29). The results are summarised in Table 5.1.

Demagnetising factor (N)	eccentricity	$T < \mathrm{T}_v$	$T > \mathrm{T}_v$
0.001	0.0706	magnetocrystalline	magnetocrystalline
0.2	0.820	shape	magnetocrystalline
0.4	0.974	shape	shape

Table 5.1: Controlling magnetic anisotropy above and below the Verwey transition T_v for three different demagnetising factors. N = 0.001 is represents spheroidal grain, whereas N = 0.4 represents an acicular grain. Assuming an ellipsoid, the eccentricity of an ellipsoid for each demagnetising factor is also shown.

At room temperature most SD grains are controlled by the shape anisotropy (Figure 5.28), *i.e.*, $N_b > N_{crit}$; at room temperature small spherical grains which are controlled by the magnetocrystalline anisotropy are superparamagnetic. It is only the largest near spherical grains, *e.g.*, volume = 1.8 $\times$ 10^{-23} m^3, diameter = 0.032 μm (Figure 5.28), which carry remanence controlled by the magnetocrystalline anisotropy. On cooling towards the Verwey transition N_b decreases for all grain sizes, *i.e.*, more grains become blocked. On cooling through the Verwey transition there is a large jump in the magnetocrystalline

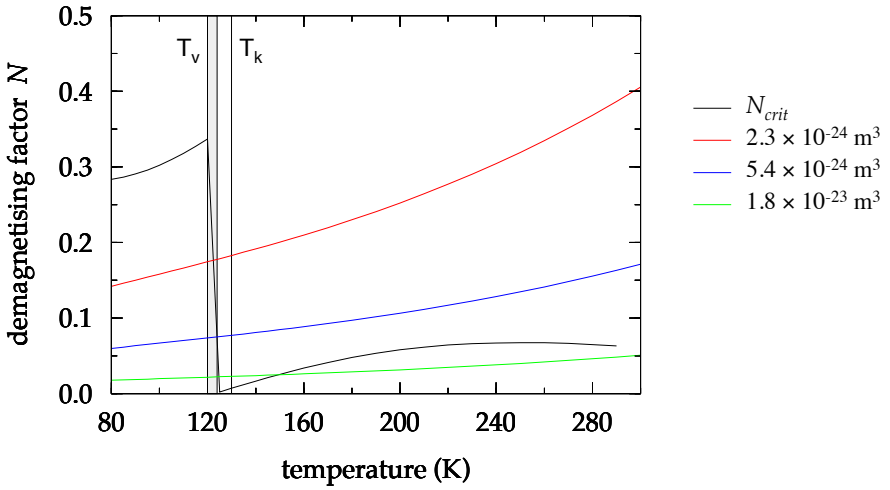


Figure 5.28: N_{crit} as a function of temperature and N_b as function of temperature for three grain volumes. Values of N above each N_b are blocked for that volume, below they are unblocked. If $N_b > N_{crit}$ all the remanence is carried by grain controlled by shape anisotropy. If $N_b < N_{crit}$ then there is a mixture of grains controlled by the shape and magnetocrystalline anisotropies. Small N values are associated with spherical grains, larger N values with acicular grains. Note a spherical grain of volume 2.3×10^{-24} m^3 has diameter of 0.016 μm, whilst a spherical grain of volume 1.8×10^{-23} m^3 has a diameter = 0.032 μm. T_v and T_k are marked, T_v as a band (120-124 K) due to the uncertainties in its value.

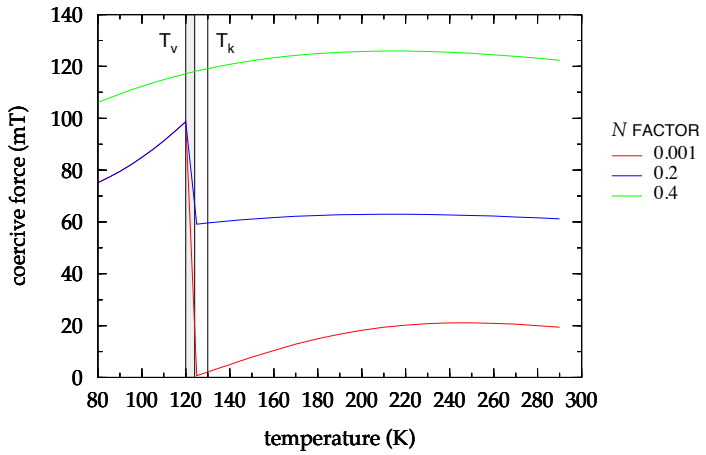


Figure 5.29: H_c as a function of temperature for various demagnetising factors. H_c is calculated for an assemblage of crystals. $N = 0.001$ represents near spheroidal grains, whereas $N = 0.4$ represents acicular grains. T_v and T_k are marked, T_v as a band (120-124 K) due to the uncertainties in its value.

anisotropy, and the magnetocrystalline anisotropy controls most aspects of SD grains, *i.e.*, $N_b < N_{crit}$. The increase in N_{crit} at T_v, means that a large percentage of SD grains will become blocked on cooling through the Verwey transition.

The aspect ratio of a SD grain strongly controls its low-temperature coercive force (Figure 5.29 and Table 5.1). Near spherical grains, *i.e.*, $N = 0.001$, are controlled by the magnetocrystalline anisotropy at all times, and their coercive force displays a large jump at T_v corresponding to the increase in the magnetocrystalline anisotropy (Figure 5.17). Grains with intermediate aspect ratios, *i.e.*, $N = 0.2$, display smaller anomalies at T_v, whilst acicular

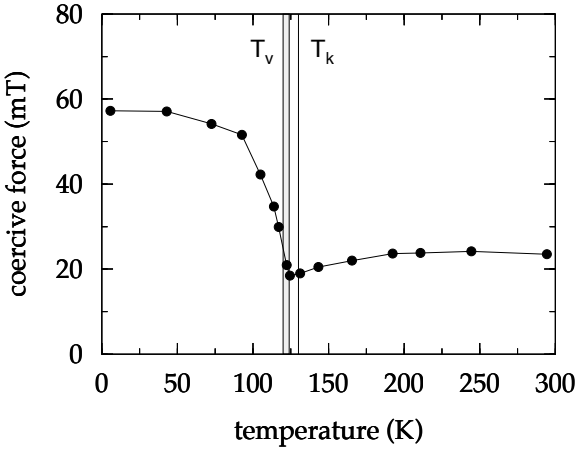


Figure 5.30: H_c as a function of temperature for near spherical 0.25 μm magnetite crystals. After Schmidbauer & Keller (1996).

aspect ratios *i.e.,* $N = 0.4$, display no anomaly at T_v (Figure 5.29).

Coercive Force as a function of low-temperature has been measured for near spherical small pseudo-single domain (PSD) crystals by Schmidbauer & Keller (1996). Their data is shown in Figure 5.30. Note small PSD grains often display similar behaviour to SD grains (Dunlop & Özdemir, 1997).

The spherical grains display similar behaviour to that predicted for grains controlled by the magnetocrystalline anisotropy (*cf.* Figures 5.29 and 5.30). The calculated coercive forces are higher.

The behaviour of the magnetocrystalline anisotropy controlled H_c (Figure 5.29) resembles the H_c curves for the hydrothermal magnetite samples *H(3.0 μm)* and *H(76 μm)* (Figure 5.27). This simply relates to the fact that the coercive force of multidomain grains is partially controlled by the magnetocrystalline anisotropy.

M_{rs}/M_s versus H_{cr}/H_c as a function of low-temperature

It is common practice to plot M_{rs}/M_s versus H_{cr}/H_c, because different domain states plot in different areas (Dunlop & Özdemir, 1997), *e.g.,* single domain grains have high M_{rs}/M_s ratios and low H_{cr}/H_c ratios. Note H_{cr}/H_c is less discriminating than M_{rs}/M_s (Thompson & Oldfield, 1986).

Figure 5.31 shows the M_{rs}/M_s versus H_{cr}/H_c plot for the two hydrothermal samples *H(3.0 μm)* and *H(76 μm)*. *H(3.0 μm)* and *H(76 μm)* both plot in the multidomain region above T_v, and show marked change on cooling through T_v. Below T_v, *H(3.0 μm)* and *H(76 μm)* are more PSD-like than they are above it, having both higher M_{rs}/M_s and lower H_{cr}/H_c ratios. This is due to anomalies in a number of controlling energies (Section 5.4), *e.g.,* the increase in the magnetocrystalline anisotropy in turn increases H_c. Below T_v, *H(3.0 μm)* plots in the area of large PSD grains grains.

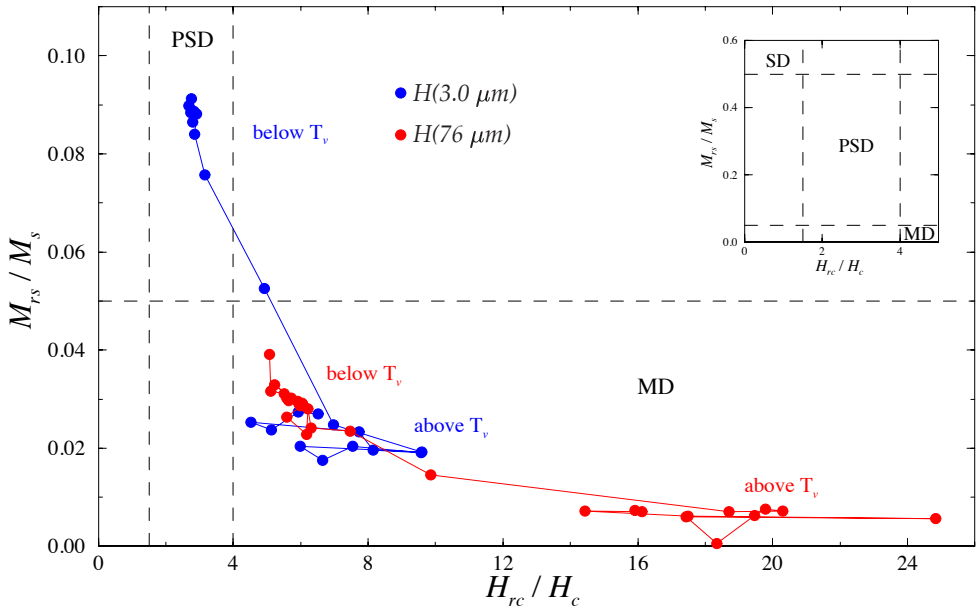


Figure 5.31: M_{rs}/M_s versus H_{cr}/H_c for the two hydrothermal samples *H(3.0 μm)* (●) and *H(76 μm)* (●).

5.8 Summary

At ≈ 120-124 K magnetite passes through a phase transition called the Verwey transition, which is marked by the reduction in hopping electrons (Section 5.2). Associated with the reduction in electron mobility are changes in all the controlling magnetic energies except the exchange energy (Section 5.4). Important to multidomain magnetite there is a very large change in both the intensity and symmetry of the magnetocrystalline anisotropy on cooling through the Verwey transition, which is attributed to changes in the electron mobility. This strongly effects the fundamental properties of magnetite like the H_c. Variations in stress and stoichiometry also affect the temperature of the Verwey transition (Sections 5.5 and 5.6). It is postulated that stress fields around dislocations will give rise to range of Verwey transition temperatures in a sample.

At ≈ 130 K the first cubic magnetocrystalline anisotropy tends to zero (Section 5.4.2). It is suggested in this chapter that T_k and the Verwey transition are separate phenomena. The temperature of the isotropic point is also affected by non-stoichiometry, however the rate of decrease is less than that for the Verwey transition.

Chapter 6

Behaviour of magnetic remanences at low-temperature

6.1 Introduction

Following on from Chapter 5 where the low-temperature properties of magnetite were discussed, in this chapter an experimental investigation of the behaviour of magnetic remanences during low-temperature cycling is presented.

When remanent magnetisation of a multidomain magnetite grain passes through the first cubic magnetocrystalline anisotropy constant at 130 K, T_k, and the Verwey transition at $\approx$ 120 K, T_v, (see Chapter 5) in zero field, it partially demagnetises (*e.g.*, Ozima *et al.*, 1964b; Halgedahl & Jarrard, 1995, Figure 5.1). There are two areas of study here; firstly the behaviour of the remanent magnetisation at low-temperatures, especially in the vicinity of T_k and T_v, and secondly the behaviour at room-temperature and above of the remaining remanent magnetisation after low-temperature treatment. The former area is discussed in this chapter, whilst the latter is discussed in Chapter 7.

Most previous investigations of the low-temperature cycling of remanences have used saturated isothermal remanences (SIRM) induced at room temperature as the initial remanence (Section 6.2). In a comparative study, the results of the low-temperature cycling of room temperature SIRMs induced in a selection of magnetite samples (hydrothermally-recrystallised, sized, magnetite grains and natural, sized, magnetite crystals (see Chapter 2 for description)) are presented in Section 6.5. To my knowledge this is the first time that the low-temperature behaviour of hydrothermal magnetites has been directly measured, which is of particular importance because previous studies (*e.g.*, Heider *et al.*, 1988a; Heider *et al.*, 1992) have suggested that synthetic crystals produced by hydrothermal recrystallisation (Chapter 2) are closer in magnetic character to natural crystals than other synthetic samples. In Section 6.5.3 the relative contribution of T_k and T_v to the total demagnetisation

of remanence during low-temperature cycling is considered, by examining the behaviour of saturating isothermal remanences to cooling through the two transitions.

It was also decided to examine the behaviour of thermoremanences (TRM and partial TRM (pTRM)) to low-temperature cycling, because there have been very few published studies which have examined this problem (Section 6.2 6.1). The results of the low-temperature cycling of TRMs are presented in Section 6.6, and the results compared to those of the low-temperature cycled SIRMs in Section 6.7.

In a subsequent chapter (Chapter 8), the experimental results found in this chapter will be compared with those from micromagnetic modelling of hypothetical, ideal single crystals subjected to theoretically identical conditions.

The remanences were measured using Quantum Design Magnetic Property Measuring Systems (MPMS). Before presenting the results, some technical difficulties and limitations encountered with the MPMSs are considered (Section 6.4).

6.2 Previous investigations of low-temperature cycling of remanent magnetisations

The study of the low-temperature cycling of remanence has never been extensive, which is mainly due to technical difficulties and lack of specialised equipment. Experimentation has either been undertaken on large samples using adapted spinner magnetometers or more recently on MPMSs, which suffer from cooling problems and relatively large residual fields (discussed Section 6.4). In theory it should be relatively straight-forward to build a low-temperature, low-residual field magnetometer with SQUID interface, however this has not been done due to the problem being too technical for in-house instrumental production and at the same time not viable enough for commercial production.

However there have been several investigations into the direct measurement of low-temperature cycling of remanent magnetisations, of which these have mainly been conducted on samples initially induced with SIRM (*e.g.*, Kobayashi & Fuller, 1968; Hodych, 1991; Halgedahl & Jarrard, 1995; King, 1996; Sahu, 1997). There have been a limited number of investigations of initial thermoremanences (TRM); namely natural samples with natural TRM (Creer & Like, 1967), natural samples with laboratory induced TRM (Ozima *et al.*, 1964b; Hartstra, 1983) and to my knowledge there is only one previous report of the low-temperature measurement of laboratory induced thermoremanence in synthetic magnetite (Ozima *et al.*, 1964b). However the low-temperature behaviour of thermoremanence is far from characterised, *e.g.*, in the most controlled investigation by Ozima *et al.* (1964b), the TRM was induced by heating synthetic samples in air, which probably partially oxidised the sample. Ozima *et al.* (1964b) realised this, did not present the data, and simply stated that "high temperature treatment [in air] might have brought in change of the physical or chemical state of the sample".

There have been many other rock magnetic low-temperature studies, however these have not relied on having absolute-zero internal residual field, *e.g.*, measurement of high-field properties (*e.g.*, Hodych, 1990; Schmidbauer & Keller, 1996, see also Chapter 5) or magnetic mineralogy studies which use low-temperature properties for identification (*e.g.*, Nagata *et al.*, 1964; Housen *et al.*, 1996).

6.3 Definition of magnetic memory

Before examining the behaviour of initial remanent magnetisation during low-temperature cooling, it is necessary to define what is meant by the expression "magnetic memory". In the literature the term "magnetic memory" is often used when describing the remanent magnetisation left after low-temperature cycling, however there are two definitions of it in the literature, here termed **definition 1** and **definition 2**. In both cases the sample is cooled from room temperature to 77 K and heated back up to room temperature in zero field.

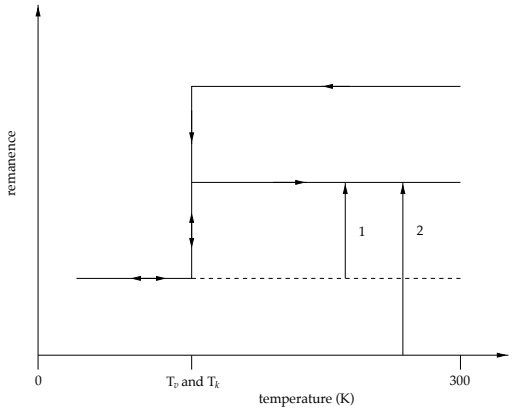


Figure 6.1: Schematic representation of a low-temperature curve, and the two magnetic memory definitions 1 and 2.

Definition 1

According to this earlier definition (*e.g.*, Ozima *et al.*, 1964b; Creer & Like, 1967) the magnetic memory is the amount of *recovery* of magnetic remanence on warming from the two transitions up to room temperature (Figure 6.1). The inverse effect has also been termed the "magnetic memory" (Nagata *et al.*, 1964), *i.e.*, samples given a SIRM at 77 K demagnetise on warming through T_v and T_k, but on cooling back to 77 K, recovery or "magnetic memory" is observed.

Definition 2

The later definition of magnetic memory (*e.g.*, Kobayashi & Fuller, 1968; McClelland *et al.*, 1996) refers to the remanent magnetisation remaining after low-temperature cycling in zero-field, regardless of whether it has *recovered* or not

(Figure 6.1). By definition 2, samples can still have magnetic memory even if there is no *recovery* in the magnetisation.

For samples which completely demagnetise below T_v, definition 1 equals definition 2, however this is the only case where the definitions are equal. On the other hand, samples which show no low-temperature transition, *e.g.*, pure maghemite, the two defintions give completely different results *i.e.*, 0 % for definition 1 and 100 % for definition 2.

The advantage of working with definition 2 over definition 1, is that it requires only two measurements both at room temperature, whereas definition 1 requires measurements at low-temperature. As a result definition 2 can easily be performed in a standard palaeomagnetic laboratory, whereas definition 1 requires more specialised equipment.

In the rest of this study "magnetic memory" will be taken to mean definition 2. The term "recovery" will be used to replace definition 1.

6.4 Notes on the technical capabilities of the MPMS

Three MPMS instruments used in this study; a MPMS2 (Department of Chemistry, University of Edinburgh, maximum field = 2 T), a MPMS5 with special low-residual field adapter (Institute for Rock Magnetism (I.R.M.), University of Minnesota, maximum field = 5 T) and another MPMS5 (Department of Chemistry, University of Oxford, maximum field = 5 T). Unfortunately the MPMS5 at the University of Oxford was purchased towards the end of this thesis, and as a result I only used it once in November 1997.

The basic MPMS (sensitivity = 1×10^{-11} Am^2) is designed to measure the magnetisation via a SQUID interface in the direction of an applied field on warming from low-temperatures (≈ 2 K $\leq T \leq 300$ K). The entire measurement sequence is fully automated, relying on some very flexible and well written software. This study required measurement of remanences during cooling from room-temperature in zero-field, which contravened the design purpose of the MPMS. Because of this unintended use, there were problems with minimising the residual field (H_{res}) and with overshooting the set temperature during cooling. These problems have been previously reported by King (1996).

The MPMS5 in Minnesota had a special low-residual field adapter which the manufacturers (Quantum Design) claimed reduced H_{res} from the standard 200μT to less than 50μT. The residual field was further reduced by running in-house external device system (EDS) code during the zero-field reset sequence. Neither the MPMS2 in Edinburgh or MPMS5 in Oxford had this low-field adapter. For all MPMS instruments H_{res} is prone to drift slightly (*pers. comm.* J. Marvin, 1996), because of this the residual field was reset before every experiment.

It is possible to adapt a MPMS to measure the magnetisation in x, y and z directions, however none of the MPMSs had this capability, *i.e.*, measurement was in the z direction only.

6.4.1 Run-time problems with the MPMS

There was a large problem with overshooting during cooling. As stated above, MPMSs are designed to run during warming.

During both cooling and warming, the measurement is taken only after the set temperature has been stabilised at each step. The system works by overshooting the target temperature before slowly iterating back to the set temperature (Figure 6.2). During warming, the system is relatively accurate, with a small overshoot which does not take long to stabilise (Figure 6.2b).

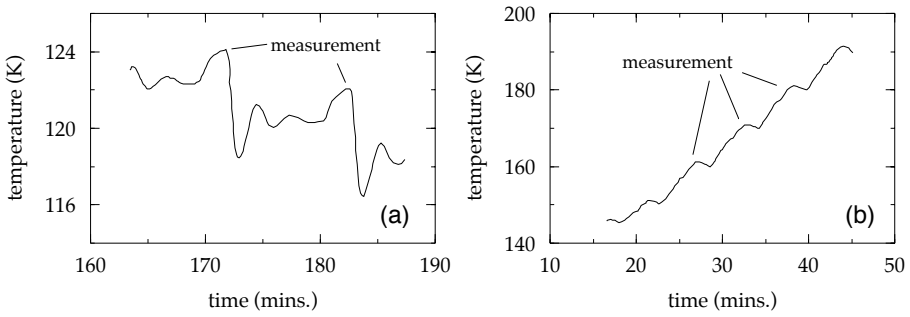


Figure 6.2: Time taken for MPMS5 in Minnesota to stabilise the temperature for measurement during a) cooling (under-cool mode on) and b) warming. The MPMS5 in Minnesota had special in-house EDS code which improved the stabilisation algorithm and reduced the stabilisation time during cooling.

During cooling, the overshoot is much greater and the time taken to stabilise is considerably greater, taking up to 20 minutes per temperature step (Figure 6.2a). Increasing the temperature step size does not significantly decrease the total measurement time, because the time taken to stabilise is approximately proportional to the size of the temperature step (*pers. comm.* B. Moskowitz, 1996). There is a special under-cool mode, which reduces the overshoot on cooling, however this facility is only available for temperatures less than 200 K and for temperature steps $\leq$ 10 K. For example for a 10 K cooling step *without* the under-cool mode, the temperature typically overshoots by $\approx$ 10 K below the required temperature for 2–3 minutes before warming to $\approx$ 5 K below the set temperature. With the under-cool mode on, the overshoot is usually $\leq$ 2 K for a 10 K step. In both cases it takes $\approx$ 15 minutes to stabilise to set temperature. In Figure 6.2a, the temperature step is only 2 K, yet it can be seen that the set temperature is overshot by as much as 1 K for 1–2 minutes.

By applying the same temperature step sequence throughout all of the experiments, any shift to lower temperatures due to overshooting on cooling, were replicated and consistent throughout all the experiments. Apart from the experiments undertaken on my second visit to the I.R.M., University of Minnesota, all the measurements were performed on samples previously vacuumed sealed in silica-quartz capsules (Chapter 2). The vacuum would be expected to increase the samples' temperature lag, and hence decrease the

undershoot experienced. However on comparison of the results from sealed and unsealed samples, there appears to be no significant difference of remanence behaviour in the region T_v and T_k (*cf.* Sections 6.5 and 6.6).

The large overshoot on cooling without the under-cool mode, meant that it was impractical to measure the magnetisation between room temperature and 200 K during cooling. Instead the samples were measured at room-temperature, taken out of the MPMS sample chamber, whilst the chamber was cooled to 190 K with an overshoot of ≈ 40 K. The samples were then returned to the chamber and left to re-equilibrate at 190 K before the measurement sequence was resumed.

One implication of the long stabilisation time during cooling, was the length of time it took to measure a complete low-temperature cycle, *i.e.*, 300 K $\rightarrow$ 70 K $\rightarrow$ 300 K. Typically the cooling curve took 8-9 hours to measure and the warming curve $2\frac{1}{2}$–3 hours. With changing of samples, re-calibration *etc.* it was possible to measure two low-temperature cycles a day.

6.4.2 Problem with back-field on inducing SIRM

There was found to be a serious problem on inducing SIRM at room temperature in "soft" multidomain (MD) magnetite using MPMSs, because there is a large back-field associated with the inducing field returned to zero. The MPMS software has options which are supposed to stop overshooting of the set field, however on returning a large saturating field ($\geq$ 2 T) to zero, there was occasionally sufficient back-field to totally demagnetise the induced SIRM. An attempt was made to reduce the back-field by manually stepping the field down, *i.e.*, 2 T $\rightarrow$ 5 mT $\rightarrow$ 0, however there was still significant demagnetisation. Instead of investigating this problem further I decided to induce room temperature SIRM using pulse magnetisers, which are standard palaeomagnetic equipment and are designed to have zero back-field (Section 1.8).

It was necessary to induce a few SIRMs below T_v, which could only be achieved using the MPMS. However because the low-temperature phase has a larger coercive force (Figure 5.27), the back-field of a manually step-downed saturating field did not produce significant demagnetisation.

6.4.3 Residual field in the MPMS sample chamber

At first there appeared to be a problem with the zero-point calibration (*pers. comm.* W. Williams, 1996), *i.e.*, the MPMS did not measure the absolute magnetisation only a relative one. However I quickly showed by measuring the magnetisation of several samples in the two possible directions, *i.e.*, normal (M_n) and reversed (M_r), that the main contribution to the offset was from a paramagnetic/diamagnetic (χ_{pd}) interaction of the sample with

the internal residual field, H_{res}. The paramagnetic/diamagnetic contribution, M_{pd}, can be related to M_n and M_r using Equation 1.1,

$$M_n = \chi_{pd} H_{res} + M_0 \tag{6.1}$$

$$M_r = \chi_{pd} H_{res} - M_0 \tag{6.2}$$

$$M_{pd} = \frac{M_n + M_r}{2} \tag{6.3}$$

where M_0 is the magnetic remanence. From Equations 6.1–6.3, the field required to produce the offset is simply given by ,

$$H_{res} = \frac{M_{pd}}{\chi_{pd}} \tag{6.4}$$

There were three separate contributing susceptibilities to χ_{pd};

$\boldsymbol{\chi_{SiO_2}}$ Diamagnetic contribution from the silica quartz (SiO_2) vacuum capsules (Chapter 2).

$\boldsymbol{\chi_{KBr}}$ Diamagnetic contribution from the KBr used to make the pellets (Chapter 2).

$\boldsymbol{\chi_{Fe_3O_4}}$ Paramagnetic contribution from magnetite itself.

See Chapter 2 for notes on the preparation of the KBr pellets and the vacuum sealing of the pellets in capsules.

For roughly half the samples it was possible to directly measure χ_{pd}, *i.e.*, using the Lake-shore AC Susceptometer (Chapter 5) or the Kappabridge susceptometer (Chapter 1), however for the rest of the samples χ_{pd} had to be calculated theoretically because the samples had been either destroyed or partially oxidised since the initial experimentation. To make the calculation of χ_{pd} using Equation 6.4, the mass of the constituent materials in each sample is required. The mass of magnetite (mean = 4.4 $\times 10^{-3}$ g) and KBr (mean = 0.15 g) had been measured for each sample during preparation of the pellets (Chapter 2), however the mass of quartz in each sample was unknown. The mean mass (0.8 g) of quartz from three samples was used in the calculation of χ_{pd} for each sample. Fortunately the uncertainty in the mass of quartz in each sample proves to be unimportant when χ_{pd} is calculated.

Using the data in Table 6.1, χ_{SiO_2} and χ_{KBr} for the mean sample (mass of SiO_2 = 0.8 g, KBr = 0.15 g and $Fe_3O_4 = 4.4 \times 10^{-3}$ g), are calculated to be -7×10^{-5} (SI) and -5×10^{-5} (SI) respectively. Using a value of 0.5 g^{-1} as the mass susceptibility for multidomain (MD) magnetite (Hartstra, 1982b; Thompson & Oldfield, 1986), gives $\chi_{Fe_3O_4} = 2.2 \times 10^{-3}$ for the mean sample. Therefore for the average sample $\chi_{Fe_3O_4} \gg \mid \chi_{SiO_2} + \chi_{KBr} \mid$. The hypothesis that diamagnetic ions were the cause of the offset can be discarded.

Ion	$\chi\,(4\pi \times 10^{-6}\ \mathrm{g}^{-1})$
Si^{4+}	-1
O^{2-}	-12
K^{+}	-13
Br^{-}	-36

Table 6.1: Diamagnetic susceptibility per gram-ion for the diamagnetic ions in each capsule. Data from Mulay & Boudreaux (1976).

Only from experiments where M_n and M_r were measured, can an estimate of H_{res} be made. However it was not until my second visit to Edinburgh to use the MPMS2 that problems with the zero-point calibration were realised, and I started measuring M_n and M_r mandatorily. This visit to Edinburgh was sandwiched between my two visits to the I.R.M. to use the MPMS5. Because of this I have only a limited number of M_n and M_r measurements from my first visit to Minnesota. Twenty five separate pairs of M_n and M_r measurements for the the MPMS2 in Edinburgh were collected, and twenty six for the MPMS5 in Minnesota.

Where M_n and M_r have been measured it is possible to calculate M_{pd} (Equation 6.3). Applying the value of M_{pd} to Equation 6.4 with either the directly measured χ_{pd} or the theoretical estimate for $\chi_{pd} \approx \chi_{Fe_3O_4}$, gives an estimate for H_{res} for each experiment.

Applying this approach to all the measured pairs of M_n and M_r, gives estimates for H_{res} of 40 μT (standard deviation $\sigma = 20\mu$T) for the MPMS5 in Minnesota and 470 μT ($\sigma = 300\mu$T) for the MPMS2 in Edinburgh. These values for H_{res}, are in the same order of magnitude as claimed by the manufacturer. The MPMS5 has a special low-field adapter to reduce $H_{res} \leq 50\mu$T. These results suggest that diamagnetic/paramagnetic contribution came from magnetite itself. The internal residual field for the Oxford MPMS5 was not calculated, however it is likely to have a similar value as the MPMS2 in Edinburgh.

There are two points of interest here; firstly from a technical view point, this demonstrates the effectiveness of the special low-field adapter and the importance in remanence experiments of using a MPMS fitted with such an adapter. Secondly and more importantly, this shows that the experiments were not performed in zero-field environments, but in fields of quite considerable size, *e.g.*, in Edinbugh, the thermoremanences were induced in a field of 100 μT (Section 6.6.1) but low-temperature cycled in a "zero-field" of 470 μT ($\sigma = 300\mu$T).

For later experiments two attempts were made to correct for the residual field and the paramagnetic contribution; firstly by measuring M_n and M_r at room temperature it was possible to split the magnetic moment into a paramagnetic contribution and a ferrimagnetic one, as described above for the calculation of H_{res}. Secondly, the effect of H_{res} on the memory (Section 6.3) was examined by subjecting the samples to the same sequence of treatments in relatively low-residual fields using standard palaeomagnetic equipment in Oxford, *i.e.*, identical thermoremanences and SIRM where induced in the samples, the remanences were then measured at room temperature, cooled to 77 K, warmed to room

temperature and remeasured. The remanent magnetisations were measured using the CCL SQUID which has maximum internal field of $\approx 1\mu$T at the top of the sample chamber, and a field ≤ 10 nT at the measuring position. The low-temperature cycling was performed in μ-metal boxes with an internal field of ≤ 100 nT (Section 1.8). The samples spent a few seconds in the earth's magnetic field during transfer from hot to cold μ-metal boxes and *vice versa*, but importantly during cooling and warming through T_v and T_k the samples were not subjected to fields of ≥ 100 nT.

To estimate the contribution from the large H_{res} in the MPMS sample chamber during low-temperature cycling, it is necessary to have a "complete set" of results for each sample, *i.e.,* to have measured both M_n and M_r on a MPMS to give the ferrimagnetic component, and to have performed subsequent low-residual field measurements in Oxford. However because the vacuum sealed samples made specially to fit into the MPMS sample chamber were rather small and fragile (Chapter 2), they had a tendency to implode during heating. Consequently there were only a few samples which survived the several heatings to have a complete set of results (Table 6.2). Coincidentally all the "complete sets" were for SIRM measured on the Edinburgh MPMS2.

sample	Edinburgh (MPMS2) ($\times 10^{-10}$ Am^2)	Oxford (CCL SQUID) ($\times 10^{-10}$ Am^2)	$100 \times \frac{\text{CCL SQUID}}{\text{MPMS2}}$
H(3.0 μm)	10.1	8.6	84.7 %
H(13 μm)	2.90	2.45	85.1 %
H(39 μm)	100.2	72.6	72.5 %
H(59 μm)	44.6	35.7	80.0 %
E(190 μm)	965.5	631.6	65.4 %
PW(3 mm)	110	86.1	78.3 %
PE(3 mm)	290	264	91.1 %
		Average	80 % ($\sigma = 9$ %)

Table 6.2: Room temperature magnetic moment of room temperature SIRM cycled to 77 K, *i.e.,* SIRM memory. The Edinburgh samples were cooled in the residual field of the MPMS2 (470 μT (σ = 300 μT)), whilst the Oxford samples in μ-metal boxes ($H_{res} \leq 100$ nT). The memory measured on the Edinburgh MPMS2 have been corrected for the paramagnetic contribution, *i.e.,* $M = \frac{1}{2} \mid M_n - M_r \mid$.

The SIRM memories measured in the low-field environment in Oxford using the CCL SQUID are on average 80 % ($\sigma = 9$ %) of the memory calculated from measurements on the MPMS2 in Edinburgh (Table 6.2). There are several possible reasons for this difference;

Calibration. The difference may have been due to a discrepancy in the absolute calibration of the magnetometers. I did check the calibration of the CCL SQUID in Oxford, however I did not personally check the calibration of any of the MPMSs used in this study.

Sample Position. There were small errors associated with repositioning samples in the MPMS for the reverse orientation measurement M_r. However a quick test found that the repositioning errors were generally ≤ 1.5 %.

Effect of variable H_{res} on memory. Until now, it has been assumed that the magnetic moment measured in the MPMS2 is a combination of a paramagnetic moment and a field-independent ferrimagnetic moment, however it is possible that the ferrimagnetic moment is partially field-dependent, *i.e.*, the resultant memory is dependent on H_{res} during low-temperature cycling. The MPMS2 and Oxford (CCL SQUID) measurements had very different internal fields during low-field cycling, estimated above at 470 μT (σ = 300 μT) and $\leq$ 100 nT respectively. It is possible that this difference in internal fields, is the cause of the difference between the memories measured in the MPMS2 and in Oxford. (Table 6.2). This problem is considered further in Section 6.5.2, where the effect of applying small fields during remanence demagnetisation is examined.

Because of the uncertainties associated with measuring the absolute magnetisation with a MPMS, comparison of the magnetic memory of my samples with the literature is not considered in this chapter, however it is in Chapter 7 where the memory is measured using the CCL SQUID in Oxford.

6.5 Low-temperature cooling of SIRM

6.5.1 Results of low-temperature cooling of SIRM

The samples were given an SIRM at room temperature by applying fields of between 1–4 T using pulse magnetisers (Section 1.8). The MPMSs were not used to induce the SIRM for two reasons; firstly on returning to zero, the saturating field gave rise to large back-fields inside the MPMS sample chamber which were found to partially demagnetise the induced SIRM (Section 6.4.2), and secondly applying large fields within the MPMS was likely to increase the previously minimised internal residual field (Section 6.4). The MPMS was used to measure the remanence during cooling and warming.

A representative selection of samples are shown in Figures 6.3 and 6.4. It should be noted that unlike the results in Chapter 4, none of the results in this chapter have been corrected for the temperature dependent behaviour of the spontaneous magnetisation (M_s), because it is ill-defined below room temperature (Section 5.3.3).

The low-temperature behaviour of the SIRMs is in good agreement with previous experiments (*e.g.*, Kobayashi & Fuller, 1968; Hodych, 1991; Halgedahl & Jarrard, 1995; King, 1996), although there are variations due to differences in the physical properties in the magnetite samples, *e.g.*, purity and dislocation density.

For all the samples there is a gradual decrease in the remanent magnetisation as they are cooled from room temperature to above T_k (Figures 6.3 and 6.4). Although this decrease on cooling below room temperature has been observed before (Hodych, 1991; Halgedahl & Jarrard, 1995) it has never been discussed. A similar demagnetisation has been observed for

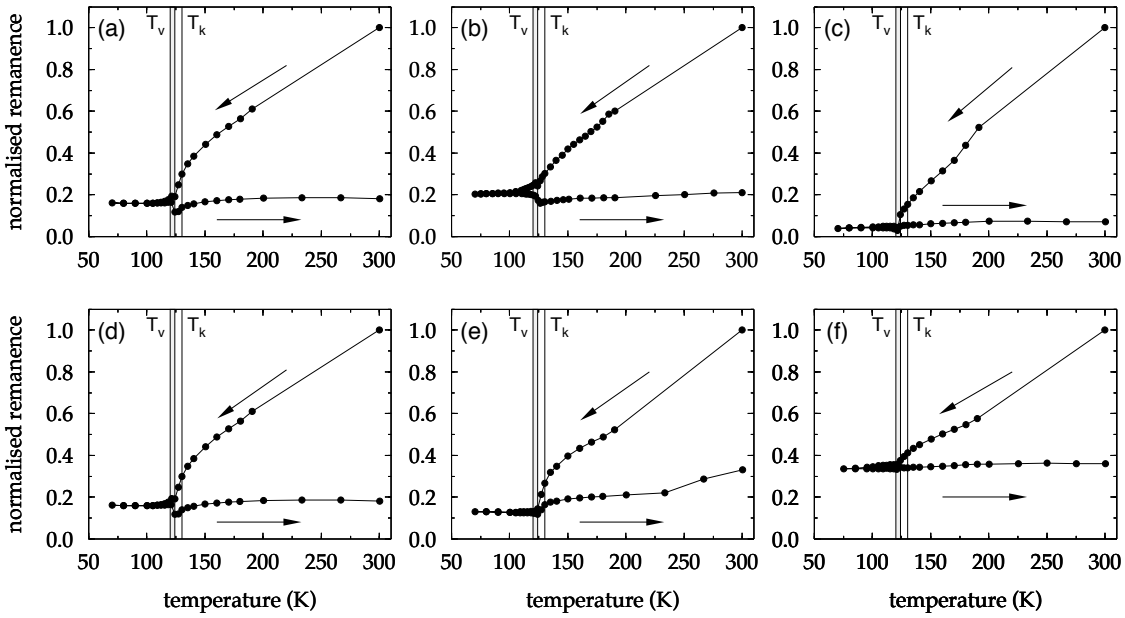


Figure 6.3: Low-temperature cycling of room temperature SIRMs induced in synthetic hydrothermal samples a) *H(3.0 μm)*, b) *H(7.5 μm)*, c) *H(24 μm)*, d) *H(39 μm)*, e) *H(59 μm)* and f) *H(108 μm)*. T_v and T_k are marked, T_v as a band (120-124 K) due to the uncertainties in its value. The remanences are normalised on their initial room temperature value.

cooling of IRMs induced above room temperature (Sugiura, 1981, and Figure 4.6), which is attributed to kinematic domain processes in Chapter 4. I suggest here that the mechanism of demagnetisation on cooling remanence between room temperature and T_k is the same kinematic process. The rate of demagnetisation is greater on cooling below room temperature compared to cooling above it (*cf.* Figure 4.6 and Figures 6.3 and 6.4), remembering that Figures 6.3 and 6.4 have not been corrected for the changes in the spontaneous magnetisation. The rate of demagnetisation increases as T_k and T_v are approached, which is probably due to corresponding decreases in the spontaneous magnetisation (Figures 5.9 and 5.14), magnetocrystalline anisotropy (Figure 5.15) and the magnetostriction constants (Figure 5.21).

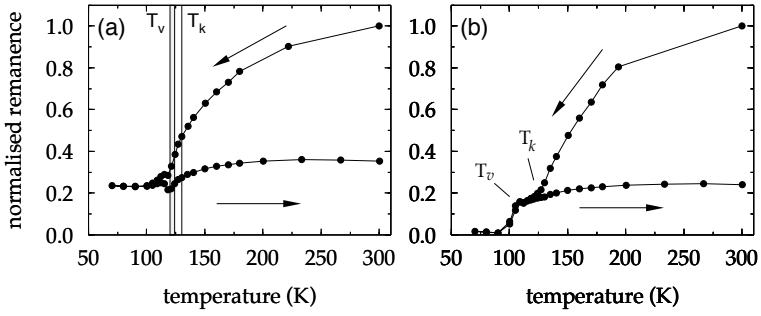


Figure 6.4: Low-temperature cycling of room temperature SIRMs induced in natural samples a) *E(190 μm)* and b) *PW(3 mm)*. The remanences are normalised on their initial room temperature value. T_v and T_k are shown for stoichiometric magnetite in a). In b) T_v and T_k are identified as the anomalies as marked.

The magnetic behaviour of all the samples (Figures 6.3 and 6.4) was strongly affected by cooling through T_k and T_v, where the controlling magnetic energies pass through large discontinuities (Section 5.4). The relative importance of T_k and T_v on the demagnetisation process is considered in Section 6.5.3.

The smaller hydrothermal crystals all display a recovery of remanence on warming from T_v and T_k to room temperature (Figures 6.3a-e). The largest sample *H(108 μm)* (Figure 6.3f) does not. However this difference is unlikely to be a grain-size effect, because the larger natural samples (Figure 6.4) display large recovery. This suggests that the size of the recovery is due to impurities or internal stresses, and is considered in more detail in Section 6.5.4.

Small impurities and internal stresses reduce the temperatures of both T_v and T_k, however T_v decreases more rapidly with increasing impurity and internal stress than T_k (see Chapter 5). The decrease in T_v and T_k due to nonstoichiometry and stress is the cause of the difference in behaviour between the natural samples (Figure 6.4) and the hydrothermal samples (Figure 6.3). For example, consider natural crystal *PW(3 mm)* (Figure 6.4b) with a trace titanium (Table 2.3), it seems reasonable to associate the anomalies at $\approx$ 110 K and $\approx$ 128 K with T_v and T_k. The exact percentage of Ti in the sample is unknown, however it is probably between 1–3 % (*pers. comm.* C. Fagg, 1995). A 2 % impurity, gives calculated values of $T_v \approx 110$ K (Figure 5.22) and $T_k \approx 125$ K (Figure 5.23). This enhanced difference between T_v and T_k can be used to address the relative importance of these two transitions (Section 6.5.3). The sample *E(190 μm)* (Figure 6.4a), was found to be almost stoichiometric (Table 2.3), and has temperatures for T_v and T_k nearly identical to the stoichiometric hydrothermal magnetites (Figure 6.3).

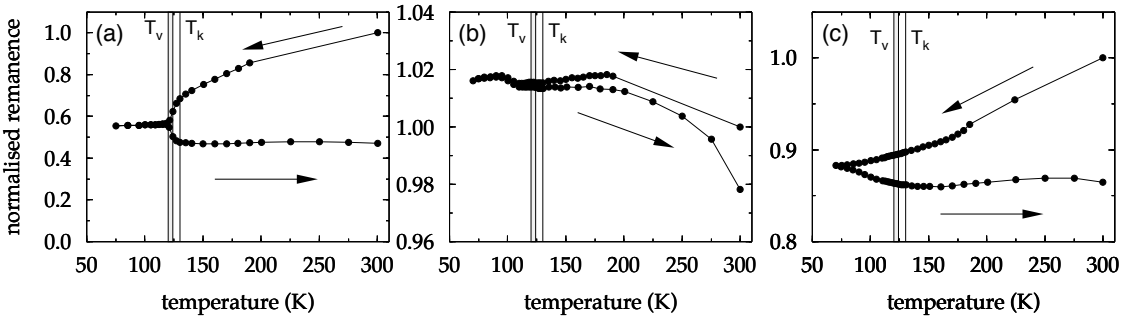


Figure 6.5: Low-temperature cycling of room temperature SIRMs induced in a) the hydrothermal seed material *H(seed)*, b) *SD(acic.)* and c) *psd-1*. T_v and T_k are marked, T_v as a band (120-124 K) due to the uncertainties in its value. *Note the difference in scales.*

A few other samples were examined, namely the hydrothermal recrystallisation seed material *H(seed)*, and the magnetite samples *SD(acic.)* and *psd-1* (Figure 6.5). On cooling the seed material (Figure 6.5a) displays similar behaviour to the hydrothermal samples (Figure 6.3), however on warming through T_v and T_k, there is further demagnetisation with no recovery on warming to room temperature.

The *SD(acic.)* sample (Figure 6.5b) displays classic low-temperature behaviour, *i.e.,* with decreasing temperature the magnetisation increases as M_s. However there is a small anomaly at 100 K, which is attributable to the Verwey transition if the *SD(acic.)* sample has been slightly oxidised, *i.e.,* partial maghemitisation of magnetite to maghemite reduces the Verwey transition temperature (Figure 5.22). The *SD(acic.)* sample had been kept in air for approximately 10 years (*pers. comm.* E. McClelland, 1995), which other studies have shown is sufficient time for small grains (≤ 1 μm) to partially oxidise (Özdemir *et al.*, 1993; Hunt *et al.*, 1995). Assuming that some degree of oxidation has occurred then it seems reasonable to assume that the anomaly at ≈ 100 K is the Verwey transition.

According to traditional theories, on cooling single domain (SD) remanence below room temperature, SD remanence should increase as M_s and should be unaffected by T_k or T_v as the remanence is thought to be controlled by the grain anisotropy. However in Section 5.7.2, using a simplified model it was shown that most SD grains are controlled by the magnetocrystalline anisotropy rather than the shape anisotropy below T_v (Figure 5.28). Only grains with high aspect ratios, *i.e.,* acicular, are controlled by the shape anisotropy above and below T_v, whilst some grains with low-aspect ratios are controlled by the magnetocrystalline anisotropy at all temperatures (Schmidbauer & Keller, 1996, Figure 5.28 and Table 5.1).

Using the coercive forces, H_c, shown in Figure 5.29, it is possible to calculate the blocking volume, v_b, for different demagnetising factors as a function of temperature (Figure 6.6) by rearranging Equation 5.4 for v_b,

$$v_b = \frac{2\mathrm{k}T(\ln C + 2\ln(2t))}{\mu_0 M_s H_c} \tag{6.5}$$

where k is Boltzmann's constant (1.381×10^{-23} JK^{-1} (Jiles, 1991)), μ_0 is the permeability of free space ($4\pi \times 10^{-7}$ Hm^{-1} (Jiles, 1991)), C is a rate constant which can be considered as the number of attempts per second that the magnetic vector tries to change direction. In Section 5.7.2, C was taken to be 10^{10} s^{-1}. The temperature dependent behaviour of M_s is taken from Figure 5.8.

Certain grain volumes ($> 20 \times 10^{-23}$ m^3, *i.e.,* diameter ≈ 0.16 μm) with low-aspect ratios and hence low demagnetising factors, *e.g.,* $N = 0.001$, are controlled by the magnetocrystalline anisotropy (Table 5.1), and unblock on cooling to just above T_v (Figure 6.6). The remanence unblocks because of the decrease in the cubic magnetocrystalline anisotropy's intensity (Figure 5.15). This value of 0.16 μm is greater than the calculated single domain threshold grain size of 0.07 μm (Williams & Wright, 1998), however experimental results (*e.g.,* Argyle & Dunlop, 1990; Dunlop & Argyle, 1997), observational data (Boyd *et al.*, 1984) and numerical models (Enkin & Williams, 1994; Fabian *et al.*, 1996; Williams & Wright, 1998) all conclude that grains slightly bigger than 0.07 μm, can under certain conditions, be in stable SD domain states. Therefore the results from this simple model have physical

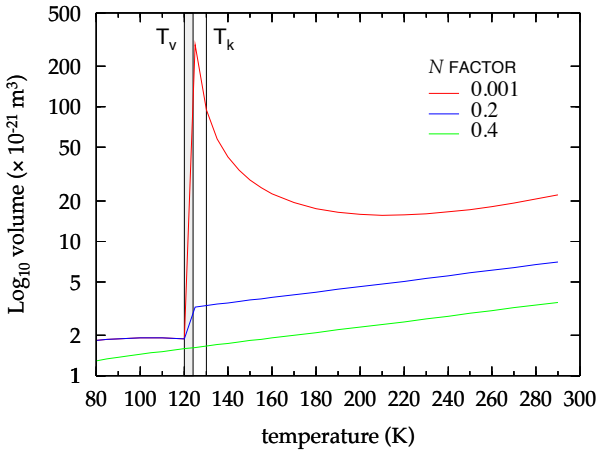


Figure 6.6: The calculated blocking volume as a function of temperature for various demagnetising factors. Grain sizes above each curve are blocked, whilst those below unblocked. N = 0.001 is represents a near spheroidal grain, whereas N = 0.4 represents an acicular grain. The temperature dependencies of the coercive forces were taken from Figure 5.29. T_v and T_k are marked, T_v as a band (120-124 K) due to the uncertainties in its value.

significance. The blocking curves of the high-aspect ratio grains, *i.e.*, $N =$ 0.2 and 0.4, are relatively unaffected by T_v (Figure 6.6).

On inspection of Figure 6.6, it is concluded that the small demagnetisation of *SD(acic.)* remanence on cycling through T_v (Figure 6.5b), is due to the unblocking of non-acicular grains.

Figure 6.5c shows the low-temperature cycling of a *psd-1* sample. This sample was supposedly MD magnetite, however it displays no remanence transition at either T_k or T_v, suggesting that the material is not. Because the demagnetisation observed on cooling SIRM from room temperature (Figure 6.5c) is known to be an MD effect and not SD (Chapter 4), the origin of this discrepancy is in the mineralogy of the sample. Similar to the *SD(acic.)* sample, the *psd-1* sample had been kept in air for $\approx$ 10 years (*pers. comm.* E. McClelland, 1995). It seems reasonable to assume that the sample showed no anomalies at T_k or T_v, because it had oxidised to maghemite. On warming from 70 K, the sample displayed irreversible behaviour identical to that described in Section 4.2.4 for partial thermoremanences on switching from cooling to heating (Figure 4.8).

6.5.2 Effect of small applied field on "zero-field" cooling

It was unknown what effect the large internal fields within the MPMSs' sample chambers (Section 6.4.3) had on the low-temperature behaviour of remanence during cooling. Because of this the effect of applying small fields during "zero-field" cooling of a room temperature SIRM was examined.

A room temperature SIRM was induced three separate times in hydrothermal sample *H(39 μm)*, and low-temperature cycled in different environments to 70 K in the MPMS2 in

Edinburgh. The different internal fields within the sample chamber were; zero-applied field, *i.e.*, the residual field H_{res}, an applied biasing field of +500 μT, and a second biasing field of −500 μT (Figure 6.7). The measurements were made on the MPMS2 in Edinburgh. Note that the applied fields' intensity was only slightly greater than the estimated value for H_{res} in the the MPMS2 sample chamber ($H_{res} = 470$ μT ($\sigma = 300$ μT)).

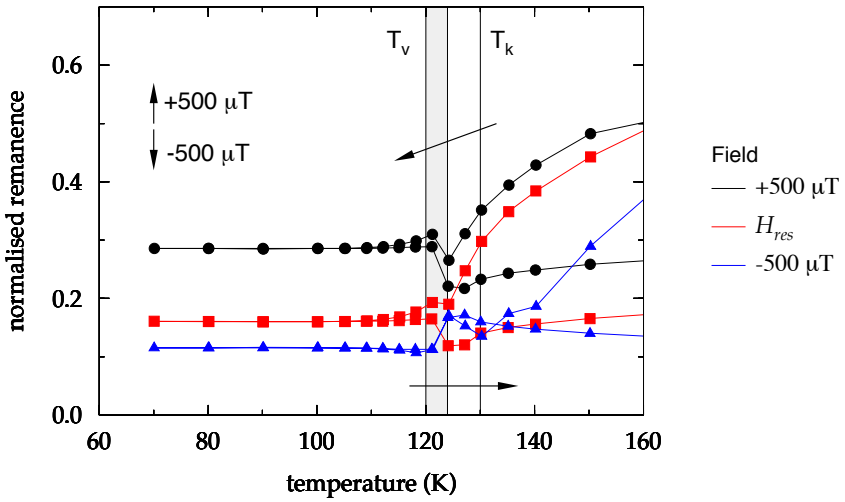


Figure 6.7: The behaviour of room temperature normalised SIRMs cooled in external fields of +500μT, residual field (H_{res}) and −500 μT in the sample *H(39 μm)*. The remanence is normalised on the room temperature SIRM. The low-temperature cycling curves were measured using the MPMS2 in Edinburgh, $H_{res} = 470$ μT ($\sigma = 300$ μT). T_v and T_k are shown, T_v as a band (120-124 K) due to the uncertainties in its value.

The effect of the biasing field is to shift the normalised magnetisation in the direction of the field (Figure 6.7), the H_{res} cooling curve lying between the low-temperature cooling curves the applied fields ± 500 μT. This is in agreement with previous studies (Yama-ai *et al.*, 1963). The H_{res} curve is fairly smooth, showing a slight anomaly in behaviour on cooling and warming through T_v/T_k (the relative importance of the transitions T_v and T_k is examined in Section 6.5.3). The shape of the +500 μT curve is similar to that of the H_{res} curve, although it is shifted in the direction of the applied field. There is a positive jump in the magnetisation in the direction of the +500 μT biasing field on cooling through T_v/T_k. The behaviour of the −500 μT is very different; the smooth cooling curves observed for the other two internal fields have been "destroyed" by the negative biasing field during cooling. There is a small negative jump in the −500 μT curve on cooling through T_v/T_k, and there is a cross-over in the H_{res} and −500 μT heating curves in the temperature range 124–130 K.

By examining the cooling curves only, a simple conclusion would be that the behaviour in the vicinity of T_v/T_k is strongly dependent on external field alone; the +500 μT curve has a positive jump, whilst the −500 μT curve a negative one (Figure 6.7). For the H_{res} curve, there is virtually no jump on cooling through T_v/T_k, suggesting that the residual field is small. In terms of the domain structure, on cooling through T_v/T_k the domain

structure is partially recorded due to changes in the controlling magnetic energies (Chapter 5). A biasing field will contribute to the partial reordering to produce a net magnetisation in the direction of the biasing field. However, this simple approach does not explain the behaviour of the magnetisation on warming from below T_v to room temperature. Consider the +500 μT curve (Figure 6.7), if the positive jump on cooling through T_v/T_k, is due to the applied field only, then the magnetisation would be expected to jump again in the direction of the biasing field or remain constant on warming back through T_v/T_k. However this is not the case; the magnetisation is partially demagnetised on warming through T_v/T_k, *i.e.,* it jumps in the opposite direction to the +500 μT field. The same observation is true for the H_{res} and -500 μT curves. The shape of -500 μT curve is very different yet the trend is the same, *i.e.,* on warming through T_v/T_k the SIRM jumps in the direction opposed to the biasing field.

In conclusion it appears, that although small fields affect the behaviour of the magnetisation at low-temperatures, it is changes in magnetite's intrinsic magnetic energies which control the general behaviour.

For the low-temperature cycling of SIRM, the size of internal residual field is relatively small compared to the total SIRM intensities, however for thermoremanences with smaller intensities the relative size from H_{res} is larger. This problem is discussed in Section 6.6.

6.5.3 Importance of T_v and T_k during low-temperature demagnetisation of SIRM

Assuming that T_k and T_v are separate transitions (see Section 5.4.2 for discussion), there are clear discrepancies in the literature as to which transition controls demagnetisation processes (see Section 5.2 for discussion). The traditional view is that it is T_k (*e.g.,* Ozima *et al.*, 1964b; Stacey & Banerjee, 1974; Shcherbakova *et al.*, 1996; Dunlop &Özdemir, 1997), whereas there is strong evidence to suggest that T_v dominates (Hodych, 1991), and finally some people have suggested that low-temperature demagnetisation is due to a combination of both transitions (*e.g.,* Halgedahl & Jarrard, 1995; Moloni *et al.*, 1996). All the SIRMs induced in stoichiometric hydrothermal magnetites samples (Figure 6.3), display continuous demagnetisation from room temperature until $\approx$ 125 K where the magnetisation shows anomalous behaviour. Further cooling to 77 K, and subsequent heating to room temperature causes little significant further demagnetisation. This temperature of 125 K, falls between the temperatures for T_k (130 K) and T_v (120-124 K), making it unclear which process controls the low-temperature demagnetisation.

Consider the influence of the controlling magnetic energies on the behaviour of SIRM domain structure on cooling from room temperature. As discussed in Section 6.5.1, a SIRM induced at room temperature partially demagnetises on cooling due to kinematic processes (Chapter 4), leaving a relatively stable domain state on approach to T_v and T_k. A first hy-

pothesis may be that on cooling to below T_v, increases in the anisotropic intensity and changes in the anisotropic symmetry effectively "freeze-in" the domain structure rather than cause further domain reordering, T_k being relatively unimportant. If this hypothesis were true, it would mean that the demagnetisation measured after low-temperature cycling to 77 K, *i.e.*, magnetic memory, is entirely due to the kinematic demagnetisation processes which occur on cooling and heating in the cubic phase of magnetite. However this is shown not to be the case by examining the behaviour of a room temperature SIRM thermally cycled near the T_v and T_k (Figure 6.8). A room temperature SIRM was induced in sample *H(39 μm)*, cooled to 190 K, and thermally cycled in the following chronology;

1. 190 K $\rightarrow$ 135 K $\rightarrow$ 150 K
2. 150 K $\rightarrow$ 125 K $\rightarrow$ 150 K
3. 150 K $\rightarrow$ 100 K $\rightarrow$ 200 K

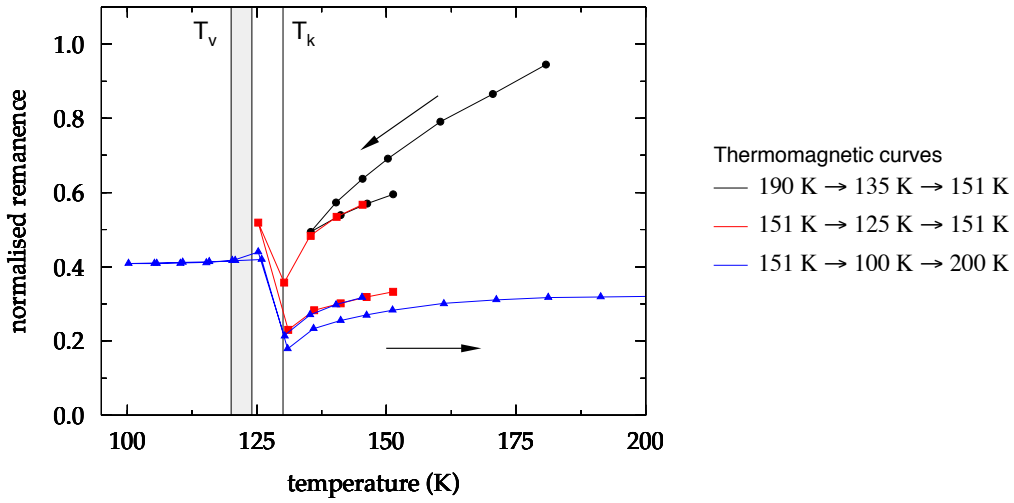


Figure 6.8: A room temperature SIRM induced in sample *H(39 μm)*, cooled to 190 K. The sample was then thermally cycled; 190 K $\rightarrow$ 135 K $\rightarrow$ 150 K $\rightarrow$ 125 K $\rightarrow$ 150 K $\rightarrow$ 100 K $\rightarrow$ 200 K. The remanence is normalised at 190 K. T_v and T_k are shown.

Figure 6.8 shows the contribution on cooling through T_v and T_k to the total demagnetisation during low-temperature cycling to 77 K. Cooling from 190 K $\rightarrow$ 135 K $\rightarrow$ 150 K significantly demagnetises the SIRM, however cooling through T_k, *i.e.*, 150 K $\rightarrow$ 125 K $\rightarrow$ 150 K, causes a demagnetisation far greater than cooling in cubic phase alone. The final cycle from 150 K $\rightarrow$ 100 K $\rightarrow$ 200 K, *i.e.*, through T_v, only produces a relatively small further demagnetisation.

From Figure 6.8, it appears that the first cubic magnetocrystalline anisotropy constant isotropic point is the dominant mechanism in the demagnetisation during low-temperature cycling. However there is still a question mark over how significant the Verwey transition

is due to problems with the overshooting (Section 6.4), *e.g.*, on cooling from 150 K $\rightarrow$ 125 K, it is possible that the sample is cooled through the Verwey transition due to overshooting (T_v = 120-124 K (Chapter 5)).

There is difficulty in differentiating between the two temperatures T_k and T_v, which is partly due to technical problems during cooling and partly to the uncertainty in the absolute temperature of T_v (Chapter 5). The variance and uncertainty in the absolute temperature of T_v has been discussed in detail in Chapter 5. By the structural-electronic model (Section 5.3.1), the variance is attributed to; different methods of determination reporting different values for T_v and secondly contamination (Section 5.5). On the other hand, according to the magneto-electronic model (Section 5.3.2) the Verwey transition is *not* a discontinuous transition, rather it is spread over a finite temperature range. The Verwey transition is generally believed to be in the temperature range 120-124 K (see Section 5.5).

The behaviour of samples with small impurities can be used to distinguish between T_v and T_k, because small impurities widen the temperature difference between T_k and T_v (Figure 6.4). Consider the natural crystal *PW(3 mm)* with a trace impurity of titanium (Figure 6.4b). In Section 6.5.1, the anomalies at $\approx$ 110 K and $\approx$ 128 K are linked with T_v and T_k respectively. On this assumption, Figure 6.4b suggests the Verwey transition strongly effects the magnetisation giving rise to a sharp decrease in the remanence, however the magnetisation is reversible across this transition. The magnetisation is irreversible to cycling across the magnetocrystalline isotropic point, T_k, implying that the low-temperature demagnetisation is controlled by T_k (Figure 6.4b). In summary the examination of Figure 6.4b clarifies that T_k and not T_v is responsible for the demagnetisation observed for the thermomagnetic curve 150 K $\rightarrow$ 125 K $\rightarrow$ 150 K in Figure 6.8.

However it should be noted, that there are errors associated with using impure samples, because not only do small impurities decrease the temperature of T_v, they also "dampen" the effects seen at T_v (Section 5.5). The small impurities in the natural sample *PW(3 mm)* (Figures 6.4b) will have reduced the relative contribution of the Verwey transition to the demagnetisation mechanism. This biases the experiment in favour of T_k.

Recently, Sahu (1997) suggested that partial demagnetisation occurs at the first transition the remanence encounters, *i.e.*, on heating from below T_v the remanence demagnetises at T_v whilst on cooling from above T_k the remanence demagnetises at T_k. To test her hypothesis an *H(39 μm)* sample was cooled to 6 K where a SIRM (H = 2.5 T) was induced, then the sample was warmed in zero field to room temperature. The results of this experiment plus the results of cooling a room temperature SIRM induced in an *H(39 μm)* sample (already presented in Figure 6.3d), are shown in Figure 6.9.

The demagnetisation process occurs at $\approx$ 124 K for the warming curve and there is anomalous behaviour in the cooling curve at $\approx$ 125 K (Figure 6.9). The relative amount of demagnetisation across T_v and T_k is much larger for the warming curve than for the cooling curve, which can be explained by considering the two domain states on approaching T_v and T_k respectively.

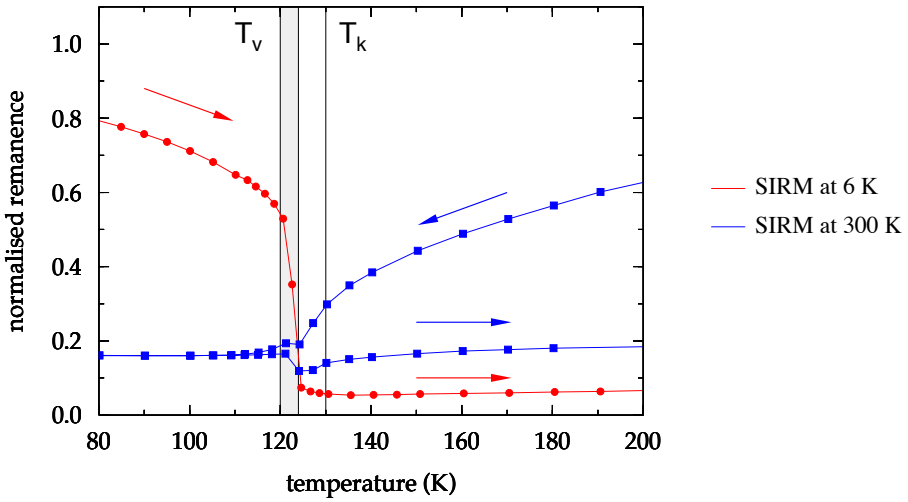


Figure 6.9: Behaviour of an *H(39 μm)* sample induced with a SIRM at 6 K and a SIRM at 300 K, to warming and cooling respectively through T_v and T_k. Both remanences are normalised by their initial SIRM. T_v and T_k are marked.

As discussed in Section 6.5.1, SIRM induced at room temperature partially-demagnetises on cooling. As expected, there is also partial-demagnetisation of the low-temperature SIRM on warming up to 124 K (Chapters 1 and 4), however as the coercive force is much greater in the monoclinic phase than in the cubic phase (Section 5.7.2), the demagnetisation on warming to 124 K is relatively small compared to the cooling curve.. The differences in the cubic and monoclinic coercive forces and the temperature ranges over which the SIRMs are heated / cooled, results in the room temperature SIRM being ≤ 40 % of its room temperature value at 140 K, whilst the low-temperature induced SIRM is only reduced to ≈ 60 % of its 6 K value at 110 K.

On warming through T_v and T_k, there are large changes in the anisotropic energies; both in symmetries and intensities (Chapter 5), which gives rise to a large drop in the coercive force (Figure 5.25). The large changes in the anisotropic energies, cause the SIRM induced at 6 K to demagnetise by both decreasing the symmetry of the magnetic structure and the intensity of magnetic anisotropy, resulting in a large demagnetisation.

On approach to T_k, the room temperature SIRM has already under gone major domain reorganisation during cooling leaving it in a relatively stable state, so although it is affected by cooling through T_k and T_v, the observed decrease is considerably less than for the warming curve.

It would appear that Sahu's (1997) theory is partially correct; the low-temperature SIRM demagnetises on warming through T_v which agrees with other studies (*e.g.*, Moskowitz 1993; Hunt *et al.*, 1995) and the low-temperature cooling of room-temperature SIRM is strongly affected by passing through T_k. However it is wrong to assume that all the demagnetisation which occurs during low-temperature cooling is due to T_k. Figures 6.3, 6.4 and 6.8 suggest that a large component of the demagnetisation is due to kinematic

processes during cooling and heating in the cubic phase (Chapter 4).

6.5.4 Effect of internal residual stress on magnetic memory

The memory which remains after low-temperature cycling is magnetically hard and is often associated with hard internally stressed areas of the grain, as is discussed in Chapter 7. In the light of this observation, many people have suggested that internal stress strongly controls the low-temperature behaviour (*e.g.*, Kobayashi & Fuller, 1968; Heider *et al.*, 1988a; McClelland & Shcherbakov, 1995).

The effect of stress is two-fold; as discussed in Section 5.6.2 it increases the breadth of the low-temperature demagnetisation in the region of T_v and T_k. Secondly it has been demonstrated that the recovery mechanism is partially associated with the degree of internal stress within the sample *i.e.*, %-recovery $\propto$ stress (Ozima *et al.*, 1964b; King, 1996). For a synthetic magnetite, Ozima *et al.* (1964b) demonstrated that annealing, *i.e.*, removing stress-inducing dislocations *etc.*, was sufficient to remove the recovery observed before annealing. King (1996) demonstrated that inducing stress increases the recovery. The mechanism of recovery has not been fully explained, however it is discussed further in Section 6.7.

The hydrothermal samples *H(3.0 μm)–H(108 μm)* displayed no or little recovery, as expected for "low-stress" samples (Figure 6.3). The natural Shetland samples *E(190 μm)* and *PW(3 mm)* (Figure 6.4) both displayed recovery, however *E(190 μm)* displayed a larger recovery than *PW(3 mm)*, which suggests that it has a higher level of internal stress. This is in agreement with room temperature hysteresis parameters which also suggest this (Chapter 3). Compared to King's (1996) results for highly stressed samples, both *E(190 μm)* and *PW(3 mm)* appear to have relatively low-internal stress.

Interestingly King (1996) also measured a 2 mm Shetland magnetite given to him by P. Aspen (University of Edinburgh) which is probably from the same location as the Shetland sample *PW(3 mm)* which I personally collected (Section 2.4). Using the MPMS2 at the Dept. of Chemistry, University of Edinburgh, King found a larger recovery and broader Verwey transition for his Shetland magnetite (Figure 6.10) than for I did for the natural Shetland sample *PW(3 mm)* (Figure 6.4b). The difference between King's and my results may be due annealing; my sample had been previously vacuum sealed in quartz capsules (Section 2.6) and heated to 600 °C on several occasions. If my samples originally carried high-residual stress, the effect of several heatings would have been to anneal the crystals, *i.e.*, reduce the level of internal residual stress. King's unheated sample would be expected to exhibit more stress related behaviour than sample *PW(3 mm)* (Figure 6.4b).

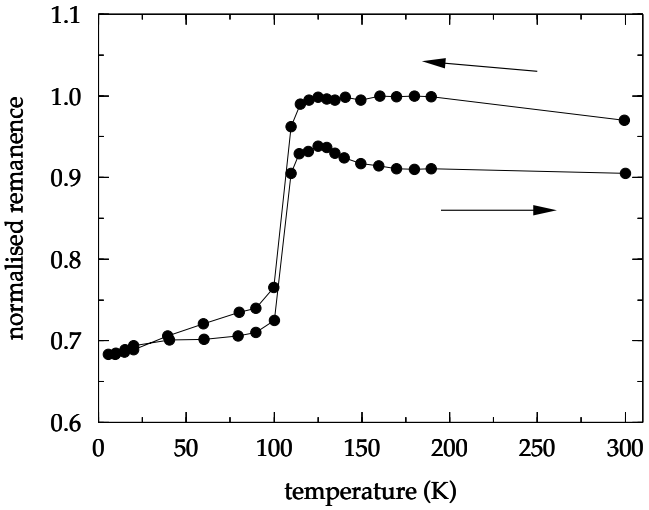


Figure 6.10: Room temperature SIRM measured in zero field as a function of temperature induced in a 2 mm size single crystal of magnetite from probably the same Shetland location as *PW(3 mm)*. After King (1996).

6.5.5 Oxidation as a source of internal stress

It has been suggested (Özdemir *et al.*, 1993) that oxidation of magnetite samples not only changes the surface stoichiometry which strongly effects their magnetic properties, but also induces internal stress due to the difference in the lattice parameters of magnetite (8.396 Å) and maghemite (8.337 Å) (Dunlop & Özdemir, 1997).

Even though the natural Shetland samples were treated by CBD treatment to remove surface oxidation products (Section 2.4.2), it is expected that some residual stress remains after the treatment. High resolution SEM photographs (Figure 2.6b) of the natural samples taken after CBD treatment and before annealing, show that the natural samples have highly cracked surfaces.

The natural samples (Figure 6.4) all exhibit recovery on heating from T_k to room temperature, which could be due to internal stress (Section 6.5.4). With the present magnetic data it is not possible to distinguish between stress induced by oxidation and stress due to other reasons, however SEM photographs (Figure 2.6b), strongly support the hypothesis that surface stress contributes to the total stress of my natural samples,

6.5.6 Note on the effect of particle interaction on the Verwey transition

As the samples were only loosely dispersed in KBr (Chapter 2), the effect of particle interaction on the behaviour of remanences at T_v and T_k must also be considered. King (1996) found that for small pseudo-single domain particles ($\approx 0.5\mu$m) particle interaction *increases* the size of the discontinuities at T_v and T_k, which compares well with other literature (*e.g.*, Moskowitz *et al.*, 1993; Özdemir *et al.*, 1993). The result of interaction can be thought of as making the assemblage of pseudo-single domain grains into a larger "multidomain-like" structure.

In the experiments conducted in this study the samples were usually much larger than 0.5 μm, so the importance of particle interaction is less (Dankers & Sugiura, 1981). The important point, however, is that particle interaction increases the effects observed at T_v, *i.e.*, any particle interactions in the samples in this study would have only increased the observed effects not decreased them.

6.6 Low-temperature cooling of thermoremanences

There have been a limited number of reports in the literature of the low-temperature behaviour of thermoremanences induced in magnetite. It was mentioned in Section 6.2, that to my knowledge there has been only one report of the low-temperature measurement of laboratory-induced thermoremanence in synthetic magnetite (Ozima *et al.*, 1964b). However the results were treated sceptically because the sample had been heated in air, and were not shown graphically.

In similar experiments to those described in Section 6.5, samples with various initial thermoremanences were measured during low-temperature cycling to 70 K, The measurements in this section and Section 6.5, were undertaken using MPMSs on four alternate visits to the Dept. of Chemistry, University of Edinburgh and the Institute for Rock Magnetism (I.R.M), University of Minnesota. These visits were followed by two days of measurement on the MPMS5 at the Dept. of Chemistry, University of Oxford (where the results in Figure 6.8 were measured). On the first three trips to use an MPMS, thermoremanences were induced using an applied field of 100 μT. This field was chosen as it was consistent with the field used in Oxford to induce thermoremanences in other experiments (Chapter 7).

Experimental evidence from the literature (*e.g.*, Day, 1977; Shcherbakov *et al.*, 1993), suggests that thermoremanence intensity is linear with applied field intensity to $\approx$ 200-300 μT for MD magnetite (Shcherbakov *et al.*, 1993). In Section 4.2.1 this relationship is experimentally verified. Therefore by applying a field of 100 μT, *i.e.*, $\approx 2 \times$ the earth's field, to induce the thermoremanences, it was assumed that the behaviour of the thermoremanences would be analogous to natural thermoremanences found in rocks. Doubling the field from the earth's field compensated for the relatively low-bulk volume content of the magnetite samples. Thermoremanence induced in fields where there is a linear relationship between thermoremanence intensity and field is usually referred to as "weak-field" thermoremanence, and thermoremanence induced in non-linear fields as "high-field" thermoremanence.

On the second trip to the I.R.M., it was decided to take advantage of the unique facilities (certainly in the field of rock magnetism) by combining high-temperature experiments on a Princeton Electronics μ-VSM (Vibrating Sample Magnetometer), with low-temperature experiments on the MPMS5. Using this combination it is possible to measure a continuous record from 2 K to 1025 K, however the use of two magnetometers can lead to calibration problems.

The results from the μ-VSM have already been described and discussed in Chapter 4, however discussion of some of the technical limitations (Section 4.2.1) are repeated here. The poor sensitivity of the μ-VSM (sensitivity = 5×10^{-9} Am^2) meant that it was not possible to measure the thermoremanence acquisition for inducing fields as low as 100 μT. To compensate for this, samples were given a thermoremanence in an inducing field of 5 mT, *i.e.*, 5000 μT. The linearity of thermoremanence intensity and applied field are discussed in detail in Section 4.2.1, where it was concluded that "high-field" thermoremanences are not analogous to natural thermoremanences, however they are of scientific interest. High-field thermoremanences are thought to be a cross-over between IRMs and weak-field thermoremanences, and were found to be relatively less stable than the thermoremanences induced in fields of 100μT (Chapter 4).

Initially it seems suitable to separate the results of the thermoremanences induced in a field of 100 μT (Section 6.6.1), with those induced in higher non-linear fields (Section 6.6.2).

Note on acquisition of thermoremanence

On the two visits to use the MPMS2 in Edinburgh and on the first trip to the I.R.M., thermoremanences were induced using standard palaeomagnetic ovens (Section 1.8). To avoid chemical alteration the samples were vacuum sealed in quartz capsules (Section 2.6). Note quartz capsules were specially made to fit into the MPMS sample chamber (Section 2.6). The number of heatings of the smaller MPMS capsules was limited, because they had a tendency to implode during heating.

On the second visit to the I.R.M. the μ-VSM was used to induce thermoremanence, which meant that the vacuum sealed capsules could not be used. The acquisition of thermoremanence using the μ-VSM has already been described in detail in Chapter 4. A set of samples from each grain size range were dispersed in KBr in the same manner as that described in Chapter 2. Here the measures taken against possible chemical alteration during thermoremanence acquisition are reiterated; firstly during the samples were heat in an inert atmosphere of He (Section 4.2.1), secondly the samples were coated in weak-diamagnetic (*pers. comm.* J. Marvin, 1997), high-temperature glue (Omega CC High Temperature Cement binder), and finally each sample from each grain size was only used once.

In Section 4.2.1, two types of thermoremanences induced in the samples. In accordance with the literature only thermoremanences cooled from T_c to room temperature in a field are termed TRM. Other thermoremanence are termed partial TRM or pTRM. The term "thermoremanences" is used generally to describe both TRM and pTRM. All the temperatures for thermoremanence acquisition are given in Celsius.

Two types of pTRM were induced in the samples;

Type 1 The samples are cooled from above T_c to T_2 in a field, where room temperature, rtp $< T_2 < T_c$ ($T_c \downarrow T_2$, H=ON; $pTRM^{T_c}_{T_2}$).

Type 2 This type of pTRM is acquired by cooling from T_c to a temperature T_1 in zero field, and from T_1 to T_2 in a field, where rtp $< T_2 < T_1 < T_c$ ($T_c \downarrow T_1$, H = OFF; $T_1 \downarrow T_2$, H=ON; $pTRM^{T_1}_{T_2}$).

In both cases below T_2, the samples were cooled in a zero field environment. Due to the importance of thermal history on the magnetic behaviour of the remanence (Sugiura, 1981; Vinogradov & Markov, 1989), samples with Type 2 thermoremanence were cooled from T_c in zero field.

6.6.1 Results of low-temperature cooling of weak-field thermoremanences

Most of the results in this section are for samples (hydrothermally recrystallised and natural magnetite samples) which have been given a "full-thermoremanence", *i.e.*, $TRM^{T_c}_{rtp}$ where rtp is room temperature, however a few weak-field partial thermoremanences were induced in the samples; $pTRM^{T_c}_{500}$, $pTRM^{500}_{rtp}$ and $pTRM^{365}_{rtp}$.

Behaviour of weak-field $TRM^{T_c}_{rtp}$

Figure 6.11 shows the results of the low-temperature cycling of TRMs induced in a field of 100 μT in hydrothermal crystals (Chapter 2). On cooling from room temperature to above T_k all the samples (Figure 6.11) display a decrease in remanence similar in appearance to that observed for both the cooling of room temperature SIRMs (Section 6.5) and cooling of partial thermoremanences above room temperature (Chapter 4). However the rate of demagnetisation for the TRMs is less than for the SIRMs. This reflects the increased stability of the TRMs.

On cooling below T_k and T_v, the smaller samples, *e.g., H(3.0 μm)* and *H(7.5 μm)* (Figures 6.11a and 6.11b respectively), display a large *increase* in the magnetisation. The relative size of this increase or jump, decreases with grain size (Figures 6.11c and 6.11d). For the largest two samples, *i.e., H(24 μm)* and *H(59 μm)* (Figures 6.11e and 6.11f), the samples demagnetise on cooling through T_k and T_v. On warming the smaller samples from 77 K (Figures 6.11a and 6.11b), the TRM is initially reversible up to $\approx$ 100 K, where it deviates from the cooling curve by continuing to increase up to T_v. In the largest samples, *i.e., H(18 μm)*, *H(24 μm)* and *H(59 μm)* (Figures 6.11d–6.11f), the TRMs are also reversible up to $\approx$ 100 K, however on further warming towards T_v there is no clear trend in the behaviour. At T_v and T_k, the jump observed on cooling is reversed for all grain sizes. The size and direction of the jump is such that in all cases there is net demagnetisation compared to the remanence before cooling through T_v and T_k; for the finer samples the warming jump is in the opposite direction to and greater than the cooling jump, (Figures 6.11a-6.11d), whereas for the coarser samples the jump is smaller than the cooling jump (Figures 6.11e-6.11f). On warming from above T_k to room temperature either no recovery or small recoveries are observed (Figure 6.11). This behaviour is similar to that for SIRM (Figure 6.3). However

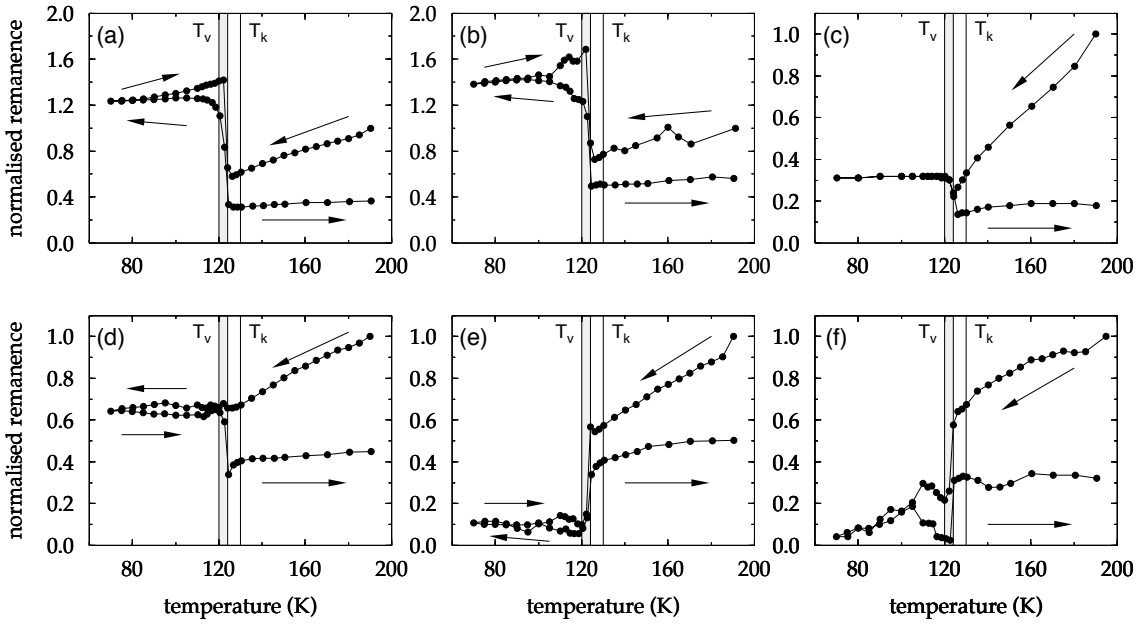


Figure 6.11: Low-temperature cycling of total TRM induced in a field of 100 μT in synthetic hydrothermal samples a) *H(3.0 μm)*, b) *H(7.5 μm)*, c) *H(13 μm)*, d) *H(18 μm)*, e) *H(24 μm)* and f) *H(59 μm). Note a) and b) have different scales from the remainder.* T_v and T_k are marked.

sample *H(24 μm)* is an exception to this general observation; it displays a relatively large recovery, which may be related to stress induced in the sample during handling.

It is immediately obvious that the low-temperature behaviour of these TRMs is markedly different to that of SIRM induced in the same samples (*cf.* Figure 6.3). This differences between thermoremanence and SIRM behaviour is discussed in Section 6.7.

The positive jump in the remanence on cooling through T_v and T_k (Figures 6.11a-6.11c) has been observed before for both SIRM (Halgedahl & Jarrard, 1995, Figure 6.12a) and TRMs induced in natural samples (Hartstra, 1983, Figure 6.12b), however because the relative size of the jumps were much smaller they were not discussed in detail.

B. Moskowitz (*pers. comm.* 1995) informed me that he once measured a similar size of jump at T_v for natural TRM in MD magnetite samples, however he was unable to repeat this observation for laboratory induced TRM in the same samples. It is uncertain as to what part oxidation played in his experiments.

The natural Shetland samples display similar behaviour during low-temperature cooling (Figure 6.13) to the hydrothermal samples (Figure 6.11), however there are differences in the detail. Firstly all the natural samples are considerably larger than the largest hydrothermal sample, *i.e., H(59 μm)*, however the behaviour of TRM induced in the natural samples is closer to the small hydrothermal grains (Figures 6.11a and 6.11b) than the largest sample *H(59 μm)* (Figure 6.11f). TRM in the natural samples appears to be more reversible to cooling and warming through T_v and T_k than for the hydrothermal crystals (Figure 6.11).

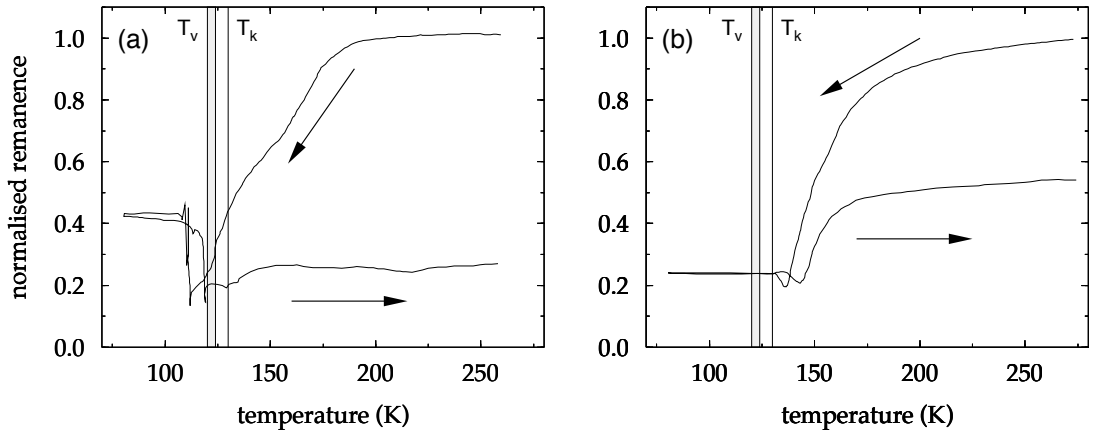


Figure 6.12: Normalised low-temperature curves for a) SIRM induced in 3 μm natural magnetite (After Halgedahl & Jarrard (1995)), and b) a TRM^{Tc}_{rtp} induced in a field of 35 μT in a natural sample with several impurities (After Hartstra (1983)). T_v and T_k are shown for stoichiometric magnetite.

Impurities decrease both T_v and T_k, however T_v decreases more rapidly with impurity than T_k (Sections 5.5 and 6.5). Because natural magnetites *E(190 μm)* and *E(250 μm)* are relatively stoichiometric (Chapter 3), the temperatures for T_v and T_k do not vary from stoichiometric magnetite; the anomalous jumps in magnetisation associated with T_v and T_k occur in a similar temperature range as stoichiometric magnetite (Figures 6.13a and 6.13b).

The natural sample *PW(3 mm)* has relatively large impurities, which reduce the temperatures for T_v and T_k. In Section 6.5 it was estimated that sample *PW(3 mm)* (≈ 2 % Ti impurity), should have reduced temperatures for T_v and T_k of $\approx$ 110 K and $\approx$ 125 K respectively. These predictions for *PW(3 mm)* are in rough agreement if the the anomaly at $\approx$ 110 K is associated with T_v, and the irreversible point at $\approx$ 125 K with T_k Figure 6.13c).

Sample *PW(3 mm)* (Figure 6.13c) can used in identifying the controlling mechanism of the anomalous jump at T_v. It appears for *PW(3 mm)* that the jump is entirely due to the Verwey transition, although it is completely reversible. The demagnetisation appears to be controlled by cycling through T_k, because the remanence is reversible to cycling through

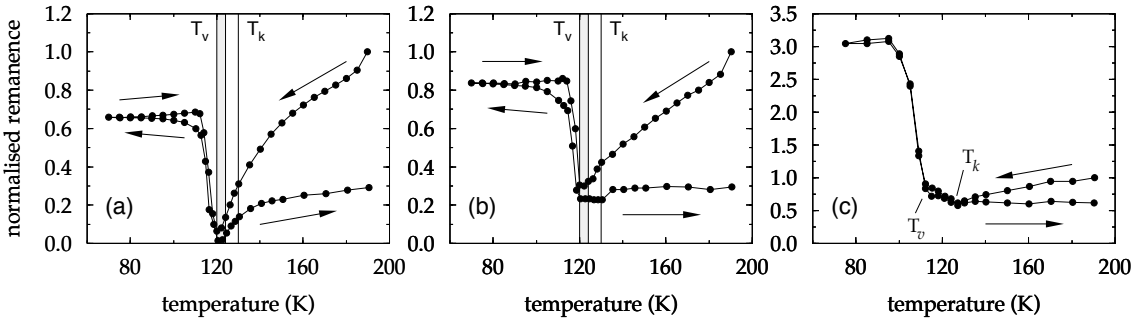


Figure 6.13: Low-temperature cycling of TRMs induced in a field of 100 μT in natural samples a) *E(190 μm)*, b) *E(250 μm)*, c) *PW(3 mm)*. T_v and T_k are shown for stoichiometric magnetite in a) and b). In c) T_v and T_k are identified as the anomalies as marked. *Note c) has a vertical different scale to a) and b).*

T_v.

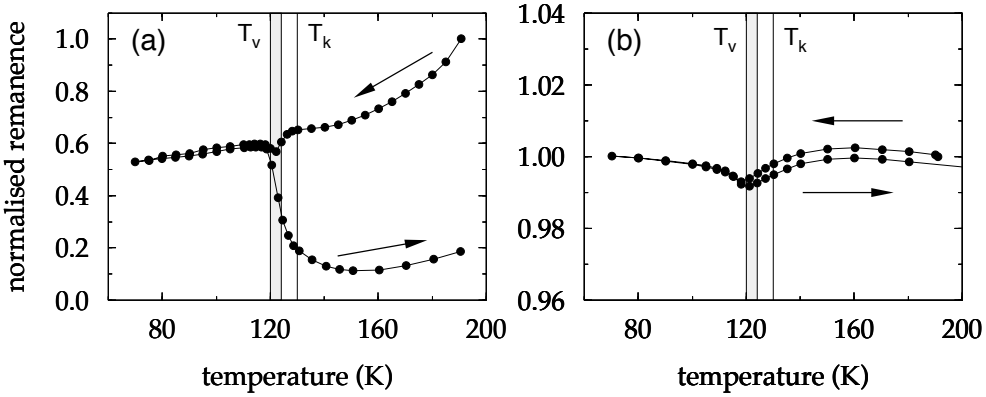


Figure 6.14: Low-temperature cycling of TRMs induced in a field of 100 μT in a) the hydrothermal seed material *H(seed)* and b) *SD(acic.). Note a) and b) have different scales.*

The seed material for the hydrothermally recrystallised samples *H(seed)*, displays no jump on cooling through T_k and T_v (Figure 6.14a); the cooling curve is almost continuous on cooling across T_v and T_k. On warming back through $T_v$and T_k, the sample displays a marked demagnetisation.

The *SD(acic.)* sample displays very similar low-temperature behaviour for TRM (Figure 6.14b) as it does for SIRM (Figure 6.5b). This is not surprising, because once a SD grain is magnetised then its subsequent behaviour is the same regardless of the method of inducement. This is not true for MD magnetites, where the very nature of the TRM and SIRM domain structure is fundamentally different.

Behaviour of weak-field partial thermoremanences

A range of pTRMs were induced in the samples; Figures 6.15 and 6.16 show low-temperature cycling curves for $pTRM^{T_c}_{500}$, $pTRM^{500}_{rtp}$ and $pTRM^{365}_{rtp}$ induced in the hydrothermal samples *H(7.5 μm)* and *H(59 μm)* respectively. Figures 6.17 and 6.18 show the low-temperature cycling curves of a $pTRM^{T_c}_{500}$ induced in natural sample *E(190 μm)* and the hydrothermal sample seed material *H(seed)* respectively.

In Figures 6.15 and 6.16, a variety of Type 1 and Type 2 thermoremanences are shown for samples *H(7.5 μm)* and *H(59 μm)*.

For *H(7.5 μm)*, $pTRM^{T_c}_{500}$ and $pTRM^{500}_{rtp}$ low-temperature cycling curves display similar behaviour to $TRM^{T_c}_{rtp}$ (Figure 6.15); the size of the anomaly at T_v is approximately equal for $pTRM^{T_c}_{500}$ and $TRM^{T_c}_{rtp}$, however it is smaller for $pTRM^{500}_{rtp}$. For $pTRM^{365}_{rtp}$ induced in *H(7.5 μm)*, the remanence was especially weak giving rise to a rather noisy signal. $pTRM^{365}_{rtp}$ did not display an anomaly at T_v. In summary it appears that for sample *H(7.5 μm)*, as the temperature range over which the remanence is acquired decreases, the anomaly decreases, *i.e.*, the anomaly at T_v is associated with remanence acquired at high-temperatures near T_c.

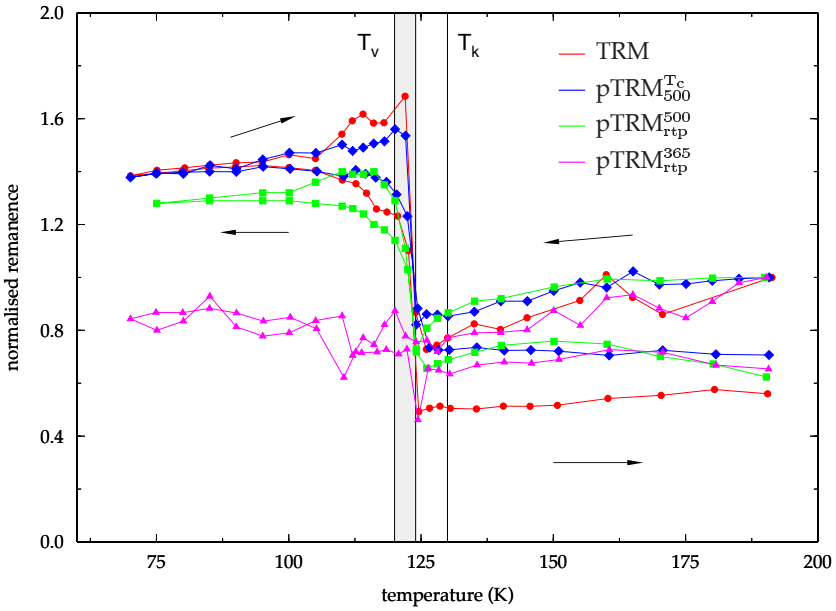


Figure 6.15: Low-temperature cycling of hydrothermal samples *H(7.5 μm)* induced with $pTRM^{Tc}_{500}$, $pTRM^{500}_{rtp}$ and $pTRM^{365}_{rtp}$ using a field of 100 μT. The TRM low-temperature cooling curve (Figure 6.11b) is also displayed. T_v and T_k are marked. The thermoremanences are normalised at 190 K.

Sample *H(59 μm)* (Figure 6.16), does not display the same relationships between pTRM and TRM behaviour as *H(7.5 μm)* (Figure 6.15); TRM displays a negative anomaly at T_v, *i.e.*, demagnetisation, whereas the three pTRMs all display a positive anomaly at T_v. However the relationship between the three pTRMs is similar to *H(7.5 μm)* (Figure 6.15), *i.e.*, the size of the anomaly decreases as the temperature over which the pTRM is acquired decreases. For *H(59 μm)*, the anomaly persists to low-temperature ranges than for *H(7.5 μm)*, *i.e.*, $pTRM^{365}_{rtp}$ displays an anomaly for *H(59 μm)* (Figure 6.16), but not for *H(7.5 μm)* (Figure 6.15). This difference is probably due variations in the blocking spectra of the two samples; the smaller *H(7.5 μm)* sample having a higher blocking spectrum than the *H(59 μm)* sample. I suggest that only domain structures trapped in deep local energy minima (LEM, Section 4.1.2) give rise to this large anomaly at T_v. In the smaller grain *H(7.5 μm)* the domain structure does not have access to particularly stable domain states during acquisition of the $pTRM^{365}_{rtp}$, however the larger *H(59 μm)* sample has a wider range of possible domain structures. Because of the differences in the number of domain states, the resultant domain configuration of a $pTRM^{300}_{rtp}$ induced in *H(59 μm)* would be expected to be more stable than a $pTRM^{300}_{rtp}$ induced in *H(7.5 μm)* sample (this hypothesis is tested in Chapter 7). In the larger sample *H(59 μm)* (Figure 6.16), TRM displays a negative anomaly at T_v whereas Type1 and Type 2 pTRM display positive anomalies. It may be assumed that in larger grains during TRM acquisition the domain structure is not finalised until low-temperatures are reached. This is confirmed by domain observation, which have shown that in hydrothermal magnetites that domain walls are readily moved by small fields at temperatures less 100 °C (Heider *et al.*, 1988b; Heider, 1990).

It seems reasonable to propose that the anomaly at T_v is associated with stability of

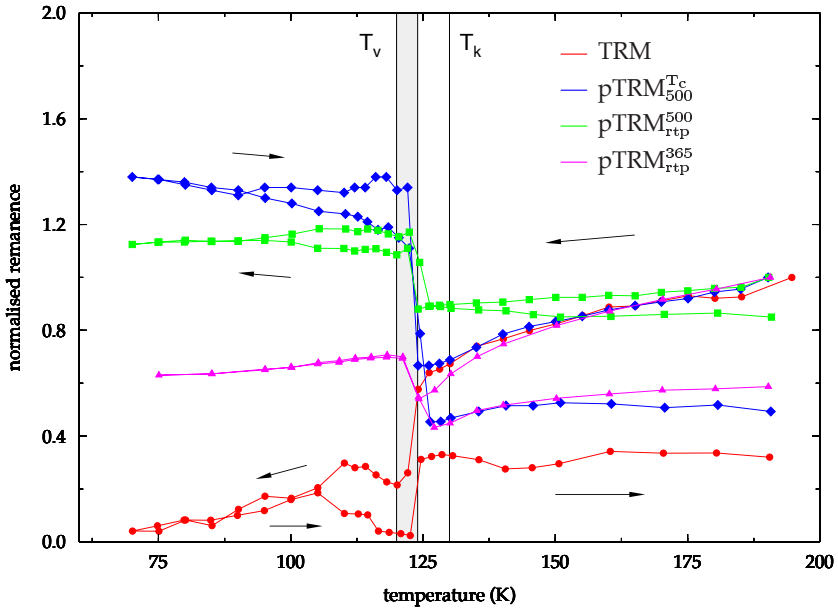


Figure 6.16: Low-temperature cycling of hydrothermal samples *H(59 μm)* induced with $pTRM^{Tc}_{500}$, $pTRM^{500}_{rtp}$ and $pTRM^{365}_{rtp}$ using a field of 100 μT. The TRM low-temperature cooling curve (Figure 6.11f) is also displayed. T_v and T_k are marked. The thermoremanences are normalised on at 190 K.

domain structure, *e.g.*, SIRM is traditionally assumed to have weak domain structures and displays no anomaly, whereas thermoremanences which are thought to be relatively stable, display an anomaly at T_v.

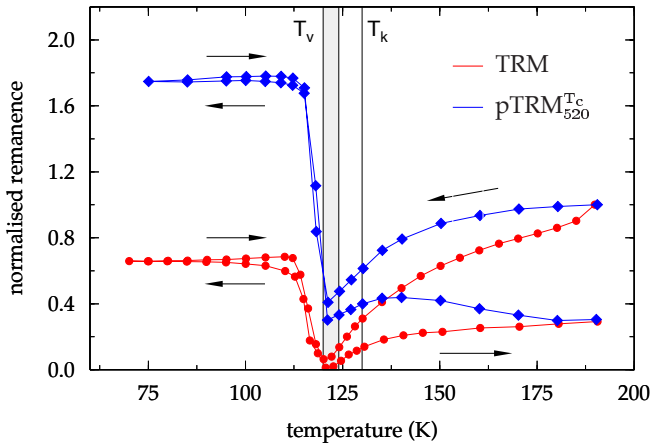


Figure 6.17: Low-temperature cycling of $pTRM^{Tc}_{500}$ induced in a field of 100 μT in natural sample *E(190 μm)*. The TRM low-temperature cooling curve (Figure 6.13c) is also displayed. T_v and T_k are marked. The thermoremanences are normalised at 190 K.

The low-temperature behaviour of a $pTRM^{Tc}_{500}$ induced in natural sample *E(190 μm)* is shown in (Figure 6.17). *E(190 μm)* displays behaviour similar to *H(7.5 μm)* (Figure 6.15); $pTRM^{Tc}_{500}$ has a smaller anomaly at T_v than TRM. That the relative demagnetisation of $pTRM^{Tc}_{500}$ on cooling to T_k is less than TRM, reflects the increased stability of $pTRM^{Tc}_{500}$. Because the grain size of *E(190 μm)* is considerably greater than either *H(7.5 μm)* or *H(59 μm)*,

they it be expected to display similar low-temperature behaviour to *H(59 μm)* (Figure 6.16), however sample *E(190 μm)* does not. The differences in behaviour may be due to either or both impurities (Table 2.3) and stress (Chapter 3).

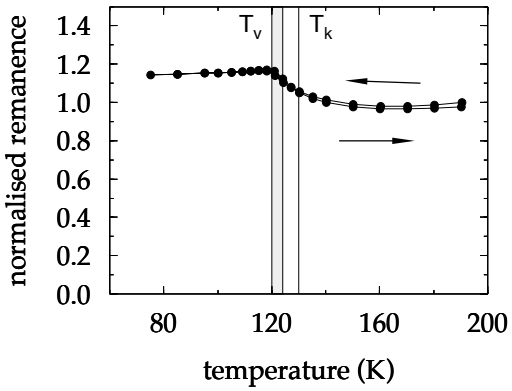


Figure 6.18: Low-temperature cycling of $pTRM^{T_c}_{500}$ induced in a field of 100 μT in hydrothermal seed material *H(seed)*. T_v and T_k are marked. $pTRM^{T_c}_{500}$ is normalised at 190 K.

The hydrothermal seed material (*H(seed)*) shows anomalous behaviour at T_v, but no substantial demagnetisation on warming to room temperature (Figures 6.18). This is probably due to the pseudo-single domain nature of the sample (Chapter 3). If we treat the sample as though it were a single-domain, then only grains with the higher coercive forces block during acquisition of a $pTRM^{T_c}_{500}$. In terms of Figure 6.6, high coercive forces are associated with high demagnetising factors. Blocked grains are less likely to demagnetise on cooling through T_v and T_k, than grains with lower coercive forces. During both SIRM and $TRM^{T_c}_{rtp}$ acquisition, lower coercive force grains are magnetised. During low-temperature cycling, the low coercive grains unblock, giving rise the demagnetisation observed at T_v (Figures 6.5a and 6.14a respectively).

6.6.2 Low-temperature behaviour of high-field partial thermoremanences

Thermomagnetic curves above room temperature for the thermoremanences discussed in this section are presented in Chapter 4.

Four different partial thermoremanence were induced in the samples; two Type 1 thermoremanences $pTRM^{T_c}_{520}$ and $pTRM^{T_c}_{480}$ and two Type 2 thermoremanences $pTRM^{550}_{450}$ and $pTRM^{450}_{300}$. A field of 5 mT (5000 μT) was used to induce the thermoremanences. As these thermoremanences were induced in high-fields, *i.e.*, $H \geq 300\mu$T where the TRM intensity is non-linear with applied field strength, it is thought that these thermoremanences have a stability and behaviour between that of SIRM and weak-field thermoremanences (Section 4.2.1). This assumption has previously been found to be true in this work for thermomagnetic curves above room temperature (see Chapter 4).

The low-temperature cooling curves of $pTRM^{T_c}_{520}$ and $pTRM^{550}_{450}$ for the hydrothermal

sample *H(7.5 μm)* are shown in Figure 6.19, and the cooling curves of $pTRM^{T_c}_{520}$, $pTRM^{550}_{450}$ and $pTRM^{450}_{300}$ for the hydrothermal samples *H(59 μm)* and *H(76 μm)* are shown in Figures 6.20 and 6.21.

In contrast to weak-field thermoremanence curves in the same sample (Figure 6.11b and 6.15), the *H(7.5 μm)* sample shows no positive jump on cooling through T_v for either of the two Type 2 pTRMs induced in the sample (Figure 6.19). On warming back to room temperature there is a large recovery. During low-temperature cooling $pTRM^{450}_{300}$ displays less demagnetisation than $pTRM^{T_c}_{520}$ (Figure 6.19b).

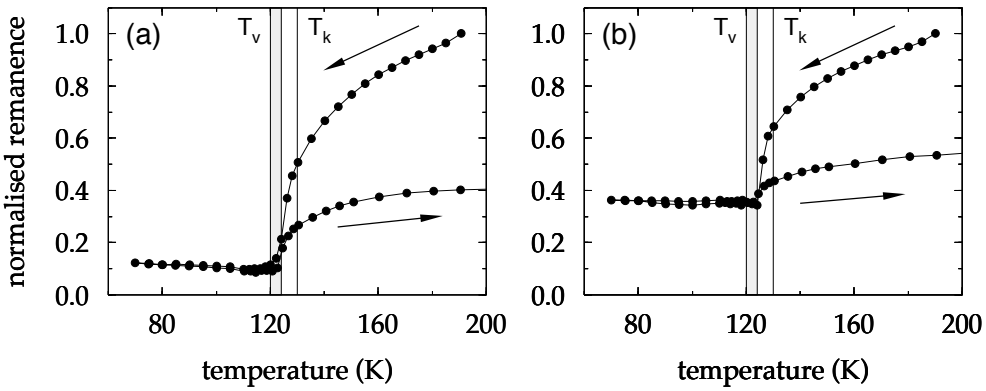


Figure 6.19: Low-temperature cycling of hydrothermal sample *H(7.5 μm)* induced with a) $pTRM^{T_c}_{520}$ and b) $pTRM^{450}_{300}$ using a field of 5 mT.

For the larger crystals *H(59 μm)* (Figures 6.20) and *H(76 μm)* (Figure 6.21), the low-temperature cooling curves all display a small anomaly on cooling through T_v. The size of the anomaly increases as the temperature at which the pTRM was acquired increases, *e.g.*, for *H(76 μm)* $pTRM^{T_c}_{520}$ anomaly $>$ $pTRM^{550}_{450}$ anomaly $>$ $pTRM^{450}_{300}$ anomaly (Figure 6.21).

The relative size of the anomaly is dependent on grain size, *e.g.*, for both $pTRM^{T_c}_{520}$ and $pTRM^{450}_{300}$ the anomaly on cooling through T_v is greatest for *H(76 μm)* followed by *H(59 μm)* and *H(7.5 μm)* (Figures 6.19, 6.20 and 6.21).

Comparing the high-field partial thermoremanences (Figures 6.19, 6.20 and 6.21) with the weak-field partial thermoremanences (Figures 6.15 and 6.16), it is readily seen that the anomaly observed is much larger for weak-field thermoremanences, for similar pTRMs induced in the same samples. The behaviour of the high-field thermoremanences is in some cases more akin to the low-temperature behaviour of SIRM (Figure 6.3). This reconfirms the ideas discussed in Chapter 4, that high-field thermoremanence has domain structures which are relatively unstable compared to weak-field thermoremanences.

Low-temperature cycling of a high-field $pTRM^{T_c}_{480}$ induced in a field of 5 mT in the natural sample *E(250 μm)* is shown in Figure 6.22, and confirms this departure in behaviour of high-field thermoremanence from weak-field thermoremanence. There is a small negative anomaly, *i.e.*, demagnetisation, observed on cooling through T_v (Figure 6.22). The general appearance is similar to the low-temperature behaviour of SIRM, *cf.* low-temperature

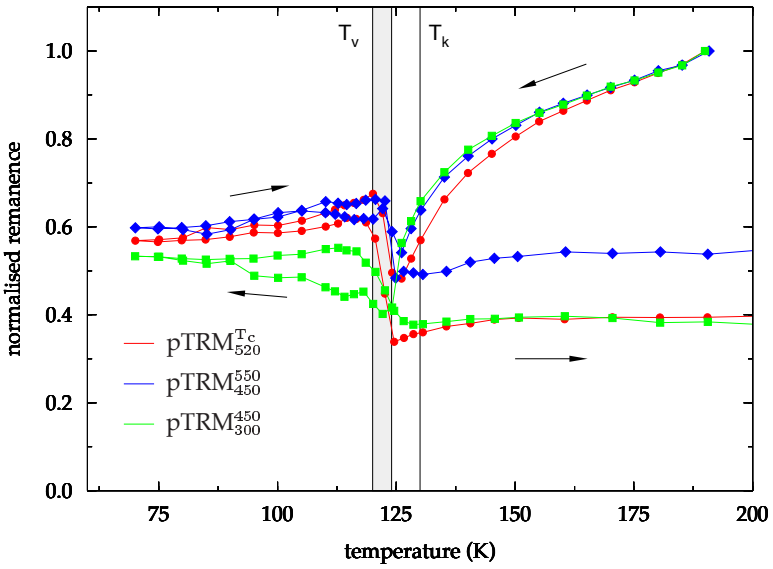


Figure 6.20: Low-temperature cycling of $pTRM^{T_c}_{520}$, $pTRM^{550}_{450}$ and $pTRM^{450}_{300}$ induced in a field of 5 mT hydrothermal sample *H(59 μm)*. T_v and T_k are marked. The thermoremanences are normalised at 190 K.

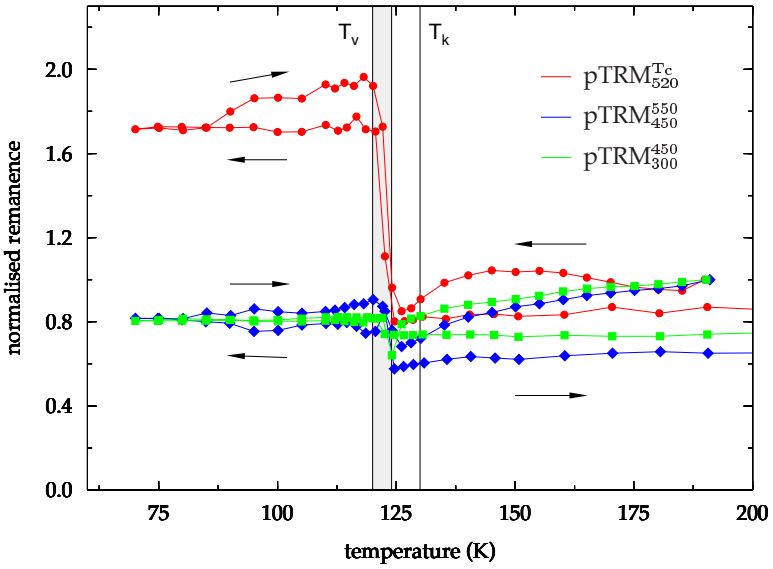


Figure 6.21: Low-temperature cycling of $pTRM^{T_c}_{520}$, $pTRM^{550}_{450}$ and $pTRM^{450}_{300}$ induced in a field of 5 mT hydrothermal sample *H(76 μm)*. T_v and T_k are marked. The thermoremanences are normalised at 190 K.

cycling curves for the natural sample *E(190 μm)*; weak-field TRM in Figure 6.13b and SIRM in Figure 6.4a. The behaviour of high-field $pTRM^{T_c}_{480}$ induced in *E(250 μm)*, confirms the departure in behaviour of high-field thermoremanence from weak-field thermoremanence.

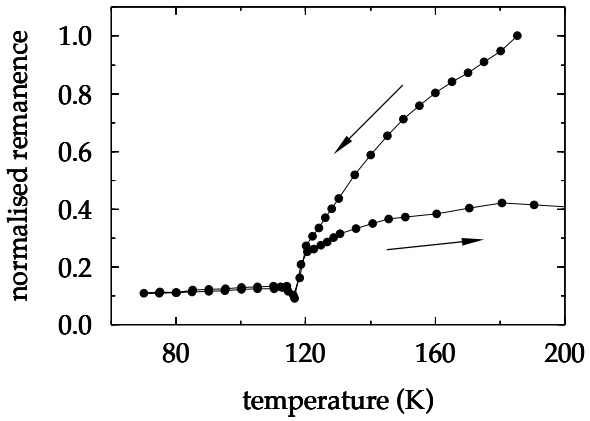


Figure 6.22: Low-temperature cycling of natural sample *E(250 μm)* induced with a $pTRM^{T_c}_{4s0}$ using a field of 5 mT.

6.7 Possible explanation for the difference between SIRM and thermoremanence low-temperature behaviour

There are large variations in the low-temperature cooling curves for the different initial remanences; SIRM (Section 6.5), weak-field thermoremanence (Section 6.6.1) and high-field thermoremanences (Section 6.6.2).

The differences in behaviour are linked to the initial domain structure, which is governed by the method of induction. It is well documented (Hartstra, 1982b; 1982a; McClelland & Shcherbakov, 1995, Chapter 7), that although SIRM has larger intensities than thermoremanences induced in the same MD samples, they are relatively less stable. The behaviour of high-field thermoremanences has not been well documented, which is partly due to difficulties with oxidation during heating but mainly because high-field thermoremanences do not occur naturally. However, reason and results such as those shown in Chapter 4, suggest that high-temperature thermoremanence has a magnetic character in between that of SIRM and weak-field thermoremanence, *i.e.,* their remanence intensity is less than a SIRM and more than a weak-field thermoremanence, and their domain structure is relatively more stable, *i.e.,* resistant to demagnetisation, than an SIRM but less stable than a weak-field thermoremanence. The results presented in this chapter agree with this theory.

So far the differences in the low-temperature behaviour of various initial remanences have been discussed, but no physical model or explanation has been given for the behaviour of these remanences on cooling and warming through T_k and T_v. An explanation of the behaviour is given below.

On cooling and warming through T_k and T_v there are significant anomalies in the spontaneous magnetisation (Figure 5.8), elastic moduli (Section 5.4.3) and the magnetostriction constants (Figure 5.21), however the temperature dependent behaviour of the magnetocrystalline anisotropy is probably the driving mechanism for the low-temperature be-

haviour. At room temperature the first cubic magnetocrystalline anisotropy constant (K_1) is negative, making the easy axis the [111] direction, and on cooling K_1 gradually increases to zero at the isotropic point T_k (Figure 5.15). From T_k to T_v, K_1 is positive making the preferred easy axis a [100] axis. However the magnitude of K_1 in the temperature range $T_v < T < T_k$ is very small, making it unlikely that this change in prefered axis is significant to domain reorganisations. On cooling through T_v to the monoclinic phase, the magnetocrystalline anisotropy is altered (Section 5.4.2), with a very large increase in intensity of the main magnetocrystalline constants (*cf.* K_1 and $\mathcal{K}_a$ (Figure 5.17)). The symmetry of the magnetocrystalline anisotropy is also dramatically reduced. This large change in the magnetocrystalline anisotropy causes H_c to increase sharply (Figure 5.27), and for SD with medium or low aspect ratios the magnetocrystalline anisotropy dominates the shape anisotropy (Figure 5.28).

Consider the behaviour of a SIRM and a weak-field $TRM^{T_c}_{rtp}$ in response to low-temperature cycling;

1. **Room temperature $\rightarrow$ T_k.** The SIRM and $TRM^{T_c}_{rtp}$ both demagnetise on cooling from room temperature, due to the mechanisms described in Chapter 4. As the magnetocrystalline anisotropy decreases, domain walls will become more flexible (Xu & Merrill, 1989; Jiles, 1991), and the rigid wall approximation breaks down. The rigid wall assumption requires that the flexure of a wall structure due to microstress issmall. This requirement is met when the magnetic anisotropy is greater than the anisotropy induced by the stress fields around a dislocation, that is (Xu & Merrill, 1989),

$$\mid -\frac{2}{3}K_1(T) + \frac{9}{2}c_{44}(\lambda_{111}(T))^2 \mid \gg \lambda\sigma \tag{6.6}$$

   where σ is the magnitude of the microstress around a dislocation and λ is the average magnetostriction constant. On cooling towards T_k, K_1 decreases (Figure 5.15) more rapidly than λ, λ_{111} or λ_{100} (Figure 5.21). The elastic modulus c_{44} also decreases on approach to T_v (Section 5.4.3). On approach to T_k, $K_1 \rightarrow 0$ and the rigid wall approximation breaks down resulting in wall flexure and wall movement (Jiles, 1991).

   At T_k, softer domain walls governed by the magnetocrystalline anisotropy widen, unpin and demagnetise (classically domain wall width $\propto \sqrt{1/K}$ (Equation 1.26). Some domain walls stay the same width, because they are controlled by the magnetoelastic anisotropy produced by the stress fields which surround pinning sites. Differences in acquisition mechanisms results in $TRM^{T_c}_{rtp}$ having more domain walls in deep LEM states than SIRM. As a consequence SIRM is more susceptible to demagnetisation on cooling through T_k.

2. **$T_k \rightarrow T_v$.** Although K_1 is positive in this region, it is relatively small. For both $TRM^{T_c}_{rtp}$ and SIRM, strongly pinned walls which did not demagnetise at T_k, will remain pinned in this temperature range. Because of this no major changes in the magnetisation are expected in this temperature range.

3. **$T_v \rightarrow$ 77 K.** On reaching T_v the crystal switches from cubic to monoclinic (Chapter 5) and there are large changes in the magnetocrystalline anisotropy. The monoclinic magnetocrystalline anisotropy has a larger intensity than the cubic magnetocrystalline anisotropy and only one easy axis; the *c*-axis (Figure 5.3). Large increases in the magnetocrystalline anisotropy, result in a reduction in the relative importance of magnetic leakage. SIRM has already undergone substantial demagnetising domain re-organisations on cooling to T_v, so the changes in the magnetocrystalline anisotropy at T_v cause little or no further domain restructuring. However the TRM, which was less affected by cooling to T_v because of its more robust domain structure, is more strongly affected. The domain structure of the TRM, is forced to realign in the *c*-direction on cooling through T_v. Some orientations of grain have their domain structure destroyed, whilst the main body domains of grains with different orientations will partially remain. However the screening closure domains become energetically unfavourable and are destroyed, giving rise to large increases in the measured magnetisation, *i.e.,* the anomaly. On cooling to 77 K high coercive domain structures will undergo further stabilisation and domain re-organisation.

4. **77 K $\rightarrow$ T_v.** Because the domain structure continued to re-organise and stabilise during cooling, at any temperature between 77 K and T_v the warming domain structure is more stable than the cooling domain structure. The stabilisation gives rise, especially in the smaller grains, to increased magnetic leakage and higher observed magnetisation. The difference between the magnetic moments of the cooling and warming curves is more apparent near T_v.

5. **$T_v \rightarrow T_k$.** On warming to above T_v, the closure domains and the other screening domains will return. Many of the central body domains which were partially realigned in the monoclinic phase, will return to their original cubic phase positions. This effect has been directly observed for surface domains by Moloni *et al.* (1996). The return of closure domains reduces magnetic leakage, which reverses the anomaly observed on cooling. However it is likely that some domains do not return to their original cubic phase positions. This results in a net demagnetisation, *i.e.,* the size of the warming anomaly is bigger than that of the cooling anomaly. On warming to T_k, the magnetisation increases as $M_s(T)$ (Figure 5.8), and appears to be partially reversible with cooling curve

6. **$T_k \rightarrow$ Room temperature.** On heating to room temperature, the magnetisation deviates from the cooling curve because of the demagnetisation which occurred on the cooling to T_k. Between T_k and room temperature, increases in the magnetocrystalline anisotropy (Figure 5.15), cause domain walls to become more rigid, which gives rise to a small recovery. Grains with more dislocations, *i.e.,* greater internal stress, will have a greater number of flexed domain walls, which become rigid on warming to T_v. Because of this stressed grains have a larger recoveries, than unstressed samples.

The high-field thermoremanences display intermediate behaviour between the weak-field thermoremanence and SIRM, which was observed (*cf.* Sections 6.5, 6.6.1 and 6.6.2).

This discussion does not explain differences in the behaviour between grain size and different types of thermoremanences, *i.e.*, $TRM^{T_c}_{rtp}$, $pTRM^{T_c}_{T_2}$ and $pTRM^{T_1}_{T_2}$. Different grain sizes have different blocking spectra; as the grain size increases the blocking spectrum decreases, *i.e.*, larger grains "block" or are pinned at lower temperatures (Dunlop & Özdemir, 1997, see also Chapter 7). However following the ideas discussed in Chapter 4, "blocked" domain walls are not locked into place, but rather whole domain structures are trapped in potential wells or LEM states. As less stable domain states demagnetise at T_k, the jump observed on cooling appears to be associated with domain structures in particularly stable LEM states. Smaller grains, *e.g.*, *H(7.5 μm)*, only have access to metastable LEM states at high temperatures during acquisition, whereas the larger grains have access to them over a wider range of temperatures (Chapters 4 and 7). This partially explains why the jump observed at T_v is still visible for $pTRM^{365}_{rtp}$ induced in *H(59 μm)* (Figure 6.16) and not for $pTRM^{365}_{rtp}$ *H(7.5 μm)* (Figure 6.15), because the *H(59 μm)* $pTRM^{365}_{rtp}$ has access to metastable LEM states on cooling, and the *H(7.5 μm)* $pTRM^{365}_{rtp}$ does not.

It was found that the jump at T_v for $TRM^{T_c}_{rtp}$ is grain size dependent (Figure 6.11), which at first is a little surprising because it was expected that all the grain sizes have an extensive range of stable LEM states available to them, which would produce a positive jump at T_v. However the larger grains show no or little jump on cooling through T_v, which contradicts the hypothesis above that the jump is related to metastable domain structures (Figure 6.11f). A possible explanation for this discrepancy is that thermoremanence acquired over a wide temperature range, *e.g.*, $TRM^{T_c}_{rtp}$, in large MD grains have domain structures which are less dependent on closure domains for the minimisation of the magnetic flux leakage, *i.e.*, the total magnetic leakage from the domain structure is minimised by the positioning of the body domains rather than closure domains. On cooling through T_v to the monoclinic phase, the destruction of unfavourably aligned closure domains would not result in a significant increase in magnetic flux leakage, *i.e.*, there would be no significant anomaly at T_v. The observed demagnetisation for the larger grains carrying weak-field $TRM^{T_c}_{rtp}$ is due the destruction of the few grains whose domain structure is completely demagnetised on cooling through T_v.

The high-field thermoremanences display a similar trends to the weak-field thermoremanences, *e.g.*, the anomaly observed at T_v increases with increasing temperature at which the pTRMs were acquired (*cf.* Figures 6.15, 6.16, 6.20 and 6.21). However the size of the anomaly is reduced for high-field thermoremanence. The high-field thermoremanences for sample *H(7.5 μm)* displays no jump at T_v, which may be because of the very high field used to induce the thermoremanences, *i.e.*, 5 mT. Domain observations of titanomagnetites (Metcalf & Fuller, 1986; Metcalf & Fuller, 1987a) have shown that occasionally grains well above the SD/MD threshold can be in unstable SD-like states after $TRM^{T_c}_{rtp}$ acquisition in fields of ≈ 1 mT (Section 4.1.1). It is possible that the high-field pTRMs acquired in the

smallest sample *H(7.5 μm)*, were in these SD-like states. High-field pTRMs were not induced in the smallest hydrothermal sample *H(3.0 μm)*. This idea was also postulated in Chapter 4, to explain the behaviour of the *H(7.5 μm)* high-field pTRMs above room temperature. If this hypothesis is correct, then it partially explains the lack of an anomaly at T_v, because the SD-like domain state would be highly unstable in a sample of this grain size, and would demagnetise on cooling through T_k in a similar manner to an SIRM (Figure 6.3). On further cooling and warming, it is expected that the *H(7.5 μm)* sample display SIRM-like low-temperature behaviour, *i.e.,* no anomaly. Dunlop & Argyle (1997) use a similar argument to explain their TRM acquisition curves in small sub-micron magnetites.

In summary, previous low-temperature studies have concentrated on the low-temperature cycling of SIRM (Section 6.2). This is partly due to technical difficulties associated with inducing thermoremanences in magnetite samples without oxidation. Without directly measuring at low-temperature several other studies have examined and compared the memory fraction remaining after low-temperature cycling of other initial remanences, *e.g.,* TRM and ARM (Dunlop & Argyle, 1991; Heider *et al.*, 1992; McClelland *et al.*, 1996). They assumed that the low-temperature behaviour of thermoremanence was similar to that of SIRM, however this study has shown that this not the case. Instead I found a significant magnetic anomaly on cooling TRM and pTRM through T_v, which has not been previously reported. The anomaly is attributed to the large increase in the magnetocrystalline anisotropy energy. The large increase in the magnetocrystalline anisotropy makes "weak" domain structures, *e.g.,* closure domains and SIRM domain structures, magnetically unfavourable. For domain states with metastable LEM body-domain structures, *e.g.,* TRM, the increase in the magnetocrystalline anisotropy energy effectively reduces the magnetic shielding, which increases the magnetic flux leakage. Importantly the magnetic anomaly observed on cooling through the Verwey transition appears to be largely reversible on warming.

Chapter 7

Origin of metastability of multidomain magnetite

7.1 Introduction

In order for palaeomagnetic studies to be successful it is important for sampled rocks to carry remanences which record the direction of the earth's magnetic field, and for this record to be magnetically stable over geological time-scales. The stability of the remanence is strongly related to the domain structure. In a first approximation of the theories developed by Néel (1949; 1955), palaeomagnetists often assume that stable remanence is carried by single domain (SD) grains, whilst multidomain (MD) remanence is magnetically soft and often of a secondary nature which is presumed to be geologically meaningless. However it has long been known that Néel's MD theory which is based on the movement and pinning of domain walls, has several deficiencies, for example it fails to predict the existence of magnetically hard components of MD remanence (Stacey, 1958; Verhoogen, 1959). This is of great significance to palaeomagnetists, because a large percentage of magnetic material in igneous rocks exists in grain sizes that are too large to be SD (Merrill, 1981).

Small grains above the SD/MD threshold (≈ 0.05 μm from experiment (Dunlop, 1973a) and ≈ 0.07 μm from theory (Williams & Wright, 1998)), exhibit decreasing stability with increasing grain size, and are termed pseudo-single domain (PSD) (Dunlop & Özdemir, 1997). As a result MD grains are usually grouped into PSD grains and "truly" MD grains. The PSD/MD grain-size threshold is ill-defined, because it is dependent on the magnetic property measured *e.g.,* thermoremanence or hysteresis parameters, and the nature of the samples, *e.g.*, natural, or synthetic crushed (stressed) or hydrothermally grown (unstressed) (Dunlop & Özdemir, 1997). Initially the value of the PSD/MD threshold was thought to be as low as 5 μm (Stacey, 1958), however over the years this value has been revised. Recent remanent coercive force (H_{rc}) experiments on hydrothermal samples suggest that the threshold is $\approx 110\mu$m (Heider *et al.*, 1996), however the grain size (d) dependency

of saturating isothermal remanence (SIRM) has been found to vary continuously as $d^{-0.5}$ to $d^{-0.65}$ (Dunlop & Özdemir, 1997) from 0.04μm to 1 mm for hydrothermal grains (Heider *et al.*, 1988a) and for natural magnetites 0.5μm to 3 mm (Özdemir & Dunlop, 1995). That recent estimates suggest a lack of a well-defined PSD/MD threshold is not important, what is however is that stability in multidomain grains is partially grain-size dependent.

Attempts to isolate and characterise the stable fraction of remanence usually consist of removing the "soft" component of the remanence by thermal, alternating-field (AF) or low-temperature demagnetisation, followed by further combinations of rock magnetic tests. (*e.g.*, Heider *et al.*, 1992; Dunlop & Xu, 1993; Argyle *et al.*, 1994; McClelland & Shcherbakov, 1995). These experiments have been rather inconclusive. At present there are two opposing ideas as to the origin of the stability; the first theory suggests that the stability is due to SD-like regions within MD structures which act independently (Verhoogen, 1959; Dunlop & Argyle, 1991; Argyle *et al.*, 1994), whereas the second theory argues that the stability is a result of stress-controlled metastable domain configurations (McClelland & Shcherbakov, 1995; McClelland *et al.*, 1996; Shcherbakova *et al.*, 1996).

In this chapter a series of experiments is presented which investigate the nature of the stable fraction of three different remanences; SIRM, thermoremanence (TRM and partial TRM (pTRM) (Chapter 4)) and anhysteretic remanent magnetisation (ARM), induced in variety of natural and synthetic crushed and hydrothermal magnetites (see Chapters 2 and 3). This study primarily investigates the stability of remanence remaining after low-temperature demagnetisation (LTD) treatment, *i.e.*, magnetic memory (see Section 6.3 for definition). In some experiments the LTD treatment step is replaced by an AF demagnetisation step calibrated to remove the same fraction of the total remanence as a LTD treatment. The term C-AFD is used to describe the calibrated AF demagnetisation step, as opposed to an AF demagnetised unblocking spectrum. The fraction remaining after C-AFD is called $\mathrm{PDT_{C-AFD}}$. Post-demagnetisation treatment (PDT) is used universally to describe the stable fraction remaining after either LTD or C-AFD treatment. The experiments on PDT remanence are compared to similar experiments which did not include a LTD or AF demagnetisation step.

In Section 7.3, the initial remanences and their corresponding magnetic memory remaining after LTD treatment are characterised. The magnetic memory ratios, *i.e.*, (memory/initial remanence) are examined, and both the initial remanence and its memory are characterised using standard techniques such as AF and thermal demagnetisation (Section 1.8.2). The sequence of these experiments closely followed the procedures of previous studies (*e.g.*, Heider *et al.*, 1992; McClelland & Shcherbakov, 1995) so that comparisons could be made. C-AFD is also calculated also in Section 7.3.

Where possible, the question of whether PDT remanence shows SD-like or MD character is considered. In particular in Section 7.5, a series of diagnostic experiments are designed to distinguish between SD and MD behaviour of PDT. These diagnostic experiments differ from most previous studies in that there is less ambiguity in the interpretation

of the results, because they examine fundamental basic differences in SD/MD behaviour, *e.g.*, blocking and unblocking spectrum.

The results in this chapter are discussed independently from the results in Chapters 6 and 8, however in Chapter 9 they are incorporated in a more general discussion.

Several of the results in this chapter have previously been reported in McClelland *et al.* (1996), but as my contribution to this paper constituted a large fraction of my work in my first year in Oxford, it seems appropriate to repeat the results here.

Most of the experiments in this chapter were undertaken in the palaeomagnetic laboratory in Oxford using the equipment previously described in Section 1.8. The results from Oxford were all measured at room temperature using either a CCL SQUID magnetometer or occasionally for stronger samples a Molspin spinner magnetometer. Remanences were induced using the equipment described in Section 1.8, and LTD treatment was applied by placing the samples in μ-metal boxes ($H_{res} \leq 100$ nT) for fifteen minutes (Section 1.8).

The only results in this chapter not measured in Oxford were the thermal demagnetisation from room temperature to T_c of "high-field" thermoremanences (Section 7.3.4), which were measured in conjunction with a sequence of experiments previously described in Chapters 4 and 6. A continuous record of thermoremanence acquisition from T_c to T_2, and subsequent zero-field cooling to 77 K and heating to T_c was recorded on my second visit to the Institute for Rock Magnetism (I.R.M.), University of Minnesota. It was necessary to use two pieces of equipment to measure the complete record; above room temperature a Princeton Electronics μ-VSM (Vibrating Sample Magnetometer), whilst below a Quantum Design Magnetic Property Measuring Systems (MPMS).

7.2 Note on terminology

The idea that the stability of MD grains is due to metastable domain configurations, has led to a slight incongruousness in terminology. Originally the term PSD was coined to describe grains just above the SD threshold which showed SD-like characteristics, *i.e.*, they appeared to have permanent magnetic moments (Stacey, 1962). However as the PSD/MD threshold has gradually increased from 5 μm (Stacey, 1962) to much larger values (described above), then the reason for using the term "PSD" must be questioned. If the stable remanence found in MD magnetites is due to SD-like inclusions with permanent moments which are shielded by softer domains, then its use is justified. However if the stability is a truly MD effect, *i.e.*, it is due to metastable domain configurations (McClelland & Shcherbakov, 1995), then its use is incorrect and misleading. Until the problem has been truly resolved (an attempt is made in the rest of this chapter) then the phrase "PSD" should be used with caution.

7.3 Relative behaviour of various magnetic remanences and their memories

Initially the relationship between magnetic memory and the initial remanence's inducing field (H) for both TRM and ARM is investigated (Section 7.3.1), for fields where TRM intensity is linearly related to field, *i.e.*, $H \leq 300$ μT (see Section 4.2.1). It was necessary to understand how both TRM and ARM memory varies with inducing field so that suitable inducing fields could be chosen in the rest of the chapter. In Section 7.3.2 the magnetic memory ratio, *i.e.*, (memory / initial remanence), is examined for various initial remanences. In the following two sections the behaviour of various initial remanences and their memories are characterised by AF demagnetisation (Section 7.3.3) and thermal demagnetisation (Section 7.3.4). In Section 7.3.6, the results of the previous three sections (Sections 7.3.2-7.3.4) are discussed and compared to similar experiments reported in the literature (*e.g.*, Heider *et al.*, 1992; McClelland & Shcherbakov, 1995; Shcherbakova *et al.*, 1996).

7.3.1 Measurement of TRM memory and ARM memory acquisition curves

In this section the behaviour of TRM and ARM memory as a function of field is examined.

As far as I am aware there is only one previous report of the measurement of TRM memory as a function of field (Ozima & Ozima, 1965) and none for ARM memory. However in their study, Ozima & Ozima (1965) did not present the TRM memory results directly only the ratio of (TRM memory / TRM) versus TRM (Figure 7.1), which does not yield any information as whether TRM memory is linear with applied field or not. It only reveals that TRM memory does not increase as rapidly with applied field as TRM.

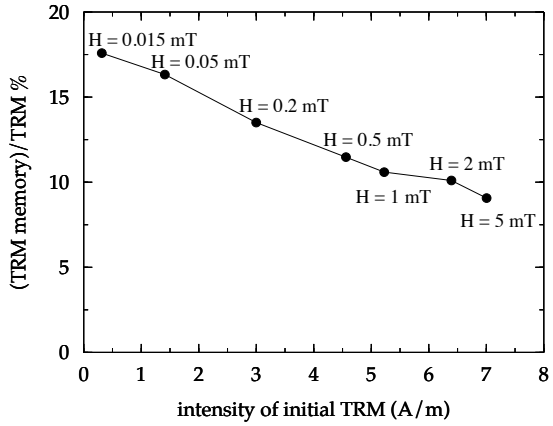


Figure 7.1: (TRM memory / TRM) versus TRM for synthetic magnetite sample with a grain size of nearly 30 μm. After Ozima & Ozima (1965).

Parry (1979) investigated IRM memory acquisition curves, and plotted the raw data (Figure 7.2). The IRM acquisition curve that Parry (1979) measured did not display a

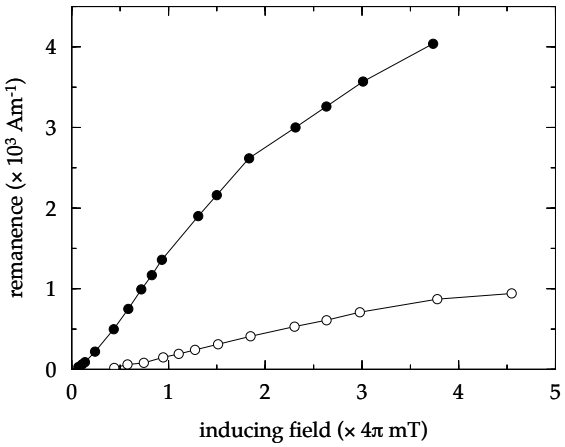


Figure 7.2: IRM (●) and IRM memory (○) plotted as a function of inducing field for natural magnetites (mean diameter = 200 μm). After Parry (1979).

smooth gradient, suggesting that several different mechanisms controlled the magnetisation. For inducing fields of ≤ 4 mT the IRM was completely destroyed on cooling to 77 K, giving zero memory, however above this field IRM memory displays a linear relationship with field up to ≈ 12 mT. Parry concluded that only domain walls which observe a micro-coercive force above 4 mT contribute to the magnetic memory.

It should be noted that IRM acquisition curves are not directly comparable with either TRM or ARM acquisition curves, because the latter remanences affect the entire coercive force (H_c) spectra whilst IRMs affect only a fraction (Dunlop & Özdemir, 1997), *i.e.*, TRM and ARM memory curves should *not* be expected to display the same behaviour as the IRM memory acquisition curve (Figure 7.2).

TRM and TRM memory acquisition curves

According to Néel's (1955) hysteretic MD theory for two domain grains the TRM intensity is $\propto H^{1/2}$ (which has since been generalised to $H^{(1-1/n)}$ for all values of H, where n is the number of domains (Dunlop & Waddington, 1975), however experimental evidence suggests this is not the case. Contrary to hysteretic theory it has been found that for MD grains in low-fields, TRM intensity is approximately linear with H (Nagata, 1961; Dunlop & Waddington, 1975; Shcherbakov *et al.*, 1993). To explain this there have been many suggestions; Néel (1955), who was well aware of this problem, applied the thermal fluctuation energy theory which he had used successfully to model SD behaviour (Néel, 1949). This introduced an effective thermal fluctuation field H_f, which he assumed for certain fields and temperatures is greater than the coercive force, and results in TRM intensity $\propto H$ for small H. The basis of Néel's MD hysteretic/thermal-fluctuation theory is still popular (*e.g.*, Dunlop & Xu, 1994; Xu & Dunlop, 1994), however there is much experimental evidence to suggest that the problem is more complicated (*e.g.*, McClelland & Sugiura, 1987; Heider *et al.*, 1988b; Heider, 1990), which has resulted in new MD TRM theories which incorporate

the linearity of TRM on H (McClelland & Sugiura, 1987; Shcherbakov *et al.*, 1993, see also Chapter 4).

It is commonly assumed that for non-interacting SD grains, TRM is approximately $\propto H$, however Dunlop & Argyle (1997, Figure 7.3) have shown experimentally that this is not the case for equidimensional synthetic magnetites. There are two possible reasons which have led to the assumption that non-interacting SD TRM $\propto H$; firstly magnetic interactions between SD grains reduces the curvature of TRM acquisition curves giving a linear MD-like appearance, *i.e.*, non-interacting grains are non-linear, but interacting are linear (Dunlop & West, 1969; Davis & Evans, 1976). And secondly it is possible that the non-linear relationship observed by Dunlop & Argyle (1997) was related to the symmetry of the grains. Acicular magnetites may display a linear relationship. To test this last possibility, TRM acquisition curves for acicular SD magnetite are examined.

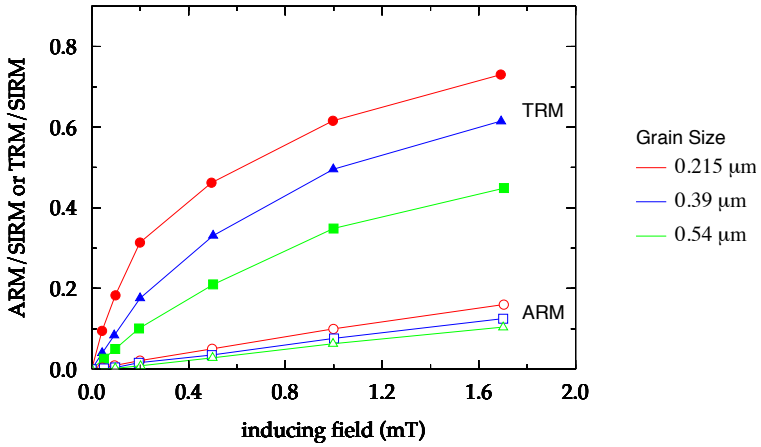


Figure 7.3: TRM (closed) and ARM (open) acquisition curves for PSD equidimensional synthetic magnetites. After Dunlop & Argyle (1997).

Assuming that Dunlop & Argyle's (1997) experimentally derived relationship is correct, then if the TRM memory acquisition curves display a non-linear relationship then this will support the idea that magnetic memory is the result of SD-like regions within the grains.

To investigate this a range of samples (hydrothermally recrystallised, synthetic crushed and natural multidomain magnetite samples, and an acicular single-domain magnetite sample, see Chapter 2 for description) were induced with a $\mathrm{TRM}^{\mathrm{T_c}}_{\mathrm{rtp}}$, *i.e.*, cooled from above T_c to room temperature in an applied field, which was measured. The samples were then cooled in a zero-field environment to 77 K, followed by warming to room temperature and re-measurement. Unfortunately, it was only possible to apply a calibrated field up to 200 μT, and an uncalibrated field up to 300 μT. This was repeated for several fields to give TRM acquisition curves. Some of the TRM acquisition curves are presented in Chapter 4.

Typical results are shown in Figure 7.4, where it can be seen that within experimental error the TRM and the TRM memory intensities are linear with applied field intensity up to

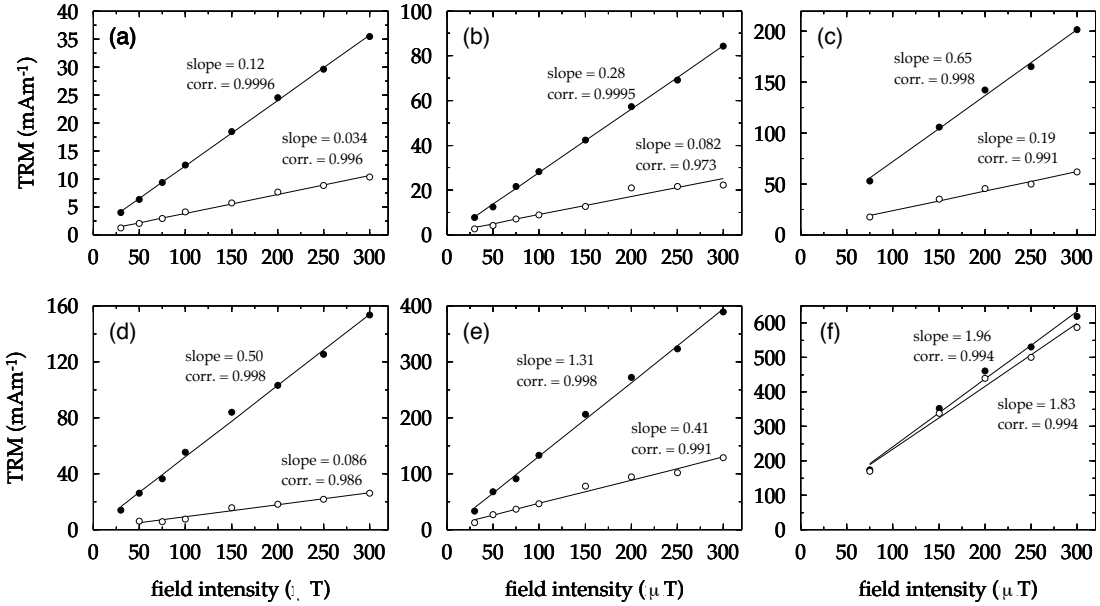


Figure 7.4: TRM (●) and TRM memory (○) intensity versus applied field for a selection of magnetites; Dankers a) *D(15-20 μm)* and b) *D(25-30 μm)*, hydrothermal synthetic c) *H(39 μm)* and d) *H(76 μm)*, e) natural *E(150 μm)* and f) *SD(acic.)*. A linear regression is fitted to each acquisition curve. The gradient (slope) and the correlation coefficient (corr.) for each linear regression is marked.

200 μT for all the synthetic and natural MD grains and the *SD(acic.)* sample. For both TRM and TRM memory above 200 μT the relationship appears to break its linearity, however that may be due to problems in the calibration of the field. It is possible, therefore, that the approximate linear relationship holds for higher field intensities. Shcherbakov *et al.* (1993) found that the linear relationship holds to only 200 μT for MD magnetite. For all the samples, *i.e.*, both SD and MD (Figure 7.4), the TRM memory increases less rapidly than TRM.

That the TRM and TRM memory of the *SD(acic.)* sample displays a linear dependency with field until 200 μT (Figure 7.4f), firstly disagrees with the recent results by Dunlop & Argyle (1997) who found that equidimensional SD magnetites displayed non-linear behaviour, and secondly it means that no conclusions about the domain state, *i.e.*, SD-like or MD-like, of TRM memory can be drawn from the results in this section. There are two possible reasons for this discrepancy; firstly the variation in the shape of the SD samples, *i.e.*, acicular and equidimensional, may alter the intrinsic difference behaviour, and secondly my *SD(acic.)* sample was not well dispersed (Section 2.6) giving rise to a large number of interactions. Grain interactions are known to produce linear acquisition curves (Dunlop & West, 1969). The equidimensional grains of Dunlop & Argyle (1997) are less likely to be affected by grain interactions, than the acicular grains.

It may be concluded that TRM memory displays a linear relationship with acquisition field up to $\approx$ 200 μT similar to TRM, however this does not reveal whether it is SD-like or MD-like in character.

ARM and ARM memory acquisition curves

If the maximum AC field is above the saturation field for the mineral in question (magnetite $\approx$ 300 mT (Thompson & Oldfield, 1986)), then ARM affects the entire grain distribution, and it has been argued that such ARMs are similar (but not identical) to TRMs acquired in the same DC field H (Nagata, 1961; Levi & Merrill, 1976). The substitution of laboratory ARM for laboratory TRM eliminates the need for heating the rock and the risk of chemically alteration, and has led to ARM analog Thellier-Thellier type palaeointensity studies and theories (Banerjee & Mellema, 1974b; Bailey & Dunlop, 1977). Because of the similarity of ARM and TRM it is common practice to compare the results for identical experiments on TRM and ARM (*e.g.*, Dunlop & Argyle, 1997). In comparable study to TRM memory acquisition described above, ARM memory acquisition is considered in here.

Since two different fields are applied during ARM acquisition (Section 1.8.2), there are two types of ARM acquisition curve, *i.e.*, variations in the AC field (van Velzen, 1994) or the DC biasing field (Nagata, 1961). Because it is the intention of this section to compare ARM memory acquisition curves with TRM memory acquisition curves, only variation in the DC bias field is considered.

There have been several investigations of ARM acquisition curves (DC-type) for MD magnetites, however these have generally been for either natural MD magnetite (Levi & Merrill, 1976) or for small PSD grains, *i.e.*, ≤ 1 μm, (*e.g.*, Sugiura, 1979; Dunlop & Argyle, 1997). In general both MD and SD magnetite display linear ARM acquisition curves at much higher fields than TRMs induced in the same sample (Figure 7.3). The rapid initial rise in TRM contrasts with the slow linear increase in ARM, TRM $\gg$ ARM for all H (Figure 7.3).

As the only published ARM acquisition curves for large MD grains that have been produced used natural samples, it seemed appropriate to measure acquisition curves for synthetic magnetite. ARM memory acquisition curves were also measured. To examine this a range of samples (hydrothermally recrystallised, synthetic crushed (Dankers samples) and natural multidomain magnetite samples, see Chapter 2 for description) were induced with ARMs. In the Oxford laboratory, the maximum AC field available was only 100 mT, *i.e.*, 200 mT less than the 300 mT ideally required to affect the entire coercive force spectrum of magnetite. However for for soft MD magnetites it is sufficient to affect the entire coercive force spectrum. As an extra precaution the starting conditions were made identical for all the experiments, by thermally demagnetising the samples, *i.e.*, cooled from above T_c in zero-field (commonly refered to in the Russian literature as the absolute zero state (AZS) (Shcherbakov *et al.*, 1993)). The maximum available DC field during ARM acquisition was 180 μT.

In a similar procedure to the thermoremanences the samples were first thermally demagnetised, induced with an ARM in a field H, measured, cooled to 77 K in liquid nitrogen and measured again. Typical results are shown in Figure 7.5.

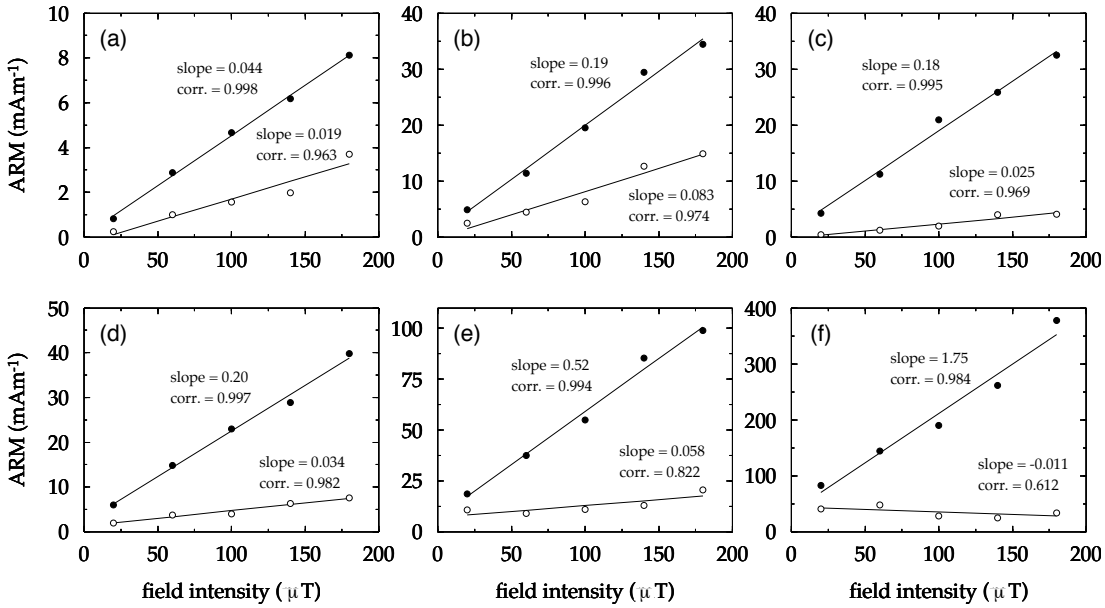


Figure 7.5: ARM (•) and ARM memory (○) intensity versus applied field for a selection of magnetites; Dankers a) *D(15-20 μm)* and b) *D(25-30 μm)*, hydrothermal synthetic c) *H(3.0 μm)* and d) *H(76 μm)*, and natural e) *E(150 μm)* and f) *PW(3 mm)*. A linear regression is fitted to each acquisition curve. The gradient (slope) and the correlation coefficient (corr.) for each linear regression is marked.

From Figure 7.5, it can be seen that ARM and ARM memory intensities are approximately linear with applied field up to the maximum inducing field of 180 μT for all the synthetic and natural MD grains. The linearity of ARM acquisition curves Figure 7.4) agrees with previous studies (Levi & Merrill, 1976, and Figure 7.3).

In a similar conclusion to that for the TRM and TRM memory acquisition curves, it may be stated that ARM memory displays a linear relationship with acquisition field up to the maximum field of 180 μT similar to TRM. This does not reveal whether the memory is SD-like or MD-like in character. To my knowledge this is the first time that ARM memory acquisition curves have been measured. ARM memory is linear with field up to 180 μT.

Comparison of TRM, TRM memory, ARM and ARM memory acquisition curves

Both TRM memory and ARM memory acquisition curves display similar behaviour in relation to the field, *i.e.*, linear upto $\approx$ 200 μT, and in relation to TRM and ARM acquisition curves respectively.

That both TRM and ARM memories increase with H is not surprising when the results in Chapter 6 are considered. In Chapter 6 it is concluded that memory is associated with metastable domain states, which are associated with thermoremanences rather than saturating isothermal remanences. For small fields, increasing H during both TRM and ARM acquisition increases the number of available local energy minima (LEM, Moon & Merrill, 1984; 1985) domains states, which in turn increases the number of possible

metastable states and the observed memory. If the field is increased further, TRM and ARM domain states will be pushed into unstable configurations, *i.e.*, the domain states become more "SIRM-like" *cf.* the behaviour of high-field thermoremanences in Chapters 4 and 6. This is reflected by the non- linearity of TRM acquisition curves above ≈ 200 μT (Figure 7.4).

That both TRM memory and ARM memory acquisition curves are linear over the same range of H as TRM and ARM are linear, reflects a linear relationship between the number of metastable domain states and H.

In Figure 7.6, acquisition curves for TRM,TRM memory, ARM and ARM memory are plotted for a selection of samples.

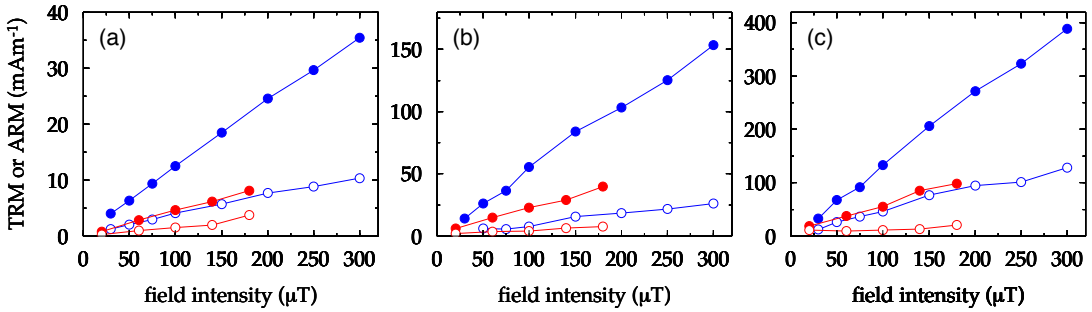


Figure 7.6: TRM (●), TRM memory (○), ARM (●) and ARM memory (○) intensity versus applied field for a selection of magnetite samples; a) Dankers *D(25-30 μm)*, b) hydrothermal synthetic *H(76 μm)* and c) natural *E(150 μm)*.

The TRM memory and ARM memory acquisition curves, have a similar relationship to each other as do TRM and ARM acquisition curves, *i.e.*, TRM memory $\gg$ ARM memory for all H (*cf.* Figure 7.3). That ARM memory does not reach the same intensity of magnetisation for the same H as TRM memory (Figure 7.6), reflects the number of metastable states available to both ARM and TRM, *i.e.*, TRM has more. The reason for this is unclear, however as the method of acquisition is completely different it is not unsurprising that there are differences. It is likely that many TRM domain configurations are not available during ARM acquisition, and/or that some TRM metastable domain configurations are obtainable during ARM acquisition, but are not metastable in the large AC field.

Interestingly, for small multidomain grains (Figure 7.3) both TRM and ARM acquisition curves are linear over the same range of remanent magnetisation, suggesting a "maximum linear magnetisation" domain state. This supports the idea that certain metastable domain configurations are unstable to the large AC field, *i.e.*, increasing the DC field decreases the relative contribution from the AC field making more TRM-like metastable domain configurations available during ARM acquisition. At some unknown field ("maximum linear magnetisation") ARM is pushed into unstable high field states in a similar manner to the TRM. Then ARM and ARM memory will display non-linear behaviour. I postulate that ARM memory at the "maximum linear magnetisation" field for ARM acqui-

sition, will have approximately the same intensity as TRM memory at the TRM "maximum linear magnetisation" field ($\approx 200\ \mu$T). To test this it is necessary to measure ARM acquisition curves for MD magnetite in larger fields than the maximum 180 μT I had available to me.

In comparison with the IRM memory acquisition curve (Figure 7.2), the ARM and TRM memory acquisition curves (Figure 7.6) display greater stability, which reflects the differences in the domain configurations.

Following the procedure of Ozima & Ozima (1965, Figure 7.1), (TRM memory / TRM) against TRM and (ARM memory / ARM) against ARM are plotted in Figure 7.7 for a selection of samples.

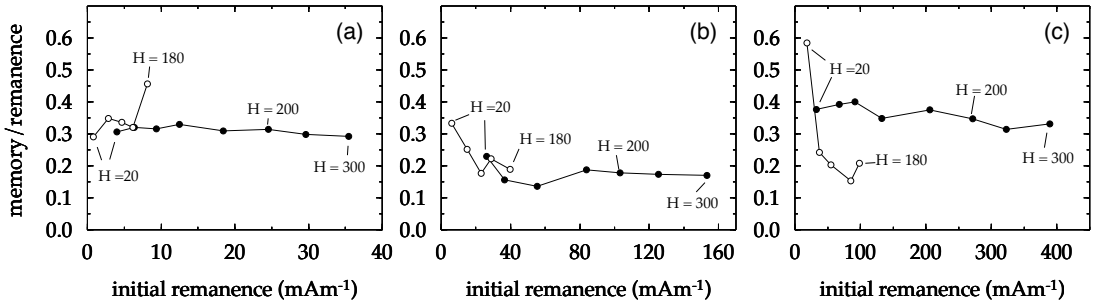


Figure 7.7: (TRM memory / TRM) against TRM (●) and (ARM memory / ARM) against ARM (○) for the selection of magnetites shown previously in Figure 7.6; a) Dankers material *D(25-30 μm)*, b) hydrothermal synthetic *H(76 μm)*and c) natural *E(150 μm)*.

(TRM memory / TRM) against TRM displays a greater linearity than (ARM memory / ARM) against ARM (Figure 7.7). This reflects differences in the number of metastable states available with increasing H; TRM has a linear increase in the number of metastable states with field, where as ARM increases in discrete jumps.

7.3.2 Magnetic memory of various initial remanences

There have been many studies which have examined the magnetic memory of various remanences for all ranges of grain size, *i.e.,* 0.03 μm–5 mm (*e.g.,* Levi & Merrill, 1976; 1978; Parry, 1979; Hartstra, 1982a; 1983; Dunlop & Argyle, 1991; Heider *et al.*, 1992; Halgedahl & Jarrard, 1995; Borradaile, 1994; Shcherbakova *et al.*, 1996). These studies have generally concentrated on SIRM and $\mathrm{TRM}^{\mathrm{Tc}}_{\mathrm{rtp}}$ memory (*e.g.,* Levi & Merrill, 1976; 1978; Heider *et al.*, 1992) however there have been several reported investigations of ARM memory (*e.g.,* Parry, 1979; Hartstra, 1983; Dunlop & Argyle, 1991). It is standard practice to normalise the magnetic memory by the initial remanence to give the "memory ratio", *i.e.,* (memory / initial remanence).

Problems arise when comparisons between memory ratios from different studies are made (Heider *et al.*, 1992; Dunlop & Özdemir, 1997), because there has been no standard

field for either TRM or ARM acquisition, and the memory ratio is dependent on the inducing field (Section 7.3.1). Fortunately the number of $TRM^{T_c}_{rtp}$ studies has been quite large, and there are several results for TRM memory induced with a field of 100 μT (Heider *et al.*, 1992; Dunlop & Xu, 1993; Argyle *et al.*, 1994; McClelland & Shcherbakov, 1995). However this is not the case for ARM memory, which has not been systematically studied to the same extent as TRM memory. A wide range of inducing fields have been used; 30 μT (Hartstra, 1982a; 1983), 55 μT and 69 μT (Levi & Merrill, 1976), 100 μT (Argyle *et al.*, 1994), 200 μT (Dunlop & Argyle, 1991) and 3.14 mT (Parry, 1979). In the only reported study of its type, Shcherbakova *et al.* (1996) investigated the magnetic memory ratios of various partial thermoremanences, both Type 1 ($pTRM^{T_c}_{T_2}$) and Type 2 ($pTRM^{T_1}_{T_2}$) (see either Section 4.2.1 or Section 6.6 for definitions).

Due to the rather sparse record of ARM memory and pTRM memory, it was decided to examine both ARM memory and pTRM memory for a range of well defined synthetic magnetites and natural magnetites. The results of $TRM^{T_c}_{rtp}$ and SIRM memory are also considered, and compared to the literature.

Experimental technique

The procedure for measuring magnetic memory is very simple; induce the remanence in the sample, measure, place the sample in liquid nitrogen inside a μ-metal box (internal field $\leq$ 100 nT) and allow the sample to re-equilibrate at that temperature, warm to room temperature and remeasure.

All the remanences were induced in the laboratory in Oxford using standard palaeomagnetic equipment (Section 1.8). SIRM was induced in a field of 0.8 T, ARM in a DC field of 100 μT and a maximum AC field of 100 mT, and TRM and pTRM in field of 100 μT. The field dependency of TRM and ARM memory is considered in Section 7.3.1. Several different thermoremanences were induced; $TRM^{T_c}_{rtp}$, $pTRM^{T_c}_{560}$, $pTRM^{T_c}_{500}$ and $pTRM^{500}_{rtp}$. The field dependency of TRM and ARM memory is considered in Section 7.3.1.

Measured memory of several different remanences

The results of the measurement of magnetic memory of all the remanences are summarised in Table 7.1. All the samples had been previously vacuum sealed in quartz capsules to remove the possibility of chemical alteration during heating (Section 2.6), however because the capsules had a tendency to implode during heating, the record shown in Table 7.1 is far from complete. The magnetic memory was aligned in the same direction as the initial remanence, except as marked in Table 7.1. The memory was found to be independent of the orientation of the sample.

Before considering the memories of ARM and pTRM it is worth comparing SIRM and TRM memories (Table 7.1), with data from the literature. The SIRM and TRM memories are plotted along with published data in Figure 7.8.

sample	SIRM %	ARM %	TRM %	$pTRM^{Tc}_{560}$ %	$pTRM^{Tc}_{500}$ %	$pTRM^{500}_{rtp}$ %
H(3.0 μm)	11	13	35		33	9 †
H(7.5 μm)	29		44		44	44
H(13 μm)	7		19			
H(18 μm)	28	23	31			55
H(24 μm)		39	34		18	59
H(39 μm)	18	9	28			38
H(59 μm)	8	24	22	35	42†	37†
H(76 μm)	12	19	24	30	16	35†
H(108 μm)	11		15			24†
D(5-10 μm)	21	57	44		40	55
D(15-20 μm)	18	58	34	26	24	52
D(20-25 μm)	27	83	54	22	27	83
D(25-30 μm)	18	43	19	18	17	54
D(30-40 μm)			18			
D(75-100 μm)	12	24†	-13†	13†	- 27†	-25†
D(100-150 μm)			-17†			32
E(150 μm)	12	21	30	41	42	16†
E(190 μm)	29	39	48	57	57	22†
E(250 μm)	20	22	49	43	78	50
E(1.5 mm)	16	18	32	51	88	
PW(1 mm)	17	65	67	61	68	69
PW(2 mm)	13		39			
PW(3 mm)	6	9	53	60		48
SD(acic.)			97			

Table 7.1: Low-temperature memory ratios for different initial remanences, *e.g.*, SIRM % = (SIRM memory/SIRM) %. A † indicates that the memory was not aligned in the same direction as the initial remanence. Negative memory ratios represents a reversal, *i.e.*, memory aligned more than 90° away from the original remanence. The thermoremanences were induced in a field of 100 μT and the ARM in a DC field of 180 μT.

Both SIRM memory and TRM memory compare favourably with previous studies (Figure 7.8); the memories decrease with increasing grain size, and TRM memory $>$ SIRM memory, which reflects differences in the stability of the two types of domain structures. In agreement with the literature (Parry, 1979; Heider *et al.*, 1992), the difference between TRM and SIRM memory increases as the grain size decreases. The reversed memories for the larger Dankers samples have been observed before for the same material (McClelland & Shcherbakov, 1995), and is discussed in detail in Section 7.3.6.

Because my hydrothermal crystals (*H(3.0 μm)–H(108 μm)*) were made using the same technique (Heider & Bryndzia, 1987) as the hydrothermal crystals of Heider *et al.* (1992), they should be expected to display similar behaviour. On comparison of both sets of hydrothermal magnetites (Figure 7.8), it is seen that the SIRM and TRM memories of my hydrothermal samples are on average slightly higher than those of Heider *et al.* (1992). A similar difference between my hydrothermal samples and those of Heider *et al.* (1992) is observed for the coercive force and the ratio of SIRM over the saturation magnetisation (Figures 3.3 and 3.4). The difference in coercive force is attributed to either grain interactions or differences in the standard deviation of grain distributions (Section 3.4.2). The

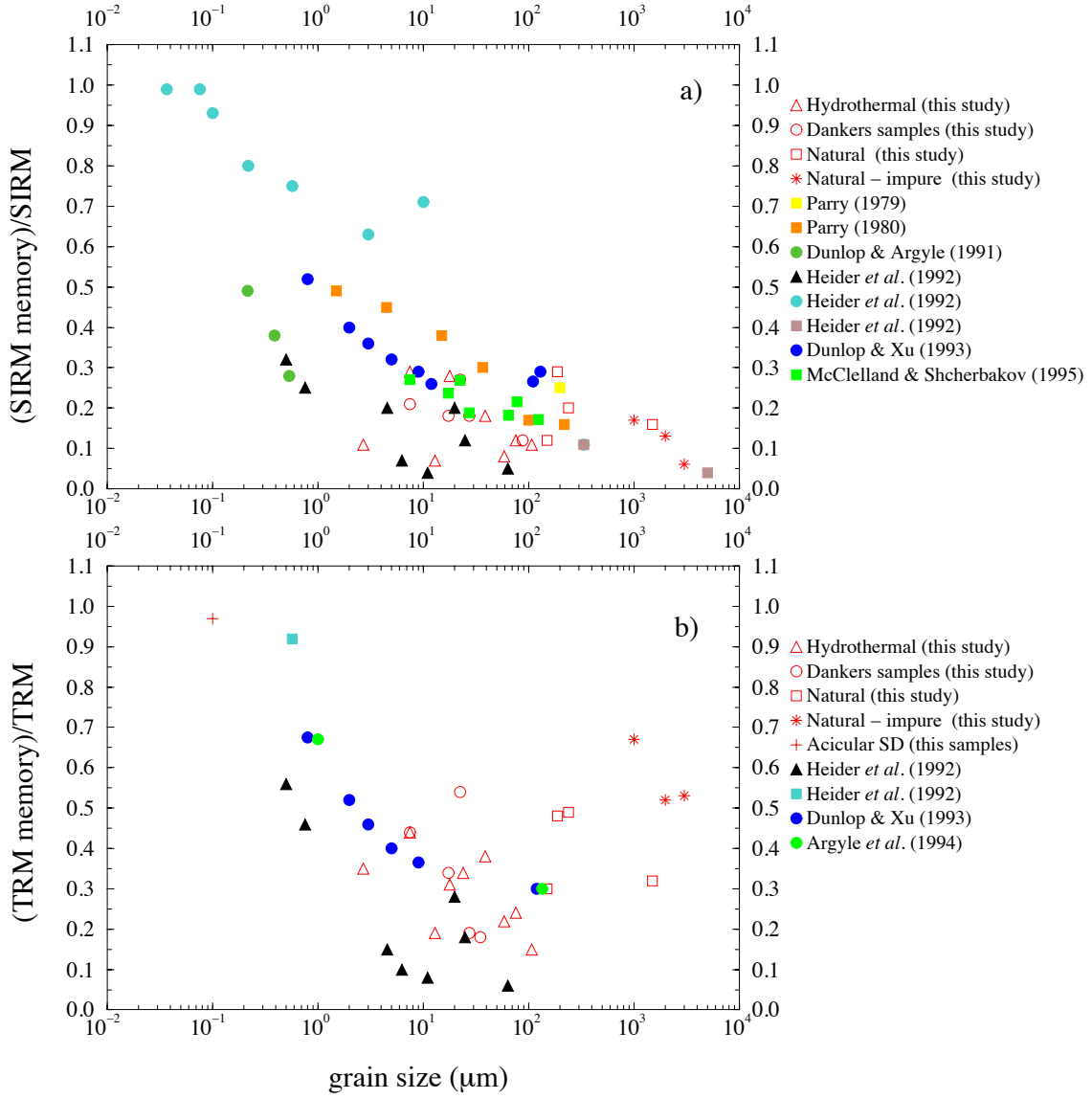


Figure 7.8: Low-temperature memory ratios for a) SIRM and b) TRM induced in 100 μT, in sized magnetites. The SIRM and 100 μT TRM memory ratios of previous studies (all synthetic magnetite) are also presented. Hydrothermal crystals are represented by △, annealed crystals by ○ and unannealed, crushed or irregular magnetites by □. My samples are represented by open symbols, *e.g.*, ○, whilst previously published data are shown as solid symbols, *e.g.*, ●. Note, because the Dankers crushed magnetites (*D(5-10 μm)–D(100-150 μm)*) had been heated on numerous occasions before this experiment, they were considered to be annealed and are represented by ○. Samples with reversed memories are not shown.

coercive forces were determined for unpressed samples, however the magnetic memories were measured on samples which had been lightly pressed into KBr pellets and sealed in vacuum capsules (Section 2.6). Lightly pressing the samples may have induced stress, which reduces demagnetisation during low-temperature cycling through the Verwey transition (T_v) and the first cubic magnetocrystalline anisotropy constant isotropic point (T_k), and increases the recovery mechanism on warming from T_k (Section 6.5.4). The net affect of stress is to increase the memory ratio (*e.g.*, Kobayashi & Fuller, 1968; Heider *et al.*,

1992). The importance of stress has been directly tested by changing the residual stress with in a sample by either inducing dislocation by pressing (Heider *et al.*, 1992; Sahu, 1997) or removing them by annealing samples (Dunlop & Argyle, 1991). These studies have confirmed that the memory ratio is strongly dependent on the internal stress. Possible differences in internal stress of the hydrothermal samples of Heider *et al.* (1992) and this study, may contribute to the difference in the magnetic memory ratios (Figure 7.8).

Two other possible mechanisms for the difference in magnetic memory ratios, *i.e.*, grain interactions and differences in grain distribution, have been discussed in detail in Section 3.4.2, where it was suggested that grain interactions in the samples of Heider *et al.* (1992) reduce the coercive force, and differences in grain distributions (my hydrothermal samples have larger standard deviations) may contribute to the variation in coercive forces. Both grain interactions and variations in grain distribution will contribute to the difference in the measured magnetic memories of the hydrothermal samples of Heider *et al.* (1992) and this study (Figure 7.8).

The Dankers samples (*D(5-10 μm)–D(100-150 μm)*), although initially crushed had been heated in vacuum sealed capsules many times, and had been effectively annealed. In fact McClelland *et al.* (1995) have previously described the same samples as annealed. On comparison with unannealed samples in Figure 7.8, it is seen that *D(5-10 μm)–D(100-150 μm)* have lower memory ratios. However they are not as low as the memory ratios of the hydrothermal crystals (Table 7.1 and Figure 7.8). The difference between the annealed samples and hydrothermal samples reflects both variations in internal residual stress and in grain shape. The hydrothermal crystals generally have regular euhedral shapes (Figure 2.3), whilst crushed grains are irregular.

The high magnetic memory ratios for the Shetland magnetite series from Evaland beach, *i.e., E(150 μm)*, *E(190 μm) E(250 μm)* and *E(1.5 mm)*, indicates that the samples have internal stress in agreement with H_c and remanent coercive force (H_{rc}) results (Chapter 3), and low-temperature measurements (Chapter 6). Impurities in magnetite samples reduce the size of the anomalies in the controlling magnetic energies at T_v and T_k (Chapter 5), which effectively increases the memory ratio (Nagata *et al.*, 1964; Hartstra, 1982a). However impurities in the Shetland magnetites from Evaland beach (*E(150 μm)–E(1.5 mm)*) were smaller than the impurities in the Shetland magnetites from Pundy Geo, *i.e., PW(1 mm)–PW(3 mm)*, which have lower magnetic memories (*cf.* Tables 2.3 and 7.1). The high magnetic memories of the samples from Evaland beach (*E(150 μm)–E(1.5 mm)*) must be attributed to stress.

The Shetland magnetites from Pundy Geo, *i.e., PW(1 mm)–PW(3 mm)*, display relatively low magnetic memory ratios compared to the literature (Figure 7.8). This suggests that the samples had very low internal residual stress, in agreement with H_{rc} measurements reported for the same material (Figure 3.5). Spectral analysis of the Pundy Geo magnetites (Section 2.4) suggests significant impurities within the samples, which contradicts the hypothesis that impurities increase the magnetic memory (Hartstra, 1982a). How-

ever if the impurities are inhomogeneous, then this may explain the low magnetic memory. Özdemir *et al.* (1993) showed that surface oxidation effects the magnetic behaviour of magnetic grains on warming through T_v by inducing stress fields at the boundary between the magnetite and and surface maghemite, its significance decreasing with increasing grain size. For the large Pundy Geo magnetites (*PW(1 mm)–PW(3 mm)*), surface oxidation products may give rise to a spectral signal however they would not be expected to effect the behaviour of the main body domains. Main body domains situated in stoichiometric stress-free regions, will dominate the magnetic signal and have low magnetic memory.

The ARM memory results (Table 7.1) were a little erratic; generally ARM memory ratio $\geq$ SIRM memory ratio, but its relationship to TRM memory ratio is less clear. For Dankers magnetite samples, *D(5-10 μm)–D(100-150 μm)*, ARM memory ratio was consistently greater than TRM memory ratio, however for the hydrothermal magnetites and the Shetland samples the ARM memory ratio was on average smaller than the TRM memory ratio (Table 7.1). In general the relationship between the ARM, SIRM and TRM memory ratios for the hydrothermal and Shetland samples is uncertain, *e.g.*, consider the Shetland samples *PW(1 mm)* and *PW(3 mm)*, they have SIRM, ARM and TRM memory ratios of 17 %, 65 % and 67 %, and 6 %, 9 % and 53 % respectively.

As stated previously, reports of ARM memory results are limited, however Dunlop & Argyle (1991) found that for small PSD magnetites ARM memories induced in a field of 200 μT were similar to "moderate-field" (1 mT) TRM memories (Table 7.2).

grain size (μm)	$\frac{\text{ARM(200 }\mu\text{T)memory}}{\text{ARM(200 }\mu\text{T)}}$ %	$\frac{\text{TRM(50 }\mu\text{T)memory}}{\text{TRM(50 }\mu\text{T)}}$ %	$\frac{\text{TRM(1 mT)memory}}{\text{TRM(1 mT)}}$ %
0.215	68	77	66
0.39	48	57	49
0.54	35	48	40

Table 7.2: Low-temperature memory ratio of ARM, TRM(50 μT) and TRM(1 mT) for synthetic magnetites. After Dunlop & Argyle (1991).

The results of Dunlop & Argyle, suggest that ARM behaves in an intermediate manner between SIRM and weak-field TRM, *i.e.*, $H \leq 300$ μT (Chapter 4), and is similar to "high-field" thermoremanences ($H = 5\ mT$) investigated in Section 6.6.2. A similar relationship between TRM, ARM and SIRM memory (TRM memory ratio $>$ ARM memory ratio $>$ SIRM memory ratio) has been observed for small natural magnetites by Hartstra (1982a; 1983, Table 7.3), however he found that this relationship breaks down for the larger grain sizes, *i.e.*, $\geq$ 15-20 μm.

Experimental evidence suggests that in MD grains ARM is sometimes trapped in metastable TRM-like domain configurations and other times in less stable SIRM-like domain configurations depending on the nature of the samples. On the application of LTD treatment, this variation in domain state gives rise to a range of ARM memories.

It might be originally thought that the cause of the high ARM ratios for Dankers

grain size (μm)	$\frac{\text{SIRMmemory}}{\text{SIRM}}$ %	$\frac{\text{ARM(30 }\mu\text{T)memory}}{\text{ARM(30 }\mu\text{T)}}$ %	$\frac{\text{TRM(30 }\mu\text{T)memory}}{\text{TRM(30 }\mu\text{T)}}$ %
< 5	70	74	87
10–15	62	55	81
15–20	50	49	78
25–30	50	49	77
150–250	34	21	54

Table 7.3: Low-temperature memory ratio of SIRM, ARM(30 μT) and TRM(30 μT) for a natural magnetite with ≈ 5 % impurity. The main impurities are MgO and Al_2O_3. After Hartstra (1983).

samples, *i.e., D(5-10 μm)–D(100-150 μm)*, compared to the hydrothermal samples is due to the increased stress within the samples, however the Shetland magnetites from Pundy Geo *E(150 μm)–E(1.5 mm)*, have relatively high internal stress yet their ARM memory ratios are small compared to the Dankers magnetites (Table 7.1). A possible explanation for the variation in ARM memory is grain size; the effect of stress maybe particularly enhanced in smaller MD grains, *cf.* samples *D(20-25 μm)* and *D(75-100 μm)* in Table 7.1. The larger grains, *i.e., E(150 μm)–E(1.5 mm)*have a greater ability to shield the stress-controlled regions, whereas the smaller grains (*D(5-10 μm)–D(100-150 μm)*) do not, giving rise to larger ARM memories.

Results of the measurement of memory ratios of three different thermoremanences ($pTRM^{T_c}_{560}$, $pTRM^{T_c}_{500}$ and $pTRM^{500}_{rtp}$) induced in a field of 100 μT in the magnetite samples are shown in Table 7.1. From the memory ratios alone there is no obvious pattern to the behaviour of thermoremanences. It is necessary to consider the low-temperature results in Chapter 6 as well. Note the memory ratios were not calculated in Chapter 6, because of errors with the residual field in the MPMS sample chamber.

The size of pTRM memory ratio reflects the stability of the initial remanence, and the availability of metastable LEM states during acquisition. In the discussion in Chapter 6, it was concluded that smaller grains acquire metastable domain configurations at higher temperatures, and that stress increases the temperature at which high metastable remanence is were acquired. The larger, low-stress grains acquire more metastable remanences at lower temperatures, *i.e.,* pTRM memory ratio increases as the temperature at the remanence is acquired decreased. Consider initially $pTRM^{T_c}_{T_2}$ type remanences: for $pTRM^{T_c}_{560}$ and $pTRM^{T_c}_{500}$, it should be expected that smaller grains or more stressed grains have more stable pTRM and higher pTRM memory ratios than the larger stress-free grains. This is found to be the case; the grain size effect is demonstrated in the Dankers samples, where there is a gradual decrease in $pTRM^{T_c}_{560}$ memory ratio with grain size, *i.e., D(15-20 μm) $>$ D(20-25 μm) $>$ D(25-30 μm) $>$ D(75-100 μm)*. The effect of stress is demonstrated by the considering the natural Shetland samples from Evaland beach *E(150 μm)–E(190 μm)*, where the $pTRM^{T_c}_{560}$ and $pTRM^{T_c}_{500}$ memory ratios $>$ $pTRM^{500}_{rtp}$ memory ratio. Whereas, for the low-stress hydrothermal and annealed magnetites there is a shift in the relationship between $pTRM^{T_c}_{560}$ and $pTRM^{T_c}_{500}$ memory ratios and the $pTRM^{500}_{rtp}$ memory ratio, *i.e.,* the $pTRM^{500}_{rtp}$ memory ratio is approximately the same as or larger than the $pTRM^{T_c}_{560}$ and $pTRM^{T_c}_{500}$ memory ratios

(Table 7.1).

These conclusions are in broad agreement with those from the only other similar study by Shcherbakova *et al.* (1996, Table 7.4). Shcherbakova *et al.* (1996) found that the memory fraction is associated with certain temperature ranges, and the metastable states for large MD grains are acquired at slightly higher temperatures than for PSD grains. They also found that stress and impurities increases the magnetic memory.

sample	origin	character	TRM %	$pTRM^{550}_{500}$ %	$pTRM^{500}_{450}$ %	$pTRM^{300}_{rtp}$ %
mt	synthetic	MD 16-60 μm	28	30	51	31
15b	granodiorite	MD	40	42	55.6	28.5
6b	dolerite	PSD	80	83.5	84	39
7b	dolerite	PSD	87	90	90	56.9
3c4	dolerite	PSD	77	97	80	49
2f	dolerite	PSD	88	84	85	56

Table 7.4: Low-temperature memory ratio of TRM and several pTRMs for one synthetic magnetite and several natural magnetites. The inducing field is not stated. After Shcherbakova *et al.* (1996).

There are a few exceptions to these general rules (Table 7.1). AF demagnetisation curves of these same memories are considered in Section 7.3.3, where this problem is examined further.

7.3.3 AF demagnetisation of initial remanence and its magnetic memory

To further understand the demagnetisation processes during LTD treatment, and to characterise the memory fraction of remanence, it has become standard practice to either examine the coercive force spectrum of memory by AF demagnetisation (Heider *et al.*, 1992; McClelland & Shcherbakov, 1995) or the unblocking spectrum by continuous (Shcherbakova *et al.*, 1996) or step-wise (Dunlop & Argyle, 1991) thermal demagnetisation (Section 1.8.2).

Previous studies have shown that the memory fraction is magnetically harder than the initial remanence (Heider *et al.*, 1992; McClelland & Shcherbakov, 1995, and Figure 7.9). This reflects the conclusions made Chapter 6, where it is postulated that the magnetic memory is associated with hard metastable domain structures and stressed grains. In Figure 7.9 it can be seen that both SIRM and SIRM memory are magnetically less stable than TRM and TRM memory, which indicates the intrinsically hard nature of TRM remanence.

In this comparative study, all the initial remanences and their memories presented in Section 7.3.2 were AF demagnetised, however only a few of remanences and memories were thermally demagnetised. The AF demagnetisation results are shown in this section, the thermal demagnetisation curves in Section 7.3.4.

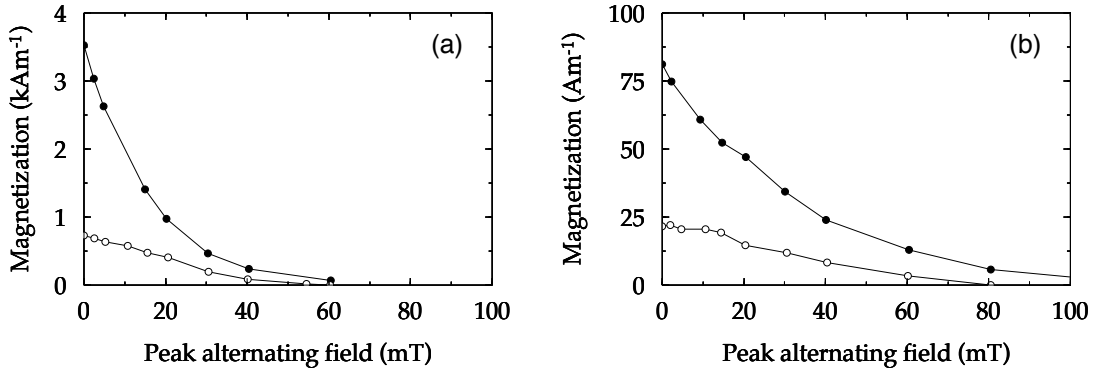


Figure 7.9: AF demagnetisation of a) SIRM and SIRM memory and b) 100 μT TRM and its memory induced in 20 μm hydrothermally grown magnetite. After Heider *et al.* (1992).

Results from AF demagnetisation

The AF demagnetisation curves were measured in Oxford using palaeomagnetic equipment described in Section 1.8. To measure the AF demagnetisation curves for both the initial remanence and its memory, it was necessary to induce the initial remanence twice, *i.e.,* induce the remanence, measure the AF demagnetisation curve, induce the remanence again, apply LTD treatment and measure the AF demagnetisation curve of the memory. The maximum applied AF demagnetisation field was 100 mT.

Typical AF demagnetisation curves and corresponding coercive force spectra are shown for; hydrothermal magnetite sample *H(3.0 μm)* in Figure 7.10, Dankers magnetite sample *D(15-20 μm)* Figure 7.11 and natural sample *E(190 μm)* Figure 7.12.

For all the AF demagnetisation curves (Figures 7.10–7.12), the initial remanence is more easily demagnetised than its memory until some AF demagnetisation field is reached (AF_{crit}) where the two AF demagnetisation curves become almost identical. Similar contrasts between initial remanences and memory have been reported previously (*e.g.,* Ozima *et al.*, 1964a; Parry, 1979; 1980; Dunlop & Argyle, 1991; Heider *et al.*, 1992; McClelland & Shcherbakov, 1995). This relationship is reflected in the coercive force spectra, where the memory has a higher coercive force spectrum than the initial remanence, *i.e.,* the memory is magnetically harder than initial remanence.

There are variations between the AF demagnetisation curves for various initial remanences, in agreement with previous studies (Heider *et al.*, 1992; McClelland & Shcherbakov, 1995). For example, consider sample *H(3.0 μm)* (Figure 7.10), the AF demagnetisation curves and the corresponding coercive force spectra for initial SIRM (Figure 7.10a and 7.10b) and $pTRM^{T_c}_{500}$ (Figure 7.10i and 7.10j) the SIRM is more susceptible to demagnetisation by small AF fields than $pTRM^{T_c}_{500}$, *i.e.,* $pTRM^{T_c}_{500}$ is magnetically harder than SIRM.

The AF demagnetisation curves for the natural sample *E(190 μm)* and the hydrothermal sample *H(3.0 μm)* are closer in appearance than the Dankers sample *D(15-20 μm)* (Figures 7.10–7.12). The shape of demagnetisation curves for magnetic memory is dependent

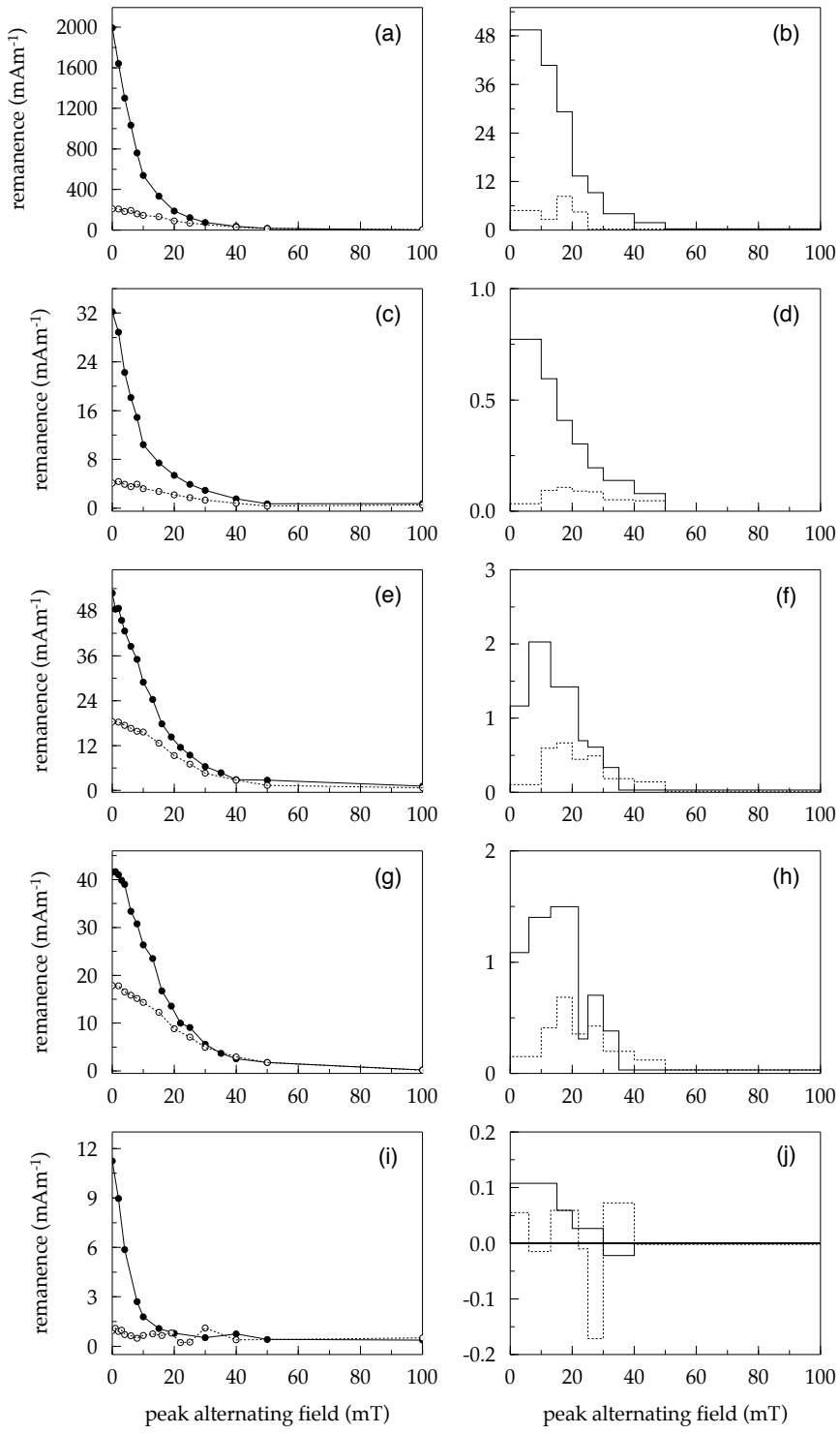


Figure 7.10: AF demagnetisation curves and corresponding coercive force spectrum for five different initial remanences (●, —) and their memories (○, - -) for the hydrothermal sample *H(3.0 μm)*. a) + b) SIRM, c) + d) ARM e) + f) TRM, g) + h) $pTRM^{Tc}_{500}$ and i) + j) $pTRM^{500}_{rtp}$. The maximum applied AF demagnetisation field was 100 mT. The thermoremanences were induced in a field of 100 μT and the ARM in a DC field of 180 μT. The volume of the samples used in the calculation of the remanence intensity is the volume of the pellet, *i.e.,* magnetite crystals plus KBr. The volume was taken to be 1 cm^3.

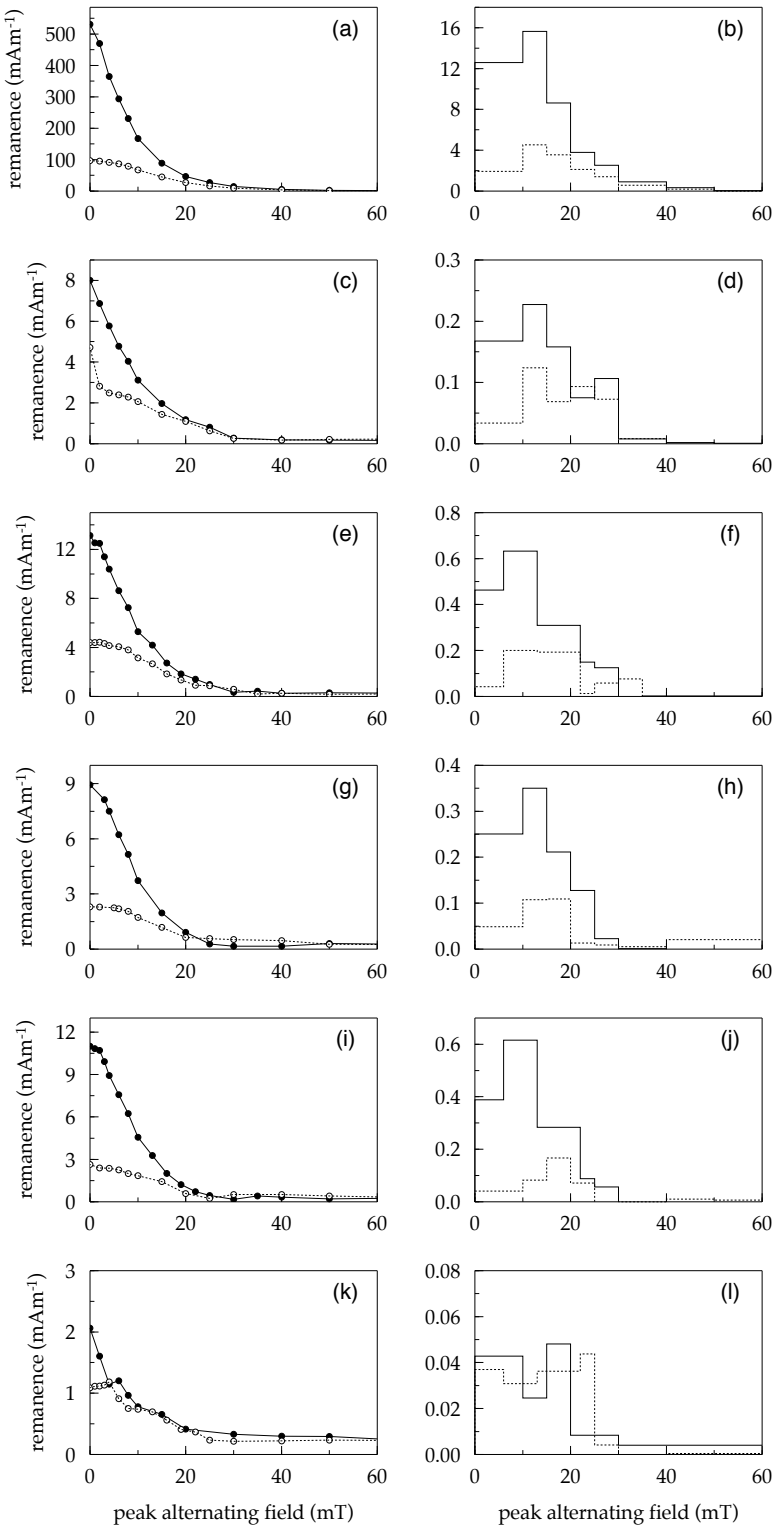


Figure 7.11: AF demagnetisation curves and corresponding coercive force spectrum for six different initial remanences (•, —) and their memories (○, - -) for my Dankers sample *D(15-20 μm)*. a) + b) SIRM, c) + d) ARM e) + f) TRM, g) + h) $pTRM^{T_c}_{560}$, i) + j) $pTRM^{T_c}_{500}$ k) and l) $pTRM^{500}_{rtp}$. The maximum applied AF demagnetisation field was 100 mT. The thermoremanences were induced in a field of 100 μT and the ARM in a DC field of 180 μT. The volume of the samples used in the calculation of the remanence intensity is the volume of the pellet, *i.e.,* magnetite crystals plus KBr. The volume was taken to be 1 cm^3.

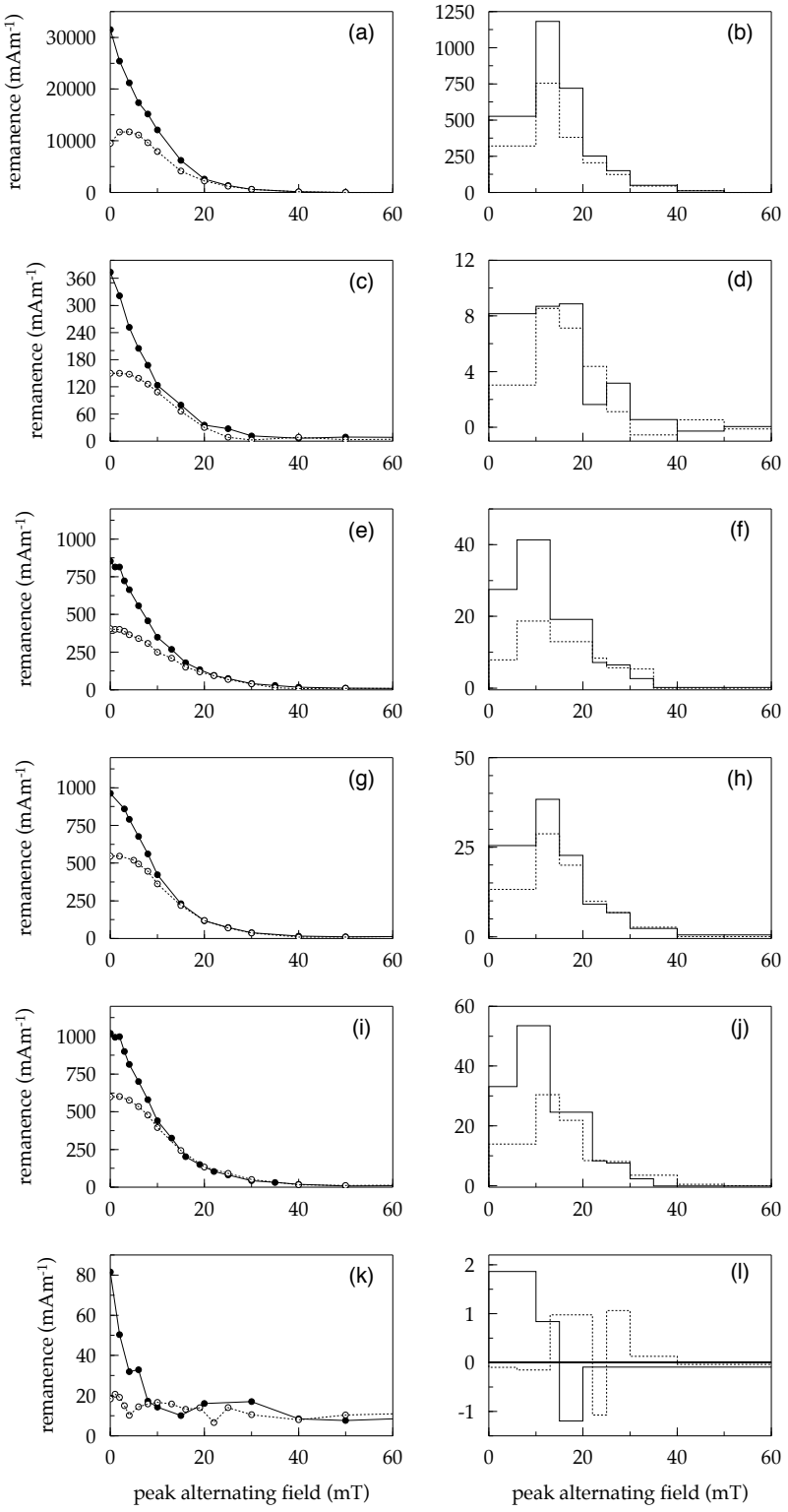


Figure 7.12: AF demagnetisation curves and corresponding coercive force spectrum for six different initial remanences (●, —) and their memories (○, - -) for the natural Shetland sample *E(190 μm)*. a) + b) SIRM, c) + d) ARM e) + f) TRM, g) + h) $pTRM^{T_c}_{560}$, i) + j) $pTRM^{T_c}_{500}$ k) and l) $pTRM^{500}_{rtp}$. The maximum applied AF demagnetisation field was 100 mT. The thermoremanences were induced in a field of 100 μT and the ARM in a DC field of 180 μT. The volume of the samples used in the calculation of the remanence intensity is the volume of the pellet, *i.e.,* magnetite crystals plus KBr. The volume was taken to be 1 cm^3.

on the memory ratio, *i.e.,* if memory ratio is large then the AF demagnetisation curve is closer to the initial remanence demagnetisation curve in appearance than the when the ratio is small (*cf.* Figures 7.10a and 7.10g). However it should be noted that the value of AF_{crit} is *not* dependent on initial memory ratio. For example, consider sample *E(190 μm)*; AF_{crit} = 22 mT for SIRM with a memory ratio of 29 % (Figure 7.12a), and for $pTRM^{500}_{rtp}$ with a memory ratio of 22 %, AF_{crit} = 10 mT (Figure 7.12k).

The AF demagnetisation curves for the Dankers sample *D(75-100 μm)* which display reversal after LTD treatment (Table 7.1), are shown in Figure 7.13.

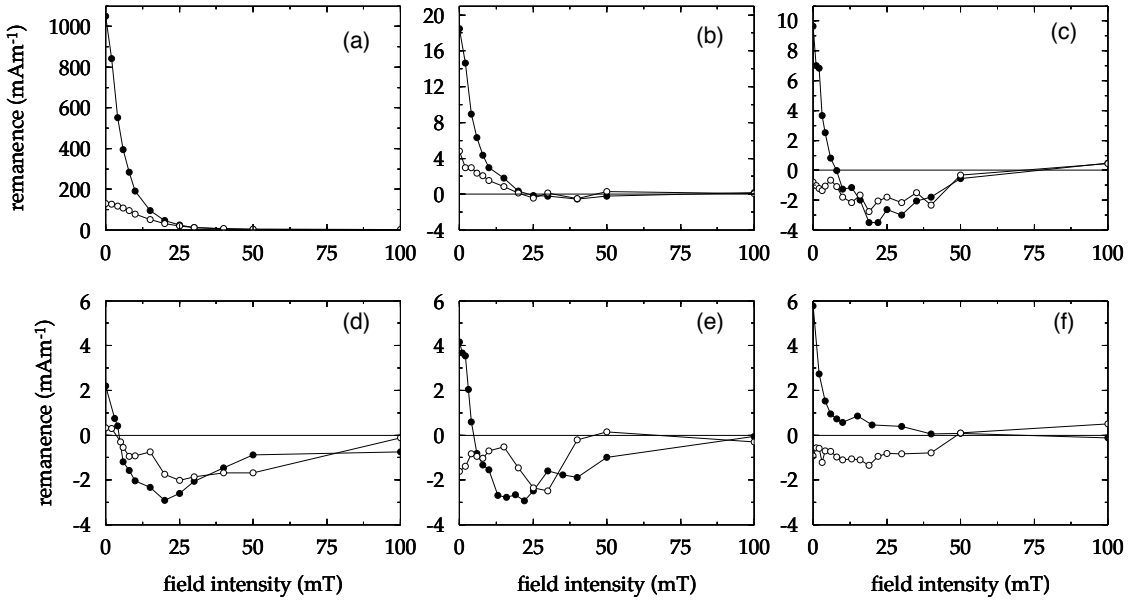


Figure 7.13: AF demagnetisation curves for six different initial remanences (•) and their memories (○) for my Dankers sample *D(75-100 μm)*. a) SIRM, b) ARM c) TRM, d) $pTRM^{T_c}_{560}$, e) $pTRM^{T_c}_{500}$ and f) $pTRM^{500}_{rtp}$. Note, the memory is corrected for its rotation from the initial remanence's orientation, making the memory ratio in this figure lower than the memory ratio given in Table 7.1. The thermoremanences were induced in a field of 100 μT and the ARM in a DC field of 180 μT. The volume of the samples used in the calculation of the remanence intensity is the volume of the pellet, *i.e.,* magnetite crystals plus KBr. The volume was taken to be 1 cm^3.

The AF demagnetisation curves for the *D(75-100 μm)* sample (Figure 7.13), are different to typical AF demagnetisation curves (Figures 7.10–7.12). This is due to the reversed component within the sample, previously observed for several of the Dankers samples' memory ratios (Table 7.1). These AF demagnetisation curves are consistent with almost identical experiments carried out on the same material (though not the same sample), by McClelland & Shcherbakov (1995). For example, compare my AF demagnetisation curves for 100 μT TRM and its memory induced in *D(75-100 μm)* (Figure 7.13c), with AF demagnetisation curves published by McClelland & Shcherbakov (1995) for the same material induced with a 50 μT TRM (Figure 7.14).

The 100 μT TRM induced in *D(75-100 μm)* (Figure 7.13c) has a relatively smaller reversed component than McClelland & Shcherbakov (1995) found for the same material

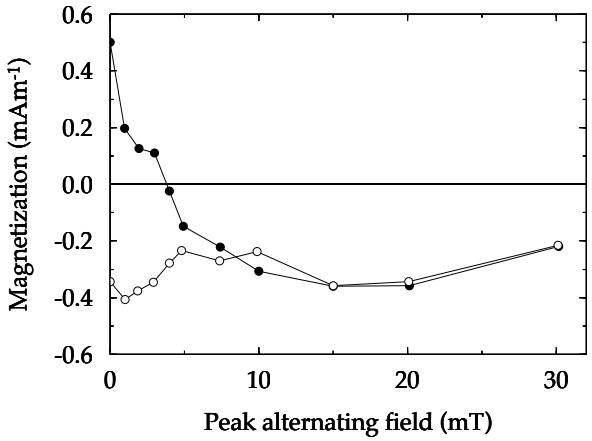


Figure 7.14: AF demagnetisation curves for 50 μT TRM (•) and 50 μT TRM memory (○) induced in same Dankers material as *D(75-100 μm)* was made from. After McClelland & Shcherbakov (1995).

induced with a 50 μT TRM (Figure 7.14). This is probably due to the difference in field. The SIRM induced in a much larger field displays no reversed fraction. ARM and ARM memory (Figure 7.13b) display no reversed component, whereas TRM and its memory does (Figure 7.13c). This again shows the unsuitability of replacing ARM by TRM in palaeointensity experiments (Banerjee & Mellema, 1974b; 1974a).

The behaviour of the thermoremanences are particularly revealing (Figures 7.13c–7.13f). $\mathrm{pTRM}^{\mathrm{T_c}}_{560}$ (Figure 7.13d) is the only thermoremanence not to have a negative memory ratio (Table 7.1), however during AF demagnetisation both the initial remanence and its memory reverse. The initial $\mathrm{pTRM}^{500}_{\mathrm{rtp}}$ remanence does not display any reversed component during AF demagnetisation (Figure 7.13f). It appears that the reversed component is associated with both the initial thermoremanence acquired at high temperatures and the memory fraction. Both high temperature pTRM and memory are attributed with high coercive forces (Heider *et al.*, 1992; McClelland & Shcherbakov, 1995, see Figures 7.10–7.12). It is appropriate to associate the reversed component in the Dankers sample *D(75-100 μm)*, with the high coercive fraction of thermoremanence.

The reversed component of both the remanence and its memory is intrinsic to the Dankers samples, as the reversed component has not been observed for studies on other magnetite samples, *e.g.*, hydrothermal samples *H(3.0 μm)–H(108 μm)*, Shetland samples (*E(150 μm)–E(1.5 mm)*), and other published data (Parry, 1979; Parry, 1980; Dunlop & Argyle, 1991; Heider *et al.*, 1992; McClelland & Shcherbakov, 1995). The reversed component of the Dankers samples is discussed in greater detail in Section 7.3.6.

It is standard to summarise AF demagnetisation curves using the parameter "median destructive field" (MDF (sometimes expressed as $H_{\frac{1}{2}}$)) (*e.g.*, Dankers & Sugiura, 1981; Hartstra, 1982b). MDF is the AF demagnetisation field taken to demagnetise half of the initial remanence, and is an indicator of magnetic hardness.

MDF values for the initial remanences and their memories are shown in the Figures 7.15–7.20. There are a few MDF results missing due to three reasons; firstly the

tendency of the vacuum sealed quartz capsules (Chapter 2) to implode during heating, secondly the repeated tumbling during AF demagnetisation caused a few of the samples to become dislodged from their mount within the quartz capsules (Chapter 2), rendering them useless for further AF demagnetisation examination. The large single crystals, *i.e.*, *E(1.5 mm)* and *PW(1 mm)-PW(3 mm)*, were particularly prone to this. Thirdly self-reversal of the larger Dankers samples makes the calculation of MDF rather meaningless. The results from *D(75-100 μm)* and *D(100-150 μm)* are not considered

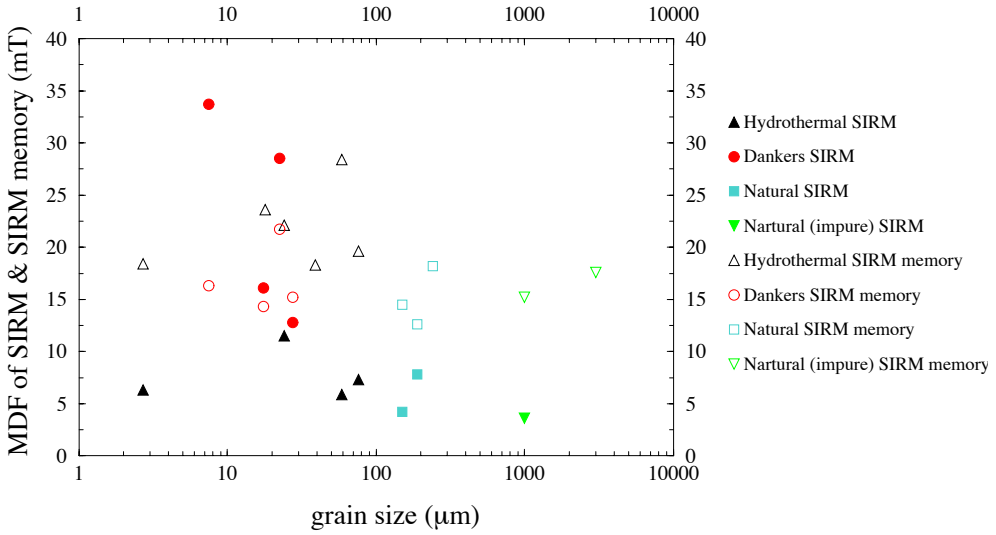


Figure 7.15: Median destructive field of SIRM (closed symbol, *e.g.*, ●) and SIRM memory (open symbol, *e.g.*, ○) for all my samples, plotted as a function of grain size. Natural = Evaland beach samples (*E(150 μm)–E(1.5 mm)*) and Natural (impure) = Pundy Geo magnetites.

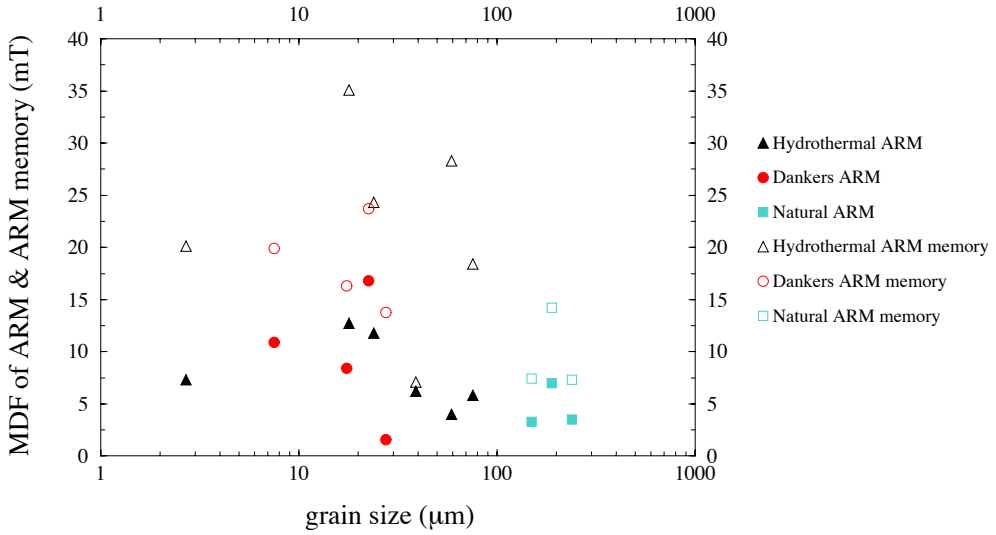


Figure 7.16: Median destructive field of 180 μT ARM (closed symbol, *e.g.*, ●) and 180 μT ARM memory (open symbol, *e.g.*, ○) for my samples, plotted as a function of grain size. Natural = Evaland beach samples (*E(150 μm)–E(1.5 mm)*) and Natural (impure) = Pundy Geo magnetites.

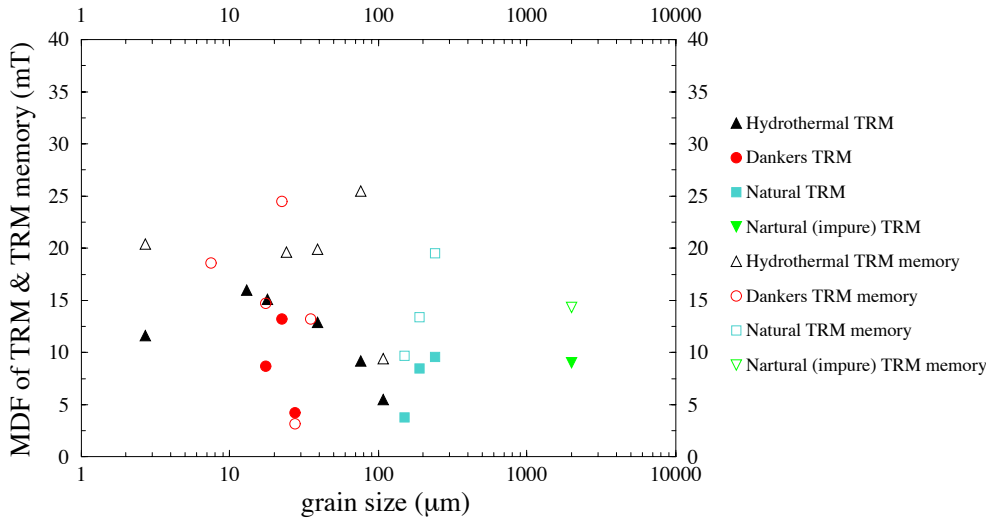


Figure 7.17: Median destructive field of 100 μT TRM (closed symbol, *e.g.*, ●) and 180 μT TRM memory (open symbol, *e.g.*, ○) for my samples, plotted as a function of grain size. Natural = Evaland beach samples (*E(150 μm)–E(1.5 mm)*) and Natural (impure) = Pundy Geo magnetites.

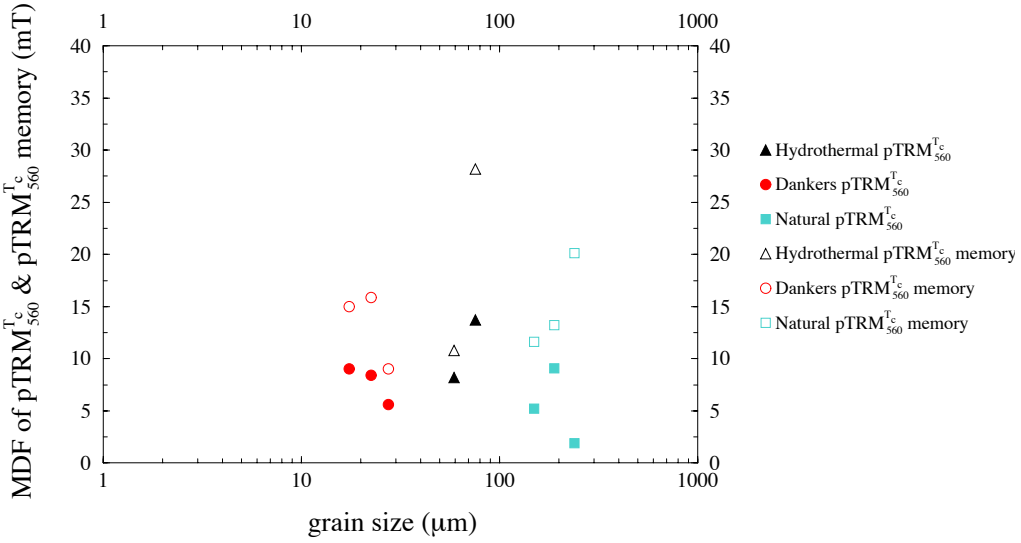


Figure 7.18: Median destructive field of 100 μT pTRM$^{T_c}_{560}$ (closed symbol, *e.g.*, ●) and 100 μT pTRM$^{T_c}_{560}$ memory (open symbol, *e.g.*, ○) for my samples, plotted as a function of grain size. Natural = Evaland beach samples (*E(150 μm)–E(1.5 mm)*) and Natural (impure) = Pundy Geo magnetites.

For all the MDF versus grains size plots (Figures7.15–7.20), there is a large scatter in the data, however there is only a slight decrease in MDF for both the initial remanence and the memory with grain size, in agreement with previous studies (Heider *et al.*, 1992). In a crude approximation: ignoring this slight grain size dependency, the average MDF for each remanence shown in the figures are summarised in Table 7.5.

Both the SIRM and ARM memories MDF values are on average twice as large as the original remanences (Figures 7.15 and 7.16 respectively and Table 7.5), however there is a greater variability in the ARM and ARM memory MDF results. This larger scatter makes

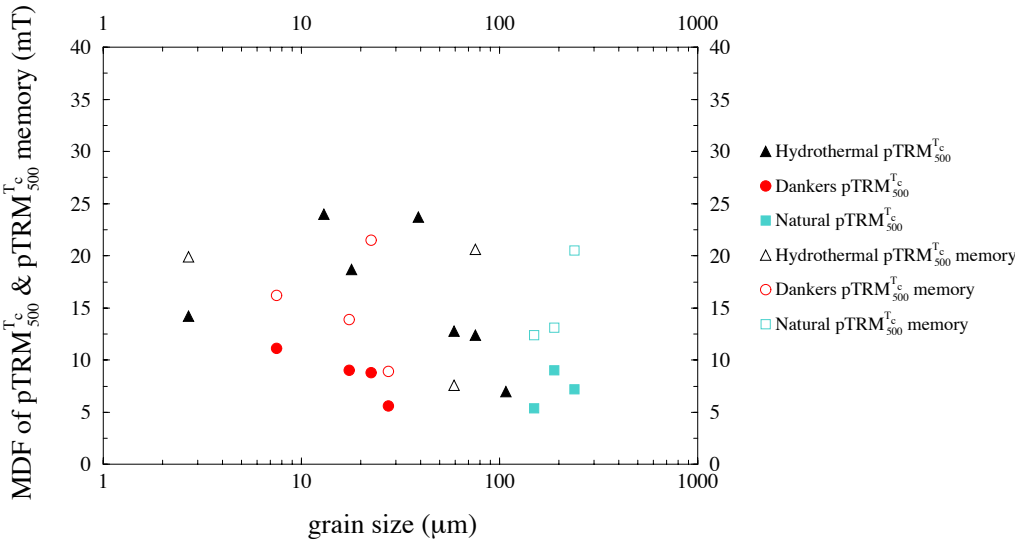


Figure 7.19: Median destructive field of 100 μT pTRM$^{T_c}_{500}$ (closed symbol, *e.g.*, ●) and 100 μT pTRM$^{T_c}_{500}$ memory (open symbol, *e.g.*, ○) for all my samples, plotted as a function of grain size. Natural = Evaland beach samples (*E(150 μm)–E(1.5 mm)*) and Natural (impure) = Pundy Geo magnetites.

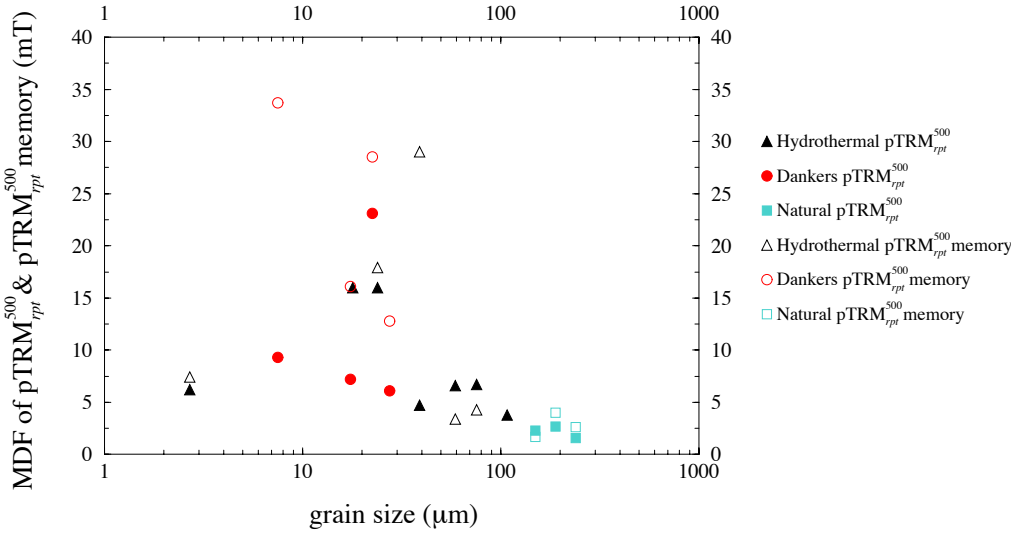


Figure 7.20: Median destructive field of 100 μT pTRM$^{500}_{rtp}$ (closed symbol, *e.g.*, ●) and 100 μT pTRM$^{500}_{rtp}$ memory (open symbol, *e.g.*, ○) for all my samples, plotted as a function of grain size. Natural = Evaland beach samples (*E(150 μm)–E(1.5 mm)*) and Natural (impure) = Pundy Geo magnetites.

the difference between the initial ARM and ARM memory less clear (Figure 7.16).

MDF values for SIRM and SIRM memory plotted as a function of grain size (Figure 7.15 and Table 7.6) are in agreement with similar results published by Heider *et al.* (1992). Heider *et al.* (1992) noted the consistency of SIRM MDF and SIRM memory MDF over several decades of grain size (Table 7.6).

There is little difference between the various types of samples for SIRM and SIRM memory MDF values (Table 7.5). SIRM and SIRM memory of the hydrothermal samples are fractionally harder compared to the other samples, *i.e.*, the hydrothermal samples have

samples	average MDF (mT)											
	S	S_{mem}	A	A_{mem}	T	T_{mem}	P1	$P1_{mem}$	P2	$P2_{mem}$	P3	$P3_{mem}$
Hydrothermal	8	22	8	22	12	19	11	20	16	16	9	12
Dankers	6	17	9	18	9	15	8	13	9	15	11	23
Natural	5	16	5	10	8	14	5	14	7	15	2	3
All samples	7	18	8	18	10	16	8	15	12	15	8	13

Table 7.5: Average MDF for different initial remanences and their memories. These averages ignore the slight grain size dependency of MDF observed in Figures 7.15– 7.20. S = SIRM, A = ARM, T =TRM, P1 = $pTRM^{Tc}_{560}$, P2 = $pTRM^{Tc}_{500}$ and P3 = $pTRM^{500}_{rtp}$, and the suffix $_{mem}$, signifies the memory of the remanence, *e.g.*, S_{mem} = the memory of SIRM. The thermoremanences were induced in a field of 100 μT and the ARM 180 μT.

study	sample description	MDF range (mT)	
		SIRM	SIRM memory
This study	PSD & MD hydrothermal, annealed & natural	6–12	12–28
Dunlop & Argyle (1991)	sub-micron synthetic	10–14	17–22
Heider *et al.* (1992)	PSD & MD synthetic	6–13	14–27

Table 7.6: MDF range for SIRM and SIRM memory for all my samples (hydrothermally grown magnetites, Dankers magnetites and natural magnetites) compared to previous studies.

larger MDF values, but not significantly so.

For ARM, there is a marked contrast in memory MDF for the different samples. The natural magnetites have an average MDF of only 10 mT whilst the hydrothermal crystals have on average MDF values of 22 mT. This difference may reflect a mistake in ignoring the small grain size dependency, because the natural magnetites are > 100 μm whilst the hydrothermal crystals are mostly < 100 μm.

Thermoremanence memories are more resistant to AF demagnetisation than the initial thermoremanences (Figures 7.17–7.20, and Table 7.5). However the contrast is less marked for thermoremanence than for SIRM or ARM because there is a large scatter (Figures 7.15–7.16). This scatter reflects the hardness of both initial thermoremanence and its memory (Table 7.5).

MDF values for TRM and TRM memory plotted as a function of grain size (Figure 7.17) are in rough agreement with similar results published by Heider *et al.* (1992).

Except for $pTRM^{500}_{rtp}$ the hydrothermal crystals display higher MDF values for thermoremanences and thermoremanence memory than the Dankers samples (Table 7.5). For the Dankers samples $pTRM^{500}_{rtp}$ has the highest MDF value of all the thermoremanences, whereas for the hydrothermal and natural samples $pTRM^{500}_{rtp}$ is the weakest (Figures 7.17–7.20, and Table 7.5)

Lowrie–Fuller Test: Comparison of AF demagnetisation curves for SIRM, ARM and TRM and their memories

Lowrie & Fuller (1971) proposed a test (commonly termed the Lowrie–Fuller test) based on AF demagnetisation curves which separate SD and PSD carriers of remanence from

MD carriers. It can be directly applied to natural remanent magnetisation (NRM) of TRM origin. The method is quick, and makes it possible to select suitable igneous rocks for further study. The Lowrie–Fuller test is based on an experimental observation that normalised AF demagnetisation curves of weak-field NRM or TRM, and high-field TRM have a different relationship for SD and PSD grains than for large MD grains of magnetite. Weak-field ARMs and SIRMs have been proposed as substitutes for weak-field TRM and high-field TRM respectively. In large MD grains, SIRM requires larger destructive fields than weak-field TRM, *i.e.,* for MD magnetite MDF is larger for SIRM than TRM. In PSD and SD grains the opposite is true. The changeover between PSD and MD grains is usually found to be in the region of 10–15 μm for magnetite (Dunlop & Özdemir, 1997).

However Heider *et al.* (1992) found a different relationship for hydrothermal magnetites, that is MDF of TRM $>$ MDF of SIRM for MD hydrothermal magnetites up to ≈ 200 μm. Heider *et al.* attributed this difference between their data and previous data (*e.g.,* Lowrie & Fuller, 1971; Johnson *et al.*, 1975; Bailey & Dunlop, 1983) to the lack of stressed regions in their crystals. This lead to a theoretical paper by Xu & Dunlop (1995), which concluded that the changes in the relationship between the microcoercive force and screening can lead to opposite Lowrie–Fuller test results, *i.e.,* MDF of TRM $>$ MDF of SIRM for low-stress MD magnetite. However, Dunlop & Özdemir (1997) point out that in natural samples, internal stress levels as low as those in the hydrothermal samples of Heider *et al.* (1992) are unlikely, making the Lowrie–Fuller test a useful grain-size discriminatory as long as the results are treated with caution.

As my hydrothermal crystals were produced using the same method (Heider & Bryndzia, 1987) as the samples studied in Heider *et al.* (1992), the results of Heider *et al.* are checked by plotting the MDF ratio $\mathrm{MDF_{TRM}}/\mathrm{MDF_{SIRM}}$ (Figure 7.21). Also plotted are the MDF ratios of memory, *i.e.,* $\mathrm{MDF^{M}_{TRM}}/\mathrm{MDF^{M}_{SIRM}}$(Figure 7.21), where $\mathrm{MDF^{M}_{TRM}}$ is MDF for TRM memory *etc.*

To investigate the suitability of using ARM as a substitute for weak-field TRM, the MDF ratios $\mathrm{MDF_{ARM}}/\mathrm{MDF_{SIRM}}$ and $\mathrm{MDF^{M}_{ARM}}/\mathrm{MDF^{M}_{SIRM}}$ are plotted in Figure 7.22.

In the largest hydrothermal magnetite, *i.e., H(76 μm)*, the $\mathrm{MDF_{TRM}}/\mathrm{MDF_{SIRM}}$ ratio is greater than one (Figure 7.21), in agreement with Heider *et al.* (1992). The natural sample *E(190 μm)*, which is thought to have a relatively high stress content (Chapter 1), also displays a $\mathrm{MDF_{TRM}}/\mathrm{MDF_{SIRM}}$ ratio greater than one. The $\mathrm{MDF_{ARM}}/\mathrm{MDF_{SIRM}}$ ratios for the larger grains are all less than one (Figure 7.22), suggesting that substituting ARM for TRM is a more effective at distinguishing between MD and PSD and SD. Alarmingly, however, it demonstrates the mistake occasionally made in the literature that ARM and TRM are similar.

The $\mathrm{MDF^{M}_{TRM}}/\mathrm{MDF^{M}_{SIRM}}$ ratio is on average slightly greater than one. This suggests that TRM memory is SD-like (Figure 7.21), whereas the $\mathrm{MDF^{M}_{ARM}}/\mathrm{MDF^{M}_{SIRM}}$ ratio for larger grains suggests that the memory is MD-like, *i.e.,* the ratio is less than one (Figure 7.22).

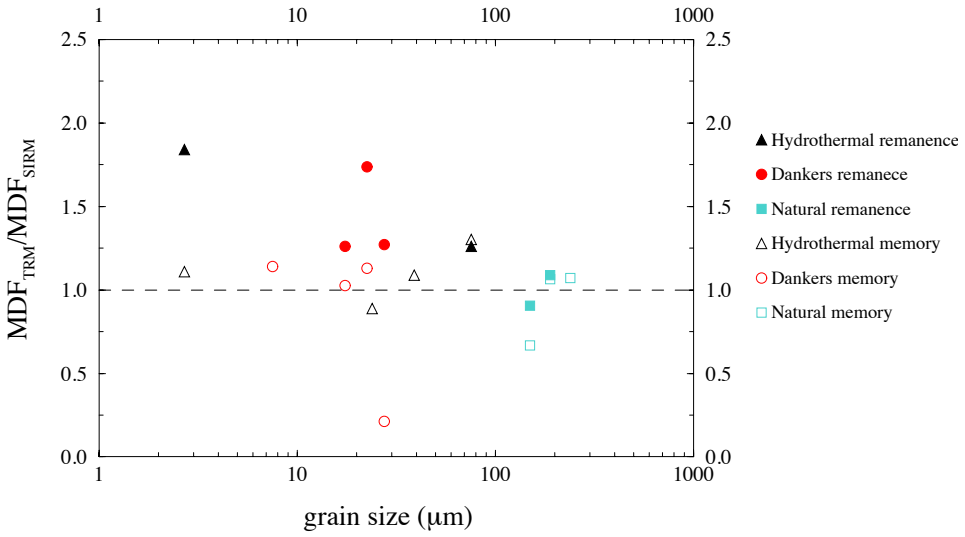


Figure 7.21: The result of the Lowrie–Fuller test expressed as the ratio median destructive fields of 100μT TRM (MDF_{TRM}) and SIRM (MDF_{SIRM}) and their corresponding memories after LTD treatment, *i.e.*, $MDF^{M}_{TRM}$and MDF^{M}_{SIRM}, plotted as a function of grain size for a selection of my samples.

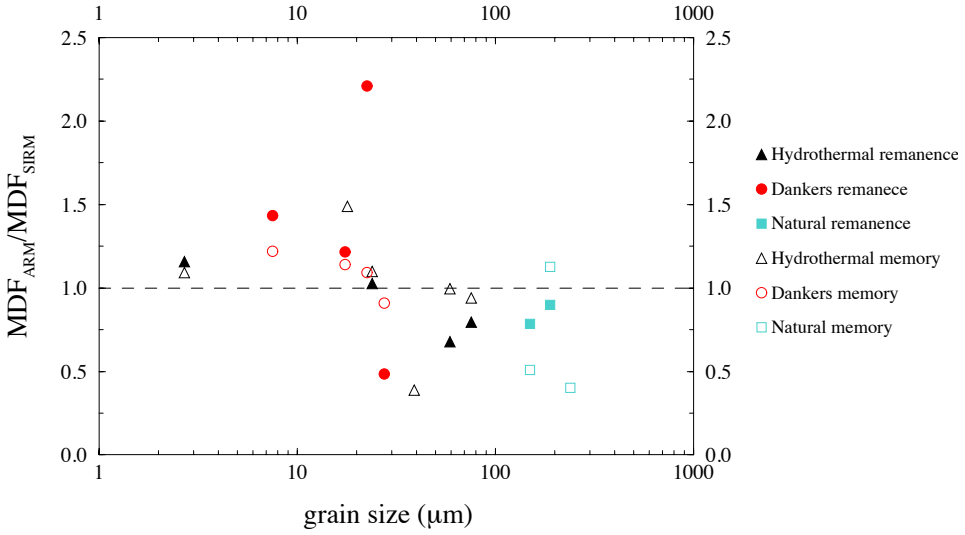


Figure 7.22: The result of the Lowrie–Fuller test expressed as the ratio median destructive fields of 180μT ARM (MDF_{ARM}) and SIRM (MDF_{SIRM}) and their corresponding memories after LTD treatment, *i.e.*, $MDF^{M}_{ARM}$and MDF^{M}_{SIRM}, plotted as a function of grain size for a selection of my samples.

As far as the Lowrie–Fuller test is concerned, the results in this section are inconclusive. Depending on whether TRM or ARM is examined the test gives different results; for large grains TRM results suggest that the remanence is SD-like, whereas ARM results suggest that the remanence is MD-like. Similar conclusions are drawn for the memories.

7.3.4 Thermal demagnetisation of initial remanence and its magnetic memory

Thermal demagnetisation allows the unblocking spectra of remanence to be examined (Section 1.8.2).

There are two separate thermal demagnetisation experiments described in this section; firstly step-wise thermal demagnetisation measured in Oxford using standard palaeomagnetic equipment (Section 1.8), and secondly continuous demagnetisation of high-field thermoremanence memory measured using a Princeton Electronics μ-VSM (Vibrating Sample Magnetometer) at the Institute for Rock Magnetism (I.R.M.), University of Minnesota. In step-wise thermal demagnetisation all the measurements are performed at room temperature, *i.e.,* the sample is heated to a given temperature, cooled and measured at room temperature, the sample is then heated to higher temperature *etc.* Continuous thermal demagnetisation differs in that the magnetisation is actually measured at high temperatures. Obviously the temperature dependence of the spontaneous magnetisation and changes in the domain structure during heating and cooling (see Chapter 4) can give very different results for continuous and step-wise demagnetisation.

The step wise thermal demagnetisation will be considered first.

Step-wise thermal demagnetisation of TRM and TRM memory

In a similar sequence of experiments to those described for AF demagnetisation, step-wise thermal demagnetisation curves for TRM and TRM memory were measured for a selection of samples: hydrothermal magnetite, Dankers magnetite and natural magnetite.

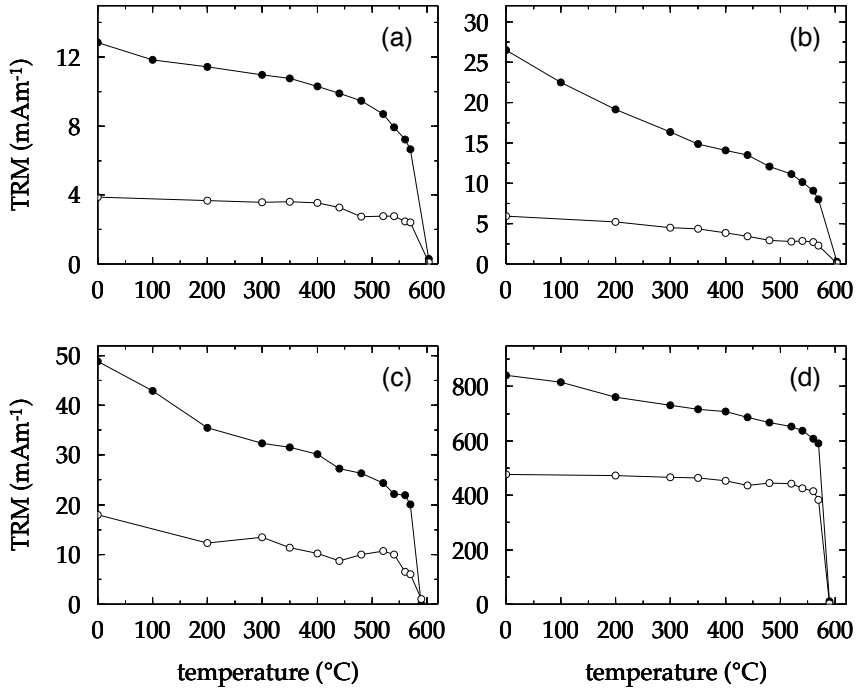


Figure 7.23: Step-wise thermal demagnetisation curves for 100 μT TRM (•) and 100 μT TRM memory (○) induced in Dankers magnetite samples a) *D(15-20 μm)* and b) *D(25-30 μm)*, c) hydrothermal sample *H(76 μm)* and d) natural Shetland magnetite *E(190 μm)*.

Typical results are shown in Figure 7.23, where it be seen that both 100 μT TRM

and 100 μT TRM memory have high unblocking spectrum, *i.e.,* they are magnetically hard, (Figure 7.23).

Both grain size and stress effect the unblocking spectra of the initial remanences; the smaller Dankers sample *D(15-20 μm)* has a higher unblocking spectrum than the larger *D(25-30 μm)* sample (*cf.* Figures 7.23a and 7.23b), and the stressed natural sample *E(190 μm)* (Figure 7.23d) has a higher unblocking spectra than the low-stress hydrothermal sample *H(76 μm)* (Figure 7.23c). The effect of grain size and stress on the unblocking spectra are well documented (Nagata, 1961; Dunlop & Özdemir, 1997).

All the TRM memories are more resistant to thermal demagnetisation than their corresponding initial remanence. However the TRM memory thermal demagnetisation curves still reflect the thermal demagnetisation curves for the total TRM (Figure 7.23), *e.g.,* both TRM and TRM memory have lower unblocking spectra for *D(15-20 μm)* than for *E(190 μm)*(*cf.* Figures 7.23b and 7.23d). This increase in unblocking spectra reflects removal of the softer components of TRM by low-temperature demagnetisation treatment.

The results in Figure 7.23 display similar characteristics those of Dunlop & Argyle (1991), who examined sub-micron PSD grains. Their thermal demagnetisation curves displayed slightly higher unblocking spectra which can be attributed to the difference in grain size.

7.3.5 Step-wise thermal demagnetisation of low-field pTRM memory

In SD magnetite, blocking and unblocking are equivalent processes and occur at almost the same temperature, however this is not the case for MD magnetites. Bol'shakov & Shcherbakova (1979) showed that $\mathrm{pTRM}_{T_2}^{T_1}$ (where $T_1 \leq T_c$) is not completely demagnetised until heated to T_c, giving rise to high temperature tails. They suggested that this is a powerful characteristic property which can be used to identify MD remanence. As there is still debate as to whether memory is SD-like or MD-like (see Chapter 7.1 for discussion), then this difference in the unblocking spectra for MD and SD magnetite is an ideal test; if $\mathrm{pTRM}_{T_2}^{T_1}$ memory completely demagnetises on cooling to T_1 then the memory is SD-like, however if the demagnetisation curves display high-temperature tails, then the $\mathrm{pTRM}_{T_2}^{T_1}$ memory is MD-like.

In this simple experiment the Dankers samples were induced with a $\mathrm{pTRM}_{rtp}^{456}$ in a field of 100μT. In accordance with other experiments in this study, the $\mathrm{pTRM}_{rtp}^{456}$ was induced by initially cooling the sample from above T_c in zero-field. LTD treatment was then applied to $\mathrm{pTRM}_{rtp}^{465}$, to produce $\mathrm{pTRM}_{rtp}^{465}$ memory. The memory then was thermally demagnetised in a step-wise manner. Thermal demagnetisation of initial $\mathrm{pTRM}_{rtp}^{465}$ was also measured. Two thermal demagnetisation curves are shown in Figure 7.24 for *D(15-20 μm)* and *D(25-30 μm)*.

For both samples the unblocking spectrum of $\mathrm{pTRM}_{rtp}^{465}$ memory does not completely demagnetise until T_c (Figure 7.24). The larger sample *D(25-30 μm)* displays a reversed

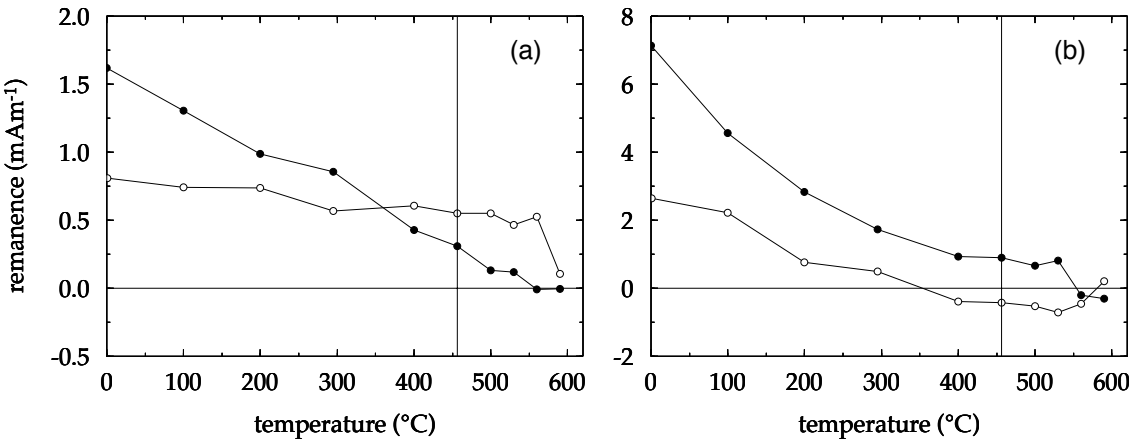


Figure 7.24: Step-wise thermal demagnetisation curves for 100 μT pTRM$^{465}_{rtp}$ (•) and pTRM$^{465}_{rtp}$ memory (◦) induced in Dankers magnetite a) *D(15-20 μm)* and b) *D(25-30 μm)*. The maximum acquisition temperature (465 °C) is marked by a horizontal line.

memory component at higher temperatures. The reversed component is likely to be of a similar origin to the reversals observed in AF demagnetisation curves for *D(75-100 μm)* (Figure 7.13). For sample*D(15-20 μm)*, the pTRM$^{465}_{rtp}$ memory demagnetisation curve is more resistant to demagnetisation than the initial remanence (Figure 7.13a).

That neither memory curve demagnetises until T_c, indicates a MD-like behaviour of memory, rather than a SD-like one as suggested by Dunlop & Argyle (1991) and Argyle *et al.* (1994).

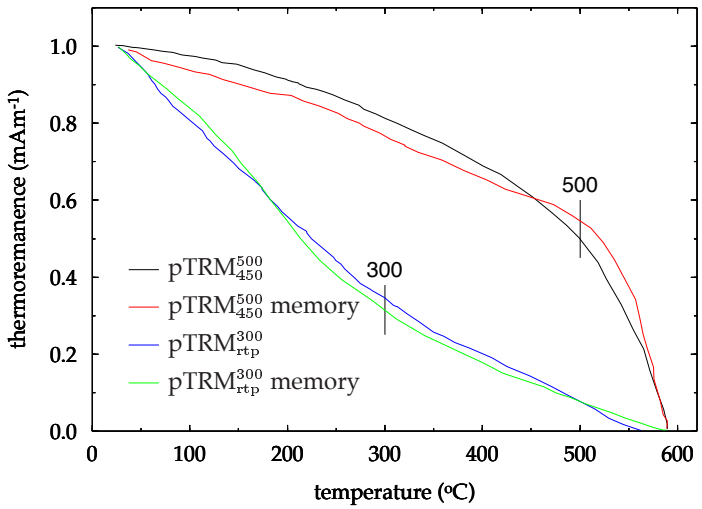


Figure 7.25: Continuous thermal demagnetisation curves for pTRM$^{500}_{450}$, pTRM$^{500}_{450}$ memory, pTRM$^{300}_{rtp}$ and pTRM$^{300}_{rtp}$ memory induced in synthetic magnetite (16–60 μm). The two lines mark the maximum acquisition temperature of the two remanences. After Shcherbakova *et al.* (1996).

Independently Shcherbakov *et al.* (1996) examined the same problem, however they used continuous rather than step-wise thermal demagnetisation (Figure 7.25). Their continuous thermal demagnetisation curves for pTRM$^{500}_{450}$, pTRM$^{500}_{450}$ memory, pTRM$^{300}_{rtp}$ and

$pTRM^{300}_{rtp}$ memory induced in a synthetic MD magnetite, do not completely demagnetise for both remanence and memory until T_c is reached (Figure 7.25). This supports the idea that pTRM memory is MD-like rather than SD-like. The continuous thermal demagnetisation curves of Shcherbakova (1996), display a higher unblocking spectra than my samples (Figure 7.24), suggesting an even greater degree of MD behaviour.

Continuous thermal demagnetisation of high-field pTRM memory

In Chapters 4 and 6 the acquisition of high-field remanences (H = 5 mT), and their behaviour on cooling from the minimum acquisition temperature (T_2) to 70 K and back to room temperature were presented. In this section the continuous thermal demagnetisation on heating the same high-field remanences from room temperature to T_c is reported. The continuous thermal demagnetisation were measured on a Princeton μ-VSM (vibrating sample magnetometer) at the Institute for Rock Magnetism, University of Minnesota. The μ-VSM and procedure have been previously described in Chapter 4. It should be noted that these samples were not vacuum sealed like the other samples in this Chapter, however they were coated in high-temperature glue (Omega CC High Temperature Cement) and were heated in an inert He environment.

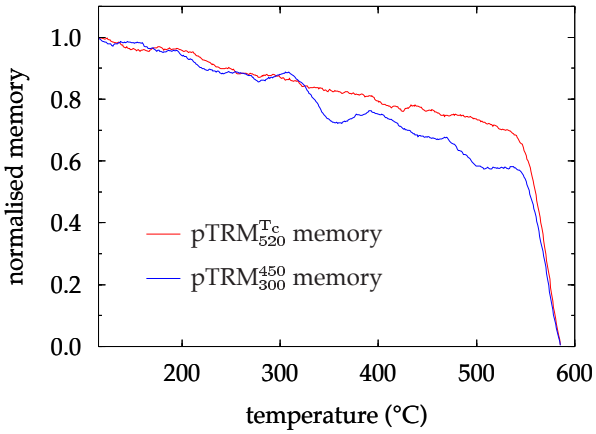


Figure 7.26: Continuous thermal demagnetisation curves for partial thermoremanence memories induced in a field of 5 mT for hydrothermal material *H(59 μm)*. The initial remanences had been cooled to 70 K using a Quantum Design MPMS (Chapter 6), to give the memories. The remanence intensities of these samples was at the lower end of the μ-VSM sensitivity, giving rise to noisy signals. The magnetisation is normalised at 100 °C.

The thermal demagnetisation curves for two partial thermoremanences induced in the hydrothermal material *H(59 μm)* are shown in Figure 7.26. The unblocking temperature spectra for 5 mT $pTRM^{T_c}_{520}$ memory and 5 mT $pTRM^{450}_{300}$ memory do not demagnetise until T_c is reached (Figure 7.26). That the 5 mT $pTRM^{450}_{300}$ memory curve does not unblock until T_c supports the idea that the pTRM memory is MD-like in nature rather than SD-like. In both these samples the memory is to seen have a much higher unblocking temperature spectrum than the continuous thermal demagnetisation curves of Shcherbakova *et al.* (1996) shown

in Figure 7.25.

The unblocking temperature spectrum for 5 mT $pTRM^{T_c}_{520}$ is higher than for 5 mT $pTRM^{450}_{300}$ (Figure 7.26). This reflects the difference in the stability of the initial domain states, and is consistent with results from untreated remanences, which show that $pTRM^{T_c}_{T_2}$ is more resistant to thermal demagnetisation than $pTRM^{T_1}_{T_2}$ (Bol'shakov & Shcherbalova, 1979).

7.3.6 Summary of previous three sections

In this section the results in the previous three sections are compared and discussed (Sections 7.3.2–7.3.4). In the three sections the magnetic memory of various remanences has been measured and characterised using a series of standard AF and thermal demagnetisation procedures. The results suggest that memory is due to metastable MD-like structures rather than SD-like inclusions, *e.g.*, the blocking/unblocking spectra are different which is indicative of MD behaviour.

The results from the three previous sections suggest that the samples can be divided into two groups;

1. Hydrothermal and natural Shetland samples.
2. Dankers samples.

The natural samples have impurities and the Evaland beach samples (*E(150 μm)–E(1.5 mm)*) have high levels of stress, however their behaviour is similar in character to the hydrothermal crystals.

The Dankers samples display reversals which has been reported previously for the same material (McClelland & Shcherbakov, 1995). The origin of the reversed component is likely to be related to the small impurities with in the sample (Section 2.2). It has been theorised and experimentally demonstrated (Banfield *et al.*, 1994; Berti & Pinna, 1996; Harrison & Putnis, 1997) that inhomogeneities in the microstructure can strongly effect the domain structure and magnetic behaviour. Harrison & Putnis (1995; 1996; 1997), have found that impurities can exsolve to leave antiparallel magnetic phases within a sample. If an impurity is magnetically hard and aligned antiparallel to the remanence, then on removal of softer remanence by either AF, thermal and low-temperature demagnetisation, a reversal is observed. That the Dankers samples display such unusual behaviour makes them unsuitable for magnetic memory investigations, and the results from the Dankers samples have to be treated with caution.

TRM and SIRM results from the hydrothermal and natural samples were in agreement with previous studies (Dunlop & Argyle, 1991; Heider *et al.*, 1992). These results

confirm the unexpected Lowrie–Fuller test results found by Heider *et al.* (1992), *i.e.,* remanences in large hydrothermal magnetites ($\approx$ 100 μm) can display apparently SD-like behaviour.

Magnetic memory appears to be associated with the high coercive force and high unblocking regions of the grains. On cooling from T_c, thermoremanences acquired at high temperatures have access to a wider range of metastable domain states, than pTRM acquired at lower temperatures. High-temperature pTRM is more likely to get trapped in deeper LEM potential wells giving rise to a higher degree of metastability. The coercive force spectra in Figures 7.10-7.12, supports this idea.

Interestingly, field-acquired remanences, *i.e.,* SIRM and ARM, display greater resistance to field demagnetisation than thermoremanence, whilst thermoremanence is more resistant to thermal demagnetisation than field remanence. It appears that this is an intrinsic property of remanence, and is retained in the memory. This further adds to the idea that memory is MD-like rather than SD-like, *i.e.,* the memory is dependent on the initial remanence type. SD-like regions are expected to be relatively independent of the type of remanence.

7.4 Characterisation of PDT_{C-AFD} and comparison with magnetic memory

In this section the AF demagnetising field required to remove the same fraction of remanence as LTD treatment is calculated to give C-AFD, *i.e.,* the AF demagnetisation field required to remove the same fraction of the initial remanence as LTD (Section 7.1). In subsequent experiments, the effect of replacing LTD treatment by C-AFD treatment is examined. Initially the stability of remanence to repeated LTD or C-AFD treatment is examined (Section 7.4.2). This is essential, because in later experiments, *e.g.,* Section 7.5, either LTD or C-AFD is repeatedly applied during the experiment. The thermal unblocking spectrum of $pTRM^{T_1}_{rtp}$ treated by C-AFD treatment is examined to determine whether the fraction remaining after C-AFD (*i.e.,* PDT_{C-AFD}) is SD-like or MD-like (Section 7.4.3). The importance of the thermal history of the initial remanence (Sugiura, 1981; Vinogradov & Markov, 1989) on the memory and PDT_{C-AFD}, is considered in Section 7.4.4.

7.4.1 Calculation of calibrated AF demagnetisation step

The experimental determination of C-AFD is straight forward;

1. Induce and measure a $TRM^{T_c}_{rtp}$ in each sample.
2. Apply LTD treatment to give a magnetic memory and measure.
3. Repeat step 1.

4. AF demagnetise incrementally the TRM in each sample until the remaining remanence equals the memory (step 2).

Typical results are shown in Figure 7.27. Due the large range in values the experiment was repeated and the results for all the samples, are summarised in Table 7.7).

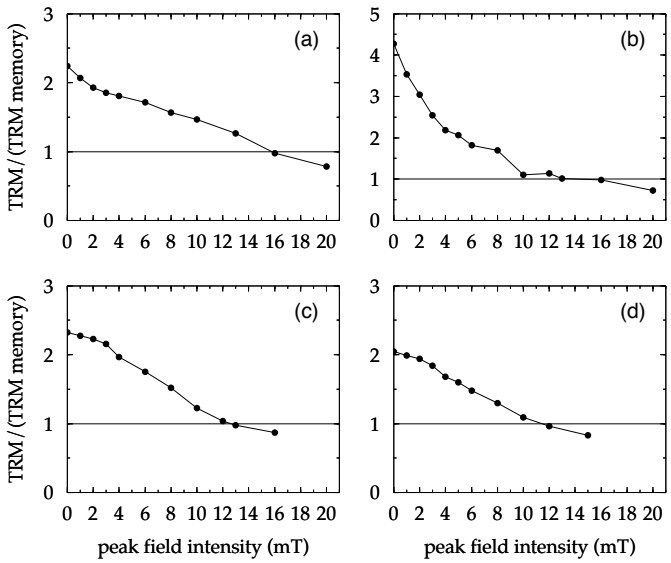


Figure 7.27: Calculation of C-AFD by AF demagnetisation of (TRM/TRM memory) induced in hydrothermal crystals a) *H(3.0 μm)* and b) *H(59 μm)*, and Dankers samples c) *D(5-10 μm)*and d) *D(20-25 μm)*. C-AFD is taken to be the AF demagnetisation field where (TRM/TRM memory) ≈ 1.

On the second calculation of C-AFD there is good repeatability (Table 7.7). There is a wide variation in C-AFD for the samples. It might be expected that the SD memory would be magnetically harder, *i.e.*, have a higher C-AFD, than some of the magnetically soft hydrothermal crystals. However the opposite is in fact the case, because the SD TRM is relatively unaffected by low-temperature cycling (Figure 6.14b), so only a small AF demagnetisation field is required to demagnetise the small fraction removed by LTD. However the application of LTD treatment causes significant demagnetisation in large hydrothermal crystals (Section 7.3.2), which increases C-AFD.

By plotting C-AFD versus memory (Figure 7.28) it can be seen that as the memory ratios increases, C-AFD decreases. It can also be seen that the different samples plot in different areas of Figure 7.28. The hydrothermal samples have particularly high C-AFD values.

7.4.2 Stability of remanence to repeated LTD or C-AFD treatment

In the experiments described in Section 7.5, either LTD or C-AFD treatment is repeatedly applied throughout the experiment. It is therefore necessary to have some understanding how remanence behaves to repeated LTD or C-AFD treatment.

sample	C-AFD (mT)	C-AFD repeat (mT)
H(3.0 μm)	20	20
H(7.5 μm)	20	16
H(13 μm)	50	50
H(18 μm)	50	50
H(24 μm)	25	30
H(39 μm)	20	20
H(59 μm)	19	13
H(76 μm)	30	35
H(108 μm)	30	35
D(5-10 μm)	13	13
D(15-20 μm)	13	13
D(20-25 μm)	12	12
D(25-30 μm)	10	10
D(30-40 μm)	9	9
D(75-100 μm)	9	9
D(100-150 μm)	40	40
E(150 μm)	8	7
E(190 μm)	20	20
E(250 μm)	7	7
E(1.5 mm)	14	13
PW(2 mm)	···	4
SD(acic.)	···	16
H(seed)	25	25

Table 7.7: Calculation of C-AFD and repeat check for most of the samples studied in this thesis.

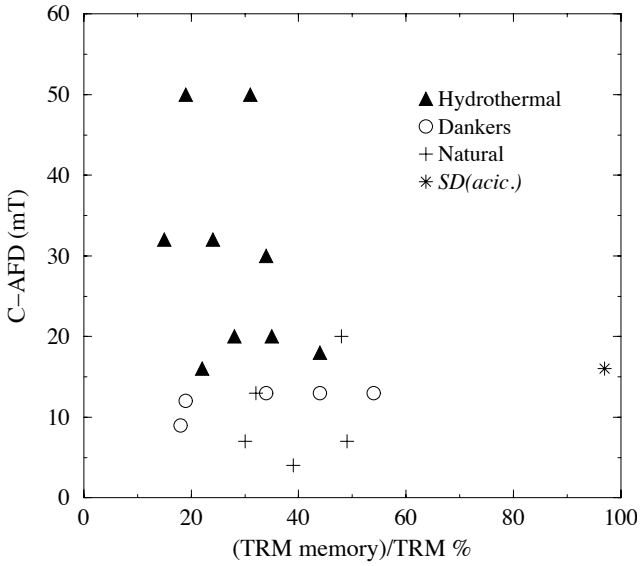


Figure 7.28: C-AFD versus TRM memory ratio for samples in this study. C-AFD decreases as TRM memory ratio increases.

This problem was examined by simply repeating LTD or C-AFD treatment to 100 μT TRM induced in the Dankers samples *D(5-10 μm)–D(100-150 μm)*. Typical results are shown in Figure 7.29.

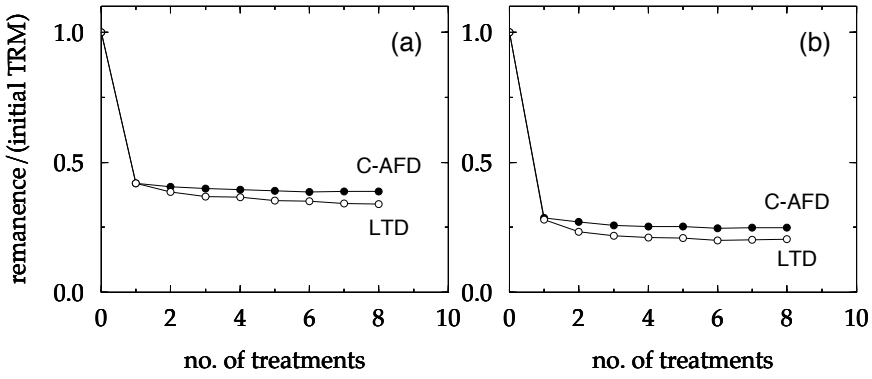


Figure 7.29: Repeated C-AFD (●) and LTD (○) treatment for initial 100 μT TRM induced in the Dankers samples a) *D(5-10 μm)* and b) *D(15-20 μm)*.

The initial remanence is more resistant to repeat C-AFD treatment than LTD treatment (Figure 7.29). The repeat LTD treatment curves compare favourably with previous studies (Merrill, 1970; Borradaile, 1994, see also Figure 7.30).

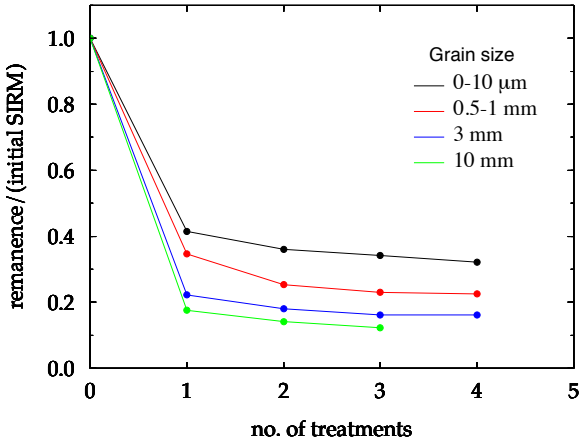


Figure 7.30: Repeated low-temperature treatments of stoichiometric magnetite samples induced with an initial 100 mT IRM. After Merrill (1970).

The difference in LTD and C-AFD cycling curves (Figure 7.29), reflects the nature of C-AFD and LTD treatment. C-AFD removes low-coercive remanence, but does not affect the rest of the domain structure. On a second application of C-AFD treatment, domain structures which were originally resistant to the AF demagnetising field, are still resistant on a second application. LTD treatment affects both high-coercive low-coercive remanence, *i.e.*, the entire domain structure is influenced by LTD treatment. On repeated application of LTD treatment, the entire domain structure is again affected, and there is a small demagnetisation.

It is seen in this study (Figure 7.29) and previous studies (Merrill, 1970; Borradaile, 1994), that after 4 or 5 five applications of LTD treatment that little further demagnetisation occurs.

Borradaile (1994) observed a "zig-zag" effect for his LTD cycles, in which odd cycles of LTD treatment give smaller memories than following even cycles. From this he suggested that odd numbers of LTD cycles were more efficient at cleaning the magnetisation than even ones. My results do *not* support this hypothesis (Figure 7.29).

7.4.3 Step-wise thermal demagnetisation of pTRM memory

In this section the experiments undertaken in Section 7.3.4 are repeated, replacing LTD treatment by C-AFD treatment. By examining the unblocking spectrum of $pTRM^{456}_{rtp}$ treated by C-AFD it is possible to distinguish whether PDT_{C-AFD} is fundamentally SD-like or MD-like in nature.

In this experiment Dankers samples were induced with a $pTRM^{456}_{rtp}$ in a field of 100μT. In accordance with other experiments in this study, the $pTRM^{465}_{rtp}$ was induced by cooling the sample initially from above T_c in zero-field. C-AFD treatment was then applied to $pTRM^{465}_{rtp}$, to give $pTRM^{465}_{rtp}$ PDT_{C-AFD}. The memory was then step-wise thermally demagnetised. Typical thermal demagnetisation curves are shown in Figure 7.31 for *D(15-20 μm)* and *D(25-30 μm)*.

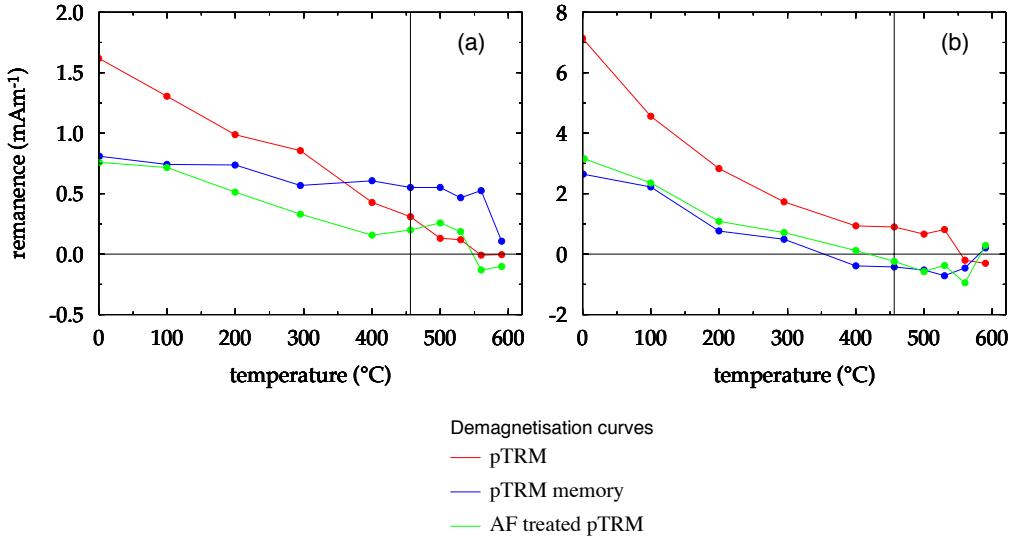


Figure 7.31: Step-wise thermal demagnetisation curves for 100 μT $pTRM^{465}_{rtp}$ and $pTRM^{465}_{rtp}$ PDT_{C-AFD} induced in Dankers magnetite, a) *D(15-20 μm)* and b) *D(25-30 μm)*. The $pTRM^{465}_{rtp}$ memory thermal demagnetisation curve, (Figure 7.24) is shown for comparison.

The unblocking spectrum of the $pTRM^{465}_{rtp}$ PDT_{C-AFD} displays similar behaviour to the memory, *e.g.*, in sample *D(25-30 μm)* PDT_{C-AFD} and memory reverse at similar temperatures (Figure 7.31b). However for *D(15-20 μm)* PDT_{C-AFD} is more susceptible to thermal demagnetisation than LTD treated memory. It is difficult to draw conclusions about the domain state for sample *D(25-30 μm)* because of the reversal, however $pTRM^{465}_{rtp}$ PDT_{C-AFD}

in sample *D(15-20 μm)* does not demagnetise until T_c (Figure 7.31a), which suggests that PDT_{C-AFD} is MD-like.

7.4.4 Dependence of thermoremanence memory on thermal history

Tanasoiu (1972) found that the ability of a magnetic grain to acquire an IRM is dependent on the initial domain structure. For a single crystal of aluminium substituted strontium hexaferrite, he observed that the IRM intensity is larger if the sample has been previously thermally demagnetised rather than AF demagnetised. The same property has subsequently been found in magnetite (*e.g.*, McClelland & Shcherbakov, 1995).

In Section 7.3.6, it is noted that remanence acquired in a field at a given temperature, *i.e.*, IRM, is more resistant to field demagnetisation than thermoremanence, and *vice versa*, *i.e.*, thermoremanence has a greater resistance to thermal demagnetisation than ARM or IRM. Assuming that an IRM is physically similar to an AC field during AF demagnetisation, then the conclusion that it is easier to induce an IRM in a thermally demagnetised domain state over an AF demagnetised domain state, is analogous to the observation that TRM is more susceptible to AF demagnetisation than IRM, *i.e.*, in both cases a field is applied to a domain state formed by thermal-equilibration. That a thermally demagnetised state has no net remanence is inconsequential, the mechanism of domain state formation is identical to a TRM. In both the domain state is rearranged into a configuration which minimises the total energy during cooling. Sometimes domain structures are trapped in LEM states. The only difference between acquisition and demagnetisation being that in the former the domain structure is minimised in the presence of a field to give a net remanence, whereas in the latter the domain structure is minimised to give zero net magnetisation.

Sugiura (1981) found that the intensity of IRM acquisition induced in MD magnetite at an elevated temperature T_1 and subsequent behaviour on either heating or cooling depends on the thermal history of the sample, *i.e.*, whether T_1 is reached by cooling from T_c in zero field or by heating from a temperature below T_1 in zero field. Vinogradov & Markov (1989) observed a similar dependency on thermal history for $pTRM_{T_2}^{T_1}$ induced in MD magnetite.

The dependency of pTRM on thermal history can be used to distinguish between MD-like and SD-like nature of a magnetic sample, because according to SD theory (Néel, 1949; Néel, 1955), SD pTRM is independent of thermal history for non-viscous samples, however MD grains are dependent on thermal history. This provides another test for the characterisation of remanence.

To examine this problem two different $pTRM_{rtp}^{400}$ were induced in the Dankers samples (*D(5-10 μm)–D(100-150 μm)*), each $pTRM_{rtp}^{400}$ having a different thermal history;

Case 1. The temperature T_1 (400 °C) was reached by cooling from T_c. $pTRM^{400}_{rtp}$ was acquired in the following sequence;

1. $T_c \downarrow 400$ °C; $H = 0$.
2. 400 °C $\downarrow$ room temperature ; $H = 100\ \mu$T.

Case 2. The temperature T_1 (400 °C) was obtained by first thermally demagnetising the sample by cooling in zero field from T_c, followed by heating in zero field from room temperature to 400 °C . The pTRM was acquired by cooling in field from 400 °C to room temperature. In summary,

1. $T_c \downarrow$ room temperature; $H = 0$.
2. room temperature $\uparrow 400$ °C; $H = 0$.
3. 400 °C $\downarrow$ room temperature ; $H = 100\ \mu$T.

In a series of experiments, both Case 1 and Case 2 $pTRM^{400}_{rtp}$ were induced in the Dankers samples, followed by C-AFD treatment. In a comparative study the C-AFD treatment step was replaced by LTD treatment. The ratio of (Case 2/Case 1) is calculated the original $pTRM^{400}_{rtp}$, $pTRM^{400}_{rtp}$ PDT_{C-AFD} and $pTRM^{400}_{rtp}$ memory (Table 7.8).

sample	(Case 2/Case 1)		
	$pTRM^{400}_{rtp}$	$pTRM^{400}_{rtp}$ PDT_{C-AFD}	$pTRM^{400}_{rtp}$ memory
D(5-10 μm)	0.96	1.08	1.07
D(15-20 μm)	0.88	1.53	0.97
D(20-25 μm)	0.99	1.22	1.1
D(25-30 μm)	0.82	0.82	1.05
D(30-40 μm)	1.12	2.45	0.8
D(75-100 μm)	0.73	2.36	...
D(100-150 μm)	0.84	1.1	0.98

Table 7.8: Ratio of the thermal histories (Case 2/Case 1) for $pTRM^{400}_{rtp}$, where for Case 1 400 °C was reached by cooling in zero field from T_c to 400 °C, and for Case 2 by heating from room temperature to 400 °C in zero field. $pTRM^{400}_{rtp}$ was induced in a field of 100 μT, and C-AFD treatment applied to give $pTRM^{400}_{rtp}$ PDT_{C-AFD}. In a repeat experiment, $pTRM^{400}_{rtp}$ was again induced LTD treatment applied to give $pTRM^{400}_{rtp}$ memory.

The ratio (Case 2/Case 1) of initial $pTRM^{400}_{rtp}$ is less than one for all the samples except *D(30-40 μm)* (Table 7.8). With the exception of the sample *D(30-40 μm)*, the ratio (Case 2/Case 1) appears to decrease with with increasing grain size. This decrease is the manifestation of the multidomain property documented by Vinogradov & Markov (1989) and Shcherbakov *et al.* (1993), *i.e.*, MD $pTRM^{T_1}_{T_2}$ (where $T_1 < T_c$) acquired by approaching T_1 in zero-field from above produces a larger remanence than a $pTRM^{T_1}_{T_2}$ acquired when T_1 is approached from below. This difference reflects a temperature dependence of domain structure. In Section 4.2.4 it was demonstrated that pTRM is irreversible to changes in the direction of heating, which reflects the temperature dependence of domain structure. If as suggested above, a thermally demagnetised domain structure is similar in character to a

TRM, then it is expected to be partially irreversible temperature dependency. Direct observation of domain structures by Bitter pattern imaging supports this hypothesis (Heider & Williams, 1988; Heider, 1990, see also Section 4.1.1)

On cooling a demagnetised sample to room temperature and back to T_1 (Case 2), the domain structure relocates to a "harder" metastable demagnetised domain state than a domain state acquired by cooling from T_c to T_1 (Case 1). The harder demagnetised domain state (Case 2), is more resistant to remanence acquisition at T_1 than the softer demagnetised domain state (Case 1), *i.e.,* for MD grains Case 1 $pTRM^{T_1}_{T_2}$ > Case 2 $pTRM^{T_1}_{T_2}$. This is seen to be the case for $pTRM^{400}_{rtp}$ (Table 7.8).

The ratios (Case 2/Case 1) for $pTRM^{400}_{rtp}$ PDT_{C-AFD} are all greater than one except for the sample *D(25-30 μm)* (Table 7.8). However this does not reflect SD-like behaviour, because SD pTRM is independent of history according to theory (Néel, 1949; Néel, 1955). If the hypothesis above is correct, the domain structure of Case 2 $pTRM^{T_1}_{T_2}$ is harder than Case 1 $pTRM^{T_1}_{T_2}$ at T_1, *i.e.,* the domain state of the initial demagnetised grain at T_1, is trapped in deeper LEM for Case 2 than Case 1. Application of C-AFD treatment, is expected to remove relatively more of the softer Case 1 $pTRM^{T_1}_{T_2}$ remanence. This in turn increases the ratio (Case 2)/(Case 1) for PDT_{C-AFD} (Table 7.8).

The ratios (Case 2/Case 1) for $pTRM^{400}_{rtp}$ memory are on average slightly greater than one (Table 7.8). The effect of LTD treatment is similar to C-AFD treatment, *i.e.,* it increases the ratio (Case 2)/(Case1) for $pTRM^{400}_{rtp}$ memory. This experiment is inconclusive in determining whether memory is SD-like or MD-like. On the one hand the ratios (Case 2/Case1) for $pTRM^{400}_{rtp}$ memory are close to one, *i.e.,* SD-like, on the other LTD treatment is expected to increase the ratio (Case 2/Case1) for $pTRM^{400}_{rtp}$. That the ratio (Case 2/Case1) for $pTRM^{400}_{rtp}$ memory is near one may be coincidence.

On average the ratio (Case 2/Case 1) for $pTRM^{400}_{rtp}$ PDT_{C-AFD}, *i.e.,* $pTRM^{400}_{rtp}$ after C-AFD treatment, is greater than the same ratio for $pTRM^{400}_{rtp}$ memory. This suggests that C-AFD treatment removes a different fraction of $pTRM^{400}_{rtp}$ than LTD treatment (Table 7.8).

7.5 Further examination of PDT_{C-AFD} and memory

In this section two experiments specifically designed to examine the nature of PDT are presented, where PDT is the general term used in this study for the fraction remaining after either C-AFD or LTD treatment. Although previous experimental evidence presented in this chapter suggests that the PDT is MD-like in character, two further tests are presented here.

In Section 7.5.1 experiments which examine the blocking/unblocking spectrum and thermal history of MD magnetites are presented, and in Section 7.5.2 Thellier-Thellier type experiments are used to examine the nature of PDT.

All the experiments in this section were performed in Oxford using the palaeomagnetic equipment described in Section 1.8.

7.5.1 Progressive remagnetisation of TRM and TRM PDT

The intensity of $pTRM^{T_1}_{rtp}$ (where $T_1 < T_c$) acquired in a thermally demagnetised MD sample, is dependent on the thermal history of the demagnetised domain state; a $pTRM^{T_1}_{rtp}$ acquired by cooling from T_c to T_1 has a greater intensity than $pTRM^{T_1}_{rtp}$ acquired on heating from room temperature to T_1 (Vinogradov & Markov, 1989; Shcherbakov *et al.*, 1993). However this relationship does not hold for either $pTRM^{T_1}_{rtp}$ PDT_{C-AFD} or $pTRM^{T_1}_{rtp}$ memory (PDT_{LTD}) (Table 7.8).

In "progressive remagnetisation" a $pTRM^{T_1}_{rtp}$ is a induced in a MD sample which has already been induced with a total TRM, *i.e.*, $TRM^{T_c}_{rtp}$. Inducing a $pTRM^{T_1}_{rtp}$ by heating from room temperature, unblocks all the TRM between room temperature and T_1, and replaces it with a $pTRM^{T_1}_{rtp}$ acquired on warming from below T_1. For MD magnetite, $pTRM^{T_1}_{rtp}$ acquired from below T_1 is expected to have a different intensity than the remanence removed. Whether $pTRM^{T_1}_{rtp}$ induced during progressive remagnetisation is greater or less than the remanence removed is not immediately apparent. On the one hand, Case 1 pTRM is greater than Case 2 pTRM (Section 7.4.4), *i.e.*, this contribution effectively *decreases* the total remanence during progressive remagnetisation, however the difference in blocking and unblocking spectra must also be considered. Because $pTRM^{T_1}_{rtp}$ does not completely demagnetise until T_c is reached, *cf.* high-temperature "tails" (Bol'shakov & Shcherbalova, 1979), each progressive $pTRM^{T_1}_{rtp}$ induced on top of a TRM, contributes to the high-temperature unblocking component above T_1, *i.e.*, inducing a $pTRM^{T_1}_{rtp}$ demagnetises all remanence with unblocking spectra less than T_1, and replaces it with a secondary remanence, most of which unblocks below T_1, however a small fraction unblocks *above* T_1. This difference in blocking/unblocking spectra effectively *increases* the net magnetisation of the high-unblocking component of the total remanence. The net contribution from the two effects, *i.e.*, differences in thermal history and in the blocking/unblocking spectra, are counter-active, *i.e.*, the former decreases the net magnetisation, the latter increases it. However it is *unlikely* that they exactly cancel out, *i.e.*, it is uncertain whether the net magnetisation increases or decreases during progressive remagnetisation. Note SD remanence has effectively identical blocking and unblocking spectra and is independent of thermal history (Néel, 1949; 1955). Therefore progressive remagnetisation of SD TRM does not alter the net magnetisation. This means that progressive remagnetisation can be used as a test for SD-like or MD-like behaviour.

To examine the uncertainty in MD behaviour during progressive remagnetisation the Dankers samples were induced with a TRM in a field of 100 μT, and then step-wise thermally remagnetised by heating the sample from room temperature to T_1, and back to room temperature in a field of 100 μT (Figure 7.32).

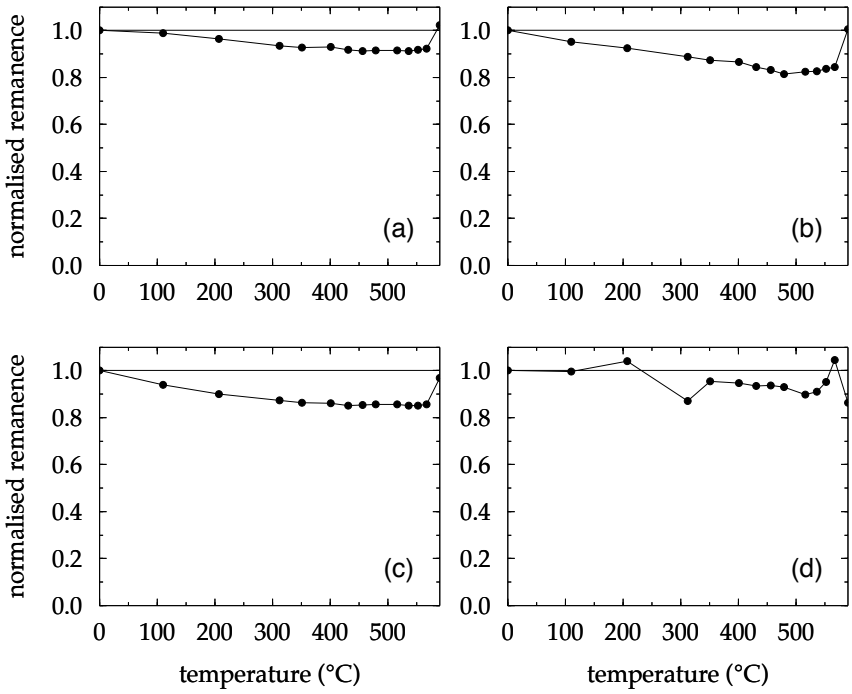


Figure 7.32: Progressive remagnetisation of 100μT TRM by 100μT pTRM for Dankers samples a) *D(5-10 μm)*, b) *D(15-20 μm)*, c) *D(20-25 μm)* and d) *D(100-150 μm)*.

It is found that the effect of progressive remagnetisation is to decrease the total intensity of remanence, *i.e.*, contribution from differences in thermal history is greater than that due to differences in blocking/unblocking spectra (Figure 7.32). It is suggested here that progressive remagnetisation provides another powerful technique in distinguishing between SD and MD behaviour.

Progressive remagnetisation of PDT

Progressive remagnetisation was used to investigate the nature and character of $\mathrm{PDT_{C-AFD}}$ and memory. The sequence of experiments was identical to that for the progressive remagnetisation of TRM (Figure 7.32), except that after each TRM or pTRM step either C-AFD treatment (Figure 7.33) or LTD treatment (Figure 7.34) was applied. The procedure is summarised below.

1. Induce $\mathrm{TRM_{rtp}^{Tc}}$.
2. Apply PDT treatment, *i.e.*, either LTD or C-AFD treatment.
3. Induce $\mathrm{pTRM_{rtp}^{T_1}}$.
4. Apply PDT treatment, *i.e.*, either LTD or C-AFD treatment.
5. Repeat steps 3 and 4, increasing T_1 until $T_1 = T_c$.

In Figures 7.33 and 7.34, the data is plotted after each PDT treatment step, *i.e.*, after C-AFD or LTD step respectively.

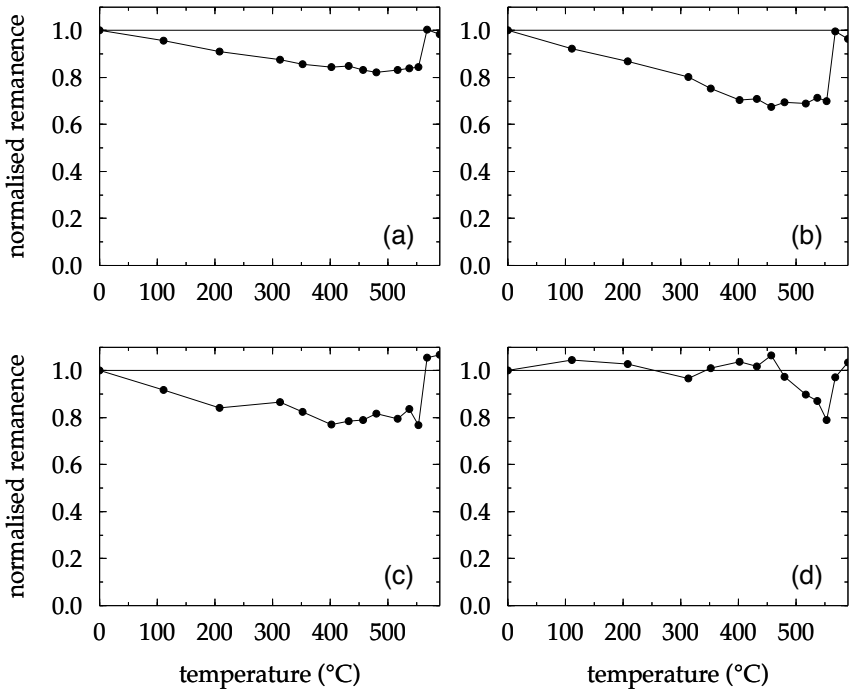


Figure 7.33: Progressive remagnetisation of 100μT TRM memory by 100μT C-AFD for Dankers samples a) *D(5-10 μm)*, b) *D(15-20 μm)*, c) *D(20-25 μm)* and d) *D(100-150 μm)*. C- AFD treatment was applied after each pTRM.

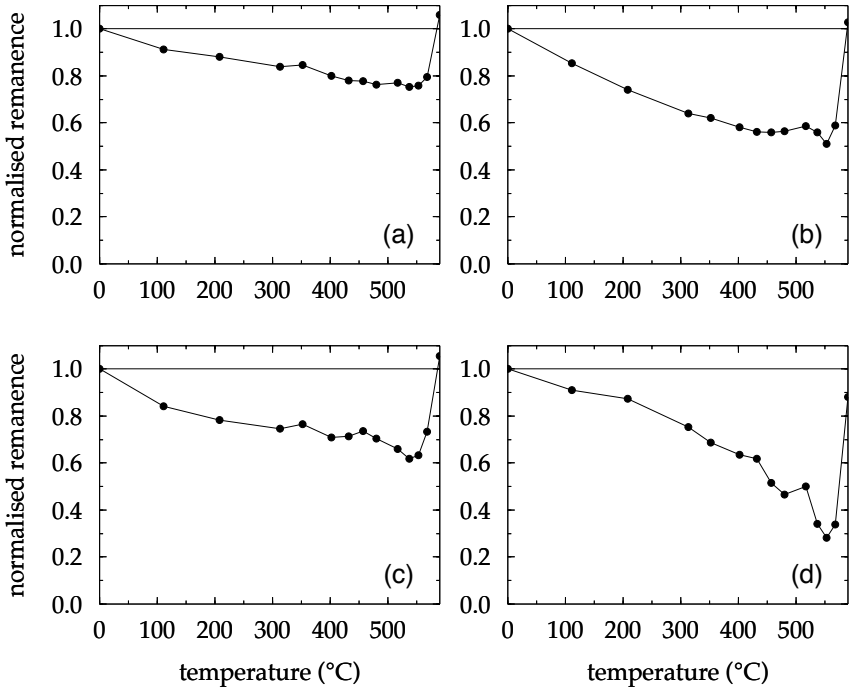


Figure 7.34: Progressive remagnetisation of 100μT TRM memory by 100μT pTRM memory for Dankers samples a) *D(5-10 μm)*, b) *D(15-20 μm)*, c) *D(20-25 μm)* and d) *D(100-150 μm)*. LTD treatment was applied after each pTRM.

There is a similar trend in behaviour for the progressive remagnetisation curves of PDT_{C-AFD} (Figure 7.33) and memory (Figure 7.34) compared to untreated remanence (Figure 7.32). Memory and PDT_{C-AFD} (by definition) are reversed for the large *D(100-150 μm)* sample (Figure 7.33d and 7.34d), in agreement with previous observations (Section 7.3.2).

Because of the repeated use of LTD and C-AFD treatment during progressive remagnetisation, the stability of TRM to repeated LTD and C-AFD treatment must also be considered (Section 7.4.2). In Table 7.9 the results are summarised by considering the maximum decrease of progressive remagnetisation of full TRM, TRM memory and TRM PDT_{C-AFD}, and the maximum decrease associated with repeated LTD and C-AFD cycling taken from Section 7.4.2 is also shown.

1	2	3	4	5	6	7	8
sample	max. % reduction			3–2–4	max. % reduction		6–2–7
	TRM rem	mem. rem	LTD cyc		PDT_{C-AFD} rem	C-AFD cyc	
D(5-10 μm)	11	18	8	-1	25	19	-5
D(15-20 μm)	14	32	14	4	49	28	7
D(20-25 μm)	13	23	10	0	38	13	12
D(25-30 μm)	14	53	30	9	59	55	-10
D(30-40 μm)	19	30	17	-6	57	82	-44
D(75-100 μm)	30	63	39	-6	12	50	-68
D(100-150 μm)	19	21	14	-16	72	53	0

Table 7.9: Maximum percentage decrease of remanence by progressive remagnetisation of initial TRM (2), TRM memory (3) and TRM PDT_{C-AFD} (6), and by repeated application of LTD treatment (4) and C-AFD treatment (7) in the Dankers samples (*D(5-10 μm)-D(100-150 μm)*). The calculation to find the contribution from repeated C-AFD or LTD treatment to PDT_{C-AFD} or memory respectively are shown in columns 5 and 8 respectively, and is discussed in the text.

For PDT_{C-AFD}, the magnitude of decrease due to progressive remagnetisation is less than the decrease of progressive remagnetisation of the full TRM (Table 7.9), by the factor associated with the contribution from repeated C-AFD cycling (Figure 7.33). It appears that the PDT_{C-AFD} progressive remagnetisation experiments simply combine the reduction of total TRM by repeat remagnetisation with the effect of repeated C-AFD treatment (Column 5 of Table 7.9).

In contrast, repeated LTD cycling causes a greater decrease in TRM than the thermal remagnetisation experiment with LTD treatment steps (Column 8, Table 7.9). The residual effect of the LTD cycling cannot be satisfactorily separated from the effect of progressive remagnetisation. If the memory were not affected by thermal remagnetisation, *i.e.*, it behaves in an SD-like manner, then the results of the thermal remagnetisation of memory, could be solely due to the effect of repeated LTD. If the memory is affected by thermal remagnetisation, *i.e.*, in a MD-like manner, then the effect of repeated LTD treatment must be removed by the intervening thermal cycles.

In summary PDT_{C-AFD} of TRM behaves in a similar manner to total TRM in response to thermal remagnetisation, suggesting that PDT_{C-AFD} is of an MD-like character, how-

ever the results from progressive remagnetisation of memory is inconclusive, *i.e.*, it is not possible to state whether the memory fraction is SD-like or MD-like.

7.5.2 Thellier-Thellier type experiments

If the NRM of a rock was acquired as a TRM in an ancient geomagnetic field (H_a) for which TRM $\propto H_a$, *i.e.*, $H < 300$ μT (Chapter 4), then (Thellier & Thellier, 1959)

$$H_a = \frac{\mathrm{NRM}}{\mathrm{TRM}_{lab}} H_{lab} \tag{7.1}$$

where TRM_{lab} is the TRM induced in the same sample in a laboratory field of H_{lab}. In theory it should be possible to simply induce a sample with a TRM_{lab} to obtain H_a, however chemical alteration often occurs at high-temperatures during acquisition of TRM_{lab}, while viscous remagnetisation can affect the lowest blocking-temperature fraction (Dunlop & Özdemir, 1997). The Thellier-Thellier method of palaeointensity determination (Thellier & Thellier, 1959) takes consideration of this and examines only partial TRM and partial NRM to determine H_a. The Thellier-Thellier method is applied by partially thermally demagnetising an initial NRM by heating in zero-field to a temperature T_1, then a $\mathrm{pTRM}^{\mathrm{T}_1}_{\mathrm{rtp}}$ is induced in a given field, and lastly the thermal demagnetisation step is repeated. The temperature T_1 is increased and the procedure repeated. There have been many variations on this basic method, *e.g.*, intermediate steps which check for chemical alteration (*e.g.*, McClelland & Briden, 1995). Ideally the plot of pTRM acquisition versus NRM demagnetisation should give a straight line, from which H_a is easily calculated (Equation 7.1).

However the Thellier-Thellier method is based on SD theory, because it assumes that the unblocking spectrum during thermal demagnetisation and the blocking spectrum during $\mathrm{pTRM}^{\mathrm{T}_1}_{\mathrm{rtp}}$ acquisition are identical. This is not true for MD grains, and often MD grains are seen as a contaminants because they cause pTRM versus NRM plots to concave downwards (Levi, 1977).

However the distinctive behaviour of MD grains during Thellier-Thellier type experiments, means that the Thellier-Thellier method can be used to classify and characterise $\mathrm{PDT}_{\mathrm{C-AFD}}$ and memory, *i.e.*, if pTRM $\mathrm{PDT}_{\mathrm{C-AFD}}$ versus NRM $\mathrm{PDT}_{\mathrm{C-AFD}}$ plots or pTRM memory versus NRM memory plots display concave behaviour of then this is indicative of MD behaviour, however if the plots display linear trends, then this suggests that $\mathrm{PDT}_{\mathrm{C-AFD}}$ and memory are SD-like.

Thellier-Thellier type curves of pTRM versus NRM for $\mathrm{PDT}_{\mathrm{C-AFD}}$ and memory were produced. A Thellier-Thellier type curve was also produced for the full thermoremanence with no LTD or C-AFD treatment. The following sequence was used to produce the Thellier-Thellier type curves,

1. Induce TRM in a field of 100 μT
2. Perform the following sequence for a range of temperature starting at 100 °C, increasing to T_c,
   (a) Thermally demagnetise the sample by heating to temperature T_1 in zero field, followed by cooling to room temperature.
   (b) Induce 100 μT $pTRM^{T_1}_{rtp}$, by heating to T_1 followed by cooling to room temperature.
   (c) Depending on the remanence under consideration, apply LTD for memory or C-AFD for PDT_{C-AFD}. This step is not applied for the full remanence.
   (d) Thermally demagnetise the sample by heating to temperature T_1 in zero field, followed by cooling to room temperature.

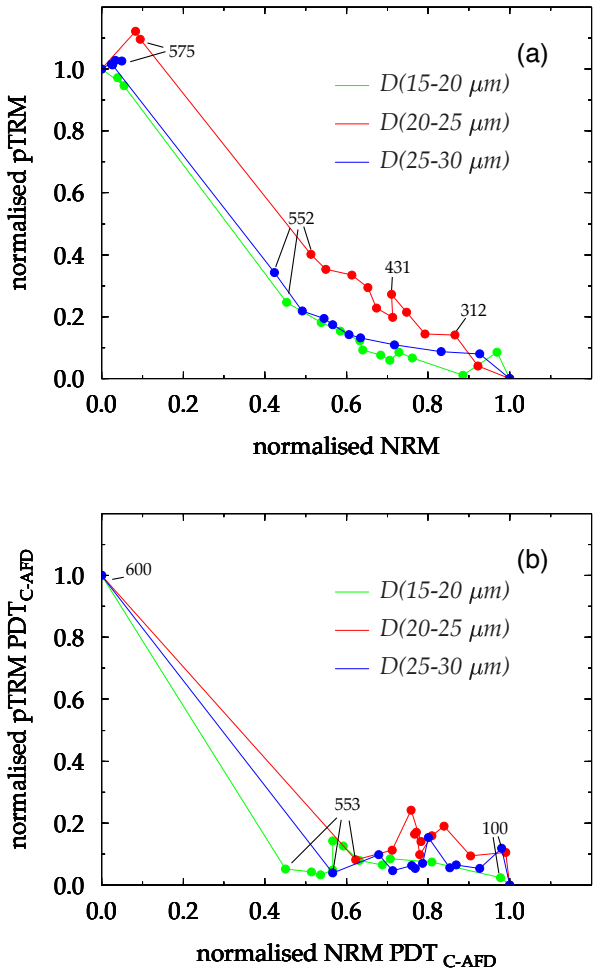


Figure 7.35: Palaeointensity plots for Dankers samples with a) initial full TRM and b) C-AFD treated TRM (PDT_{C-AFD}). Note in b all the measurements are *after* C-AFD treatment. Temperatures marked are in Celsius.

I personally measured the Thellier-Thellier curves for full remanence and PDT_{C-AFD}, however I am indebted to Rick Thomas who measured the Thellier-Thellier curves for memory in the summer of 1994, just before I started this D.Phil. The results from Rick

Thomas's work have been previously published in McClelland *et al.* (1996). All the Thellier-Thellier type experiments were undertaken using Dankers samples *D(5-10 μm)-D(100-150 μm)* (Figures 7.35 and 7.36). Only the smaller Dankers samples are considered here, because the larger samples display self-reversal on the application of C-AFD or LTD treatment (Table 7.1). Note in Figures 7.35b and 7.36, all the measurements are *after* C-AFD or LTD treatment respectively.

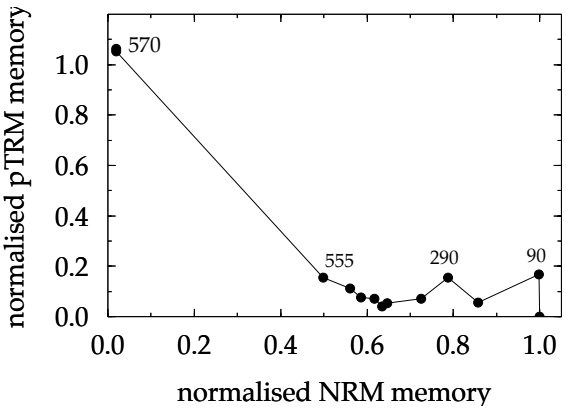


Figure 7.36: Palaeointensity plot for Dankers sample *H(3.0 μm)* with a LTD treated TRM (memory). Note in all the measurements are *after* LTD treatment. Temperatures marked are in Celsius. Measured by R. Thomas.

All the Dankers samples display MD-like behaviour for raw TRM , TRM PDT_{C-AFD} and TRM memory (Figures 7.35 and 7.36), *i.e.,* the pTRM versus NRM, pTRM PDT_{C-AFD} versus NRM PDT_{C-AFD} and pTRM memory versus NRM memory plots are concave rather than linear (SD-like).

It is easier to demagnetise the initial TRM than it is to replace it with a pTRM (Figure 7.35a), which results in a slope of pTRM versus NRM curve which is much greater than one up to temperature's between 530-550 °C. The pTRM versus NRM plots for the raw remanence (Figures 7.35a) are in agreement with previous data for MD magnetite (Levi, 1977).

The curvature of the plots is enhanced by both C-AFD and LTD treatment, suggesting that both PDT_{C-AFD} and memory are MD-like in character.

Chapter 8

Micromagnetic models of pseudo-single domain grains near the Verwey Transition

8.1 Introduction

In this chapter, results of numerical micromagnetic models for 0.05–0.6 μm cubic grains of magnetite in the vicinity of the Verwey transition (120–124 K, T_v) are presented.

In Chapter 6, the low-temperature behaviour of saturation isothermal remanences (SIRM) and various kinds of thermoremanence (*e.g.*, $TRM^{T_c}_{rtp}$, $pTRM^{T_c}_{T_2}$ and $pTRM^{T_1}_{T_2}$ (see either Chapter 4 or 6 for definitions)) induced in hydrothermal and natural crystals was examined. The low-temperature cycling of thermoremanence gave some very unexpected results (Section 6.6), which was explained in terms of metastable and unstable domain structures, however no analytical formulation was made. As the experimental evidence has not completely elucidated the low-temperature behaviour of domain structure, it was decided to examine this problem by simulating low-temperature cycling of SIRM and thermoremanences using three-dimensional micromagnetic modelling (Schabes & Bertram, 1988; Williams & Dunlop, 1989).

The monoclinic phase of magnetite has never been investigated using micromagnetic models before, so before simulating the low-temperature cycling experiments described in Section 6.6; a preliminary investigation of the monoclinic phase of magnetite is considered (Section 8.3). The simulated low-temperature cycling models are considered in Section 8.4.

Initially the micromagnetic algorithm used in this study is considered (Section 8.2).

8.2 Micromagnetic Models

Theoretical models are achieved by minimising the total energy of a specified number of magnetic moments with respect to each other. The problem is complicated by the need to calculate the long range non-linear magnetostatic interaction between each magnetic moment in the model.

Early attempts to solve this problem constrained the domain structure into pre-determined blocks of varying width. These type of constrained models are commonly called Rhodes-Rowlands-Amar (RRA) models after the ideas of Rhodes & Rowlands (1954) and Amar (1958), and there have been many rock magnetic papers which have based their calculation on this type of formulation (*e.g.,* Shcherbakov & Markov, 1982; Moskowitz & Banerjee, 1979; Argyle & Dunlop, 1984; Moskowitz & Halgedahl, 1987; Shcherbakov *et al.*, 1990; Shcherbakov & Tarashchan, 1990; Xu & Merrill, 1990b). RRA models are relatively easy to calculate, however they suffer by being highly constrained.

Advances in computer technology have allowed for the calculation of non-uniform solutions based on the micromagnetic equations formulated by Brown (1963). These types of models have gradually reduced the number of constraints by firstly allowing the magnetisation to vary freely in one dimension, *i.e.,* no pre-determined domain structure (Enkin *et al.*, 1987; Newell *et al.*, 1990), followed by two dimensions (LaBonte, 1969; Xu *et al.*, 1994) and lastly three dimensions (Schabes & Bertram, 1988; Williams & Dunlop, 1989). With each increase in the degree of freedom, the computational power and time required also increases.

Whether one and two dimensional models produce realistic domain states, has been disputed by Williams & Wright (1998). Their argument against one and two-dimensional models, follows from the observation that these models always yield higher energy domain states than three dimensional models, which suggests that in reality domain structures are minimised spatially in three dimensions, not in two dimensional slices. It should be noted that magnetite found in rocks is usually finite in all directions, *i.e.,* it is three dimensional.

Micromagnetic models have recently been vastly improved by the implementation of fast-Fourier-transform (FFT) algorithms to the three-dimensional optimisation process (Fabian *et al.*, 1996; Wright *et al.*, 1997). This has extended the grain-size range which can be studied by reducing the number of calculations from to N^2 to $N\log N$ (where N is the number of elements into which the grain is sub-divided), *e.g.,* the FFT model enables the equilibrium magnetisation to be predicted using a resolution of $64 \times 64 \times 64$ magnetic moments per grain, in 16 hours CPU time compared with a resolution of $12 \times 12 \times 12$ in 24 hours using previous models (Wright *et al.*, 1997). Recent advances in computation power and the implementation of FFT to the algorithm, means that it has now become feasible to study not only the domain structure of pseudo-single domain (PSD) grains up to 4.0 μm at a high resolution of $64 \times 64 \times 64$ (Wright *et al.*, 1997), but also the variation of domain structure with external field (Williams & Dunlop, 1995; Williams & Wright, 1998)

and temperature (Winklhofer *et al.*, 1997, this study).

In accordance with most previous studies (*e.g.*, Williams & Dunlop, 1989; Winklhofer *et al.*, 1997) only cubic grains are considered in this thesis. Synthetic and natural magnetites can be either rhombic dodecahedron, octahedral or cubic (Heider & Bryndzia, 1987, Chapter 2), however Williams & Wright (1998) modelled micromagnetic structures of both cubic and octahedral shape and found that both the coercive force (H_c) and the normalised saturation remanence (M_{rs}/M_s) were largely invariant to different grain geometries. They concluded that roughly equidimensional grains behave in a similar manner.

8.2.1 The Discrete Micromagnetic Model

The basic algorithm used to model the results in this chapter was fully described by Wright *et al.* (1997), to whom I am grateful for letting me use the code. Here a only a brief description of the algorithm and the changes made to accommodate the low-temperature phase are given. As it was the intention to model both the inducement of thermal remanences and low-temperature cycling to $\approx$ 70 K it was necessary to include the temperature dependency of the various constants and variables between 70 K and T_c (851 K).

The model subdivides the cubic grain of length d into a number (n) of finite element sub-cubes of length Δ, which are assumed to be homogeneously magnetised (Figure 8.1). All the sub-cubes have equal magnetic magnitude, but their magnetisation can vary in direction, making it possible to completely describe each sub-cube by a constant magnetisation, M_l, a colatitude ϕ_l and azimuth angle θ_l.

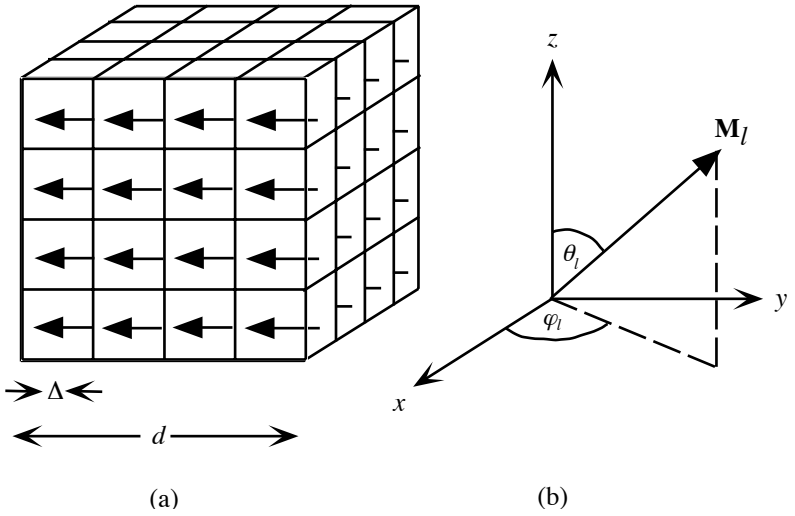


Figure 8.1: The geometry of the micromagnetic model. a) A cubic crystal of edge length d is subdivided into $N = n^3$ sub-cubes each of length Δ. In the above cube $n = 4$. b) Each element has a magnetisation of constant magnitude (M_l), and can be defined in terms of the azimuthal angle (θ_l) and the colatitude (ϕ_l). After Wright *et al.* (1997).

To calculate the domain structure its necessary to optimise the total free magnetic

energy (E_{tot}). The total free magnetic energy (Equation 1.12) is the sum of the exchange energy E_{ex}, the external field energy E_h, the magnetostatic energy E_d and the anisotropy E_{anis}. The effect and nature of these energies have been described previously in Chapter 1. Here only the formulation used in this model is described.

Exchange energy

The exchange energy E_e is given by

$$E_e = A\sum_{i=1}^{n}(\nabla m)_{\mathbf{i}}^2\Delta^3 \tag{8.1}$$

where A is the exchange constant. Above room temperature, $A(T)$ was taken to vary as $M_s^{1.7}(T)$ (Heider & Williams, 1988). Below room temperature, there are no reported measurements leading directly to the calculation of $A(T)$, however $A(T) \propto$ the exchange integral (Dunlop & Özdemir, 1997), which has been measured below room temperature (Alperin *et al.*, 1967; Torrie, 1967). The exchange integral appears to be unaffected by the Verwey transition, and does not vary significantly from the room temperature value. It was therefore assumed that $A(T)$ did not vary below room temperature. This is a crude assumption, but to my knowledge the data required to determine $A(T)$ below room temperature, has not been reported in the literature. It should be not that the exchange integral which controls the exchange energy E_e, is *not* the same as the Vonsovskiĭ exchange integral which gives rise to the anomaly in M_s at T_v (Figure 5.8). The two exchange interactions are mutually independent. It is therefore possible for M_s to display a low-temperature anomaly, and $A(T)$ not to. The temperature dependence of M_s used in this model, is shown in Figure 1.17 for $T > 273$ K, and in Figure 5.8 for $T \leq 273$ K.

External field energy

The external field energy E_h is given by

$$E_h = -\mu_0 M_s \sum_{i=1}^{n} \mathbf{H_e} \cdot m_{\mathbf{i}}\Delta^3 \tag{8.2}$$

where $\mathbf{H_e}$ is the external field with magnitude H and direction ϕ_H and θ_H, and μ_0 denotes the permeability of free space.

Magnetostatic energy

The magnetostatic energy E_d is given by

$$E_d = -\frac{\mu_0 M_s}{2} \sum_{i=1}^{n} \mathbf{H_{d},}i \cdot m_\mathbf{i} \Delta^3 \tag{8.3}$$

where $\mathbf{H_d}, i$ is the magnetic field at the location m_i due to each magnetic dipole in the system.

Anisotropy energy

In Chapter 1, E_{anis} was defined as the sum of the magnetocrystalline, magnetostrictive and magnetoelastic anisotropy energies.

Magnetocrystalline anisotropy In accordance with the ideas previously discussed in Section 5.4.2, the magnetocrystalline anisotropy energy was split into high-temperature cubic phase (E_k^c) and the low-temperature monoclinic phase (E_k^m), defined by Equations 1.20 and (5.1) respectively.

After considering Figure 5.17 and Figures 5.18–5.20, it can be readily seen that the K_2 term in Equation 1.20, and the terms $\mathcal{K}_{aa}$, $\mathcal{K}_{bb}$ and $\mathcal{K}_{ab}$ in Equation 5.1 are relatively small, and are in some cases smaller than the errors associated with the other anisotropy constants. For simplicity, it seems reasonable to reduce the two Equations 1.20 and 5.1 to

$$E_k^c = K_1(\alpha_1^2\alpha_2^2 + \alpha_2^2\alpha_3^2 + \alpha_3^2\alpha_1^2) \tag{8.4}$$

$$E_k^m = \mathcal{K}_a\alpha_k^2 + \mathcal{K}_b\alpha_b^2 - \mathcal{K}_u\alpha_{111}^2 \tag{8.5}$$

where the constants K_1 and $\mathcal{K}_i$, and the directional cosines (α) are expressed with the original Equations 1.20 and 5.1. In terms of the discrete model, these two energies are given by

$$E_k^c = \sum_{i=1}^{n} [K_1(\alpha_1^2\alpha_2^2 + \alpha_2^2\alpha_3^2 + \alpha_3^2\alpha_1^2)]\Delta^3 \tag{8.6}$$

$$E_k^m = \sum_{i=1}^{n} [\mathcal{K}_k\alpha_k^2 + \mathcal{K}_b\alpha_b^2 - \mathcal{K}_u\alpha_{111}^2]\Delta^3 \tag{8.7}$$

The temperature dependence of the magnetocrystalline constants used in the model are shown in Figure 8.2. A transition temperature for T_v of 119 K was chosen. This temperature is slightly lower than the values usually quoted for pure magnetite, *i.e.*, 120-124 K (*e.g.*, Aragón *et al.*, 1985; Gridin *et al.*, 1996; Rozenberg *et al.*, 1996), however this is the measured value for T_v in the papers from which $\mathcal{K}_i$ was taken. It is

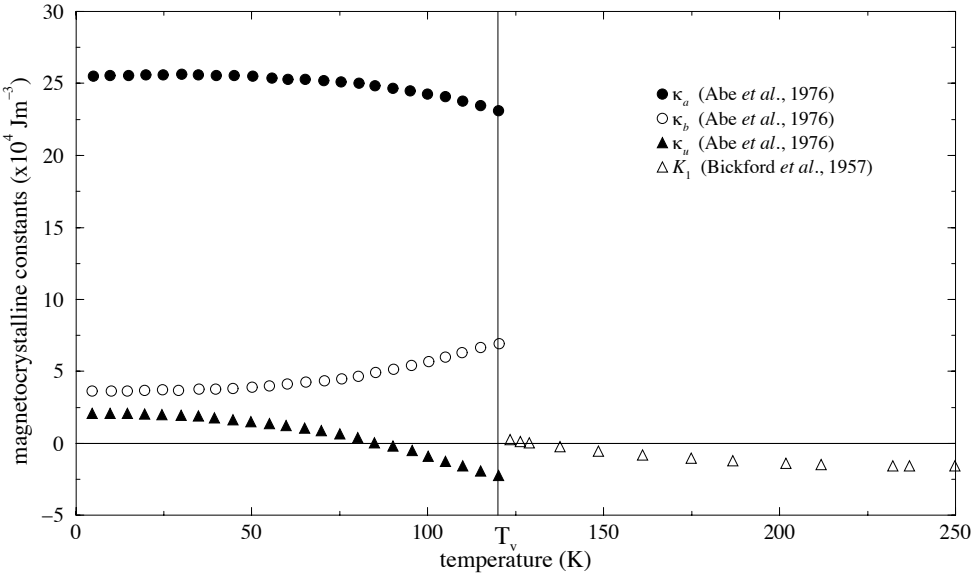


Figure 8.2: Temperature dependence of the magnetocrystalline constants used in the model. $\mathcal{K}_i$ are the low-temperature monoclinic constants (Equation 8.7), whilst K_1 is the cubic constant (Equation 8.6).

possible that the samples used to determine $\mathcal{K}_i$ were not 100 % stoichiometric magnetite, which would reduce the temperature of T_v fractionally. It only takes an oxygen deficiency of ≈ 0.2 % to reduce T_v by ≈ 5 K (Honig, 1995, Figure 5.22).

Following the ideas discussed by Ye *et al.* (1994, Chapters 1 and 5), it should be noted that the magnetocrystalline anisotropy "constants" in Figure 8.2 are not strictly $K_1, \mathcal{K}_i$ but $K_1', \mathcal{K}_i'$, *i.e.*, $K_1, \mathcal{K}_i$ plus a magnetostrictive contribution. However this magnetostrictive contribution is *not* the magnetostrictive anisotropy energy, and should be treated as a small error. In theory it is possible to obtain $K_1, \mathcal{K}_i$ by either direct measurement using ferromagnetic-resonance (FMR) as suggested by Ye *et al.* (1994) or by simply removing the experimentally measured magnetostrictive term from $K_1', \mathcal{K}_i'$ (*e.g.*, Kąkol *et al.*, 1991; Sahu & Moskowitz, 1995). However with regard to FMR, there are very few reports of its use in determining the magnetocrystalline anisotropy constants (Bickford Jr., 1949; 1950), and these few reports only cover the temperature range $T_v < T \leq$ room temperature. The latter method of calculating $K_1, \mathcal{K}_i$ is fraught with errors, because for magnetite the values of the magnetostrictive constants are often smaller than the error in the measurement of $K_1', \mathcal{K}_i'$. It was decided to be consistent across the entire temperature range and use $K_1', \mathcal{K}_i'$ instead of $K_1, \mathcal{K}_i$.

Magnetostrictive anisotropy This term was not included in the model because there are as yet unresolved technical difficulties in incorporating it for spatially independent crystals, *i.e.*, single crystals (*pers. comm.* W. Williams, 1997). Fabian & Heider (1996) have managed to incorporate it in an elastically infinite medium, *i.e.*, for magnetic crystals embedded in an infinitely large rock matrix which has identical elastic parameters to the magnetic crystals. For example, this inability to resolve the boundary

conditions results in an overestimation of the elastic properties of volcanic rocks by approximately 2-3 times.

The significance of its omission can be estimated by considering the characteristic sample size (d_{crit}) above which the magnetostrictive term is thought to dominate the domain structure, given by Fabian *et al.* (1996),

$$d_{crit} = \frac{8\sqrt{A|K_1, \mathcal{K}_a|}}{c_{44}\lambda_{111}^2} \tag{8.8}$$

It is possible calculate d_{crit} as a function of temperature (Figure 8.3). The thermal behaviours of the "constants" used in the calculation of d_{crit} were taken from the following sources; Heider & Williams (1988), Abe *et al.* (1976), Fletcher & O'Reilly (1974), Moskowitz (1993a) and Tsuya *et al.* (Tsuya *et al.*, 1977, Figure 5.21). A is assumed to be constant below zero, and c_{44} constant for all temperatures.

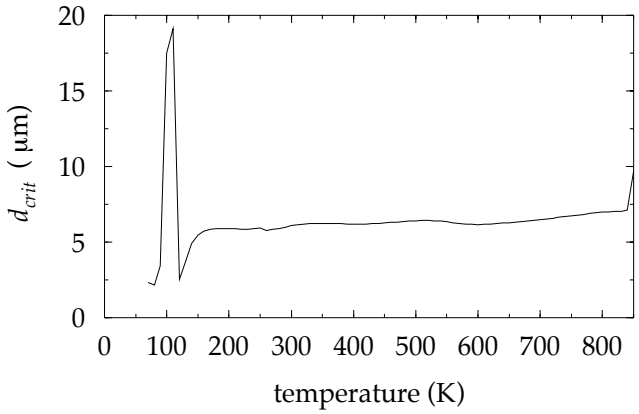


Figure 8.3: d_{crit} plotted as a function of temperature using equation 8.8. Above the line the magnetostrictive self-energy starts to dominate.

It is seen that nowhere in the temperature range of interest in the model does d_{crit} fall significantly below the maximum grain size modelled in this study, *i.e.*, 4 μm. However Figure 8.3 should be treated with *caution* because there are large uncertainties in both $\mathcal{K}_a$ (Figure 5.17) and λ_{111} (Figure 5.21) near T_v, and it is uncertain if this relationship for d_{crit} is valid as $\mathcal{K}_a$ and λ_{111} tend to zero at T_v. For example as λ_{111} tends to zero, the value of λ_{100} becomes significant (Figure 5.21), however λ_{100} has not been included in the calculation of d_{crit}.

Magnetoelastic anisotropy The models in this study were for stress free samples, *i.e.*, no dislocations and no external stress, making the contribution from the magnetoelastic anisotropy zero (Equation 1.24).

The total magnetic energy previously given in Equation 1.12, is simplified for the model to

$$E_{tot} = E_{ex} + E_h + E_d + E_k \tag{8.9}$$

E_{tot} is optimised by the conjugate-gradient method (Press *et al.*, 1986), to give the local energy minimum (LEM) and its domain state. Note that this algorithm does not always find the absolute energy minimum, rather it locates a stable LEM state. However this is in agreement with domain observations which have found that metastable states are common (*e.g.*, Metcalf & Fuller, 1986; Metcalf & Fuller, 1987a; Metcalf & Fuller, 1987b; Halgedahl, 1991, see also Chapter 4).

The magnetisation in each sub-cube represents the averaged magnetisation direction of many hundreds of atomic magnetic dipole moments for which it is assumed that the magnetisation is a continuous vector. This effectively puts a lower limit on the resolution of the model; Δ must be greater than ≈ 0.005 μm (Williams & Wright, 1998). The maximum size of Δ is limited by the complexity of the domain structure modelled. This is because in the calculation of E_{ex}, it is assumed that the angle between neighbouring magnetisation vectors is less than $\approx 15^\circ$. The most complicated structures are expected to be in domain walls, which in magnetite have a typical width of $\approx 0.1 - 0.2$ μm (Williams *et al.*, 1992a; Proksch *et al.*, 1994). For the exchange energy in a domain wall to be correctly calculated, then a sub-cube size of ≈ 0.01 μm should be sufficient to model any domain structure in magnetite. The largest grid which can be readily modelled is $64\times64\times64$ (Wright *et al.*, 1997; Williams & Wright, 1998), which puts an upper limit on the grain size of 0.64 μm. However Williams & Wright (1998) argue that cubic grains above 1.0 μm can still be modelled, provided it is realised that neither the absolute energies or the domain structures are exact. They propose that as long as domain walls are represented by ≈ 4 or more sub-cubes, then the results still reflect the general domain structure, even though there may be differences in the detail. Williams & Wright (1998) present calculations for the domain structure of a 4.0 μm cubic grain using a resolution of $64 \times 64 \times 64$.

Generally the CPU time taken to optimise a domain structure is related to the number of cells within the cube, *e.g.*, a $30\times30\times30$ cube takes approximately $27\times$ longer to optimise than a $10 \times 10 \times 10$ cube depending on initial domain state and complexity of domain structure.

It should be noted that the model does *not* include the the effect of thermal fluctuations, which are thought to be important in determining the domain structure (Dunlop & Özdemir, 1997). Attempts have been made to incorporate an approximation to thermal fluctuations by simulated annealing (Thomson *et al.*, 1994), though this addition consumes vast amounts of computational time, which made its use impractical in this study. However this study is primarily concerned with the magnetic behaviour of remanences below room temperature, where the importance of thermal-fluctuations is greatly reduced. Its exclusion is not expected to be significant at low-temperatures. The only problem may arise in the simulation of thermoremanences, however it is not the intention of the present study

to model the acquisition of thermoremanences. The simulated thermoremanences should only be treated as crude approximations for thermoremanence domain states.

The model of Wright *et al.* (1997) allows for the results from one minimisation to be used as the initial guess of the next, as long as the grid size remains fixed. This makes it possible to simulate variations of temperature, external field and grain size, and hence model rock magnetic properties like hysteresis parameters and chemical remanence acquisition.

The relationship between the model axis (x,y,z), cubic axis phase ([100],[010],[001]) and monoclinic phase axis (a,b,c) is shown in Figure 8.4.

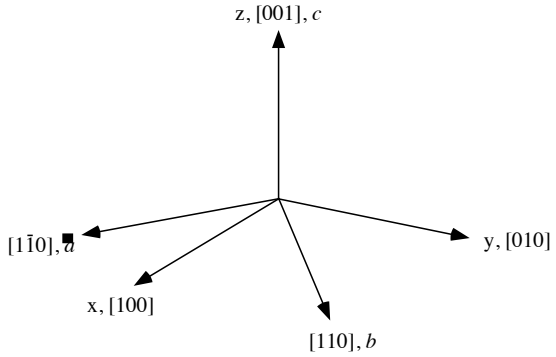


Figure 8.4: The relationship between the model axis (x,y,z), cubic phase axis ([100],[010],[001]) and monoclinic phase axis (a,b,c). In the cubic phase the [111] (and [$\bar{1}$11], [1$\bar{1}$1], [$\bar{1}\bar{1}$1] *etc.*) is the easy axis above 130 K, and the [100] (and [$\bar{1}$00], [001], [0$\bar{1}$1] *etc.*) between T_v and 130 K. In the monoclinic phase the c axis is the easy direction, yet the a axis is much harder than the b axis (Figure 8.2).

8.3 Domain structure in the monoclinic phase of magnetite near the SD/MD transition

In this section the domain structures of small cubic grains of magnetite in the monoclinic phase are examined.

8.3.1 Test for the critical SD size

The large increase in the magnetocrystalline anisotropy on cooling through T_v (Figure 8.2), should be expected to effect the critical single-domain size, d_o (Section 1.5). There are two approaches for estimating d_o; firstly by considering where the domain wall thickness $\rightarrow d_o$ (Néel, 1947), and secondly by calculating where the energies for single-domain and two-domain structures are equal (Kittel, 1949a). The former gives the relationship $d_o \propto \sqrt{1/K_u}$, while the later finds $d_o \propto \sqrt{K_u}$, where K_u is the uniaxial anisotropy. Obviously these two results are contradictory. On the one hand Néel's criteria appears to be more realistic for the cubic phase, as the two-domain structure used in the Kittel approximation

does not exist in micromagnetic models solutions. Micromagnetic models for the cubic phase predict a single domain $\leftrightarrow$ vortex structural transition (Fabian *et al.*, 1996; Williams & Wright, 1998, Figures 8.6a and 8.6b). However the other micromagnetic models calculate d_o by minimising the energy, in a similar manner to the Kittel's criteria.

On cooling to the monoclinic phase of magnetite, the large increase in magnetocrystalline anisotropy decreases the wall width which according Kittel's (1949a) simple approximation is $\propto \sqrt{1/K_u}$. A decrease in wall width would be expected to alter the domain structure. Using Néel's criteria to compare the monoclinic critical domain size d_o^m at 100 K with the cubic critical domain size d_o^c at 300 K, gives $d_o^m \approx (K_1(300K)/\mathcal{K}_i(100K))^{1/2} d_o^c \approx 0.25 d_o^c$. Taking d_o^c to be $\approx 0.07\mu$m at room temperature (Williams & Wright, 1998), gives an estimate for $d_o^m \approx 0.02\mu$m. Similarly, using Kittel's criteria gives $d_o^m \approx 4 d_o^c \approx 0.28\mu$m. It should be noted that these calculations are for uniaxial anisotropy, which the monoclinic phase clearly is not.

Stability of domain structure in the monoclinic phase of magnetite

It was initially intended to calculate the monoclinic SD critical size using a simple procedure described in Fabian *et al.* (1996) and Williams & Wright (1998) to estimate the SD critical size at room temperature, *i.e.*, simply starting with an initial SD/flower state, the grain dimension is increased until a vortex is formed. This is then repeated in reverse, decreasing the grain size until a SD/flower state is energetically favourable. However on application to the monoclinic phase, this approach proved to be unsuccessful because the energy barrier between the SD and vortex/2-domain state is too high for an unconstrained transition to occur, even for very large/small grain sizes. These high energy barriers are reflected by the large coercive forces measured for the monoclinic phase (Belov, 1993; Schmidbauer & Keller, 1996, Figure 5.26).

Instead a constrained model, similar to that described by Enkin & Williams (1994) was used to examine the critical SD grain size. This approach works by constraining two groups of cells on opposing sides of the cube. The two groups of cells are constrained to the angles $\Phi_{y=1}$ and $\Phi_{y=7}$, which are rotated through 360° at some step interval, usually 10-15°. For each angle of $\Phi_{y=1}$ and $\Phi_{y=7}$, the total energy of the domain is minimised with respect to the magnetisation direction of all the other cells, *i.e.*, the directions of all the unconstrained cells magnetic moments are allowed to realign to minimise the total energy, the constrained cells remained fixed during this optimisation to the angles $\Phi_{y=1}$ and $\Phi_{y=7}$. For different orientations of $\Phi_{y=1}$ and $\Phi_{y=7}$, the optimised magnetic energy varies. By plotting the energy of each domain structure for the two degrees of freedom, *i.e.*, $\Phi_{y=1}$ and $\Phi_{y=7}$, it is possible to generate a contour map of the energy surface for $\Phi_{y=7}$ versus $\Phi_{y=1}$.

Working with a resolution of $7 \times 7 \times 7$, Enkin & Williams (1994) constrained two groups of four cells on the top and bottom, *i.e.*, the $z = 1$ and $z = 7$ planes. In the monoclinic phase, constraining cells in the z-plane forces the alignment of the constrained cells

to go through the energetically unfavourable a-axis. To avoid this, cells were constrained in the y plane (the x plane would have equally sufficed), *i.e.,* on the $y = 1$ and the $y = 7$ plane for a $7 \times 7 \times 7$ cubic cell. Unfortunately due to the high energy barriers in the monoclinic phase, it was necessary to constrain 16 cells in each group for the domain structure to display uniform behaviour. The layout of the constrained cells in the four planes $y = 1$, $y = 2$, $y = 6$ and $y = 7$, are shown in Figure 8.5. The layout in the planes $y = 1$ and 7 are identical, similarly for planes $y = 2$ and 6. Eight of the cells were constrained in the $y = 2$ and the $y = 6$ planes. This represents 9.3 % of the total number of cells within the $7 \times 7 \times 7$ model, which is approximately on the upper limit for this type of constrained model (*pers. comm.* W. Williams, 1997).

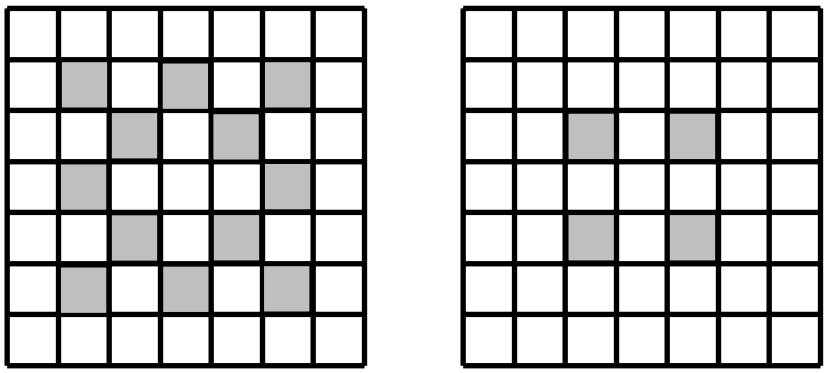


Figure 8.5: Schematic diagram showing the positioning of the constrained cells. The two groups of cells, *i.e.,* $y = 1$ and 2 and $y = 6$ and 7) are constrained to the angles $\Phi_{y=1}$ and $\Phi_{y=7}$ and are rotated through 360° in the y plane.

There are two basic stable LEM states available to the magnetite cubes smaller than 0.3 μm at 110 K;

1. single domain/flower domain (Figure 8.6c).
2. two domain/vortex state structures (Figure 8.6d).

On comparison with similar cubic phase structures (Figure 8.6a and 8.6d), the large increase in the magnetocrystalline anisotropy on cooling through T_v (Figure 8.2), cause the domain structures to rotate towards the z direction. This reduces the flowering in the SD-like state (*cf.* Figures 8.6a and 8.6c), and the monoclinic vortex is closer in appearance to Kittel's (1949a) "classical" two domain structure without closure domains (*cf.* Figures 8.6b, 8.6d and 8.7).

Figure 8.8 shows the energy for the two possible LEM states for the monoclinic phase of magnetite at 110 K as a function of grain size. Energy surfaces at 110 K for grain sizes

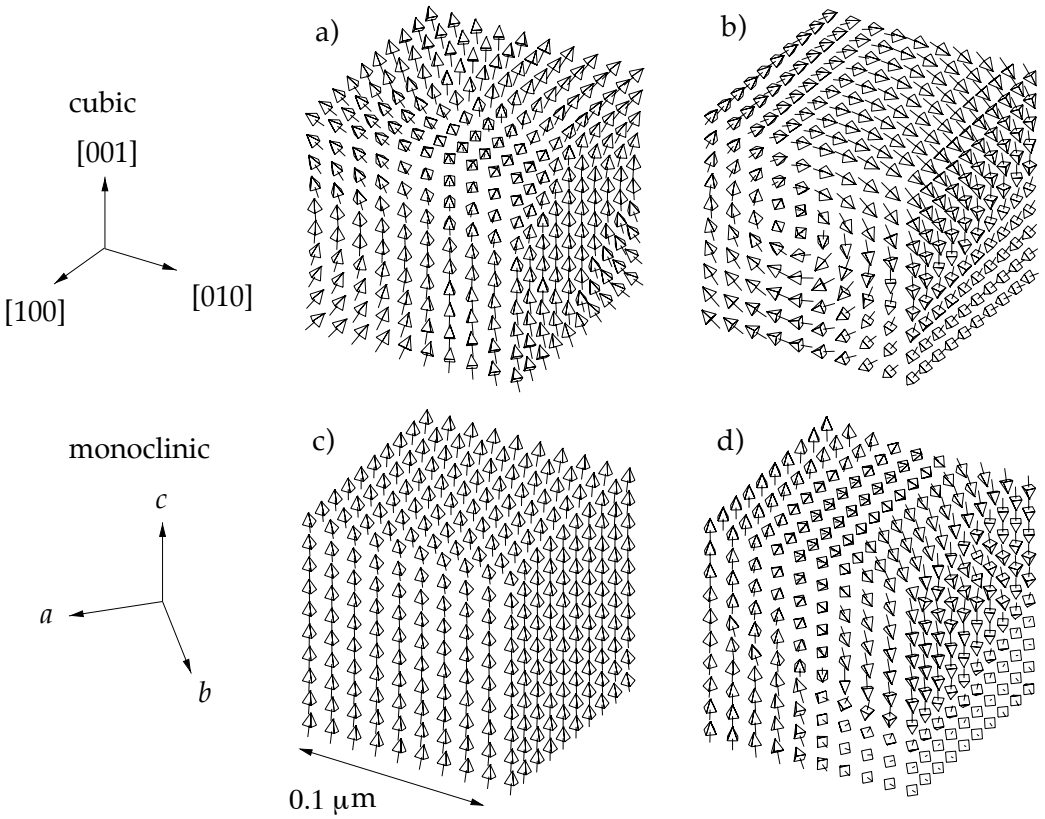


Figure 8.6: The two types of LEM states that can exist for cubic grains of size 0.10 μm in both the cubic phase (a & b) and the monoclinic phase (c & d). For the cubic phase at 300 K a) flower state, where the magnetisation flowers out at the grain surface, and b) vortex tate, where the magnetisation curls around a central core. And for the monoclinic phase at 110 K c) SD/flower state, with greatly reduced flowering compared to the cubic phase flower state, and d) two-domain/vortex state, which has greatly reduced curl compared to the cubic phase vortex state. The monoclinic vortex phase resembles Kittel's (1949a) "classical" two domain structure (Figure 8.7).

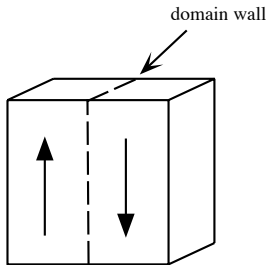


Figure 8.7: Kittel's (1949a) "classical" model of a two domain grain without closure domains. Shown previously in Figure 1.9b.

0.08 μm to 0.3 μm are shown in Figures 8.9–8.13. The energy surfaces correspond to the domain structure after minimisation of the unconstrained cells. Each calculation is independent of each other. Ideally it would have been more appropriate to follow the technique of Enkin & Williams (1994), who used the solution from one set of constrained angles as the initial starting solution for the next set, *e.g.*, the final solution from ($\Phi_{y=1} = 15^\circ$, $\Phi_{y=7} = 30^\circ$) is used as the initial solution for ($\Phi_{y=1} = 15^\circ$, $\Phi_{y=7} = 45^\circ$). However due to the high mag-

netocrystalline anisotropy, the unconstrained cells rotated less quickly than the constrained ones, until they were antiparallel to local constrained cells. Obviously this was incorrect. In an attempt to resolve this problem and to obtain homogeneous domain structures, half of the unconstrained cells were initially aligned parallel to $\Phi_{y=1}$, and the other half to the cells $\Phi_{y=7}$.

As a comparison the energy surface for a 0.06 μm cube of magnetite at 300 K, *i.e.*, in the cubic phase, is shown in Figure 8.14. A cube edge of 0.06 μm is just below $d_o^c \approx 0.07$ μm at 300 K (Enkin & Williams, 1994; Williams & Wright, 1998). Figure 8.14 compares reasonably well with identical energy surfaces published by Enkin & Williams (1994)

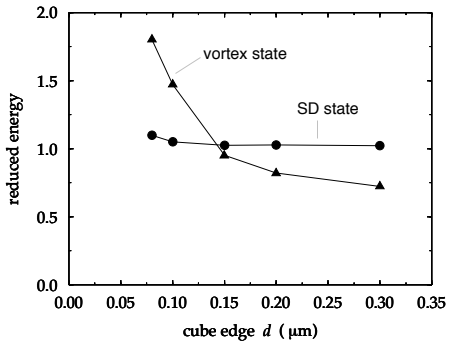


Figure 8.8: The reduced energy of LEM states as a function of grain size at 110 K, where the reduced energy is the total energy normalised by the energy of a cube uniformly magnetised along the easy axis. The line marked "SD" corresponds to the SD/flower state, and the line marked "vortex" corresponds to the vortex/2-domain LEM state. The critical size of a transition from single domain (Figure 8.6c) to 2 domain/vortex structure (Figure 8.6d), occurs at ≈ 0.14 μm. Because of the high energy barriers between the two possible states (Figures 8.9– 8.13), there is a wide range of grain sizes over which the two domain states can co-exist.

From Figures 8.8-8.13, it can be seen that for a grain of dimension 0.1 μm at 110 K, the SD/flower state is energetically the most favourable state. However for a grain size of 0.15 μm the 2-domain/vortex state is slightly more favourable, and on increasing to 0.2 μm its energy decreases further. In the monoclinic phase the energy barriers to be surmounted on swapping between antiparallel SD/flower states or between SD/flower states and 2-domain/vortex states are larger than those found in the cubic phase of magnetite (*cf.* Figures 8.9–8.13 and Figure 8.14). For example consider two domain structures just below d_o; in the cubic phase the maximum reduced energy barrier to be overcome on switching between antiparallel domain states is ≈ 0.2 (Figure 8.14), whilst in the monoclinic phase a reduced energy barrier of ≈ 1.1 has to be overcome (Figure 8.10).

The deep LEM potential wells, was the cause of the difficulty in determining d_o^m using the method of Williams & Wright (1998). This resistance to changes in the domain structure can be inferred from the three fold increase in the coercive force observed on cooling through T_v (Schmidbauer & Keller, 1996, Section 5.7.2).

The monoclinic phase has LEM SD states at $\Phi_{y=1} = 0\,^\circ$, $\Phi_{y=7} = 0\,^\circ$, and the cubic phase at $\Phi_{y=1} = 45^\circ$ $\Phi_{y=7} = 45^\circ$, and there are similar differences for the orientation of the vortex

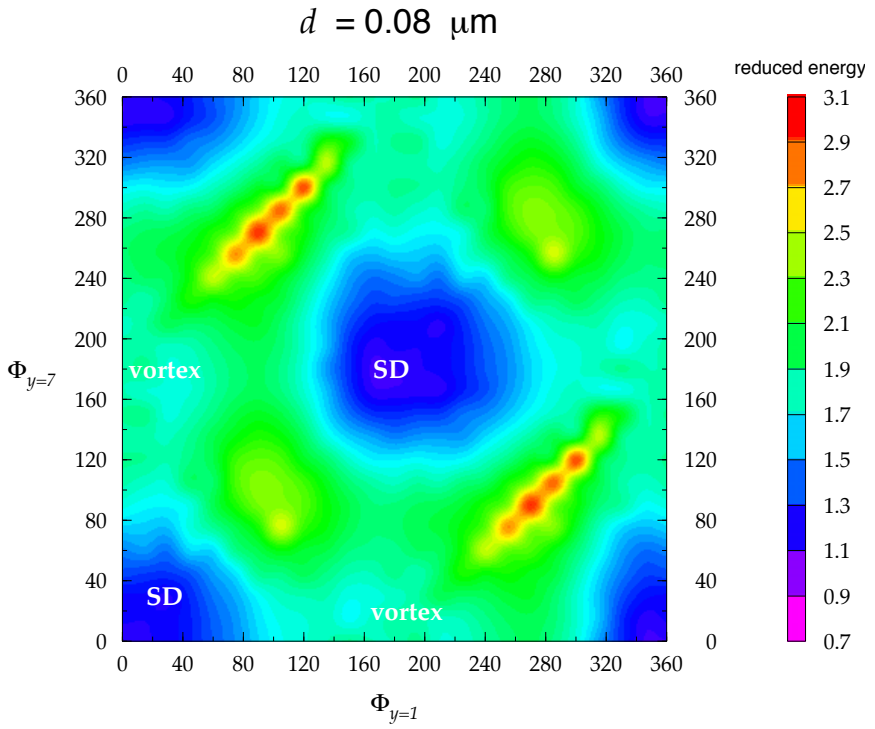


Figure 8.9: Energy surfaces for 0.08 μm cube of magnetite in the monoclinic phase at 110 K. The favourable SD ($\Phi_{y=1} = \Phi_{y=7}$) and vortex ($\Phi_{y=1} = 180° + \Phi_{y=7}$) states are marked. The model used a resolution of $7 \times 7 \times 7$.

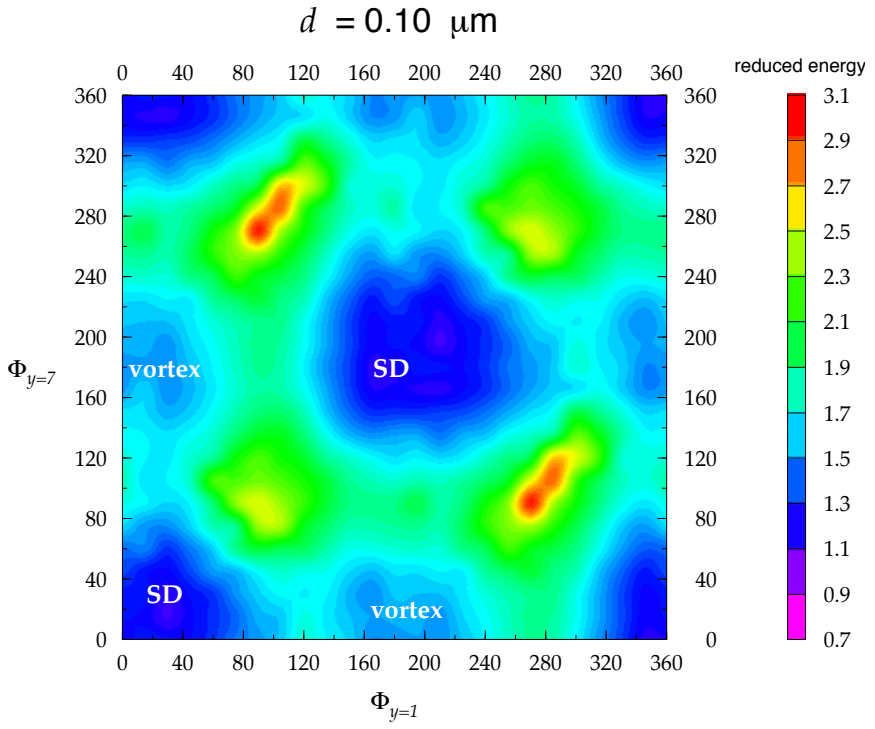


Figure 8.10: Energy surfaces for 0.1 μm cube of magnetite in the monoclinic phase at 110 K. The favourable SD ($\Phi_{y=1} = \Phi_{y=7}$) and vortex ($\Phi_{y=1} = 180° + \Phi_{y=7}$) states are marked. The model used a resolution of $7 \times 7 \times 7$.

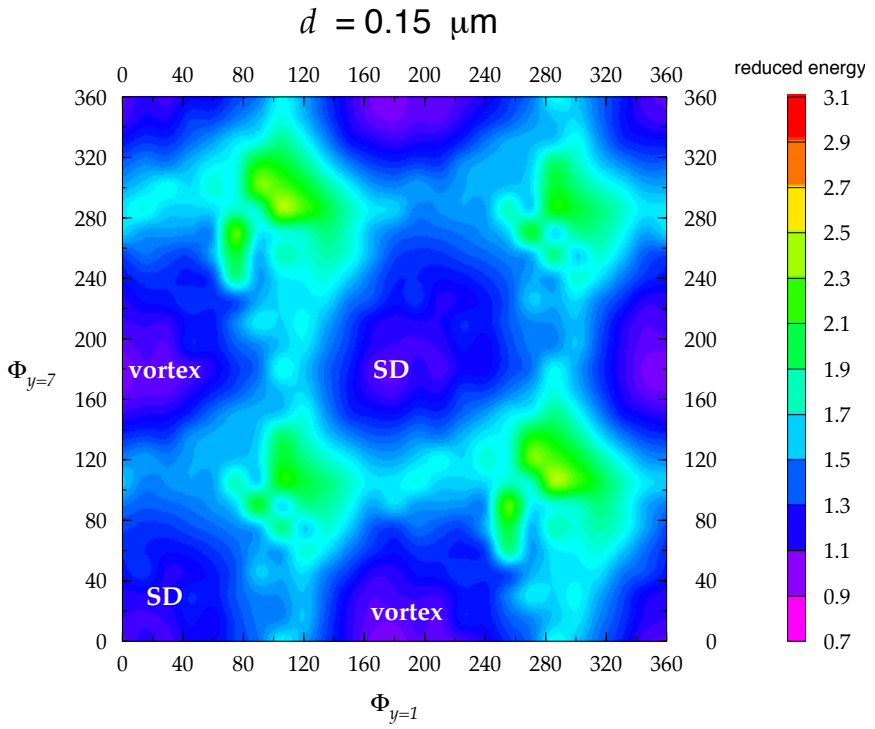


Figure 8.11: Energy surfaces for 0.15 μm cube of magnetite in the monoclinic phase at 110 K. The favourable SD ($\Phi_{y=1} = \Phi_{y=7}$) and vortex ($\Phi_{y=1} = 180° + \Phi_{y=7}$) states are marked. The model used a resolution of $7 \times 7 \times 7$.

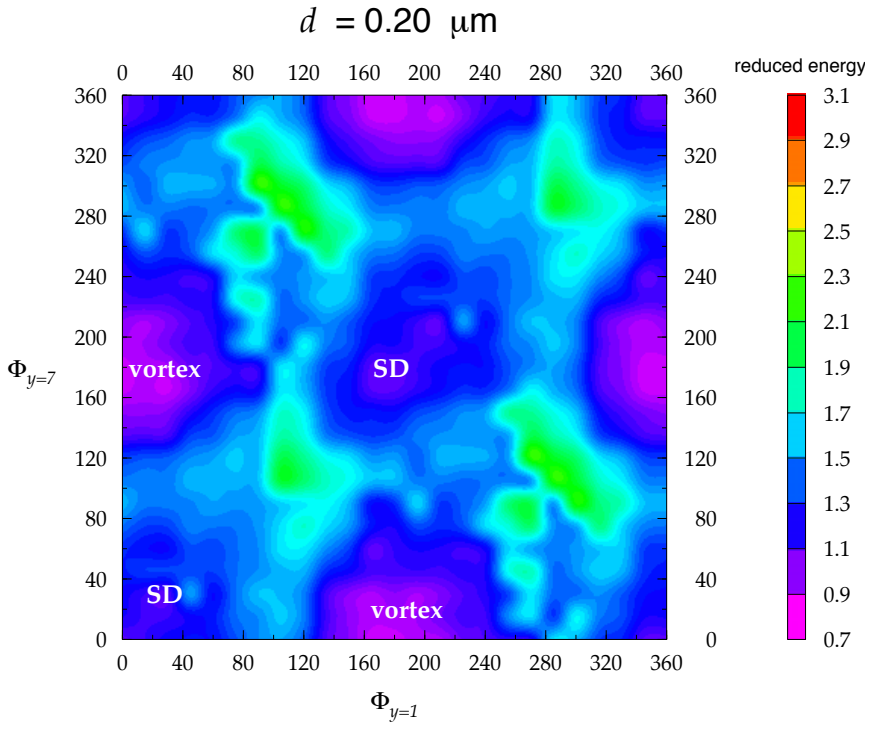


Figure 8.12: Energy surfaces for 0.20 μm cube of magnetite in the monoclinic phase at 110 K. The favourable SD ($\Phi_{y=1} = \Phi_{y=7}$) and vortex ($\Phi_{y=1} = 180° + \Phi_{y=7}$) states are marked. The model used a resolution of $7 \times 7 \times 7$.

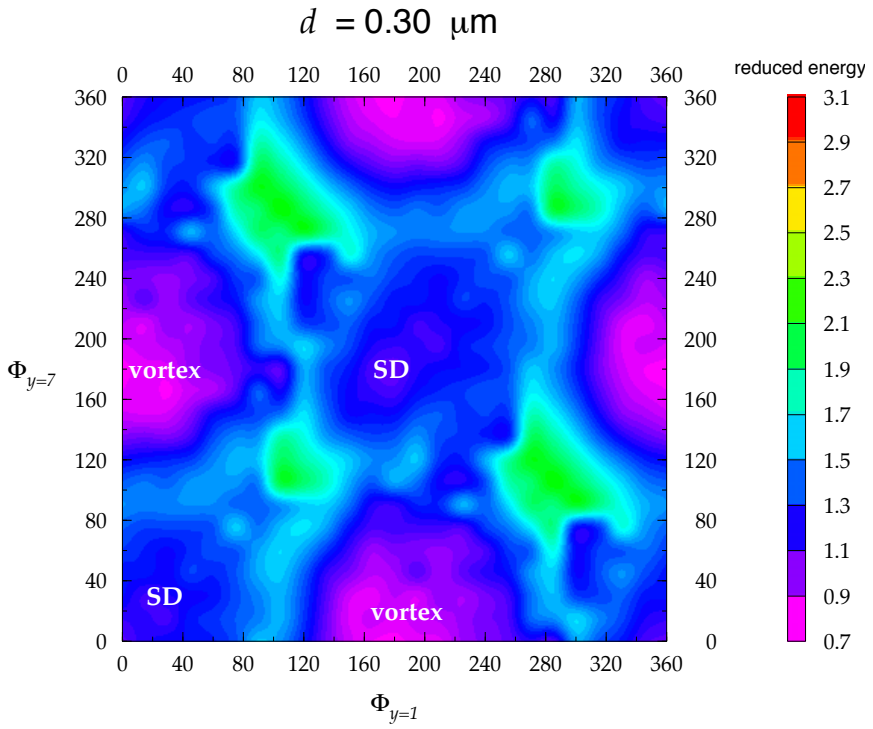


Figure 8.13: Energy surfaces for 0.30 μm cube of magnetite in the monoclinic phase at 110 K. The favourable SD ($\Phi_{y=1} = \Phi_{y=7}$) and vortex ($\Phi_{y=1} = 180° + \Phi_{y=7}$) states are marked. The model used a resolution of $7 \times 7 \times 7$.

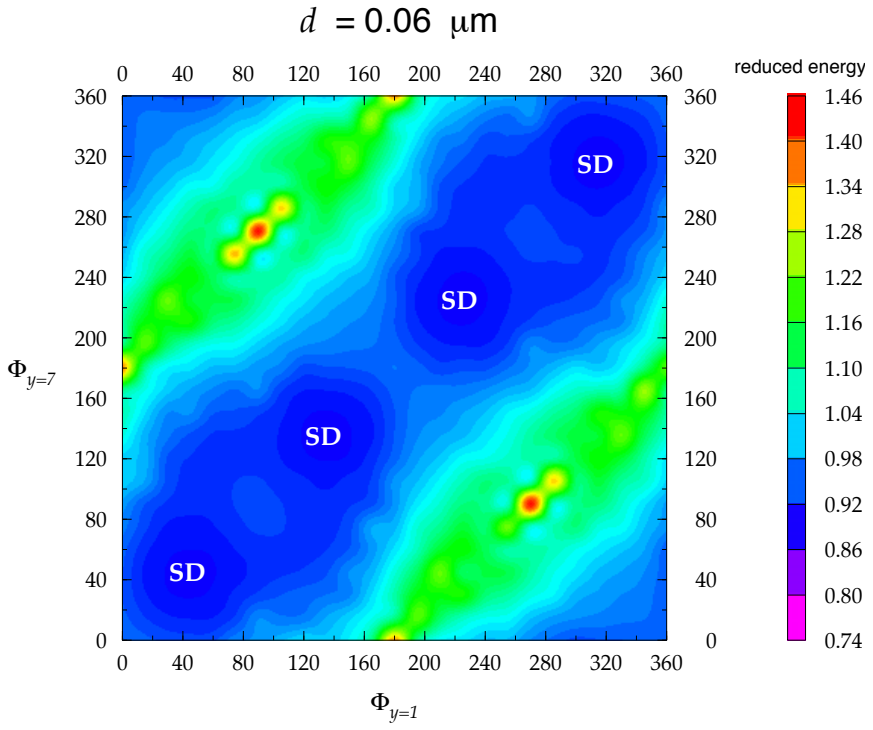


Figure 8.14: Energy surfaces for 0.06 μm cube of magnetite in the cubic phase at 300 K. 0.06 μm is just below the d_o^c ($\approx$ 0.07 μm). The LEM potential wells are much shallower than those observed for the monoclinic magnetite grains of similar sizes, *cf.* Figures 8.9–8.13. The favourable SD states are marked. The model used a resolution of $7 \times 7 \times 7$.

LEM states. This is due to the preferred magnetocrystalline anisotropy easy axis in the cubic and monoclinic phase.

The transition from SD $\leftrightarrow$ 2-domain/vortex occurs at $\approx 0.14\mu$m, and is much closer to the Kittel's (1949a) estimate of 0.28 μm, than to Néel's (1949) of 0.02 μm. This can be partially explained by examining the domain structure of 0.1 μm grain in both the SD/flower-state and the 2-domain/vortex at both 110 K and 300 K (Figure 8.6). The SD/flower state has less flowering at 110 K that at 300 K, and on cooling the vortex state from 300 K to 110 K, the energy is minimised by the magnetisation aligning in the easy *c*-direction, producing a relatively thin "domain wall". Both the SD and 2-domain/vortex structures in the monoclinic phase are close in appearance to the "classic domain" structures described by Kittel (1949a, see also Figure 1.9) and used in his calculation for d_o. It should be noted that both Kittel's and Néel's predictions were for a uniaxial symmetry which the monoclinic phase is not.

In conclusion, on cooling through the Verwey transition the SD-critical size increases from 0.07 μm to 0.14 μm. However the high resistance to changes in the domain structure in the monoclinic phase means that it is unlikely that grains already in vortex states will denucleate domain walls to become SD.

8.3.2 Orientation of magnetic moments in vortex structures in the monoclinic phase

The nature of the monoclinic magnetocrystalline anisotropy differs considerably from the cubic phase, which has been modelled many times (*e.g.*, Williams & Dunlop, 1989; Williams & Dunlop, 1990). On cooling through the Verwey transition the intensity of the magnetocrystalline anisotropy increases sharply (Figure 8.2), and the symmetry changes. The monoclinic phase has one very hard direction *i.e.,* the *a*-direction (Figure 5.20). Because of the high anisotropy the magnetic moments align in the *a*-plane, *i.e.,* away from the *a*-axis, at all times, even in domain walls and in the centre of vortex structures. For example in the cubic phase at room temperature, the surface moments of a vortex structure in a 0.1 μm grain align along the direction of the grain boundaries (Figure 8.15a), however on cooling to below room temperature the surface moments which were partially aligned in the *a*-direction in the cubic phase (Figure 8.15a), rotate into the *a*-plane in the monoclinic phase, *i.e.,* away from the hard *a*-axis (Figure 8.15b).

8.4 Simulated low-temperature cycling of remanences

The behaviour of different kinds of remanence (SIRM and thermoremanences) to low-temperature cycling was modelled in grains in the size range 0.1–0.6 μm. These models simulated the low-temperature experiments reported in Chapter 6.

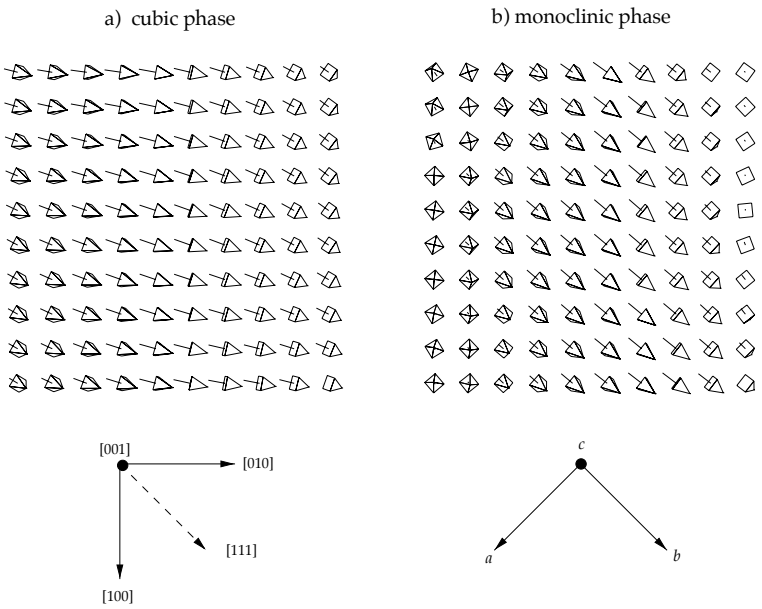


Figure 8.15: The surface z plane of vortex structure in a 0.1 μm grain at a resolution of $10 \times 10 \times 10$ in a) cubic phase (300 K) and b) monoclinic (110 K). In the monoclinic phase the domain walls are orientated away from the *a*-axis towards the *b*-axis.

The importance of the initial orientation of remanence during simulated low-temperature cycling is considered in Section 8.4.1 where SIRM is simulated in different directions.

Two different orientations of SIRM were modelled in cubic grains at room temperature, by simulating a saturating field of 2 T in the direction of both the x-axis (SIRM$_x$) and z-axis (SIRM$_z$). The SIRMs were modelled, by optimising the domain structure in field, followed by optimisation of the same domain structure in zero-field at the same temperature. To simulate the low-temperature cycling the domain structure was optimised at 20 K intervals in zero-field down to 150 K, and then in smaller steps to 70 K with domain structure optimisation as frequent as every 2 K near T_v. On subsequent simulated warming, the temperature steps followed the same pattern of as the cooling temperature steps, but reversed.

Low-temperature cycling of thermoremanence was modelled in a similar manner to SIRM, *i.e.,* the domain structure was optimised at regular temperature intervals during simulated cooling from T_c to 70 K, with a field applied between appropriate temperatures (Section 8.4.2). The temperature sequence used for SIRM was repeated for thermoremanences. All the temperature steps above 150 K being of 20 K. It was not the intention of this study to model the domain structure of thermoremanences during acquisition, because the algorithm did not include the effect of thermal fluctuations. Instead it was hoped that the modelled thermoremanence domain structures approximated to real thermoremanences. However because the grain size under consideration, *i.e.,* $\leq$ 0.6 μm, is less than the lower limit of domain observation (see Section 4.1.1), then only the low-temperature behaviour of magnetic remanence) can be used as a comparison (Chapter 6).

Two types of thermoremanences were simulated in the model (previously defined in Chapter 4 and 6);

Type 1 The samples are cooled from above T_c to T_2 in a field, where room temperature, rtp $< T_2 < T_c$ ($T_c \downarrow T_2$, $\mathbf{H_e}$ = ON; $pTRM^{T_c}_{T_2}$).

Type 2 This type of thermoremanence is simulated by cooling from T_c to a temperature T_1 in zero field, and from T_1 to T_2 in a field, where rtp $< T_2 < T_1 < T_c$ ($T_c \downarrow T_1$, $\mathbf{H_e}$ = OFF; $T_1 \downarrow T_2$, H=ON; $pTRM^{T_1}_{T_2}$).

In both cases the inducing field $\mathbf{H_e}$ was in the x-axis direction with an intensity of 50 μT. The 0.1 μm cubes were modelled using a $20 \times 20 \times 20$ resolution, whilst the 0.3 μm and 0.6 μm cubes with a resolution of $30 \times 30 \times 30$.

8.4.1 Solutions for $SIRM_x$ and $SIRM_z$

0.1 μm cubic grains

The initial room temperature SIRM domain structure for 0.1 μm cubes of magnetite is a flower state, with the moment aligned in the direction of the applied field. $SIRM_x$ and $SIRM_z$ are identical apart from orientation (*cf.* Figures 8.16a and 8.17a), with a reduced remanent magnetisation at 270 K of 0.92 % (Table 8.1). The reduced magnetisation is the magnetisation of the modelled grain (M) normalised by the magnetisation of a cube uniformly magnetised along the easy axis (M_{SD}), *i.e.*, for a "perfect" SD grain with its moment aligned along the easy axis the $M/M_{SD} = 1$.

On cooling through the Verwey transition the domain structure of the $SIRM_z$ remains aligned in the z-axis (Figures 8.17b), whilst the entire domain structure of the $SIRM_x$ rotates so that the net moment is 8° from the z axis (Figure 8.16b). The small horizontal component of the $SIRM_x$ moment is aligned at an angle $\phi = 224°$, *i.e.*, in direction of the monoclinic b axis (Figure 8.4). Unfortunately it is difficult to see this 8° in deviation θ in Figure 8.16b. In both cases there is a reduction in flowering of the domain structure; the reduced remanent magnetisation at 117 K increases to 0.94 for $SIRM_z$ and 0.96 $SIRM_x$ (Table 8.1). On warming to room temperature, $SIRM_z$ (Figure 8.16c) remains aligned in the direction of the z-axis, whilst $SIRM_x$ rotates further towards the z-axis, reducing the offset to less than 3° (Figure 8.16c). The degree of flowering returns to its initial value of 0.92 for both cases.

It can be concluded that the net effect of the low-temperature cycling of SIRM in 0.1 μm cubic grains is to align the magnetic moment in the direction of the monoclinic c-axis (z-axis), and destroying fraction of the remanence carried by grains whose magnetisation was not aligned in the z-axis.

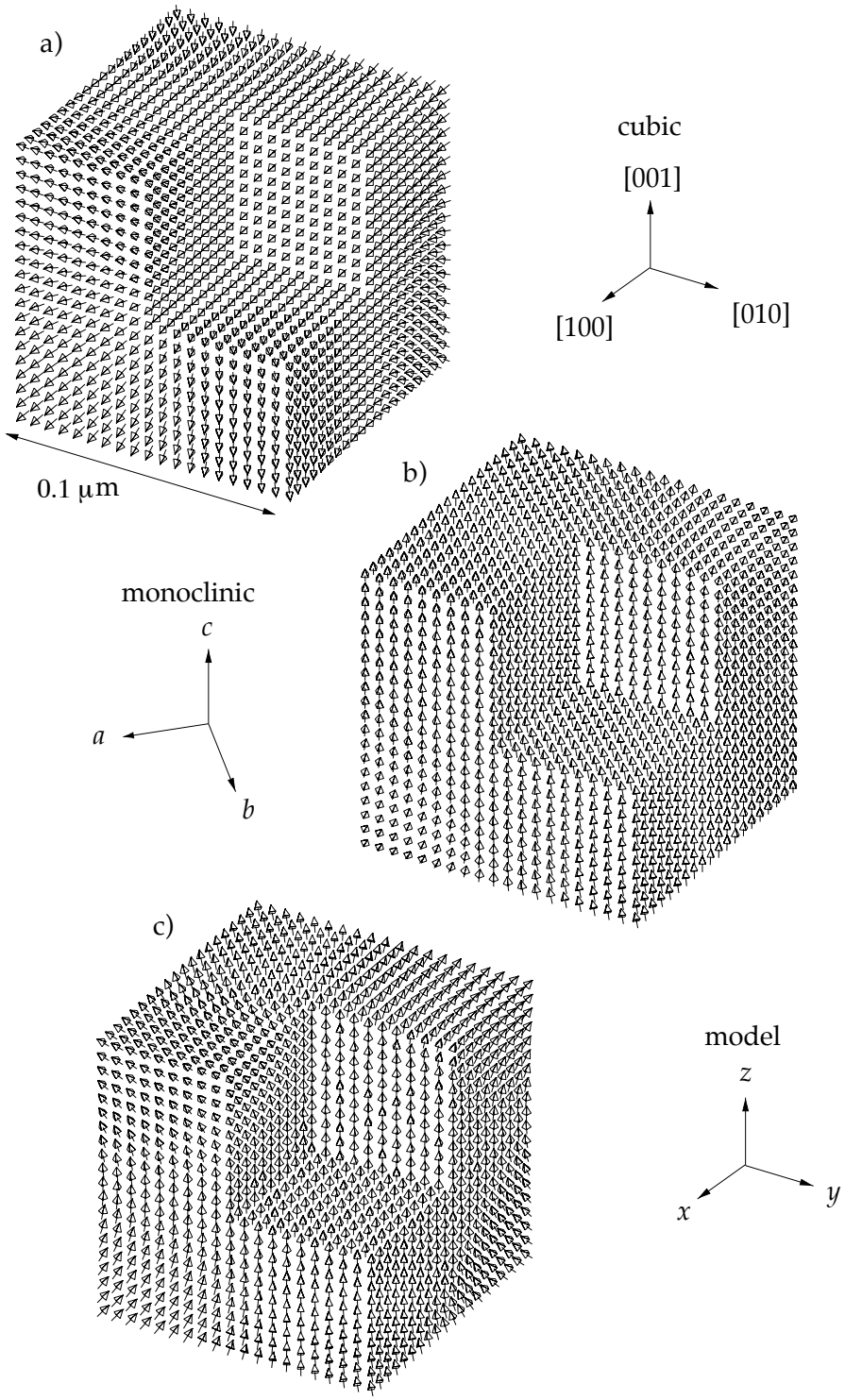


Figure 8.16: Domain structure of a 0.1 μm cubic grain with a simulated SIRM$_x$ a) before simulated cooling at 270 K, b) in the monoclinic phase after cooling to 117 K, and c) at 270 K after simulated low-temperature cycling. To model the SIRM$_x$ a field of 2 T was applied in the x direction.

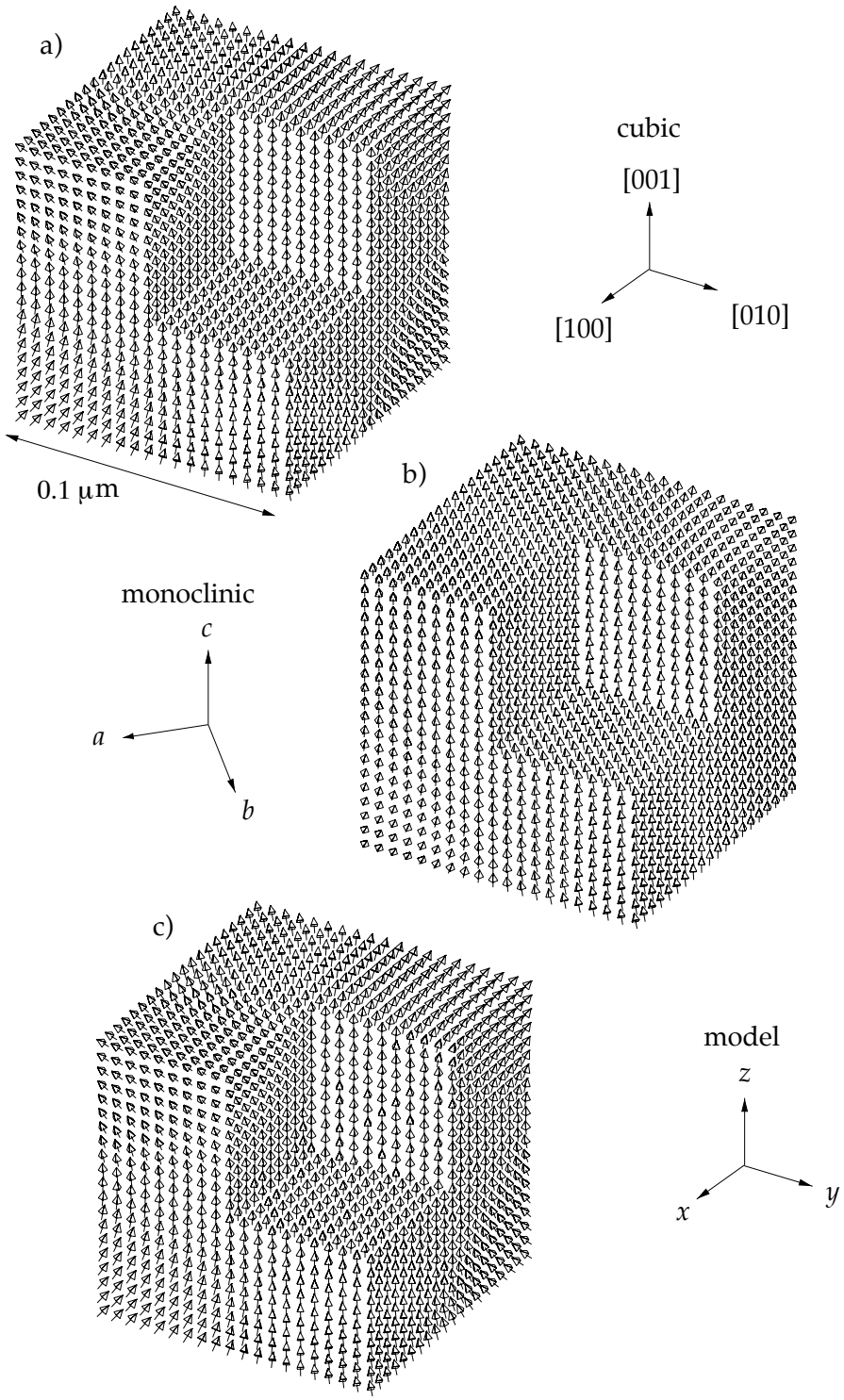


Figure 8.17: Domain structure of a 0.1 μm cubic grain with a simulated SIRM$_z$ a) before simulated cooling at 270 K, b) in the monoclinic phase after cooling to 117 K, and c) at 270 K after simulated low-temperature cycling. To simulate the SIRM$_z$ a field of 2 T was applied in the z direction.

treatment	0.1 μm		0.3 μm		0.6 μm	
	M/M_{SD}	θ, ϕ	M/M_{SD}	θ, ϕ	M/M_{SD}	θ, ϕ
			SIRM$_x$			
initial	0.92	90°, 0°	0.09	92°, 355°	0.01	90°, 5°
monoclinic	0.96	8°, 224°	0.25	54°, 355°	0.27	44°, 359°
memory	0.92	3°, 225°	0.04	95°, 6°	0.01	76°, 357°
			SIRM$_z$			
initial	0.92	0°, 0°	0.17	5°, 1°	0.01	0°, 347°
monoclinic	0.94	3°, 1°	0.24	24°, 191°	0.06	37°, 166°
memory	0.92	1°, 1°	0.01	6°,198°	0.01	2°, 165°

Table 8.1: Intensity and direction of reduced SIRM$_x$ and SIRM$_z$ during simulated low-temperature cycling for three grain sizes; 0.1 μm, 0.3 μm and 0.6 μm. "Initial" is the reduced SIRM at 270 K before simulated cooling, "monoclinic" the reduced SIRM at 117 K in the monoclinic phase of magnetite after simulated cooling from room temperature, and "memory" is the reduced SIRM remaining at 270 K after simulated low-temperature cycling.

0.3 μm cubic grains

For 0.3 μm cubic grains carrying induced SIRM$_x$ and SIRM$_z$, the initial domain structure consisted of central body domain with four large domains towards at each corner which can be thought of as *very* large closure domains (Figure 8.18). The central body domain is partially aligned in the direction of the easy axis, *i.e.,* [111]. For some unknown reason the reduced magnetisation of the SIRM$_x$ is half the intensity of SIRM$_z$ (Table 8.1). The net magnetisation of both SIRMs is misaligned from the inducing field by $\leq 5°$.

On cooling from room temperature, the basic domain structure remains; there is only a small increase in the size of the large closure domains. The net magnetisation and its orientation do not alter significantly. The domain structure and magnetisation are relatively unaffected by T_k, however on cooling through T_v there is a sudden change in the structure. Due to the large increase in the magnetocrystalline anisotropy (Figure 8.2), the magnetic moments align themselves either in the c (model z) direction or the b (cubic [110]) direction, *i.e.,* in the a plane, which causes the large changes to the domain structure. The body domain of the initial SIRM$_z$ is aligned near the c direction, and is therefore unaffected by cooling through the Verwey transition. However the large closure domains and the structures surrounding them become energetically unstable (Figure 8.20). The magnetic moments near the closure domains rotate to align in the a-plane, reducing the size of the closure domains. The reduced efficiency of the closure domain and the rotation of magnetic vectors away from the direction of the a-axis, causes the net magnetisation to increase and to lie close to or in the a-plane (Table 8.1).

Compared to SIRM$_z$, the effect of cooling an SIRM$_x$ domain structure through the Verwey transition is far greater (*cf.* Figures 8.19 and 8.20). This is because the central body domain in the cubic phase, is aligned at only 45° from the hard a-axis. On cooling through the Verwey transition the the main body domain rotates towards the c axis, in a similar manner to 0.1 μm SIRM$_x$ (Figure 8.16). The closure domains similarly rotate, and the net

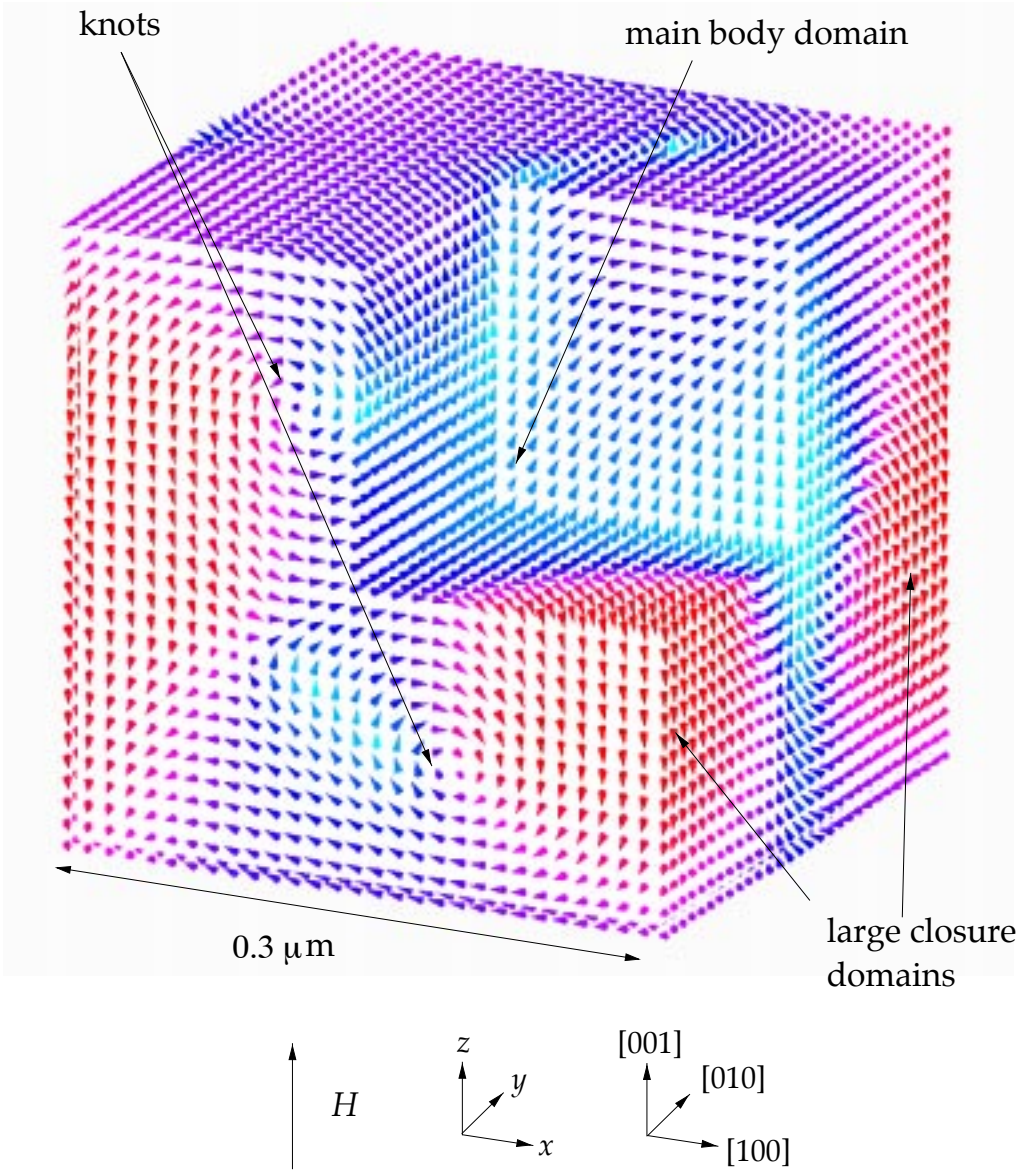


Figure 8.18: The domain structure of 0.3μm cubic grain of induced with SIRM$_z$ at 270 K. The model resolution is $30 \times 30 \times 30$. There is one well defined body domain, with large closure domains at each corner. Associated with the closure domains are are vortex-like "knots". The domain structure of SIRM$_x$ is similar apart from orientation. The direction of the inducing field is marked.

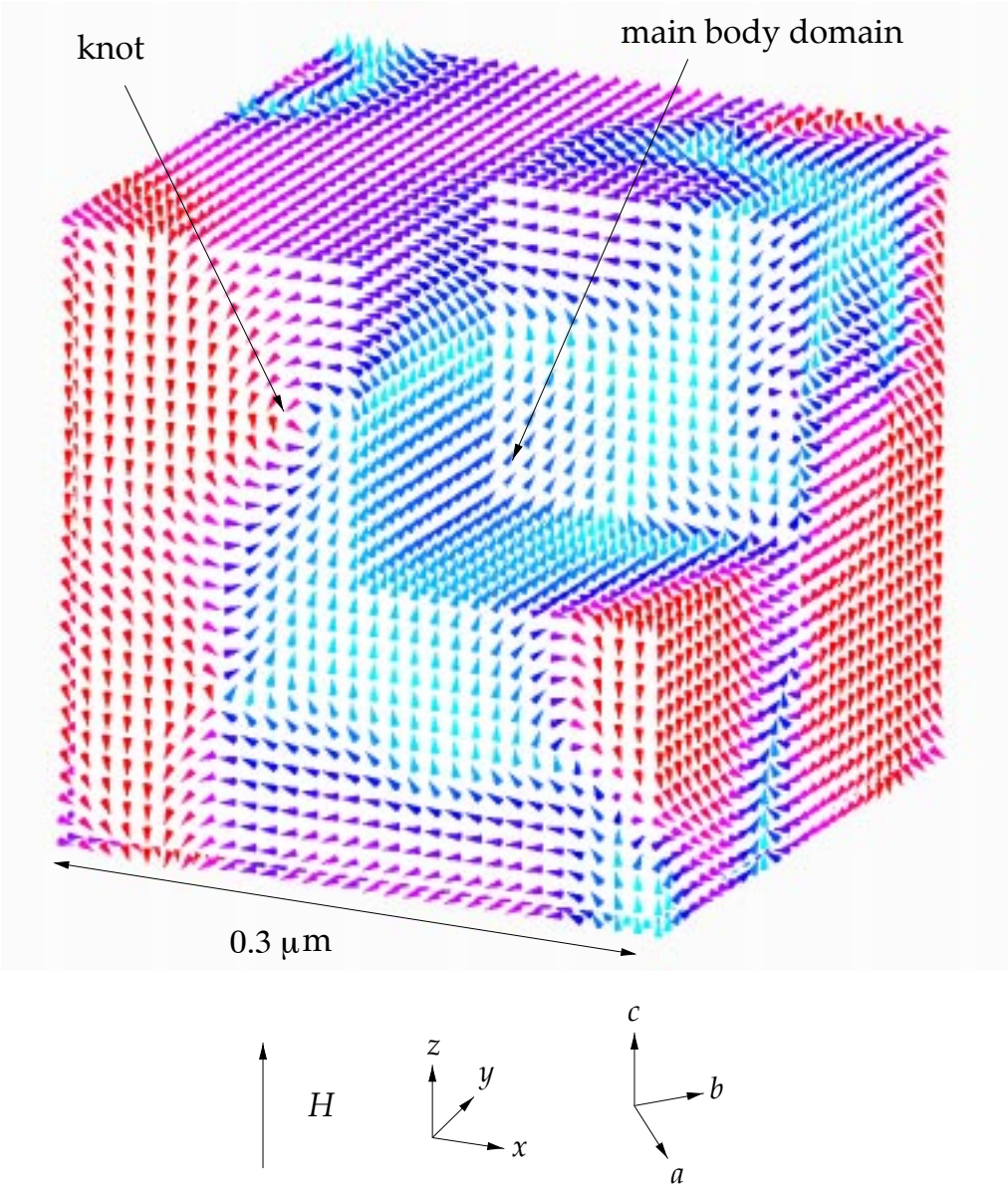


Figure 8.19: The domain structure of 0.3μm cubic grain of magnetite at 117 K, induced with a SIRM$_z$ at 270 K. The model resolution is 30 $\times$ 30 $\times$ 30. On cooling through T$_v$, the large increase in the magnetocrystalline anisotropy forcing the magnetic vectors to lie in the *a* plane. The central body domain survives cooling through T$_v$, however the closure domains are strongly effected. The direction of the inducing field is shown.

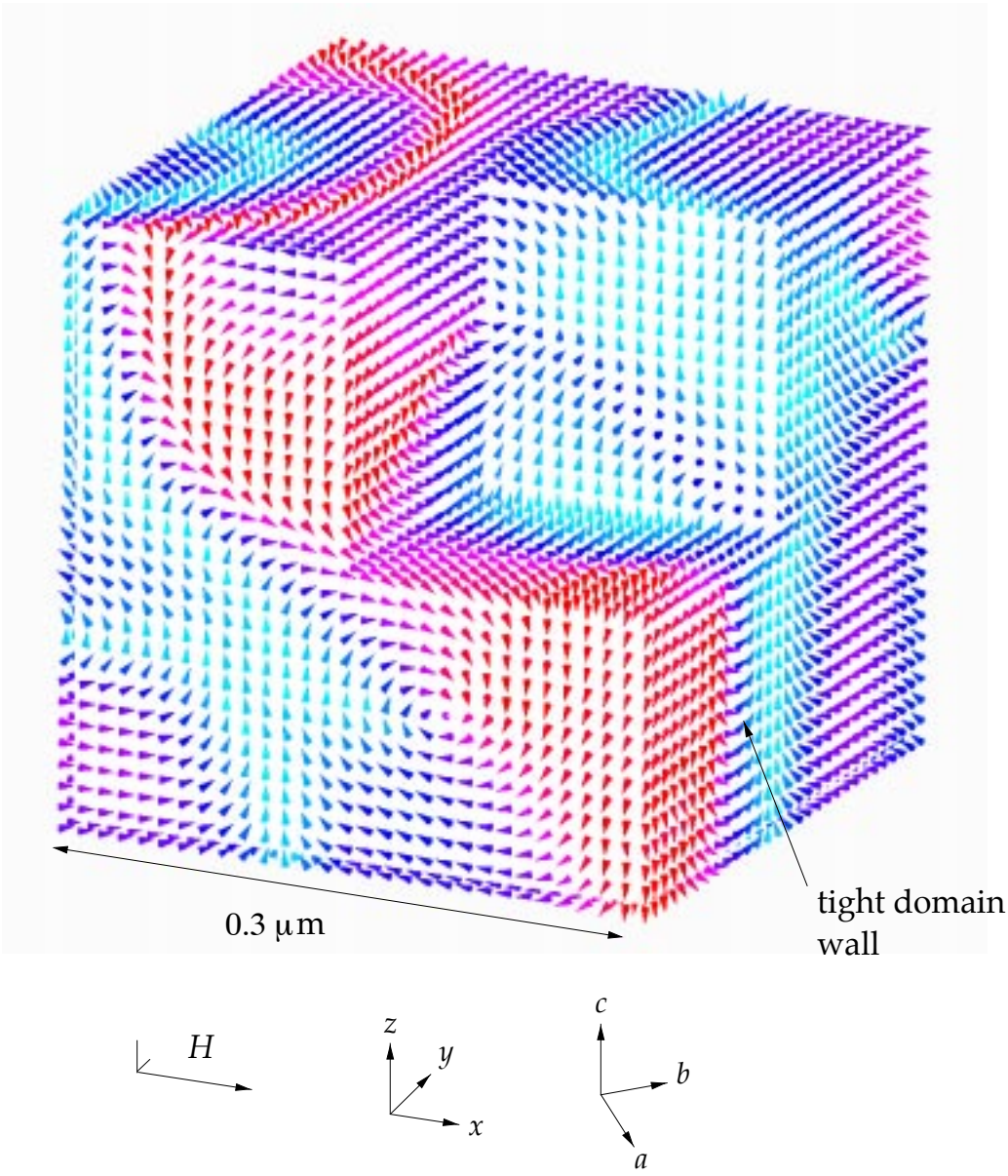


Figure 8.20: The domain structure of 0.3μm cubic grain of magnetite at 117 K, induced with a SIRM$_x$ at 270 K. The model resolution is $30 \times 30 \times 30$. On cooling through T_v, the large increase in the magnetocrystalline anisotropy causes the magnetic vectors to lie in the a plane, and the magnetisation becomes more multidomain like

magnetisation is aligned at 54° from the *c,z* axis (Table 8.1). The structure becomes more multidomain-like (Figure 8.19).

For both SIRM$_x$ and SIRM$_z$ in the monoclinic phase, the closure domains partially join to give the domain structure an appearance similar to Kittel's (1949) classic three domain structure (Figure 8.21). The SIRM$_x$ structure is angled at $\theta = 54^\circ$ whilst SIRM$_z$ at $\theta = 24^\circ$ (Table 8.1).

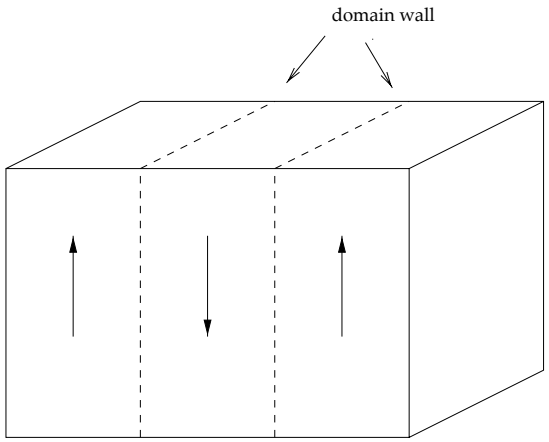


Figure 8.21: Kittel's (1949) "classical" model of a three domain grain without closure domains.

On warming back through T$_v$, SIRM$_z$ forms a "double vortex" structure, *i.e.*, two vortices at either end of the grain rotating in opposite directions (Figure 8.22). Similar double vortices have been reported for elongated grains (Fabian *et al.*, 1996). The domain structure has a low-magnetic flux leakage, and the net magnetisation is reduced. However the net magnetisation still has a "memory" of its original orientation and rotates back towards its initial direction (Table 8.1).

The SIRM$_x$ forms a single vortex structure, yet the central vortex path does not pass from one side of the grain to the other, *e.g.*, a (001) plane to a (002) plane, rather it travels from a (010) plane to a (001) plane (Figure 8.23). The net magnetisation is greatly reduced due to the vortex structure, however it partially realigns itself with the initial direction (Table 8.1).

0.6 μm cubic grains

This was the largest grain size examined during simulated low-temperature cycling, because below T$_v$ the domain structure is very multidomain making it on the upper limit for a model resolution of $30 \times 30 \times 30$.

The initial remanences SIRM$_x$ and SIRM$_z$ both have simple domain structures which are slightly more complicated than vortex structure shown in Figure 8.6c. The initial reduced remanences are of the order 0.01 (Table 8.1), which is in agreement with the results

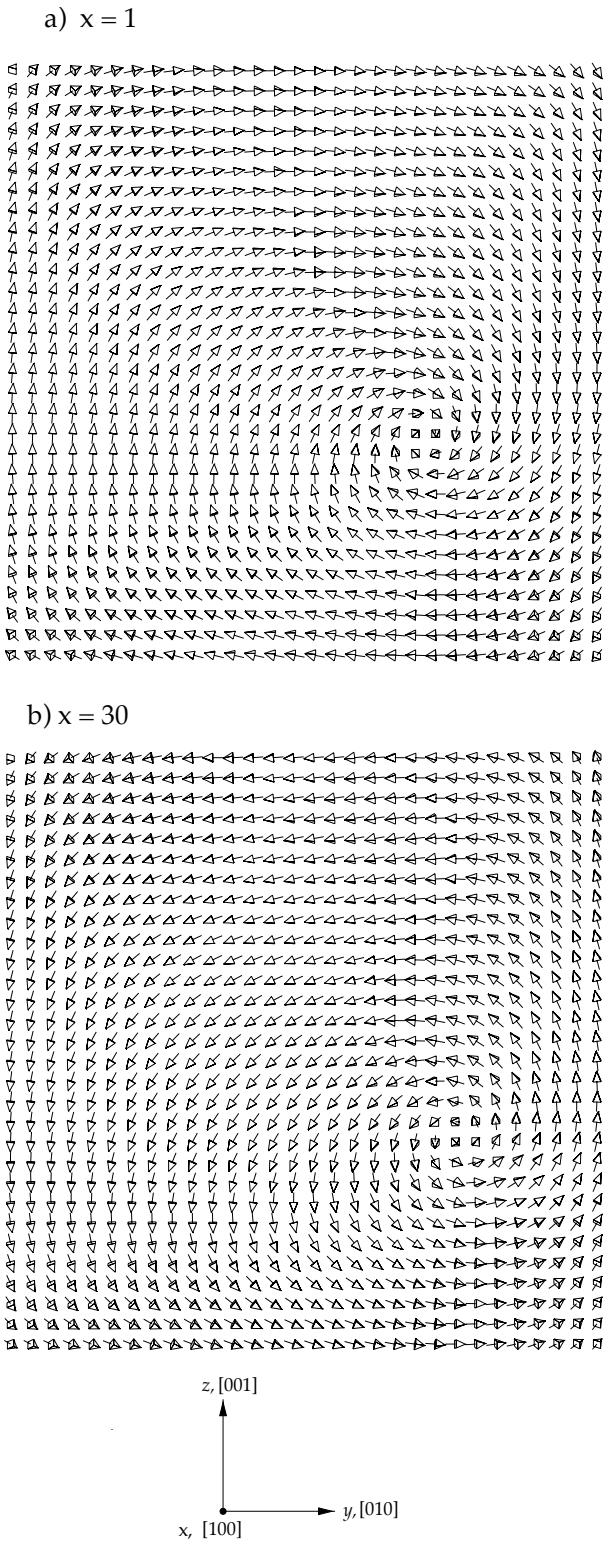


Figure 8.22: Two slices of the domain structure of $SIRM_z$ in a 0.3μm cubic grain of magnetite at 270 K after simulated cooling to 70 K; a) $x = 1$ and b) $x = 30$. The two vortices rotate in opposite directions. The overall domain structure resembles a double vortex; each vortex rotating in opposite directions. The initial $SIRM_z$ was induced at 270 K. The model resolution is $30 \times 30 \times 30$.

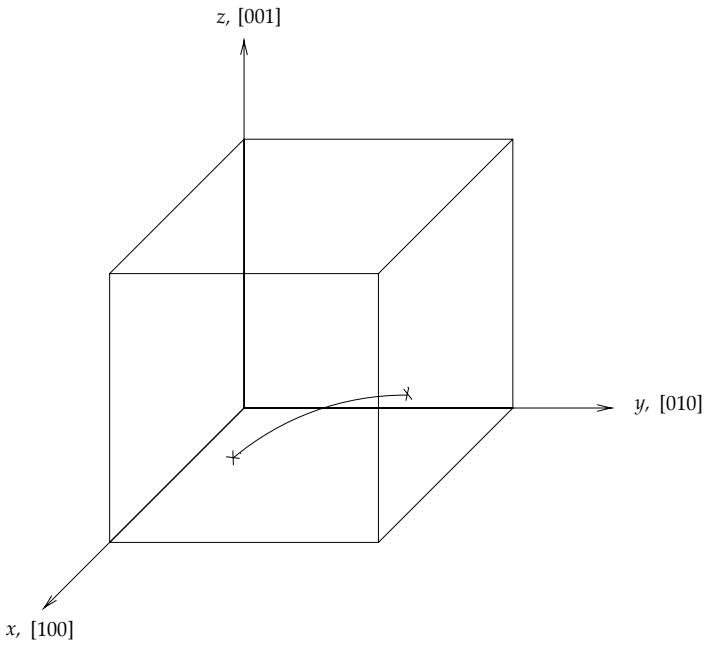


Figure 8.23: Schematic diagram showing the central vortex path for SIRM$_x$ simulated in a cube of side 0.3 μm after warming above T$_v$. The model resolution is $30 \times 30 \times 30$.

of Williams & Wright (1998). The initial SIRMs are not perfectly aligned in the direction of the simulated inducing field; the angle ϕ is seen to rotate slightly (Table 8.1). This reflects the effect of the magnetocrystalline anisotropy. Unlike the smaller grain sizes, there is significant changes in the domain structure during cooling between room temperature and T$_v$ (Figure 8.24).

On cooling below T$_v$, the domain structure changes radically, the magnetic moments aligning away from the a-axis. In similar behaviour to the other grain sizes, SIRM$_x$ rotates towards the c,z-axis ($\theta = 44^\circ$), whilst SIRM$_z$ is rotated away from the z-axis ($\theta = 37^\circ$). For both SIRM$_x$ and SIRM$_z$ and the overall domain appearance becomes more multidomain-like (Figure 8.25). There is increased leakage of magnetisation, and the net magnetisation increases.

There are a few discontinuities in the domain structure, *i.e.*, 180° jumps in neighbouring sub-cell orientations, and it is debatable as to how accurate a resolution of $30 \times 30 \times 30$ is at modelling the domain structure below T$_v$.

On warming back through T$_v$, both SIRM$_x$ and SIRM$_z$ become simple vortex structures (Figure 8.6b). The small reduced remanence returns to its original orientation and intensity (Table 8.1).

The difference between SIRM$_x$ and SIRM$_z$ low-temperature behaviour decrease as the grain size increases.

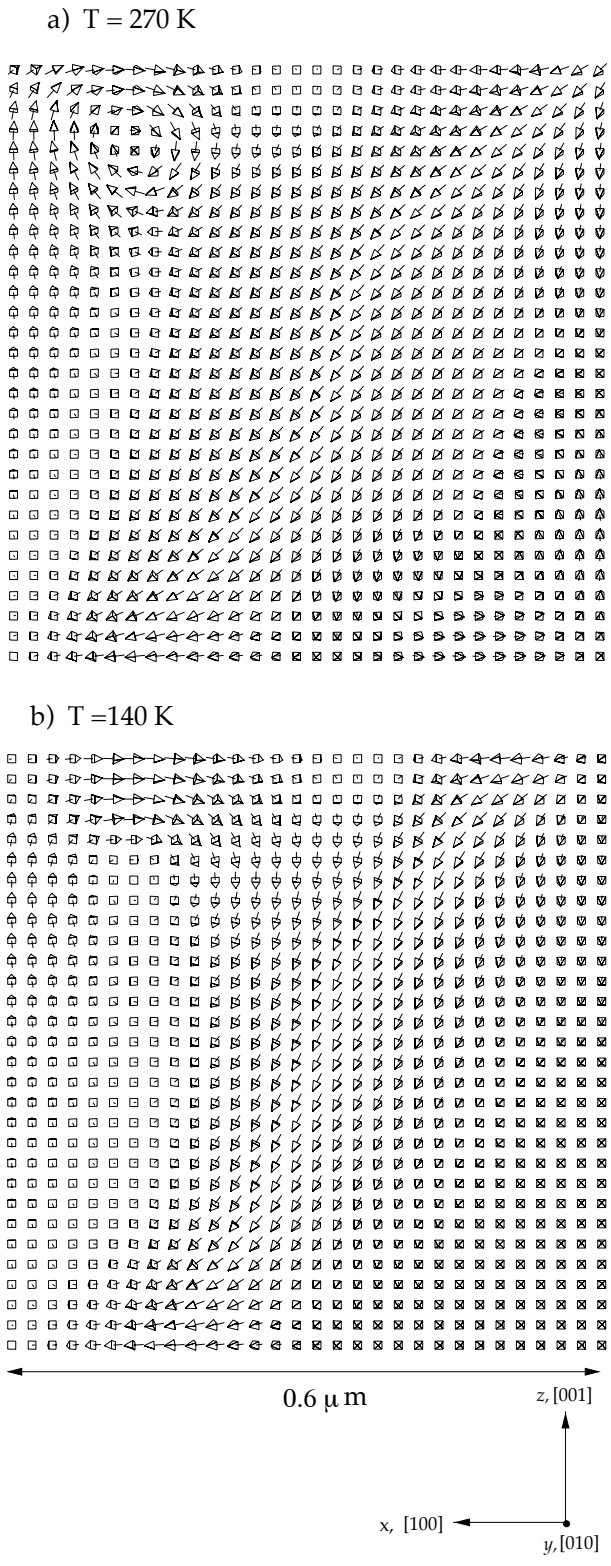


Figure 8.24: Two slices of the domain structure of SIRM$_z$ ($y = 7$) in 0.6 μm cubic grain of magnetite at a) 270 K and b) after cooling to 140 K. The model resolution is $30 \times 30 \times 30$.

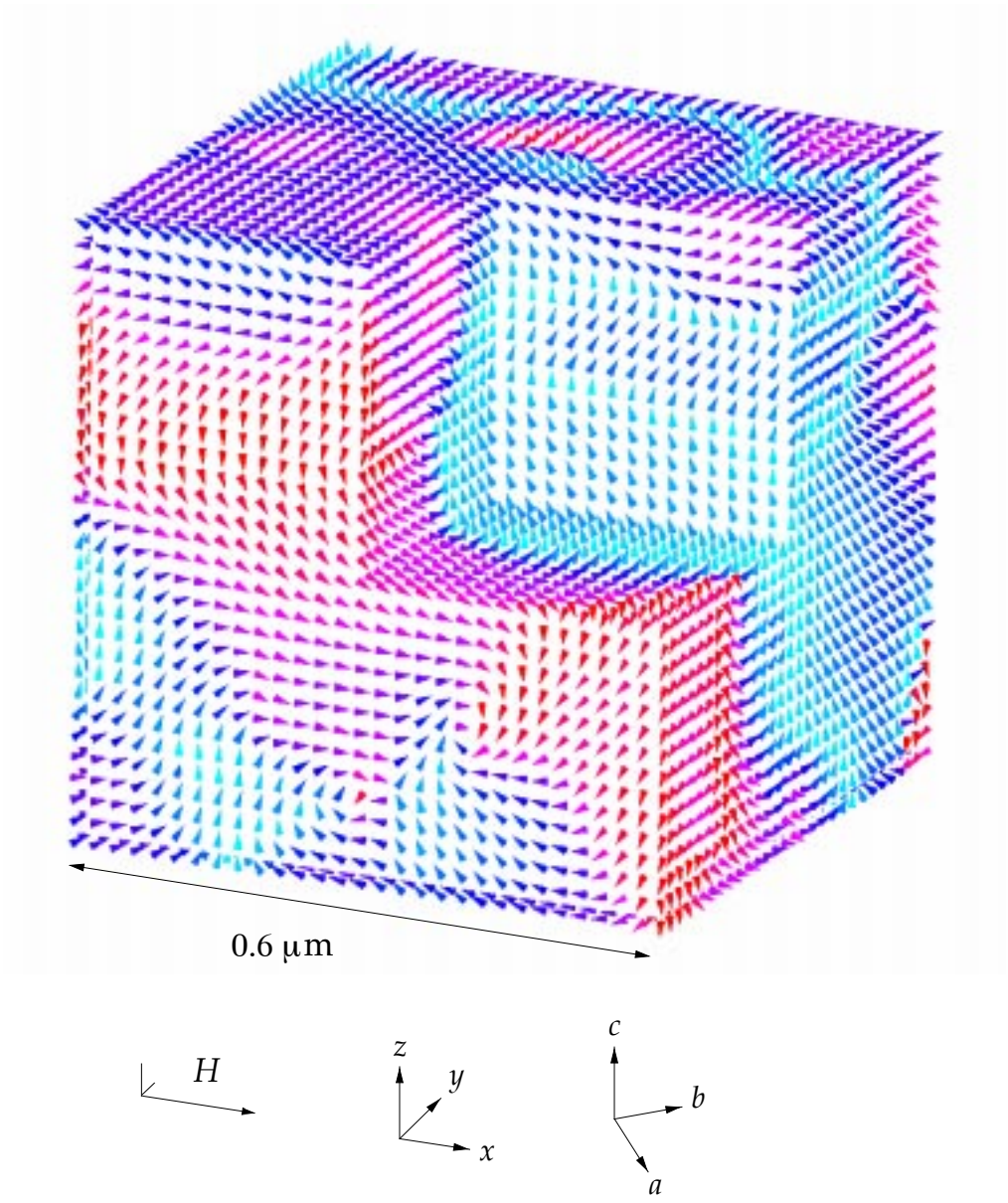


Figure 8.25: The domain structure of 0.6μm cubic grain of magnetite at 117 K, induced with a SIRM$_x$ at 270 K. The model resolution is 30 $\times$ 30 $\times$ 30. On cooling through T_v, the large increase in the magnetocrystalline anisotropy causes the magnetic vectors to lie in the *a* plane, and the magnetisation becomes more multidomain like. The direction of the inducing field is shown.

8.4.2 Behaviour of thermoremanences

Three different thermoremanence were induced in three grain sizes 0.1 μm, 0.3 μm and 0.6 μm; namely a "full" thermoremanence $TRM^{T_c}_{rtp}$, a type 1 $pTRM^{T_c}_{477}$ and a type 2 $pTRM^{477}_{rtp}$ (where rtp is room temperature). All the thermoremanences were induced in the x direction. The thermoremanences were induced in one direction only because of the large amount of CPU time required to model several different thermoremanences in three different grain sizes. Thermoremanences were induced in the x direction, because they are expected to display greater changes on cooling through T_v than thermoremanences induced in the z direction. In accordance with previous chapters both T_1 and T_2 in $pTRM^{T_1}_{T_2}$ are given in Celsius.

0.1 μm cubic grains

For the 0.1 μm grain size, the low-temperature behaviour of the simulated thermoremanences induced in the x axis does not vary significantly from that of $SIRM_x$. This is because the initial thermoremanence domain structures were flower states aligned in the x direction, similar to the initial $SIRM_x$ flower state (Figure 8.16a). There were small differences in the degree of flowering (Table 8.2).

For all the thermoremanences the the initial remanence is that of a flower state aligned in the x direction, which on cooling to the monoclinic phase rotates towards the z axis until θ = 14–21° (Table 8.2). The small component in the z plane is aligned in the b direction (Figure 8.4). On warming to 270 K the magnetic moment rotates towards the x-axis until θ = 4–14°. However there are differences in detail; the angle of the net magnetisation is dependent of the type of thermoremanence, *e.g.*, $pTRM^{T_c}_{477}$ memory ($\theta = 4°$) is closer to the z axis than $pTRM^{477}_{rtp}$ memory ($\theta = 14°$). For all three thermoremanences at 270 K, $\phi \approx 225°$ (Table 8.2). This is in the direction of an easy axis in the cubic phase of magnetite. There is no significant difference between the intensity of the reduced magnetisations.

remanence	initial		monoclinic		memory	
	M/M_{SD}	θ, ϕ	M/M_{SD}	θ, ϕ	M/M_{SD}	θ, ϕ
$TRM^{T_c}_{rtp}$	0.91	90°, 0°	0.95	15°, 224°	0.92	6°, 225°
$pTRM^{T_c}_{477}$	0.92	90°, 0°	0.96	14°, 224°	0.92	4°, 225°
$pTRM^{477}_{rtp}$	0.92	90°, 0°	0.93	21°, 225°	0.92	14°, 228°

Table 8.2: Intensity and direction of simulated reduced $TRM^{T_c}_{rtp}$, $pTRM^{T_c}_{477}$ and $pTRM^{477}_{rtp}$ during low-temperature cycling for 0.1 μm cubic grains. The thermoremanences were induced in the x direction. "Initial" is the reduced remanence at 270 K before simulated cooling, "monoclinic" the reduced remanence at 117 K in the monoclinic phase of magnetite after simulated cooling from room temperature, and "memory" is the reduced remanence remaining at 270 K after simulated low-temperature cycling. Both T_1 and T_2 in $pTRM^{T_1}_{T_2}$ are in Celsius.

0.3 μm cubic grains

As the grain size is increased, the flower state cannot be accommodated due to the increased internal demagnetising energy. Instead all three thermoremanences take a simple vortex structure similar to that shown in Figure 8.26. However the orientation of the vortex path depends on the type of thermoremanence, *i.e.*, $\mathrm{pTRM}^{\mathrm{T_c}}_{\mathrm{T_2}}$ and $\mathrm{pTRM}^{\mathrm{T_1}}_{\mathrm{T_2}}$. The simulated $\mathrm{TRM}^{\mathrm{T_c}}_{\mathrm{rtp}}$ (Figure 8.26) and $\mathrm{pTRM}^{\mathrm{T_c}}_{477}$ both have central vortex paths approximately in the x direction, whilst the $\mathrm{pTRM}^{477}_{\mathrm{rtp}}$ vortex path is aligned in the x direction (Figure 8.27). The vortexes are slightly anti-symmetric to accommodate the small net remanence.

On cooling through T_v, the vortex domain states of the three thermoremanences all form structures which resemble Kittel's (1949) two domain structure (see Figures 8.28 and 8.29). There is an increase in the magnetic flux leakage, and the reduced remanence increases for all three thermoremanences. The $\mathrm{pTRM}^{477}_{\mathrm{rtp}}$ vector is seen to be "weaker", because it rotates furthest from the x direction on cooling through the Verwey transition (Table 8.3).

On warming to room temperature, the vortex structures return. The vortex structures have a higher degree of symmetry than before cooling, and the reduced magnetisation is less than the initial value. The initial orientation is partially returned for all three thermoremanences.

remanence	initial		monoclinic		memory	
	M/M_{SD}	θ, ϕ	M/M_{SD}	θ, ϕ	M/M_{SD}	θ, ϕ
$\mathrm{TRM}^{\mathrm{T_c}}_{\mathrm{rtp}}$	0.03	90°, 359°	0.39	43°, 350°	0.003	83°, 6°
$\mathrm{pTRM}^{\mathrm{T_c}}_{477}$	0.04	90°, 337°	0.26	56°, 350°	0.007	88°, 331°
$\mathrm{pTRM}^{477}_{\mathrm{rtp}}$	0.02	91°, 357°	0.35	41°, 348°	0.03	83°, 0°

Table 8.3: Intensity and direction of simulated reduced $\mathrm{TRM}^{\mathrm{T_c}}_{\mathrm{rtp}}$, $\mathrm{pTRM}^{\mathrm{T_c}}_{477}$ and $\mathrm{pTRM}^{477}_{\mathrm{rtp}}$ induced in the x direction, simulated low-temperature cycling for 0.3 μm cubic grains. "Initial" is the reduced remanence at 270 K before simulated cooling, "monoclinic" the reduced remanence at 117 K in the monoclinic phase of magnetite after simulated cooling from room temperature, and "memory" is the reduced remanence remaining at 270 K after simulated low-temperature cycling. Both T_1 and T_2 in $\mathrm{pTRM}^{\mathrm{T_1}}_{\mathrm{T_2}}$ are given in Celsius.

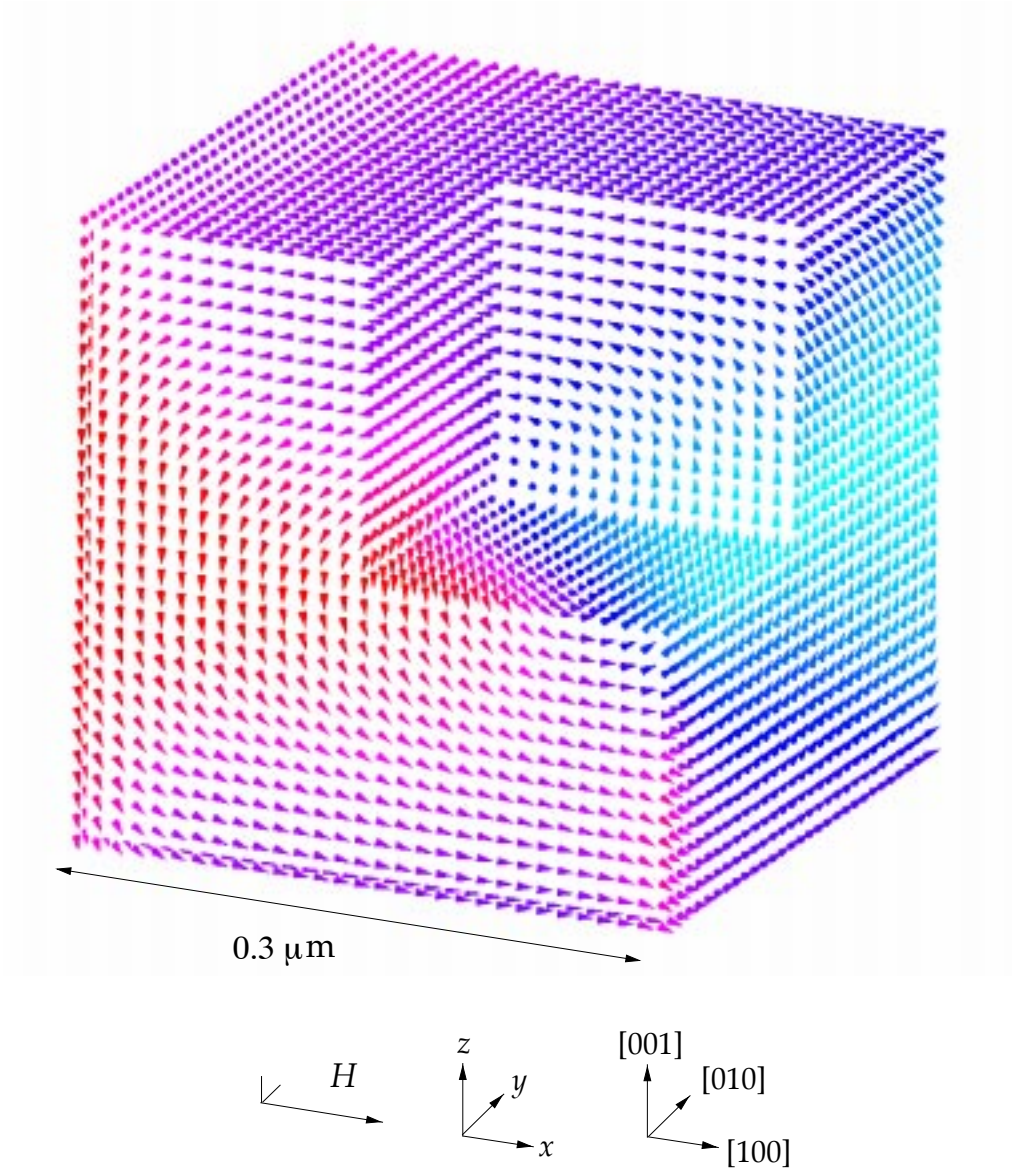


Figure 8.26: The domain structure of 0.3μm cubic grain of magnetite at 300 K, induced with a TRM in the x direction. The orientation of the inducing field is shown.

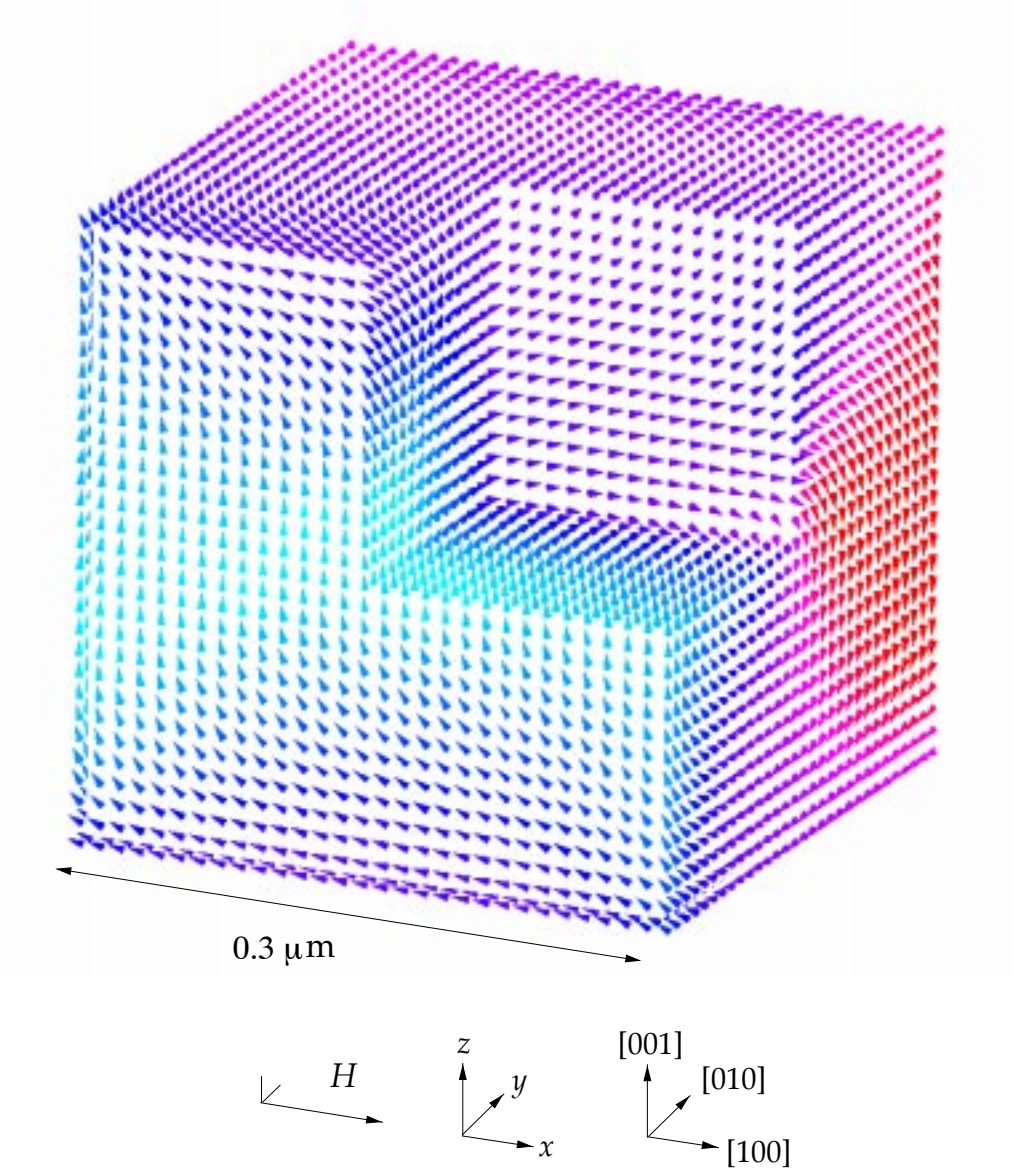


Figure 8.27: The domain structure of 0.3μm cubic grain of magnetite at 300 K, induced with a $\mathrm{pTRM}^{477}_{\mathrm{rtp}}$ in the x direction. The orientation of the inducing field is shown.

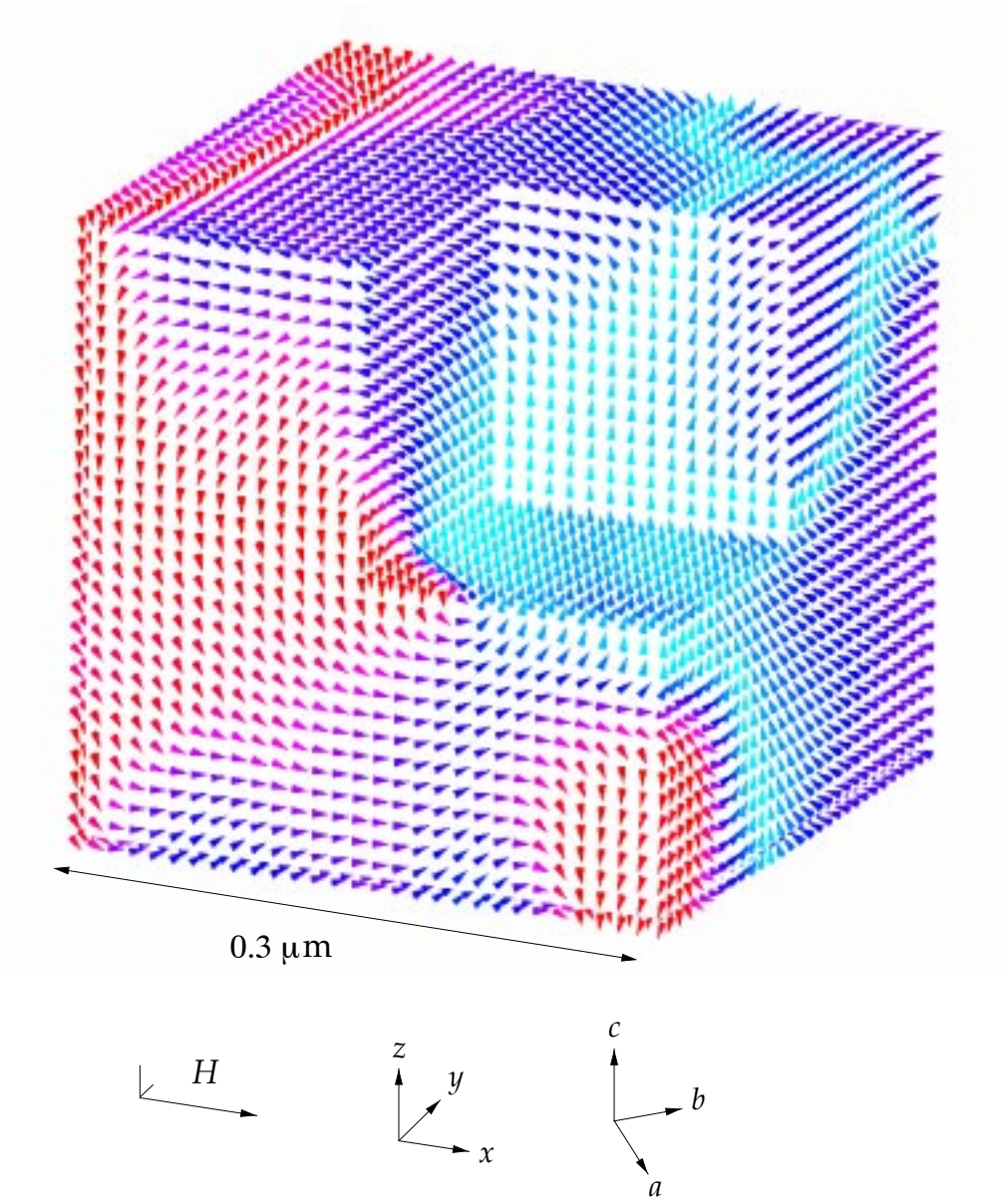


Figure 8.28: The domain structure of 0.3μm cubic grain of magnetite at 117 K, induced with a TRM in the x direction. The model resolution is 30×30×. On cooling through T_v, the large increase in the magnetocrystalline anisotropy causes the magnetic vectors to lie in the a plane, and the magnetisation becomes more multidomain like

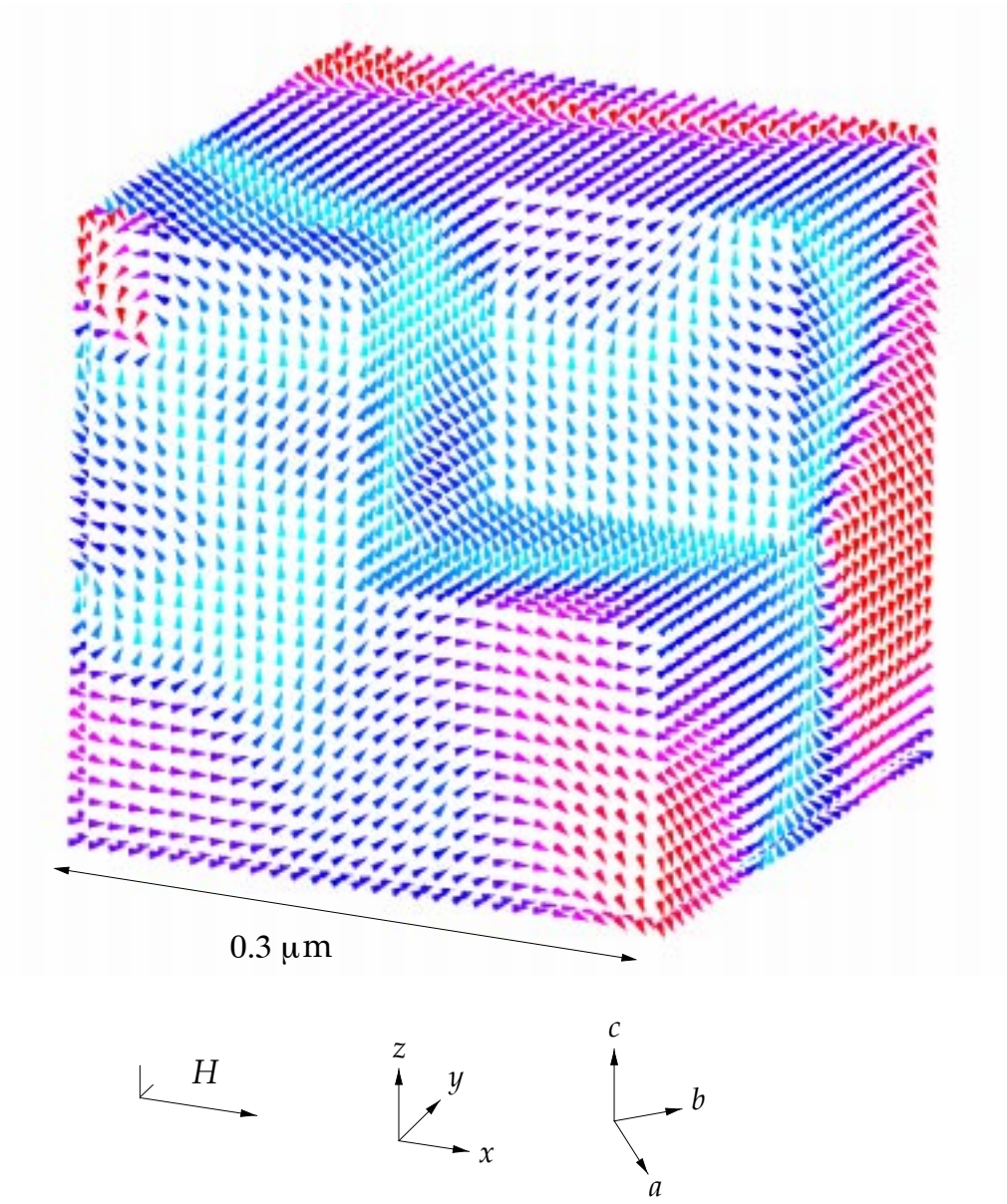


Figure 8.29: The domain structure of 0.3μm cubic grain of magnetite at 117 K, induced with a $pTRM_{1tp}^{477}$ in the x direction. The model resolution is 30×30×. On cooling through T_v, the large increase in the magnetocrystalline anisotropy causes the magnetic vectors to lie in the a plane, and the magnetisation becomes more multidomain like

0.6 μm cubic grains

In 0.6 μm grains, the initial $\mathrm{TRM}^{\mathrm{T_c}}_{\mathrm{rtp}}$ and $\mathrm{pTRM}^{477}_{\mathrm{rtp}}$ domain structures at 270 K have simple multidomain structures. As an example the domain structure of $\mathrm{TRM}^{\mathrm{T_c}}_{\mathrm{rtp}}$ at 270 K is shown in Figure 8.30. The magnetic vectors in the centre of grain are partially aligned in the direction of the K_1 cubic anisotropy. The reduced magnetisation of all three thermoremanences is very low, however the small remanences are closely aligned to the direction of the inducing field (Table 8.4).

The simulated thermoremanences, become more multidomain on cooling through T_v, and the magnetic vectors align in the a plane (Figure 8.31). As with the smaller grains, the net magnetisation increases and rotates away the direction of the applied field towards the monoclinic c-axis. The degree of rotation, *i.e.*, the rotation of θ, is related to the initial thermoremanence; $\mathrm{pTRM}^{477}_{\mathrm{rtp}} > \mathrm{TRM}^{\mathrm{T_c}}_{\mathrm{rtp}}$ (Table 8.4). $\mathrm{TRM}^{\mathrm{T_c}}_{\mathrm{rtp}}$ has a greater intensity than $\mathrm{pTRM}^{477}_{\mathrm{rtp}}$ (Table 8.4). However the domain structures are non-uniform and it is debatable how reliable the model is at this resolution.

On subsequent warming to room temperature, both $\mathrm{TRM}^{\mathrm{T_c}}_{\mathrm{rtp}}$ and $\mathrm{pTRM}^{\mathrm{T_c}}_{477}$ become vortex states, with central vortex paths approximately in the [100] and [010] directions respectively. The net magnetisations partially return to the original orientations (Table 8.4), however the intensities are reduced with respect to the initial values.

remanence	initial		monoclinic		memory	
	M/M_{SD}	θ, ϕ	M/M_{SD}	θ, ϕ	M/M_{SD}	θ, ϕ
$\mathrm{TRM}^{\mathrm{T_c}}_{\mathrm{rtp}}$	0.02	90°, 351°	0.11	63°, 347°	0.01	93°, 351°
$\mathrm{pTRM}^{\mathrm{T_c}}_{477}$	0.03	93°,358°	0.03	18°,178°	0.01	1°,3°

Table 8.4: Intensity and direction of simulated reduced $\mathrm{TRM}^{\mathrm{T_c}}_{\mathrm{rtp}}$ and and $\mathrm{pTRM}^{477}_{\mathrm{rtp}}$ induced in the x direction, simulated low-temperature cycling for 0.6 μm cubic grains. "Initial" is the reduced remanence at 270 K before simulated cooling, "monoclinic" the reduced remanence at 117 K in the monoclinic phase of magnetite after simulated cooling from room temperature, and "memory" is the reduced remanence remaining at 270 K after simulated low-temperature cycling. Both $\mathrm{T_1}$ and $\mathrm{T_2}$ in $\mathrm{pTRM}^{\mathrm{T_1}}_{\mathrm{T_2}}$ are given in Celsius.

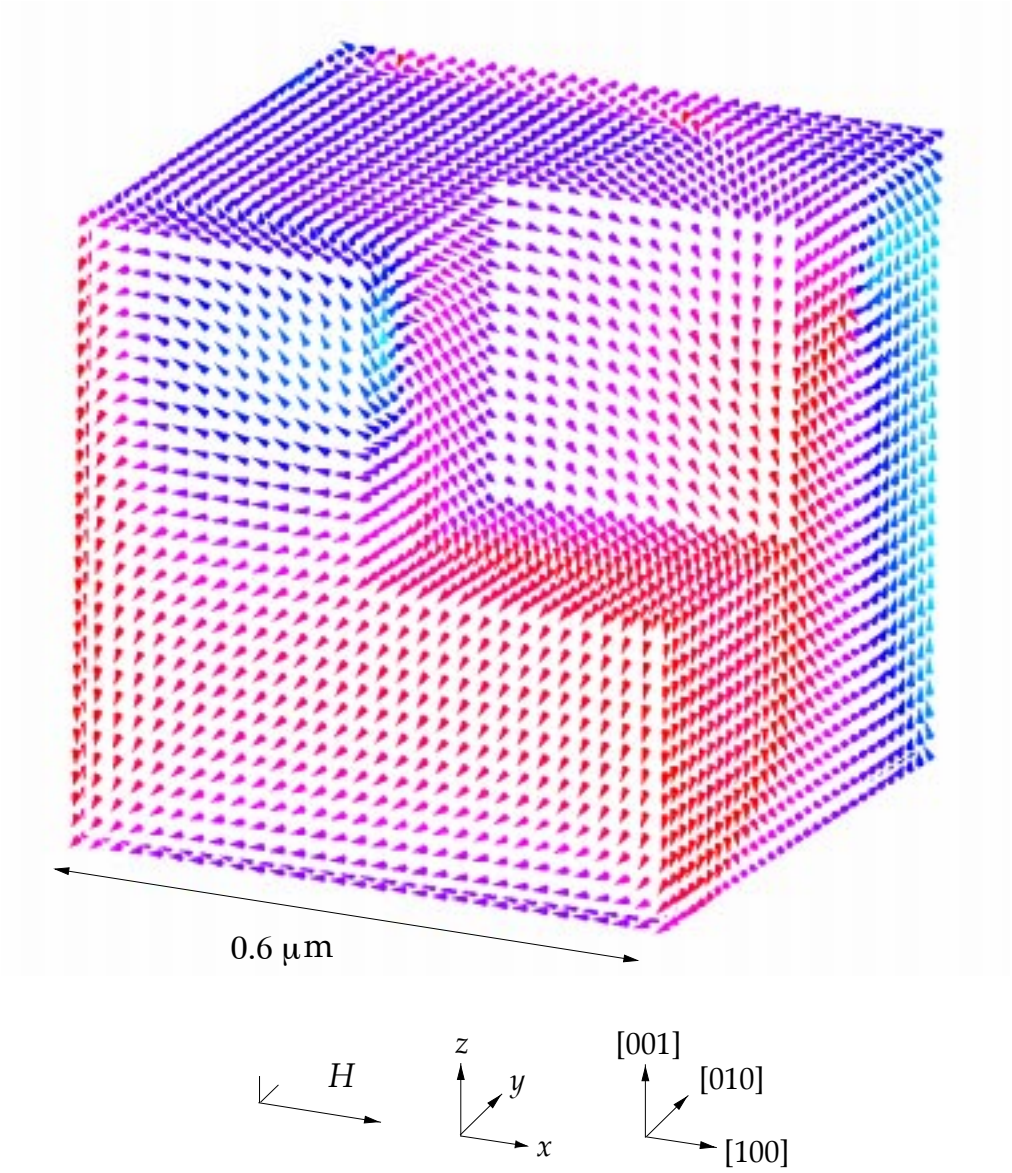


Figure 8.30: The domain structure of 0.6μm cubic grain of magnetite at 270 K, induced with a TRM in the x direction. The model resolution is $30 \times 30 \times 30$. The direction of the inducing field is marked.

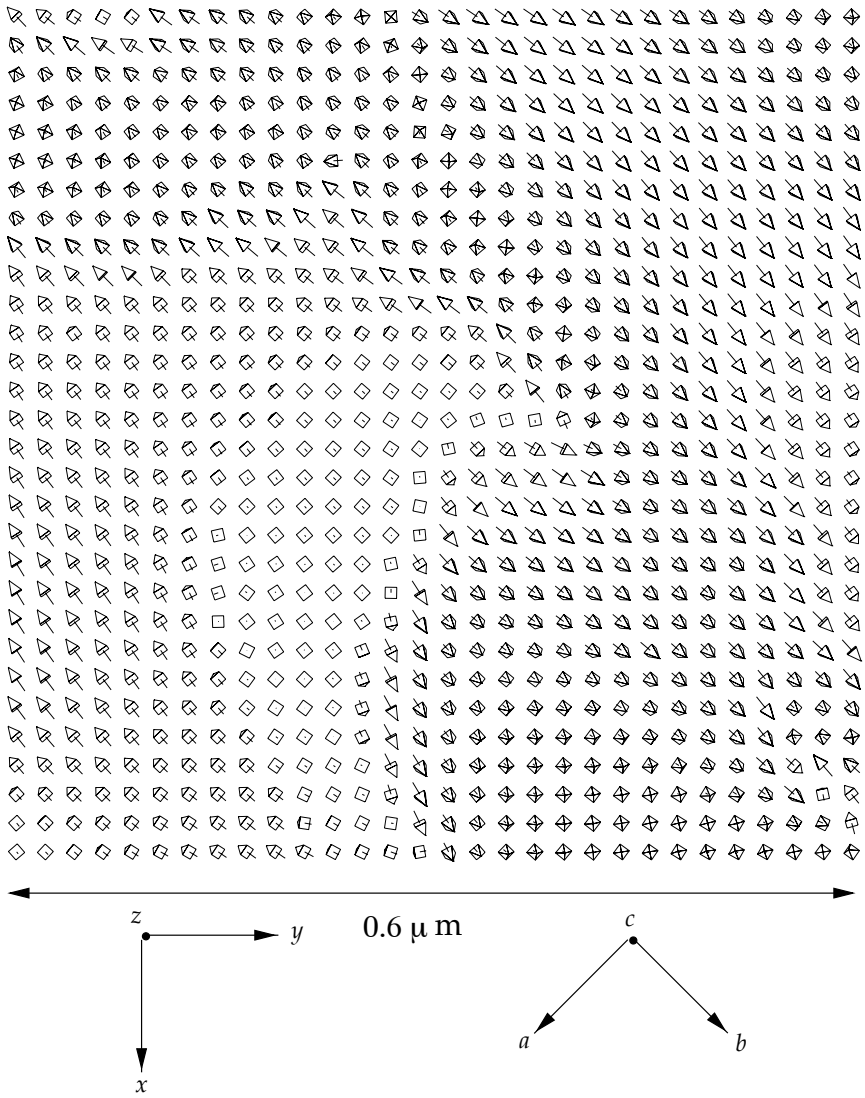


Figure 8.31: A slice of the domain structure of TRM ($z = 7$) in 0.6μm cubic grain of magnetite at 117 K. The model resolution is $30 \times 30\times$. The magnetic vectors are all aligned in the *a* plane, *i.e.,* away from the hard *a*-axis.

8.5 Comparison with experimental results

The simulated low-temperature behaviour of remanent magnetisation and the magnetic memory ratio, *i.e.*, the ratio of (remanence memory / remanence), are compared with experimental results presented in Chapters 6 and 7.

Some considerations have to taken into account when comparing experimental and theoretical results; mainly that the experimental results are for samples containing an assemblage of randomly orientated grains, whereas the theoretical results are for single crystals. It is theoretically possible to calculate the low-temperature domain structure behaviour for remanences induced with a large number of discrete field angles, however due to computational capabilities it was not feasible.

8.5.1 Remanent magnetisation versus temperature

There have been several experimental investigations which have directly measured the remanent magnetisation during low-temperature cycling, however these have mostly been conducted on SIRMs (*e.g.*, Kobayashi & Fuller, 1968; Halgedahl & Jarrard, 1995; King, 1996, this study Chapter 6), with only a limited number of investigations of thermoremanences (*e.g.*, Ozima *et al.*, 1964b; Creer & Like, 1967; Hartstra, 1983, this study Chapter 6). The results for the low-temperature cycling of thermoremanence presented in Chapter 6, are the most reliable to date, because they were performed using hydrothermal magnetite crystals induced with laboratory thermoremanence and vacuum sealed in quartz capsules, which prevent chemical alterations. The experimental results presented in Chapter 6) are for slightly larger grains than those simulated in this model. As the samples were made by hydrothermal recrystallisation (Heider & Bryndzia, 1987, Chapter 2) they are relatively defect free (Chapter 3) and comparable in magnetic behaviour to the simulated grains which were theoretically "perfect". The experimental results were only measured in one direction, *i.e.*, the direction of the initial magnetisation. The modelled magnetisation is treated accordingly.

Before comparing the experimental and numerical results it should be noted that as the model is rather simplified, only the trends in behaviour are of interest here. The low-temperature cycling results for the hydrothermal sample *H(7.5 μm)* are shown in Figure 8.32, and the simulated low-temperature cycling results for a 0.3 μm cubic grain are shown in Figure 8.33. The simulated cycling results for the 0.1 μm cubic grains are not shown because they vary only as the spontaneous magnetisation, and the models for the 0.6 μm because of doubts in the accuracy in using a $30 \times 30 \times 30$ resolution to model the monoclinic phase.

There is reasonably good agreement between the experimental trends and simulated low-temperature cycling behaviour (Figures 8.32 and 8.33).

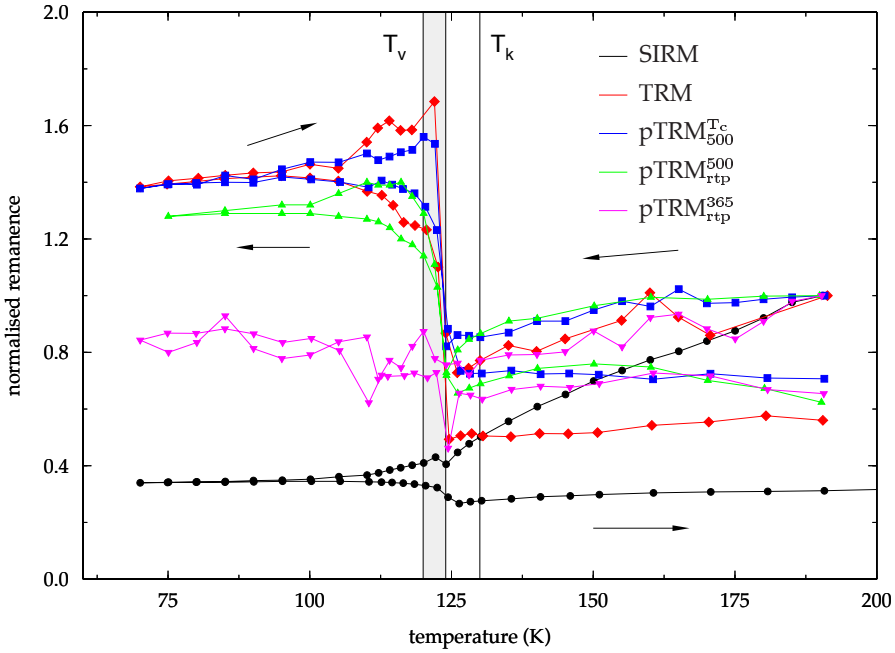


Figure 8.32: Low-temperature cycling of different initial thermoremanences induced in hydrothermal sample *H(7.5 μm)*, containing an assemblage of randomly orientated samples. The remanence is normalised at 190 K. The experimental results were previously presented in Chapter 6.

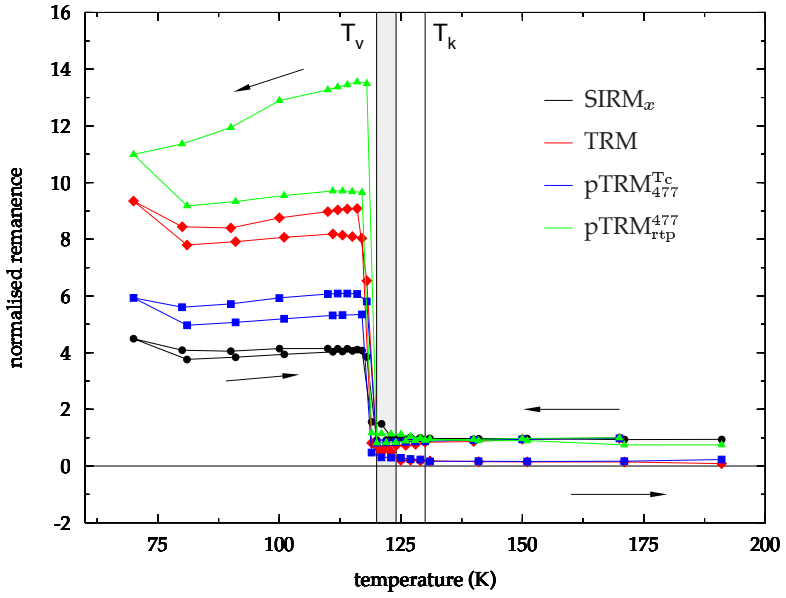


Figure 8.33: Simulated low-temperature cycling of different initial thermoremanences $SIRM_x$ induced in a single 0.3μm cube. $SIRM_x$ rather than $SIRM_z$ is shown, because all the thermoremanences were induced in the x direction. The remanence is normalised at 190 K.

Interestingly the theory confirms the large positive anomaly in the magnetisation observed on cooling through T_v (*cf.* Figures 8.32 and 8.33), which has never been reported outside this study. The size of the modelled anomaly in the remanent magnetisation, is larger than that observed experimentally. This is probably due to three factors; firstly simplifications in the model, *e.g.,* the model did not include the effect thermal fluctuations, magnetostrictive anisotropy and crystal defects. Secondly the experimental results are for an assemblage of randomly orientated magnetite grains and the model only for single crystals induced with a remanence in the x direction. Remanence induced in the z is less likely to display Lastly the experimental results are for a larger grain size than in the model. Increasing the grain size increases the amount of shielding, which is expected to reduce the large positive anomaly. There is a positive anomaly observed in the modelled low-temperature cycling curve for $SIRM_x$ (Figure8.33), although none is observed for SIRM induced in the natural sample (Figure 8.32).

The model also confirms the relative behaviour of the SIRM and thermoremanences, *i.e.,* the thermoremanences have larger anomalies at T_v, in agreement with the experimental results. However the modelled Type 2 pTRM, *i.e.,* $pTRM^{477}_{rtp}$, has a bigger anomaly than the Type 1 pTRM $pTRM^{T_c}_{477}$, in disagreement with the experimental results (Figure 8.33) which found that Type 2 pTRM, *e.g.,* $pTRM^{500}_{rpt}$, has a smaller anomaly at T_v than Type 1 pTRM, *e.g.,* $pTRM^{500}$(Figure 8.32). This discrepancy may be a fault of the program; the model appears to take several temperature steps to optimise the monoclinic domain structure, *cf.* the decrease in the magnetisation of $pTRM^{477}_{rpt}$ on cooling from T_v to 70 K (Figure 8.32). In reality the domain structure would be expected to optimise instantaneously. It must also be remembered, that the model does *not* include simulated annealing (Thomson *et al.*, 1994), and hence it only crudely approximates the domain structure of thermoremanences. That the model does not correctly simulate the relative behaviour of *different* pTRM Types reflects the insensitivity of the program.

In general the model does predict that thermoremanences have larger anomalies at T_v, than SIRM in agreement with experimental evidence, and this support the ideas in Chapter 6, that the anomaly at T_v is due to metastable LEM states, often associated with thermoremanences.

8.5.2 Magnetic memory

The ratio of the room temperature remanent magnetisation to the post-low-temperature cooled remanent magnetisation is called the magnetic memory. Experimentally this ratio is easy to determine as all the measurements are made at room temperature.

Most reported measurements have concentrated on SIRMs and "full" TRMs, *i.e.,* $TRM^{T_c}_{rtp}$, with only a limited number of memory studies for pTRM (Shcherbakova *et al.*, 1996).

All the experimental measurements of memory ratio for sub-micron grains have been

for assemblages of randomly orientated samples. Because the behaviour of memory is dependent on the inducing field direction (Table 8.1), before comparing the model with the experimental data it is necessary to get some estimate for the memory ratio of a group of randomly orientated grains. This can be achieved by using the results from $SIRM_x$ and $SIRM_z$, to calculate $SIRM_{av}$. $SIRM_{av}$ is calculated assuming that $\frac{1}{3}$ of grains have the low-temperature *c*-axis in the x,y and z respectively. As $SIRM_y$ is symmetrical with $SIRM_x$, then the average behaviour of non-interacting grains is given by

$$SIRM_{av} = \frac{SIRM_z + 2SIRM_x}{3} \tag{8.10}$$

The modelled memory ratios for $SIRM_x$, $SIRM_y$, $SIRM_{av}$ and TRM are compared with experimental results in Figure 8.34. The results for $SIRM_x$, $SIRM_z$ and TRM are either much lower than the experimental values if they are induced in the x direction, *i.e.*, $SIRM_x$ and TRM, or much higher if in the z direction, *i.e.*, $SIRM_z$. However $SIRM_{av}$ gives reasonably good agreement with the experimental results (Figure 8.34a). The $SIRM_{av}$ memory ratios for 0.1 μm and 0.3 μm cubes are slightly lower than the results of Dunlop & Argyle (Dunlop & Argyle, 1991). This may be due to two possible reasons; the model is for "ideal" crystals with no internal stress which is thought to increase the memory ratio (Heider *et al.*, 1992, Chapter 7). Secondly the difference may be due to the crude method of approximating $SIRM_{av}$. The $SIRM_{av}$ memory ratio for 0.6 μm is slightly higher that the 0.1 μm and 0.3 μm cubes, however I suspect this is due to errors associated with modelling the monoclinic domain structure with only a resolution of $30 \times 30 \times 30$.

8.6 Conclusions

The monoclinic phase is magnetically harder than the cubic phase due to large increases in the anisotropy. This causes the SD-critical size to increase on cooling through T_v from 0.07 μm to 0.14 μm (Figure 8.8).

The behaviour of SIRMs and TRMs to low-temperature cycling is revealing. For the 0.1 μm grains the behaviour of the SIRMs and TRMs is dominated by the switching of the flower structure to the easy z-axis. On repeating the $SIRM_x$ low-temperature cycling experiment for a 0.05 μm cube, it was found that the flower state rotates to align in the *b* axis, rather than the easier *c* axis, on cooling through T_v. It would appear that there is some critical elongation and/or grain size where the shape anisotropy dominates the anisotropy, and suppresses the rotation from the cubic [100] direction to the monoclinic *c*-axis.

For the larger models, *i.e.*, 0.3 μm and 0.6 μm, $SIRM_x$, $SIRM_z$ and TRM rotate from the cubic orientation on cooling through T_v. However on warming to 270 K, the original directions are partially recovered. The orientation of SIRM displays a greater recovery than thermoremanence on warming to room temperature, however the memory ratio of SIRM

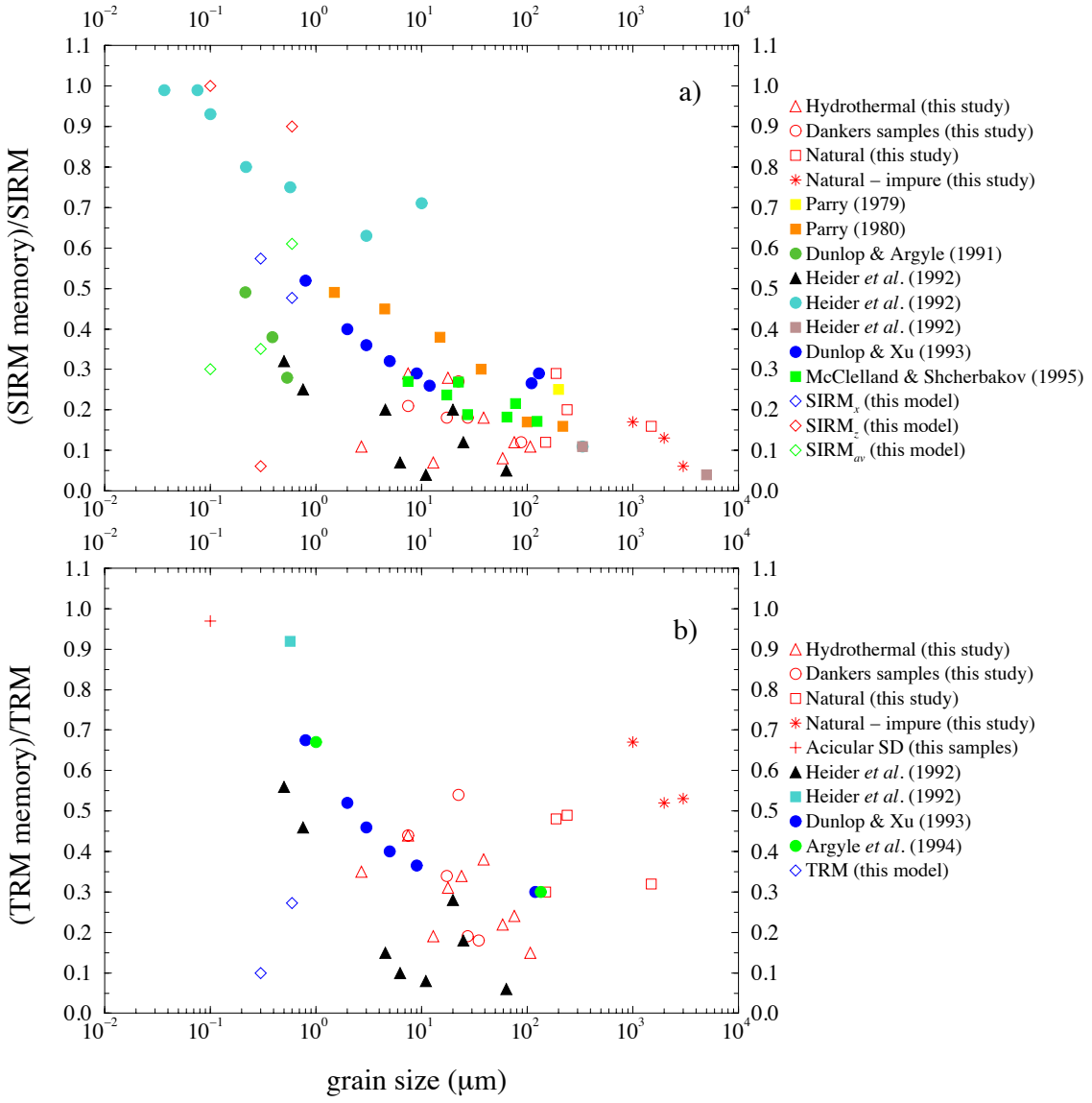


Figure 8.34: Low-temperature memory ratios for a) SIRM and b) TRM induced in sized magnetites. The model results are represented by a ◇. In figure a) SIRM$_x$, SIRM$_y$, SIRM$_{av}$ are shown, whilst in b) only TRM is presented. It should be noted that SIRM$_x$, SIRM$_y$ and TRM memory ratios are only for single crystals. The experimental coding; hydrothermal crystals are represented by △, annealed crystals by ○ and unannealed, crushed or irregular magnetites by □. My samples are represented by solid symbols, *e.g.*, ○, whilst previously published data are shown as open symbols, *e.g.*, ●. Note, because the Dankers crushed magnetites (*D(5-10 μm)–D(100-150 μm)*) had been heated on numerous occasions before this experiment, they were considered to be annealed and are represented by ○. Samples with reversed memories are not shown. The experimental results have been shown previously in Figure 7.8.

is lower than that of thermoremanence because the SIRM domain structures rearrange to reduce the magnetic flux leakage. The difference in memory ratio suggests that SIRM is intrinsically "weaker" than thermoremanence.

For $pTRM^{477}_{rtp}$ in 0.3 μm grains, the net magnetisation rotates further than $SIRM_x$, TRM or $pTRM^{T_c}_{477}$ on cooling through T_v. And the original direction is not recovered on warming through T_v. For $pTRM^{477}_{rtp}$ in a 0.6 μm grain the original direction is not recovered on warming to the cubic phase. This difference in the ability to recovery the original orientaiton on cycling through T_v, suggests the TRM is trapped in a deeper, more flexible LEM states than $pTRM^{477}_{rtp}$.

The simulated low-temperature remanence curves display similar trends to the experimental data (*cf.* Figures 8.32 and 8.33). The large increase in the remanent magnetisation on cooling to the monoclinic phase is due to the high anisotropy at low-temperatures. Here is a paradox, the domain structure becomes more multidomain but at the same time has a higher remanent magnetisation. This is partially due to the high energy barriers which must be overcome for the domain structure to reorganise. The increase in the energy barriers on cooling to the monoclinic phase is reflected in the three fold increase in the coercive force observed on cooling through T_v (Belov, 1993; Schmidbauer & Keller, 1996, Section 5.7.2).

This model assumes that during the phase change from cubic to monoclinic at T_v, that all areas of a grain are orientated in the same direction, however this is unlikely to be the case as experimental evidence has shown that a variety of twin structures occur (Otsuka & Sato, 1986; Miyamoto & Chikazumi, 1988). The twin structures are due to the *c*-axis aligning in different directions in different areas of a magnetite grain, *i.e.*, on cooling through T_v the *c*-axis can align in anyone of six orientations. It has been suggested (Moloni *et al.*, 1996), that the twin-domains in the monoclinic phase are magnetically independent *i.e.,* the grain behaves magnetically like a polycrystal, however this is unlikely to be the case as twin-domain walls have been shown to move easily in an external field (Otsuka & Sato, 1986).

Theory suggests that there should be an interaction between the twin-domains and the magnetic domains (Houchmandzadeh *et al.*, 1991) . It is postulated here that this interaction reduces the remanent magnetisation below T_v (Figure 8.33), and partially explains the difference between the experimental and theoretical results (Figure 8.32). It is uncertain how large the interaction is.

The exclusion of magnetostriction during simulated low-temperature cycling would expected to have a significant effect, especially at T_k where $K_1 \rightarrow 0$. On cooling through T_v, there are anomalies in both the magnetostrictive and elastic constants (Chapter 5). An improvement to the model is to include magnetostriction.

There is no strong evidence from the models to suggest that T_k controls the demagnetisation process during low-temperature cycling.

Chapter 9

Conclusions

This chapter presents the conclusions of the thesis.

The main aim of the thesis was to investigate the origin of the stability of remanence in multidomain magnetite, with particular reference to the stability of remanence during low-temperature treatment.

A series of experiments was designed to examine the stability of multidomain magnetite, using a selection of characterised synthetic and natural samples. The stability of thermoremanence above room temperature was examined in Chapter 4, the stability of remanence during low-temperature cycling was investigated in Chapter 6 and the stability of remanence after low-temperature treatment, *i.e.*, above room temperature was investigated in Chapter 7. In Chapter 8 a micromagnetic simulation of low-temperature cycling was considered.

The results in Chapter 4 confirmed the kinematic theories for thermoremanence behaviour on cooling below the acquisition temperature, developed by McClelland & Sugiura (1987) and Shcherbakov *et al.* (1993). These theories incorporate a temperature dependent domain structure, which breaks away from the classical theories of Néel (1949, 1955) which are based on the idea of blocked or fixed domain structures. Previous experimental evidence of this phenomena is sparse. These studies have only examined crushed or natural magnetites, which have either high-stress or impurities respectively. In this study similar experiments are reported for characterised low-stress hydrothermal crystals. The results from the hydrothermal crystals agree with previous observations for crushed and natural magnetites, and support the kinematic model. Markov *et al.* (1983) have reported experimental evidence which is only in partial agreement with the kinematic models, namely they found that the observed decrease or demagnetisation on cooling partial thermoremanence below its minimum acquisition temperature *decreases* with increasing inducing field. However the kinematic model predicts an *increase*. In a series of experiments designed to examine this problem (Section 4.2.2) I measured an *increase* of magnetisation, in agreement with the predictions of the kinematic model. Unfortunately there is no clear

reason for the difference between the data reported by Markov *et al.* (1983) and reported in this study.

In Chapters 5–8 the behaviour and stability of remanence at low-temperatures was examined. The physics of the Verwey transition (T_v) and the magnetocrystalline anisotropy isotropic point (T_k) were discussed in detail in Chapter 5. King (1996) argued that T_v and T_k are in fact the same transition, however in Chapter 5 experimental data is presented which refutes King's hypothesis, and I argue that T_v and T_k are separate transitions. The two proposed theories for the Verwey transition, *i.e.*, structural-electronic (Zuo *et al.*, 1990; Mishra & Satpathy, 1993) and magneto-electronic (Belov, 1993; Belov, 1996a) were discussed in detail in Chapter 5. Experimental evidence from both this study and previous investigations support the magneto-electronic model in favour over the structural-electronic model, however it is realised that there is strong experimental in support of the structural-electronic model (Hargrove & Kündig, 1970; Rubinstein & Forester, 1971). Central to the magneto-electronic model is an anomaly in the spontaneous magnetisation (Belov, 1993, Figure 5.14), which to my knowledge has not been discussed in rock magnetic literature. The anomaly in the spontaneous magnetisation was verified experimentally in this study using hydrothermal magnetite samples. The anomaly in the spontaneous magnetisation has not been considered in structural-electronic models.

Although the anomaly in the spontaneous magnetisation is significant ($\approx 20\ \%$) it is the anomaly in the magnetocrystalline anisotropy which dominates the low-temperature behaviour. On cooling through the Verwey transition the intensity of the magnetocrystalline anisotropy increases sharply, and the symmetry of the magnetocrystalline anisotropy reduced (Section 5.4.2). Using micromagnetic models (Chapter 8), it is calculated that the changes in the magnetocrystalline anisotropy increase the (single domain/multidomain) threshold size from 0.07 μm at room temperature to 0.14 μm at 110 K in the low-temperature phase.

In Chapter 6 the behaviour of various remanences during low-temperature cycling was measured. Previous studies have concentrated on the low-temperature cycling of SIRM, however in this study thermoremanence was considered in detail. During low-temperature cooling I observed that the remanences initially demagnetised on cooling from room temperature to T_k. In this thesis it is suggested that the physical processes which control this demagnetisation are identical to the kinematic processes (McClelland & Sugiura, 1987; Shcherbakov *et al.*, 1993) which occur on cooling thermoremanence above room temperature, *i.e.*, the same kinematic processes which occurs on cooling remanence above room temperature continues to operate below room temperature. The rate of demagnetisation increases on approach to T_k, suggesting that the kinematic processes are partially controlled by the magnetocrystalline anisotropy. At the Verwey transition the behaviour of the magnetisation is dependent on both the remanence and the physical properties of the sample, *e.g.*, grain size and stress. SIRM does not display any significant behaviour on cooling through T_v, however thermoremanences were found to display anomalous be-

haviour on cooling through T_v. Large positive anomalies, *i.e., increases* in the magnetisation, are observed for thermoremanence acquired at high temperatures. Stressed samples with small grain sizes were found to display the largest anomalies on cooling through T_v. High-temperature thermoremanence acquired in stressed samples with small grain sizes is normally associated with hard magnetic remanence. Characterisation of initial thermoremanence and the thermoremanence remaining after low-temperature cycling, *i.e.,* thermoremanence memory, confirms the hypothesis that remanence which displays large anomalies on cooling through T_v is magnetically hard, *i.e.,* the large positive anomalies are associated with metastable remanence.

The origin of the anomaly in thermoremanence at T_v is discussed in Chapter 6, and it is concluded that it is related to the large increase in the magnetocrystalline anisotropy. I propose that because of the large increase of the magnetocrystalline anisotropy energy on cooling to the low-temperature phase, the relative importance of magnetic leakage decreases, and closure domains are destroyed. Central body domains align with an easy axis. Micromagnetic models support this hypothesis, for example vortex structures which reduce the total magnetic energy in the cubic phase by reducing magnetic leakage, on cooling through T_v become similar in appearance to Kittel's (1949a) classic two-domain grains (Figure 1.9b) which have higher magnetic leakage.

On warming through the Verwey transition the anomaly in the thermoremanences was found to be partially reversible; there was usually a a small net demagnetisation on warming through T_v. I interpret this small demagnetisation to be due to either areas of a domain structure or entire domain structures of a grain being irreversible to cooling through the Verwey transition, however most domain structures were reversible to cooling through the Verwey transition. On warming from T_v to room temperature the thermomagnetic curve was found to differ from the cooling curve. The small recovery observed on warming to room temperature was explained in terms of flexible domain walls (Chapter 6).

It has been suggested that the cause of the large demagnetisation observed on cooling is due to either T_k, T_v or both (*e.g.,* Shcherbakova *et al.*, 1996; Hodych, 1990; Halgedahl & Jarrard, 1995). However in this study it was found that the magnetisation was partially reversible to cooling and warming through the Verwey transition, and no significant demagnetisation anomaly was observed at T_k. Examination of low-temperature demagnetisation curves, especially SIRM cooling curves, suggests that the demagnetisation occurs on cooling to T_k, *i.e.,* due to the kinematic processes discussed in Chapter 4. Consider Figure 4.8; simply cooling $pTRM_{300}^{450}$ from 300 °C, followed by heating back to 300 °C was sufficient to cause significant demagnetisation. This study suggests that a large percentage of the demagnetisation which is associated with low-temperature cycling, occurs on cooling to T_k rather than at T_k. This mechanism of demagnetisation has never been proposed as a method of demagnetisation during low-temperature treatment. The rate of demagnetisation due to kinematic processes is greater when K_1 is small, *i.e.,* near T_k (Chapter 6) and

near T_c (McClelland & Sugiura, 1987).

Simulated low-temperature cycling using micromagnetic models does not fully explain the low-temperature behaviour (Chapter 8). The models predict the importance of T_v, but not T_k. Note the micromagnetic results are only for single crystals, for an assemblage of crystals the calculated anomaly at T_v for the thermoremanences is expected to be less. The micromagnetic models were limited by; grain size, the fact that only single crystals were examined, and by the omission of important physical mechanisms, *e.g.,* thermal fluctuations and magnetostriction. However the model was very *successful* in predicting the relative behaviour of the different remanence during low-temperature cycling through T_v, *e.g.,* in agreement with experiment, the anomaly of $pTRM^{T_c}_{T_2}$ is greater than $pTRM^{T_1}_{T_2}$.

Experimental evidence collected in Chapter 7, suggests that memory and the fraction remaining after calibrated AF demagnetisation treatment (Chapter 7) is truly multidomain. Previous studies have examined features such as AF demagnetisation curves, however examination of the unblocking spectrum of $pTRM^{T_1}_{T_2}$ is a thought to be a better indicator of the true nature of remanence, *i.e.*, SD-like or MD-like (Bol'shakov & Shcherbalova, 1979). By examining the thermal demagnetisation for $pTRM^{T_1}_{T_2}$ memory it was concluded that magnetic memory is truly MD. These experiments above room temperature refute the idea suggested by D. Clark (*pers. comm.* 1997) that the anomaly at T_v is due to the unshielding of SD-like remanence. as this suggests that the the carriers of the remanences are in fact metastable body domains. The origin of stability is attributed deep local energy minima (LEM) domain states which are only available to domain structures during thermoremanence acquisition at high-temperatures. The deep LEM states are probably also available to ARM during acquisition, but the large AC field makes them unstable.

Further Work

The origin of the metastable remanence has not been fully resolved in this thesis, it has only been demonstrated that it is MD. To find the origin it is necessary to examine the microstructure. An attempt was made at this using TEM microscopy, however I did not start this project until the middle of my 3rd year, and it soon because apparent, that although I would have time to examine samples, I would not have time to master the art of preparing samples for TEM study. There have been a few studies which have examined the microstructure in magnetite grains (*e.g.,* Banfield *et al.*, 1994; Berti & Pinna, 1996) but never extensively in *pure* magnetite grains. This is an area which needs further investigation.

A second area of interest not discussed in this study is the possibility of an interaction of twin-structures with the domain structures below T_v. When magnetite is cooled through the Verwey structure the cubic symmetry is destroyed and replaced with a simpler (monoclinic or triclinic) structure with a small rhombohedral distortion. The cubic structure has a higher degree of symmetry than the monoclinic structure. On cooling through T_v, the crystals structure has to "choose" an orientation, *i.e.,* the *c*-axis can align in one of

three possible orientations. It is uncertain how the orientation of the *c* axis is determined, yet its orientation strongly affects the magnetocrystalline anisotropy which in turn effects the magnetic domain structure. It has been experimentally observed that in different regions of a grain the *c*-axis is aligned in different orientations (Otsuka & Sato, 1986). This gives rise to both twin-structures (Iida, 1980; Otsuka & Sato, 1986) and spontaneous strain (Salje, 1993). The twin-structures are separated by twin-domain walls similar to magnetic domain walls, and the spontaneous strain is expected to interact with the magnetism (*cf.* Equation (1.21). According to Houchmandzadeh *et al.* (1991), there is an interaction between magnetic domain walls and the twin-domain walls which has been observed for magnetite by Otsuki & Sato (1986) and Moskowitz (*pers. comm.* 1997); the twin domain walls are found to move easily in the presence of a magnetic field. The existence of twin-structures below the Verwey transition, but none above means that the Verwey transition is a ferroelastic phase transition (Salje, 1993, *pers. comm.* E. Salje, 1997).

To fully understand the low-temperature behaviour of remanence in MD magnetite it will be necessary to determine the size of the interaction between the magnetic domain structure with the ferroelastic domain structure. This could be determined using a combination of TEM and MFM.

The experiments which examined the low-temperature cycling of thermoremanence (Chapter 6), need to be repeated in a very low-field environment, *i.e.*, at least < 100 nT, ideally ≤ 10 nT.

Synthesis

This thesis has found that the origin of metastability is due to MD-like structures in agreement with McClelland & Shcherbakov (1995) and McClelland *et al.* (1996) rather than SD-like regions as suggested by Argyle *et al.* (1994) . The metastable structures are associated with thermoremanence acquired at high-temperature near T_c. The stability increases as the grain size is reduced, and the internal stress is increased. On cooling through the Verwey transition, stable domain structures give rise to large reversible anomalies in the magnetisation which has not been documented before. The positive anomalies and the stability of MD structures is supported by micromagnetic models.

Due to the anomalous low-temperature behaviour of thermoremanence it is suggested that low-temperature demagnetisation treatment should not be used alone as a "magnetic-cleaning technique". For example it was found that large SD grains irreversibly rotate their entire moments towards the monoclinic magnetocrystalline easy axis on cooling through T_v, whereas for large MD grains the rotation is *partially* reversible, *i.e.*, the direction of the primary remanence is partially rotated after LTD treatment and the original remanence direction is lost. In both cases the primary remanence orientation is lost, making LTD treatment inappropriate as a "magnetic-cleaning technique".

Bibliography

Abe, K., Miyamoto, Y., & Chikazumi, S. 1976. Magnetocrystalline anisotropy of low-temperature phase of magnetite. *J. Phys. Soc. Japan*, **41**(6), 1894–1902.

Abrikosov, A.A. 1968. Formulation of bound states of conduction-electron with localised spins in metals. *Soviet Phys. JETP*, **26**(3), 641–646.

Aharoni, A. 1985. Domain wall pinning at planer defects. *J. Appl. Phys.*, **58**, 2677–2880.

Aksenova, E.V., Gorbach, V.N., & Mamalui, V.N. 1987. Investigation of magnetostriction of magnetite near the Verwey temperature. *Sov. Phys. Solid State*, **29**(3), 1149–1152.

Allen, T. 1990. *Particle size measurement*. 4th. edn. London: Chapman & Hall.

Alperin, H.A., Steinsvoll, O., Nathans, R., & Shirane, G. 1967. Magnon scattering of polarised neutrons by the diffraction method: measurements on magnetite. *Phys. Rev.*, **154**(2), 508–514.

Amar, H. 1958. Magnetization mechanism and domain structure of multidomain particles. *Phys. Rev.*, **111**, 149–153.

Ambatiello, A., Fabian, K., & Hoffmann, V. 1995. Changes in the magnetic domain structures of magnetite during heating up to the Curie temperature (abstract). *Page B96 of: I.U.G.G. XX1 Gen. Ass., Abstracts*.

Anderson, P.W. 1956. Ordering and antiferromagnetism in ferrites. *Phys. Rev.*, **102**(4), 1008–1013.

Aragón, R. 1992. Influence of non-stoichiometry on the Verwey transition. *Phys. Rev. B*, **46**(9), 5328–5333.

Aragón, R., Buttrey, D.J., Shepherd, J.P., & Honig, J.M. 1985. Influence of non-stoichiometry on the Verwey transition. *Phys. Rev. B*, **31**(1), 430–436.

Arai, K.I., Ohmori, K. Tsuya, N., & Iida, S. 1976. Magnetostriction of magnetite in the vicinity of the low-temperature transition. *Phys. stat.sol (a)*, **34**, 325–330.

Argyle, K., & Dunlop, D. 1984. Theoretical domain structure in multidomain magnetite particles. *Geophys. Res. Lett.*, **11**(3), 185–188.

Argyle, K., & Dunlop, D. 1990. Low-temperature and high-temperature hysteresis of small multidomain magnetites (215-540 nm). *J. Geophys. Res.*, **95**(B5), 7069–7083.

Argyle, K.S., Dunlop, D.J., & Xu, S. 1994. Single Domain Behaviour of Multidomain Magnetite Grains (abstract). *Eos (Trans. Am. Geophys. Un.)*, **75**(Fall Meeting suppl.), 196.

Bailey, M.E., & Dunlop, D.J. 1977. On the use of anhysteretic remanent magnetization in paleointensity determination. *Phys. Earth Planet. Inter.*, **13**, 360–362.

Bailey, M.E., & Dunlop, D.J. 1983. Alternating field characteristics of pseudo-single-domain (2–14 μm) and multidomain magnetite. *Earth Planet. Sci. Lett.*, **294**, 335–352.

Banerjee, S.K. 1991. Magnetic Properties of Fe-Ti. *In:* Lindsley, D.H. (ed), *Reviews in Mineralogy Volume 25 - Oxide Minerals: Petrologic and magnetic significance*. Washington D.C.: Mineralogical Society of America.

Banerjee, S.K., & Mellema, J.P. 1974a. Lunar paleointensity from three Apollo 15 crystalline rocks using an A.R.M. method. *Earth Planet. Sci. Lett.*, **23**, 185–188.

Banerjee, S.K., & Mellema, J.P. 1974b. A new method for the determination of paleointensity from the A.R.M. properties of rocks. *Earth Planet. Sci. Lett.*, **23**, 177–184.

Banfield, J.F., Waskilewski, P.J., & Veblen, D.R. 1994. TEM study of relationships between microstructure and magnetic properties of strongly magnetized magnetite and maghemite. *Am. Min.*, **79**, 654–667.

Bean, C.P., & Livingston, J.D. 1959. Superparamagnetism. *J. Appl. Phys.*, **30**(4), 120S–129S.

Belov, K.P. Goryaga, A.N, Sheremet'ev, V.N., & Pronin, V.N. 1985a. Interrelation of magnetic and electronic subsystems in orthorhombic phase magnetite. *Sov. Phys. Solid State*, **27**(6), 1101.

Belov, K.P. Goryaga, A.N, Sheremet'ev, V.N., & Naumova, O.A. 1985b. The nature of the small contribution to the magnetostriction of Fe^{2+} ions ins spinel. *JETP Lett*, **42**(3), 117–119.

Belov, K.P. 1982. Spin-reorientation transition in magnetite as an example of spinodal decomposition in a magnetic system. *JETP Lett.*, **36**, 146–149.

Belov, K.P. 1993. Electronic processes in magnetite (or "Enigmas in magnetite"). *Physics-Uspekhi*, **36**(5), 380–391.

Belov, K.P. 1994. Anomalies of the magnetoresistance of ferrites. *Physics-Uspekhi*, **37**(6), 563–575.

Belov, K.P. 1996a. Ferrimagnets with a "weak" magnetic sublattice. *Physics-Uspekhi*, **39**, 623–634.

Belov, K.P. 1996b. On the nature of a low-temperature transition in magnetite. *JETP*, **36**, 1152–1155.

Berti, G., & Pinna, E. 1996. Microstructure of magnetite from XRPD data in relation to magnetism. *Mater. Sci. Forum*, **228-231**, 839–844.

Bickford Jr., L.R. 1949. Ferromagnetic Resonance Absorption in Magnetite. *Phys. Rev.*, **76**, 137–138.

Bickford Jr., L.R. 1950. Ferromagnetic Resonance Absorption in Magnetite Single Crystals. *Phys. Rev.*, **78**(4), 449–457.

Bickford Jr., L.R., Pappis, J.R., & Stull, J.L. 1955. Magnetostriction and permeability of magnetite and cobalt-substituted magnetite. *Phys. Rev.*, **99**(4), 1210–1214.

Bickford Jr., L.R., Brownlow, J.M., & Penoyer, R, F. 1957. Magnetocrystalline anisotropy in cobalt-substituted magnetic single crystals. *Proc. I.E.E.*, **B104**, 238–244.

Bitter, F. 1931. On inhomogeneities in the magnetization of ferromagnetic materials. *Phys. Rev.*, **38**, 1903–1905.

Blackett, P.M.S. 1956. *Lectures on Rock Magnetism*. Jerusalem: Weizmann Science Press of Israel.

Bleaney, B.I., & Bleaney, B. 1965. *Electricity and magnetism*. 2nd edn. London: Oxford University Press.

Bol'shakov, A.S, & Shcherbalova, V.V. 1979. A thermomagnetic criterion for determining the domain structure of ferrimagnetics. *Izv., Acad. of Sci., USSR, Phys. Solid Earth*, **15**, 111–117.

Borradaile, G.J. 1994. Low-temperature demagnetisation and ice-pressure demagnetisation in magnetite and hematite. *Geophys. J. Int.*, **116**, 578–584.

Boyd, J.R., Fuller, M., & Halgedahl, S. 1984. Domain wall nucleation as a controlling factor in the behaviour of fine magnetic particles in rock. *Geophys. Res. Lett.*, **11**(3), 193–196.

Bozorth, R.M. 1951. *Ferromagnetism*. D. van Nistrand Co., Inc., New Jersey.

Brown, A.P., & O'Reilly, W. 1996. The magnetic hysteresis properties of ball-milled monodomain titanomagnetite $Fe_{2.4}Ti_{0.6}O_4$. *Geophys. Res. Lett.*, **23**(20), 2863–2866.

Brown, W.F., Jr. 1963. *Micromagnetics*. John Wiley, New York.

Brunhes, B. 1906. Recherches sur la direction d'aimantation des roches volcaniques. *J. Physique*, **5**, 705–724.

Calhoun, B.A. 1954. Magnetic and electric properties of magnetite at low-temperatures. *Phys. Rev.*, **94**(6), 1577–1585.

Chainani, A., Yokoya, T., Morimoto, T., Takahashi, T., & Todo, S. 1996. Electronic structure of Fe_3O_4 across the Verwey transition. *J. Electron Spect. Rel. Pheb.*, **78**, 99–102.

Chakravarty, A.S. 1980. *Introduction to the magnetic properties of solids*. London: Wiley & Sons.

Clark, D.A. 1983. Comments on Magnetic Petrophysics. *Bull. Aust. Soc. Explor. Geophys.*, **14**, 49–62.

Collinson, D.W. 1983. *Methods in rock magnetism and palaeomagnetism - techniques and instrumentation*. London: Chapman and Hall.

Creer, K.M., & Like, C.B. 1967. A low temperature investigation of natural remanent magnetisation of several igneous rocks. *Geophys. J. R. Astron. Soc.*, **12**, 301–312.

Crew, D.C., Farrant, S.H., McCormick, P.G., & Street, R. 1996. Measurement of magnetic viscosity in a Stoner-Wohlfarth material. *J. Magn. Magn. Mater.*, **163**, 299–312.

Cullen, J.R., & Callen, E. 1971. Band theory of multiple ordering and the metal-semiconductor transition in magnetite. *Phys. Rev. Lett.*, **26**(5), 236–238.

Cullen, J.R., & Callen, E. 1973. Multiple ordering in magnetite. *Phys. Rev. B*, **7**(1), 397–402.

Dankers, P. 1978. *Magnetic properties of dispersed natural iron-oxides of known grain size*. Ph.D. thesis, State University of Utrecht.

Dankers, P. 1981. Relationship between median destructive field and remanent coercive forces for dispersed natural magnetite, titanomagnetite and hematite. *Geophys. J. R. Astron. Soc.*, **64**, 447–461.

Dankers, P., & Sugiura, N. 1981. The effects of annealing and concentration on the hysteresis properties of magnetite around the PSD-MD transition. *Earth Planet. Sci. Lett.*, **56**, 422–428.

David, P. 1904. Sur la stabilité de la direction d'aimantation dans quelques roches volcaniiques. *C. R. Acad. Sci. Paris*, **138**, 41–42.

Davis, P.M., & Evans, M.E. 1976. Interacting single domain properties of magnetite intergrowths. *J. Geophys. Res.*, **81**, 989–993.

Day, R. 1977. TRM and its variation with grain size. *J. Geomag. & Geoelec.*, **29**, 233–265.

Day, R., Fuller, M., & Schmidt, V.A. 1977. Hysteresis properties of titanomagnetites: grain size and compositional dependence. *Phys. Earth Planet. Inter.*, **13**, 260–267.

de Boer, C.B., & Dekkers, M.J. 1996. Grain-size dependence of the rock magnetic properties of natural maghemite. *Geophys. Res. Lett.*, **23**(20), 2811–2814.

De Grave, E., Persoons, R.M., Vanderberghe, R.E., & de Bakker, P.M.A. 1993. Mössbauer study of the high-temperature phase of Co-substituted magnetites, $\mathrm{Co}_x\mathrm{Fe}_{3-x}\mathrm{O}_4$. I. $x \leq 0.04$. *Phys. Rev. B*, **47**(10), 5881–5893.

Domenicali, C.A. 1950. Magnetic and electric properties of natural and synthetic single crystals of magnetite. *Phys. Rev. B*, **78**, 459–467.

Dunlop, D.J. 1971. Hematite: intrinsic and defect ferromagnetism. *Science*, **169**, 858–860.

Dunlop, D.J. 1973a. Superparamagnetic and single-domain threshold sizes in magnetite. *J. Geophys. Res.*, **78**, 1780–1793.

Dunlop, D.J. 1973b. Theory of magnetic viscosity of lunar and terrestrial rocks. *Rev. Geophys. Space Phys.*, **11**, 851–901.

Dunlop, D.J. 1983. Viscous magnetisation of 0.04-100μm magnetites. *Geophys. J. R. astr. Soc.*, **74**, 667–687.

Dunlop, D.J., & Argyle, K.S. 1991. Separating multidomain and single-domain-like remanences in pseudo-single-domain magnetites (215-540 nm) by low-temperature demagnetisation. *J. Geophys. Res.*, **96**(B2), 2007–2017.

Dunlop, D.J., & Argyle, K.S. 1997. Thermoremanence, anhysteretic remanence and susceptibility of submicron magnetites: Nonlinear field dependence and variation with grain size. *J. Geophys. Res.*, **102**(B9), 20199–20210.

Dunlop, D.J., & Özdemir, Ö. 1997. *Rock Magnetism: Fundamentals and Frontiers*. Cambridge University Press.

Dunlop, D.J., & Waddington, E.D. 1975. The field dependence of thermoremanent magnetization igneous rocks. *Earth Planet. Sci. Lett.*, **25**, 11–25.

Dunlop, D.J., & West, G.F. 1969. An experimental evaluation of single domain theories. *Rev. Geophys.*, **7**, 709–757.

Dunlop, D.J., & Xu, S. 1993. A comparison of methods of granularity and domain structure determination (abstract). *Eos (Trans. Am. Geophys. Un.)*, **74**(Fall Meeting suppl.).

Dunlop, D.J., & Xu, S. 1994. Theory of partial thermoremanence in multi-domain grains: 1. repeated identical barriers to wall motion (single coercivity). *J. Geophys. Res.*, **99**(B5), 9005–9023.

Dunlop, D.J., Newell, A.J., & Enkin, R.J. 1994. Transdomain thermoremanent magnetization. *J. Geophys. Res.*, **99**(B10), 19741–19755.

Enkin, R., , & Dunlop, D.J. 1987. A micromagnetic study of pseudo-single domain remanence in magnetite. *J. Geophys. Res.*, **92**(B12), 12726–12740.

Enkin, R.J., & Williams, W. 1994. Three-dimensional micromagnetic analysis of stability in fine magnetic grains. *J. Geophys. Res.*, **99**(B1), 611–618.

Everitt, C.W.F. 1962. Thermoremanent magnetization: III. Theory of Multidomain grains. *Philos. Mag.*, **7**(76), 599–616.

Fabian, K., & Heider, F. 1996. How to include magnetostriction in micromagnetic models of titanomagnetite grains. *Geophys. Res. Lett.*, **23**(20), 2839–2842.

Fabian, K., Kirchner, A., Williams, W., Heider, F., Leibl, T., & Huber, A. 1996. Three-dimensional micromagnetic calculations for magnetite using FFT. *Geophys. J. Int.*, **124**, 89–104.

Farrell, D.M. 1972 (June). *A study of the infra-red absorption in the oxidation of magnetite to maghemite and hematite*. Tech. rept. IR 72-18. Mines Branch, Dept. of Energy, Mines and Resources, Ottawa.

Fine, P., & Singer, M.J. 1989. Contribution of ferrimagnetic minerals to oxalate- and dithionite-extractable iron. *Soil. Sci. Soc. Am. J.*, **53**, 191–196.

Fletcher, E.J., & O'Reilly, W. 1974. Contribution of Fe^{2+} ions to the magnetocrystalline anisotropy constant K_1 of $Fe_{3-x}Ti_xO_4$ ($0 < x < 0.1$). *J. Phys. C.: Solid State Phys.*, **7**, 171–178.

French, A.P., & Taylor, E.F. 1978. *An introduction to quantum physics*. London: Chapman and Hall.

Fukuma, K., & Dunlop, D.J. 1997. Monte Carlo simulation of two-dimensional domain structures in magnetite. *J. Geophys. Res.*, **102**(B3), 5135–5143.

Geiß C.E., Heider, F., & Soffel, H.C. 1996. Magnetic domain observations on magnetite and titanomaghemite grains (0.5-10 μm). *Geophys. J. Int.*, **124**, 75–88.

Gillot, B. 1994. Infrared spectrometric investigation of the submicron metastable cation-deficient spinels in relation to order-disorder phenomena and phase transition. *Vibrational Spectroscopy*, **6**, 127–148.

Gleitzer, C. 1997. Electrical properties of anhydrous iron oxides. *Key Engineering Materials*, **125-126**, 355–418.

Goss, C.J. 1987. *Chemical remanent magnetisation and phase transformations in iron oxide minerals*. Ph.D. thesis, University of Cambridge.

Gridin, V.V., Hearne, G.R., & Honig, J.M. 1996. Magnetoresistance extremum at the first-order Verwey transition in magnetite (Fe_3O_4). *Phys. Rev. B*, **53**(23), 15518–15521.

Halgedahl, S.L. 1991. Magnetite domain patterns observed on synthetic Ti-rich titanomagnetite as a function of temperature and in states of thermoremanent magnetization. *J. Geophys. Res.*, **96**(B3), 3943–3972.

Halgedahl, S.L., & Fuller, M. 1980. Magnetic domain observations of nucleation processes in fine particles of intermediate titanomagnetite. *Nature*, **288**, 70–72.

Halgedahl, S.L., & Fuller, M. 1983. The dependence of magnetic domain structure upon magnetization state with emphasis on nucleation as mechanism for pseudo-single-domain behaviour. *J. Geophys. Res.*, **88**, 6505–6522.

Halgedahl, S.L., & Jarrard, R.D. 1995. Low temperature behaviour of single domain through multidomain magnetite. *Earth Planet. Sci. Lett.*, **130**, 127–139.

Hargrove, R.S., & Kündig, W. 1970. Mössbauer measurements of magnetite below the Verwey transition. *Solid State Comm.*, **8**, 303–308.

Harrison, R.J., & Putnis, A. 1995. Magnetic properties of the magnetite-spinel solid solution: saturation magnetization and cation distributions. *Am. Min.*, **80**, 213–221.

Harrison, R.J., & Putnis, A. 1996. Magnetic properties of the magnetite-spinel solid solution: Curie temperatures, magnetic susceptibilities, and cation ordering. *Am. Min.*, **81**, 375–384.

Harrison, R.J., & Putnis, A. 1997. Interaction between exsolution microstructures and magnetic properties of magnetite-spinel solid solution. *Am. Min.*, **82**, 131–142.

Hartmann, U. 1987. A theoretical analysis of Bitter-pattern evolution. *J. Magn. Magn. Mater.*, **68**, 298–304.

Hartstra, R.L. 1982a. A comparative study of the ARM and $I_{\rm sr}$ of some natural magnetites of the MD and PSD grain size. *Geophys. J. R. Astron. Soc.*, **71**, 497–518.

Hartstra, R.L. 1982b. Grain-size dependence of initial susceptibility and saturation magnetisation-related parameters of four natural magnetites in the PSD-MD range. *Geophys. J. R. Astron. Soc.*, **71**, 477–495.

Hartstra, R.L. 1983. TRM, ARM and Isr of two natural magnetites of MD and PSD grain size. *Geophys. J. R. Astron. Soc.*, **73**, 719–737.

Heddle, M.F. 1878a. The Geognosy and mineralogy of Scotland, Orkney and Shetland. Island of Unst. *Mineralog. Mag.*, **2**, 12–35.

Heddle, M.F. 1878b. Islands of Uya, Haaf Grunay, Fetlar, and Yell. *Mineralog. Mag.*, **2**, 106–133.

Heddle, M.F. 1878c. The Mainland. *Mineralog. Mag.*, **2**, 155–90.

Heider, F. 1988. *Magnetic properties of hydrothermally grown Fe_3O_4 crystals*. Ph.D. thesis, University of Toronto.

Heider, F. 1990. Temperature dependence of domain structure in natural magnetite and its significance for multi-domain TRM models. *Earth Planet. Sci. Lett.*, **65**, 54–61.

Heider, F., & Bryndzia, L.T. 1987. Hydrothermal growth of magnetite crystals (1 μm to 1 mm). *J. Crystal Growth*, **84**, 50–56.

Heider, F., & Williams, W. 1988. Note of temperature dependence of exchange constant in magnetite. *Geophys. Res. Lett.*, **15**(2), 184–187.

Heider, F., Dunlop, D.J., & Sugiura, N. 1988a. Magnetic properties of hydrothermally recrystallised magnetite crystals. *Science*, **236**, 1287–1290.

Heider, F., Halgedahl, S.L., & Dunlop, D.J. 1988b. Temperature dependence of magnetic domains in magnetite crystals. *Geophys. Res. Lett.*, **15**, 499–502.

Heider, F., Dunlop, D.J., & Soffel, H.C. 1992. Low temperature and alternating field demagnetisation of saturation remanence and thermoremanence in magnetite grains (0.037 μm to 5 mm). *J. Geophys. Res.*, **97**(B6), 9371–9381.

Heider, F., Zitzelsberger, A., & Fabian, K. 1996. Magnetic-susceptibility and remanent coercive force in grown magnetite crystals from 0.1 μm to 6 mm. *Phys. Earth Planet. Inter.*, **93**, 239–256.

Hodych, J.P. 1986. Evidence for magnetostrictive control of intrinsic susceptibility and coercive force of multidomain magnetite in rocks. *Phys. Earth Planet. Inter.*, **42**, 184–194.

Hodych, J.P. 1990. Magnetic hysteresis as a function of low temperature in rocks: evidence for internal stress control of remanence in multi-domain and pseudo-single-domain magnetite. *Phys. Earth Planet. Inter.*, **64**, 21–26.

Hodych, J.P. 1991. Low-temperature demagnetisation of saturation remanence in rocks bearing multidomain magnetite. *Phys. Earth Planet. Inter.*, **66**, 144–152.

Hoffmann, V.and Schäfer, R., Appel, E., Hubbert, A., & Soffel, H. 1987. First domain observations with the magneto-optical Kerr effect on Ti-ferrites in rocks and synthetic equivalents. *J. Magn. Magn. Mater.*, **71**, 90–94.

Honderich, J. (ed). 1995. *The Oxford companion to Philosophy*. Oxford: Oxford University Press.

Honig, J.M. 1995. Analysis of the Verwey transition in magnetite. *J. Alloys & Compounds*, **229**, 24–39.

Honig, J.M., & Spałek, J. 1992. Elementary formulation of the Verwey transition in magnetite via order-disorder formalism. *J. Solid State Chem.*, **96**, 115–122.

Hook, J.R., & Hall, H.E. 1991. *Solid state physics*. 2nd edn. London: Wiley & Sons.

Houchmandzadeh, B., Lajzerowicz, J., & Salje, E. 1991. Order parameter coupling and chirality of domain walls. *J. Phys. Condens. Matter*, **3**, 5163–5169.

Housen, B.A., Banerjee, S.K., & Moskowitz, B.M. 1996. Low-temperature magnetic properties of siderite and magnetite in marine sediments. *Geophys. Res. Lett.*, **23**(20), 2843–2846.

Hu, Z., Yamg, X., Hsia, Y., Jiang, X., Chen, X., & He, Y. 1991. The investigation of magnetite microcrystals. *Hyperfine Interactions*, **68**, 421–424.

Hunt, C.P., Singer, M.J., Kletetshka, G., Tenpas, J., & Verosub, K.L. 1995. Effect of citrate-bicarbonate-dithionite treatment on fine-grained magnetite and maghemite. *Earth Planet. Sci. Lett.*, **130**, 87–94.

ICDD. 1986. *Mineral Powder Diffraction File: Data Book*. Swarthmore, U.S.A: International Centre for Diffraction Data.

Iida, S. 1980. Structure of at Fe_3O_4 low temperature. *Phil. Mag. B*, **42**(3), 349–376.

Iizumi, M., Koetzle, T.F., Shirane, G., Chikazumi, S., Mastsui, M., & Todo, S. 1982. Structure of magnetite (Fe_3O_4) below the Verwey transition temperature. *Acta. Cryst.*, **B38**, 2121–2133.

Isida, S., Suzuki, M., Todo, S., Môri, T., & Siratori, K. 1996. Pressure effect on the elastic constants of magnetite. *Physica B*, **219 & 220**, 638–640.

Jackson, J.D. 1975. *Classical electrodynamics*. 2nd edn. New York: Wiley & Sons.

Jiles, D. 1991. *Magnetism and Magnetic Materials*. London: Chapman and Hall.

Johnson, H.P., Lowrie, W., & Kent, D.V. 1975. Stability of of anhysteretic remanent magnetization in fine and course magnetite and maghemite. *Geophys. J. R. Astron. Soc.*, **41**, 1–10.

Kąkol, Z. 1990. Magnetic and transport properties of magnetite in the vicinity of the Verwey transition. *J. Solid State Chem.*, **88**, 104–114.

Kąkol, Z., & Honig, J.M. 1989. Influence of deviations from ideal stoichiometry on the anisotropy parameters of magnetite $Fe_{3-\delta}O_4$. *Phys. Rev. B*, **40**(13), 9090–9097.

Kąkol, Z., Sabol, J., & Honig, J.M. 1991. Magnetic anisotropy of titanomagnetites $Fe_{3-x}Ti_xO_4$, $0 \leq x \leq 0.55$. *Phys. Rev. B*, **44**(5), 2198–2204.

King, J. 1996. *Magnetic properties of arrays of magnetite particles produced by the method of electron beam lithography (EBL)*. Ph.D. thesis, University of Edinburgh.

King, J., Williams, W., Wilkinson, C.D.W., McVitie, S., & Chapman, J.N. 1996. Magnetic properties of magnetite arrays produced by the method of electron lithography. *Geophys. Res. Lett.*, **23**(20), 2847–2850.

Kittel, C. 1949a. Physical theory of ferromagnetic domains. *Reviews of Modern Physics*, **21**(4), 541–583.

Kittel, C. 1949b. Theory of the Formation of Powder patterns on ferromagnetic crystals. *Phys. Rev.*, **76**(10), 1527.

Kittel, C. 1975. *Introduction to solid state physics*. 5th edn. New York: Wiley & Sons.

Kobayashi, K., & Fuller, M. 1968. Stable remanence and memory of multidomain materials with special reference to magnetite. *Phil. Mag.*, **18**, 601–624.

Koenigsberger, J.G. 1938. Natural residual magnetism of eruptive rocks. *Terr. Magn. Atoms. Elec.*, **43**, 119–130 & 299–320.

Kozłowski, A., Kąkol, Z., Kim, D., Zalecki, R., & Honig, J.M. 1996. Heat capacity of $Fe_{3-\alpha}M_{\alpha}O_4$ (M=Zn, Ti, $0 \leq \alpha \leq 0.04$). *Phys. Rev. B*, **54**(17), 12093–12098.

Krane, K.S. 1988. *Introductory Nuclear Physics*. London: Wiley & Sons.

Kronmüller, H. 1977. Theory of the magnetic after-effect by valency fluctuations in magnetite. *J. Magn. Magn. Mater.*, **4**, 280–286.

Kronmüller, H., Schützenauer, R., & Walz, F. 1974. Magnetic after-effects in magnetite. *Phys. Stat. Sol. (A)*, **24**, 487–494.

LaBonte, A.E. 1969. Two-dimensional Bloch-type domain walls in ferromagnetic films. *J. Appl. Phys.*, **40**, 2450–2458.

Landau, L., & Lifshitz, E. 1935. On the theory of the dipseriosn of magnetic permeability in ferromagnetic bodies. *Phys. Z. Soujet.*, **8**, 153–167.

Lee, E.W. 1955. Magnetostriction and magnetomechanical effects. *Rept. Prog. Phys.*, **18**, 184–229.

Levi, S. 1977. The effect of magnetite particle size on paleointensity determinations of the geomagnetic field. *Phys. Earth Planet. Inter.*, **13**, 245–259.

Levi, S., & Merrill, R.T. 1976. A comparison of ARM and TRM in magnetite. *Earth Planet. Sci. Lett.*, **32**, 171–184.

Levi, S., & Merrill, R.T. 1978. Properties of single-domain, pseudo-single domain and multidomain magnetite. *J. Geophys. Res.*, **83**, 309–323.

Liboff, R.L. 1992. *Introduction to quantum mechanics*. 2nd edn. New York: Addison-Wesley Publishing.

Liese, H.C. 1967. An infrared absorption analysis of magnetite. *Am. Min.*, **52**, 1198–1205.

Liu, X., Rolph, T., & Bloemendal, J. 1995. The Citrate-Bicarbonate-Dithionate (CBD) removable magnetic component of Chinese loess. *Quaternary Proceedings*, **4**, 53–58.

Longworth, G., Becker, L.W., Thompson, R., Oldfield, F., Dearing, J.A., & Rummery, T.A. 1979. Mössbauer effect and magnetic studies of secondary iron oxides in soils. *J. Soil Sci.*, **30**, 93–100.

Lowrie, W., & Fuller, M. 1969. Effect of annealing on coercive force and remanent magnetisations in magnetite. *J. Geophys. Res.*, **74**(10), 2698–2710.

Lowrie, W., & Fuller, M. 1971. On the alternating field demagnetisation characteristics of multidomain thermoremanent magnetisation in magnetite. *J. Geophys. Res.*, **76**(26), 6339–6349.

Markov, G.P., Shcherbakov, V.P., Bol'shakov, A.S., & Vinogradov, Yu.K. 1983. On the temperature dependence of the partial thermoremanent magnetization of multidomain grains. *Izv., Acad. of Sci., USSR, Phys. Solid Earth*, **19**(8), 625–630.

Matijević, E. 1993. Preparation and properties of uniform size colloids. *Chem. Mater.*, **5**, 412–426.

Matsui, M., Todo, S., & Chikazumi, S. 1977. Magnetisation of the low temperature phase of Fe_3O_4. *J. Phys. Soc. Japan*, **43**, 47–53.

McClelland, E. 1996. Theory of CRM acquired by grain-growth, and its implications for TRM discrimination and paleointensity determination in igneous rocks. *Geophys. J. Int.*, **126**(1), 271–280.

McClelland, E., & Briden, J.C. 1995. An improved methodology for Thellier-type paleointensity determination in igneous rocks and its usefulness for verifying primary thermoremanence. *J. Geophys. Res.*, **101**(B10), 21995–22013.

McClelland, E., & Shcherbakov, V.P. 1995. Metastability of domain state in MD1 magnetite: consequences for remanence acquisition. *J. Geophys. Res.*, **100**(B3), 3841–3857.

McClelland, E., & Sugiura, N. 1987. A kinematic model of TRM acquisition in multidomain magnetite. *Earth Planet. Sci. Lett.*, **46**, 9–23.

McClelland, E., Muxworthy, A.R., & Thomas, R.M. 1996. Magnetic properties of the stable fraction of remanence in large multidomain (MD) magnetite grains: single-domain or MD? *Geophys. Res. Lett.*, **23**(20), 2831–2834.

McElhinny, M.W. 1973. *Palaeomagnetism and plate tectonics*. Cambridge: Cambridge University Press.

McKie, D., & McKie, C. 1974. *Crystalline Solids*. London: Thomas Nelson & Sons.

Mehra, O.P., & Jackson, M.L. 1960. Iron oxide removal from soils and clays by a dithionite-citrate system buffered with sodium bicarbonate. *Clays Clay Miner.*, **7**, 317–327.

Merrill, R.T. 1970. Low-temperature treatment of magnetite and magnetite-bearing rocks. *J. Geophys. Res.*, **75**(17), 3343–3349.

Merrill, R.T. 1981. Toward a better theory of thermal remanent magnetization. *J. Geophys. Res.*, **86**(B2), 937–949.

Metcalf, M., & Fuller, M. 1986. Domain observations of titanomagnetites from room temperature to Curie point and the nature of thermoremanent magnetism in fine particles. *Nature*, **321**, 847–849.

Metcalf, M., & Fuller, M. 1987a. Domain observations of titanomagnetites during hysteresis at elevated temperatures and thermal cycling. *Phys. Earth Planet. Inter.*, **46**, 120–126.

Metcalf, M., & Fuller, M. 1987b. Magnetic remanence measurements of single particles and the nature of domain patterns in titanomagnetites. *Geophys. Res. Lett.*, **14**(12), 1207–1210.

Metcalf, M., & Fuller, M. 1988. A synthetic TRM induction curve for fine particles generated from domain observations. *Geophys. Res. Lett.*, **15**, 503–506.

Millar, R.W. 1929. The heat capacities at low-temperature of Ferrous Oxide magnetite and cuprous and cupric oxides. *J. Amer. Chem. Soc.*, **51**, 215–222.

Mishra, S.K., & Satpathy, S. 1993. Energetic stabilisation of the Mizoguchi structure for magnetite by band-structure effects. *Phys. Rev. B*, **47**(10), 5564–5570.

Miyamoto, Y., & Chikazumi, S. 1988. Crystal symmetry of magnetite in low temperature phase deduced from magnetoelectric measurement. *J. Phys. Soc. Japan*, **57**(6), 2040–2050.

Mizoguchi, M. 1978a. NMR Study of the low-temperature phase of Fe_3O_4. Electron ordering analysis. *J. Phys. Soc. Japan*, **44**(5), 1512–1520.

Mizoguchi, M. 1978b. NMR Study of the low-temperature phase of Fe_3O_4. I. Experiments. *J. Phys. Soc. Japan*, **44**(5), 1501–1511.

Moloni, K., Moskowitz, B.M., & Dahlberg, E.D. 1996. domain structures in single crystal magnetite below the Verwey transition as observed with a low-temperature magnetic force microscope. *Geophys. Res. Lett.*, **23**(20), 2851–2854.

Moon, T., & Merrill, R.T. 1984. The magnetic moments of non-uniformly magnetized grains. *Phys. Earth Planet. Inter.*, **34**, 186–194.

Moon, T., & Merrill, R.T. 1985. Nucleation theory and domain states in multidomain magnetic material. *Phys. Earth Planet. Inter.*, **37**, 214–222.

Moon, T.S. 1991. Domain states in fine particle Fe_3O_4 and titanomagnetite. *J. Geophys. Res.*, **96**(B6), 9909–9923.

Morin, J. 1950. Magnetic susceptibility of α-Fe_2O_3 and Fe_2O_3 added titanium. *Phys. Rev.*, **78**, 819–820.

Moskowitz, B.M. 1980. Theoretical grain size limits for single-domain, pseudo-single domain and multidomain behavior in titanomagnetite (x = 0.6) as a function of low-temperature oxidation. *Earth Planet. Sci. Lett.*, **47**, 286–293.

Moskowitz, B.M. 1993a. High-temperature magnetostriction of magnetite and titanomagnetites. *J. Geophys. Res.*, **98**(B1), 359–371.

Moskowitz, B.M. 1993b. Micromagnetic study of the influence of crystal defects on coercivity in magnetite. *J. Geophys. Res.*, **98**(B10), 18011–18026.

Moskowitz, B.M., & Banerjee, S.K. 1979. Grain size limits for pseudosingle domain behaviour in magnetite. *IEEE Trans. Magn.*, **MAG-15**, 1241–1246.

Moskowitz, B.M., & Halgedahl, S.L. 1987. Theoretical temperature and grain-size dependence of domain state in X = 0.6 titanomagnetite. *J. Geophys. Res.*, **92**(B10), 10667–10682.

Moskowitz, B.M., Frankel, R.B., & Bazylinski, D.A. 1993. Rock magnetic criteria for the detection of biogenic magnetite. *Earth Planet. Sci. Lett.*, **120**, 283–300.

Mulay, L.N., & Boudreaux, U. 1976. *Theory and Application of Molecular diamagnetism*. New York: Wiley-Interscience.

Muxworthy, A.R. 1994. *Analysis of the time and temperature dependence of an assemblage of SD magnetite grains*. Undergraduate thesis, University of Edinburgh.

Mykura, W. 1976. *British regional geology: Orkney and Shetland*. N.E.R.C., Institute of Geological Sciences. Edinburgh: Her Majesty's Stationary Office.

Nagaev, É.L. 1971. Conductivity of magnetic semiconductors in the case of strong coupling between carriers and localised spins. *Sov. Phys. Solid State*, **13**(4), 961–967.

Nagata, T. 1961. *Rock Magnetism.* revised edn. Tokyo: Mazuren Company Ltd.

Nagata, T., Kobayashi, K., & Fuller, M.D. 1964. Identification of magnetite and hematite in rocks by magnetic observation at low temperature. *J. Geophys. Res.*, **69**, 2111–2120.

Néel, L. 1947. Propriétés d'un ferromagnétique cubique en grain fins. *C. R. Acad. Sci. Paris*, **224**, 1488–1490.

Néel, L. 1949. Theory of the magnetic after effect in ferromagnetics in the form of small particles, with applications to baked clays. *Ann. Géophys.*, **5**, 99–136.

Néel, L. 1955. Some theoretical aspects of rock magnetism. *Adv. Phys.*, 191–242.

Newell, A.J., Dunlop, D.J, & Enkin, R.J. 1990. Temperature dependence of critical sizes, wall widths and moments in two-domain magnetite grains. *Phys. Earth Planet. Inter.*, **65**, 165–176.

Oersted, H.C. 1820. Experiment on the effects of a current on the magnetic needle. *Ann. Phil.*, **16**.

O'Grady, K., Lewis, V.G., & D.P.E., Dickson. 1993. Alternating gradient force magnetomery: Applications and extension to low temperatures (invited). *J. Appl. Phys.*, **73**(10), 5608–5613.

Okudera, H., Kihara, K., & Matsumoto, T. 1996. Temperature dependence of structure parameters in natural magnetite: Single crystal X-ray study from 126 K and 773 K. *Acta. Cryst.*, **B52**, 450–457.

O'Reilly, W. 1984. *Rock and Mineral Magnetism*. Glasgow: Blackie & Sons Ltd.

Otsuka, N., & Sato, H. 1986. Observation of the Verwey transition in Fe_3O_4 by high-resolution electron microscopy. *J. Solid. State Chem.*, **61**, 212–222.

Ozaki, M., & Matijević, E. 1985. Preparation and magnetic properties of monodispersed spindle-type γ-Fe_2O_3 particles. *J. Coll. Inter. Sci.*, **107**(1), 199–203.

Özdemir, Ö. 1990. High-temperature hysteresis and thermoremanence of single-domain maghemite. *Phys. Earth Planet. Inter.*, **65**, 125–136.

Özdemir, Ö., & Dunlop, D.J. 1989. Chemico-viscous remanent magnetisation in the Fe_3O_4-γFe_2O_3 system. *Science*, **243**, 1043–1047.

Özdemir, Ö., & Dunlop, D.J. 1993. Magnetic domain structures on a natural single crystal of magnetite. *Geophys. Res. Lett.*, **20**(17), 1835–1838.

Özdemir, Ö., & Dunlop, D.J. 1995. Single-domain state in a large (3 mm) multidomain magnetite crystal (abstract). *Eos (Trans. Am. .Geophys. Un.)*, **76**(Fall Meeting suppl.), F160.

Özdemir, Ö., & Dunlop, D.J. 1997. Effect of crystal defects and internal stress on the domain structure and magnetite properties of magnetite. *J. Geophys. Res.*, **102**(B9), 20211–20224.

Özdemir, Ö., & O'Reilly, W. 1982. High-temperature properties of synthetic monodomain titanomaghemites. *Earth Planet. Sci. Lett.*, **57**, 437–447.

Özdemir, Ö., Dunlop, D.J., & Moskowitz, B.M. 1993. The effect of oxidation on the Verwey transition in magnetite. *Geophys. Res. Lett.*, **20**(16), 1671–1674.

Özdemir, Ö., Xu, S., & Dunlop, D.J. 1995. Closure domains in magnetite. *J. Geophys. Res.*, **100**(B2), 2193–2209.

Ozima, Minoru, & Ozima, Mituko. 1965. Origin of thermoremanent magnetization. *J. Geophys. Res.*, **70**(6), 1363–1369.

Ozima, Minoru, Ozima, Mituko, & Nagata, T. 1964a. Low-temperature treatment as an effective means of "magnetic cleaning" of natural remanent magnetisation. *J. Geomag. & Geoelec.*, **16**, 37–41.

Ozima, Mituko, Ozima, Minoru, & Akimoto, S-T. 1964b. Low-temperature characterisation of remanent magnetisation of magnetite - Self-reversal and recovery phenomena. *J. Geomag. & Geoelec.*, **16**, 165–177.

Parkinson, W.D. 1983. *Introduction to Geomagnetism*. Edinburgh: Scottish Academic Press.

Parry, L.G. 1965. Magnetic properties of dispersed magnetite powders. *Phil. Mag.*, **11**, 303–312.

Parry, L.G. 1979. Magnetization of multidomain particles of magnetite. *Phys. Earth Planet. Inter.*, **19**, 12–30.

Parry, L.G. 1980. Shape-related factors in the magnetisation of immobilized magnetite particles. *Phys. Earth Planet. Inter.*, **22**, 144–154.

Pauthenet, R., & Bochirol, L. 1951. Aimantation spontanée des ferrites. *J. Phys. Rad.*, **12**, 249–251.

Pecharromán, C., González-Carreño, T., & Iglesais, J.E. 1995. The infrared dielectric properties of maghemite, γ-Fe_3O_3, from reflectance measurement on pressed powders. *Phys. Chem. Minerals*, **22**, 21–29.

Pénicaud, M., Siberchicot, B., Sommers, C.B., & Kübler, J. 1992. Calculated electronic band structure and magnetic moments of ferrites. *J. Magn. Magn. Mater.*, **103**, 212–220.

Persoons, R. M., & De Grave, E. 1989. On the Verwey transition in cobalt-substituted magnetite as determined ^{57}Fe Mössbauer spectroscopy. *Solid State Comm.*, **72**(10), 977–980.

Pokhil, T.G., & Moskowitz, B.M. 1997. Magnetic domains and domain walls in pseudo-single-domain magnetite studied with magnetic force microscopy. *J. Geophys. Res.*, **102**(B10), 22681–22694.

Press, W. H., Flannery, B. P., Teukolsky, S. A., & Vetterling, W. T. 1986. *Numerical Methods.* Cambridge University Press.

Proksch, R.B., Foss, S., & Dahlberg, E.D. 1994. High resolution magnetic force microscopy of domain wall fine structures. *IEEE Trans. Magn.*, **30**, 4467–4472.

Rae, A.I.M. 1992. *Quantum Mechanics*. 3rd edn. Bristol: Institute of Physics Publishing.

Readman, P.W., & O'Reilly, W. 1972. Magnetic properties of oxidized (cation-deficient) titanomagnetite, $(Fe, Ti, \square)O_4$. *J. Geomag. & Geoelec.*, **24**, 69–90.

Rhodes, P., & Rowlands, G. 1954. Demagnetising energies of uniformally magnetised rectangular blocks. *Proc. Leeds Philos. and Lit Soc.*, June, 191–210.

Roquet, J. 1954. Sur les rémanences des oxydes de fer et leur intérêt en géomagnetisme (transl. J. Briden). *Ann. Géophys.*, **10**, 226–247 & 282–325.

Rozenberg, G.Kh., Hearne, G.R., Pasternak, P.M., Metcalf, P.A., & Honig, J.M. 1996. Nature of the Verwey transition in magnetite (Fe_3O_4) to pressures of 16 GPa. *Phys. Rev. B*, **53**(10), 6482–6487.

Rubinstein, M., & Forester, P.W. 1971. Investigation of the insulating phase magnetite by NMR and the Mössbauer effect. *Solid State Comm.*, **9**, 1675–1679.

Sahu, S. 1997. *An experimental study on the effects of stress on the magnetic properties of magnetite*. Ph.D. thesis, University of Minnesota.

Sahu, S., & Moskowitz, B.M. 1995. Thermal dependence of magnetocrystalline anisotropy and magnetostriction constants of single crystal $Fe_{2.4}Ti_{0.61}O_4$. *Geophys. Res. Lett.*, **22**, 449–452.

Salje, E.K.H. 1993. *Phase transitions in ferroelastic and co-elastic crystals*. Student edn. Cambridge: Cambridge University Press.

Samiullah, M. 1995. Verwey transition in magnetite: Finite-temperature mean-field solution of the Cullen-Callen model. *Phys. Rev. B*, **51**(16), 10352–10356.

Schabes, M.E., & Bertram, H.N. 1988. Magnetisation processes in ferromagnetic cubes. *J. Appl. Phys.*, **64**(3), 1347–1357.

Schmidbauer, E., & Keller, R. 1996. Magnetic properties and rotational hysteresis of Fe_3O_4 and γ-Fe_2O_3 particles ~ 250 nm in diameter. *J. Magn. Magn. Mater.*, **152**, 99–108.

Schmidt, V.A. 1973. A multidomain model of thermoremanence. *Earth Planet. Sci. Lett.*, **20**, 440–446.

Schrieffer, J.R. 1974. *Theory of superconductivity*. New York: W.A. Benjamin Inc.

Shcherbakov, V.P., & Markov, G.P. 1982. Theory of thermoremanent magnetisation in a multidomain grain of inhomogeneous magnetic hardness. *Izv., Acad. of Sci., USSR, Phys. Solid Earth*, **18**(9), 681–689.

Shcherbakov, V.P., & Tarashchan, S.A. 1990. Domain structure of titanomagnetite grains with closure domains. *Phys. Earth Planet. Inter.*, **65**, 177–187.

Shcherbakov, V.P., Tarashchan, S.A., & Lamash, B.E. 1990. Domain structure of PSD- and MD-grains and its temperature dependence. *Phys. Earth Planet. Inter.*, **63**, 23–31.

Shcherbakov, V.P., McClelland, E., & Shcherbakova, V.V. 1993. A model of multidomain thermoremanent magnetisation incorporating temperature-variable domain structure. *J. Geophys. Res.*, **98**(B4), 6201–6216.

Shcherbakova, V.V., Shcherbakov, V.P., Schmidt, P.W., & Prevot, M. 1996. On the effect of low-temperature demagnetisation on TRM and pTRMs. *Geophys. J. Int.*, **127**, 379–386.

Shive, P.N. 1969. Dislocation control of magnetisation. *J. Geomag. & Geoelec.*, **21**(2), 519–529.

Sholpo, L.Ye., Ivanov, V.A., & Borisova, G.P. 1991. Thermomagnetic effects of reorganization of domain structure. *Izv., Acad. of Sci., USSR, Phys. Solid Earth*, **27**(7), 617–623.

Siratori, K., & Kino, Y. 1980. A note on the magnetic anisotropy of Fe_3O_4. *J. Magn. Magn. Mater.*, **20**, 87–90.

Skipetrova, L.A. 1978. *Effect of cation-cation exchange on the magnetic properties of ferrites with spinel structure (in Russian).* Ph.D. thesis, Moscow State University.

Slonczewski, J.C. 1958. Origin of magnetic anisotropy in $Co_xFe_{3-x}O_4$. *J. App. Phys.*, **29**, 448–449.

Smith, P.J. 1968. Pre-Gilbertian conceptions of terrestrial magnetism. *Tectonophysics*, **6**, 499–510.

Smith, P.J., & Needham, J. 1967. Magnetic declination in medieval China. *Nature*, **214**, 1213–1214.

Smith, P.P.K. 1979. The identification of single-domain titanomagnetite particles by means of transmission electron microscopy. *Can. J. Earth Sci.*, **16**, 375–379.

Smith, P.P.K. 1980. The application of Lorentz electron microscopy to the study of rock magnetism. *Pages 125–128 of: Inst. Phys. Conf. Ser.* Bristol: Institute of Physics.

Soffel, H.C. 1971. The single domain-multidomain transition in natural intermediate titanomagnetites. *Z. Geophys.*, **37**, 451–470.

Stacey, F.D. 1958. Thermo-remanent magnetization of multidomain grains in igneous rocks. *Phil. Mag.*, **3**, 1391–1401.

Stacey, F.D. 1962. A generalized theory of thermoremanence, covering the transition from single domain to multi-domain magnetic grains. *Phil. Mag.*, **7**, 1887–1900.

Stacey, F.D., & Banerjee, S.K. 1974. *The Physical principles of rock magnetism*. London: Elsevier.

Stacey, F.D., & Wise, K.N. 1967. Crystal dislocations and coercivity in fine grained magnetite. *Aust. J. Phys.*, **20**, 507–513.

Stancil, D.D. 1993. *Theory of Magnetostatic Waves*. New York: Springer-Verlag.

Stephenson, A. 1981. Gyroremanent magnetisation in a weakly anisotropic rock sample. *Phys. Earth Planet. Inter.*, **25**, 163–166.

Stephenson, A., & Collinson, D.W. 1974. Lunar magnetic field palaeointensities determined by an anhysteretic remanent magnetization method. *Earth Planet. Sci. Lett.*, **23**, 200–228.

Stumpf, C., Hoffmann, V., Ambatiello, A., Zitzelberger, A., & Soffel, H.C. 1997. Micromagnetic observations on synthetic single-crystal titanomagnetites (Fe(3-x)Ti(x)O(4))with varying Ti-content:cubic-style magnetic domain patterns on TM60 and TM63 (abstract). *Page p. 69 of: I.A.G.A. 97, Abstracts*.

Sugiura, N. 1979. ARM, TRM and magnetic interactions: Concentration dependence. *Earth Planet. Sci. Lett.*, **42**, 451–455.

Sugiura, N. 1981. A new model for the acquisition of thermoremanence by multidomain magnetite. *Can. J. Earth Sci.*, **18**, 789–794.

Syono, Y. 1965. Magnetocrystalline anisotropy and magnetostriction of Fe_3O_4-Fe_2TiO_4 series - with special application to rock magnetism. *Japan. J. Geophys.*, **4**, 71–143.

Tanasoiu, T. 1972. The influence of demagnetisation on the domain structure of hard magnetic minerals. *IEEE Trans. Magn.*

Thellier, E. 1938. Sur l'aimantation des terres cuites et ses applications géophysiques. *Ann. Inst. Phys. Globe Univ. Paris*, **16**, 157–302.

Thellier, E., & Thellier, O. 1959. Sur l'intensité du champ magnétique terrestre dans le passé historique et geologique. *Ann. Géophys.*, **15**, 285–376.

Thompson, R., & Oldfield, F. 1986. *Environmental Magnetism*. London: Allen and Unwin Publishers.

Thomson, L.C., Enkin, R.J., & Williams, W. 1994. Simulated annealing of three dimensional micromagnetic structures and simulated thermoremanent magnetization. *J. Geophys. Res.*, **99**, 603–606.

Torrie, B.H. 1967. Spin-waves in magnetite at a temperature below the electronic ordering transition. *solid State Comm.*, **5**, 715–717.

Träuble, H. 1969. The influence of crystal defects on magnetisation processes in ferromagnetic single crystals. *Chap. 13 of:* Berkowitz, A. E., & Kneller, E. (eds), *Magnetism and Metallurgy*. San Diego: Academic Press.

Tsuya, N., Arai, K.I., & Ohmori, K. 1977. Effect of magnetoelastic coupling on the anisotropy of magnetite below the transition temperature. *Physica*, **86-88B**, 959–961.

Uhl, M., & Siberchicot, B. 1995. A first-principles study of exchange integrals in magnetite. *J. Phys.: Condens. Matter*, **7**, 4227–4237.

van Velzen, A. 1994. *Magnetic minerals in Pliocene and Pleistocene marine marls from southern Italy: Rock magnetic properties and alteration during thermal demagnetisation*. Ph.D. thesis, State University of Utrecht.

Verhoogen, J. 1959. The origin of thermoremanent magnetization. *J. Geophys. Res.*, **64**(12), 2441–2449.

Verwey, E.J.W. 1935. The crystal structure of γ-Fe_2O_3 γ-Al_2O_3. *Z. Krist.*, **91**, 65–69.

Verwey, E.J.W. 1939. Electronic conduction of magnetite (Fe_3O_4) and its transition point at low-temperature. *Nature*, **44**, 327–328.

Verwey, E.J.W., & Haayman, P.W. 1941. Electronic conductivity and transition point of magnetite ("Fe_3O_4"). *Physica*, **VIII**(9), 979–987.

Verwey, E.J.W., & Heilmann, E.L. 1947. Physical properties and cation arrangement of oxides with spinel structures. I. Cation arrangement in spinels. *J. Chem. Phys.*, **15**(4), 174–180.

Verwey, E.J.W., Haayman, P.W., & Romeijn, F.C. 1947. Physical properties and cation arrangement of oxides with spinel structures. II. Electronic conductivity. *J. Chem. Phys.*, **15**(4), 181–187.

Vinogradov, Yu.K., & Markov, G.P. 1989. On the effect of low temperature heating on the domain state of multidomain magnetite. *Pages 31–39 of: Investigations in rockmagnetism and palaeomagnetism (in Russian)*. Moscow: Institute of Physics of the Earth.

Vlag, P., Rochette, P., & Dekkers, M.J. 1996. Some additional hysteresis parameters for a natural (titano)magnetite with known grain size. *Geophys. Res. Lett.*, **23**(20), 2803–2806.

Vonsovskiĭ, S.V. 1946. On the exchange interaction of the valence and inner electrons in ferromagnetic (transition) metals. *J. Phys.*, **10**, 468–475.

Waldron, R.D. 1955. Infrared spectra in ferrites. *Phys. Rev.*, **99**(6), 1727–1735.

Walz, F., & Kronmüller, H. 1990. Point defects in electron-irradiated stoichiometric magnetite. *Phys. Stat. Sol. (B)*, **160**, 661–671.

Walz, F., & Kronmüller, H. 1991. Evidence for a single-stage Verwey transition in perfect magnetite. *Phil. Mag. B*, **64**(5), 623–628.

Walz, F., & Kronmüller, H. 1994. Analysis of magnetic point-defect relaxations in electron-irradiated magnetite. *Phys. Stat. Sol. (B)*, **181**, 485–498.

Weertman, J., & Weertman, J. R. 1992. *Elementary Dislocation Theory*. Oxford: Clarendon Press.

Williams, W. 1986. *The effect of time and temperature on magnetic remanence*. Ph.D. thesis, University of Cambridge.

Williams, W., & Dunlop, D.J. 1989. Three-dimensional micromagnetic modelling of ferromagnetic domain structure. *Nature*, **377**, 634–637.

Williams, W., & Dunlop, D.J. 1990. Some effects of grain shape and varying external magnetic fields on the magnetic structure of small grains of magnetite. *Phys. Earth Planet. Inter.*, **65**, 1–14.

Williams, W., & Dunlop, D.J. 1995. Simulation of magnetic hysteresis in pseudo-single-domain grains of magnetite. *J. Geophys. Res.*, **100**(B3), 3859–3871.

Williams, W., & Walton, D. 1986. Demagnetisation of viscous moments. *Geophys. J. R. astr. Soc.*, **85**, 453–459.

Williams, W., & Wright, T.M. 1998. High resolution micromagnetic models of fine grains of magnetite. *J. Geophys. Res.* Submitted.

Williams, W., Enkin, R.J., & Milne, G. 1992a. Magnetic domain wall visibility in Bitter pattern imaging. *J. Geophys. Res.*, **97**(B12), 17433–17438.

Williams, W., Hoffmann, V., Heider, F., Göddenhenrich, T., & Heiden, C. 1992b. Magnetic force microscopy imaging of domain walls in magnetite. *Geophys. J. Int.*, **111**, 417–423.

Wilson, M.T. 1994. Infrared methods. *In:* Russel, J.D., & Fraser, A.R. (eds), *Clay mineralogy: spectroscopic and chemical determinative methods*. London: Chapman and Hall.

Winklhofer, M., Fabian, K., & Heider, F. 1997. Magnetic blocking temperature of magnetite calculated with a three-dimensional micromagnetic model. *J. Geophys. Res.*, **102**(B10), 22695–22709.

Worm, H.-U., & Markert, H. 1987. The preparation of dispersed titanomagnetite particles by glass-ceramic method. *Phys. Earth Planet. Inter.*, **46**, 263–269.

Worm, H.-U., Ryan, P.J., & Banerjee, S.K. 1991. Domain size closure domains, and the importance of magnetostriction in magnetite. *Earth Planet. Sci. Lett.*, **102**, 71–78.

Wright, T.M., Williams, W., & Dunlop, D.J. 1997. An improved algorithm for micromagnetics. *J. Geophys. Res.*, **102**(B6), 12085–12094.

Xu, S., & Dunlop, D.J. 1994. Theory of partial thermoremanence in multi-domain grains: 2. effect of microcoercivity distribution and comparison with experiment. *J. Geophys. Res.*, **99**(B5), 9025–9033.

Xu, S., & Dunlop, D.J. 1995. Towards a better understanding of the Lowrie–Fuller test. *J. Geophys. Res.*, **100**, 22533–22542.

Xu, S., & Dunlop, D.J. 1996. Micromagnetic modelling of Bloch walls with Néel caps in magnetite. *Geophys. Res. Lett.*, **23**(20), 2819–2822.

Xu, S., & Merrill, R.T. 1989. Microstress and microcoercivity in multidomain grains. *J. Geophys. Res.*, **94**(B8), 10627–10636.

Xu, S., & Merrill, R.T. 1990a. Microcoercivity, bulk coercivity and saturation remanence in multidomain materials. *J. Geophys. Res.*, **95**(B5), 7083–7090.

Xu, S., & Merrill, R.T. 1990b. Thermal variations of domain wall thickness and number of domain in magnetic rectangular grains. *J. Geophys. Res.*, **95**(B13), 21433–21440.

Xu, S., & Merrill, R.T. 1992. Stress, grain size and magnetic stability of magnetite. *J. Geophys. Res.*, **97**(B4), 4321–4329.

Xu, S., Dunlop, D.J., & Newell, A.J. 1994. Micromagnetic modelling of two-dimensional domain structures in magnetite. *J. Geophys. Res.*, **99**(B5), 9035–9044.

Xu, W., Peacor, D.R., Van der Voo, R., Dollase, W., & Beaubouef, R. 1996. Modified lattice parameter/Curie temperature diagrams for titanomagnetite/titanomaghemite within the quadrilateral Fe_3O_4-Fe_2TiO_4-Fe_2O_3-Fe_2TiO_5. *Geophys. Res. Lett.*, **23**(20), 2811–2814.

Yama-ai, M., Ozima, Minoru, & Nagata, T. 1963. Self-reversal of remanent magnetisation of magnetite at low-temperature. *Nature*, **197**, 444–445.

Ye, J., & Merrill, R.T. 1995a. Residual stress and domain structure. *J. Geophys. Res.*, **100**(B6), 9995–10002.

Ye, J., & Merrill, R.T. 1995b. Use of renormalization group theory to explain the large variation of domain states observed in titanomagnetites and implications for paleomagnetism. *J. Geophys. Res.*, **100**(B9), 17899–17907.

Ye, J., Newell, A.J., & Merrill, R.T. 1994. A re-evaluation of the magnetocrystalline anisotropy and magnetostriction constants. *Geophys. Res. Lett.*, **21**(1), 25–28.

Yoshida, J., & Iida, S. 1979. X-ray study of the phase transition in magnetite. *J. Phys. Soc. Japan*, **47**(5), 1627–1633.

Zhang, Z., & Satpathy, S. 1991. Electron states, magnetism and the Verwey transition. *Phys. Rev. B*, **44**(24), 13319–13331.

Zhou, Z-J., & Ya, J-J. 1992. Sputtering iron oxide films by a water vapour process. *J. Magn. Magn. Mater.*, **115**, 87–98.

Zuo, J.M., Spence, J.C.H., & Petuskey, W. 1990. Charge ordering in magnetite. *Phys. Rev. B*, **42**(13), 8451–8464.

Appendix A

Identification of magnetic minerals by infrared spectroscopy

A.1 Introduction

The results of a preliminary investigation of the use of infrared spectroscopy as a method of identifying minerals of rock magnetic interest are presented. To my knowledge, there are no reports in the literature of its use in rock magnetic investigations.

Compared to other spectral techniques, *e.g.,* X-ray diffraction (XRD) or Mössbauer spectroscopy, infrared spectrometry is a relatively fast method of mineral identification. It was decided to examine its suitability for use in rock magnetism.

Initially the infrared spectra of common magnetic minerals are considered in Section A.3. In Section A.4, the accuracy of infrared spectrometry for identifying small traces of maghemite in the presence of magnetite is examined. The ability to detect low-concentrations of maghemite in the presence of magnetite was of particular interest to the work in Chapter 2, and to rock magnetism in general. The accuracy of infra-red spectroscopy is compared to that from other available methods.

A Mattson Galaxy 5020 Fourier transform infrared spectrometer with DTGS detector located in the University of Oxford Museum of Natural History, was utilised in these experiments. The introduction of the Fourier transform to the interpretation of infrared spectroscopy in recent years has vastly improved the accuracy and measurement time (*pers. comm.* M. Price, 1996).

A.2 Method

Whole crystals of a sample are first ground in bulk using a pestle and mortar until the sample has a fine "silky" texture. A small amount (0.5-1mg) of the ground sample is mixed

with ground potassium-bromide powder (250 mg) and pressed into pellets. Potassium bromide acts as a diluent which is optically transparent to the mid-infrared radiation.

If the sample is not ground to a size finer than the wavelength region of absorption (wavenumber = 400-1600 cm^{-1}) then this causes the spectra to be diffuse and assymetrical. This is due to the Christiansen effect (Farrell, 1972). It is not desirable to compensate for this effect by over-grinding, because grinding itself leads to lattice distortion, which in turn produces weak peaks that may shift main peaks.

The pellets are mounted in the spectrometer and scanned 50 times at 4.0 cm^{-1} wavenumber resolution over the range 4000-400 cm^{-1} wavenumbers. The absorption spectra are measured. Scanning takes about two minutes to carry out (including the measurement of the background spectrum), and the whole process from raw sample to the acquisition of a spectrum takes approximately fifteen minutes.

The analysis of the spectra was achieved using an infrared spectrometry support software called First™.

A.3 Common magnetic minerals

In this section the measurement of the infrared spectra from pure iron oxide, iron hydroxide and titanomagnetite samples are presented. No iron sulphides were examined. Specimens of natural magnetite, hematite, goethite (α-FeO(OH)) and ilmenite ($FeTiO_3$) samples were kindly provided by the University of Oxford Museum of Natural History. These were either of well-formed pristine crystals or from mineral specimens which had previously been identified by XRD. Reference spectra were obtained for high-purity magnetite (Johnson-Matthey, 99.999 % pure Fe_3O_4) and maghemite (BASF, γ-Fe_2O_3). The maghemite was kindly provided by Dr. W. O'Reilly. XRD analysis of this maghemite sample confirmed the purity of the sample to within the accuracy of the XRD spectrometer (≤ 5 %).

The infrared spectra of the reference samples in the range 750-400 cm^{-1} are shown in Figure A.1. These compare well with cited spectra (Liese, 1967; Farrell, 1972; Gillot, 1994; Wilson, 1994).

Infrared absorption results from the excitation of internal vibrations of atoms relative to each other, of groups of atoms relative to the crystal structure or of vibrations of the lattice itself. In examining the infrared absorption spectra of magnetite and its oxidation products, only two basic vibrational modes have to be considered. One is the stretching vibration of the Fe-O bonds, and the other is the bending or deformation of the angle between the three atoms O-Fe-O or Fe-O-Fe, where Fe and O are the anchor atoms respectively (Farrell, 1972). The stretching vibration is considerably more intense than the deformation vibration, and gives rise to the main peaks, *e.g.*, the strong absorption peak at 574 cm^{-1} in magnetite (Figure A.1a), (Farrell, 1972). The deformation vibration (Fe-O-Fe) is the cause of the shoulder at 630 cm^{-1} in hematite (Figure A.1b) (Farrell, 1972).

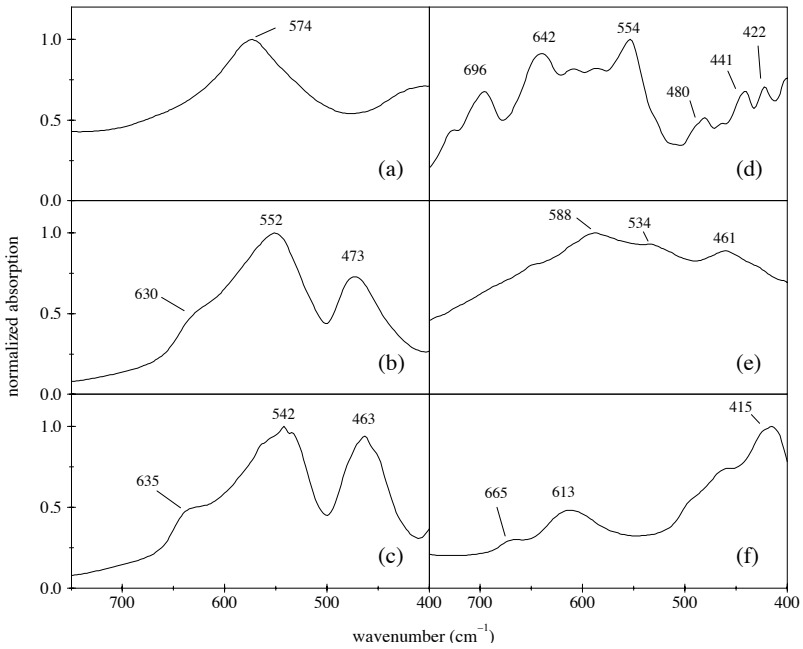


Figure A.1: Infrared spectra for; (a) magnetite, (b) specular hematite, (c) hematite (kidney ore), (d) maghemite, (e) ilmenite and (f) goethite.

Hematite has two common habits, metallic grey crystals (specular hematite), and tightly intergrown crystals giving a red botryoidal appearance (kidney ore). Although their spectra are generally similar (Figure A.1b and Figure A.1c), there are differences in the detail. The two main peaks at 542 cm^{-1} and 463 cm^{-1} for kidney ore are shifted to the higher frequencies 552 cm^{-1} and 473 cm^{-1} for specular hematite (Wilson, 1994). Maghemite's spectrum (Figure A.1d) has a sharp, distinctive pattern, while that of ilmenite is broad (Figure A.1e). The only reference hydrous iron oxide to be measured was goethite (α-FeO(OH)). Its spectrum is very different to the anhydrous iron oxide spectra, with distinctive peaks at 903 cm^{-1}, 801 cm^{-1}, 613 cm^{-1} and 415 cm^{-1} (Figure A.1f). Lepidocrocite (γ-FeO(OH)) has strong peaks at 1022 cm^{-1}, 742 cm^{-1} and 474 (cm^{-1} (Wilson, 1994). The spectra of the hydrous iron oxide minerals are also distinctive in having a large absorption peak from the O-H bond between 3150-3180 cm^{-1} (Wilson, 1994).

A.4 Detection of maghemite in the presence of magnetite

There are only a limited number of investigations which use infrared spectrometry to examine magnetite and maghemite (Waldron, 1955; Liese, 1967; Farrell, 1972; Gillot, 1994; Pecharromán *et al.*, 1995). None of these studies have tried to quantify the magnetite:maghemite ratio.

Four magnetite samples were mixed with between 0.2 % and 16 % maghemite to examine the ability of infrared spectroscopy to detect secondary maghemite in the presence of magnetite (Figure A.2). To test repeatability, three sets of pellets were made from the

source material, *i.e.*, the source material was ground three separate times. In Figure A.2, two repeat measurements for two similar magnetite:maghemite ratios are shown.

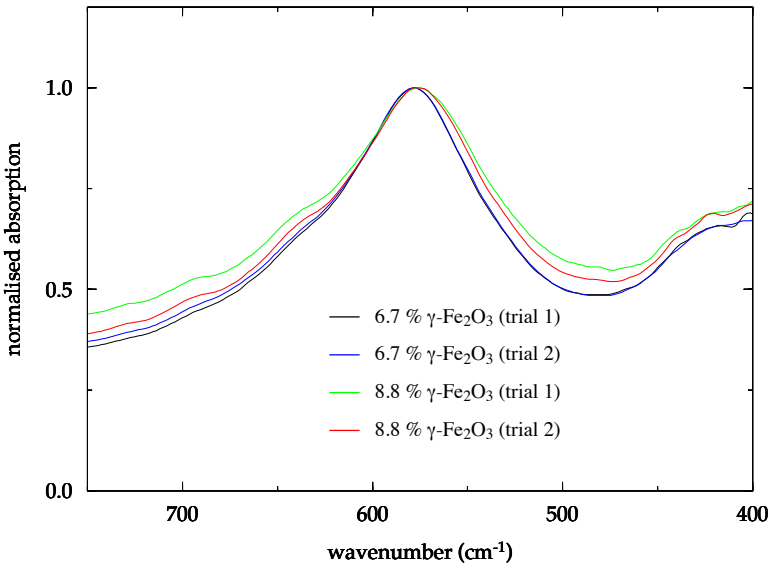


Figure A.2: Infrared reference spectra for two magnetite samples with differing maghemite content. The two trials were for material which had been ground independently during sample preparation.

It is seen in Figure A.2, that the variation in repeatability is greater than the variation between the different magnetite:maghemite ratios. Similar variations were observed for the other concentrations of maghemite. There was still a significant difference in repeatability for 16 % maghemite.

A.5 Conclusions

Fourier transform infrared spectrometry was found to be a very fast spectral method of determining the primary magnetic mineral. Compared to XRD and Mössbauer spectroscopy, its sample preparation and measurement time of only fifteen minutes per sample is substantially less. In comparison, it took approximately two days to measure one sample using the Mössbauer spectrometer with a weak ^{57}Co source at the Institute for Rock Magnetism (I.R.M.), University Minnesota.

However infrared spectrometry was found to be less accurate than either XRD or Mössbauer spectroscopy at detecting maghemite in the presence of magnetite. Infrared spectrometry could not accurately detect magnetite:maghemite ratios as low as 6:1. In comparison the calibrated Mössbauer spectrometer at the I.R.M. is able to detect a magnetite:maghemite ratio as high as 20:1 (*pers. comm.* P. Solheid, 1996). The XRD in Oxford could detect a ratio of approximately 10:1 (*pers. comm.* C. Fagg, 1995). Because it was the intention of this study to find an accurate method of determining the magnetite:maghemite ratio, infrared spectrometry was not investigated further.

Appendix B

Bitter pattern imaging at high temperatures

B.1 Introduction

Bitter pattern imaging is a technique developed by Bitter (1931) to examine magnetic domain structures. It is achieved by placing fine magnetic particles suspended in oil or water on top of a highly polished surface of a magnetic crystal. The colloid particles are attracted to the high field regions, *i.e.,* domain boundaries, and the resulting patterns can be easily observed with a microscope (Bozorth, 1951).

Although Bitter patterns may be quite sharp at room temperature, they fade gradually with increasing temperature (*e.g.*, Heider *et al.*, 1988b; Halgedahl, 1991). It is theoretically possible to calculate the domain wall visibility with increasing temperature, however to my knowledge no such calculations have been reported in the literature. In the appendix, the decrease in domain wall visibility with increasing temperature is calculated for magnetite and titanomagnetite.

B.2 Calculation of domain wall visibility as a function of temperature

The effect of temperature on the optical contrast parameter, $\sigma(T)$, can be calculated by considering the density of the colloidal particles in the vicinity of the domain walls (Kittel, 1949b; Williams *et al.*, 1992a). For simplicity it is easier to consider the relative temperature dependent optical contrast, *i.e.,* $\sigma(T)/\sigma(\mathrm{T_0})$ where $\mathrm{T_0}$ is room temperature. An expression for $\sigma(T)/\sigma(\mathrm{T_0})$ is obtained by combining Equation 13 of Hartmann (1987) and Equation 9 of Williams *et al.* (1992a);

$$\frac{\sigma(T)}{\sigma(\mathrm{T_0})} = C\left(\frac{\rho M_s^c(T)}{T}\right)^2 \tag{B.1}$$

where C is a constant, ρ is the surface charge density of the mineral under examination and $M_s^c(T)/T$ is the temperature dependent behaviour of the colloidal particles ($M_s^c(T)$ = spontaneous magnetisation for the colloidal particles). Note, Equation B.1 does not include the thermal randomisation of the colloidal particles which increases with increasing temperature. Therefore Equation B.1 overestimates $\sigma(T)$, especially at higher temperatures.

The surface charge density is calculated by considering the stray fields in the vicinity of a domain wall (Williams *et al.*, 1992a). For a classical 180° Néel or Bloch wall of thickness $\delta_{\mathrm{w}} = \pi\sqrt{A(T)/K_u(T)}$, (see Equation 1.26, where $A(T)$ and $K_u(T)$ are the exchange constant and generalised uniaxial anisotropy constant respectively), ρ is given by (Williams *et al.*, 1992a);

$$\rho_{N\acute{e}el} = \rho_{Bloch} = \frac{2M_s^m(T)\delta_{\mathrm{w}}(T)}{\pi} \approx 2M_s^m(T)\left(\frac{A(T)}{K_u(T)}\right)^{\frac{1}{2}} \tag{B.2}$$

where M_s^m is the spontaneous magnetisation of the mineral under consideration. For a classical 180°wall, $K_u(T)$ is given by (Xu & Merrill, 1990b),

$$K_u(T) = \mid -\frac{2}{3}K_1(T) + \frac{9}{2}c_{44}(\lambda_{111}(T))^2 \mid \tag{B.3}$$

where K_1, c_{44} and λ_{111} are respectively the first cubic magnetocrystalline anisotropy, an elastic modulus and the cubic magnetostriction anisotropy constants for the [111] crystallographic direction (see Chapter 1).

Therefore, for a classical 180°Néel or Bloch wall, $\sigma(T)/\sigma(\mathrm{T_0})$ is given by,

$$\frac{\sigma(T)}{\sigma(\mathrm{T_0})} = C\frac{(M_s^m(T))^2(M_s^c(T))^2A(T)}{T^2(\mid -\frac{2}{3}K_1(T) + \frac{9}{2}c_{44}(\lambda_{111}(T))^2 \mid)} \tag{B.4}$$

In most recent rock magnetic Bitter pattern observations, the colloidal particles have been magnetite itself (*e.g.*, Heider *et al.*, 1988b; Halgedahl, 1991; Özdemir *et al.*, 1995; Geiß *et al.*, 1996; Özdemir & Dunlop, 1997). Other fine magnetic particles can be used, but magnetite has long been established for use in Bitter pattern observations and is still popular (Kittel, 1949a; Bozorth, 1951). The magnetite particles are usually suspended in a low-viscosity ferrofluid (Heider, 1988; Geiß *et al.*, 1996).

Figure B.1 shows the calculated temperature dependence of $\sigma(T)$ for magnetite and titanomagnetite $Fe_{2.39}Ti_{0.61}O_4$ (TM61). To calculate the temperature dependency

of $\sigma(T)$, data from the following sources was used: for magnetite; Bickford Jr. (1950), Pauthenet & Bochirol (1951), Fletcher & O'Reilly (1974), Heider & Williams (1988) and Moskowitz (1993a), and for titanomagnetite; Moskowitz & Halgedahl (1987) and Sahu & Moskowitz (1995). The temperature dependency of the magnetite variables are discussed in greater detail in Chapters 1 and 8.

Near T_c, there are large errors in anisotropies for magnetite, and in the exchange energy and anisotropies for $Fe_{2.39}Ti_{0.61}O_4$. To my knowledge, the exchange constants for $Fe_{2.39}Ti_{0.61}O_4$ or TM60 have never been measured above room temperature. Previous models dependent on the thermal variance of A for TM60 ($Fe_{2.4}Ti_{0.6}O_4$), have either left the temperature dependent behaviour as a variable, *e.g.*, Moskowitz & Halgedahl (1987 let it vary between $\propto M_s^1$ and $\propto M_s^3$, or have assumed that it behaves in the same manner as magnetite, *i.e.*, $A(T) \approx M_s^{1.7}$ (Moon, 1991). For $Fe_{2.39}Ti_{0.61}O_4$ $A(T)$ was allowed to vary as $A(T) \propto M_s^{1.5}$ and $\propto M_s^3$ (Figure B.1b).

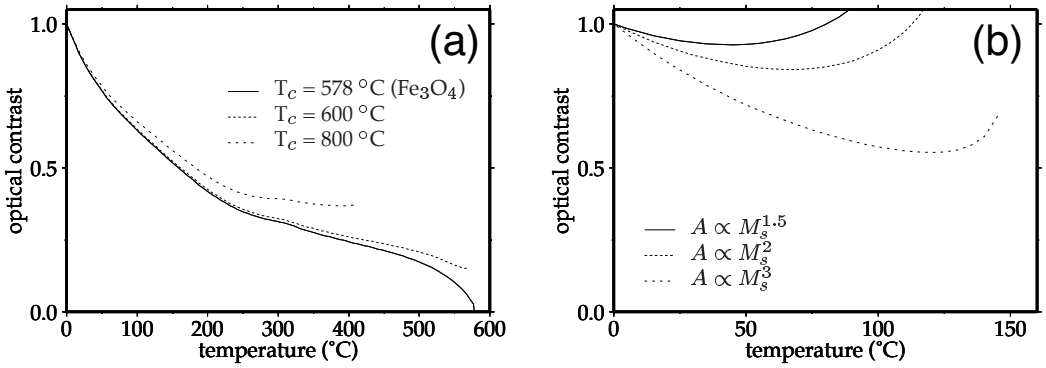


Figure B.1: Calculated normalised optical contrast as a function of temperature. a) magnetite (T_c = 578 °C), with varying Curie temperatures for colloidal particles. b) titanomagnetite $Fe_{2.39}Ti_{0.61}O_4$ (TM61,(T_c = 150 °C) with variations in the thermal behaviour of $A(T)$ (see text). Only magnetite colloidal particles are considered in Figure b). The curves are cut off when an upward trend begins, see text for explanation.

The curves in Figure B.1 are cut off when they start to show an increase in $\sigma(T)$ at high temperatures near T_c. This unrealistic upward trend, is due to errors in $A(T)$ and $K_u(T)$ at high temperatures which strongly effect the behaviour of $\sigma(T)$ (Equation B.4). Numerical models predict less variation in domain wall width with temperature than the classical domain wall width used in this model (*e.g.*, Newell *et al.*, 1990; Shcherbakov & Tarashchan, 1990; Xu & Merrill, 1990b). If the thermal dependency of domain wall width calculated from the numerical models, was applied to Equation B.4, this would reduce the upward trend in $\sigma(T)$ as T_c is approached (Figure B.1).

For magnetite (Figure B.1a), the effect of increasing the Curie temperature of the colloidal particles increases $\sigma(T)$ at higher temperatures. Heider and co-workers (1988b; 1990) had problems with reduced optical contrast at higher temperatures; up to $\approx$ 350 °C Bitter patterns could still be observed but the contrast was too low for photographs to be taken above $\approx$ 200 °C. From Figure B.1a, a rough guide to the minimum visible optical con-

trast can be obtained by considering $\sigma(T)/\sigma(\mathrm{T_0})$ at 350 °C, *i.e.*, $\sigma(T)/\sigma(\mathrm{T_0}) \approx 0.35$. It can be assumed 0.35 is approximately the lower visible limit of $\sigma(T)/\sigma(\mathrm{T_0})$. I suggest here, that using a different colloidal powder with a higher Curie temperature than magnetite, should improve the quality of Bitter pattern images at high temperatures. However due to errors in $K_u(T)$ at high temperatures and uncertainties in the contribution from thermal randomisation of the colloidal particles, it is not possible to put a quantitive value on this improvement.

For titanomagnetites observed using colloidal, magnetite powder, Equation B.1 predicts $\sigma(T)/\sigma(\mathrm{T_0}) > 0.35$ for the selection of $A(T)$ dependencies shown in Figure B.1b. This suggests that the domain structures should be observable at temperatures relatively close to T_c. This has been found to be the case, *e.g.*, Halgedahl (1991) observed domain structures for $Al_{0.1}Mg_{0.1}Fe_{2.2}Ti_{0.6}O_4$ within ≈ 10 °C of the Curie temperature at 70-75 °C, where presumably the classical domain wall approximation breaks down and the field gradients around the domain wall become too low to attract the magnetite fine powder.

In summary it should be realised that the disappearance of a domain wall with temperature may be due to reduced optical contrast, rather than denucleation of domain wall. However by continuous observation it is possible to distinguish between the two possibilities, as Halgedahl (1991) demonstrated.